

11 57
875 1
NASA Conference Publication 10181

Seals Code Development Workshop

*Proceedings of a workshop held at
NASA Lewis Research Center
Cleveland, Ohio
June 14–15, 1995*



NASA Conference Publication 10181

Seals Code Development Workshop

*Proceedings of a workshop
held at and sponsored by
the NASA Lewis Research Center
Cleveland, Ohio
June 14–15, 1995*



National Aeronautics and
Space Administration

Office of Management

**Scientific and Technical
Information Program**

1996

PREFACE

1. Large changes in direct operating costs plus interest (DOC +I) for a small investment in seal technology particularly for small engines are supported by OEM's and well documented by Munson and Steinetz. For example, development of a film riding rim seal could reduce SFC by 1.8% in the regional engine and 5% in the turboshaft engines.

1.1. Engine secondary flows, cooling and parasitic, are 15 to 18 percent of the power stream flows (up to 3 % per blade row); parasitic losses are 5 to 6% for regional and 8 to 9 % for turboshaft. Seals and multiply connected cavities represent the interactive fluid dynamic interface coupling.

1.2. Effective thermal management of engine flows calls for a clean sheet design approach.

2. Many IHPTET II goals have been met in tests, however, IHPTET III goals are difficult to achieve. And, without the seals/secondary/primary flow interactions program, phase-III goals can not be met - neither can AST or HSR goals. Critical sealing parameters include:

High surface speeds 1650 ft/sec
High operating temperatures 1600 F
Larger structural and aerodynamic loading (up to 2x for HSR)
Transonic flow fields

3. All rotating systems have runout and dynamic unbalance. Seals should be and in many cases are used to enhance rotor stability

3.1 All seals must afford compliance either by clearance control or compliant materials. Reduced engine dynamics or tolerance to shaft excursion implies closer control of leakages. Reduction of leakages implies increases in engine pressure ratios, larger operating envelopes, and higher efficiencies.

3.2 Smaller clearances imply increased sensitivity to dynamics, e.g., unshrouded rotor stages.

3.3 Applications of seal enhanced rotor stability to magnetic bearings will reduce dynamic bearing load, control power, and backup bearing requirements as well as dampers.

3.4 Seals were the nemeses of the SSME turbopumps until Black, von Pragneau, Fleming, Childs, Hendricks, Rocketdyne, NASA et al. provided data and developed methods to stabilize these turbomachines seals and bearings. The success of the program represents a major milestone in Space Exploration.

4. Significant benefits of tribopairing of interface materials can be derived in general and for brush seals in particular.

4.1 Bristle and bare shaft material transfers in both heated air and cryogenic testing leaves interface wear and life to be the Achilles heal of the brush seal.

4.2 Coatings for cryogenic operations as well as heated air should be supported. For example, solid lubricant additive hard coatings as PMS 212 and its modifications (e.g., Triboglide), Teflon impregnated Cr, ceramics as aluminum oxide, zirconia, silicon nitride or carbide sleeves in addition to hardened and bare metallic shafts.

4.3 New brush bristle materials and applications program, both metallic and ceramics, should be initiated.

4.4 For direct bristle shaft contact, watch the shaft interface for metallurgical changes and cracking propagation. With highly loaded surfaces bare rubbing may induce microcrack defects that lead to shaft failures (aero engines), while such surface defects may be of little consequence for very large low speed rotors (aeroderivative engines).

4.5 Large diameter brush seals (diameter > 30 inch) are being fabricated for both aero and aeroderivative gas turbine engines. The use of brush configurations looks promising.

4.6 Finger seals afford low cost compliant sealing; hysteresis problems require further analysis and materials tribopairing problems are similar to the brush seal system.

5. New data and dynamic testing results have led Childs et al. to reexamine the linear theory and conclude it to be insufficient to predict the instabilities associated with honeycomb stators interfacing with labyrinth or smooth rotors. These systems may require frequency dependent solutions and a two model solution is being prepared by Childs et al. The current approach is to identify transfer functions as in controls modeling.

$$\begin{bmatrix} F_x \\ F_y \end{bmatrix} = \begin{bmatrix} D & E \\ -E & D \end{bmatrix} \begin{bmatrix} x \\ y \end{bmatrix} \quad \text{Where} \quad \begin{aligned} D &= K_d (S + a)/(S + b) \\ E &= K_e/(S + b) \end{aligned}$$

The INDSEAL code work, per Shapiro's analysis anticipates frequency dependent results but is not adequate to handle flow details of the honeycomb type. Honeycomb types can only be simulated in INDSEAL through average wall roughness; however, hole depth and effective cell parameters are significant and honeycomb seals reduce the effective fluid bulk modulus (and sonic speed) which can not be handled in INDSEAL. A coupled acoustic solution will be required as conventional time dependent CFD (SCISEAL) for high frequencies becomes inaccurate and expensive; coupled aeroacoustic-aeroelastic and shock effects will also enter.

6. New and used codes in various states of development are available. Some are available to the US industrial community and others are available for an initial investment. These codes are beginning to find utility in the prediction of cavity flows, seal leakages, and rotordynamics. A partial listing of such codes is limited to those discussed by Athavale, Braun, Pelfrey, SanAndres, and Shapiro at this workshop with more detail found herein. Some NASA sponsored Conference Publications are also cited.

- INDSEAL** Industrial design version of seals code (Face, narrow groove theory spiral groove , shaft with Ng-Elrod Turbulence model, labyrinth (USAF version), dynamics). Data and numerical comparisons are given in this and previous workshops (Roberts, Keba, Childs, San Andres, Scharrer to cite a few)
- in general, flows and stiffnesses are usually comparable, while damping and “cross”or “quadrature dyanmic stiffness” terms often disagree.
Available to US industry through NASA Lewis Research Center
- SCISEAL** Scientific 3-D time accurate version of seals code (interactive multiply connected power/secondary/seal flow shaft seal flow fields with conjugate heat transfer) 33-validation tests are available including multiple connected cavities in UTRC SSME turbopump simulation and Allison T-56/501D, 4-stage turbine. Available to US industry through NASA Lewis Research Center
- HYDROFLEX**
HYDROTRAN Bulk-flow code for evaluation of static and rotordynamic force characteristics of laminar or turbulent flow hydrostatic/hydrodynamic bearings, e.g, damper seals, and journal , externally pressurized pocket, tilting pad, simple foil bearings. Transient response of point mass rotor supported on rigid surface bearings. Extensively validated with available experimental data.
Available through Texas A&M University Technology Licensing Office.
- HYDROB3D** Pratt-Whitney code for 3-D fluid film bearing hydrodynamics (based on work of Braun/Dzodzo (B&C Engr. Akron Ohio))
- FLOWCON1** Brush seals 2-D laminar CFD modeling including full flow field; also for pin-fin flow devices and equivalent porous media flows. Fully validated robust code (University of Akron)
- FLOWCON2** Power stream/secondary/seal cavity flows axisymmetric laminar CFD modeling (University of Akron)
- RSR -** RSR Software library for seals and bearings including examples
- PUBLICATION** Seals Flow Code Development annual NASA Conference Publications date from 1991.
- Rotordynamic Instability Problems in High-Performance Turbomachinery are available as biannual NASA Conference Publications dating from 1980.
- Rotordynamic coefficient data sets available for labyrinth, honeycomb, smooth (tapered, stepped, constant clearances), and helically grooved seals. (Prof. Childs, Texas A&M Turbomachine Labs)

7. New emphasis is required on oil/air sealing flows, as customer driven sealing requirements (Hendricks, Seals Code Development 1993). Oil vapors and coking smells are obnoxious at best and health hazards at worst to the customer.

7.1 Ullah, Allied Signal, is instituting a consortium to enhance life of oil seals by 10 and reduce the leakage of oil smoke into the cabin. Seals have high temperatures, incorrect tracking, and coking. The effects of wear and sudden rise in seal temperature for a throttle chop are under investigation. Several programs have end of 95 deadlines.

7.2 Inputs from the two-phase programs of Hughes et al. (Carnegie-Mellon retired), Hsu et al. (NASA retired) two-phase and mist flows, Allison cooling work (Dr. Paul), Yasuna (Carnegie-Mellon) transient flows, Zimmerman (MTU-Siemans) two-phase flows in oil heat exchangers, Marek fuels coking, Meyer and Linne (NASA) heat transfer, Glahn et.al. (Universitat Karlsruhe) and others should be used as a nucleus for the program. Seals programs at Allison and Purdue could also contribute to lip sealing.

8. Fluid film devices are receiving much attention in turbomachines.

8.1 Some bearings, are integrated into the IHPRT program at Phillips AFB. Fluid film bearings offer compact, low part count turbomachines.

8.2 Alternately, Si₃N₄ ceramic ball bearing tests are looking for 6.3M DN and the Dimofte wave bearing is shown to have high resistance to whirl and operates well within the clearance when whirl does occur.

8.3. Hydrostatic pocket film characterization requires a fully 3-D simulation. The effects are pronounced in shallow and deep pocket flows as within the restrictor. In some cases, multiple fluid passes from the restrictor to the pocket edge and back are required before the fluid exits the pocket/restrictor. The vonPragneau type seal/bearing afford good stability and is often coupled with the hydrostatic pockets.

8.4 Film riding seals as the aspirating seal, leaf seal, film riding brush and potentially the finger seal, and proposed rim seals take advantage of the "lubricant film", however very small clearances (e.g., 0.4 mil) with critical flatness in harsh environments affords design challenges.

9. Turbulence measurements for code validation at 25 and 50 percent eccentricities will continue under Morrison at Texas A&M with consortium sponsorship.

10. The What's coming section includes structural-thermohydrodynamic coupling, predictive maintenance/monitoring, flow balancing throughout the engine, active/passive seals for rotor stabilization (fan stabilization), strict environmental restraints, increased aeroderivative enhancements, emphasis on film riding sealing, large diameter seal research, counter rotating systems, and acoustic coupling.

10.1. **SUGGESTED GOAL: Clean Sheet Approach to Engine Design** ; specifically reduce the number of compressor and turbine stages, increase reliability/life, and improve dynamic response. Studies to date assume cooling and power stream requirements are known and satisfied. Interactively this is an incompatible assumption; the clean sheet approach is required.

10.2 WHAT'S NEEDED (Under section 10.2, the percentages are given for aero and aeroderivative gas turbines)
(Greater percentages are anticipated for space propulsion turbomachines)

10.2.1. RIM SEALS (order of 2 percent payoff)

Rim seals appear in both the compressor and the turbine. They afford the highest payoff , the biggest challenge and provide the greatest opportunity for a new engine. The subtle warning we are providing is that proper engineering of the seals will lead the manufacturers to a clean sheet engine that will indeed be revolutionary as blades, stators, drums, cavities, radial and axial dimensions are not constrained by conventional means.

To properly deal with rim seals will involve time unsteady (or suitable effective stress parameters) interactive multicavity power/secondary and seal flow characteristics:

A. Start with the inlet flow parameters and determine the characteristics of the compressor, the combustor, and the turbine with the exhaust parameters all satisfying the environmental constraints.

B. This sounds a lot like NPSS (numerical propulsion simulation system), and it is to some extent.

C. At this point we propose using all that's available, including the interactive multicavity power/secondary/seal flow code SCISEAL- CFSPACE and -ADPAC (Allison).

D. New unstructured grid coding will enhance the solutions in the Euler form, and these serve as first order solutions for the Navier Stokes forms plus conservation equations (energy, mass, continuity, strain).

E. The new features of these codes will be the interaction with the strain codes to produce the displacements associated with rotational and thermal management effects (nonuniformly heated components with aerodynamic and centrifugal loads).

F. The dynamics of such machines and their response to the seals have - to this point- not been integrated into the engine analyses; however in our approach, these seals become a major source of engine stability.

G. Controlled vortex generation would permit different platform flows and thermal management scenarios. The basis remains in the lid-driven flow studies (Athavale et.al. AIAA93-0390) and the success of the swirl brake in controlling unwanted flow fluctuations (Childs and Ramsey: NASACP3122). With some insight, such "tire-tracking" of the seal tips and blade/vane curvature could be used to control flow. The seal tips through blade tip treatments and shroud cellular materials (Bill, Wolak, Wisander, NASA TP 1835 (1981); Tolokan, Jarrabet, Howe, ISROMAC (1992), p.571) and stator/rotor curvature (Huber, Rowey,

Ni; AIAA-85-1216; Dring, Sprout, Weingold ASME95-GT-190) could be used to control stall and enhance efficiency.

10.2.2. TIP SEALS (order of payoff 1-2 percent, depends on analyst)

The same arguments are given for tip seals; depends how the air losses are accounted for by the engine analysis, but these seals provide the opportunity to reconfigure the shroud and case in the same manner as the RIM SEAL. A potential key factor is the unsteady interaction between the vortex shedding of the tip and hub regions with the subplatform cavities. When margins are close to instability or singular points small perturbations can affect large changes in the entire system. (e.g., fluid amplifiers). (e.g., see also Yamamoto et.al. ASME93-GT-404; Weingold et al. ASME95-GT-380; Dring et al. ASME95-GT-190).

10.2.3. CDP SEALS (order of 1 percent payoff)

The most expensive air in the engine is immediately downstream of the compressor. Several engine companies are looking to “stopper the leakage” However, we know through analysis and TEST RESULTS (NASA TM 106360/ ARL-MR-232) that the major benefits are not the parasitic air recovery but the enhancement of the pressure ratio across the engine.

10.2.4. OIL/AIR SEALS (CUSTOMER DRIVEN REQUIREMENT - HIGHEST PAYOFF)

Cabin borne smells of oil and fuel are unacceptable to the paying customer and usually occur after the engine is in service costing 1000 to 10000 times the initial investment to correct the problem in the design phase. Air oil seals involve tracking the particle laden fuel, and oil as it flows through the engine and egresses through the exhaust. Clean compressor air is affected by leakages and subsequent ingestion of the air into the cabin either through these ducts or as “sucked” in from the exhaust sources.

11. Emphasis is shifting toward supporting of both the engine and component industries. NASA and these workshops will attempt to accommodate industrial requests and expand the base to include manufacturing. The latter will require non-disclosure agreements among the participants.

12. Future meetings:

Sept.-Oct.

NASA Interactive Seals Secondary Power Stream Workshops will be limited representation to OEM’s and their designees.

June

Joint Propulsion Conference

Seal/Secondary/Power Stream Flows Sessions will be public forum.

Liang

Seals code development overview and dissemination of INDSEAL and SCISEAL codes

Hendricks

Rotordynamic coefficient data sets available for labyrinth, honeycomb, smooth (tapered, stepped, constant clearances), and helically grooved seals.

SCISEAL successfully extended to compute multiple connected cavity flows with seals interacting with the power stream with validation using UTRC SSME HPFP simulated configuration results and turbine rig data.

Rim seal flow ingress/egress for small static displacements simulating and eccentric rotor showed increased seal-neck heating for the forward facing step and diffuse heating for the backfacing step.

Numerical simulation of the pressure in a synchronous whirling seal (Morrison water rig data) indicated similar axial-circumferential mapping at fixed radial position; however, the magnitudes are about 2/3 that of the experiment. Local radial-circumferential contours show qualitative agreement with higher experimental shear.

SiC fiber testing on bare and coated rotors show decreases in friction with speed. Haynes 25 alloy fiber testing shows decreasing wear at elevated temperatures.

New sealing technology including piezoelectric face seals, compliant metallic leaf, and finger seals are discussed.

Steinetz

AST Goals: reduce DOC+I up to 5%

SCF up to 10%

NOx over 50%

Noise by 7dB

2.5% can be gained by seals

Seals / Secondary Air Delivery goals:

Evaluate low leakage seals and cavity design requirements

Demonstrate seal/secondary air flow in engines

Validated time resolved/average CFD

Aspirating seal, rim seal development, with current research proposals under evaluation

Cooperative programs with Allied Signal, Cross, Technetics, Williams, USAF, US Army

T-700 engine test data demonstrated over 1% reduction in SFC replacing BOM CDP labyrinth seal with a dual brush seal. These tests clearly demonstrated that the compressor pressure ratio increased thereby changing flows throughout the entire engine.

New SBIR starts for brush CFD analysis and a floating brush seal was initiated. Shape ;memory alloy clearance control testing moves into phase II. Compliant high temperature seals to over 1500F continue with evaluation of seal durability..

Proctor

A 2" diameter Haynes-25 standard construction brush seals were tested up to 4.3 hours in cryogenics nitrogen and hydrogen at surface speeds of approx. 300 and 540 fps. Flow data for a single brush were 0.5 to 0.3 that of a 12-tooth labyrinth for pressure drops to 175 psi. Teflon impregnated chromium and chromium carbide coatings are preferable to zirconium oxide and uncoated inconel 718.

Addy

Data for SiC brush and a finger seal are compared to 4-tooth labyrinth seal illustrating some hysteresis of the finger seals with enhanced performance over that of the brush and labyrinth.

Mayhew

IHPDET initiative to double turbine engine capability by 2000; thrust/weight over 100% and compressor exit temperature by +400F. Secondary flow impact on the engine HPC: 4.4% efficiency and HPT 4.2 % efficiency. Sealing requirements 1400 to 1650 fps and over 1600 F Brush seal development Haynes 25 and 214 with 130 psi pressure drop for single seal. Coatings as Al₂O₃ and CrC (triboglide) have been evaluated. High speed testing at P&W to 1500F and 1650fps. Toward a ceramic brush exceeding the 1600F goal. Hybrid and all ceramic seals are being investigated. A user friendly secondary gas path analysis code is being developed. Brush seals are in the F119 and F100-PW-229 engines. IHPDET goals can not be met without the seals/secondary air programs.

Lowenthal

Sealol brush seals with backplate relief (low hysteresis design) show lower leakage over time and respond more favorably to excursions than conventional Sealol designs. Testing includes speeds to 1080 fps, temperatures to 1200F and pressures to 130 psid and seal diameters to 9 inches (not all applicable to the same test). Projected for NTC-76 demonstrator engine.

Bagepealli

Aspirating seal geometries and loadings from seals codes are reported. The primary components of the aspirating seal are a labyrinth seal axial seal combined with a cavity fed inner face seal and a hydrostatically fed outer face seal. Windmilling restarts (6) and ten other operational envelope characteristics are cited. Film and rotor growth parameters are given.

Shapiro

INDSEAL: GCYLT, ICYL, (cylindrical seals gas turbulent and incompressible laminar)
GFACE,IFACE (face seals, gas and incompressible)
SPIRALG,SPIRALI (spiral groove seals, gas and incompressible)
DYSEAL (dynamic seal analyses)
KTK (labyrinth seal, from USAF)
KBS (knowledge based system)

GCYLT : uses G-factors for Poiseuille and Couette turbulence coefficients. Ng-Elrod models
SPRIALI : is updated to include turbulence and inertia, but maintains the narrow groove theory
KTK : labyrinth seal code handles straight or stepped seals
DYSEAL: provides dynamics for the seal geometry
KBS: knowledge based system, which remains to be expanded into reality

Roberts

Comparison between Muijderman spiral groove bearing (Philips Tech. Labs, 1966) for a 324 mm x 388 mm seal operating at 320 m/s(1000 fps), 700C(1300F) and pressure drop of 1350 kPa(200psi) and SPIRALG show significant departures. Below 10 microns (0.04 mils) one would suspect the results of either code and above 100 microns (0.4 mils) some transition to turbulence is expected. No comparison to data are cited. In any case the thermoelastic effects would have significant influence on the results.

Keba

Comparisons of L/D=1 hydrostatic bearing run at Texas A&M and a generic L/D=0.37 hydrostatic bearing run at Rocketdyne with code predictions are provided. In general the flow rates and direct stiffness as predicted by HYDROPAD and ICYL code are similar; however significant differences appear in cross-coupled stiffness and damping predictions. These results illustrate that the codes are not accurately modeling the physics.

Athavale, Ho, Przekwas

SCISEAL capabilities for cylindrical seals and multiply connected cavity flows interacting with the power stream are delineated. Colocated grids, high order differencing, turbulence models, rough walls. Multi domain solution methodology. Efficient solutions for entrance regions and seal clearances, stepped and straight labyrinth seals, rim seals, face seals, conjugate heat transfer, passive scalar transport (mass transport) 2D/3D treatments. Rotor loads, torques, and rotordynamic coefficient calculations; full CFD solutions for centered orbits and small perturbation methods for eccentric seals. The validation effort includes some 33 validation cases.

Results are presented for:

Synchronous whirling water seal data of Morrison (Texas A&M, 1992 and 1995)

Illustrates good qualitative comparison between measured and calculated results for average velocities. Note that these methods do not calculate the Reynolds stress tensor; however the Reynolds stress tensor is a measured result of Morrison. A more fundamental approach is required in the computations.

Rims seal gas ingestion (Graber et al UTRC 1987)

The comparison with data are quite good. These are averaged quantities and smear the local

details - like any good integration scheme.

Allison engine turbine cavity data (Munson and Forry of Allison)

Comparison with two different seal clearances illustrates how gas may be ingested into the disc cavities and how non uniform heating of the discs can occur. While the simulation in static the inference of dynamics can be made, i.e., rotor perturbations

Large scale rig UTRC/MSFC SSME HPFTP (Daniels and Johnson, 1993)

These results illustrate that the cavities are connected and the analysis must support multiple connected cavities that interact with the power streams if the correct flow and mass distributions are to be computed.

San Andres

Description of HYDROFLEX code to calculate flows in bearings and seals. Considers laminar, transition and turbulent flows with surface roughness and variable thermophysical properties. 32 force impedance coefficients for stiffness and damping The code handles cylindrical seals and bearings with hydrostatic or hydrodynamic forces. HYDROTRAN provides force response to transient loads. Fixes to improve dynamic stability in hydrodynamic journal bearings: Pneumatic Hammer (limit recess axial length and reduce recess volume; use end seal restrictors or wear rings; change type of fluid inlet restriction, i.e., inherent compensation) Hydrodynamic Instability: (use rough bearing surface; fluid injection against shaft rotation; introduce bearing asymmetry; use flexible pad bearing geometry, i.e., flexure pad bearings) Reduced load and capacity and direct stiffness are to be traded off for dynamic stability. Flexure pivot tilting pad hydrostatic bearing has no restriction for hydrodynamic stability. HYDROFLEX has been extensively validated with available experimental data for water/oil/liquid hydrogen/liquid nitrogen hydrostatic bearings, water/liquid nitrogen damper seals, oil and air journal bearings and tilting pad bearings, oil flexure-pivot tilting pad bearings, and other applications.

Pelfrey

Analytical models of Reddecliff and Vohr were Reynolds equation finite difference solutions which accounted for turbulence in hydrostatic bearings but has some convergence problems at high eccentricity and clearances. HYDROB could account for grooves and is a finite element code with better turbulence and inertia modeling and has no convergence problems. At present HYDROFLEX and HYDROTRAN provide a 2-D bulk flow model finite difference solution with transient and compliant bearing pad capability. RSR Software library includes a 2-D incompressible bulk flow model for thrust bearings; however HYDROB is used for compressible thrust bearings. MTI INDSEAL codes are cited. HYDROB3D (Braun/Dzodzo) full 3-D Navier Stokes finite difference finite volume accounts for turbulence and inertia and does not assume uniform pocket pressure. Pocket flows are highly 3-dimensional and code validation comparisons with experimental data are excellent. Further testing of components will include LH2 and LOX at Phillips and MSFC as well as ARPA TRP under a 4 yr \$15M program with NASA/MSFC. The vonPragneau damper bearing geometries are to be tested as a part of the IHP RPT program.

It is important to note the accomplishments of the PW ATD turbopumps; building on technological advancements the pump has hours (vs minutes) of operational time - a significant achievement.

Parallel processing using up to 500 engineering workstations, equivalent to 50 Cray XMP's , can provide solutions overnight.

Palazzolo, Venkataraman, Padavala
Ryan, Vallely, Funston

A code is presented for liquid annular seals as a joint effort between Texas A&M and NASA-MSFC. Details are not provided; however the bulk flow model is similar to that of San Andres. References to INDSEAL and SCISEAL are absent as are comparisons. Comparisons with the data of Iwatsubo indicates good agreement for fixed and flexible surfaces. The latter appears difficult to assess.

Ullah

Air/oil seals that result in oil-in-cabin or smoke-in-cabin odors are a major cause of customer complaints and warranty costs at Allied Signal. A consortium of various Allied Signal business units and research center along with Arizona State Univ. and Georgia Tech. has been established. Their current goals are to increase seal life by at least 10 times and understand the fundamentals such as coking that is believed to be a primary contributor to the seal leakage problem. Current problems being addressed include: Improving the thermal management of seals by improved modeling/analysis methods; obtaining heat transfer data for active cooling schemes (jets, proprietary film cooling etc); prediction of seal face tracking dynamics; understanding oil coking mechanisms; and quantifying coking rates. Steady state thermal management models are being studied first with 1995 year end deadlines; coking research is expected to continue through 1996; and ,transient problems, such as sudden rise in seal temperatures during a throttle chop, will be addressed thereafter.

Munson, Stienetz

Results of a comparative study of engine internal airflow systems for regional (AE-3007) and turboshaft (LHTEC T801) illustrate 50% of leakage through 2 turbine blade/vane gaps; Sealing effort at few locations yield large returns (regional or turboshaft). Development of a film riding rim seal could reduce SFC by 1.8% in the regional engine and 5% in the turboshaft engines. The potential for a clean sheet approach to engine design can provide even larger gains. Better sealing is an inexpensive way to boost engine performance.

Dimofte, Hendricks

Unloaded journal bearing with a wave can operate over a range of speed free of subsynchronous whirl. When whirl occurs the equilibrium radius is less than the bearing clearance and the bearing runs stably. At large clearances the two wave exhibits whirl frequencies near 1/4 synchronous while the three wave whirl frequencies are close to 1/2 synchronous. At small clearances, both exhibit half synchronous whirl at increased whirl thresholds.

TABLE OF CONTENTS

SEALS CODE DEVELOPMENT WORKSHOP INTRODUCTION Anita D. Liang, NASA Lewis Research Center	1-0 <i>omit</i>
TURBOMACHINE SEALING Robert C. Hendricks, NASA Lewis Research Center	5-1
AEROSPACE SEAL REQUIREMENTS Bruce M. Steinetz and Robert C. Hendricks, NASA Lewis Research Center	41-2
CRYOGENIC BRUSH SEAL TEST RESULTS Margaret P. Proctor and James F. Walker, NASA Lewis Research Center	55-3
RESULTS OF CONTACTING SEAL TESTING AT NASA LEWIS RESEARCH CENTER Gene Addy, NASA Lewis Research Center	67-4
AIR FORCE SEAL PROGRAMS Ellen R. Mayhew, Wright Laboratory, Wright Patterson Air Force Base	73-5
PRDA-II AND III BRUSH SEAL DEVELOPMENT PROGRAMS AT EG&G Robert G. Loewenthal, EG&G Mechanical Components Technology Group Research and Development	81-6
ASPIRATING SEAL DEVELOPMENT: ANALYTICAL MODELING AND SEAL TEST RIG Bharat Bagepalli, General Electric Company	89-7
INDUSTRIAL COMPUTER CODES Wilbur Shapiro, Wilbur Shapiro & Associates, Inc.	115-8
COMPARISON OF SPIRALG PERFORMANCE PREDICTIONS WITH A SPREAD SHEET SOLUTION Martyn G. Roberts, Atlanta Engineering, Rolls-Royce, Inc.	139-9
COMPARISON OF CODE PREDICTIONS TO TEST MEASUREMENTS FOR TWO ORIFICE COMPENSATED HYDROSTATIC BEARINGS AT HIGH REYNOLDS NUMBERS John E. Keba, Rocketdyne Division, Rockwell Corporation	145-10
SCISEAL: A CFD CODE FOR ANALYSIS OF FLUID DYNAMIC FORCES IN SEALS M.M. Athavale, Y.-H. Ho, and A.J. Przekwas, CFD Research Corporation	159-11
THERMOHYDRODYNAMIC ANALYSIS OF CRYOGENIC LIQUID TURBULENT FLOW FLUID FILM BEARINGS Luis San Andres, Mechanical Engineering Department, Texas A&M University	191-12
THE ACOUSTIC INFLUENCE OF CELL DEPTH ON THE ROTORDYNAMIC CHARACTERISTICS OF SMOOTH-ROTOR/HONEYCOMB-STATOR ANNULAR GAS SEALS Dara W. Childs, Mechanical Engineering Department, Texas A&M University	209-13

WALL SHEAR STRESS, WALL PRESSURE AND NEAR WALL VELOCITY FIELD RELATIONSHIPS IN A WHIRLING ANNULAR SEAL Gerald L. Morrison, Robert B. Winslow, and H. Davis Thames III, Turbomachinery Laboratory, Texas A&M University	211	-14
P&W CRYOGENIC FLUID-FILM BEARING AND SEAL TECHNOLOGY DEVELOPMENT AND IMPLEMENTATION Philip C. Pelfrey, Pratt & Whitney	223	15
INTERSTAGE DISK-CAVITY/BRUSH SEAL NUMERICAL FLOW VISUALIZATION STUDY V.V. Kudriavtsev and M.J. Braun, Department of Mechanical Engineering, The University of Akron	237	16
TWO-DIMENSIONAL DYNAMIC SIMULATION OF A CONTINUOUS FOIL BEARING M.J. Braun, F.K. Choy, M. Dzodzo, and J. Hsu, Department of Mechanical Engineering, The University of Akron	267	17
THREE DIMENSIONAL FLOW AND PRESSURE PATTERNS IN A HYDROSTATIC JOURNAL BEARING M.J. Braun and M.B. Dzodzo, Department of Mechanical Engineering, The University of Akron	281	18
THREE DIMENSIONAL FLOW AND PRESSURE PATTERNS IN A SINGLE POCKET OF A HYDROSTATIC JOURNAL BEARING M.J. Braun and M.B. Dzodzo, Department of Mechanical Engineering, The University of Akron	285	19
LIQUID ANNULAR SEAL RESEARCH Alan B. Palazzolo, Balaji Venkataraman, and Sathya S. Padavala, Department of Mechanical Engineering, Texas A&M University; and Steve Ryan, Pat Vallely, and Kerry Funston, NASA George C. Marshall Space Flight Center	299	20
SEALS RESEARCH AT ALLIEDSIGNAL M. Rifat Ullah, AlliedSignal Engines, AlliedSignal, Inc.	315	-21
INNOVATIVE SEALING TECHNOLOGY FOR NEXT GENERATION SUBSONIC ENGINES John Munson, Allison Engine Company, and Bruce Steinetz, NASA Lewis Research Center	327	22
FRACTIONAL WHIRL MOTION IN WAVE JOURNAL BEARINGS Florin Dimofte and Robert C. Hendricks, NASA Lewis Research Center	337	-23
COLOR PLATES	341	
ATTENDANCE LIST	353	

01/17/11

SEALS CODE DEVELOPMENT WORKSHOP INTRODUCTION

Anita D. Liang
NASA Lewis Research Center
Cleveland, Ohio

SEALS CODE DEVELOPMENT WORKSHOP

WORKSHOP OBJECTIVES

- **PRESENT WORK PERFORMED UNDER NASA CONTRACT NAS3-25644, "NUMERICAL/ANALYTICAL/EXPERIMENTAL STUDY OF FLUID DYNAMIC FORCES IN SEALS"**
- **PROVIDE A FORUM FOR INFORMATION EXCHANGE BETWEEN THE GOVERNMENT AND INDUSTRY ON SEAL/BEARING TECHNOLOGY DEVELOPMENT**

WORKSHOP DELIVERABLES

- **CONFERENCE PROCEEDINGS TO BE DISTRIBUTED IN SEPTEMBER, 1995**
- **CODES TO BE DISSEMINATED IN JUNE - JULY, 1995**

NASA CONTRACT NAS3-25644

OBJECTIVE	DEVELOP CODES FOR ANALYZING AND DESIGNING OPTIMIZED ADVANCED SEALS FOR FUTURE AEROSPACE AND ADVANCED ROCKET ENGINE SYSTEMS
ORIGINAL SCOPE	<ul style="list-style-type: none">● SEVEN YEAR EFFORT● DEVELOP 3-D CFD SCIENTIFIC CODES● COMPILE AND GENERATE SETS OF VERIFIED 2-D INDUSTRIAL CODES● GENERATE A KNOWLEDGE BASED SYSTEM TO BE COUPLED TO THE CODES● TECHNOLOGY TRANSFER VIA WORKSHOPS● CODE VALIDATION VIA PUBLISHED DATA, IN-HOUSE TEST WORK AND COOPERATIVE PROGRAMS● PROGRESS MONITORED BY A PEER REVIEW PANEL

CLOSE-OUT OF NASA CONTRACT NAS3-25644

- **CONTRACT RE-NEGOTIATED IN FY94 AS A FIXED PRICE CONTRACT**
- **CONTRACT CLOSE-OUT IN FY95**
- **FINAL DELIVERABLES FROM MECHANICAL TECHNOLOGY, INC.**

INDUSTRIAL CODES (INDSEAL) - ICYL, GCYLT, IFACE, GFACE, SPIRALG, SPIRALI, DYSEAL, AND KTK

SCIENTIFIC CODE (SCISEAL) - MULTIDOMAIN CODE WITH ROTORDYNAMIC CAPABILITY

- **EXECUTABLES TO BE DISSEMINATED IN JUNE - JULY, 1995**
- **SOURCE CODES TO BE DELIVERED BY THE END OF CY1996 TO COSMIC OR EQUIVALENT**
- **CODE DEVELOPMENT ACTIVITIES WILL BE COORDINATED WITH OTHER PROGRAMS AND FUND SOURCES**

ISSUES TO BE ADDRESSED BY THE PEER REVIEW

INDUSTRIAL CODE OPERATING ENVIRONMENT

FUTURE WORKSHOPS

SI-07

39443

TURBOMACHINE SEALING

Robert C. Hendricks
NASA Lewis Research Center
Cleveland, Ohio

Overview

Designers and customers are demanding higher performance turbomachine systems that have long life between overhauls and satisfy the more restrictive environmental constraints. This overview provides sources of design data, numerical, and experimental results along with selected new seal configurations and static sealing challenges such as in the combustors.

The following categories are presented:

1. Seal Rotordynamic Data Base (experimental analytical program: Dr. Childs at Texas A&M)
2. Secondary Flow Interactions (validation studies with Dr. Athavale at CFDRC, Huntsville AL)
3. Contact Sealing (selected types with finger seal model)
4. Environmental Constraints (emphasis on combustors)
5. What's Coming

1. Seal Rotordynamic Data Base

At least 95-percent of the published data for dynamic coefficients of annular gas seals available in the world today were generated under grant NAG3-181 with Dr. Dara Childs at Texas A&M University. These data and the Workshop Proceedings will continue to serve as resource materials and validation test results for analysis codes, future experimentation, and design.

Rotordynamic coefficient characterization of several different seal configurations including labyrinth, honeycomb, brush, cylindrical, spiral grooved, and damper. Stiffness and damping coefficients were assessed for centered whirling seals where the force input was horizontal and the rotor suspended as a pendulum. Flow rates, pressure and accelerometer measurements were taken to define the forces and leakages and displacements monitored by Bently probes. A limited amount of eccentric rotor data (static eccentricity) results were taken.

For small motion about a centered position, the linear reaction-force model for gas path annular seals becomes

$$\begin{pmatrix} F_x \\ F_y \end{pmatrix} = \begin{pmatrix} K & k \\ -k & K \end{pmatrix} \begin{pmatrix} x \\ y \end{pmatrix} + \begin{pmatrix} C & c \\ -c & C \end{pmatrix} \begin{pmatrix} \dot{X} \\ \dot{Y} \end{pmatrix}$$

and test data are available on the following seal configurations (figure 1, ref. 3):

- (a) Tooth-on-stator labyrinths
- (b) Tooth-on-rotor labyrinths, smooth stators
- (c) Tooth-on-rotor labyrinths, honeycomb stator
- (d) Interlocking seals
- (e) Brush seals (4,5, and 6 stages)
- (f) Smooth seals, constant clearances
- (g) Smooth seals, tapered geometries
- (h) Smooth seals, step configuration
- (i) Honeycomb seals
- (j) Helically-grooved stator/smooth-rotor seals

This program was the first to demonstrate the remarkable advantages of the honeycomb seals as compared to see-through or interlocking labyrinth seals contrary to some early German test results which suggested honeycomb should be avoided. However, because of the large damping the long honeycomb seals are much better than the labyrinth seals, and leak less. These seals are now gaining acceptance as replacements for labyrinth seals in centrifugal compressors and steam turbines.

The brush seal results still remain the only available set of dynamic measurements and reduce the cross-coupling to nearly zero. As a result brush seals generally improve the rotordynamics of gas turbine engines.

See-through annular teeth-on-stator configurations are slightly more stable than teeth-on-rotor configurations; for teeth-on-rotor and smooth and honeycomb stators are comparable. Interlocking seals showed substantial reductions in direct damping.

Helically-grooved-stator/smooth-rotor seals showed that a negative cross coupling could be achieved, which opposes forward whirl. Analytical treatments of the turbulent flows and commercialization remains to be explored.

Swirl brakes showed that significant reductions in cross-coupling can be achieved; for the SSME HPOTP the reduction could be a factor of two. These brakes have found commercial applications in the electric power industry particularly where labyrinth seals are involved.

The testing of eccentric seals with smooth bores showed the seal to be more sensitive to

eccentricity than predicted and a continued effort is needed.

Swirl brake characteristics were explored and have been introduced to stabilize several turbomachines in the field as well as new designs.

2. Secondary Flow Interactions

Fluid flows within an engine or turbomachine are coupled. The power stream and the secondary flow streams that cool components, function as working or purge fluids are coupled through the seal and cavity flow fields. The behavior of these flows becomes critical to the thermal management of the component and ultimately to the performance of the turbomachine. Flow studies in a turbine and within the UTRC simulated SSME HPFTP (figure 2, ref. 1) provided validation studies of the SCISEAL code and the CFD-ACE codes.

As turbomachine power systems mature the ability to refine component efficiencies declines with efforts focused on small percentage gains. In conventional turbomachine analyses interaction between the power stream and the secondary flow paths such as beneath the blade platforms, beyond the blade/vane tips, around the diffuser, and combustor sections are not coupled. For large changes in efficiencies this approach is valid; however, for small changes the coupling becomes of major significance. Current numerical and experimental work is focused on determining the interaction between the power stream and multiply-connected multicavity sealed secondary flow fields and conjugate thermomechanical response.

UTRC HPFTP Simulation

The results of a recent numerical study of the experimental work of Daniels and Johnson at UTRC using CO₂ as the tracer gas (ref. 4) suggests the following:

1. Multiple cavity analyses capture interactive power/secondary flow stream effects that can not be realized for uncoupled single cavity treatments; in short, uncoupled results are inadequate for determining small changes in performance. For the UTRC simulation of the SSME HPFTP a flow thread is defined that works its way through the upstream first stage rotor seal throughout the dual rotor cavities and exits downstream of the second stage rotor seal.
2. Generally there is good agreement with the experimental results for gas ingestion and flow egress, although the egress was lower than calculated. Tables I, II, III, ref. 1.
3. Comparisons of the concentrations (CO₂) in the central cavity regions was good but only fair agreement at the blade shanks. The shanks were simulated as rotating slots and such simulations are known to be inadequate as the flow field is complex 3-D with spiral and angled jetting from

the holes. A second reason for disagreement could be in the scanning of the prints for grinding.

4. The purge cooling thread (figure 3, ref. 1) tends to provide cooling for the front side of rotor 1 and aft side of rotor 2. The ingested gas effects the aft part of rotor 1 and the front side of rotor 2. Such nonuniform cooling and heating leads to nonuniform stress in the rotors.

5. These results illustrate that small changes in seals and cavity flows effect flows throughout the entire engine or turbomachine. Further, these results are corroborated by test results from the T-700 (figure 4, ref. 11) where the compressor discharge seal was changed out to a dual-brush seal. The engine performance showed a SFC decrease of at least one percent (figure 5, ref. 11). The seal flows were reduced but more importantly, the compressor discharge pressure was increased implying changes throughout the entire engine.

6. With the strength of these numerical tools, the experimental data, and design expertise, it is suggested that the entire secondary flow path and seal design be reevaluated. Those cooling and purge gases that are of marginal importance can be eliminated along with the structural distress associated with such holes. Further it is suggested that this **'clean sheet' approach be applied** to all the associated components with thought given to active controls for a more efficient long life low maintenance engine.

Turbine Interstage Seal

A study of pressure and thermal effects in a labyrinth seal between stage 1-2 turbine disk cavities provide the validation results. For orientation, the turbine vane is shown in white and the color results represent the flow field computations. The geometry is that of a six-tooth-on-rotor - labyrinth seal with a smooth stator. The clearances were fixed at 0.012 inch and 0.024 inch. The analysis shows the following results:

1. When the labyrinth seal clearances are small (0.012 in.), turbine gas ingestion into the cavity is limited and cavity temperatures appear uniform, especially in the seal area.(figure 6) (Blue to blue-green color). However when the seal clearances are opened by operations or design to 0.024 inch, the powerstream flow is ingested into the cavity and appears to heat the labyrinth seal as well. If the rotor is whirling in some manner the thermal distortions on the disk and the labyrinth seal teeth will be nonuniform as there is a large thermal gradient across the first tooth. Such nonuniformities can lead to durability problems.

2. The pressure drops reflect the increased leakage flows with the major gradient across the first tooth (figure 7). The increased loading coupled with the thermal effects can increase the durability problem.

Vortex Control

In a lid-driven flow blade simulation, the blade flow carryover initiated a vortex on the opposite wall (pressure side) (figure 8, ref. 10). While these vortices are usually confined to the upper 10 to 20 percent of the blade they represent a considerable loss of performance. The concept of introducing counter and co-rotating vortices could be used to control vortex losses, noise sources, and stall margins. The vortices could be introduced by controlled jets or swirl vanes in the platforms of the stators.

Unsteady Ingestion

Turbomachine rotation is eccentric to some degree, with whirl representing an extreme orbital motion that can destroy a machine (figure 9, ref. 10). The fluid ingestion due to the rotor being offset half of the seal clearance into the power stream is significant; also the fluid egress due to the rotor being half a seal clearance below the power stream is large. While the coupled effects were not studied, the inference is that unsteady thermomechanical distress can become acute under dynamic loadings.

Acoustics

Not addressed due to the lack of data, but of major significance is the acoustic fields generated and transmitted by the multiple cavities and their associated seals. A part of the long range seals code development program, but this program funding has been stopped.

Synchronous Whirling Annular Seal - Experimental

The measurements of turbulence in a 0.5 eccentric synchronous whirling annular seal operating at a Reynolds number of 24,000 and a Taylor number of 6,600 was measured using a 3-color laser Doppler anemometer system. Flush mounted pressure and shear stress probes measured the normal and shear stresses along the stator. Phased averaged pressure and shear along with mean velocities and turbulence kinetic energy (at 0.16 clearance from the stator wall) were measured. The results are complex and do not follow conventional seal models:

1. The mean pressure decreases rapidly at the seal inlet as the flow accelerates into the clearance gap resulting in large shear stresses and flow fluctuations (figure 10, ref. 2).
2. The coherence levels are large (.8 -.9) for pressure and shear as rotor whirl dominates the development of the flow field. Pressure is high on the pressure side of the rotor and low on the suction side with shear stress being nearly 90-degrees out of phase.
3. Progressing through the seal, pressure and shear stress fluctuations decrease as turbulence levels decrease with the axial and tangential velocities becoming more uniform (figure 11, ref. 2).

4. The mean shear stress angle steadily increases from 15-degrees at the inlet to 35-degrees at the outlet with a sudden increase to 45-degrees outside of the seal within the 'plenum'. The circumferential velocity steadily increases with a sudden decrease in axial velocity at the exit.
5. At the exit the axial velocity is largest on the pressure side as compared to the suction side at the inlet resulting in the phase averaged velocity becoming negative on the pressure side and positive on the suction side at the seal exit.
6. The simple assumptions of no circumferential variation in pressure or shear stress and the assumption that the axial velocity will be maximum within the maximum clearance are invalid. Modeling of the flow field becomes a difficult task.

Synchronous Whirling Annular Seal - Numerical

The code SCISEAL was applied to the synchronous whirling annular seal data (see figures 10, 11). Transforming the system to a rotating frame made the flow quasi steady. In this framework the flow fields showed fair to good agreement with the experiment and generally consistent picture of the flow physics. experimental turbulence is anisotropic, but the isotropic k-e model was used in the numerical calculations. Before validation can be accepted, the low-Reynolds model or multi-layer models should be applied to the data. Although further measurements are desirable now that the codes are available, funding for the effort has been curtailed.

3. Contact Sealing

Brush seals

Brush seals suffer from high incipient wear, which reduces their effectiveness. Attempts to identify rub-runner coatings and tribological pairing to reduce wear have not been to successful and perhaps the better solution is to permit the bristles to rub an uncoated or sacrificial layer of the shaft.

Ceramic brush developments, currently centered on SiC bristles, indicate that SiC is a good cutting tool. Tribological pairing of SiC, Al₂O₃, and glass with various coatings provided some initial screening of the fibers and SiC was the fiber of choice with tuft testing carried out at surface speeds (500 <V_s< 1100 ft/s) (figure 12, ref. 12). standard rub-runner coatings such as CrC was stripped by the SiC fibers and other coatings were sought. One coating developed for wear reduction was co-sprayed PSZ with boron-nitride added for dry high temperature lubrication and more conventional coatings, plasma sprayed PSZ and vapor deposited PSZ, alumina, and Triboglide (not available for testing) were also selected. Tuft testing of the SiC running against coated rotors indicated that none of the coatings provided good wear characteristics. friction coefficient was also high and in some cases decreased a little with running speed (figure 13, ref. 12). Although the ceramics afford a hard surface, the operation on

bare shaft 17-4PH proved to be an equally good rub tolerant surface to the SiC.

In separate tuft testing at low surface speeds (< 80 ft/s) showed a significant reduction in wear at 650C even though the friction coefficient was nominally the same (figure 14, ref. 5).

Four compliant seal concepts (finger seals, piezoelectric-controlled face seals, and shaped memory-alloy shroud seals) while not in "use" have significant potential. In most cases, the contacting seals experience rapid incipient wear.

Alternate contact seals

While a significant amount of effort has been given to brush seals and face seals (hydrostatic, hydrodynamic, aspirating, ring lift-off) development efforts continue on new types of seals (figure 15, ref. 16 and figure 16, ref. 15, and refs. 6, 9, 13, and 17).

Shaped-memory alloys are used for attachment pins and are being investigated for use in a shroud seal. For example, a compressor ring could be designed so that when steady state temperature is reached, the ring would contract to less than 1 percent of the diameter. Such a design would permit a relative expansion between a magnesium case and nickel alloy blades and provide good blade tip sealing at cruise conditions. Response to in flight dynamics remains to be evaluated.

Piezoelectric face seal elements can be designed to provide face coning. Coning controls both seal stability and leakage. One such experimental test configuration had a carbon-faced, piezoelectric, active-controlled elements placed on both sides of a rotor. purpose to the seal was to reduce the consumption of onboard helium and still separate cryogenic oxygen and hot hydrogen-rich steam (figure 17, ref. 10).

Leaf seals combine the noncontacting features of fluid film seals and the compliant nature of the brush seal. leaf seal consists of several thin sheets or leaves that resemble sections of lip seals wiping the shaft. A second set of overlapping leaves completes sealing and the leaves can be straight or angle cut. leaves have mismatched curvature with respect to the shaft for lift off with 300-500 micro-inch at the leading edge to perhaps twice that at the trailing edge. leaf flexes in the radial direction to accomodate thermomechanical behavior and axial and angular misalignments. Under no rotation, there is a net closing force to keep the leaves in contact with the shaft (figure 18, ref. 10).

Finger seals are of simple construction. seal consists of two or more axially stacked, radially compliant, overlapping disks or diaphragms that resemble and are often referred to as "hockey sticks"(figure 19, ref. 7). fingers which are separated by gaps can have straight or logarithmic curvature and usually are of constant thickness. overlapping disks arrays form a compliant seal. Finger seals can be fabricated by several techniques, e.g., photoetched or machined from a variety of materials such as metal, plastic, or ceramics. assembly is held together by simple riveting and the final configuration can be ground and lapped depending on the use. These seals leak less than 1/10th of a conventional labyrinth, but current versions suffer from hysteresis problems.

An elementary leakage model was developed based on the brush seal bulk flow model and provides guidance for parametric variations and design (figure 20, ref. 7)

4. Environmental Constraints

Most communities have adapted some form of environmental controls and requirement for leakage control, emissions, and noise (e.g., see ref. 8). For example, the high speed research program is dedicated to achieving about 5g of NO_x per kg-fuel burned.

Gas turbine exhausts CO, CO₂, H₂O, unburned hydrocarbons (UHC), particulate matter mostly in the form of carbon, NO_x and excess O₂, and N₂. While CO₂ and H₂O are commonplace they contribute to the global warming and are reduced only by burning less hydrocarbons. In industrial gas turbines sulfur and oxides are also a problem and requires removal prior to combustion. Controlling the combustion temperature between 1680K and 1900K is considered by some as the temperature range for low emissions (CO<25 and NO_x< 15 ppm) and represents the underlying principles in staged, variable geometry, and premixed combustors.

International Civil Aviation Organization (ICAO) has set standards that involve the emission index(g/kg-fuel), the SFC(kg fuel/hr-kN), and the time of operation (hr) for the landing takeoff cycle (LTO) (see Table IV).

$$\text{Emissions (g/kN)} = \text{EI} \times \text{SFC} \times \text{Time in LTO mode}$$

For the commercial powerplants, emissions of 10-20 ppm NO_x are being sought and can possibly be met by consuming natural gas.

These complex combustors require static seals, and several types are proposed including the use of brush and rope seals (figure 21, ref. 14). Loss of high emission laden gases or injection of fuel or air at the improper locations will lead to excessive engine emissions.

5. What's Coming

- A. Conjugate problems with coupled structural interactions with different time scales as a potential problem.
- B. Monitoring components for longevity (life) and predictive maintenance
- C. Flow balancing through the compressor/turbine multiple cavities and subplatform flows
- D. Active/passive seals rotordynamics for stabilizing both the aero and aero-derivative engine

- E. Strict environmental restraints on fluid leakages and engine emissions
- F. Aeroderivative systems increases in efficiencies by controlled subplatform flows and perhaps the use of separate cooling fluids
- G. Increased shift toward face seals for special applications (high payoff) but labyrinths will not go away for a long time.
- H. Large diameter seals, segmented, brush, face, lift, and floating types.
- I. Counter-rotating systems.

Selected References

1. Athavale, M.M., Przekwas, A.J., Hendricks, R.C., Steinetz, B.M. (1995) Numerical Analysis of Intra-Cavity and Power-Stream Flow Interactions in Multiple Gas-Turbine Disk-Cavities. Int. Gas Turbine and Aeroengine Congress and Expo., Houston TX, June 5-8, 1995, Paper 95-GT-325. NASA TM 106886.
2. Athavale, M.M., Hendricks, R.C., Steinetz, B.M. (1995) Numerical Simulation of Flow in a Whirling Annular Seal and Comparison with Experiments. To be presented at the Joint Propulsion Conference, San Diego CA.
3. Childs, D. W. (1995) Summary of Seal Rotordynamic Data NASA NAG3-131. Final Report 1995. Texas A&M Turbomachine Laboratories.
4. Daniels, W.A., and Johnson, B.V. (1993), Experimental Investigation of Turbine Disk Cavity Aerodynamics and Heat Transfer, Contract NAS8-37462, UTRC Report 93-957878-27.
5. Fellenstein, James A. and DellaCorte, Christopher: (1995) A New Tribological Test for Candidate Brush Seal Materials Evaluation. Society of Tribologists and Lubrication Engineers, Chicago, IL, May 15-20, 1995. DOE/NASA/50306-6; NASA TM-106753.
6. Glienicke, J., Launert, A., Schlums, H., and Kohring, B. (1993) Non-Contacting Gas Lubricated Face Seals for High p.v -Values. Seals Code Development-93, NASA CP10136, p.367.
7. Hendricks, R.C., O'Halloran, B., Arora, G., Addy, H.E., Flowers, J., Carlile, J., and Steinetz, B.M. (1994): Advances in Contact Sealing. Advanced Earth to Orbit Propulsion Technology Conference, Huntsville AL, May 16-19, 1994. US Army Research Laboratories.
8. Hendricks, R.C. (1993) Environmental and Customer-Driven Seal-Requirements. Seals Flow Code Development-93. Hendricks, R.C. and Liang, A.D. Eds., NASA CP 10134, p.67.
9. Hendricks, R.C., Liang, A.D., Childs, D.W., and Proctor, M.P. (1992) Development of Advanced Seals for Space Propulsion Turbomachinery. 1992- Aerospace Atlantic Int. Conf.

And Expo., SAE, Dayton OH April 6-10, 1992. NASA TM 105659.

10. Hendricks, R.C., Steinetz, B.M., Athavale, B.M., Przekwas, A.J., Braun, M.J., Dozozo, M.I., Choy, F.K., Kudriavtsev, V.V., Mullen, R.L., and Von Pragenau, G.L. (1995) Interactive Development of Seals, Bearings, and Secondary Flow Systems with the Power Stream. to be published Interanational Journal of Rotating Machinery. Presented at the Fifth International Symposium on Transport Phenomena and Dynamics of Rotating Machinery (ISROMAC-5) Kaanapali, HI, May 8-11, 1994.

11. Hendricks, R.C., Griffin, T.A., Kline, R.R., Csavina, K.R., Pancholi, A., and Sood, D. (1994) Relative Performance Comparison Between Baseline Labyrinth and Dual-Brush Compressor Discharge Seals in a T-700 Engine Test. Int. Gas Turbine and Aeroengine Congress and Expo., The Hague Netherlands, June 13-16, 1994. NASA TM 106360. ARL-MR-118.

12. Howe, Harold: Brush Seal Shaft Wear Resistant Coatings. Contract NAS3-27383, Final Report March 1995.

13. Leefe, S., (1992) Dynamics of Face Seals for High Speed Turbomachinery. Seals Flow Code Development-92, NASACP 10124, p 197.

14. Lefebvre, A.H. : (1995) The Role of Fuel Preparation in Low Emissions Combustion. Int. Gas Turbine and Aeroengine Congress and Expo., Houston TX, June 5-8, 1995, Paper 95-GT-465.

15. Munson, John (1993) Compressor Discharge Film Riding Face Seals. Seals Flow Code Development-93 NASA CP 10136 , p.219.

16. Pope, A.N. (1991) Areas of Seal R&D at GE. Seals Flow Code Development-91. Hendricks, R.C. and Liang, A. D. Eds., p 109.

17. Withers, P.A. (1992) High Pressure Compressor Delivery Brush Seal of the International Aero Engines (IAE) V2500-A1 Gas Turbine Engine. Seals Flow Code Development-92, NASA CP 10124. P 275.

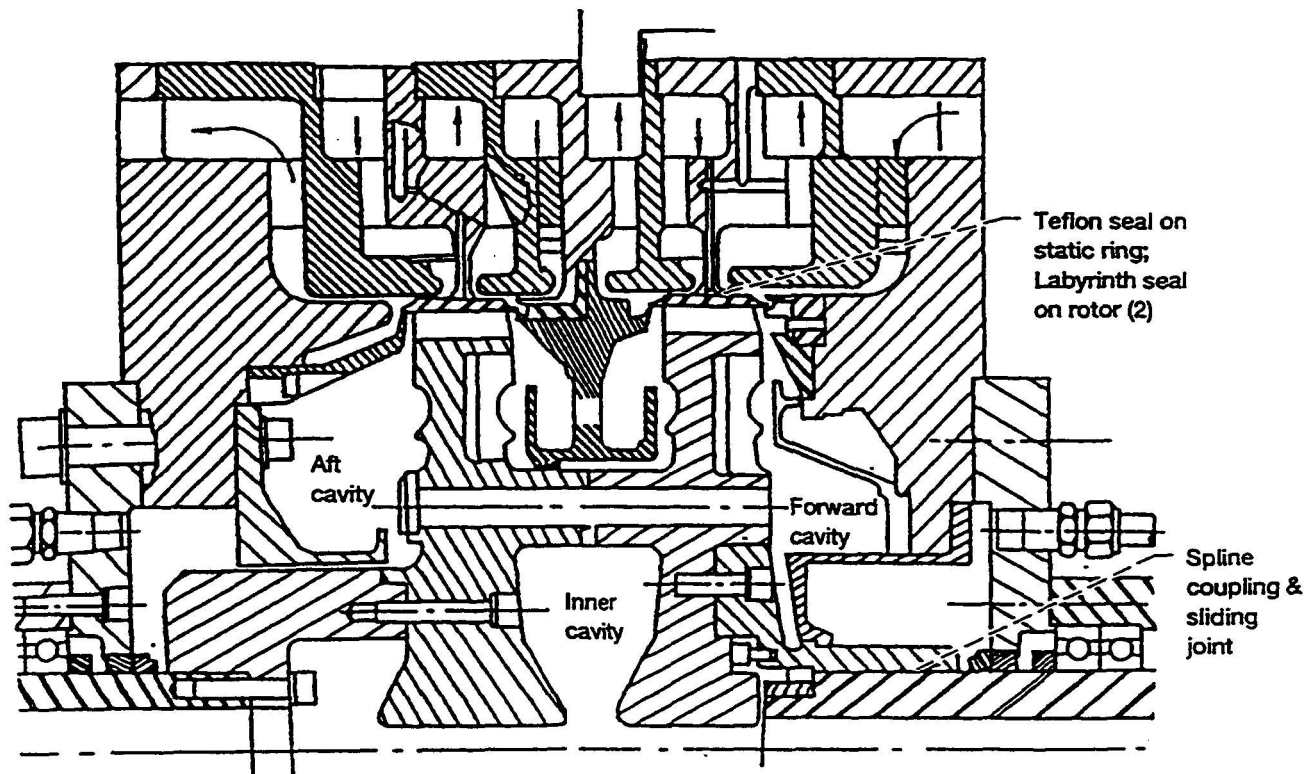
TABLE III—COMPARISON OF GAS SOURCE MEASUREMENTS AND CALCULATIONS FOR FLOW CONDITIONS BASELINE RUN 202 (SEE TABLE I). SEE FIGURE 4 FOR PROBE LOCATIONS

	ϕ_{12} F1	ϕ_{13} F2	ϕ_{14} F3	ϕ_{01} F4	ϕ_{03} F5
Region I - Forward cavity					
A23 - numerical	0.278	4×10^{-5}	0	0.721	0.001
experimental	.09	0	0	.93	0
A24 - numerical	0.978	1×10^{-4}	0	0.021	2×10^{-4}
experimental	.96	0	0	.09	0
Region II - Center cavity and rotor I					
C44 - numerical	0.232	0.03	0	0.465	0.273
experimental	.24	.12	.03	.32	.28
C42 - numerical	0.150	0.378	0	0.299	0.173
experimental	.22	.18	.03	.31	.22
A8 - numerical	0.194	0.194	0	0.388	0.223
experimental	.09	.67	0	.13	.11
A5 - numerical	0.003	0.987	0	0.006	0.004
experimental	.03	.9	0	.05	.04
C39 - numerical	0.002	0.992	0	0.004	0.002
experimental	.07	.71	.03	.1	.04
Region III - Center cavity and rotor II					
B30 - numerical	0.039	0.838	0	0.078	0.045
experimental	.06	.77	.03	.08	0
B26 - numerical	0.070	0.708	0	0.140	0.082
experimental	.22	.22	.03	.29	.22
B23 - numerical	0.216	0.102	0	0.431	0.251
experimental	.24	.12	.03	.33	.26
C25 - numerical	0.218	0.091	0	0.436	0.254
experimental	.24	.11	.02	.33	.25
C33 - numerical	0.097	0.598	0	0.193	0.112
experimental	.2	.19	.03	.31	.23
C29 - numerical	0.223	0.068	0	0.447	0.261
experimental	.23	.11	.02	.33	.25
Region IV - Aft cavity and rotor II					
C11 - numerical	0.006	0.012	0.956	0.011	0.007
experimental	.08	.03	.77	.07	.07
B10 - numerical	0.213	0.109	0.004	0.425	0.248
experimental	.21	.12	.06	.34	.3

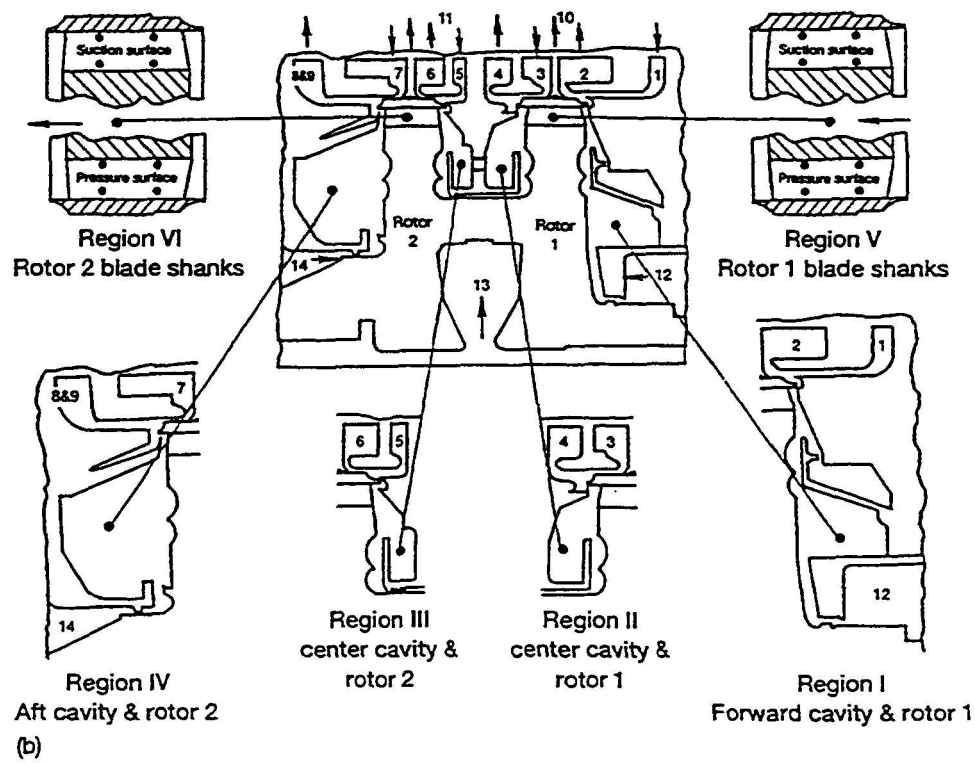
TABLE IV. ICAO Gaseous Emissions Standards

Emission	Subsonic turbojet/turbofan New, takeoff thrust >26.7kN	Supersonic turbojet/turbofan
HC	19.6	$140(0.92)^{**}Pr_{\text{takeoff}}$
CO	118	$4550/(Pr_{\text{takeoff}})^{**}1.03$
NOx	$40 + 2Pr_{\text{takeoff}}$	$36 + 2.42Pr_{\text{takeoff}}$

Pr = engine pressure ratio



(a)

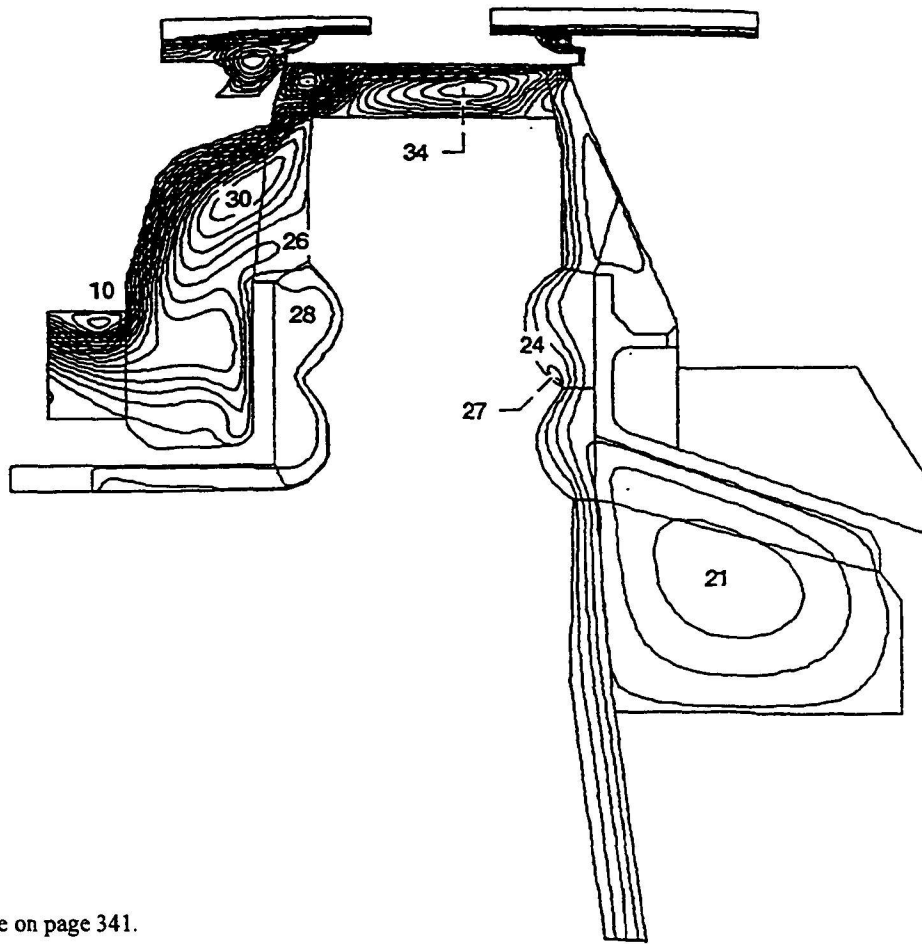


(b)

Figure 2 —(a) Large-scale model of SSME HPFTP disks and cavities - from Daniels and Johnson (1993). (b) Model seal region and gas source/exit locations - from Daniels and Johnson (1993). (c) Flow domain showing the computational grid and the definition of various flow streams and rim seal locations.

Contour levels

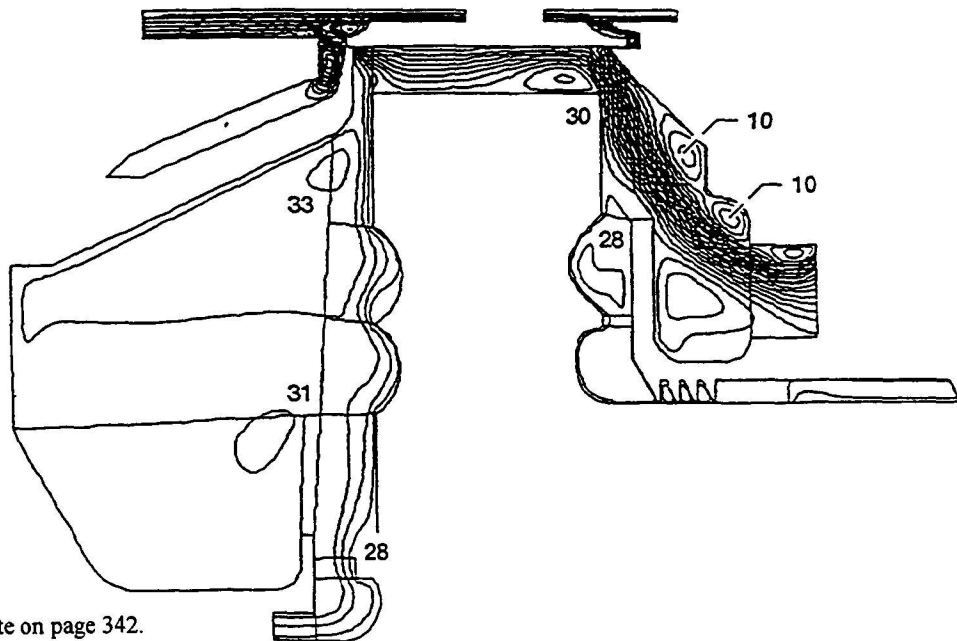
3	-6.540E-02
6	-5.850E-02
9	-5.160E-02
12	-4.470E-02
15	-3.780E-02
18	-3.090E-02
21	-2.400E-02
24	-1.710E-02
27	-1.020E-02
30	-3.300E-03
33	3.600E-03
36	1.050E-02
39	1.740E-02



(a) See color plate on page 341.

Contour levels

3	-6.540E-02
6	-5.850E-02
9	-5.160E-02
12	-4.470E-02
15	-3.780E-02
18	-3.090E-02
21	-2.400E-02
24	-1.710E-02
27	-1.020E-02
30	-3.300E-03
33	3.600E-03
36	1.050E-02
39	1.740E-02



(b) See color plate on page 342.

Figure 3 —(a) Streamline pattern in regions I, II and the connecting blade shank region. (b) Streamline pattern in regions III, IV, connecting blade shank region and the slot in the stator support. (c) Flow detail at seals 1, 2, and blade shank region to illustrate the complex vortical structure and Mainpath flow ingestion.

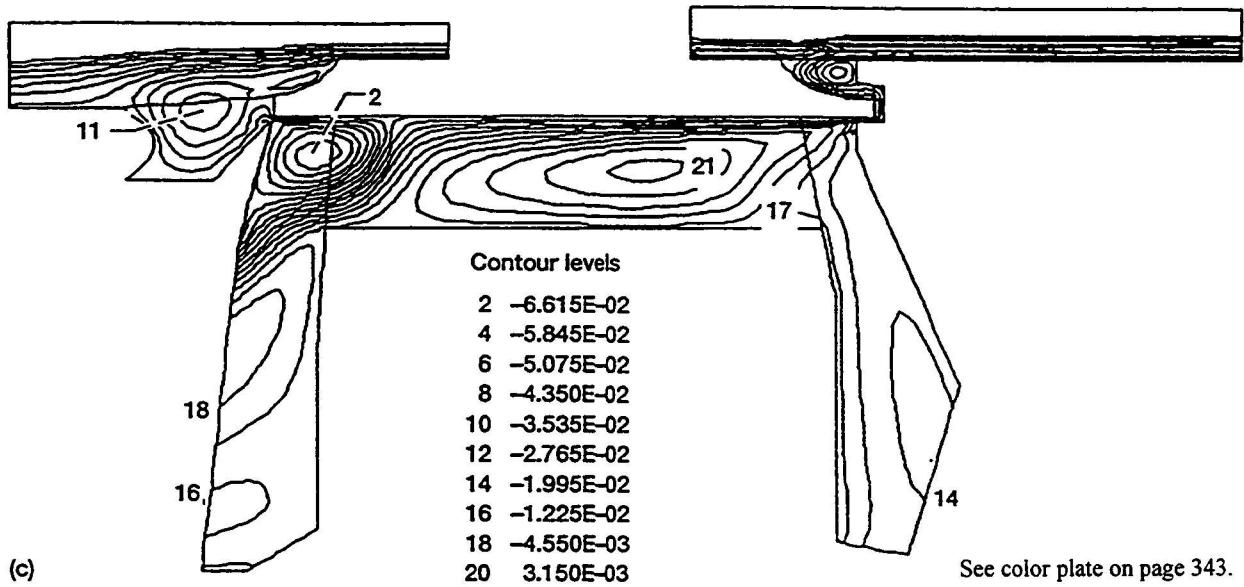
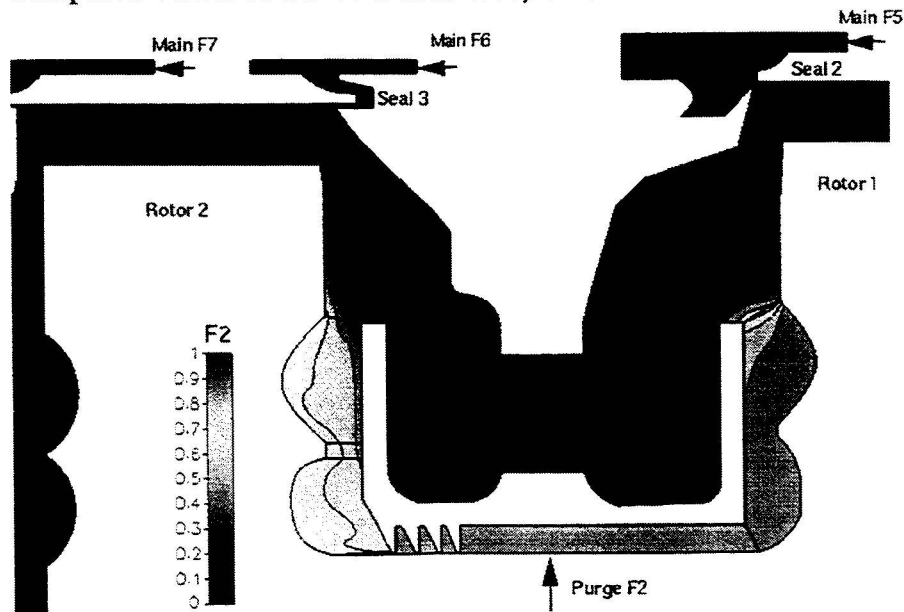


Figure 3 —Concluded. (c) Flow detail at seal 1, 2, and blade shank region to illustrate the complex vortical structure and main-path flow ingestion.

Mixture Fraction (Concentrations)

Computed Values of F2 Concentrations, Run No. 202



See color plate on page 345.

Figure 3 **Ingestion of main-path flow in multiple gas-turbine disc cavities**
UTRC/MSFC Large Scale Rig

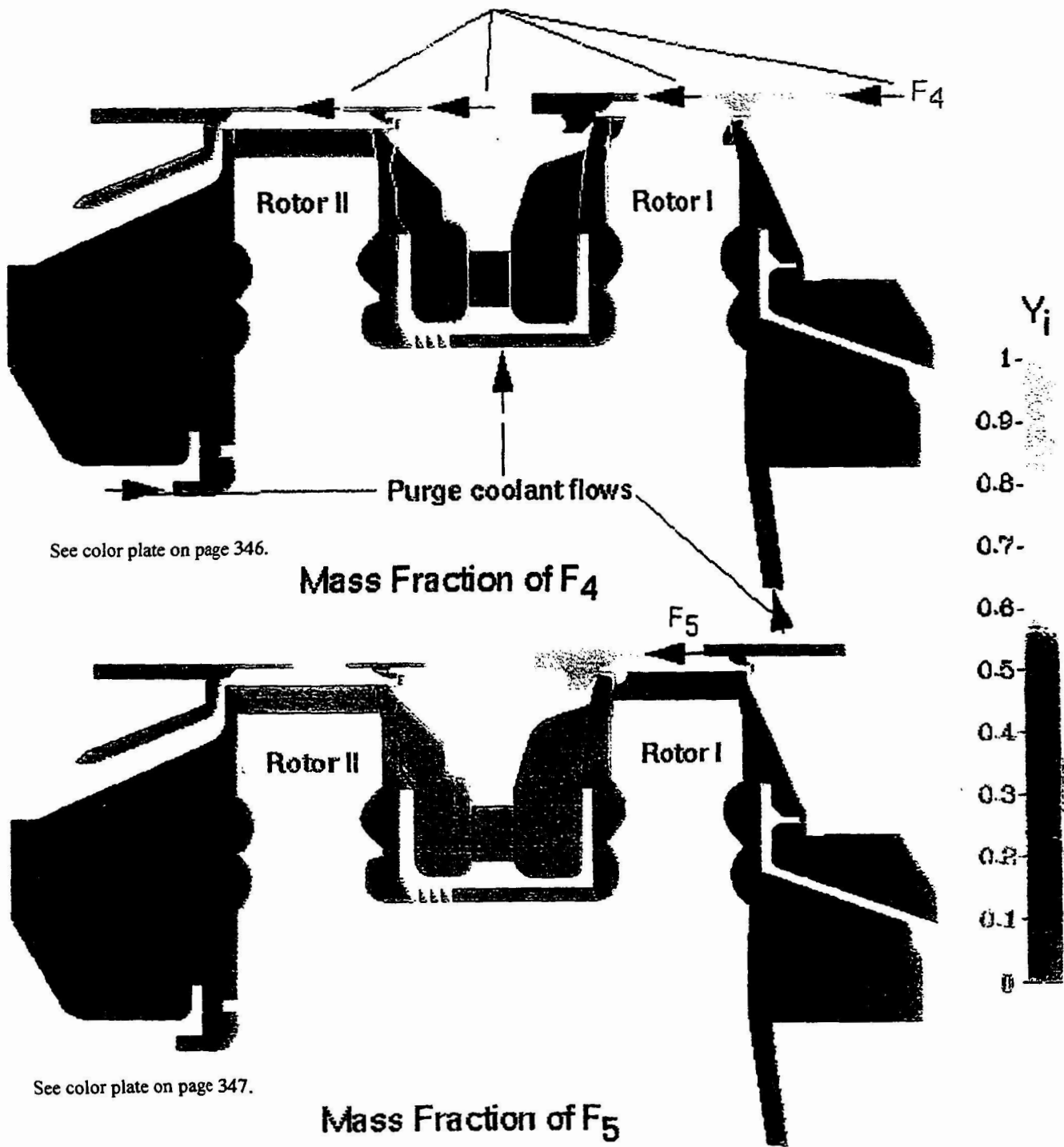
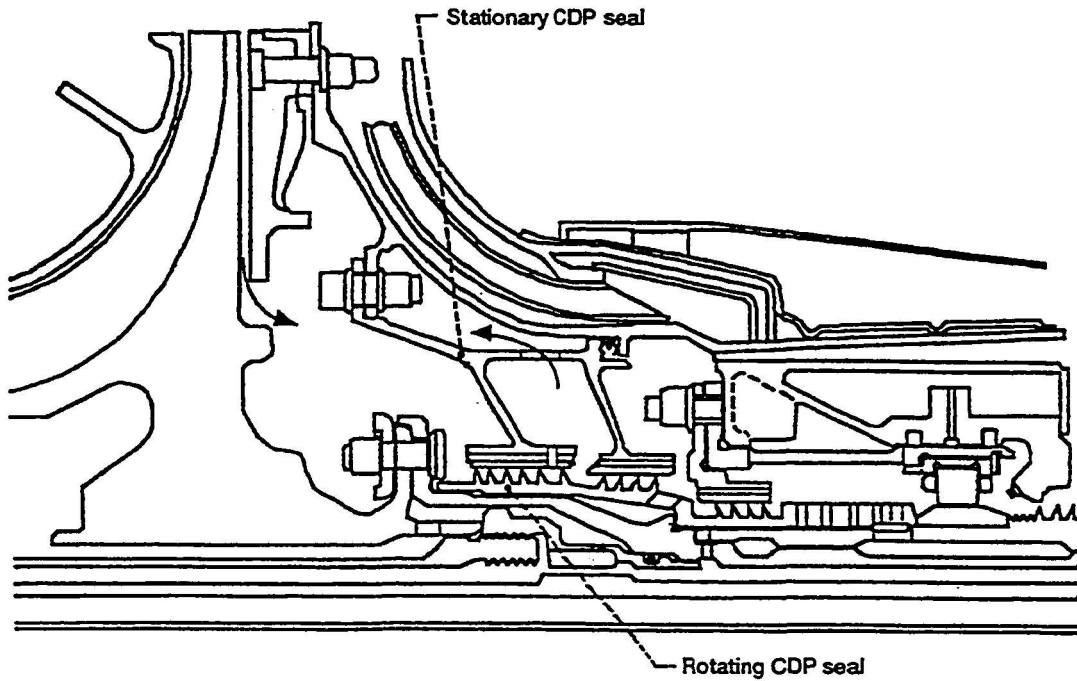
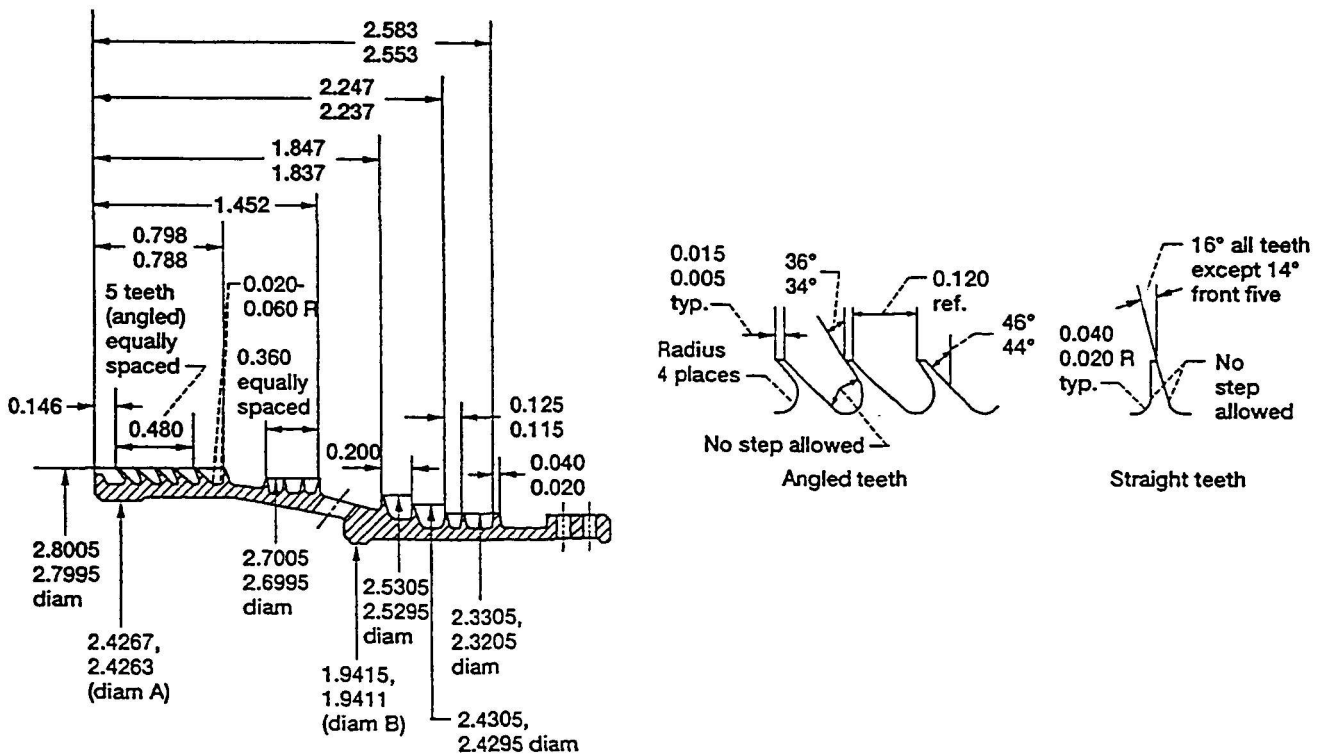
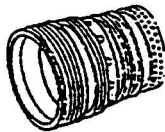


Figure 3 Ingestion of main-path flow in multiple gas-turbine disc cavities
UTRC/MSFC Large Scale Rig



(a) Labyrinth seal package and airflow.



(b) Schematic of labyrinth compressor discharge seal. (Seal teeth and axis established by diameters A and B to be concentric within 0.003 full indicator reading. No steps allowed on tooth face or at fillet radius. All dimensions are in inches.)

Figure 4—Labyrinth compressor discharge seal system.

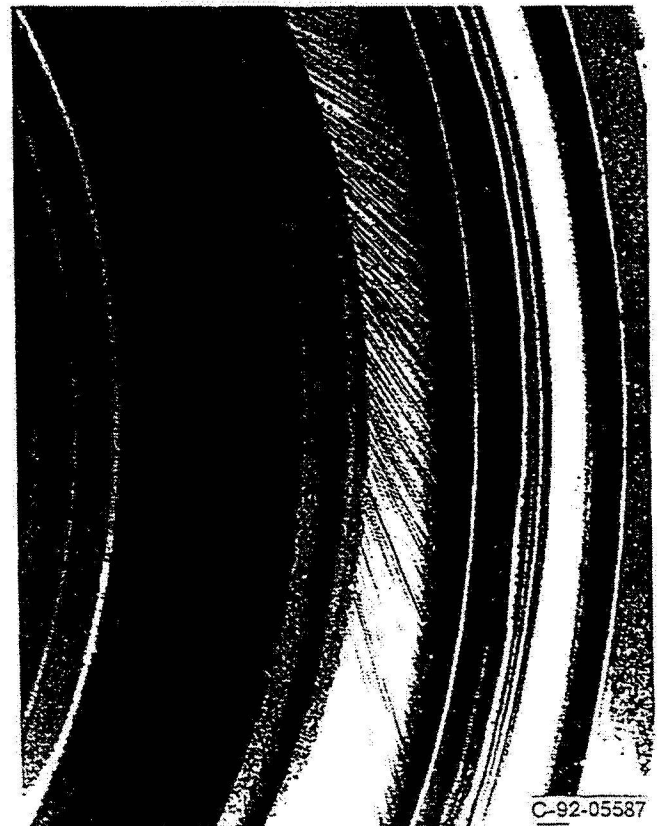
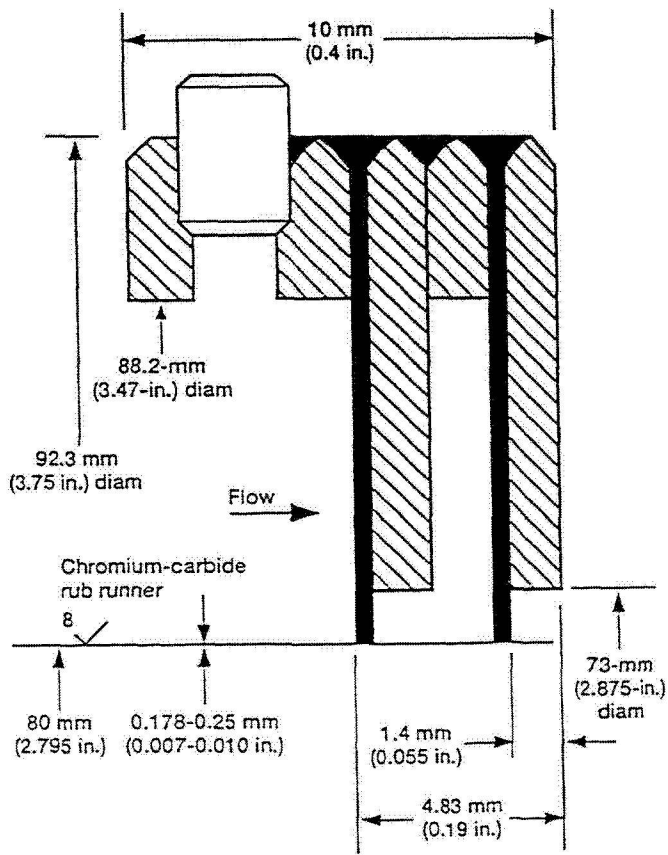
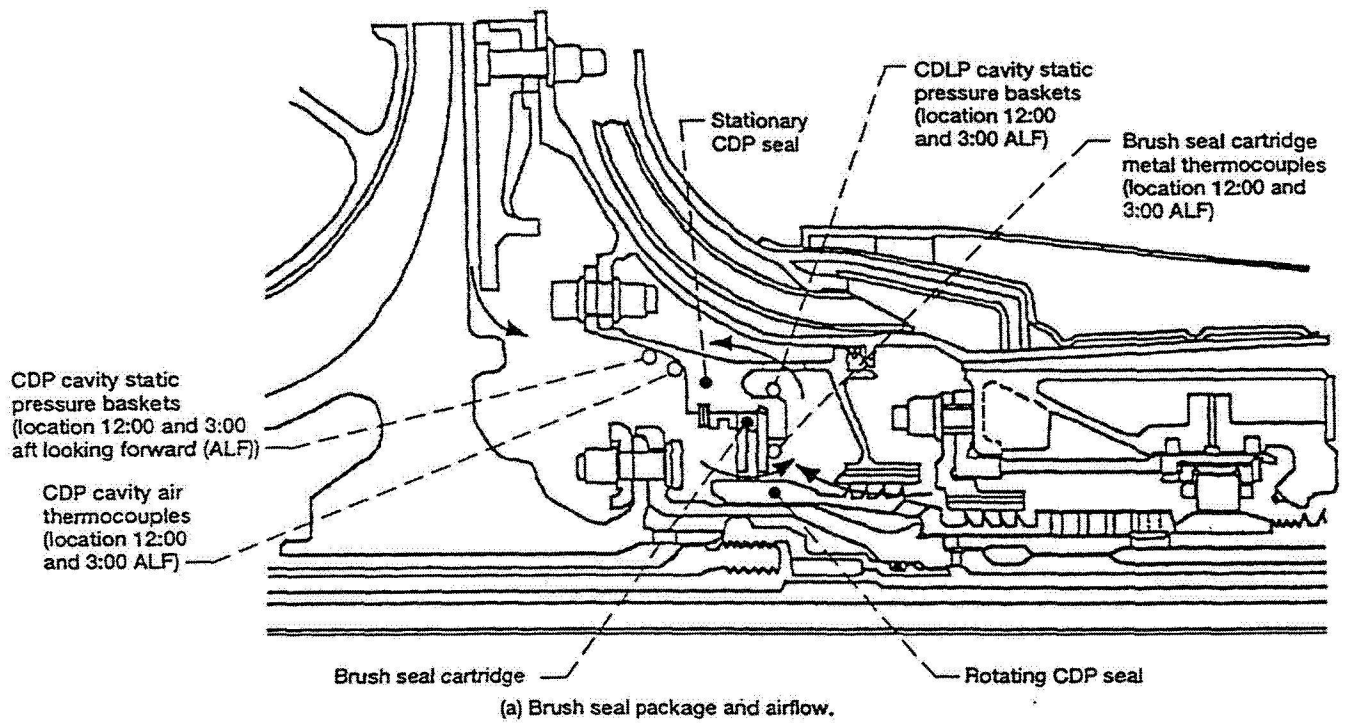


Figure 4 —Dual-brush compressor discharge seal system and schematic of airflow.

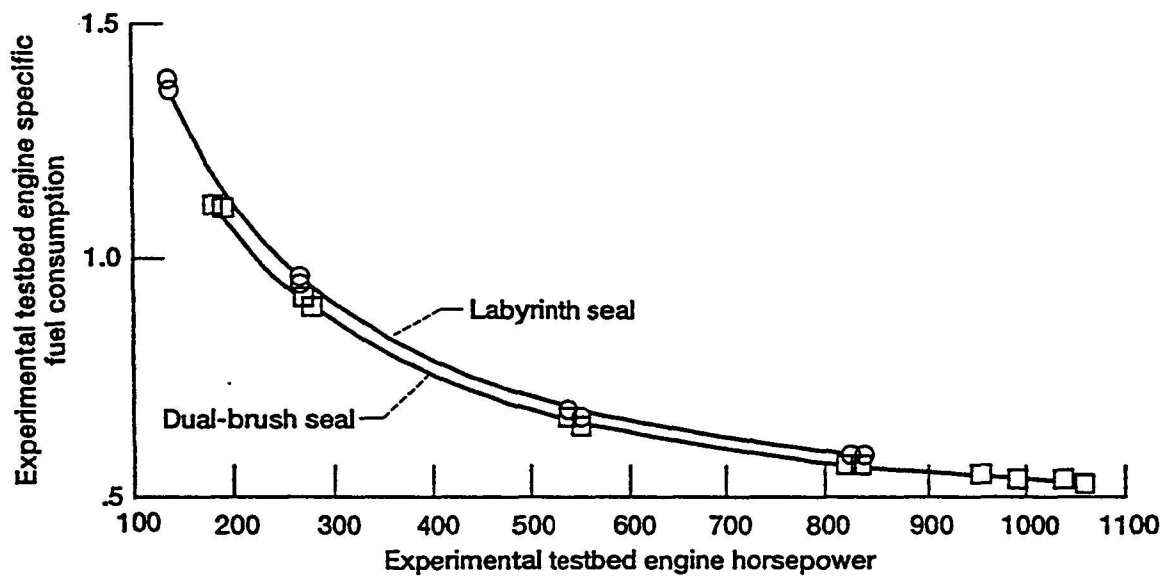
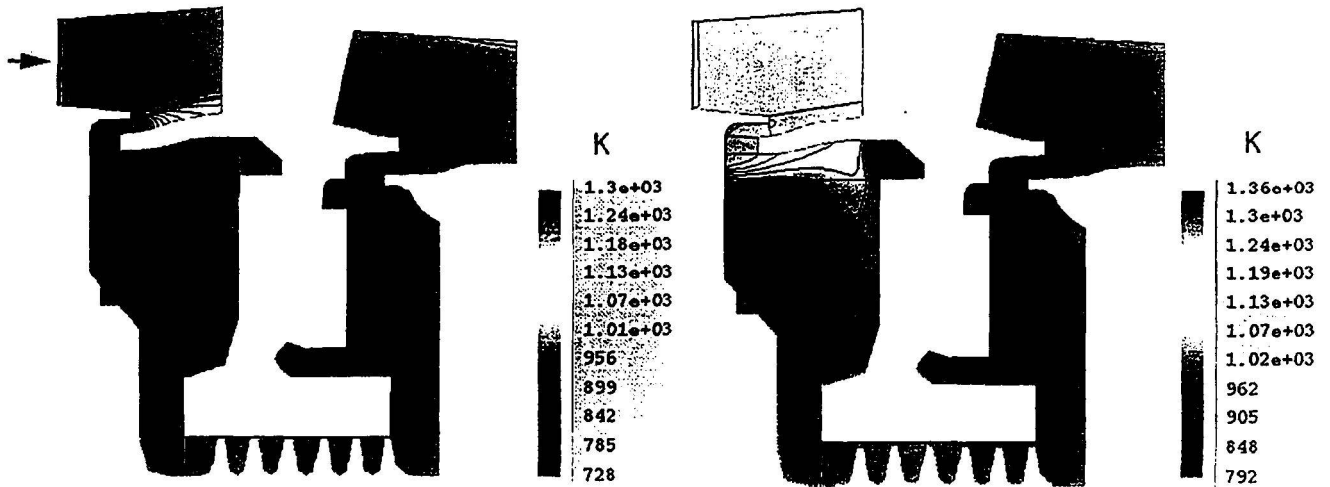


Figure 5 —Experimental testbed engine specific fuel consumption as a function of horsepower.

Figure 6 Temperature contours

Stage 1-2 Disk Cavities



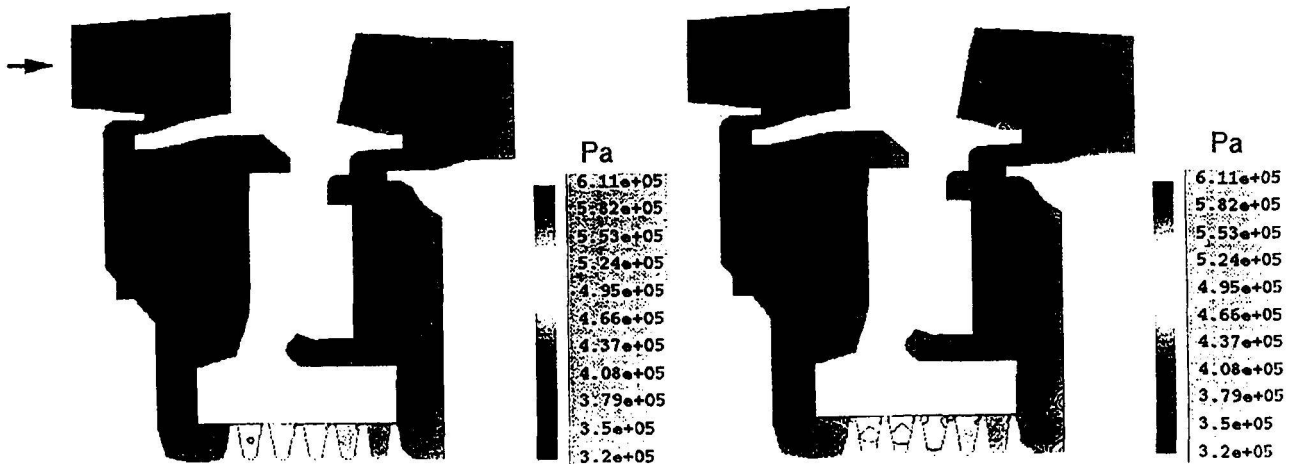
A. Labyrinth seal clearance = 0.012 in.

B. Labyrinth seal clearance = 0.024 in.

See color plate on page 348.

Figure 7 Stream Function

Stage 1-2 Disk Cavities



A. Labyrinth Seal clearance = 0.012 in.

B. Labyrinth Seal clearance = 0.024 in.

See color plate on page 349.

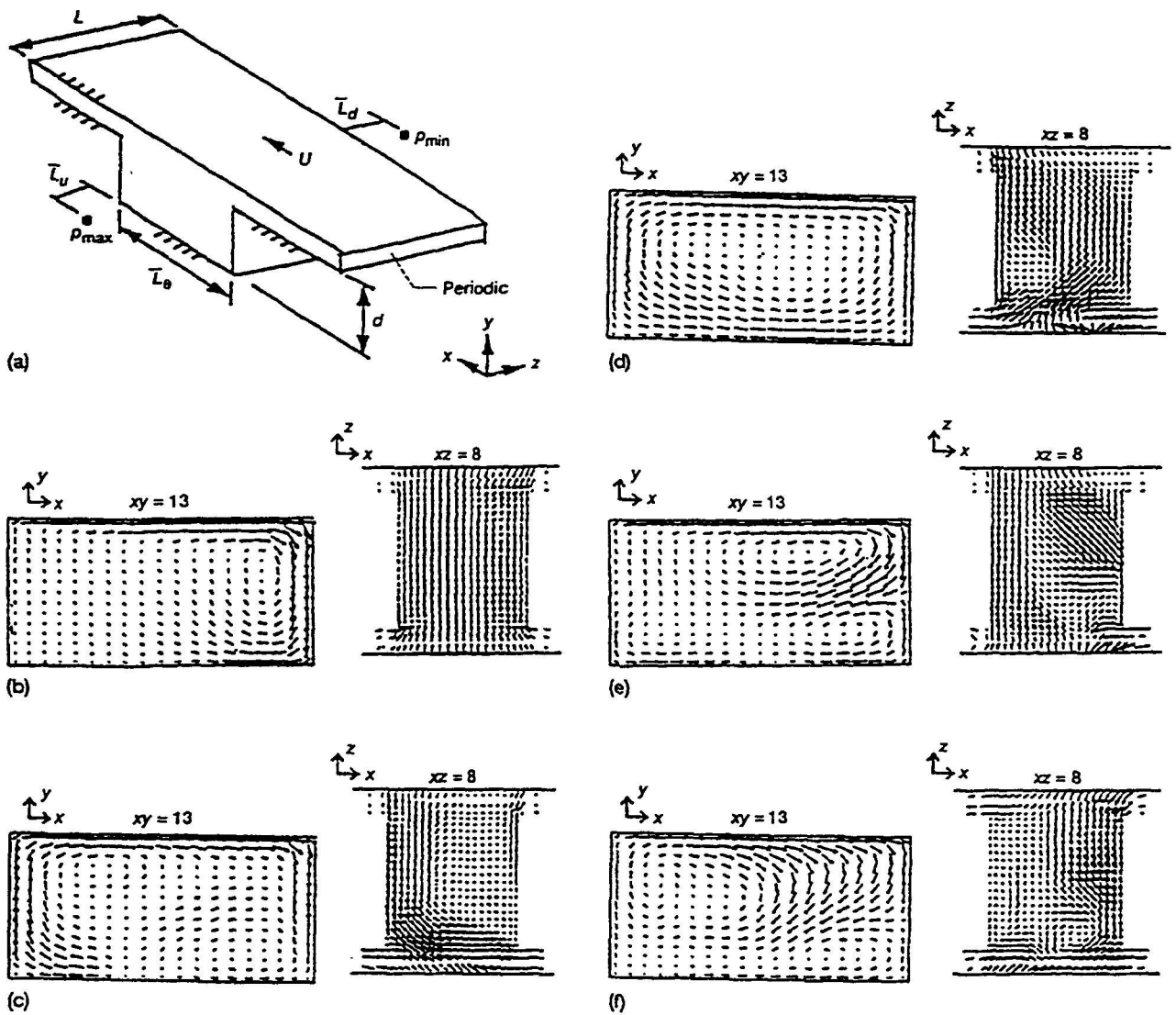


Figure 8 Velocity vector plots for a lid-driven cavity simulating a turbine blade passage at axial plane $xy = 13$ (near midplane) and radial plane $xz = 8$ (near midplane). (a) Flow geometry. (b) Base test case velocity vector plots at three selected axial planes: $xy = 4$ (near inlet), $xy = 22$ (near exit and radial planes), $xz = 1$ (near cavity bottom), $xy = 15$ (near cavity top). (c) Inlet corotating vortex injection near pressure side of simulated blade. (d) Inlet corotating vortex injection near suction side of simulated blade. (e) Inlet counterrotating vortex injection near pressure side of simulated blade. (f) Inlet counterrotating vortex injection near suction side of simulated blade.

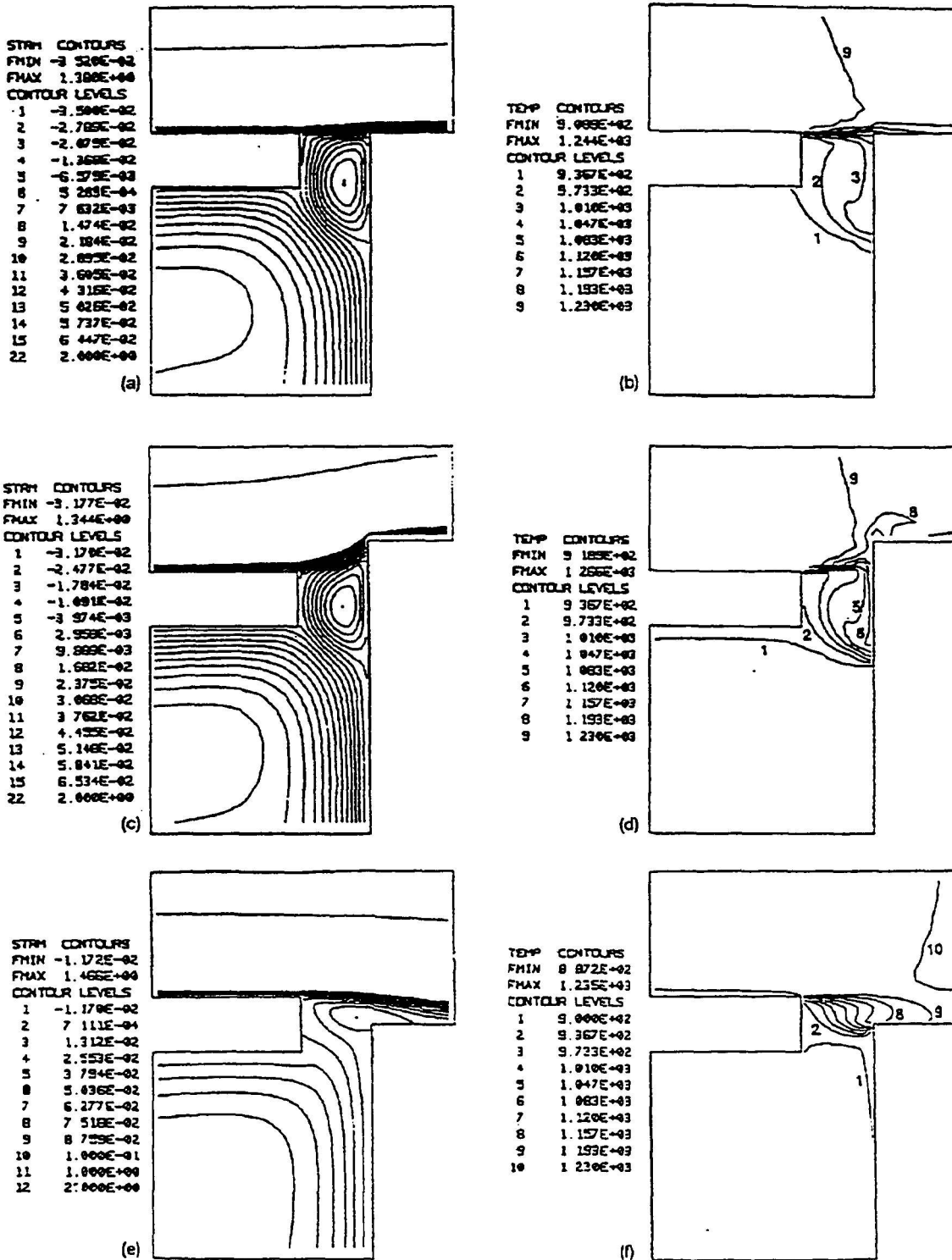


Figure 9 Streamline and isotherm contours near rim seal neck for simulated rotor-stator mismatch operation where $R = R_{cs} + e$. Base level case $C_q = 7200$ (see also fig. 37). (a) Eccentricity $e = 0$, streamlines. (b) $e = 0$ (isotherms). (c) $e = -0.5$ (seal neck thickness t), streamlines. (d) $e = -0.5$ (seal neck thickness t), isotherms. (e) $e = 0.5$ (seal neck thickness t), streamlines. (f) $e = 0.5$ (seal neck thickness t), isotherms.

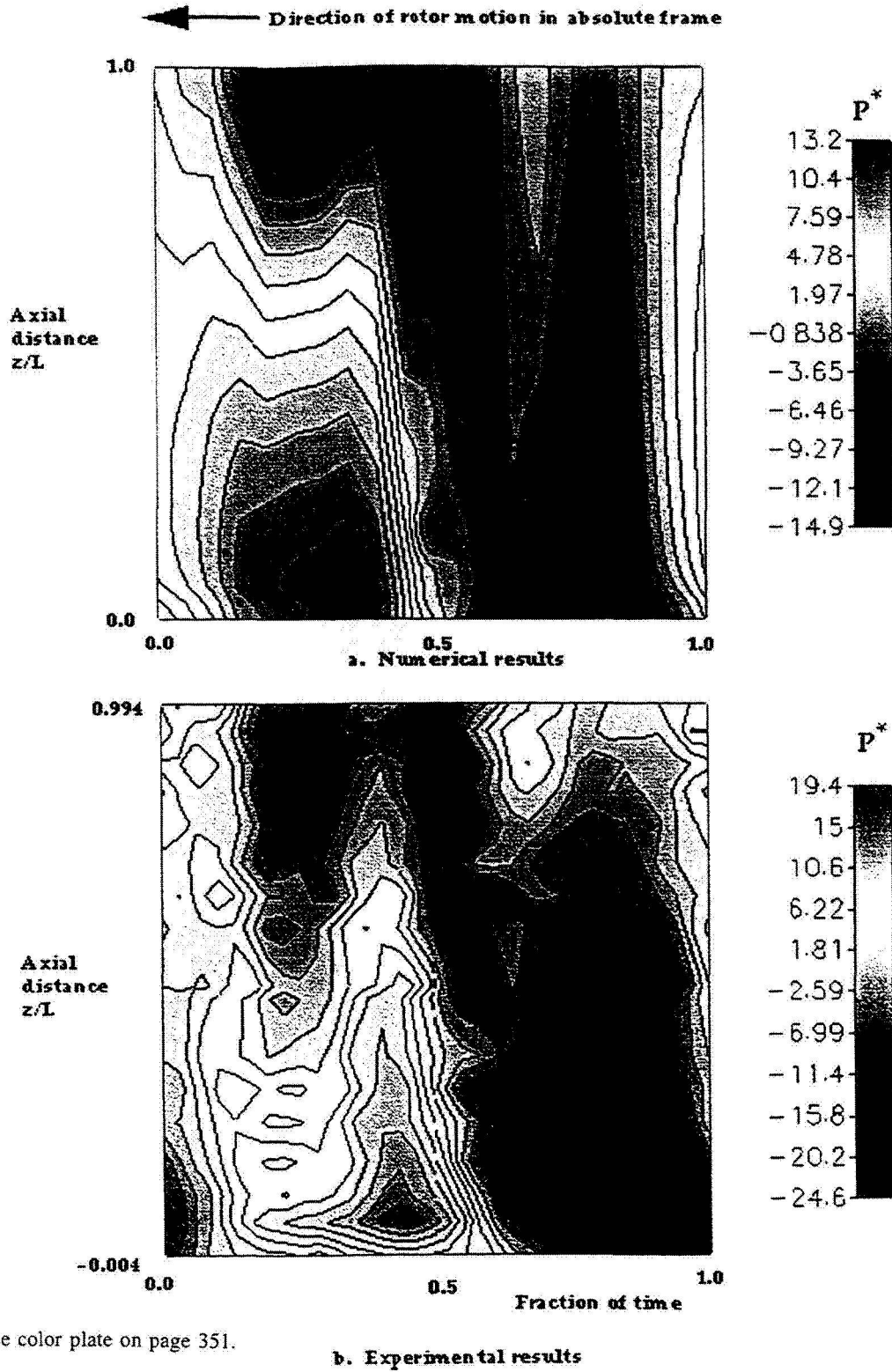
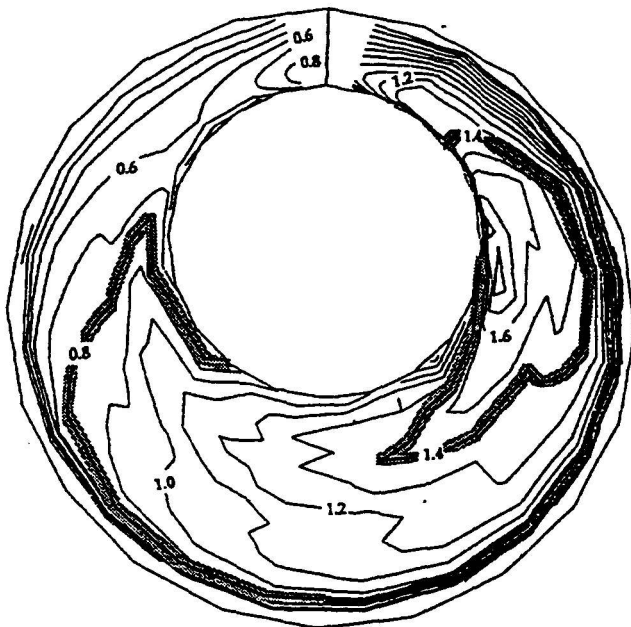


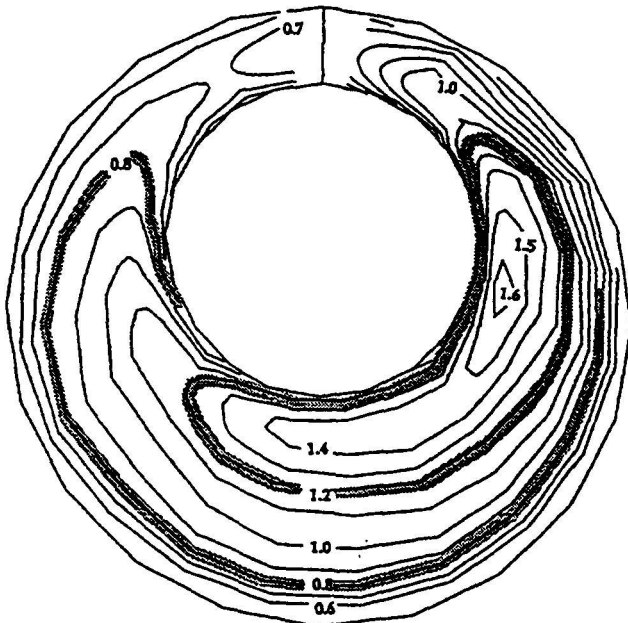
Figure 10 Comparison of the calculated and experimental non-dimensional pressures on the stator wall, $P^* = PL / (C\Delta P) ..$



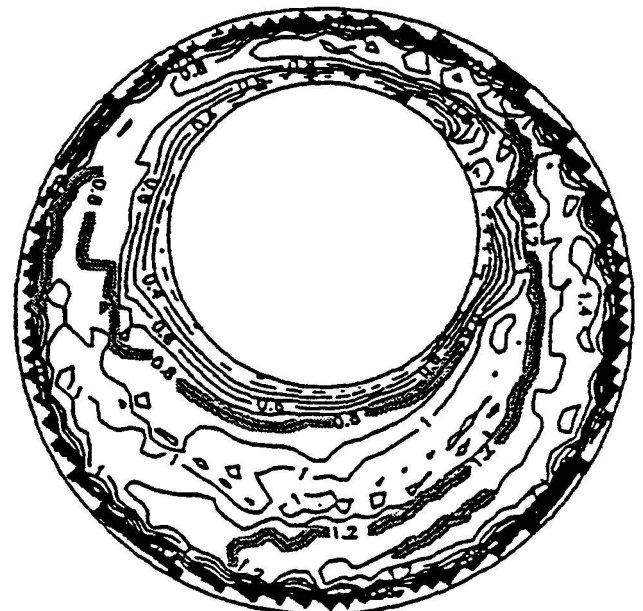
(a) $x/L = 0.00125$



$x/L = 0.0$



(b) $x/L = 0.2125$

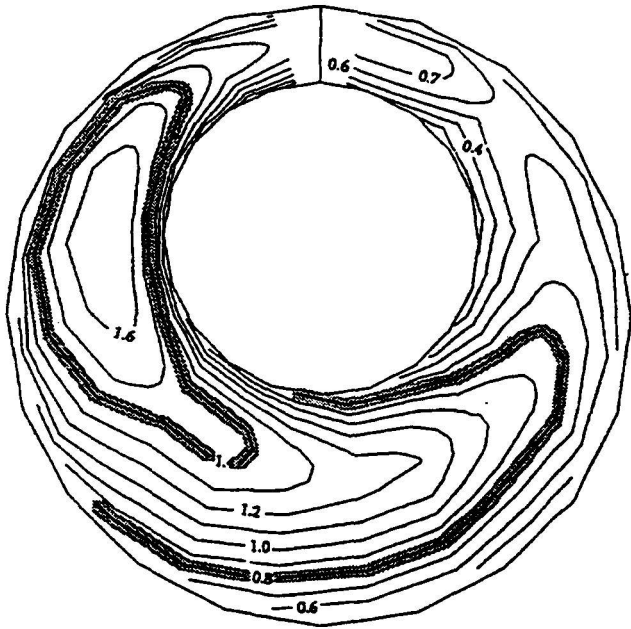


$x/L = 0.22$

Numerical

Experimental

Figure 11 —Contours of u_x/U_m at various cross-sections along the seal axial length x . Seal whirl and spin in counter-clockwise direction. Seal clearance exaggerated for clarity.



(e) $x/L = 0.9875$

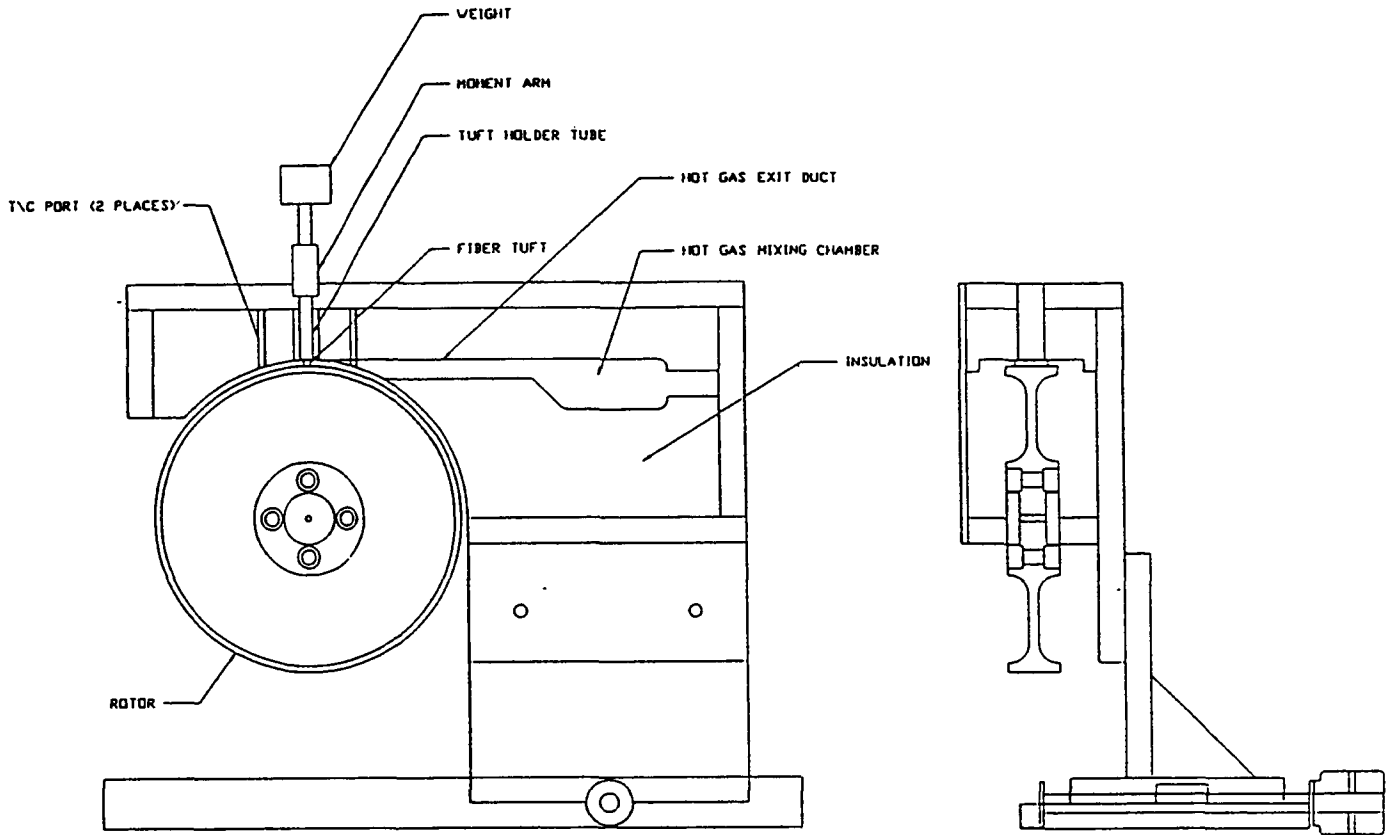
Numerical



$x/L = 0.99$

Experimental

Figure 11 —Concluded.

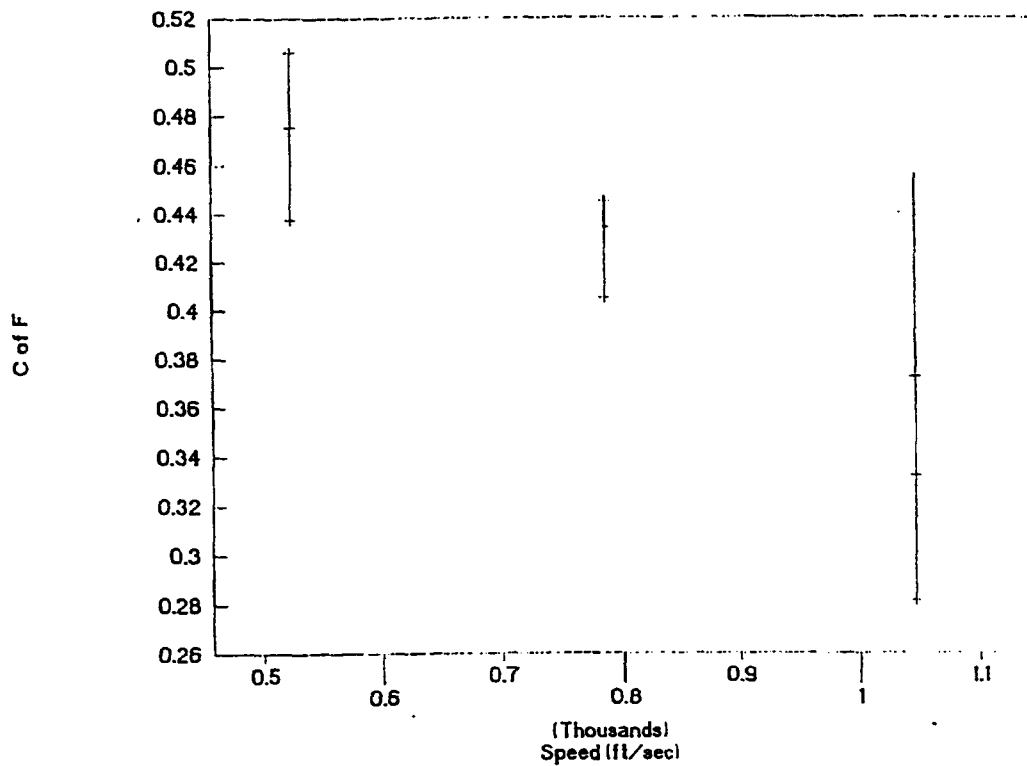


SECTION VIEWS OF FIBER / COATING TEST RIG

Figure 12, Reference 12

SiC on BN/PSZ

Cold Air(7.5 acfm) / Large Wt.



SiC on Bare Rotor

Ambient Air / Large Wt.

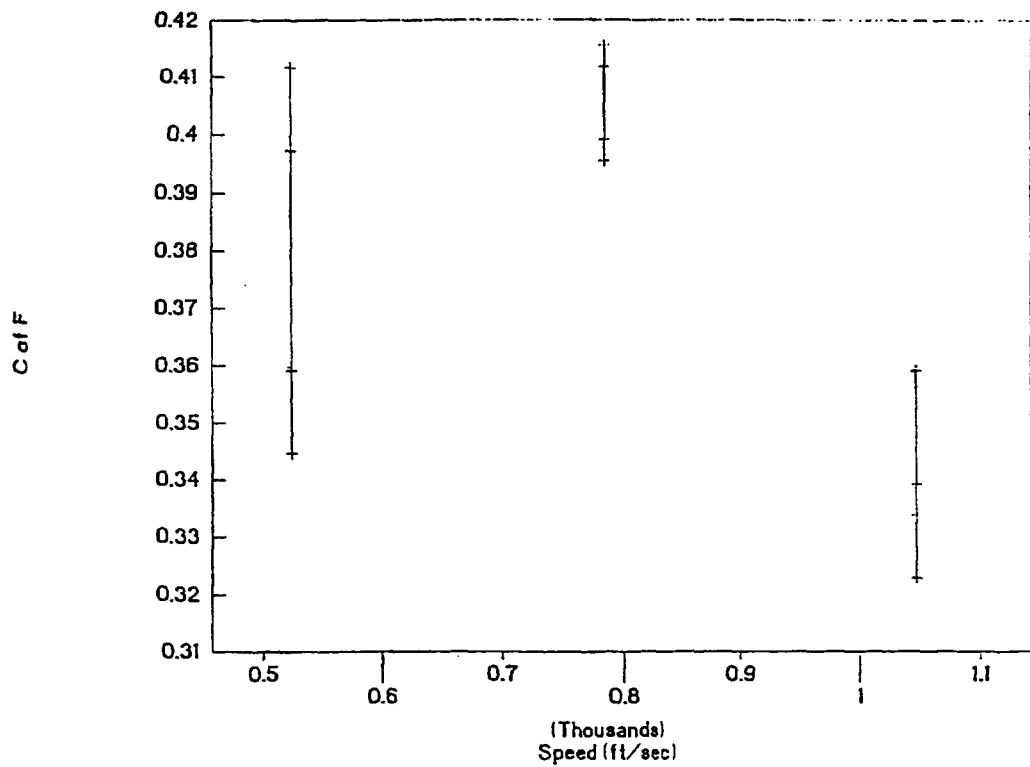
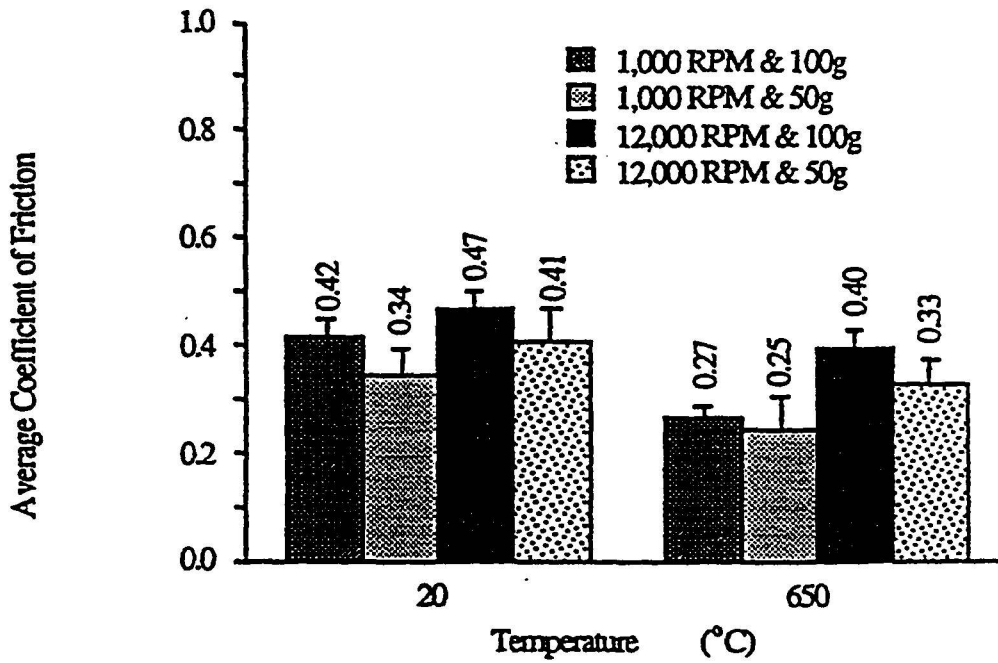
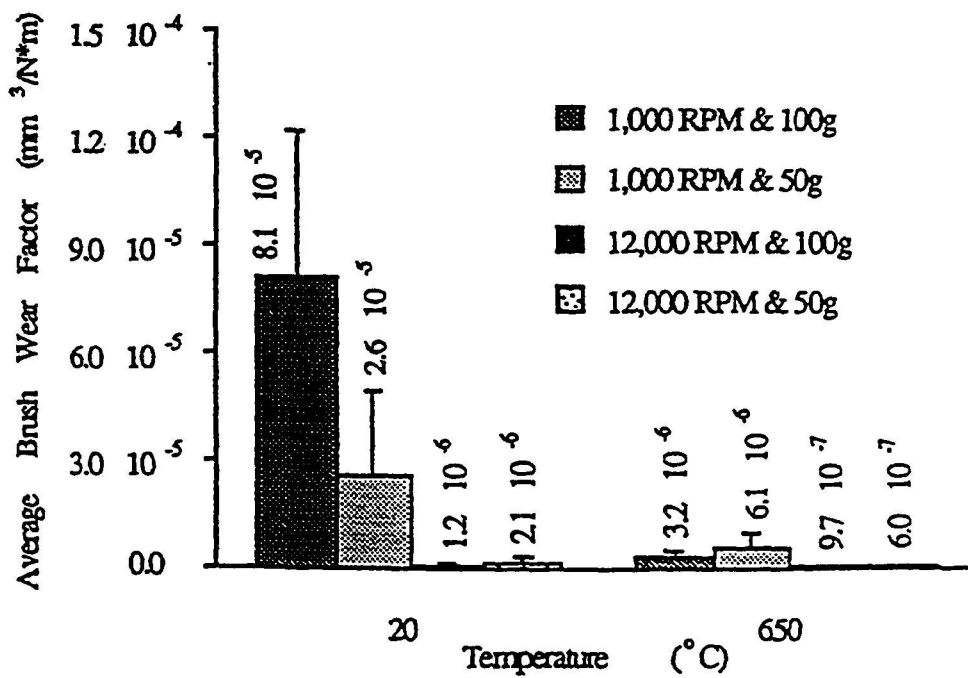


Figure 13

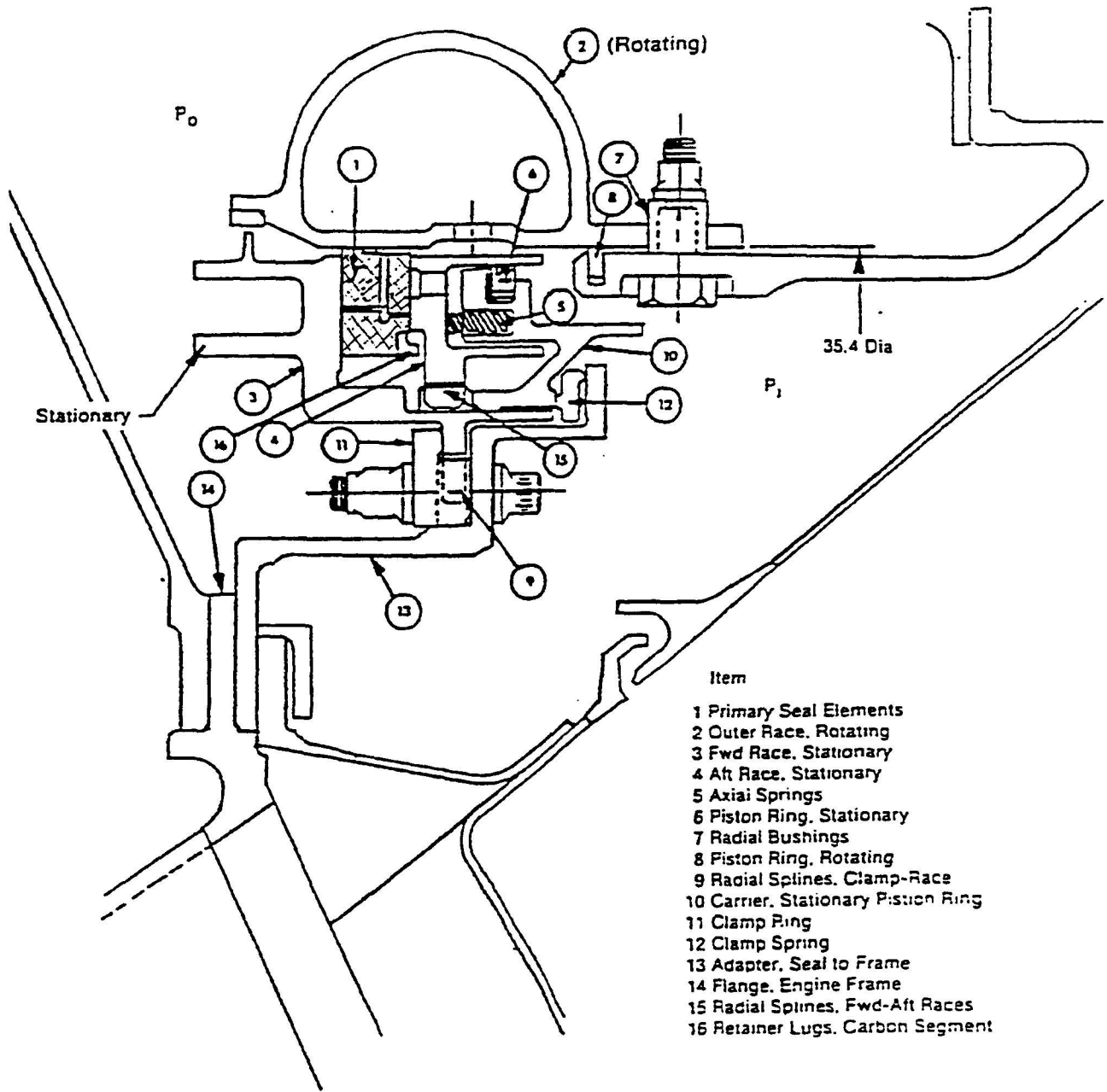


—Average friction coefficient of H25 tufts vs. I718 journal under various test conditions. Error bars represent standard deviation of averages of 9 test runs.



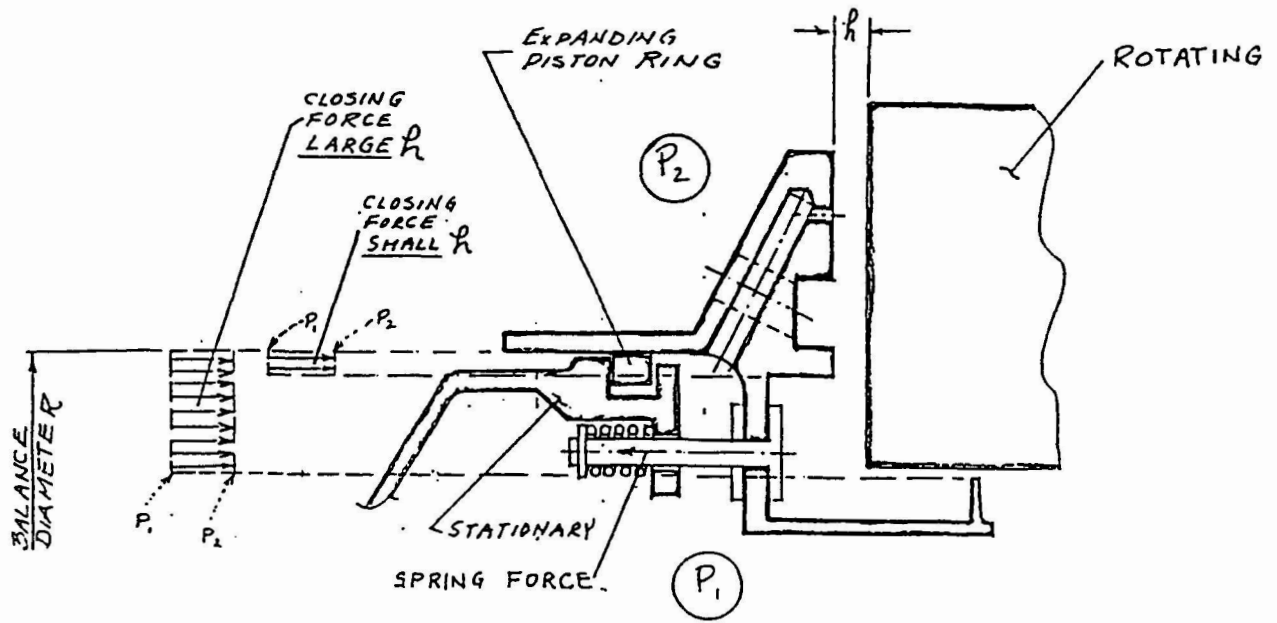
—Brush wear factor, in $\text{mm}^3/\text{N}\cdot\text{m}$ for H25 cobalt based superalloy bristles sliding against I718 nickel based superalloy shaft. Wear factor goal for adequate wear life is $10^{-8} \text{mm}^3/\text{N}\cdot\text{m}$.

Figure 14, Reference 5

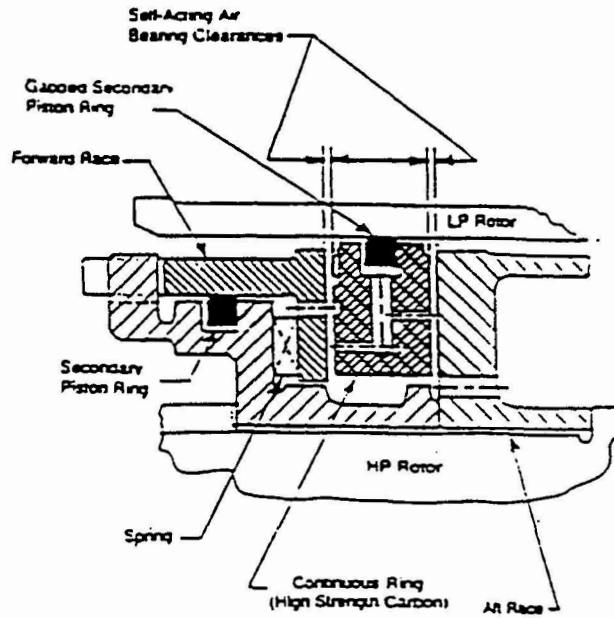


LARGE DIAMETER HYDROSTATIC SEAL

Figure 15, Reference 16



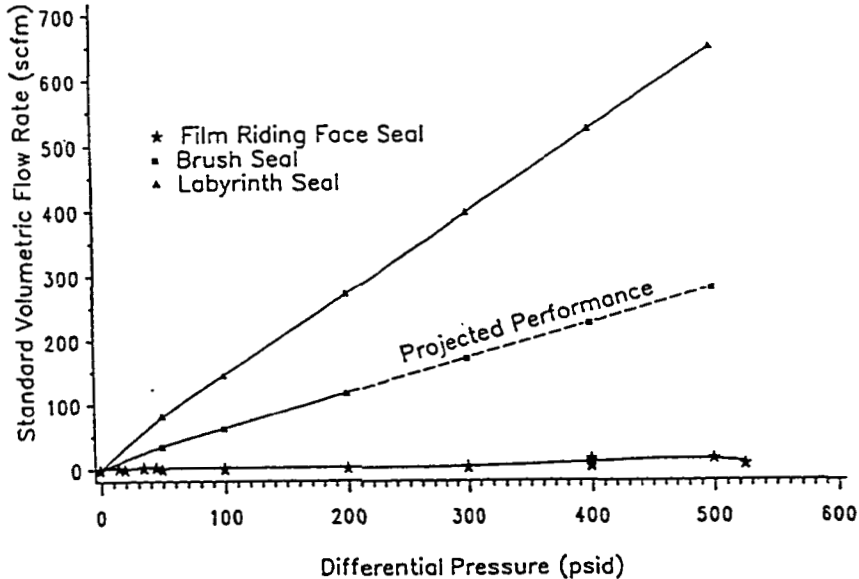
ASPIRATING GAS BEARING FACE SEAL



CONTINUOUS RING SEAL DESIGN

Figure 15 Concluded

Low Leakage of FRFS will provide substantial reduction in cycle specific fuel consumption:



- 1.5% relative to Labyrinth seal system
- 0.5% relative to Projected multi-stage brush seal

Figure 16, Reference 15

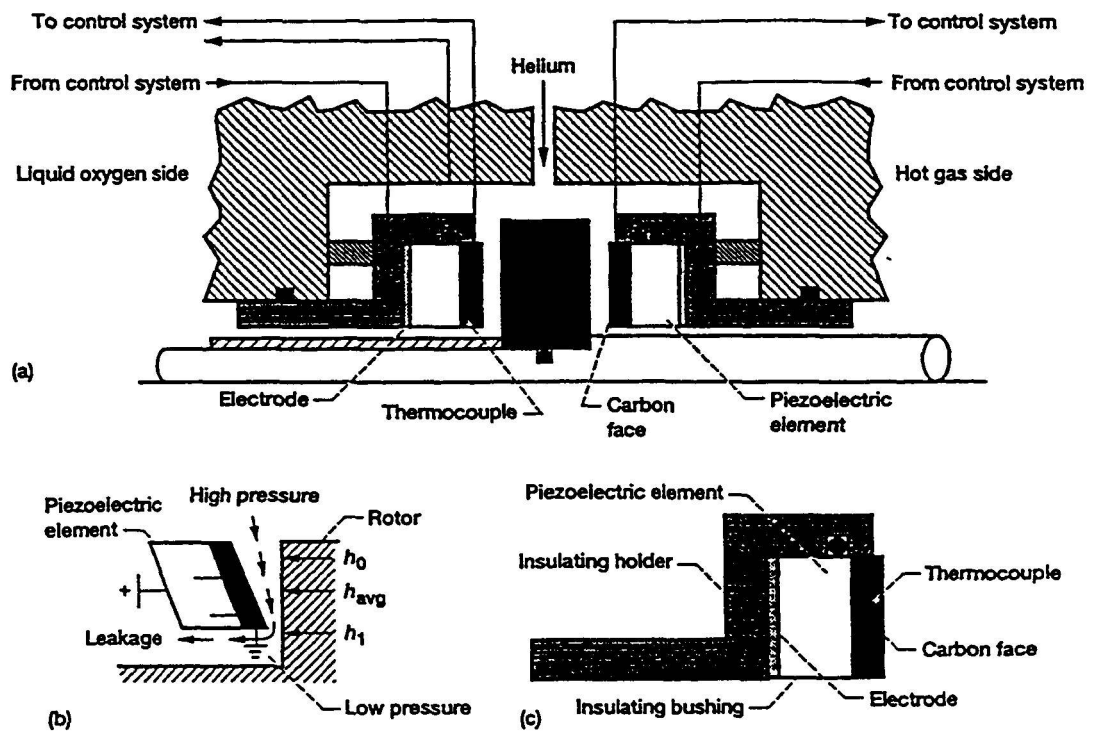


Figure 17 —Piezoelectric face seal configuration. (a) Helium purge seal (clearance greatly exaggerated). (b) Coned deformable face assembly. Coning, $\delta = h_0 - h_1$. (c) Face holder and deformable face assembly.

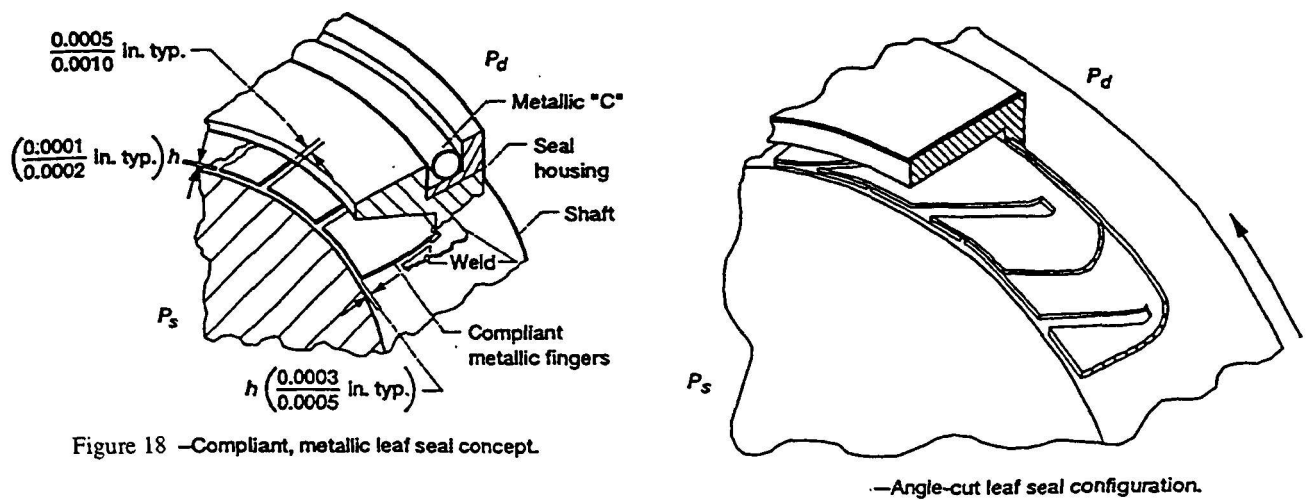
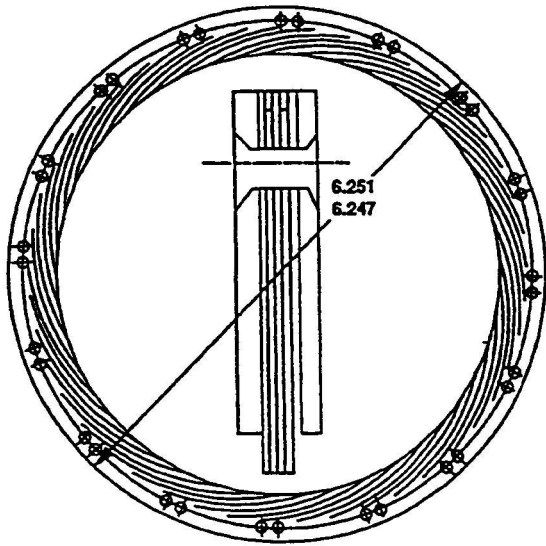
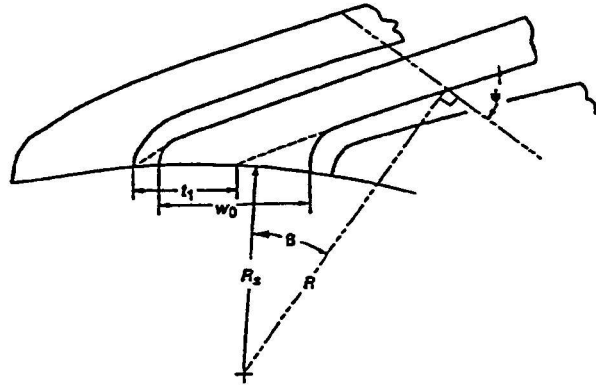


Figure 18 —Compliant, metallic leaf seal concept.

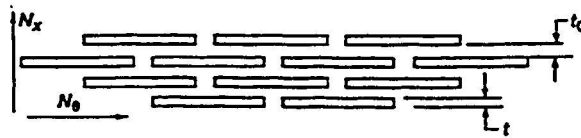
—Angle-cut leaf seal configuration.



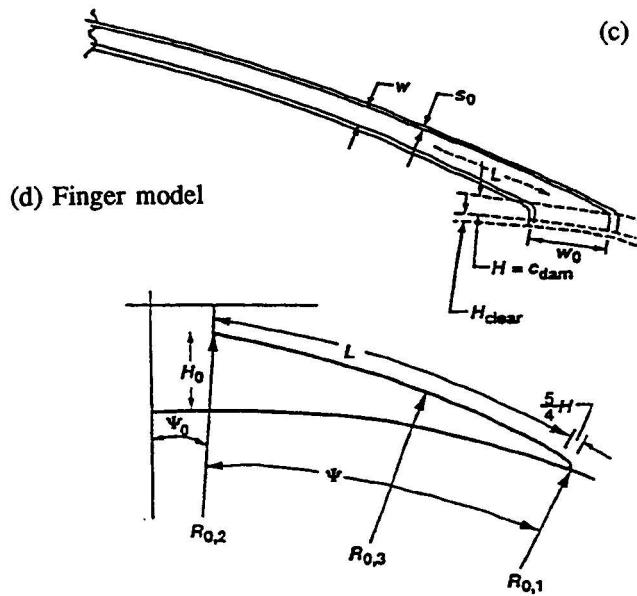
(a) Configuration



(b) Finger geometry at the interface



(c) Staggered fingers



(d) Finger model

Figure 19 —Finger seal model. $N_x = 4$; $s_0 = 0.006$ in.; $w = 5 s_0$;
 $w_0 = 5 w$; $H = 0.040$ in.; $H_0 = 0.375$ in.; $R_{0,1} = 4.1$ in.; $R_{0,3} = 4.3$ in.;
 $\psi = 31^\circ$; $\psi_0 = 6^\circ$; $t = 0.010$ in.; $t_0 = 0.02 t e^{-(\Delta P/2P_3)}$.

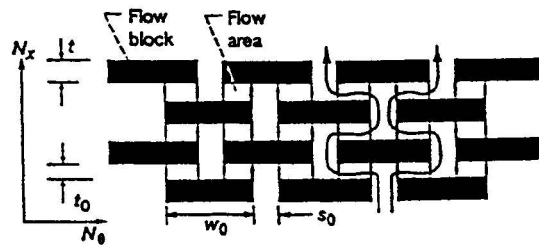


Figure 20 —Idealized finger seal footprint model.

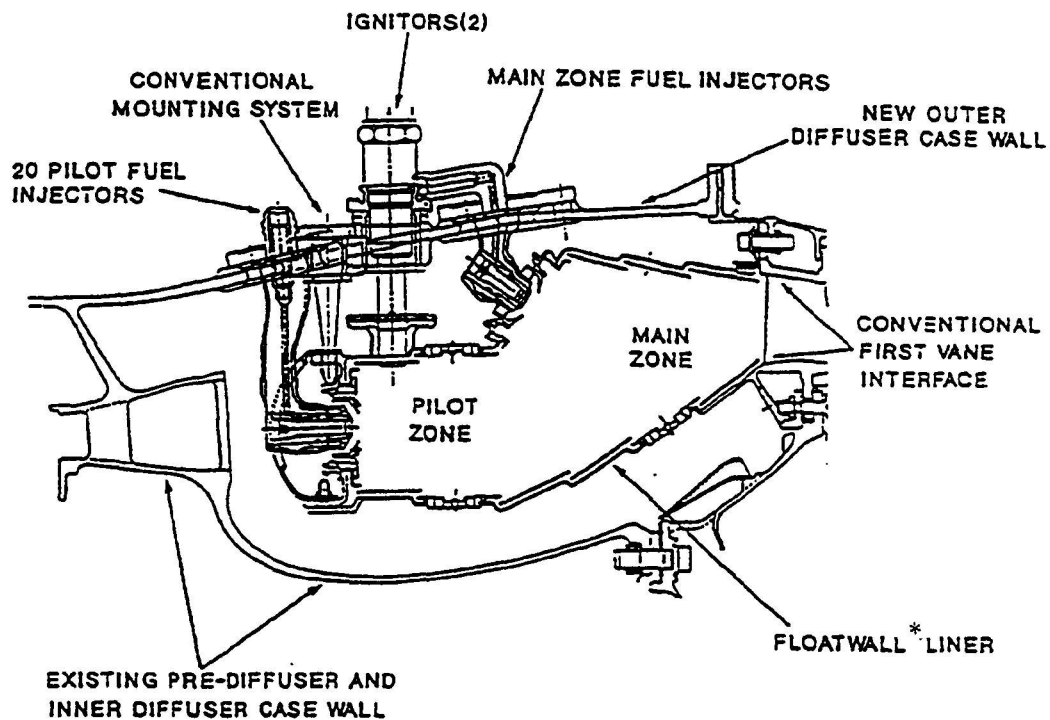


Figure 21, Reference 14 Pratt and Whitney axially-staged combustor

* Floatwall is a tradename of a product manufactured by the Pratt & Whitney. Trade names or manufacturers' names are used in this report for identification only. This usage does not constitute an official endorsement, either expressed or implied, by the National Aeronautics and Space Administration.

AEROSPACE SEAL REQUIREMENTS

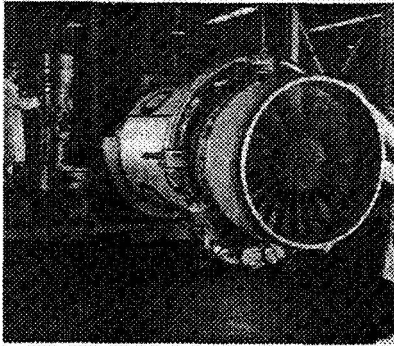
Bruce M. Steinetz and Robert C. Hendricks
NASA Lewis Research Center
Cleveland, Ohio

Cycle studies have shown the benefits of increasing engine pressure ratios and cycle temperatures to decrease engine weight and improve performance of commercial turbine engines. NASA is working with industry to define technology requirements of advanced engines and engine technology to meet the goals of NASA's Advanced Subsonic Technology Initiative. As engine operating conditions become more severe and customers demand lower operating costs, NASA and engine manufacturers are investigating methods of improving engine efficiency and reducing operating costs. A number of new technologies are being examined that will allow next generations engines to operate at higher pressures and temperatures. Improving seal performance - reducing leakage and increasing service life while operating under more demanding conditions - will play an important role in meeting overall program goals of reducing specific fuel consumption and ultimately reducing direct operating costs. This paper provides an overview of the Advanced Subsonic Technology Program goals, discusses the motivation for advanced seal development, and highlights seal technology requirements to meet future engine performance goals.

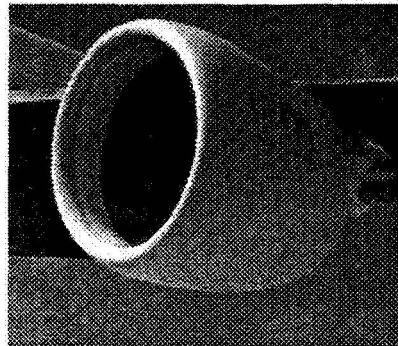
Outline

- o **AST Program**
- o **Joint NASA/Army Program**
- o **SBIR Seals Development**
- o **Compliant Seal Development (In House)**

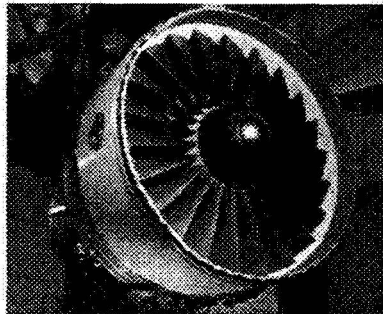
Modern Commercial Engines



Allison-AE3007



General Electric-GE90



Pratt & Whitney-PW4084

CD-94-64752

Advanced Subsonic Technology Initiative General Program Goals

Reduce:

- Direct operating costs (+ interest) by up to 5%
- Engine fuel burn up to 10%
- Engine oxides of emission by $\geq 50\%$
- Noise by 7dB

Strengthen U.S. competitiveness into next century and beyond.

CD-94-64756

Advanced Subsonic Technology

14.3 Seals/Secondary Air Delivery

Goal:

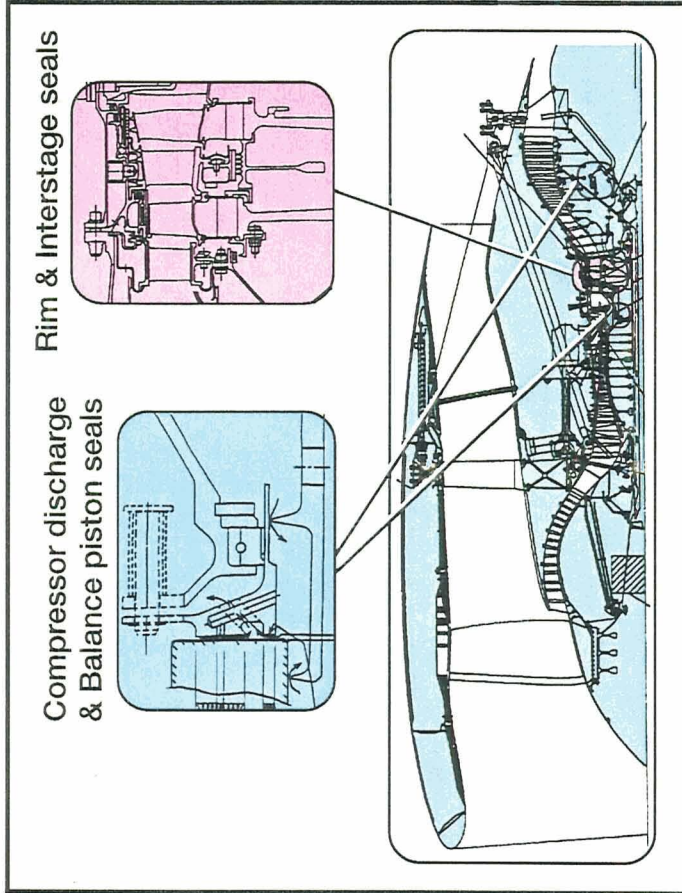
Develop and demonstrate advanced seals and design/analysis methods to meet AST engine goals.

Approach:

Assess feasibility of required sealing technologies through component testing. Demonstrate seal performance under engine-simulated conditions. Transition mature seal technologies to engine service.

Schedule:

- + Evaluate performance of robust, low leakage, large diameter seal FY96
- + Demonstrate large diameter seal in engine test FY99
- + Measure time averaged/time resolved rim seal cavity conditions FY97
- + Validate comprehensive secondary/main flow analysis tool FY97
- + Demonstrate performance of CDP seal in gas generator/engine test FY00



Funding:

WBS	FY96	FY97	FY98	FY99	FY00	FY01	TOTAL
14.3	1337	1932	3105	3250	1100	0	10,724

CD-95-70819

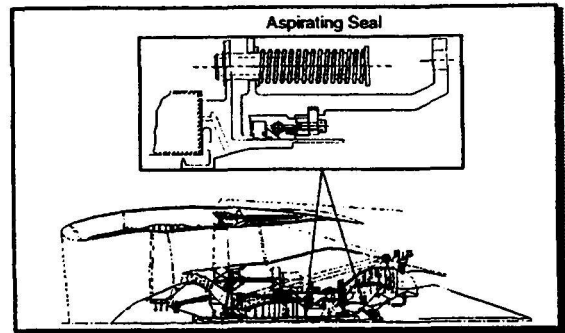
Transport Aircraft Seal Technology Benefits 2005 EIS

Seal Technology	Study Engine	Co.	System Level Benefits
Balance Piston Aspirating Seals (3ea)	GE90/AST Transport	GE	-1.29% SFC
Film Riding Face Seals CDP/Preswirl Locations	AST Regional	Allison	-.76% SFC
Adv. Tech. Brush Seals Turbine Rim Locations (2 ea)	AST Regional	Allison	-1.67% SFC
Film Riding Circumferential Seals Turbine Rim Locations (2 ea)	AST Regional	Allison	-1.8% SFC
Turbine Blade Tip Active Clearance Control	AST Regional	Allison	-1.36% SFC
Compressor Blade Tip Passive Clearance Control	T-55	Allied/ Lycoming	-.3% SFC

Aspirating Seal Development

Objective:

Investigate feasibility of large (36") diameter aspirating seals for turbine balance piston locations and demonstrate in engine test.



Approach:

- + Perform sub-scale and full-scale seals tests to optimize seal characteristics
- + Demonstrate ability to safely follow once-per-rev and maneuver tilt rotor run-outs
- + Evaluate seal's resistance to potential dust-ingestion
- + Develop and validate analytical methods to perform seal sensitivity studies under off-design conditions.
- + Test seal on engine test bed and evaluate acceptability for engine service.

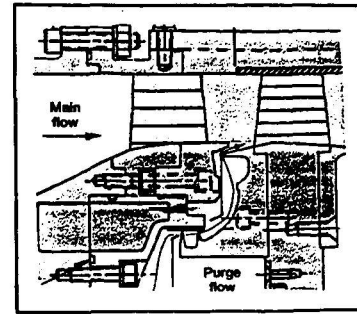
Near Term Schedule:

- +Evaluate performance of robust, low leakage, large diameter seal FY96

UTRC Cavity/Rim Seal Experiment

Objectives:

Characterize turbine cavity/rim seal environment and develop an optimized design to minimize purge requirements and mitigate hot gas ingestion.



Approach:

- + Obtain time-avg./time-resolved pressure and velocity distributions to examine rim seal ingestion mechanisms for an AST high work turbine.
- + Develop physical models of ingestion processes
- + Develop improved/optimized design concept based on operating conditions
- + Determine film cooling benefits of purge on gas-path side of blade platform
- + Evaluate nature of purge flow entering main stream and identify potential effects on turbine efficiency.
- + Document findings in usable format for anchoring advanced time-avg./time-resolved 3-D CFD analyses techniques.

Schedule:

Complete fabrication/instrumentation of airfoils and rim seal cavity model	2Q FY95
Complete baseline geometry experiments	1Q FY96
Complete parametric geometry experiments	4Q FY96
Complete improved geometry experiments	2Q FY97
Deliver complete data set	3Q FY97

NASA Research Announcement (NRA)

Elements:

- + Two step (PRDA-like) process:
 - Company submission of abstracts responding to NRA Topics of Interest
 - Company submission of full-proposals
- + Term: FY96 - FY00 with possible large-scale technology demonstration FY00-01

Schedule:

June 2	Receipt of abstracts
June	NASA Technical review of abstracts
July 7	Letter of encouragement for full proposals and detailed costs.
August 23	Receipt of full proposals
end Oct.	Final proposal evaluation complete
January	Contracts awarded

Joint NASA/Army Seal Program

Why Seals?

- High return on technology \$ investment
Same performance goals possible through modest investment in the technology development
(e.g. 1/5th to 1/4th cost of obtaining same performance improvements re-designing/re-qualifying the compressor)
- Close correlation between percentage leakage reduction and percentage increased thrust or decreased SFC
- New seal technologies offer significant leakage reductions assisting in meeting engine goals

TURBINE ENGINE SEAL DEVELOPMENT NASA/ARMY

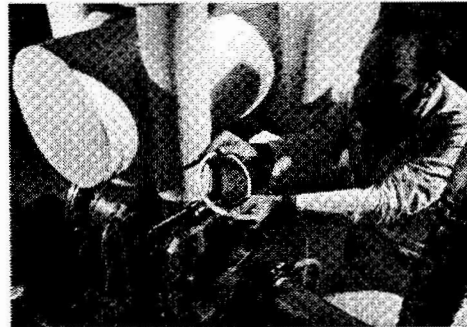
OBJECTIVE

- Develop durable, high temperature seals to meet demands of next generation subsonic and supersonic engines.

DELIVERABLES

- Validated analytical codes and data bases for use in design of high temperature, high speed brush, contacting and other advanced seals.

P.O.C. B.M. Steinetz/R.C. Hendricks



PROG SCHEDULE

TASKS	FY	93	94	95	96	97
In-house bench tests; data analysis; flow modeling; material screening.		[Hatched bar]				
CFD brush seal analyses NASA/CFDRC SBIR I & II.				[Hatched bar]	[Hatched bar]	
Advanced concept development: high temp. brush; floating ring brush; contacting seal.		[Hatched bar]				
Upgrade seal test facility (temps. to 1500° F; accelerated life).				[Hatched bar]	[Hatched bar]	
Engine tests.						[Hatched bar]

Accomplishments FY 93-95

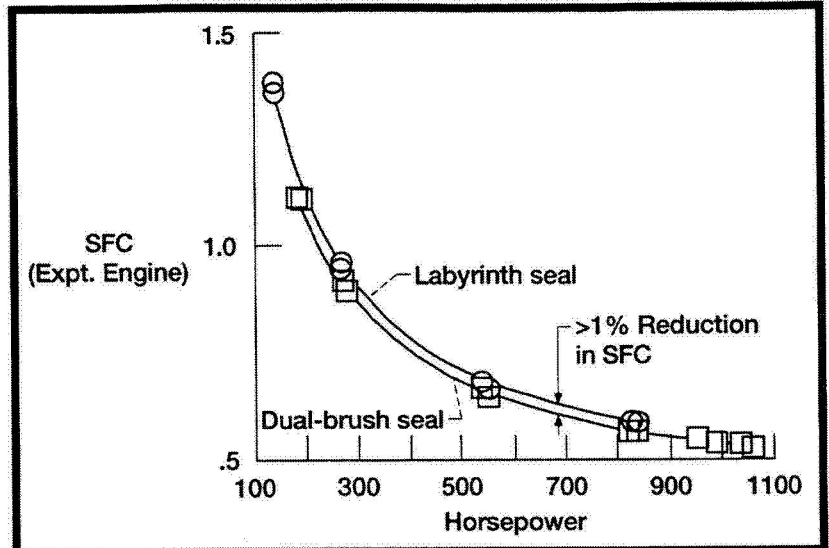
- Allison/NASA/Army seal study identifies large (2-5%) SFC reductions implementing advanced seals in IHPTET/AST engines.
- Demonstrated a 1% reduction in T-700 SFC substituting a dual brush seal for labyrinth CDP seal.
- Tested advanced seals for William's, Allied Signal, Cross and Technetics.
- Successfully tested first-ever ceramic brush seals to ~1000 F.
- Evaluated friction/wear of H25 brush segments vs. TiC, Al2O3, Zr2O3, and DLC diamond coatings. (R.T. & 1200 F).
- Began SBIRs to:
 - + develop a low wear floating ring brush seal
 - + develop CFD flow model of brush seals with frictional heating

Plans FY 95-97

- Complete design/fabrication of high temperature seal rig upgrades.
- Test advanced seal concepts (brush, contact, floating brush, other).
- Perform coupled secondary-to power-stream (including transonics) calculations with industry/validate methods.
- Initiate coupled fluid/thermal/structural solver for seal design.

CD-95-71305

Brush Seals are Promising Alternative to Conventional Labyrinth Seals



Requirements to meet next generation engine goals:

- Improved designs for life and reliability
- High temperature materials/coatings
- Improved high temperature lubricants

P.O.C. Bob Hendricks (216) 977-7507
Bruce Steinetz (216) 433-3302

CD-94-68758

SBIR Seal Development

Hybrid Floating Brush Seal Feasibility Study

NASA SBIR Phase I
B&C Engineering/University of Akron

Objective:

Assess feasibility of unique hybrid floating brush seal to reduce brush seal wear by floating brush seal in an air-bearing carrier.

Approach:

- + Perform design analyses to size hydrostatic air bearing to float brush seal carrier
- + Design/build hybrid seal
- + Evaluate seal feasibility using University of Akron facilities

Schedule:

Complete design	March, 95
Complete fabrication	June, 95
Complete feasibility demonstration	June, 95

Potential Customers:

- + Aircraft engine industry
- + Durametallic Seal Company
- + Power generation industry
- + Other

CFD Brush Seal Analysis

NASA SBIR Phase I
CFD Research Corp.

Objective:

Develop integrated thermal/fluid/structures brush seal analysis methodology

Approach:

- + Adapt unstructured 3-D Navier Stokes code to model the fluid flow through porous brush
- + Implement the conjugate heat transfer and frictional heating capabilities to assess brush seal thermal response to brush-rotor friction and local flow conditions.
- + Validate analysis tools using available experimental data.
- + Initiate the development of dedicated brush seal flow model that can be coupled with global secondary-air system analysis procedures.

Schedule:

CFD code and automatic grid generation adapted to brush seal	April, 95
Complete brush seal flow/heat transfer initial simulations	June, 95

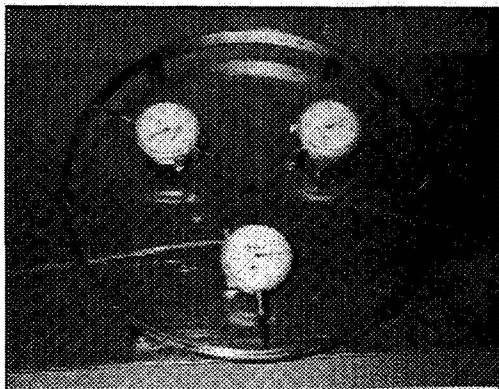
Customers:

Brush seal vendors
Aircraft engine and power generation industries.

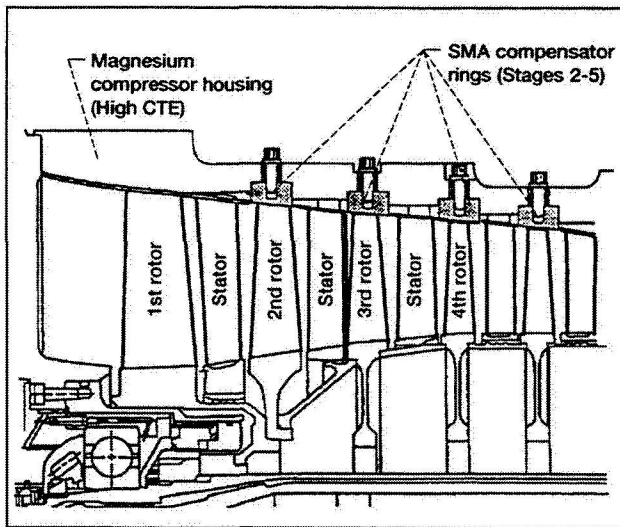
Shape Memory Alloy Compensator Ring For Compressor Clearance Control

Memry Technologies/Lycoming

Prototype Compensator Ring
Phase 1



Advanced Development
Engine Compressor Demonstration
Phase 2



CD-94-69910

Compliant Seal Development

High Temperature Compliant Seal Development In-House

Objective:

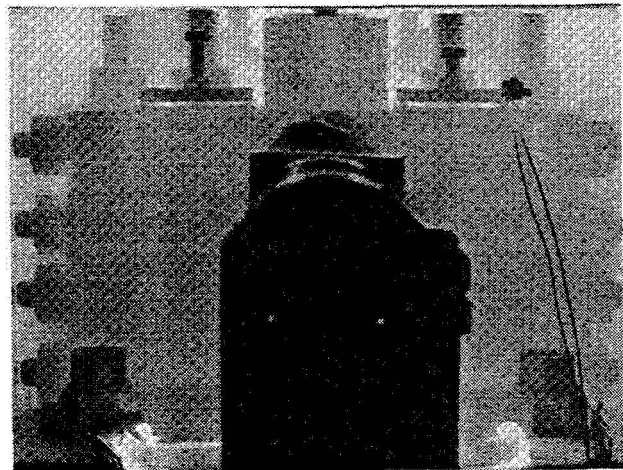
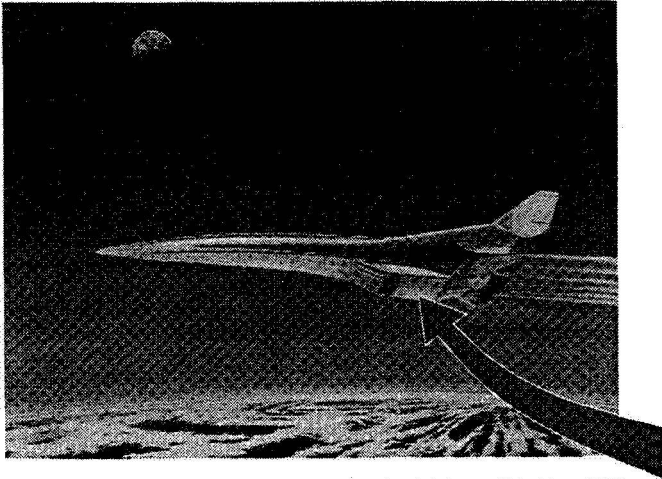
Develop high temperature compliant seals for high temperature structural interfaces to minimize leakage and permit relative component growth, minimizing thermal stresses.

Approach:

- + Develop advanced compliant seal concepts for ≥ 1500 F service.
- + Evaluate performance characteristics
 - + high temperature leakage and durability.
 - + flexibility and compliance retention with cycling
 - + manufacturability, scalability.
- + Develop design guides to predict leakage and seal compliance over operating temperature regime.
- + Provide technology to engine and industrial partners.

Goals:

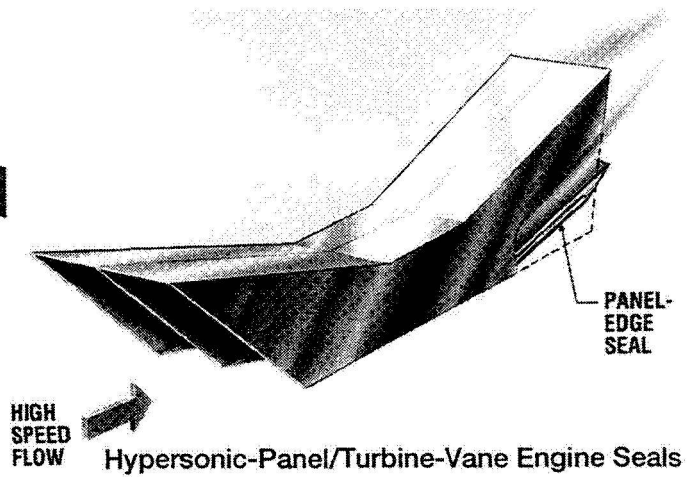
- + Develop necessary facilities to evaluate advanced compliant seals at temperatures to 1500 F.
- + Extend NASP-derived high temperature compliant seal technology to meet HSR, IHPTET, and industrial-partner goals.



1500°F Seal Testing

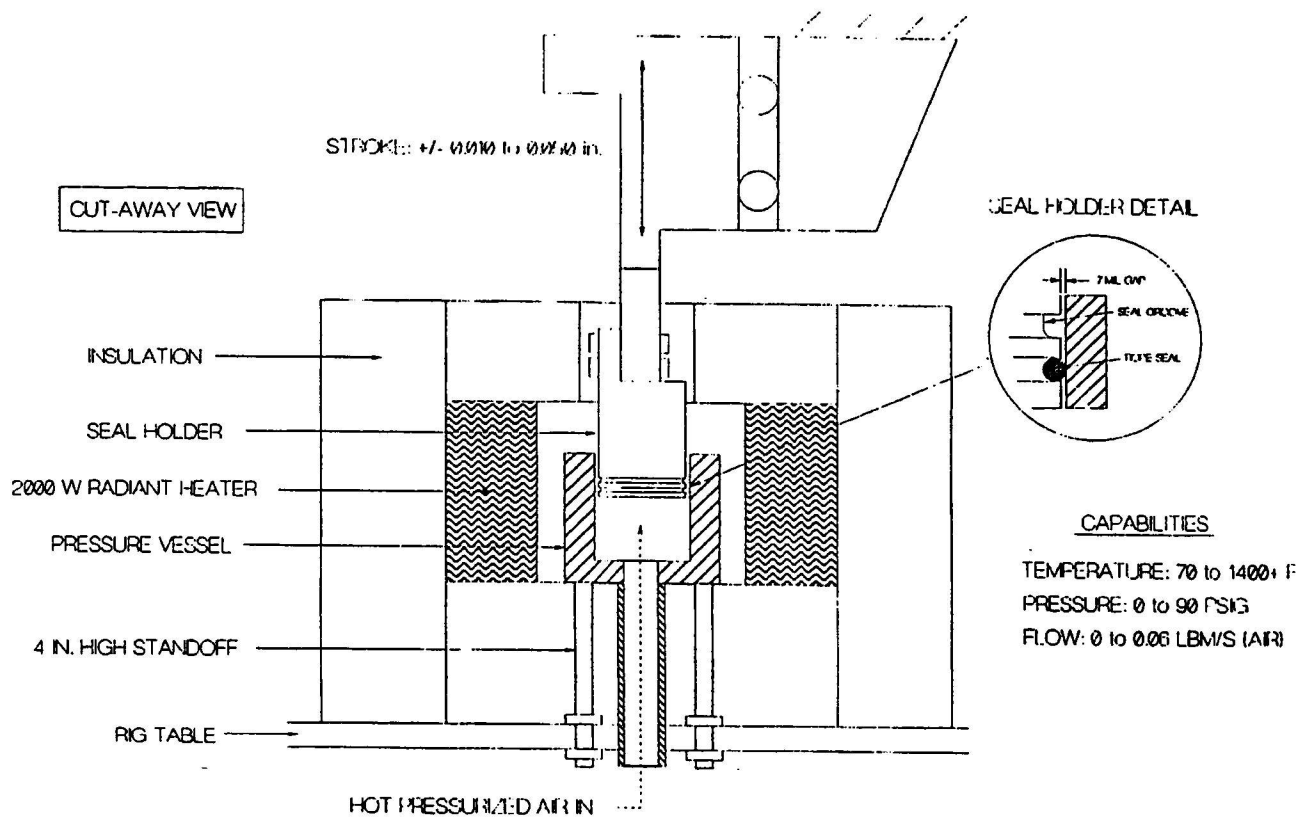
Lewis Demonstrates 1500°F Compliant Seal Technology

Customers: GE IHPTET; NASP/HYSTEP



CD-94-70758

HIGH-TEMPERATURE FLOW AND DURABILITY RIG



Summary

- **NASA and industry partners are pursuing engine performance advancements to reduce fuel burn, reduce operating costs, and ensure industry competitiveness into the next century and beyond.**
- **Advancements in seal technology will play an important role in achieving AST performance goals.**
- **Significant reductions in SFC are possible through implementing advanced seal technology. Engine studies show that over 2.5% reduction in SFC is possible applying advanced seals to a few locations.**
- **Costs of developing advanced engine seals are a small fraction of re-designing & re-qualifying complete compressor or turbine components with comparable performance improvements.**

53-37

39445

CRYOGENIC BRUSH SEAL TEST RESULTS

Margaret P. Proctor and James F. Walker
NASA Lewis Research Center
Cleveland, Ohio

Brush seals are compliant, contact seals that have long-life, low-leakage characteristics desirable for use in rocket engine turbopumps. 50.8-mm (2.0 inch) diameter brush seals with a nominal initial radial interference of 0.127-mm (0.005 inch) were tested in liquid nitrogen at shaft speeds up to 35,000 rpm and differential pressure loads up to 1.21 MPa (175 psi) per brush. The measured leakage rate of a single brush was 2-3 times less than that measured for a 12-tooth, 0.127-mm (0.005 inch) radial clearance labyrinth seal used as a baseline. Stage effects were studied and it was found that two brush seals with a large separation distance leaked less than two brushes tightly packed together. The maximum measured groove depth on the Inconel 718 rotor was 25.4 μm (0.001 inch) after 4.31 hours of shaft rotation. The Haynes-25 bristles wore approximately 25.4-76.2 μm (0.001-0.003 inch) under the same conditions.

Three seal runner coatings, chromium carbide, Teflon impregnated chromium, and zirconium oxide, were tested in liquid hydrogen at 35,000 and 65,000 rpm with separate 50.8 mm diameter brush seals made of Haynes-25 bristles and having a nominal initial radial interference of 129 μm . Two bare Inconel-718 rotors were also tested as a baseline. The test results revealed significant differences between the wear characteristics of the uncoated and coated seal runners. At both speeds the brush seal with the bare Inconel-718 seal runner exhibited significant bristle wear with excessive material transferring to the runner surface. In contrast, the coated seal runners inhibited the transfer and deposit of bristle material. The chromium carbide coating showed only small quantities of bristle material transferring to its surface. The Teflon impregnated chromium coating also inhibited material transfer and provided some lubrication. This coating, however, is self-sacrificing. The Teflon remained present on the low speed runner, but it was completely removed from the high speed brush seal, which was tested considerably longer. The tests of the Teflon coating revealed the importance of using a lubricating and low friction coating for brush seals to reduce bristle and seal runner wear. The zirconium oxide coating exhibited the greatest amount of coating wear, while the brushes incurred only slight wear. Further testing of ceramics is recommended before making a final judgement on the viability of ceramic coatings for brush seals because of the contrast between the results reported by Carlile and the results presented herein. Strictly based on the results presented hereinabove, the chromium carbide and Teflon impregnated chromium coatings were considered preferable to the uncoated Inconel-718 and zirconium oxide coatings because of their good wear resistance and characteristics to inhibit bristle material wear and transfer to the seal runner.

SUMMARY OF LN2 BRUSH SEAL TEST RESULTS

- LEAKAGE FOR A SINGLE BRUSH SEAL WAS 2-3 TIMES LESS THAN FOR A 12-TOOTH LABYRINTH SEAL.
- THE MAXIMUM TEMPERATURE RISE FOR A SINGLE BRUSH SEAL WAS LESS THAN 30K (50R) AND OCCURRED AT 0.172 MPa (25 PSID) ACROSS THE SEAL AND 35,000 RPM. (THIS TEMPERATURE RISE WOULD BE GREATER WITH NO PRESSURE DROP.)
- A STATIC BLOWOUT TEST DEMONSTRATED SEALING CAPABILITY UP TO 3.79 MPa (550 PSID). THE SEAL LIMIT WAS NOT OBTAINED.
- THE POWER LOSS FOR A SINGLE BRUSH AT 35,000 RPM AND 1.21 MPa (175 PSID) WAS 1824 W (1.73 BTU/S).
- TWO BRUSHES FAR APART LEAK LESS THAN TWO BRUSHES TIGHTLY PACKED.
- ROTOR WEAR WAS APPROXIMATELY 19 μm (0.00075 MILS) AND BRISTLE WEAR WAS 25.4-76.2 μm (1-3 MILS) AFTER 4-1/2 HOURS.

CRYOGENIC BRUSH SEAL

OBJECTIVE: TO EVALUATE SEAL COATINGS FOR CRYOGENIC BRUSH SEAL APPLICATION BY TESTING VARIOUS MATERIALS ON SEAL RUNNERS IN A CRYOGENIC BRUSH SEAL TEST RIG.

- CHROMIUM CARBIDE (CrC)
- TEFLON IMPREGNATED CHROMIUM
- ZIRCONIUM OXIDE (ZrO₂)
- UNCOATED INCONEL-718 (BASELINE)

BACKGROUND:

THE IMPORTANCE OF GOOD MATERIAL SELECTION WAS REVEALED IN THE 1ST YEAR OF TESTING CRYOGENIC BRUSH SEALS AT NASA LERC. WHILE THE EFFORT FOCUSED ON LEAKAGE RATE PERFORMANCE IN LIQUID NITROGEN (LN2), PRELIMINARY DATA WAS TAKEN IN LIQUID HYDROGEN (LH2). IN LH2, THE UNCOATED INCONEL-718 SEAL RUNNER AND THE BRUSH MADE OF HAYNES-25 BRISTLES EXHIBITED POOR TRIBOLOGICAL PERFORMANCE. BRISTLE WEAR WAS EXCESSIVE AND BRISTLE MATERIAL TRANSFERRED TO THE RUNNER CAUSING GALLING DUE TO LIKE-ON-LIKE METAL CONTACT.

CROSS SECTION OF CRYOGENIC BRUSH SEAL TESTER

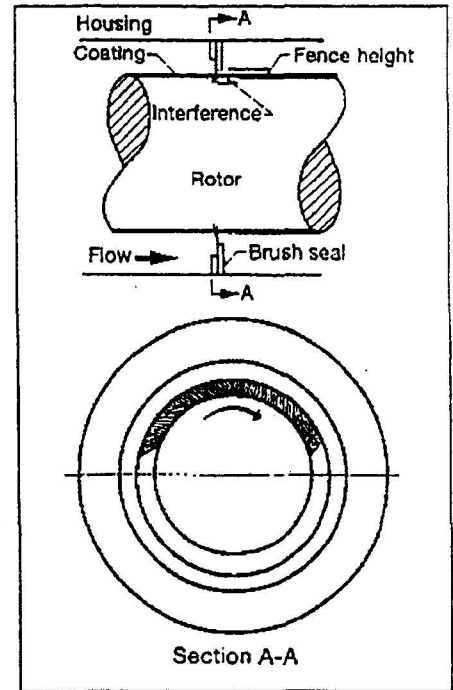
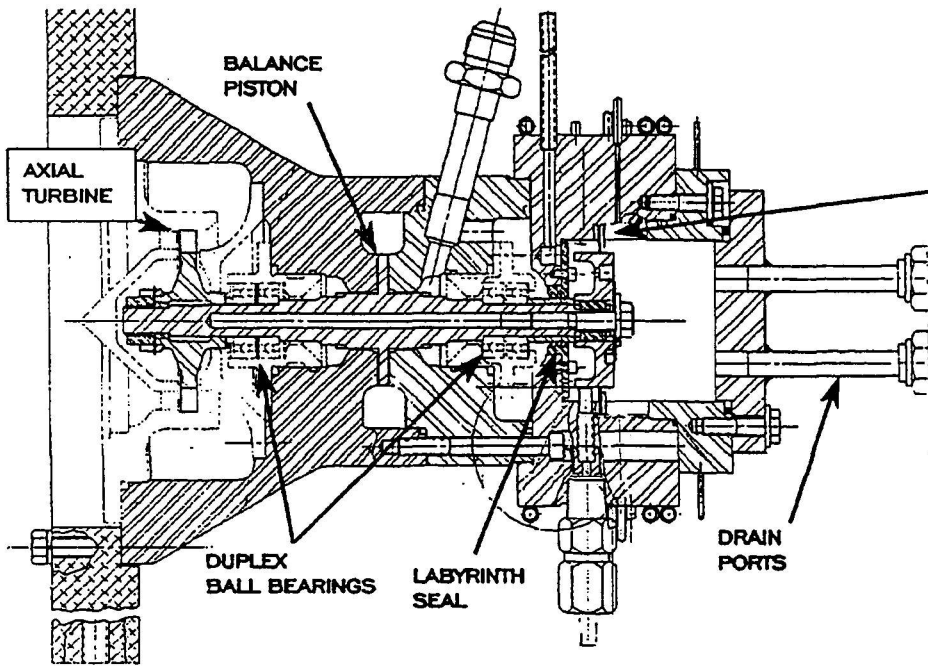
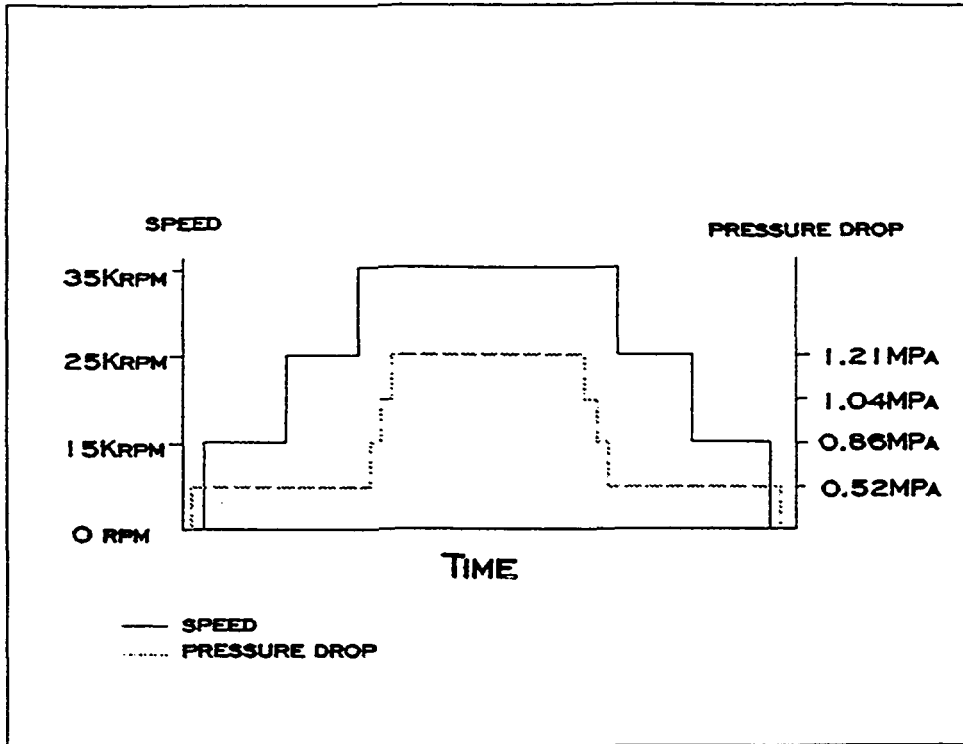


FIGURE 2. BRUSH SEAL

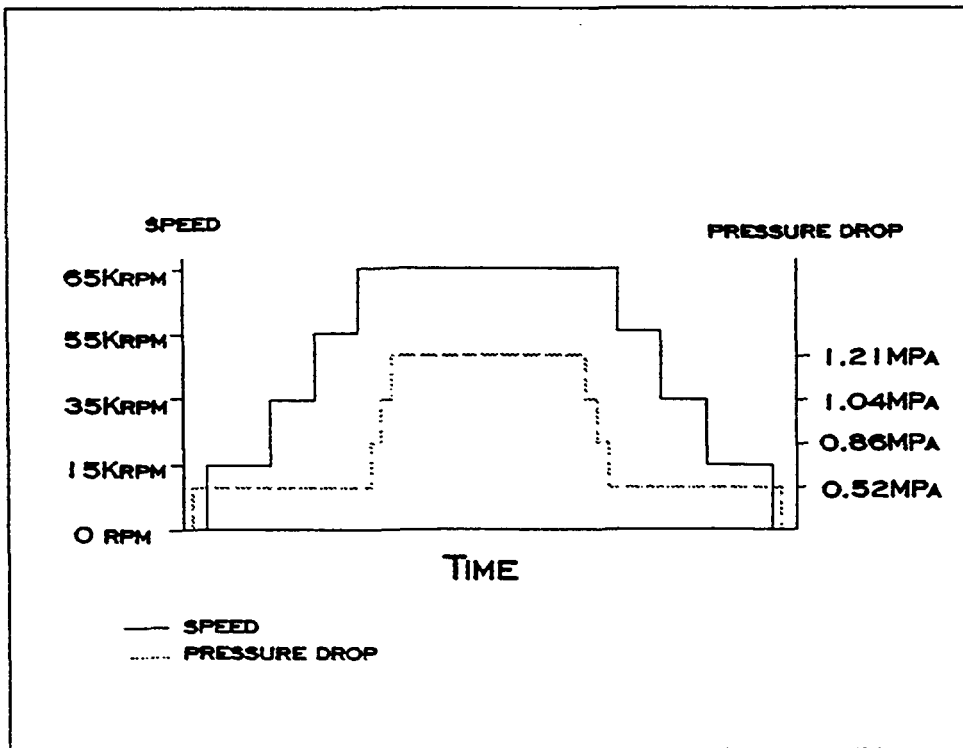
SEAL RUNNER PROPERTIES

SEAL RUNNER COATING	COATING DEPOSITION PROCESS	COATING THICKNESS (mm)	SURFACE FINISH (RMS- μ m)	COATING HARDNESS (Rc)	INTERFERENCE FIT (μ m)	TEST SPEED (rpm)
INCONEL-718 (UNCOATED)	-	-	.3	46	135	35,000
INCONEL-718 (UNCOATED)	-	-	.3	38	129	65,000
Cr C	Plasma sprayed	100	.3	67	120	35,000
CrC	Plasma sprayed	100	.3	66	128	65,000
Cr+Teflon	Cr electro-deposit and ground. Then Teflon impregnated into fissures created by chemically etching the Cr.	50.8	.6	50	130	35,000
Cr+Teflon	Cr electro-deposit and ground. Then Teflon impregnated into fissures created by chemically etching the Cr.	50.8	.9	60	130	65,000
ZrO ₂	Plasma sprayed onto 100 μ m thick AMI 973 bond coat	203	.4	67	132	35,000
ZrO ₂	Plasma sprayed onto 100 μ m thick AMI 973 bond coat	203	.4	62	132	65,000

TEST PROFILES



TEST SPEED : 35,000 RPM.



TEST SPEED : 65,000 RPM.

EVALUATION TECHNIQUES

- **SEAL RUNNER WEAR QUANTIFICATION:**

A SURFACE PROFILOMETER WAS USED TO MEASURE SURFACE TRACES PERPENDICULAR TO THE BRUSH TRACK AT FOUR LOCATIONS EQUALLY SPACED AROUND THE CIRCUMFERENCE AFTER EACH TEST.

- **BRISTLE WEAR QUANTIFICATION:**

AN OPTICAL COMPARATOR WAS USED TO MEASURE I.R. OF THE BRUSH AT MULTIPLE LOCATIONS EQUALLY SPACED AROUND THE CIRCUMFERENCE OF THE BRUSH AFTER EACH TEST. RADIAL WEAR WAS BASED ON THE AVERAGE OF THE MEASURED VALUES, AND DETERMINABLE ONLY IF THE MEASURED VALUES BEFORE AND AFTER A TEST WERE STATISTICALLY DIFFERENT.

- **SEAL RUNNER AND BRISTLE WEAR CHARACTERISTICS:**

A SCANNING ELECTRON MICROSCOPE WITH A BACK SCATTER DETECTOR AND X-RAY ENERGY DISPERSIVE ELEMENTAL ANALYSIS WAS USED TO INVESTIGATE MATERIAL TRANSFER BETWEEN THE BRISTLES AND THE SEAL RUNNER.

UNCOATED INCONEL-718 SEAL RUNNER

EXCESSIVE BRISTLE WEAR AND MATERIAL TRANSFER TO THE SEAL RUNNER PROMOTED GALLING DUE TO LIKE-ON-LIKE METAL CONTACT.

35,000 RPM:

BRISTLE RADIAL WEAR: $64 \mu\text{m}$

RUNNER BUILDUP: $12 - 15 \mu\text{m}$

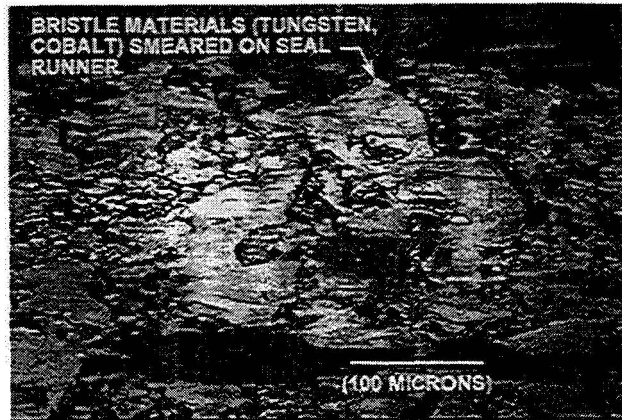
(213 Km and 43 min)

65,000 RPM:

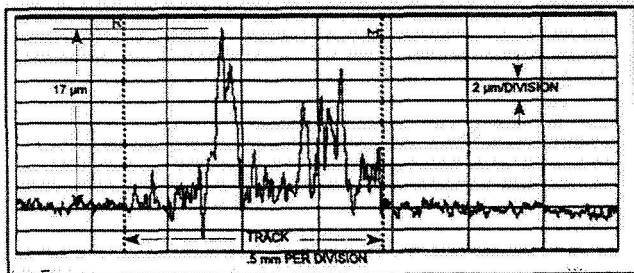
BRISTLE RADIAL WEAR: $41 \mu\text{m}$

RUNNER BUILDUP: $9 - 17 \mu\text{m}$

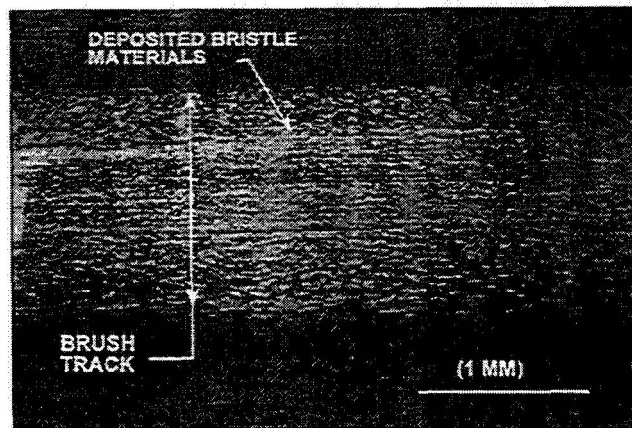
(300 Km and 38 min)



MAGNIFICATION OF THE TRACK'S EDGE ON SEAL RUNNER.

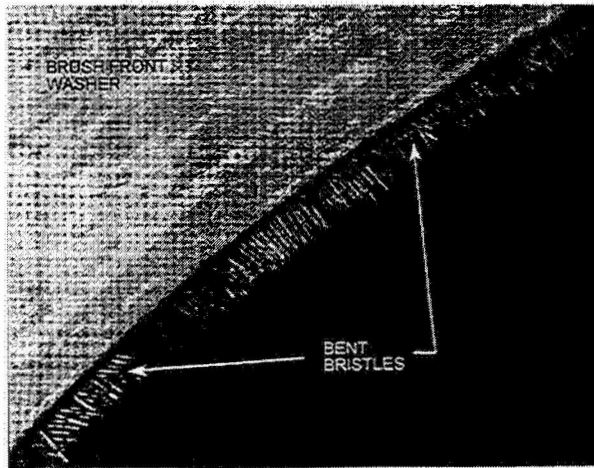


PROFILOMETER TRACE SHOWS BUILD-UP OF MATERIAL ACROSS THE TRACK.



SEM MICROGRAPH OF SEAL RUNNER TAKEN IN BACK-SCATTER

BRUSH TESTED WITH UNCOATED INCONEL-718 SEAL RUNNER



BRISTLE DAMAGE LIKELY CAUSED BY MATERIAL GALLING.

CHROMIUM CARBIDE COATED SEAL RUNNER

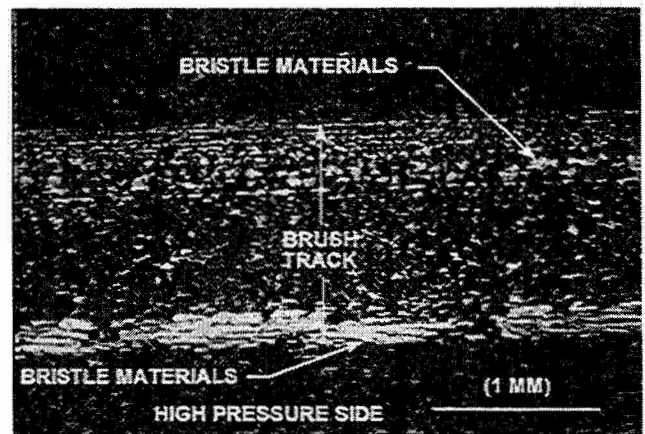
THE CrC COATING REDUCED BRISTLE MATERIAL TRANSFER TO THE SEAL RUNNER AND BRISTLE WEAR.

35,000 RPM:

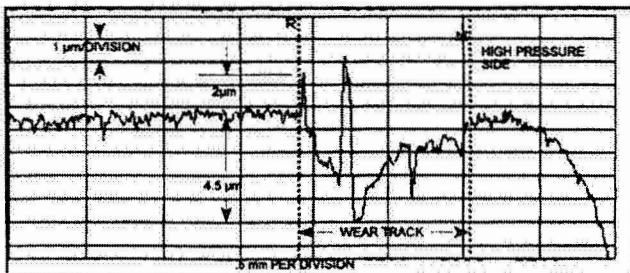
BRISTLE RADIAL WEAR : 25 μm
 COATING RADIAL WEAR : 3 - 6 μm
 (223 Km and 51 min)

65,000 RPM:

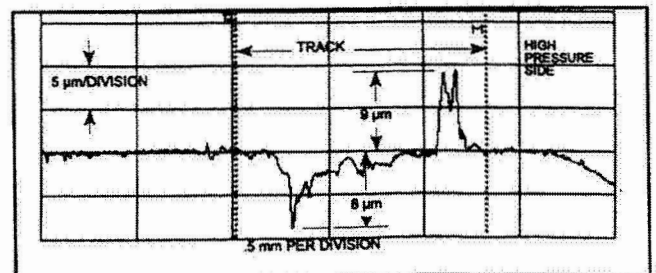
BRISTLE RADIAL WEAR : 38 μm
 COATING RADIAL WEAR : 7 - 20 μm
 (450 Km and 58 min)



BRISTLE MATERIAL SMEARED AT THE HIGH PRESSURE SIDE OF SEAL TESTED TO 65,000 RPM AND SPARSELY SMEARED OVER REST OF TRACK.



PROFILOMETER TRACE OF WEAR TRACK ON RUNNER TESTED AT 35,000 RPM.

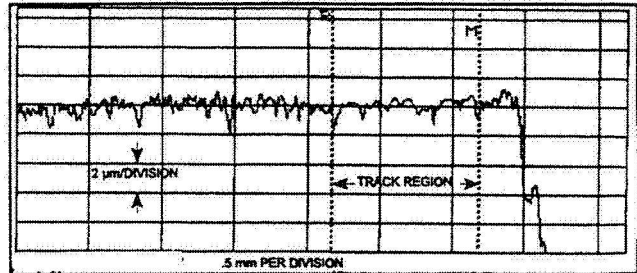


PROFILOMETER TRACE OF WEAR TRACK ON RUNNER TESTED AT 65,000 RPM.

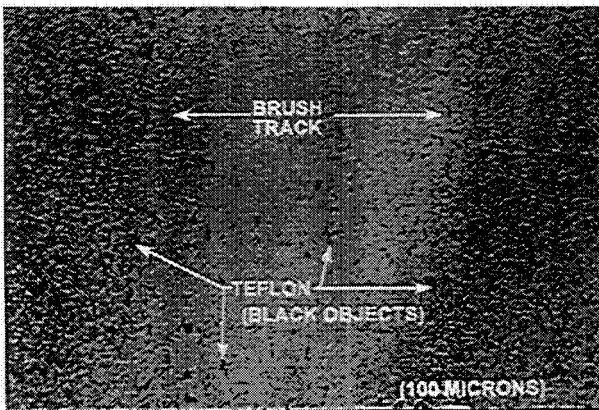
**TEFLON IMPREGNATED CHROMIUM COATED SEAL RUNNER TESTED
AT 35,000 RPM**

THE COATING EXHIBITED NEGLIGIBLE SEAL RUNNER AND BRISTLE WEAR WHICH IS ATTRIBUTED TO THE LUBRICATING PROPERTIES OF THE COATING.

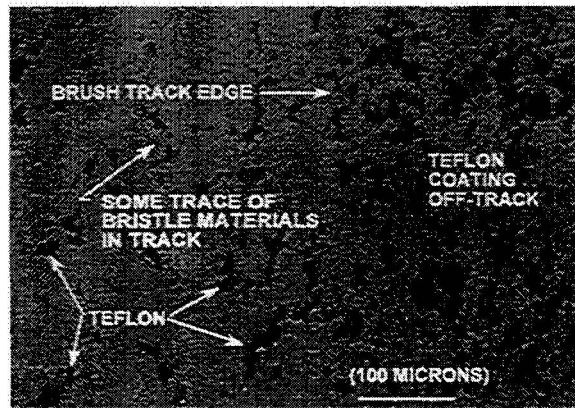
SEAL ACCUMULATED 86 Km and 28 minutes.



PROFILOMETER TRACE SHOWS NEGLIGIBLE WEAR AFTER 86 KILOMETERS OF LINEAR SLIDING DISTANCE.



BRUSH TRACK TAKEN WITH THE SEM USING A BACK SCATTER DETECTOR.

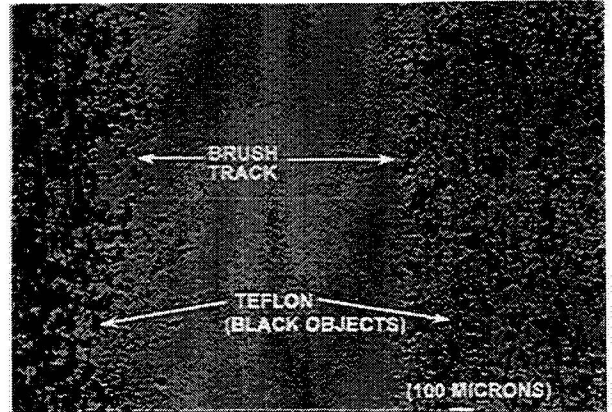


EDGE OF BRUSH TRACK REVEALS TEFLON REMAINING IN THE TRACK WITH SOME BRISTLE MATERIAL ALSO PRESENT.

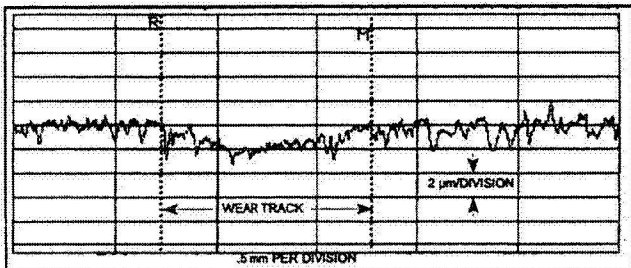
**TEFLON IMPREGNATED CHROMIUM COATED SEAL RUNNER TESTED
AT 65,000 RPM**

AT HIGH SPEEDS, THE COATING INCURRED SLIGHT WEAR BUT THE BRISTLES SHOWED SIGNIFICANT WEAR THAT OCCURED DURING THE THIRD AND LAST TEST SUGGESTING THE TEFLON IS A SELF-SACRIFICING PROTECTIVE FILM.

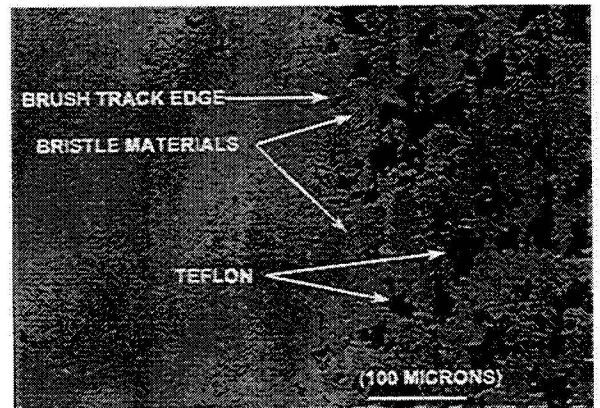
BRISTLE RADIAL WEAR : 56 μm
 COATING RADIAL WEAR : 2 - 10 μm
 (577 Km and 66 minutes)



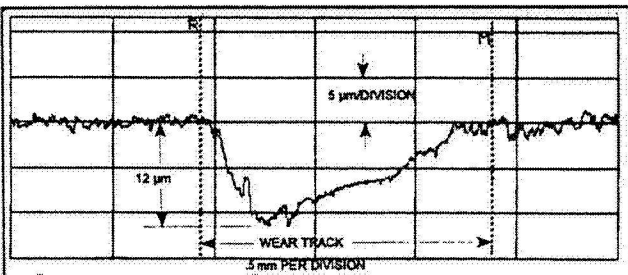
BRUSH TRACK



PROFILOMETER TRACE OF THE MINIMUM WEAR DEPTH.



EDGE OF BRUSH TRACK



PROFILOMETER TRACE OF THE MAXIMUM WEAR DEPTH.

TRIBOLOGICAL PERFORMANCE SUMMARY

35,000RPM

SEAL RUNNER COATING	ACCUMULATIVE TEST DURATION (min)	ACCUMULATIVE LINEAR SLIDING DISTANCE (Km)	ACCUMULATIVE BRISTLE WEAR (μm)	MAXIMUM RADIAL SEAL RUNNER WEAR (μm)
INCONEL-718 (UNCOATED)	43	213	64	-17 (DEPOSITED)
CrC	51	223	25	6
Cr+TEFLON	28	86	(NEGLIGIBLE)	(NEGLIGIBLE)
ZrO ₂	47	222	5	90

65,000 RPM

SEAL RUNNER COATING	ACCUMULATIVE TEST DURATION (min)	ACCUMULATIVE LINEAR SLIDING DISTANCE (Km)	ACCUMULATIVE BRISTLE WEAR (μm)	MAXIMUM RADIAL SEAL RUNNER WEAR (μm)
INCONEL-718 (UNCOATED)	38	300	41	-17 (DEPOSITED)
CrC	58	450	38	20
Cr+TEFLON	66	577	56	12
ZrO ₂	48	337	18	85

CONCLUDING REMARKS

- THE COATINGS REDUCED BRISTLE WEAR AND TRANSFER OF BRISTLE MATERIAL TO THE SEAL RUNNERS AS COMPARED TO THE UNCOATED SEAL RUNNER.

- THE GOOD PERFORMANCE OF THE TEFLON IMPREGNATED CHROMIUM COATING REVEALED THE IMPORTANCE OF USING A LUBRICOUS (LOW FRICTION) MATERIAL TO REDUCE BRISTLE AND SEAL RUNNER WEAR.

- THE SEVERE WEAR OF THE ZIRCONIUM OXIDE COATING IS ATTRIBUTED TO POOR CERAMIC COATING QUALITY AS SUBSTANTIATED BY THE LOW COATING HARDNESS. FURTHER INVESTIGATION OF CERAMICS FOR BRUSH SEAL APPLICATION IS WARRANTED.

- BASED ON THE RESULTS OBTAINED IN THIS EFFORT, THE TEFLON IMPREGNATED CHROMIUM AND THE CHROMIUM CARBIDE COATINGS ARE CONSIDERED PREFERABLE TO THE ZIRCONIUM OXIDE COATING AND UNCOATED INCONEL-718.

RESULTS OF CONTACTING SEAL TESTING AT NASA LEWIS RESEARCH CENTER

Gene Addy
NASA Lewis Research Center
Cleveland, Ohio

34-07
39446

Advanced technology initiatives such as the Integrated High Performance Turbine Engine Technology (IHPTET) program and the Advanced Subsonic Technology (AST) program have recognized that advancements in seal technologies are a key element of the overall effort to improve gas turbine performance and efficiency. These improvements in performance and efficiency call for reduced seal leakage while requiring the seals to operate at higher temperatures and surface speeds.

The High Temperature/High Speed Seals Test Facility at NASA's Lewis Research Center has evolved as a result of the combined efforts of three separate federal government entities. The U.S. Air Force had the rig built under contract by Teledyne CAE in Toledo, Ohio and a series of brush seal tests were conducted at Teledyne as part of the contract. At the conclusion of the contract, the USAF chose to locate the rig at NASA Lewis based on Lewis' proposal for continued seal testing under its seal programs. Support for seal testing in this facility at Lewis is a combined effort of the Vehicle Propulsion Directorate of the U.S. Army Research Laboratory located at Lewis and NASA Lewis. The U.S. Army provides primary technical support for rig operation while NASA provides primary research and development capability.

Testing has been underway at Lewis in this test rig since April 1993. Various contacting seals such as brush and finger seals, as well as labyrinth seals have been tested to surface speeds of 1100 feet per second, temperatures to 1100 degrees Fahrenheit and pressure differentials to 100 psid. Various rotor coatings have also been tested including aluminum oxide, chromium carbide and zirconia as well as an uncoated Inconel 718 rotor.

Brush seals with bristles made of cobalt based alloys (i.e. Haynes 25) and with bristles made of silicon carbide have been tested for leakage performance at high speeds and high temperatures. Finger seals made of Inconel X750 (a nickel based alloy) have also been performance tested. Results from these tests will be presented and discussed.

One sealing technology which has been gaining wider use is brush seals. These seals have been shown to reduce leakage over the widely used labyrinth seals and have the added advantage of being able to withstand significant shaft excursions without incurring permanent damage. However, the higher temperatures of up to 1600 degrees F and surface speeds up to 1600 ft/sec targeted by the technology initiatives will require use of materials other than the cobalt and nickel based materials, such as the Haynes and Inconel alloys, currently used for the bristles in the brushes.

Silicon carbide is one such substitute material for the bristles. It has shown good resistance to wear while maintaining its strength, stiffness, and resistance to oxidation at temperatures to 1600 degrees F. It can also be formed into the small diameter filaments of approximately 0.003 inch needed for the brushes.

HIGH TEMPERATURE/HIGH SPEED SEALS TEST PROGRAM

Objective:

To apply the low leakage and displacement-tolerant characteristics of contacting seal designs to the high speed, high temperature conditions in gas turbomachinery

Participants:

- U.S. Army Research Laboratory
- U.S. Air Force Wright Laboratory
- NASA Lewis Research Center
- Gas Turbine Industry
- Seal Manufacturing Companies

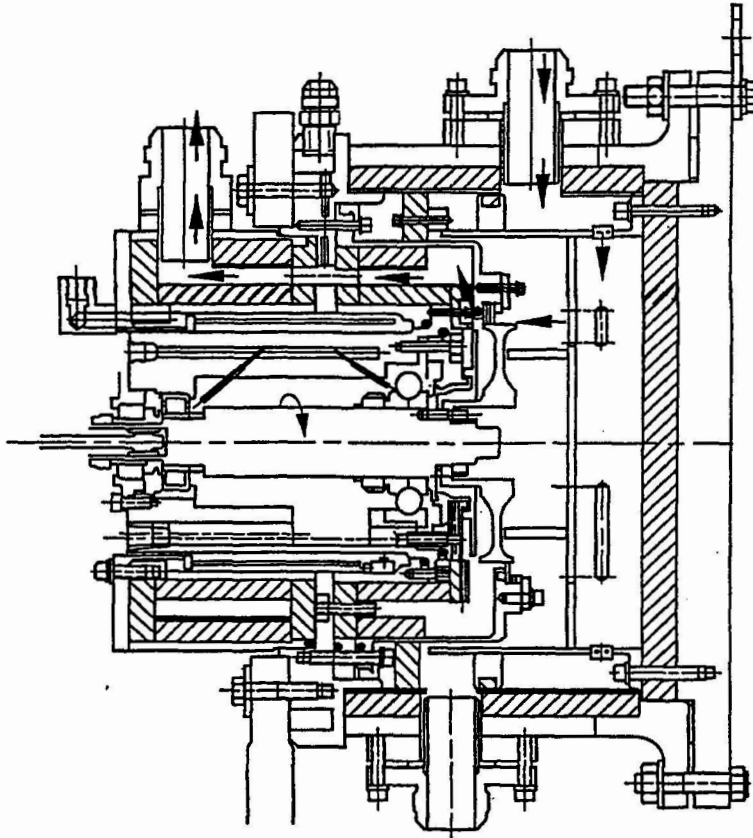
Industry Partners:

- Allied Signal Engines
- Cross Manufacturing
- Technetics
- Williams International

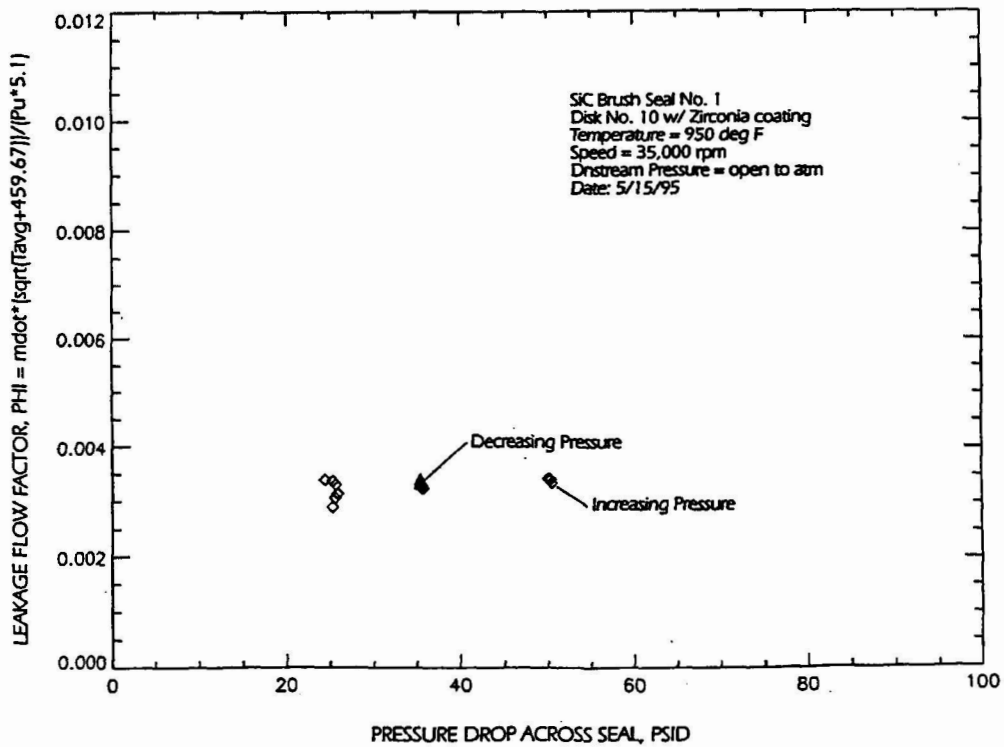
Rig Capabilities:

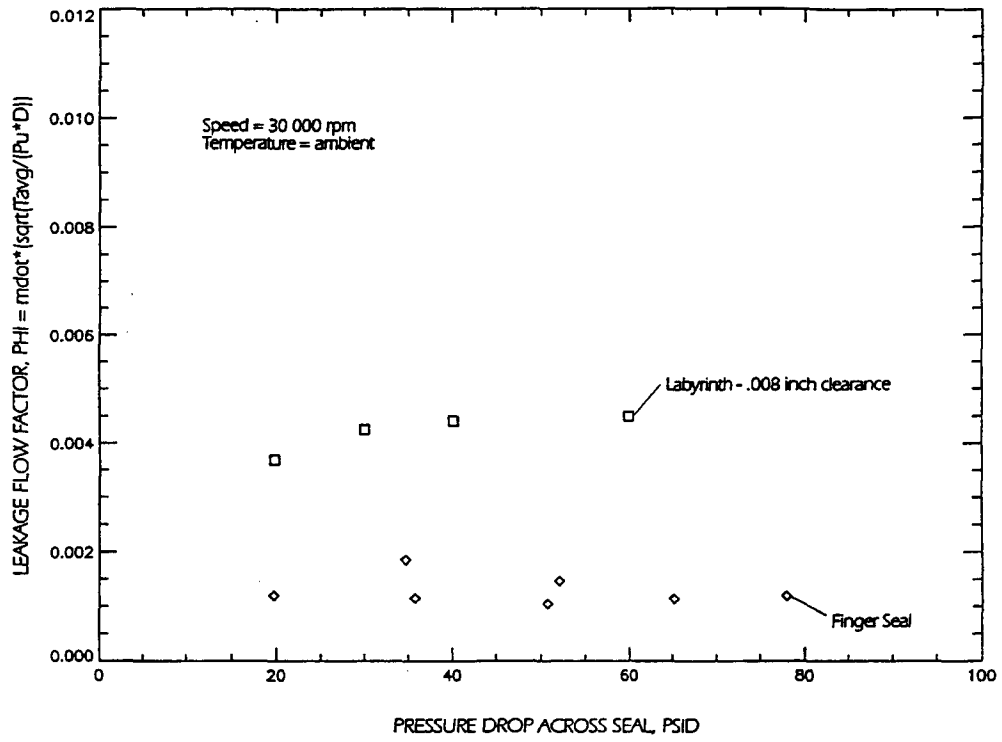
- Surface speeds to 1100 fps
- Pressure differences across seal to 100 psi
- Temperatures to approx. 1200 F

Air Flow Path During Brush Seal Test



CD-92-61559





AIR FORCE SEAL PROGRAMS

Ellen R. Mayhew
Wright Laboratory
Wright Patterson Air Force Base
Wright Patterson Air Force Base, Ohio

55-07

39447

Seal technology development is an important part of the Air Force's participation in the Integrated High Performance Turbine Engine Technology (IHPTET) initiative, the joint DOD, NASA, ARPA, and industry endeavor to double turbine engine capabilities by the turn of the century. Significant performance and efficiency improvements can be obtained through reducing internal flow system leakage, but seal environment requirements continue to become more extreme as the engine thermodynamic cycles advance towards these IHPTET goals. Seal technology continues to be pursued by the Air Force to control leakage at the required conditions. This presentation briefly describes current seal research and development programs and gives a summary of seal applications in demonstrator and developmental engines.

OUTLINE

- **INTEGRATED HIGH PERFORMANCE TURBINE ENGINE TECHNOLOGY (IHPTET) INITIATIVE**
- **AIR FORCE SEALS R&D PROGRAMS**
- **ENGINE APPLICATIONS**
 - IHPTET DEMONSTRATORS
 - PRODUCTION MILITARY ENGINES
- **FUTURE DIRECTIONS**
- **CONCLUSIONS**

IHPTET INITIATIVE

- **JOINT DOD/NASA/ARPA EFFORT**
- **GOAL: DOUBLE TURBINE ENGINE PROPULSION CAPABILITY BY THE TURN OF THE CENTURY**
 - FIGHTER/ATTACK ENGINE GOALS
 - » FN/WT +100%
 - » COMPRESSOR EXIT TEMP +400F

 - SIMILAR TURBOSHAFT/PROP AND EXPENDABLE ENGINE GOALS
- **PHASED APPROACH FOR NEAR TERM AND LONGER TERM PAYOFFS**
 - PHASE I DEMO COMPLETED 1994 (+30%)
 - PHASE II DEMO 1997 (+60%)
 - PHASE III DEMO 2003 (+100%)
- **SIGNIFICANT SECONDARY FLOW IMPACT ON ENGINE PERFORMANCE**
 - HPC: EFF +4.4% ==> TIT -85F OR FN +7.6%
 - HPT: EFF +4.2% ==> TIT -93F OR FN +9.7%
 - REDUCE/ELIMINATE LPT COOLING AIR
- **SECONDARY FLOWS GROUPED UNDER IHPTET COMPRESSOR TECHNOLOGY DEVELOPMENT**
 - 60% LEAKAGE REDUCTION GOAL
- **ADVANCED CYCLES POSE CHALLENGES IN SEAL OPERATING ENVIRONMENT**
 - CURRENT SEALS RESEARCH (FOR 1997 ENGINE DEMOS)
 - » 1400-1650 FT/SEC
 - » 1600F

CURRENT AIR FORCE PROGRAMS

EG&G: ADVANCED BRUSH SEAL DEVELOPMENT PROGRAM

- **OBJECTIVE:** DEVELOP A BRUSH SEAL DESIGN METHODOLOGY FOR MAN-RATED ENGINE APPLICATIONS (UP TO 1400F/1400FPS)
- **APPROACH:**
 - SEAL DESIGN OPTIMIZATION VIA RIG TEST AND CFD
 - TRIBOPAIR TESTING AND EVALUATION AT ELEVATED CONDITIONS
- **ACCOMPLISHMENTS:**
 - “LOW HYSTERESIS” DESIGN OPTIMIZED FOR LOW WEAR
 - » REDUCED BRISTLE FLUTTER
 - » ELIMINATED BRISTLE PUSH-DOWN EFFECT
 - 130 PSID SINGLE-STAGE CAPABILITY SUCCESSFULLY DEMONSTRATED
 - CFD MODELING OF BRISTLE TIP LIFT-OFF FORCES IN PROGRESS
 - TRIBOPAIR INVESTIGATION IN PROGRESS

P&W: HIGH SPEED BRUSH SEAL DEVELOPMENT PROGRAM

- **OBJECTIVE:** DEMONSTRATE HIGH-SPEED/HIGH-TEMPERATURE OPERATION FOR IHPTET PHASE II DEMONSTRATOR ENGINES
- **APPROACH:**
 - APPLICATION STUDY OF PHASE II ENGINE/MISSION FLIGHT CYCLE FOR SURFACE SPEED AND TEMPERATURE REQUIREMENTS
 - DESIGN/FABRICATE/RIG TEST BRUSH SEALS TO VERIFY THEIR CAPABILITY AT PHASE II CONDITIONS
- **ACCOMPLISHMENTS:**
 - APPLICATION STUDY COMPLETED
 - » REQUIREMENTS TO 1500F, 1650 FT/SEC
 - PRELIMINARY DESIGN OF BRUSH SEAL CONCEPTS COMPLETED
 - RIG ADAPTIVE HARDWARE DESIGN/FABRICATION IN PROGRESS

CURRENT AIR FORCE PROGRAMS

TECHNETICS: CERAMIC BRUSH SEALS

- **OBJECTIVE:** DEVELOP A FULLY OR PARTLY CERAMIC BRUSH SEAL FOR APPLICATIONS FROM 1600F - 2000F
- **APPROACH:**
 - PERFECT MANUFACTURING METHODS
 - RIG TEST FOR PERFORMANCE, ROTORDYNAMICS, AND WEAR
 - FABRICATE HYBRID SEAL FOR TEST IN A DEMONSTRATOR ENGINE
- **ACCOMPLISHMENTS:**
 - MANUFACTURING TRIALS OF ALL-CERAMIC SEALS DEMONSTRATED LONG TERM PROMISE
 - “HYBRID” CERAMIC BRISTLE/METALLIC HOLDER SEALS CURRENT FOCUS (1600F GOAL)
 - » CERAMIC COATINGS SHOWED BEST DURABILITY IN WEAR TESTS
 - HIGH CERAMIC/CERAMIC FRICTIONAL HEATING, WEAR DEBRIS CONCERNS
 - LINE-ON-LINE DESIGN MAY BE DESIRABLE FOR CERAMIC BRUSH SEALS
 - » HYBRID SEAL TESTS IN PROGRESS

SCIENTIFIC RESEARCH ASSOCIATES: ADVANCED SECONDARY GAS PATH METHODOLOGY

- **OBJECTIVE:** DEVELOP A SECONDARY GAS PATH DESIGN SYSTEM BASED ON A 3-D NAVIER-STOKES CODE
- **APPROACH:**
 - APPLY GRAPHICAL USER INTERFACE (GUI) TECHNOLOGY TO MAKE CFD DESIGNER-FRIENDLY
 - EXERCISE ON A DEMONSTRATOR ENGINE CAVITY AND COMPARE TO TEST RESULTS
- **ACCOMPLISHMENTS:**
 - GUI NEARLY COMPLETE
 - USER TESTING IN PROGRESS
 - DEMONSTRATOR ENGINE COMPUTATIONS COMPLETE
 - ENGINE CURRENTLY IN TEST

IHPTET DEMONSTRATOR ENGINE SEAL APPLICATIONS

- **BRUSH SEAL TESTING TO DATE**
 - TURBINE AND COMPRESSOR APPLICATIONS
 - HAYNES 25 AND HAYNES 214 BRISTLES
 - ALUMINUM OXIDE, CHROME CARBIDE COATINGS
 - 20-80% REDUCTION IN LEAKAGE OVER LAB SEALS
 - GENERALLY GOOD DURABILITY
TURBINE AND COMPRESSOR APPLICATIONS
- **FUTURE TESTING**
 - BRUSH SEALS PLANNED FOR ALL DEMO ENGINES
 - HIGHER SURFACE SPEEDS, TEMPERATURES
 - EXPANDED ARRAY OF BRISTLE AND COATING MATERIALS
 - ADVANCED CONFIGURATIONS

AIR FORCE PRODUCTION ENGINES ADVANCED SEALS

- **F119 ENGINE**
 - 4 STATIC BRUSH SEALS
 - 2 DYNAMIC BRUSH SEALS IN LPT
- **F100-PW-229 ENGINE**
 - DYNAMIC BRUSH SEAL IN LPT

FUTURE DIRECTIONS

SEAL TECHNOLOGY

- **INCREASED TEMPERATURE REQUIREMENTS**
 - ALL-CERAMIC BRUSH SEALS
 - » SPECIALLY DESIGNED FIBERS, COATINGS
- **NON-CONTACTING SEALS**
 - WEAR BENEFITS, HIGH PRESSURE CAPABILITY

APPLICATIONS

- **FULL INTEGRATION OF ADVANCED SEAL TECHNOLOGY INTO ENGINE DESIGNS**
 - NOT ONLY “SHOWCASE” TECHNOLOGY OR QUICK FIXES

CONCLUSIONS

- **EXTENSIVE SEALS RESEARCH HAS BEEN CONDUCTED IN PURSUIT OF THE IHPTET GOALS**
 - ADVANCED BRUSH SEAL MATERIALS AND DESIGNS
 - » NEW TEMPERATURE/SPEED REGIMES
 - » EXTENDED SEAL LIFE
 - DESIGNER-FRIENDLY TOOLS FOR EFFICIENT SECONDARY GAS PATH DESIGN
 - » 3-D NAVIER-STOKES FOR THE DESIGNER
- **PUSHING FOR ADVANCED SEAL TECHNOLOGY IN IHPTET DEMONSTRATOR ENGINES**
- **WORKING WITH PROGRAM OFFICES TO TRANSITION SEAL TECHNOLOGY**

PRDA-II AND III BRUSH SEAL DEVELOPMENT PROGRAMS AT EG&G

Robert G. Loewenthal
EG&G Mechanical Components Technology Group
Research and Development
Cranston, Rhode Island

56-37
39448

1990-1995

These programs come under the Integrated High Performance Turbine Engine Technology (IHPTET) program.

EG&G Mechanical Components Technology Group R&D completed a **Brush Seal Development Program** under PRDA-II in late 1992. We started the **Advanced Brush Seal Development program**, under PRDA-III, in 1993 and will complete it in 1996. Both programs have been funded by the United States Air Force. In the first program, we made significant gains in the area of tribopairs (bristle materials vs. shaft coatings) and the "Low Hysteresis" design for brush seals. These were reported in two AIAA Propulsion Conference papers (copies available), and the "Low Hysteresis" design has been patented. Seals were delivered for test in an Air Force demonstrator at Allison. In PRDA-III, goals are to increase the pressure sealing capability, and the surface speeds and temperatures at which brush seals can be used. We have conducted part of the design and testing and have tested brush seals successfully at more severe conditions than in the previous program. We are continuing with the program, and will complete it in time to furnish brush seals for an Air Force Demonstrator test in 1997.

PRDA II/III Brush Seal Programs

PRDA-II

- Developed Low Hysteresis Design - Patent issued.
 - AIAA and Propulsion Journal Papers
- Optimized Tribopairs with extensive test program.
 - AIAA Paper

PRDA-III Goals

- Single Stage Seal for Higher Pressure. 150psid
- Design for High Surface Speed. 1200-1400fps
- Increase Temperature Capability. 1200-1400°F
- Reduce Pressure Closure to decrease wear.



US005401036A

***United States Patent** [19]

[11] **Patent Number:** 5,401,036

Basu

[45] **Date of Patent:** Mar. 28, 1995

- [54] BRUSH SEAL DEVICE HAVING A RECESSED BACK PLATE
- [75] Inventor: Prithwish Basu, Pawtucket, R.I.
- [73] Assignee: EG & G Sealol, Inc., Cranston, R.I.
- [21] Appl. No.: 35,072
- [22] Filed: Mar. 22, 1993
- [51] Int. Cl.⁶ F16J 15/447
- [52] U.S. Cl. 277/53
- [58] Field of Search 277/51, 53, 188 R; 415/173.5, 174.5

1523768 11/1989 U.S.S.R. 277/53
 2014951 9/1992 WIPO 277/53

Primary Examiner—William A. Cuchlinski, Jr.
Assistant Examiner—John E. Beres
Attorney, Agent, or Firm—Finnegan, Henderson, Farabow, Garrett & Dunner

[57] **ABSTRACT**

A brush seal device for sealing a high pressure area from a low pressure area. The brush seal device comprises an annular retaining plate having a first side facing the high pressure area and a second side opposite the first side, and an annular back plate having a first side facing the low pressure area and a second side opposite the first side, the second side of the back plate having an outer peripheral portion and an inner peripheral portion. A plurality of bristles are between the second side of the retaining plate and the outer peripheral portion of the second side of the back plate such that they extend inwardly from the outer peripheral portion of the second side of the back plate. The inner peripheral portion of the second side of the back plate has a recessed surface formed therein to inhibit the plurality of bristles from contacting the inner peripheral portion of the second side of the back plate.

[56] **References Cited**

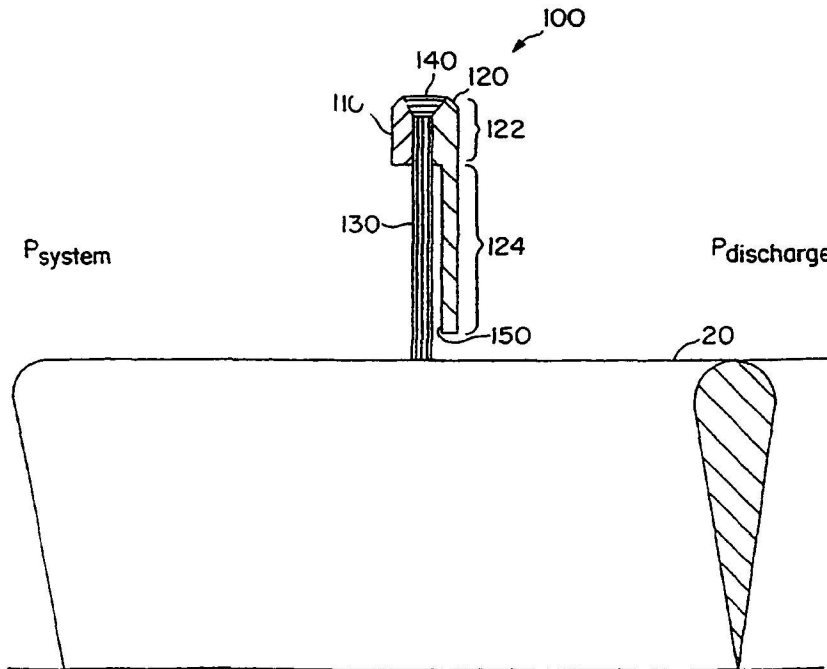
U.S. PATENT DOCUMENTS

- 4,202,554 5/1980 Snell 277/53
- 5,029,875 7/1991 Spain et al. 277/53 X
- 5,066,024 11/1991 Reisinger et al. 277/53
- 5,071,138 12/1991 Mackay et al. 277/53 X
- 5,106,104 4/1992 Atkinson et al. 277/53 X
- 5,108,116 4/1992 Johnson et al. 277/53
- 5,201,530 4/1993 Kelch et al. 277/53

FOREIGN PATENT DOCUMENTS

- 0293140 11/1988 European Pat. Off. 277/53
- 2021210 11/1979 United Kingdom .
- 1598926 9/1981 United Kingdom .
- 2258277 2/1993 United Kingdom 277/53

43 Claims, 7 Drawing Sheets



*Published, with permission, from EG&G Mechanical.

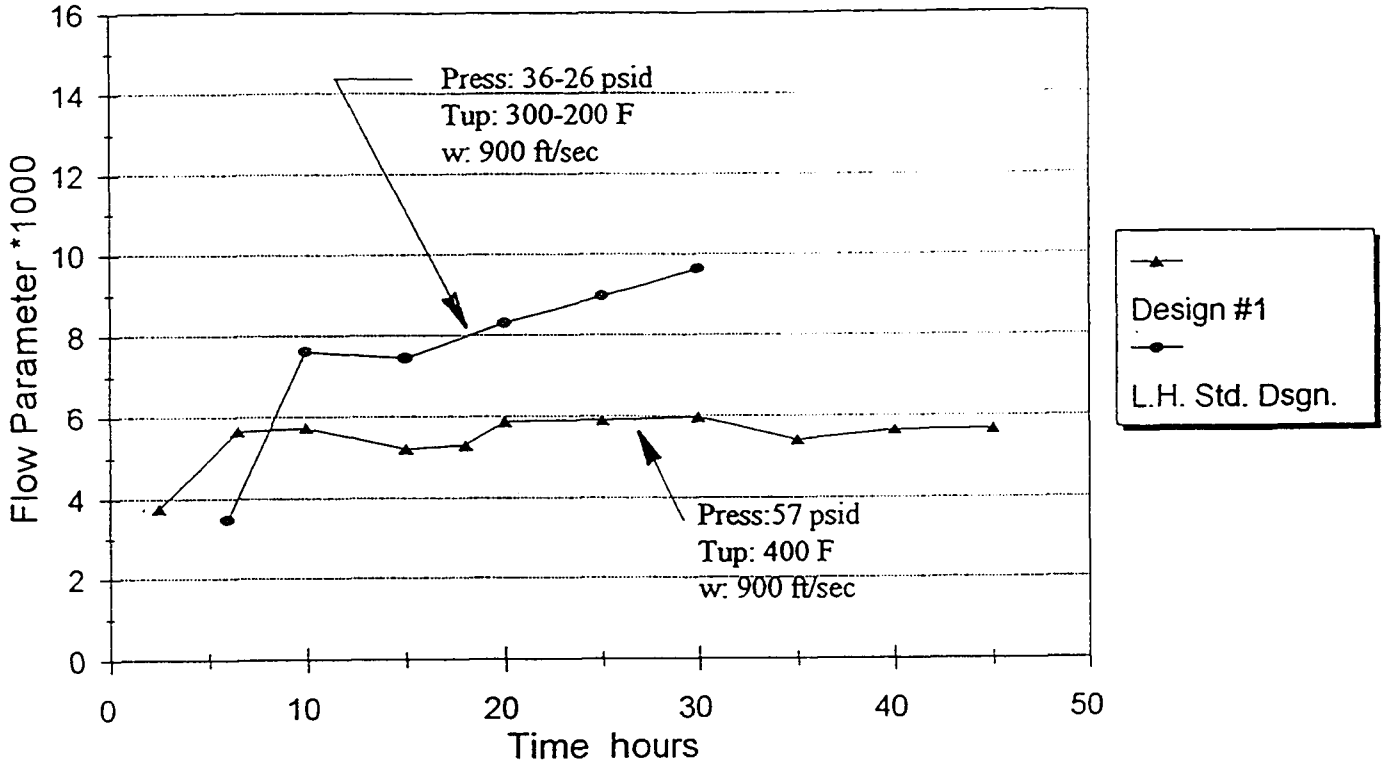
Brush Seal Testing 1990-1995

- **Maximum conditions of successful testing brush seals to date:**
 - **Highest temperature ever tested - 1200°F**
 - **Highest surface speed ever tested - 1080 feet per second**
 - **Highest pressure differential across a single stage seal - 130psid**

 - **Tested 9 inch diameter seal with .019 inch radial excursions for 500 cycles,**
 - **Pressure differential for that test - 57psid.**
 - **Low Hysteresis design. 500°F 950fps.**
 - **Total test time - 80 hours.**
 - **Brush seal tested satisfactorily.**

Flow Parameter History

Design Comparison



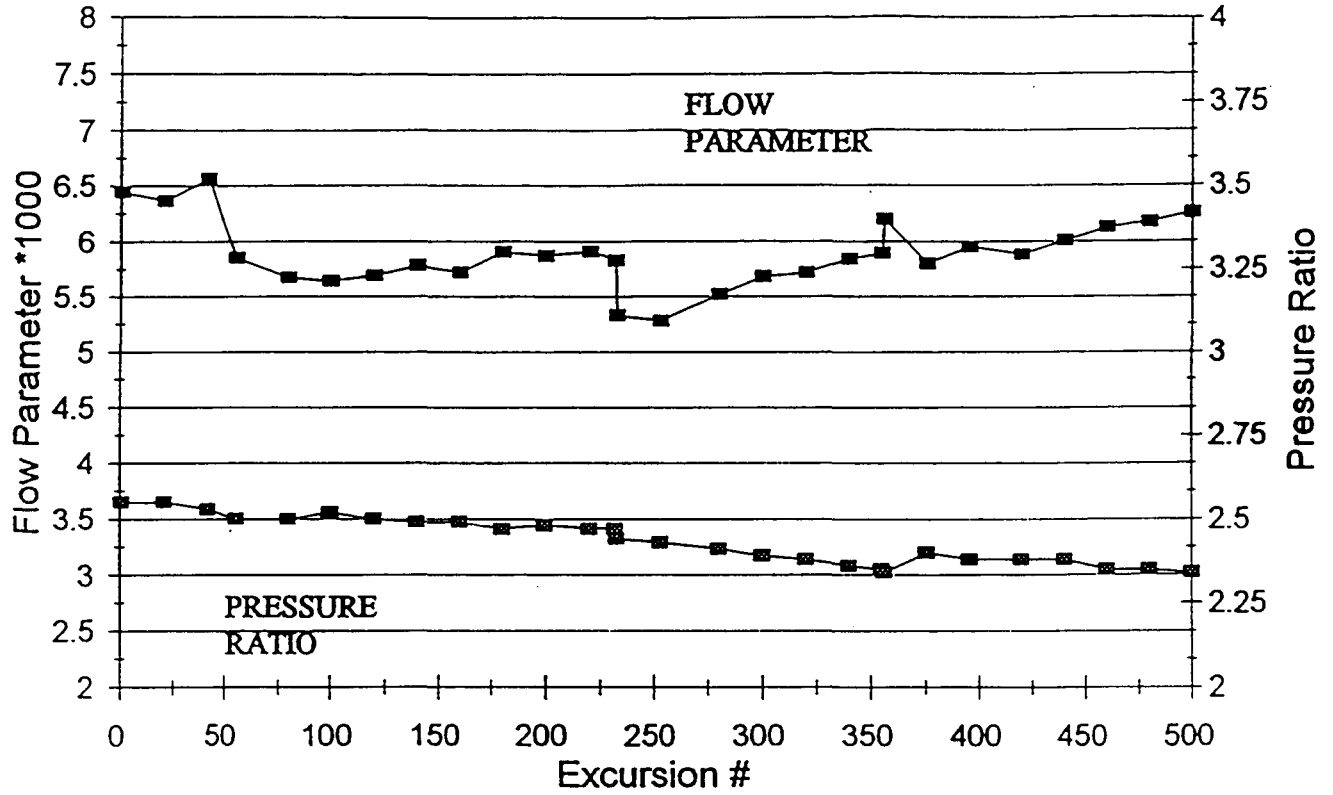
Flow Parameter

$$\Phi = (\dot{m}\sqrt{T}) / (PuDi)$$

\dot{m} = lbmass
 T = temperture in °Rankine
 Pu = upstream pressure psi a
 Di = ID in feet

Excursion Performance

Design#1



Flow Parameter

$$\Phi = (\dot{m}\sqrt{T}) / (P_u D_i)$$

\dot{m} = lbmass

T = temperture in °Rankine

P_u = upstream pressure psia

D_i = ID in feet

- Moving toward best design for IHPTET Goals.
- XTC-76 - New demonstrator engine being built by a GE and Allison team.
- Positions in the engine being selected for demonstration of the PRDA-III seal technology.
- PRDA-III Advanced Brush Seal Development Program will complete in late 1996.

ASPIRATING SEAL DEVELOPMENT: ANALYTICAL MODELING AND SEAL TEST RIG

Bharat Bagepalli
General Electric Company
Schenectady, New York

57-07
39449

ABSTRACT

This effort is to develop large diameter (22 - 36 inch) Aspirating Seals for application in aircraft engines. Stein Seal Co. will be fabricating the 36-inch seal(s) for testing. GE's task is to establish a thorough understanding of the operation of Aspirating Seals through analytical modeling and full-scale testing. The two primary objectives of this project are to develop the analytical models of the aspirating seal system, to upgrade using GE's funds, GE's 50-inch seal test rig for testing the Aspirating Seal (back-to-back with a corresponding brush seal), test the aspirating seal(s) for seal closure, tracking and maneuver transients (tilt) at operating pressures and temperatures, and validate the analytical model.

The objective of the analytical model development is to evaluate the transient and steady-state dynamic performance characteristics of the seal designed by Stein. The transient dynamic model uses a multi-body system approach: the Stator, Seal face and the rotor are treated as individual bodies with relative degrees of freedom. Initially, the thirty-six springs are represented as a single one trying to keep open the aspirating face. Stops (Contact elements) are provided between the Stator and the seal (to compensate the pre-load in the fully-open position) and between the rotor face and Seal face (to detect rub). The secondary seal is considered as part of the stator. The film's load, damping and stiffness characteristics as functions of pressure and clearance are evaluated using a separate (NASA) code GFACE. Initially, a laminar flow theory is used. Special two-dimensional interpolation routines are written to establish exact film load and damping values at each integration time step. Additionally, other user-routines are written to read-in actual pressure, rpm, stator-growth and rotor growth data and, later, to transfer these as appropriate loads/motions in the system-dynamic model. The transient dynamic model evaluates the various motions, clearances and forces as the seals are subjected to different aircraft maneuvers: Windmilling restart; start-ground idle; ground idle-takeoff; takeoff-burst chop, etc. Results of this model show that the seal closes appropriately and does not ram into the rotor for all of the conditions analyzed.

The rig upgrade design for testing Aspirating Seals has been completed. Long lead-time items (forgings, etc.) have been ordered.

Analytical Modeling of Aspirating Seals

- **TRANSIENT DYNAMICS**
 - Time Variation of Aspiration Motion in Moving From One Operating Regime to Another
- **STEADY STATE DYNAMICS**
 - The Behavior and Dynamic Characteristics of the Aspirating Seal in the Vicinity of an Operating Regime under Cyclic Perturbations

Transient Dynamics Cases

Windmilling Restart (6 cases)

Initial closure to ground idle

Ground idle to takeoff

Takeoff to ground idle chop (deceleration)

1/5000 maneuver

Ground idle to takeoff via worst case burst

Takeoff to worst case chop ground idle

Takeoff to cruise

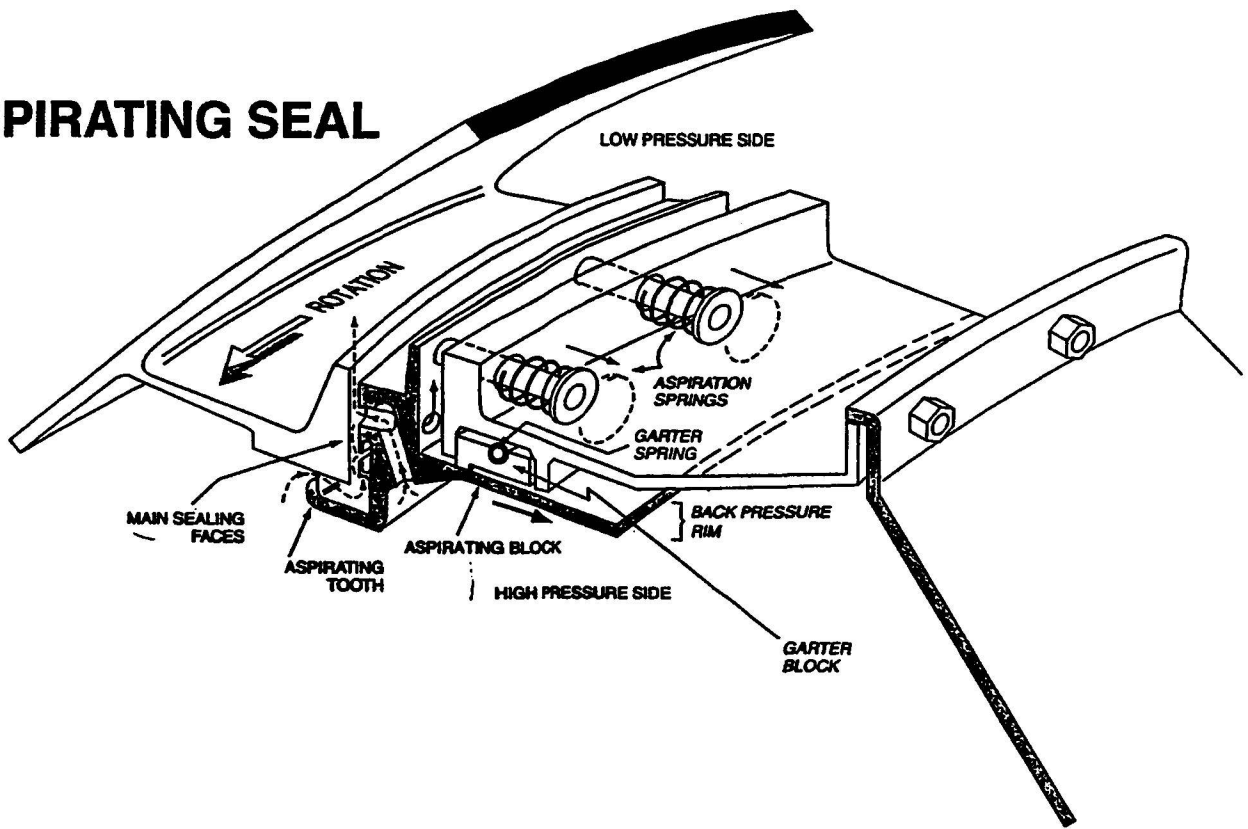
Steady State Dynamics Cases

Ground Idle

Take Off

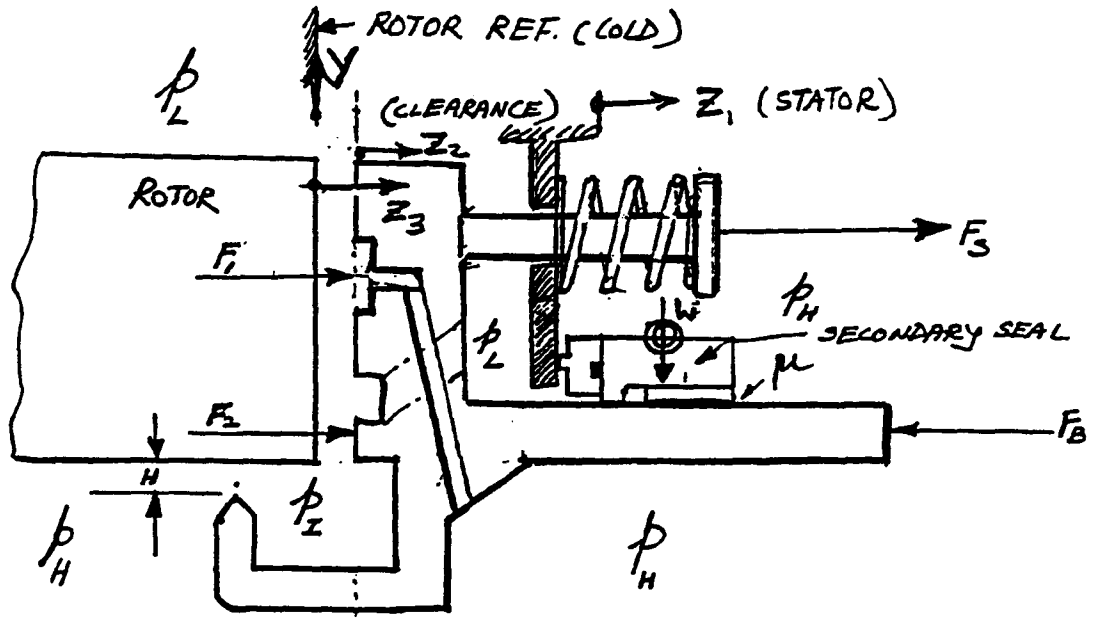
Cruise

ASPIRATING SEAL



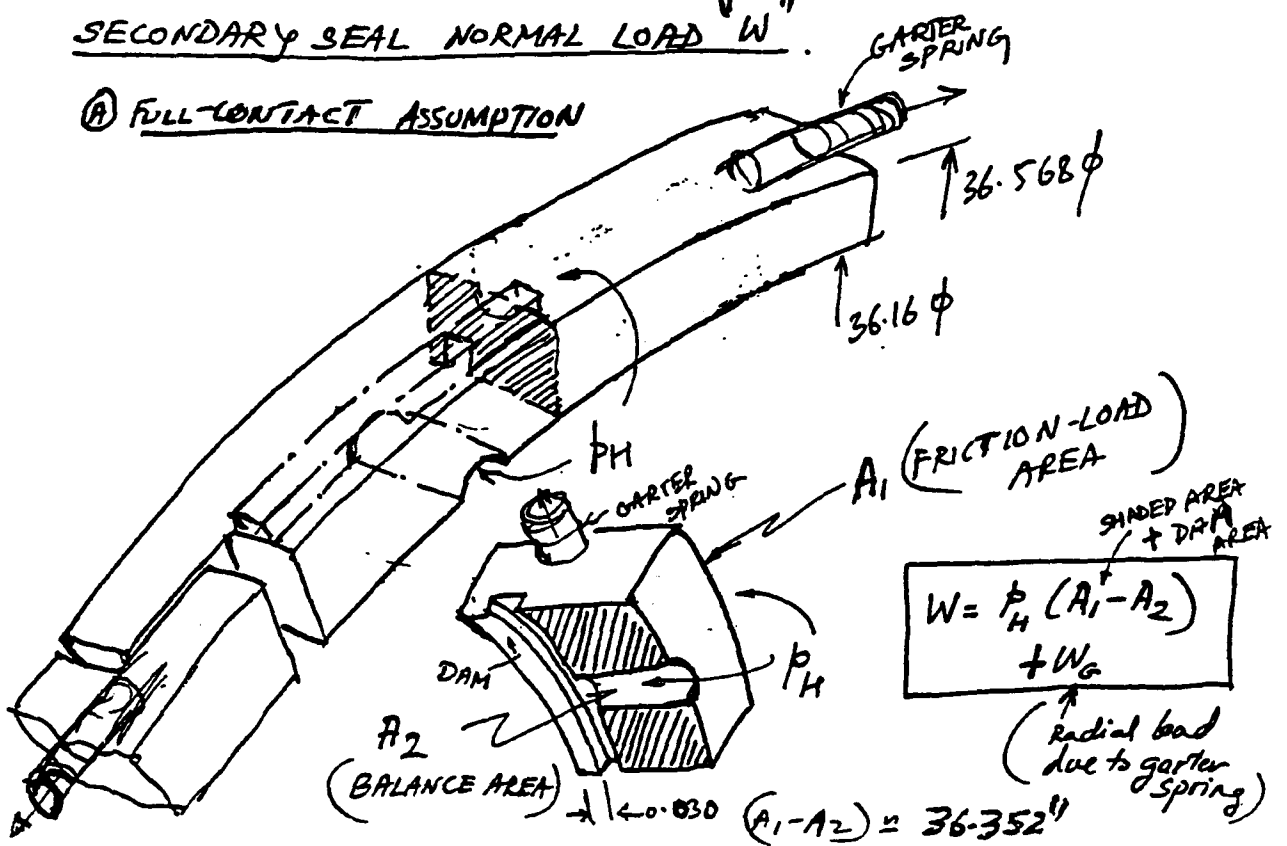
ASPIRATING FACE SEAL

TRANSIENT-DYNAMICS MODEL

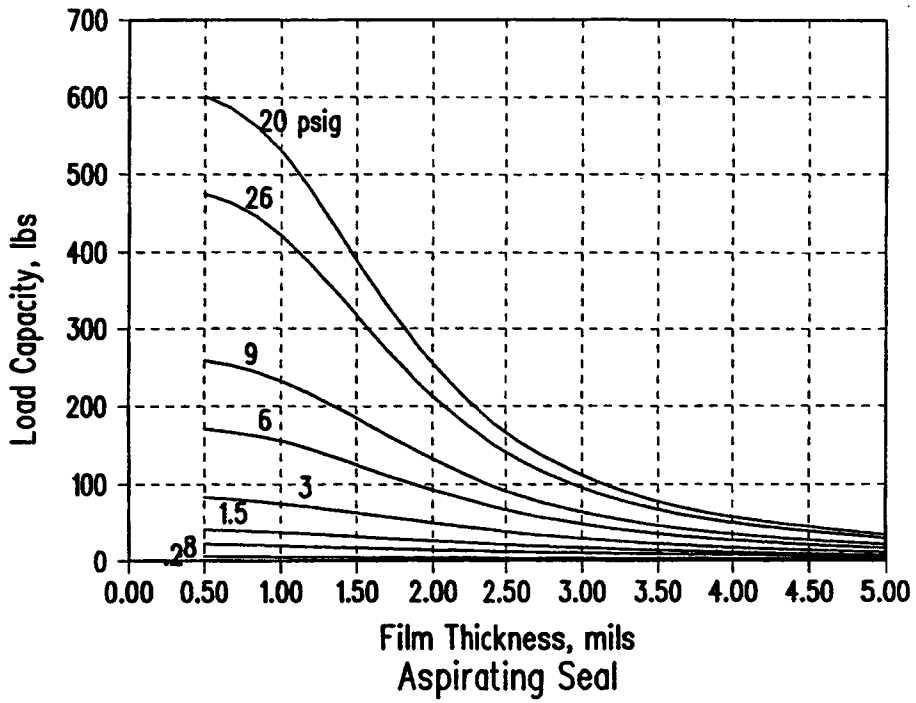


SECONDARY SEAL NORMAL LOAD "W"

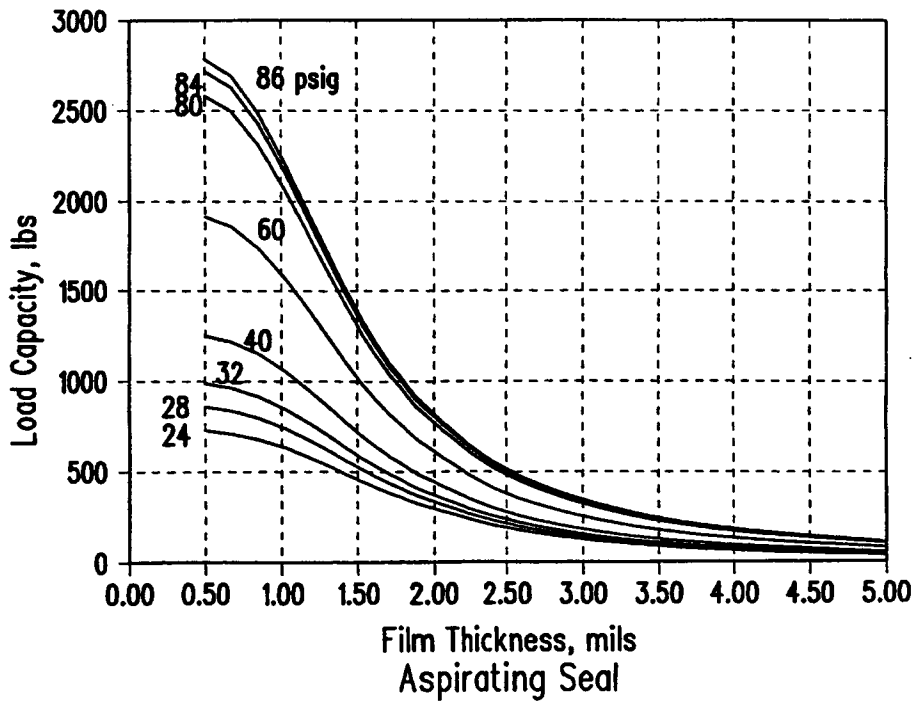
Ⓐ FULL-CONTACT ASSUMPTION



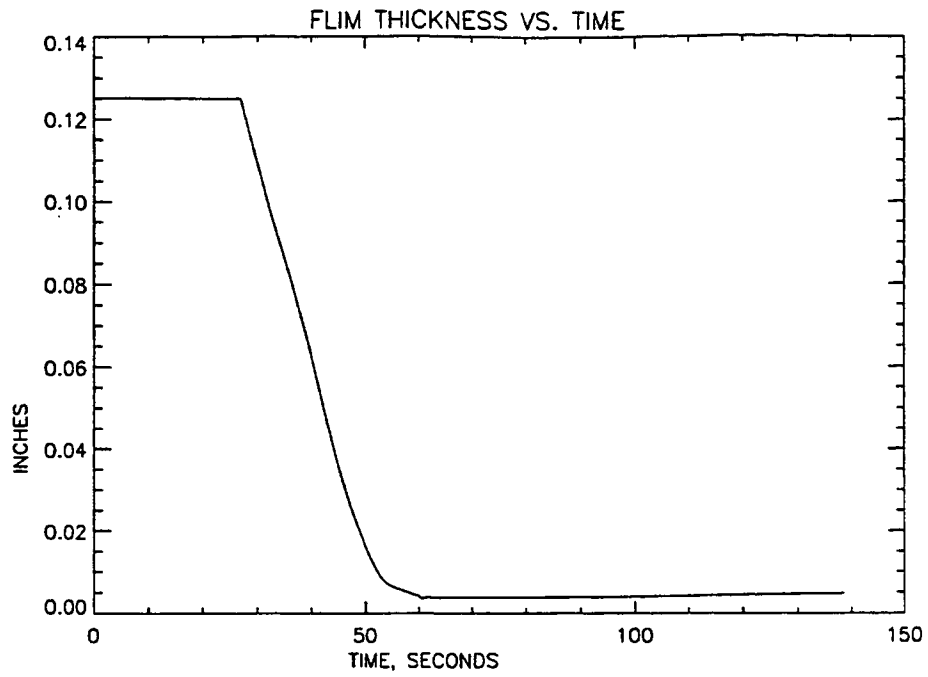
F1 - Load Capacity



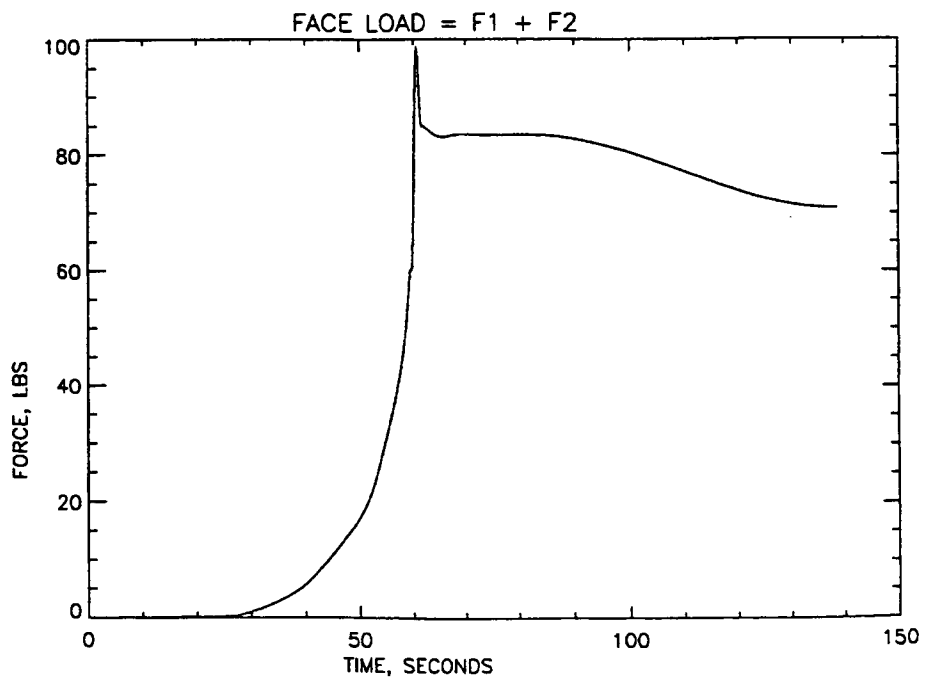
F1 - Load Capacity



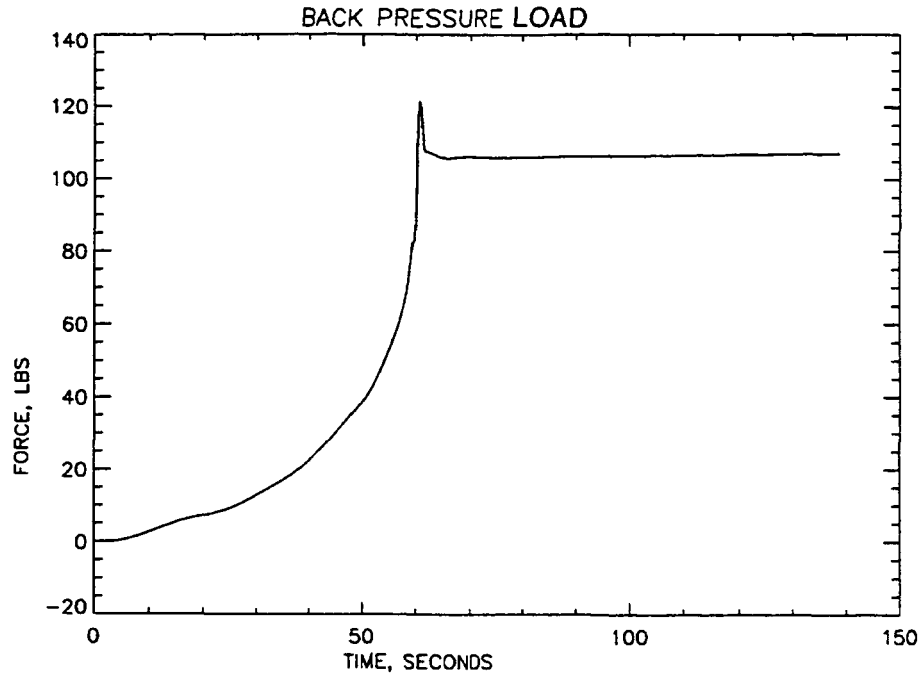
Seal Closure to GI



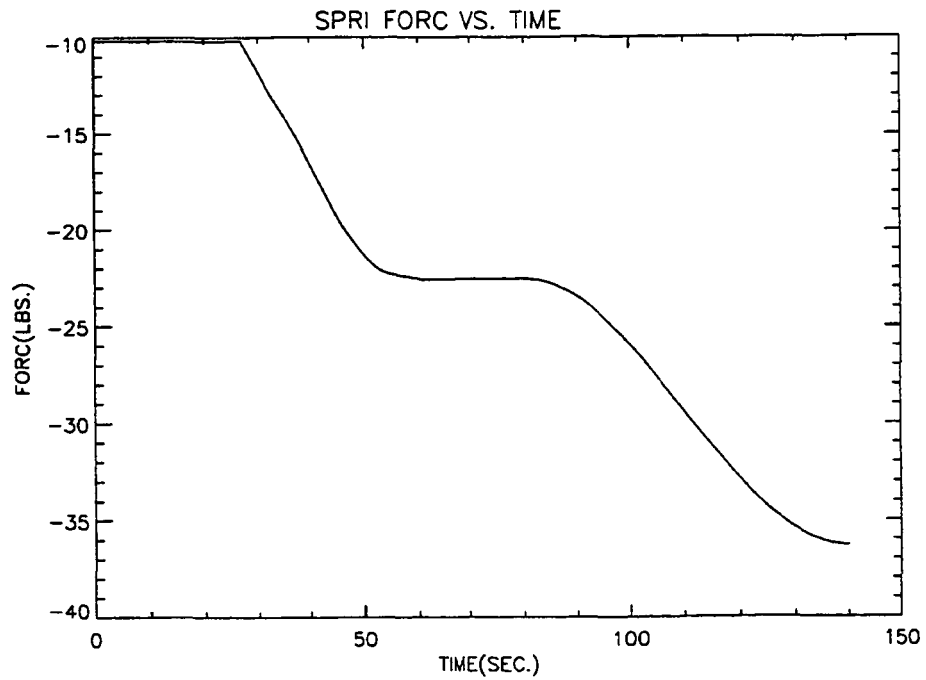
Seal Closure to GI



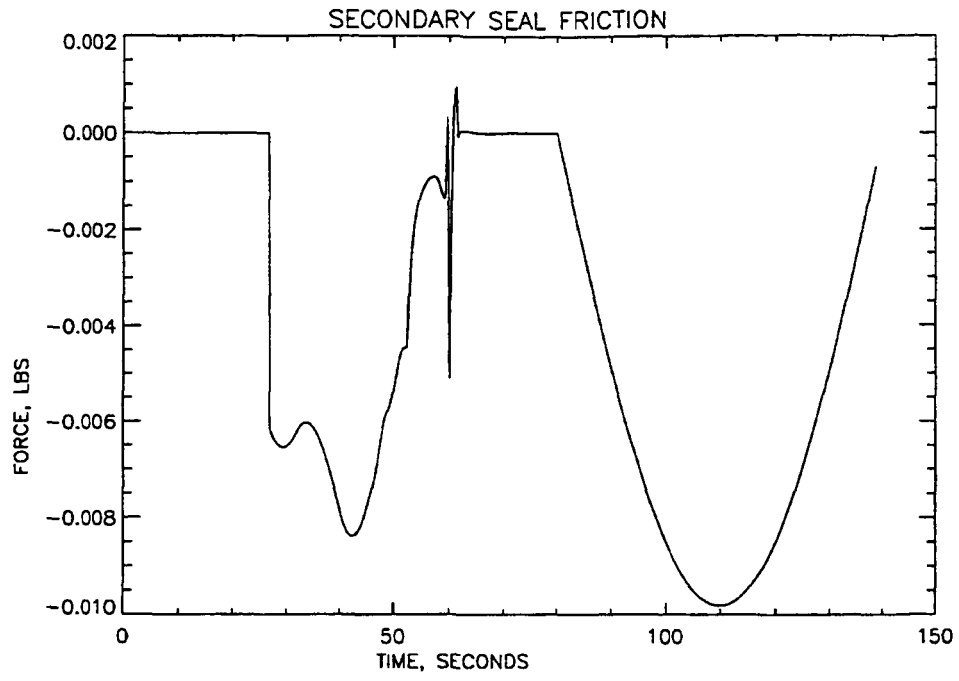
Seal Closure to GI



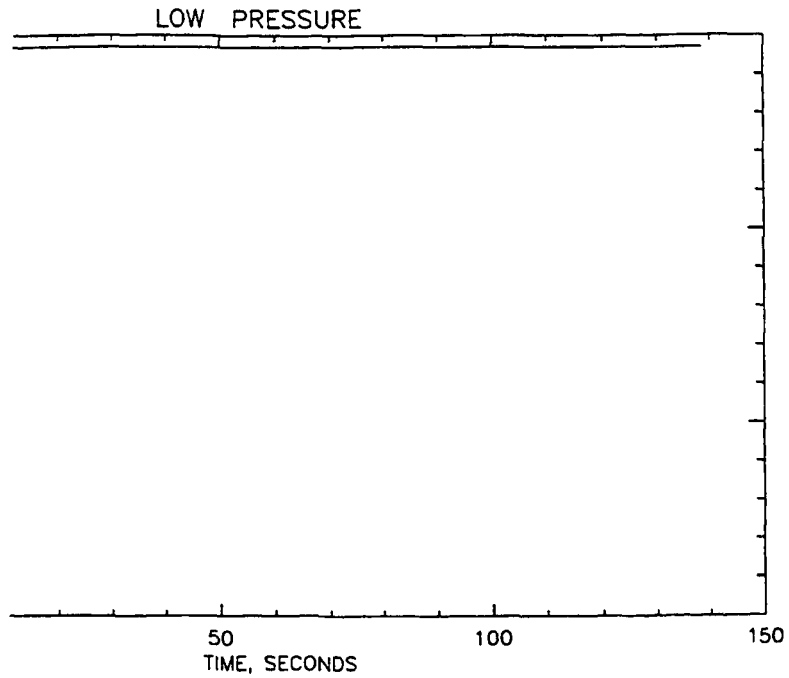
Seal Closure to GI



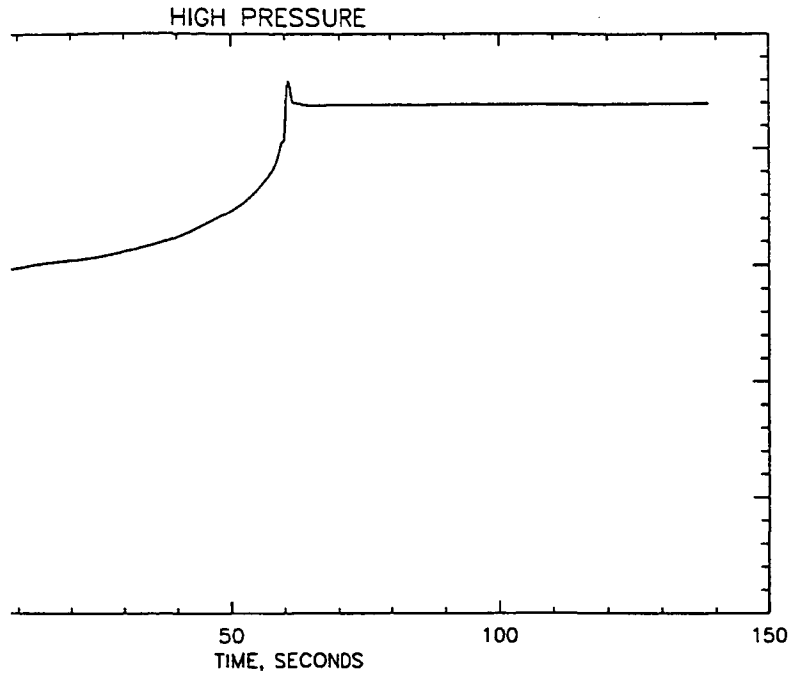
Seal Closure to GI



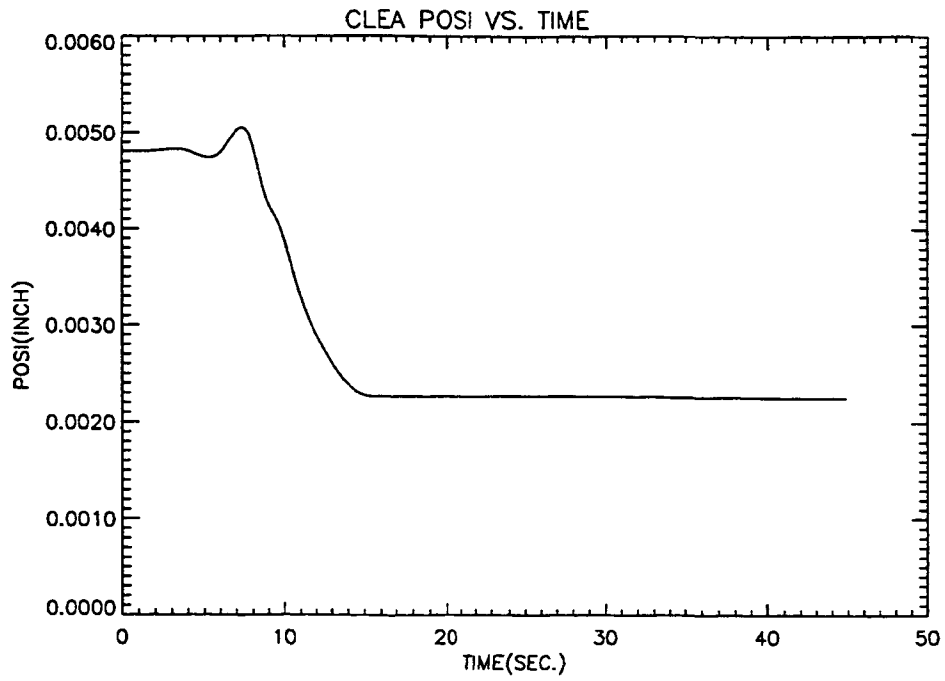
Seal Closure to GI



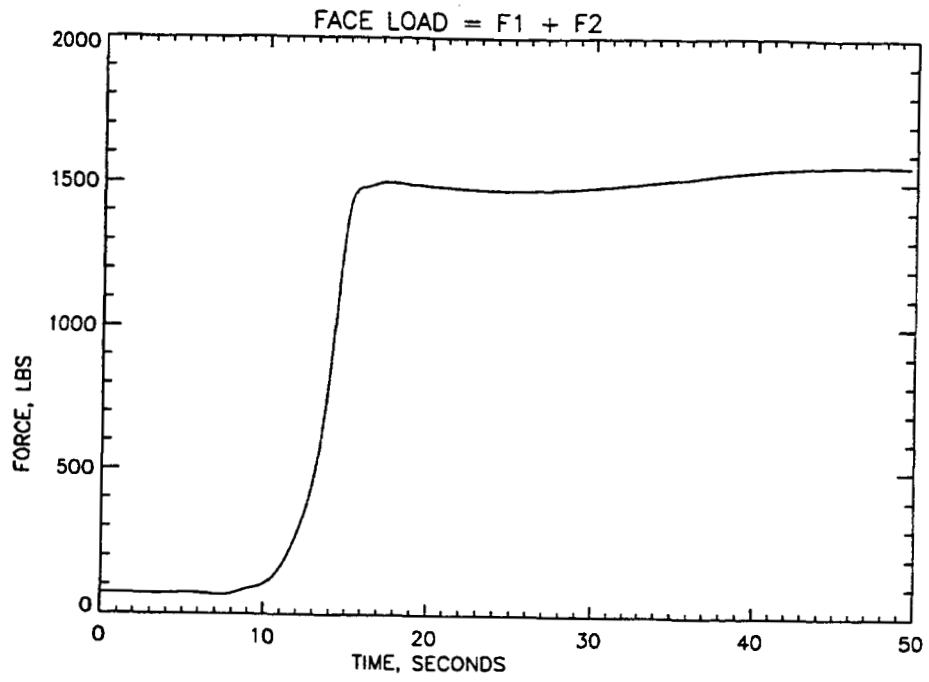
Seal Closure to GI



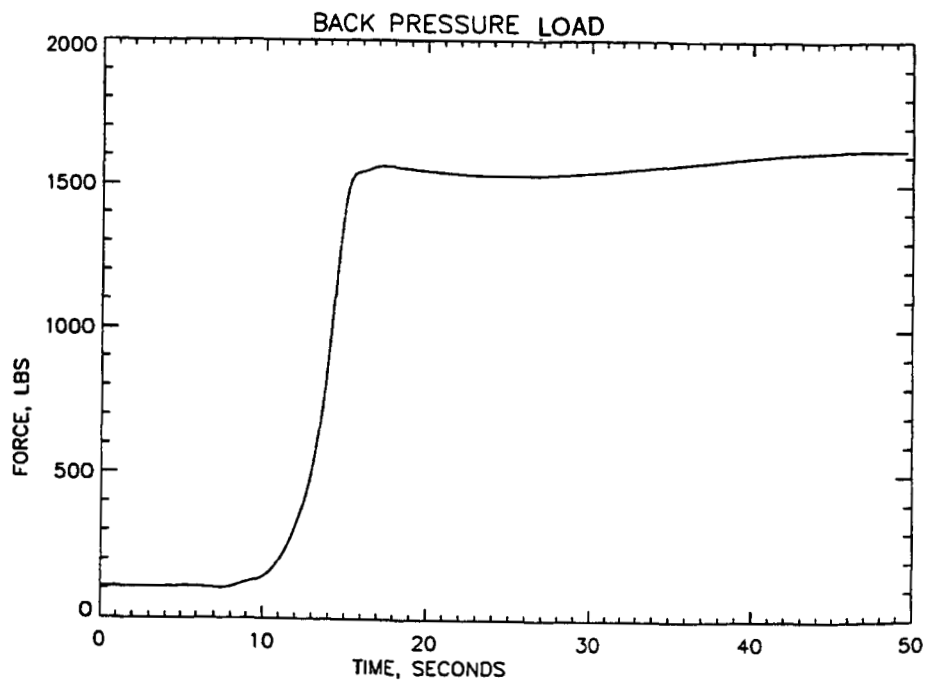
GI to Takeoff



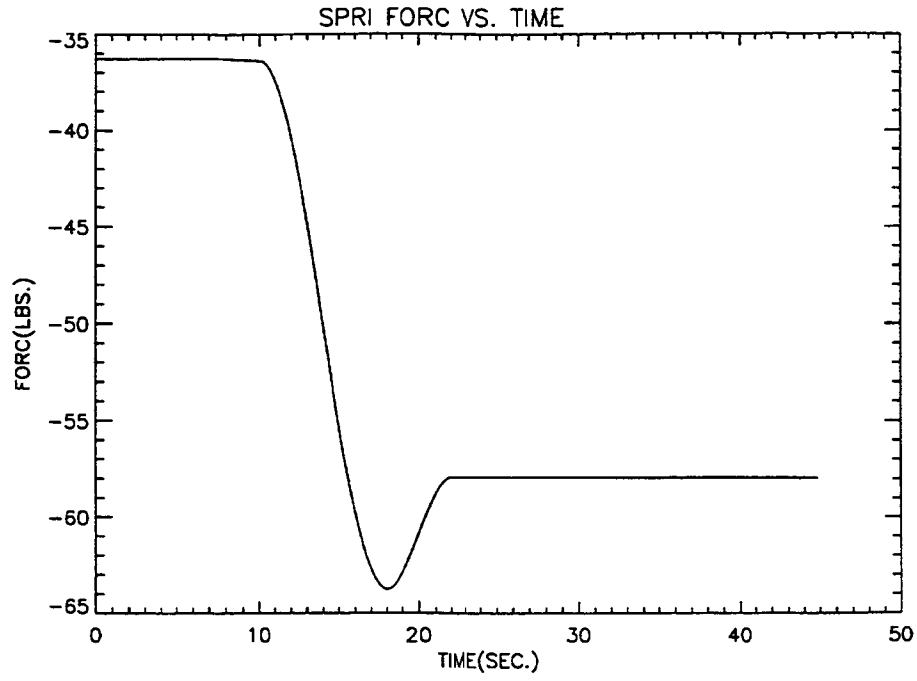
GI to Takeoff



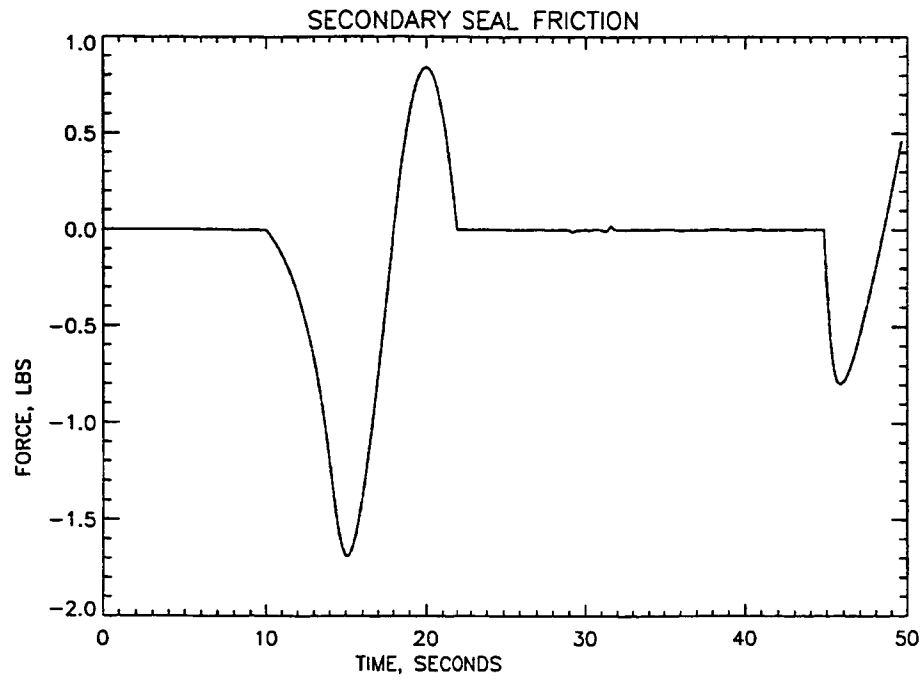
GI to Takeoff



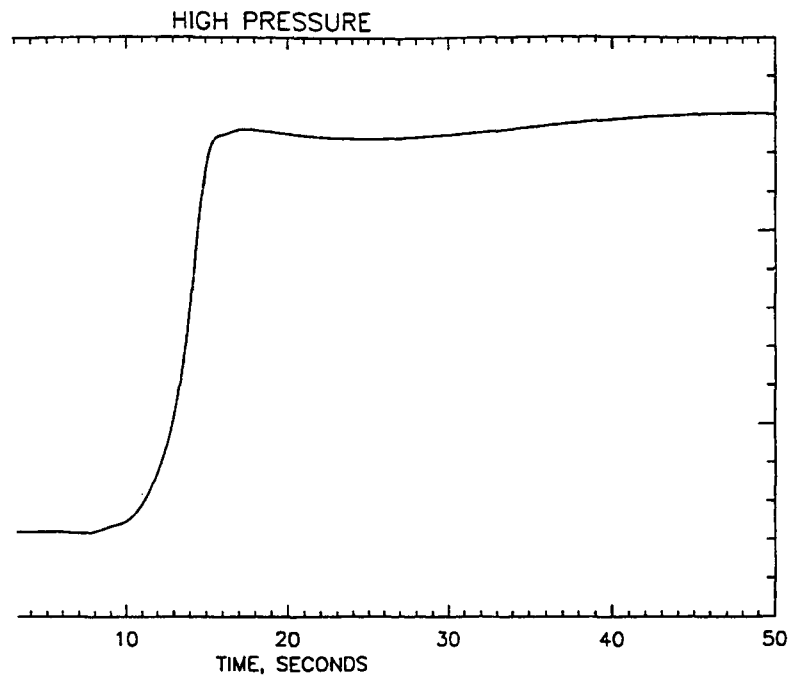
GI to Takeoff



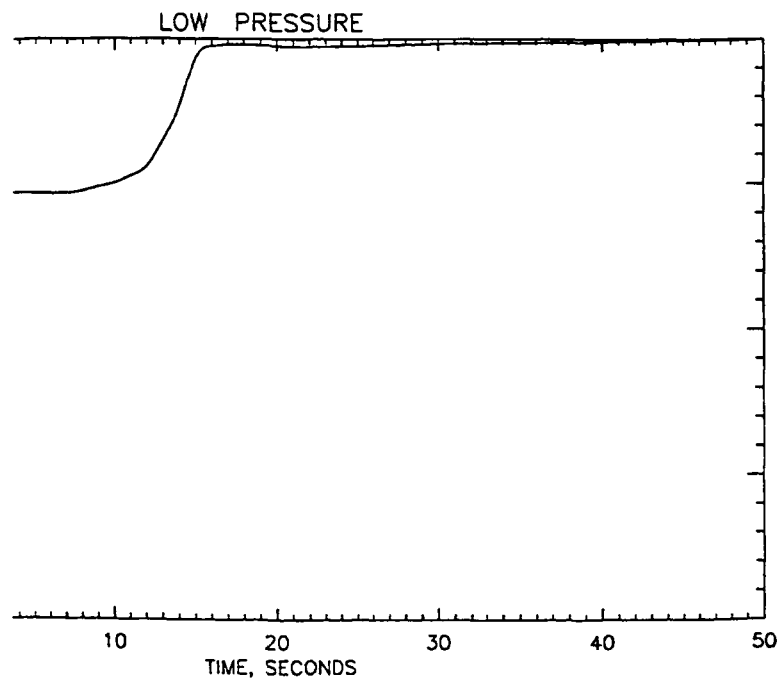
GI to Takeoff



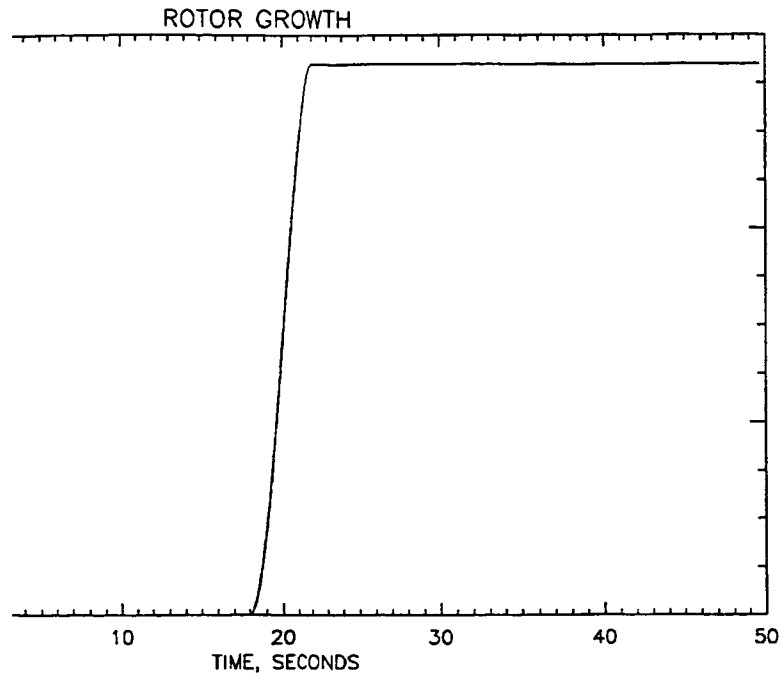
GI to Takeoff



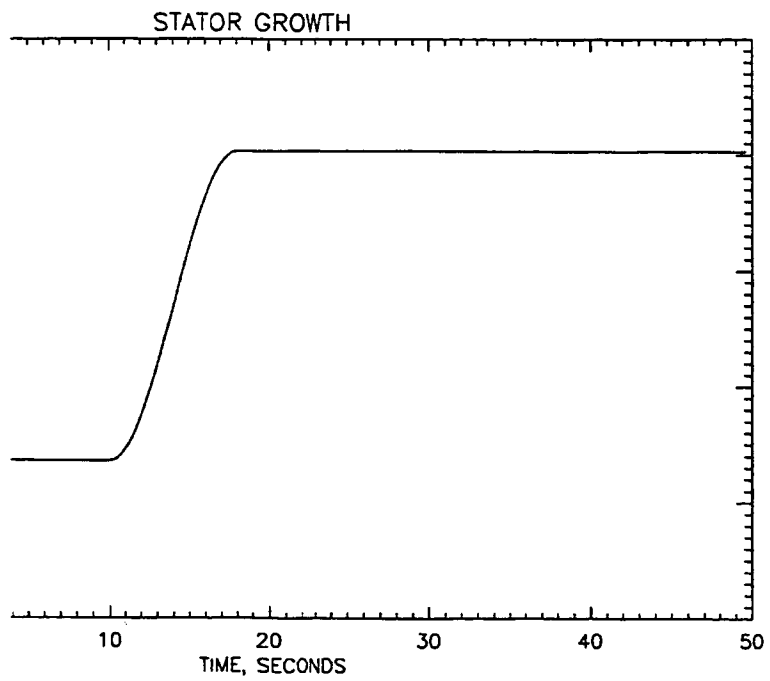
GI to Takeoff



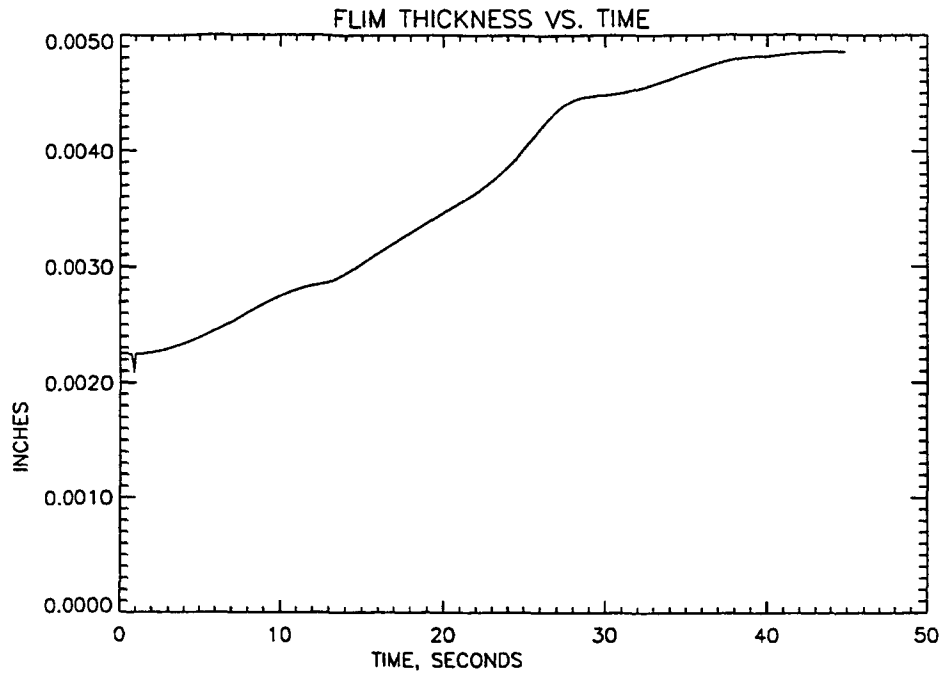
GI to Takeoff



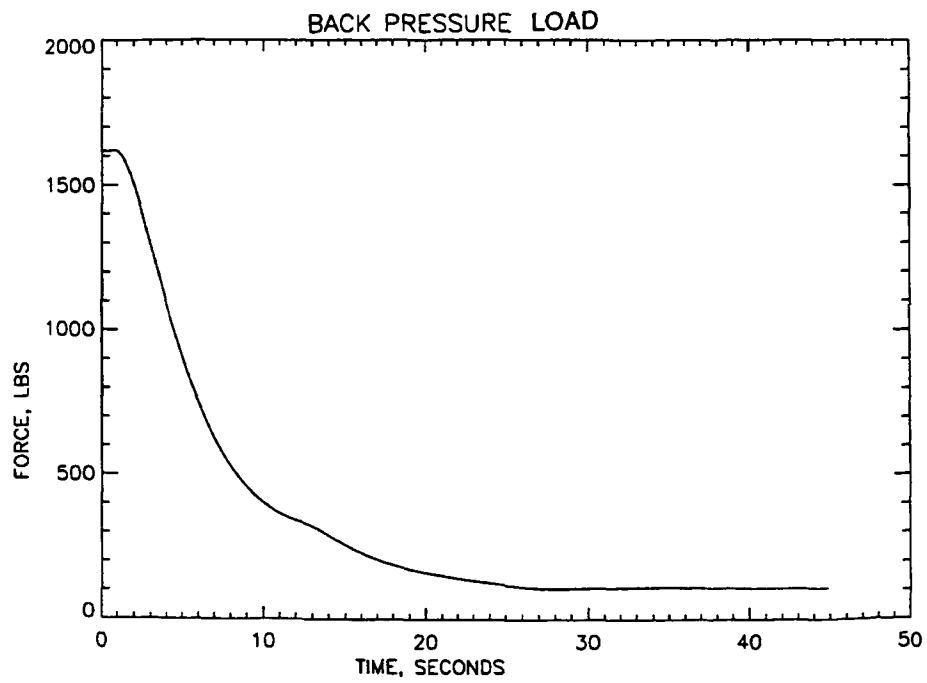
GI to Takeoff



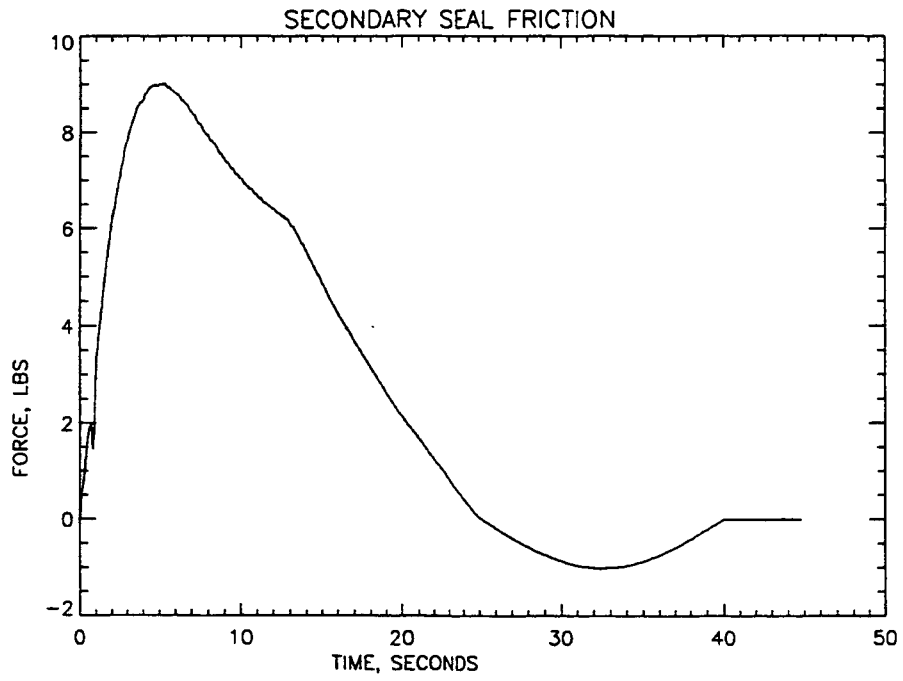
Chop to GI



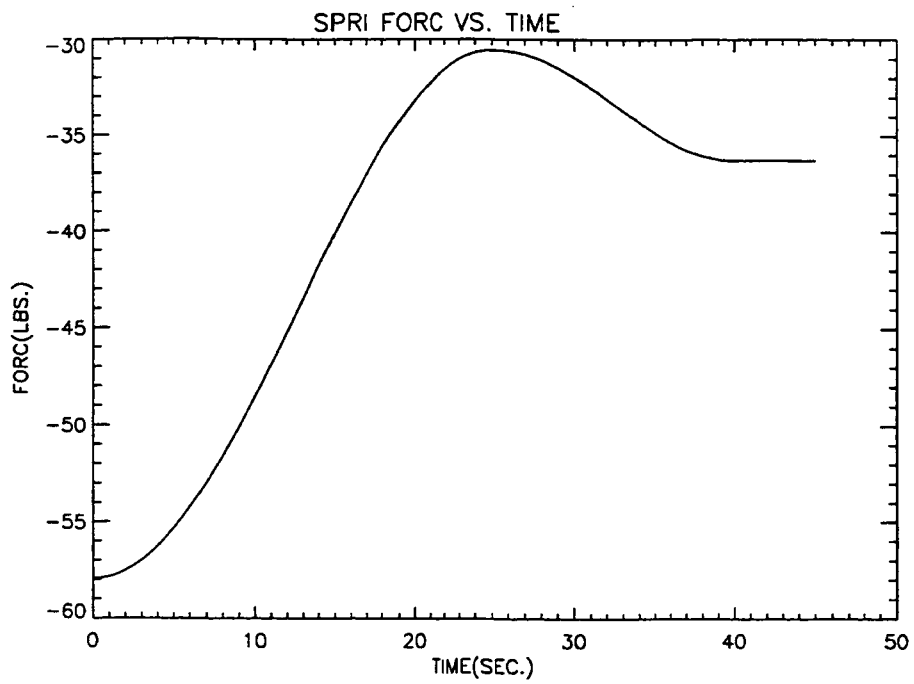
Chop to GI



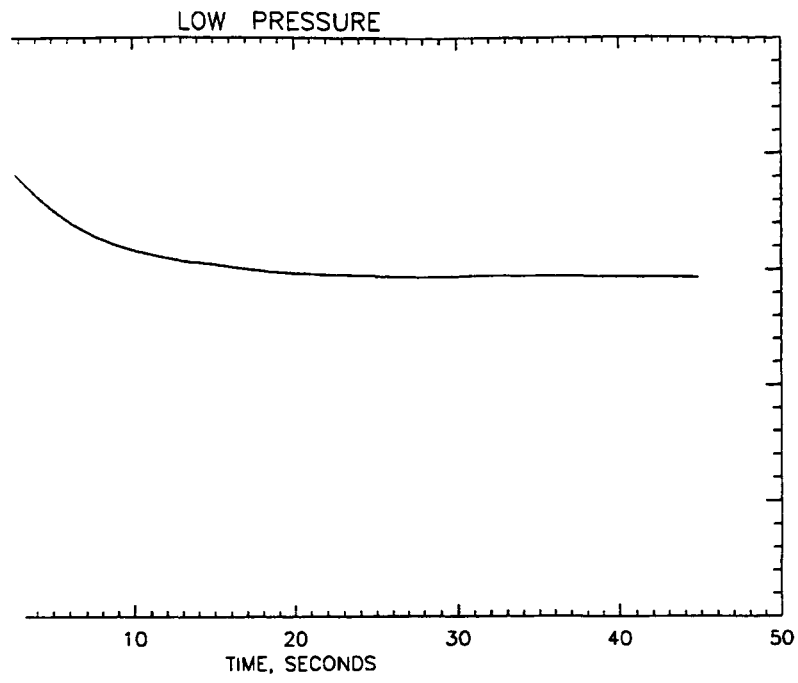
Chop to GI



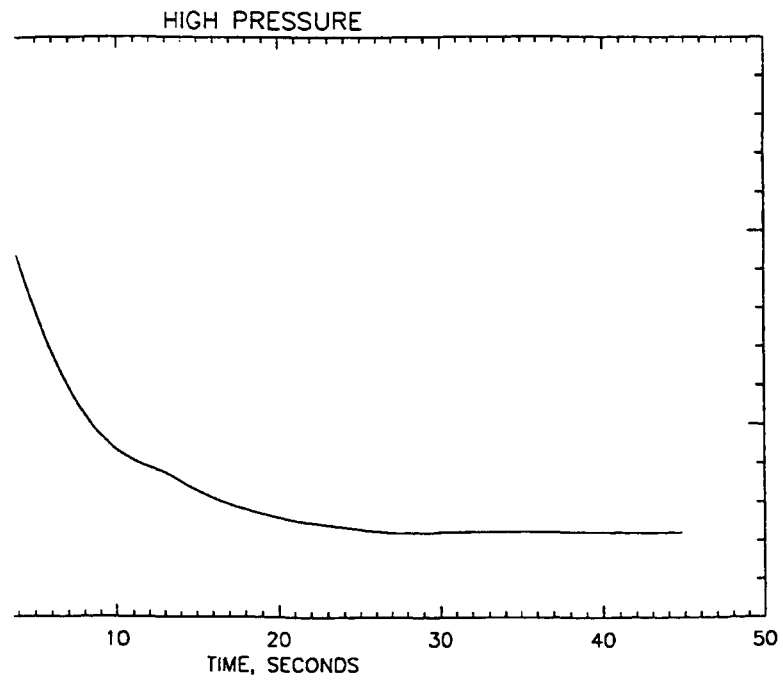
Chop to GI



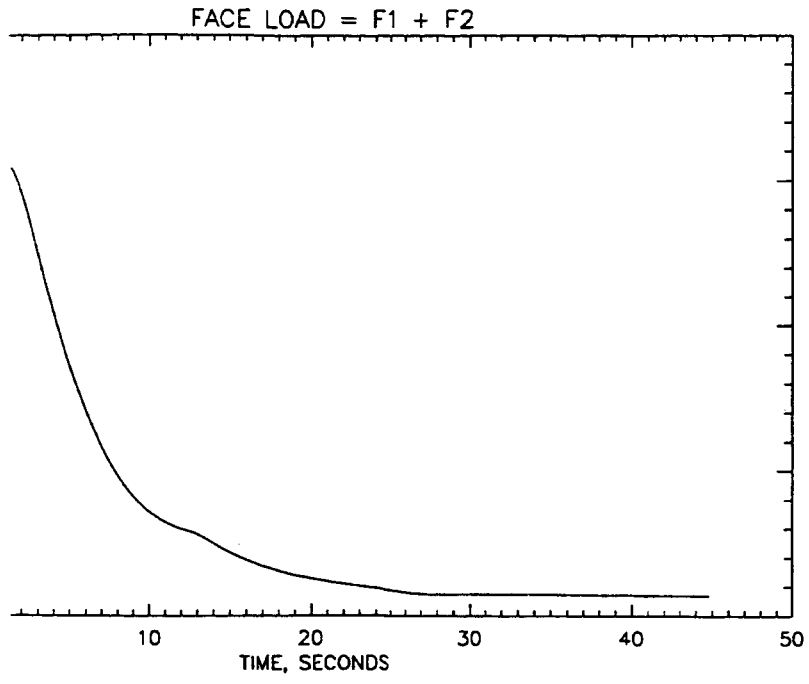
Chop to GI



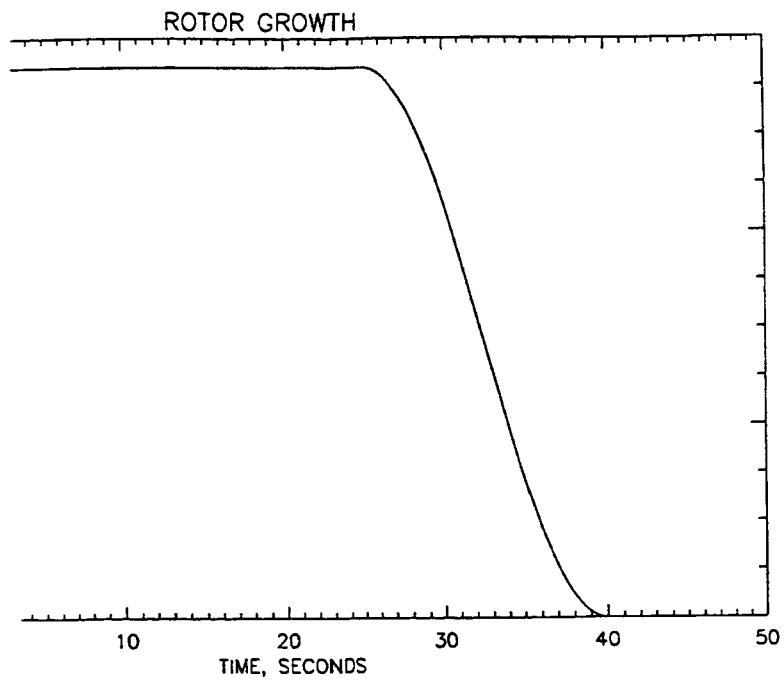
Chop to GI



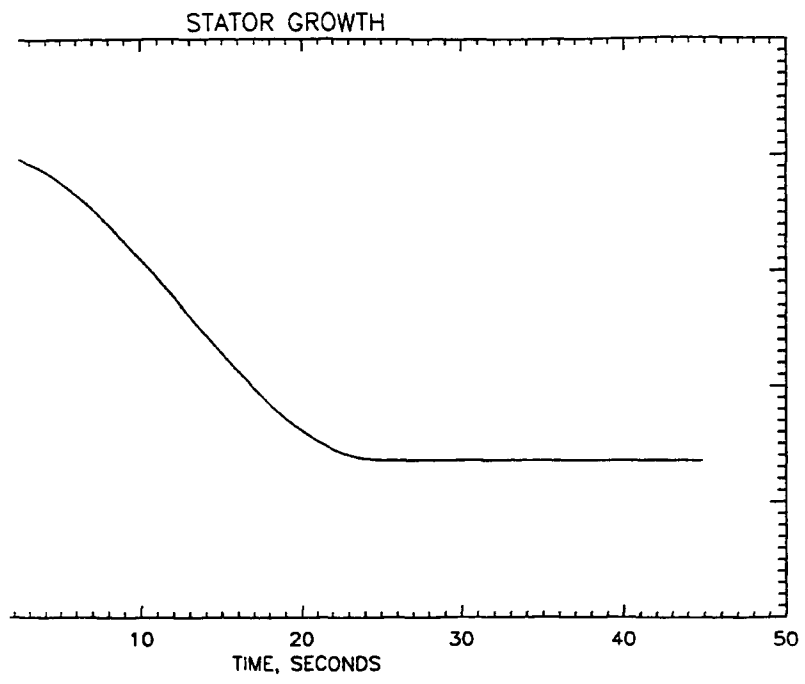
Chop to GI



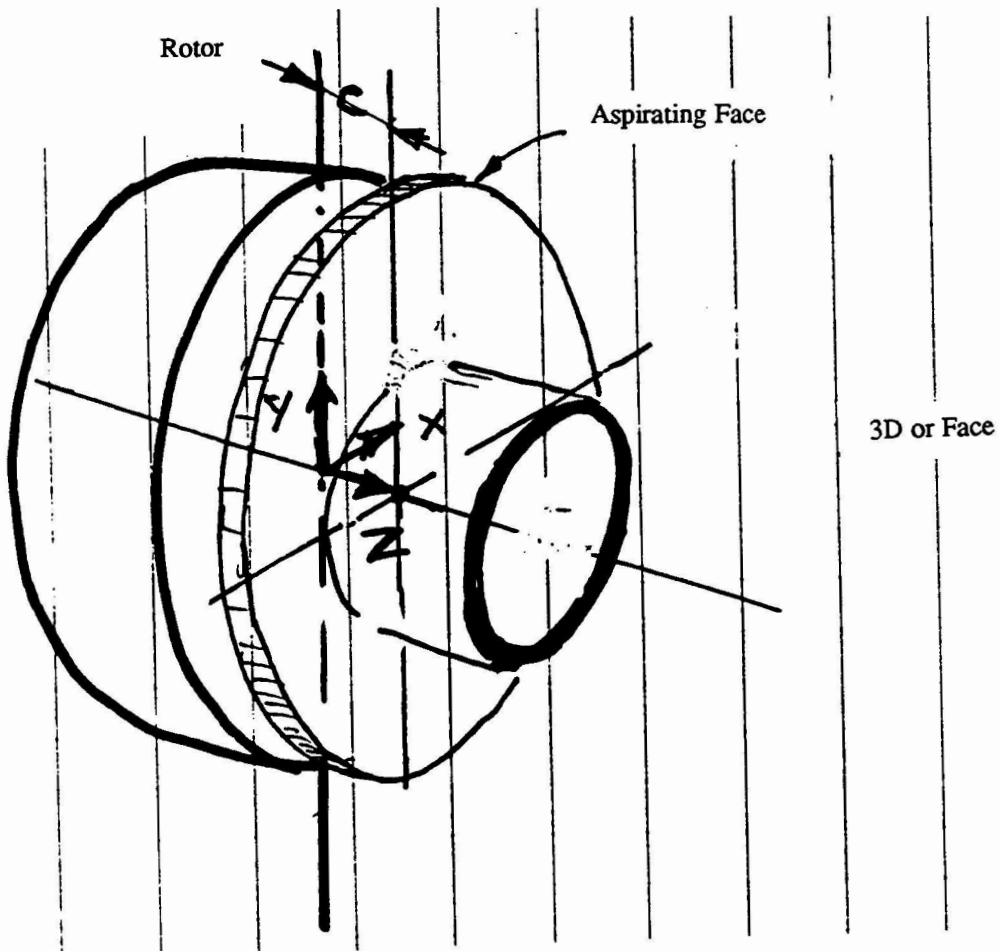
Chop to GI



Chop to GI



STEADY STATE DYNAMICS



Axial Perturbations: $\pm\Delta x, \pm\Delta y, \pm\Delta z$

Angular Perturbations $\pm\Delta\theta_x, \pm\Delta\theta_y$

Result in runout at seal face (TIR)

Nominal Design Requirement:

$\pm\Delta x, \pm\Delta y, \pm\Delta z = \pm 2$ mils (?)

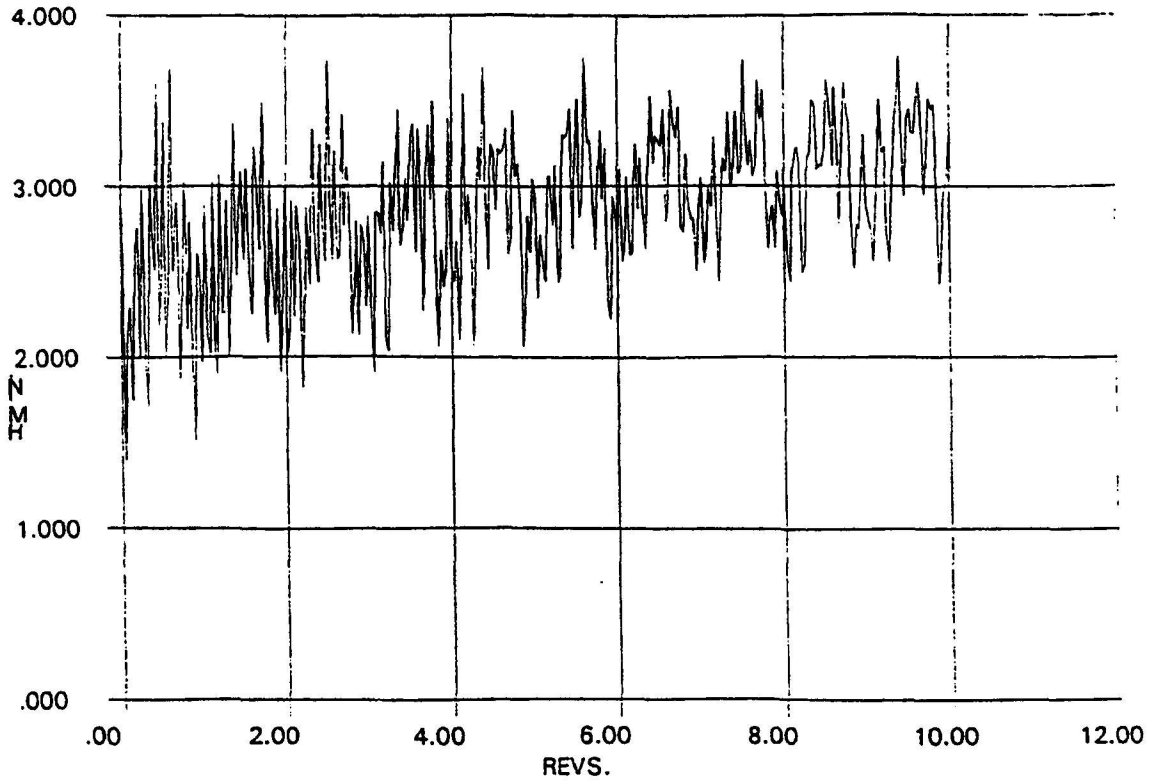
TIR = ± 10 mils at 36 in.

APPROPRIATE DEGREES OF FREEDOM, (5)
STIFFNESSES, AND INERTIAS OF THE SEAL ARE CONSIDERED

DYNAMIC ANALYSIS OF SEALS

HMIN.

GE ASPIRATING SEAL, CRUISE CONDITIONS, CASE 2

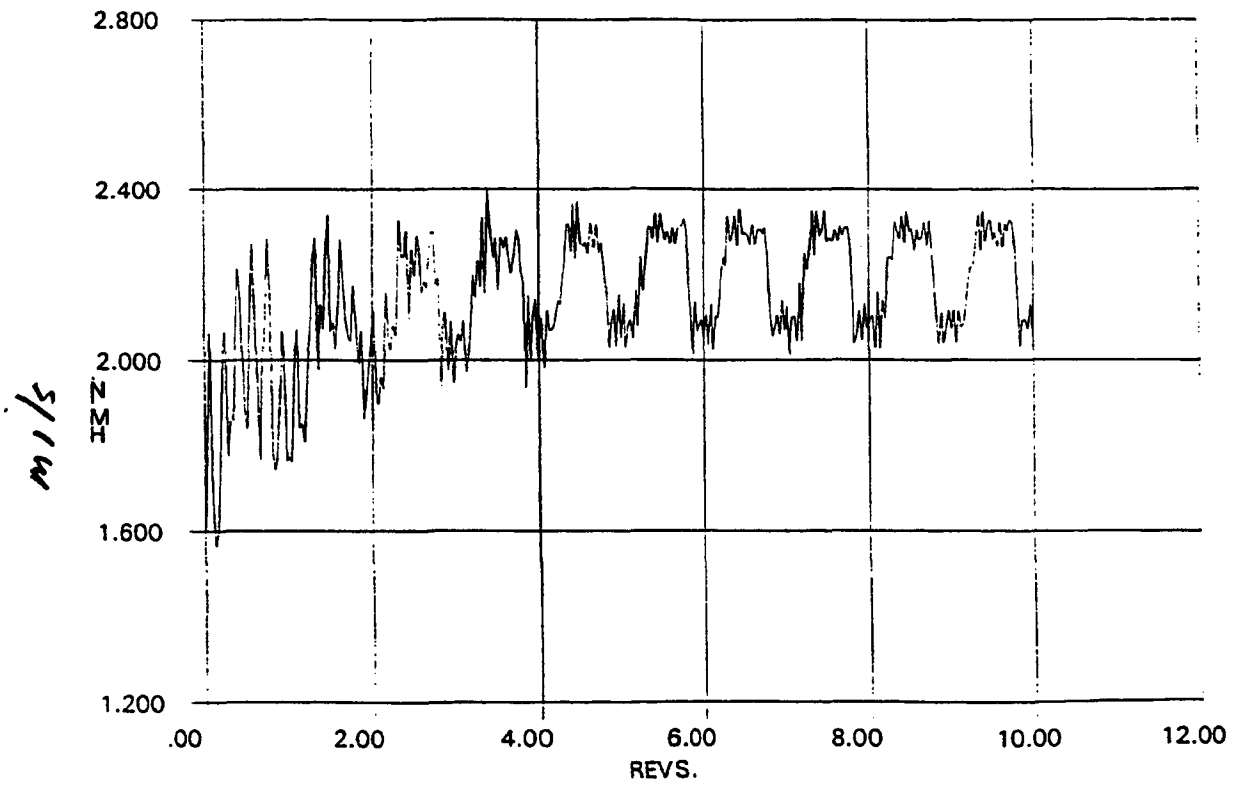


Minimum Film Thickness
equilibrium = 2.25 mils

GROOVED

DYNAMIC ANALYSIS OF SEALS
GE ASPIRATING SEAL, TAKEOFF CONDITIONS, CASE 2

— HMIN. $\omega / .03'' e / \omega$



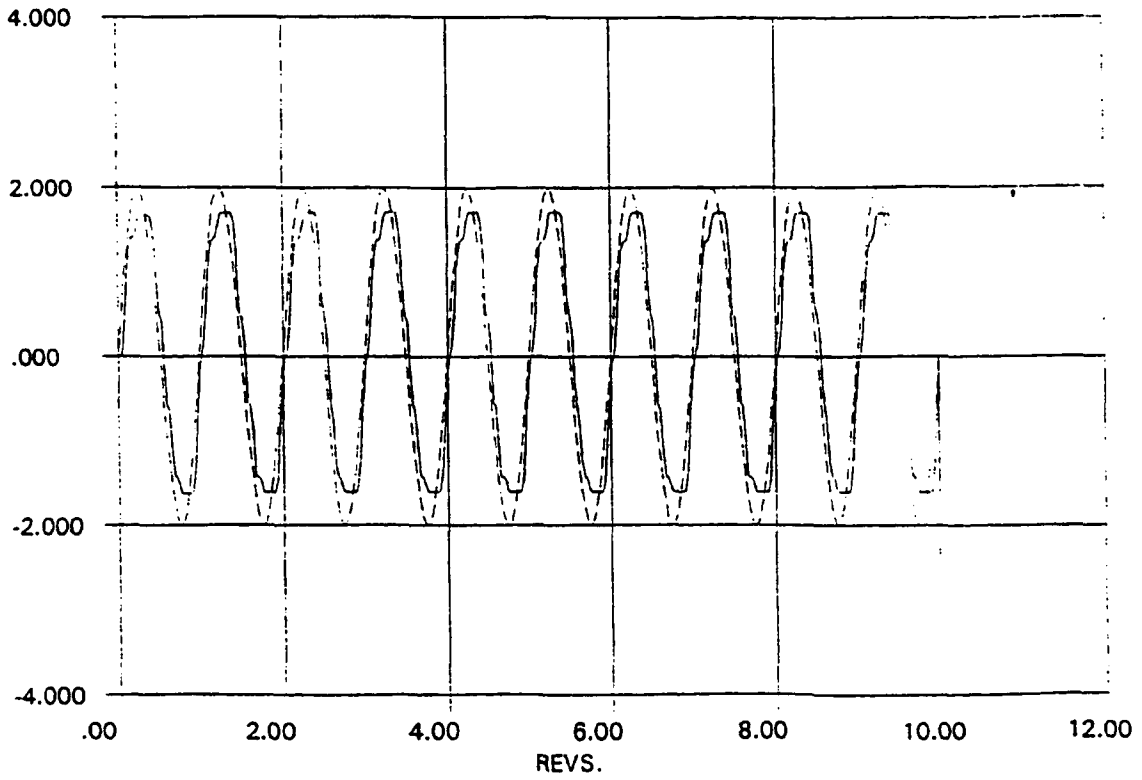
$X_0 = Y_0 = Z_0 = 2$ mils
misalignment = ± 10 mils TIR

GROOVED

DYNAMIC ANALYSIS OF SEALS

— ZS-DISP.
- - - Z-DISPL.

GE ASPIRATING SEAL, IDLE CONDITIONS, CASE 2



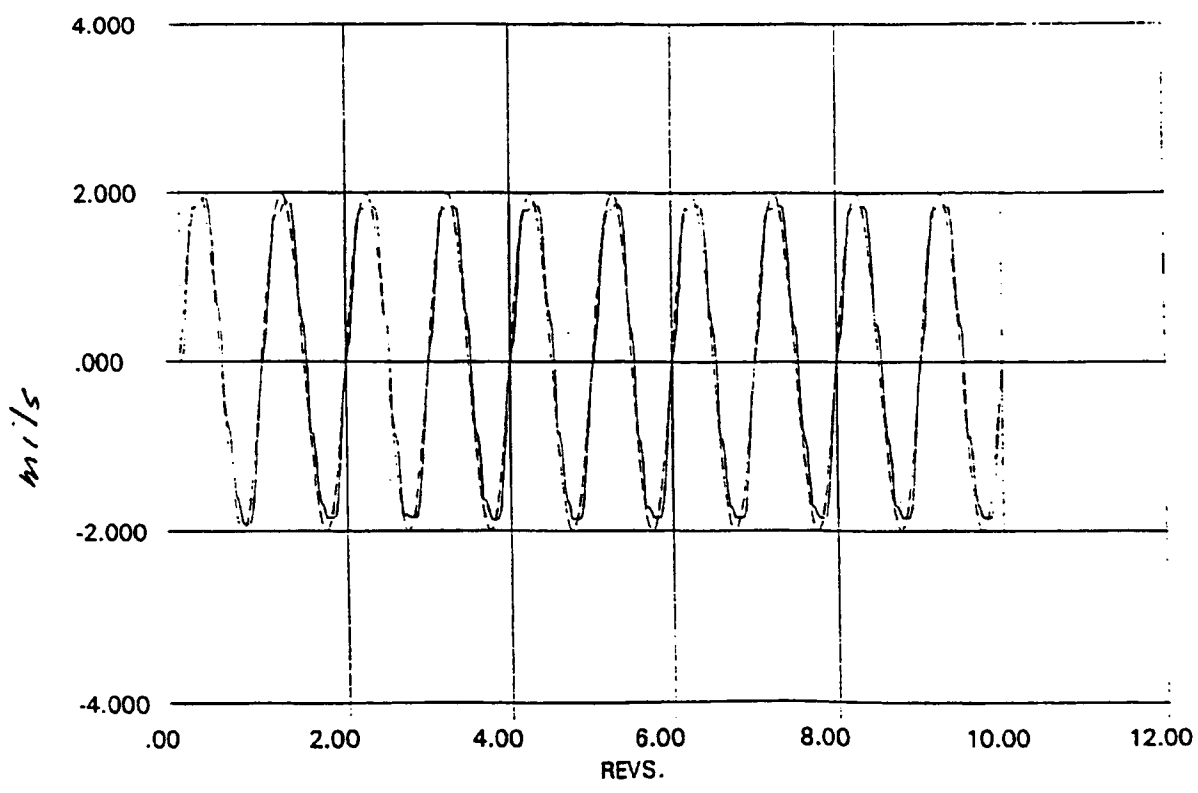
$X_0 = Y_0 = Z_0 = 2$ mils
misalignment = ± 10 mils TIR

Axial Vibrations
Synchronized

GROOVED

DYNAMIC ANALYSIS OF SEALS
GE ASPIRATING SEAL, CRUISE CONDITIONS, CASE 2

--- ZS-DISP.
- - - Z-DISPL.



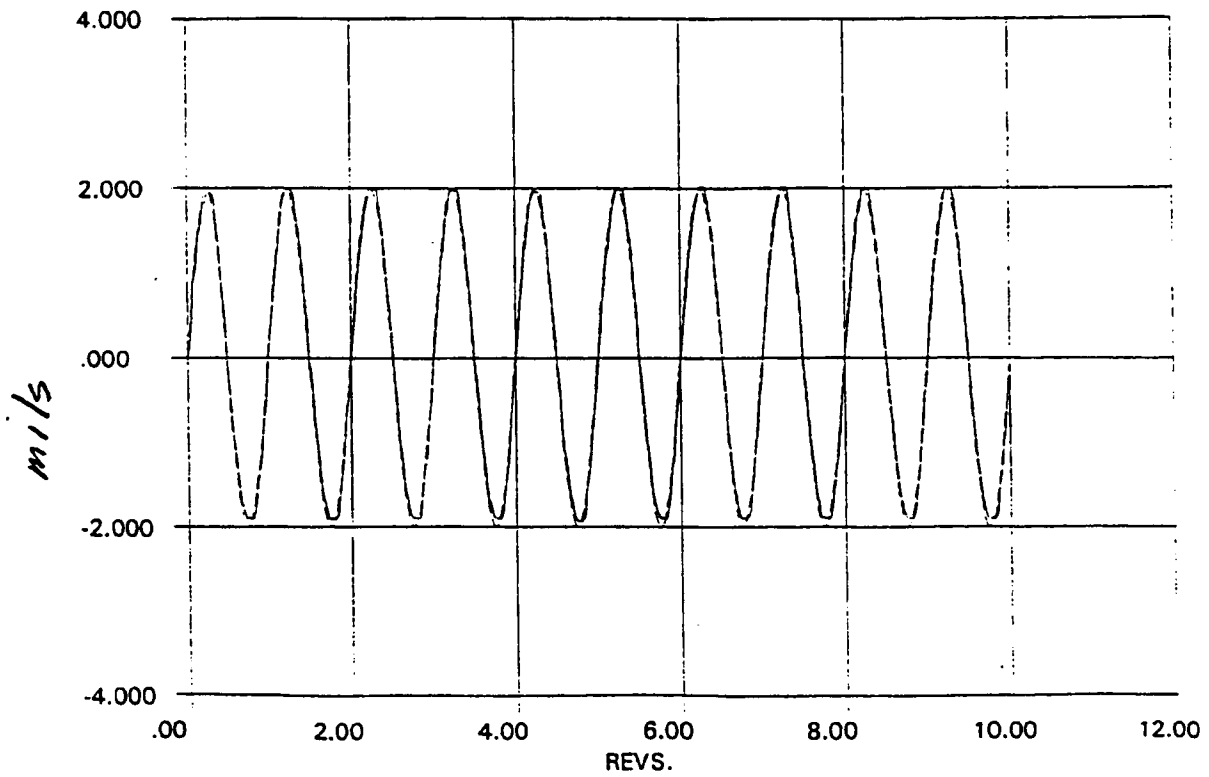
$X_0 = Y_0 = Z_0 = 2$ mils
misalignment = ± 10 mils TIR
 $f = 0.2$

Axial Vibrations
Synchronized

GROOVED

DYNAMIC ANALYSIS OF SEALS
GE ASPIRATING SEAL, TAKEOFF CONDITIONS, CASE 2

— ZS-DISP. SEAL
- - - Z-DISPL. ROTOR



Aspirating Seal Test

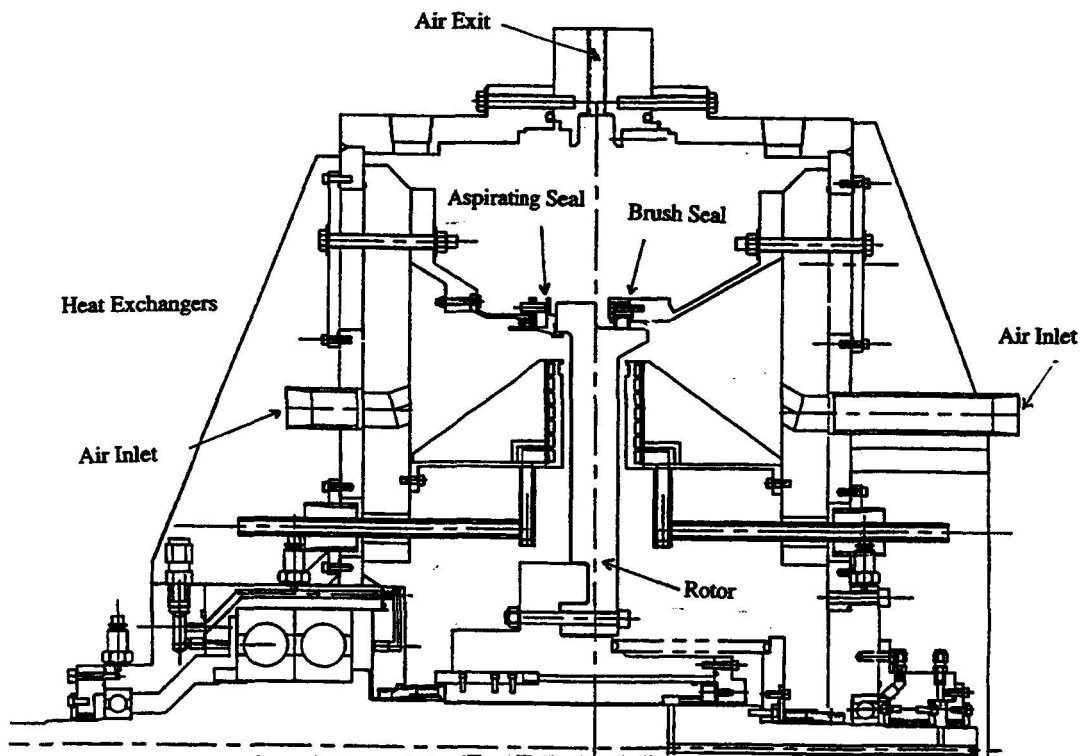
Test Program Objectives

- Phase I*
- Determine seal closing pressure.
 - Determine seal leakage at cruise and take off pressure conditions at room temperature, at 400° F and at operating temperature.
 - Demonstrate seal tracking capability over full range of relative axial motion.
- Phase II*
- Determine seal behaviour under maneuver deflections -- tilt mechanism.
 - Determine seal behaviour with rotor runout -- 0.005" and 0.010" TIR machined into rotor.

Test Rig Capabilities

- Aspirating seal and brush seal inlet air flow measured independently; inlet pressure controlled independently.
- Rotor can be moved axially $-.35/+ .95$ ".
- Aspirating seal cone designed to allow retrofit of tilt mechanism.
- Aspirating seal instrumentation includes:
 - 1 accelerometer -- axial for rub detection
 - 3 prox probes -- axial for film thickness measurement
 - 3 thermocouples -- seal exit air temperature measurement

Aspirating Seal Test Rig



INDUSTRIAL COMPUTER CODES

Wilbur Shapiro
Wilbur Shapiro & Associates, Inc.
Niskayuna, New York

58-61

39450

Industrial Codes

- ▶ **GCYLT***
 - ▶ **GFACE**
 - ▶ **SPIRALG**
 - ▶ **SPIRALI***
 - ▶ **IFACE**
 - ▶ **ICYL**
 - ▶ **DYSEAL****
 - ▶ **KTK****
 - ▶ **KBS****
- * Updated**
**** New**

GCYLT

(Gas - Cylindrical-Turbulent)

▶ **Multi-Geometry Code**

- **Steps**
- **Tapers**
- **Hydrostatic**

GCYLT - Turbulent Theory

Reynolds equation for turbulent compressible flow for journal bearings is as follows:

$$\frac{1}{R^2} \frac{\partial}{\partial \theta} \left(p h^3 G_z \frac{\partial p}{\partial \theta} \right) + \frac{\partial}{\partial z} \left(p h^3 G_z \frac{\partial p}{\partial z} \right) = 6\mu\omega \frac{\partial(p h)}{\partial \theta} + 12\mu \frac{\partial(p h)}{\partial t}$$

The equation is made dimensionless with the following definitions. (Upper case variables are dimensionless).

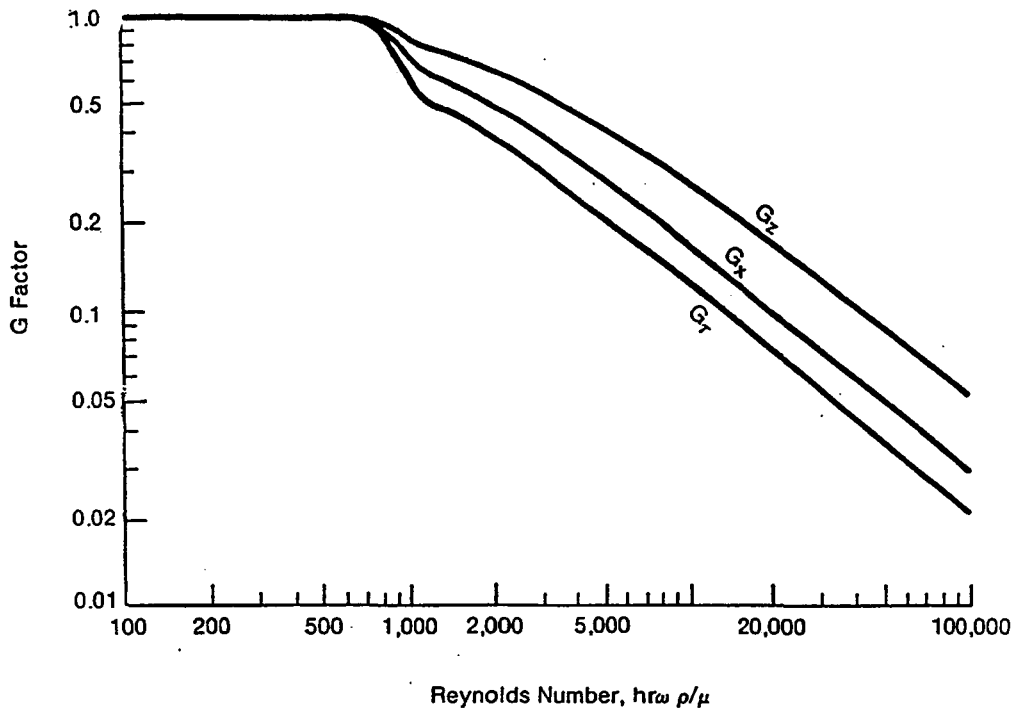
$$Z = z/R, \quad H = h/C_o, \quad T = t/t_o, \quad P = p/p_o,$$

$$\Lambda = \frac{6\mu\omega R^2}{p_o C_o^2}, \quad t_o = \frac{12\mu R^2}{p_o C_o^2}, \quad G_z \text{ and } G_z = \text{turbulence modifiers}$$

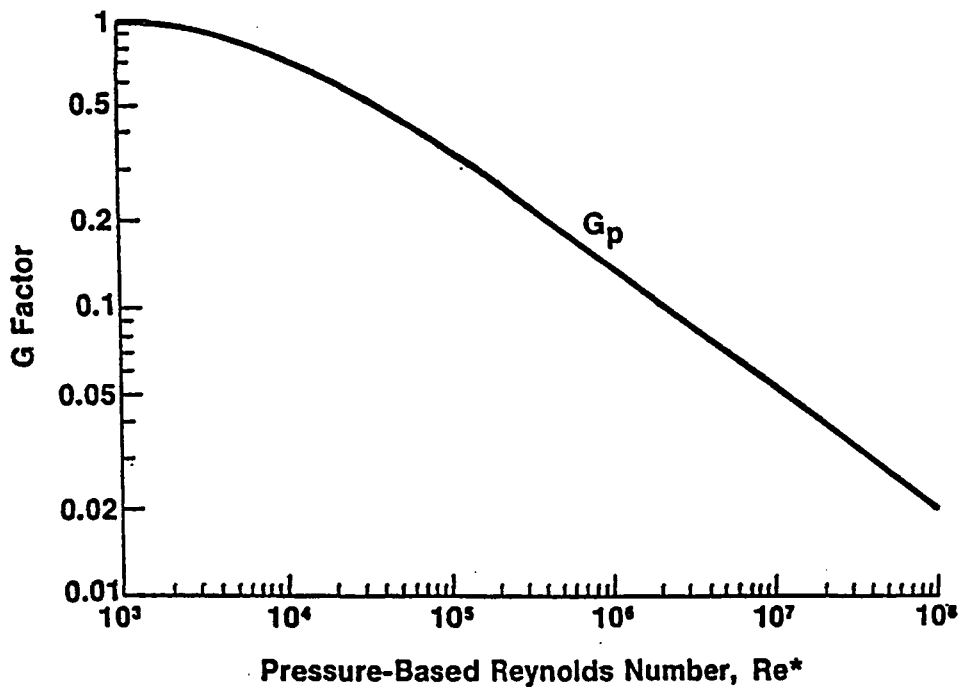
Substituting the dimensionless variables into the turbulent Reynolds equation produces dimensionless equation.

$$\frac{\partial}{\partial \theta} \left(P H^3 G_z \frac{\partial P}{\partial \theta} \right) + \frac{\partial}{\partial Z} \left(P H^3 G_z \frac{\partial P}{\partial Z} \right) = \Lambda \frac{\partial(P H)}{\partial \theta} + \frac{\partial(P H)}{\partial T}$$

Couette Turbulence Coefficients



Poiseuille Turbulence Coefficients



GCYLT - Turbulent Theory (Continued)

The turbulent G factors are dependent upon the Couette and Poiseuille Reynolds numbers which are at each grid point^[2].

The Couette Reynolds number is

$$Re = \frac{CR\omega p_c}{\mu G_c T_c} P H_c$$

where the subscript c refers to the cell corner point (e.g., for Q_{12} , $P_c = P_1$). The Poiseuille Reynolds number is defined as:

$$R_c^* = R_{c0}^* |\nabla P| H_c^3 P_c$$

$$\text{where } R_{c0}^* = \frac{C^3 p_c^2}{\mu^2 R G_c T_c}$$

$$G_x = \text{Min}[G_x(R_c), G_x(R_c^*)]$$

$$|\nabla P| = \left[\left(\frac{\partial P}{\partial \theta} \right)^2 + \left(\frac{\partial P}{\partial Z} \right)^2 \right]^{1/2}$$

$$G_z = \text{Min}[G_z(R_c), G_z(R_c^*)]$$

GCYLT Comparisons

Couette Turbulence Comparison

		GCYLT	GBEAR
h_{min}	mils	0.252	0.252
W	lb	1270	1269
γ	deg	4.92	4.63
HP	hp	1.2	1.2
Q	lb/s	-	-
K_{xx}	lb/in.	43,740	40,917
K_{xy}	lb/in.	6,458,000	6,443,64
K_{yx}	lb/in.	-5,062,000	1
K_{yy}	lb/in.	919,000	-
D_{xx}	lb-s/in.	1920	5,058,81
D_{xy}	lb-s/in.	-270.7	6
D_{yx}	lb-s/in.	334.3	813,689
D_{yy}	lb-s/in.	2649	1936
M_c	lb	16	-166
ω_c	rpm	23,987	-147
			2650
			12
			24,064

N = 50,000 rpm $P_a = 14,700$ psig
 $R_{\omega} = 48,995$ Excitation Frequency = 0

Poiseuille Turbulence Comparison

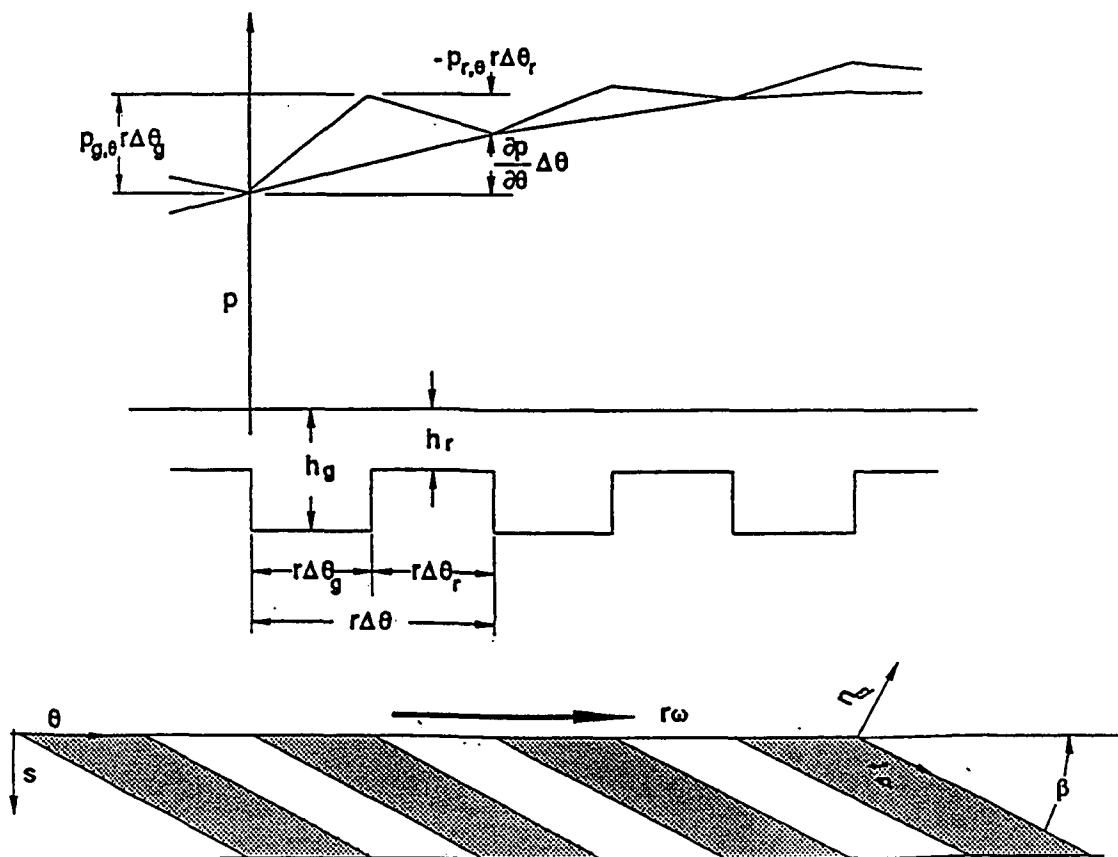
		GCYLT	GBEAR
h_{min}	mils	0.25	0.25
W	lb	9.513	9.449
γ	deg	0.03	0
HP	hp	9.48×10^{-5}	9.43×10^{-5}
Q_t	lb/s	.0270	.0267
K_{xx}	lb/in.	10.05	-
K_{xy}	lb/in.	46,170	47,271
K_{yx}	lb/in.	-38,860	-37,188
K_{yy}	lb/in.	23.16	0.78
D_{xx}	lb-s/in.	728.7	739
D_{xy}	lb-s/in.	-0.60	-
D_{yx}	lb-s/in.	0.82	0.88
D_{yy}	lb-s/in.	862.7	875
M_c	lb	-0.35	-2.8
ω_c	rpm	511	497

N = 1000 rpm $P_a = 14,700$ psig
 $P_d = 500$ psig Excitation Frequency = 0

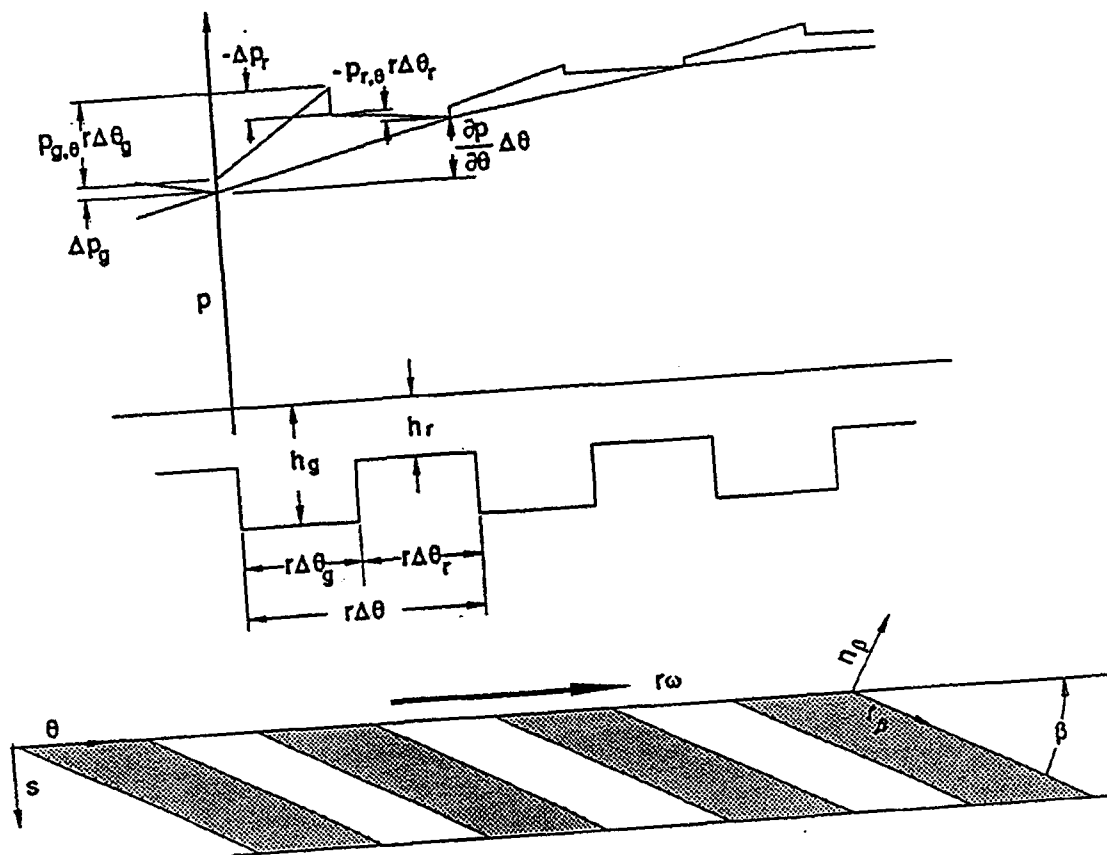
SPIRALI (Spiral-Groove - Incompressible)

- ▶ Spiral Groove Seals
- ▶ Parallel Grooves
- ▶ Helical Grooves
- ▶ Arbitrary Axi-Symmetric Geometry
- ▶ Cylindrical and Face
- ▶ Turbulence and Inertia
- ▶ Limitations
 - ▶ Concentric
 - ▶ Hir's Bulk Flow Model
 - ▶ Narrow Groove Theory

SPIRALI - Local Inertia Neglected



SPIRALI -Local Inertia Included



SPIRALI - Ungrooved Cylindrical Seal Comparison

Table 1. Comparison of test cases 5 - 8 with data published by D. W. Childs (Ref. 4)

	$u_p = r_p \omega / 2, L/D = 2$		$u_p = r_p \omega / 2, L/D = 1$		$u_p = 0, L/D = 2$		$u_p = 0, L/D = 1$	
	SPIRALI	Childs	SPIRALI	Childs	SPIRALI	Childs	SPIRALI	Childs
Q (cm ³ /s)	4006.	4019.	1771.	1779.	3989.	4019.	1767.	1779.
K _{xx} (MN/m)	18.90	18.65	10.79	9.756	18.58	18.52	13.25	12.48
K _{yy} (MN/m)	4.127	4.213	91.78	94.05	-3027	-3000	75.18	77.61
B _{xx} (KN-s/m)	21.89	22.35	487.2	500.6	21.89	22.47	489.5	502.2
B _{yy} (KN-s/m)	1.140	1.206	102.9	107.5	.8518	.8932	89.26	93.39
A _{xx} (kg)	3.020	3.200	272.6	285.3	3.003	3.189	272.1	285.3

Childs, D. W. "Finite Length Solutions for Rotor Dynamic Coefficients of Turbulent Annular Seals, ASME, J. Lub. Tech., V105,3, (1983),pp 437-445

SPIRALI - Definition of Coefficients

Overall Seal Discharge Coefficient

$$C_d = \frac{\Delta P}{\frac{1}{2} \rho V^2}$$

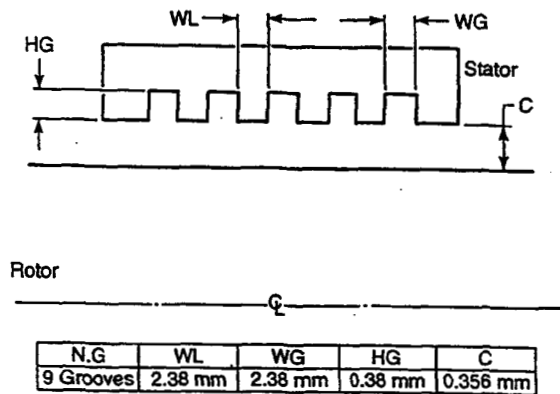
Radial Force Coefficient

$$-f_r = K + c\omega - M\omega^2 = K_{ef} - M_{ef}\omega^2$$

Tangential Force Coefficient

$$-f_\theta = C\omega - k = C_{ef}\omega$$

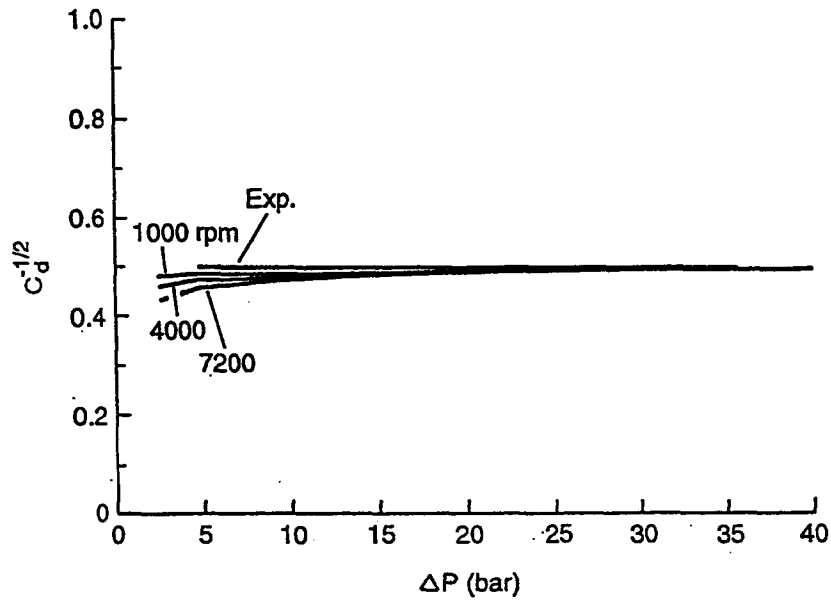
SPIRALI - Parallel Groove Pressure Breakdown Seal



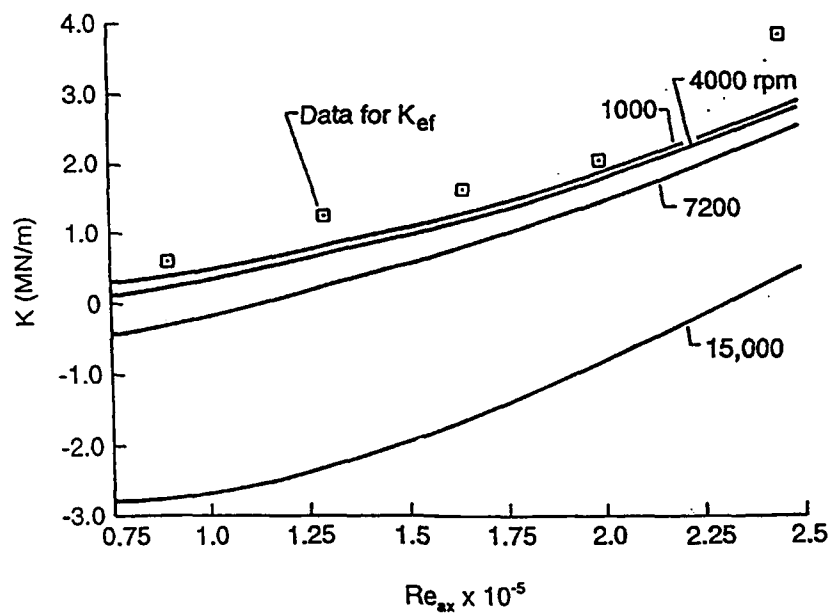
Radius = 50.8 mm

Childs, D. W., Nolan S. A., Kilgore J. J., "Test Results for Turbulent Annular Seals Using Smooth Rotors and Helically Grooved Stators", ASAME, J. Trib. V 112, 2, (1990), pp 254-258

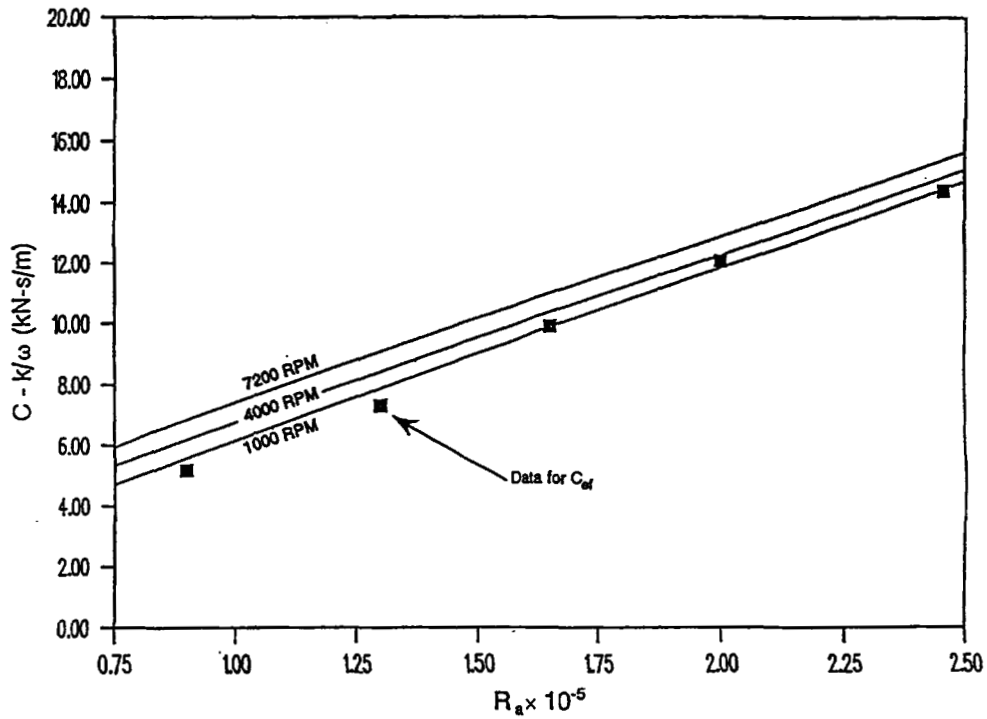
SPIRALI - Parallel Groove, Flow Coefficient



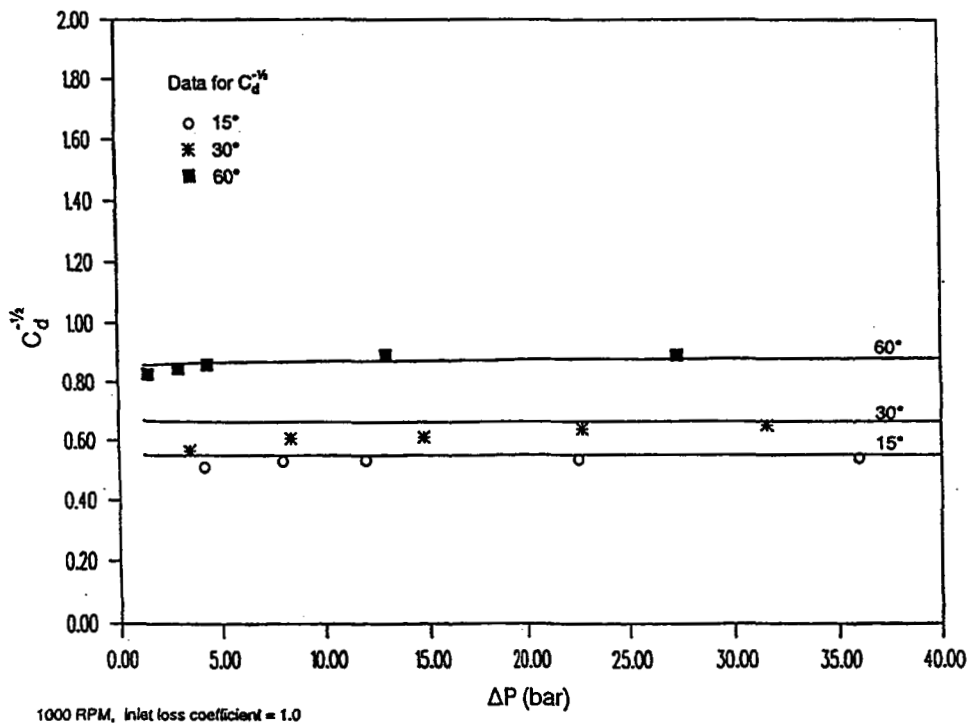
SPIRALI - Parallel Groove, Direct Stiffness



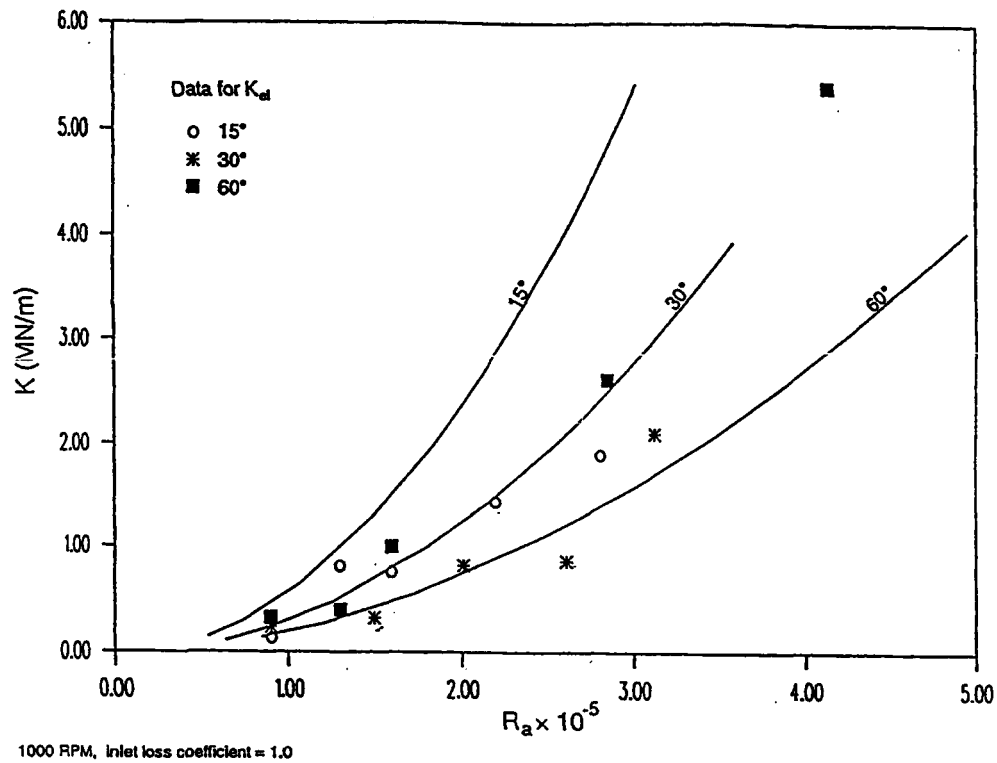
SPIRALI - Parallel Groove, Damping



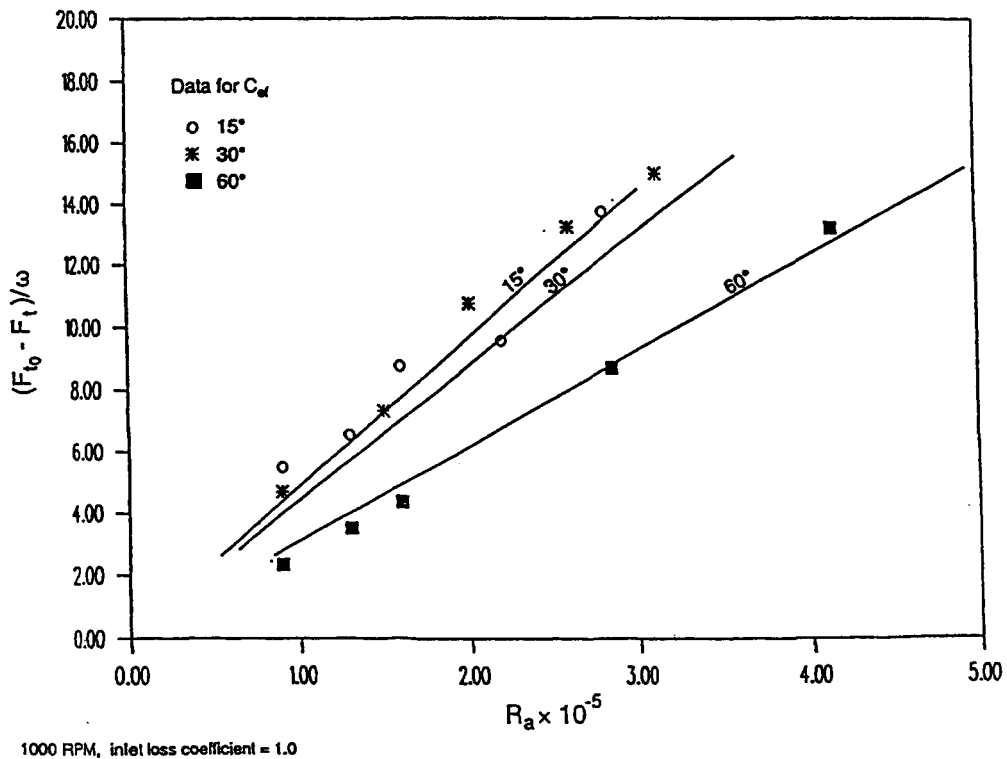
SPIRALI - Helical Groove Flow



SPIRALI - Helical Groove - Direct Stiffness



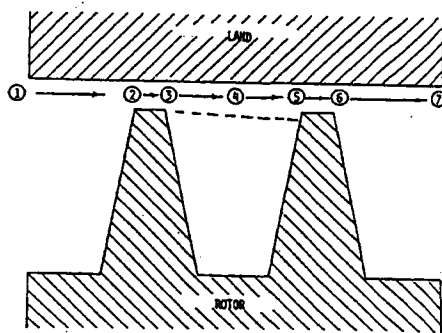
SPIRALI - Helical Groove - Effective Damping



KTK - Labyrinth Seal Code

- ▶ Knife to Knife Approach (KTK)
- ▶ Empirically Based
- ▶ Leakage and Internal Pressure Distribution
- ▶ Optimun Geometry Option
- ▶ Straight or Step Seals
 - Flow going up or down the step

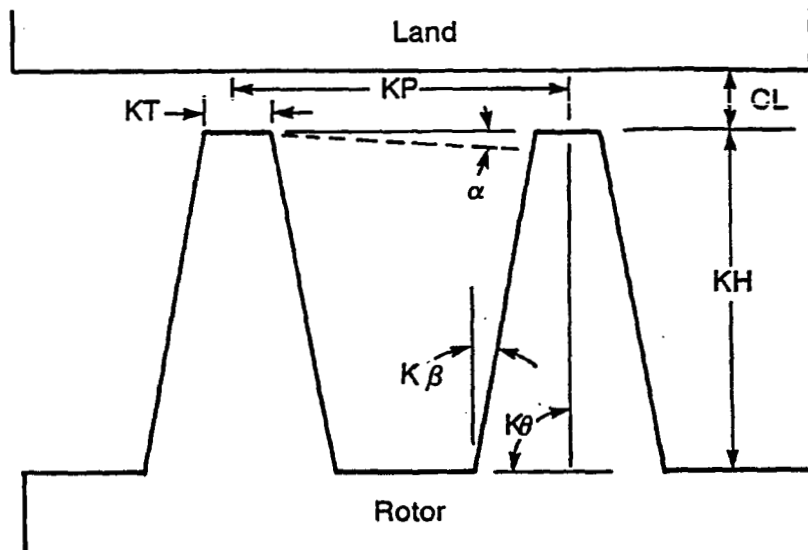
KTK - Labyrinth Seal Code - Loss Zones



- ▶ Contraction 1 to 2, 4 to 5
- ▶ Venturi and Friction - 2 to 3, 5 to 6
- ▶ Partial or Full Expansion 3 to 4, 6 to 7

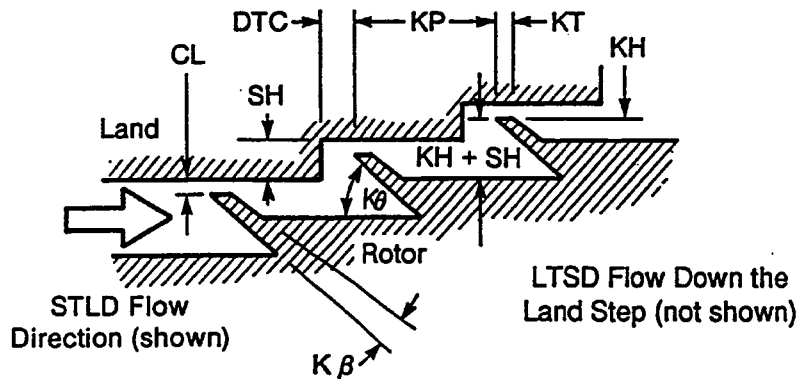
KTK - Labyrinth Seal

Code - Straight Seal Parameters



KTK - Labyrinth Seal

Code - Step Seal Parameters



Geometric parameters for straight and stepped seals

- Knife height (KH)
- Knife pitch (KP)
- Number of knives (KN)
- Knife angle ($K\theta$)
- Knife tip thickness (KT)
- Knife taper angle ($K\beta$)
- Knife tip leading edge radius (KR)
- Clearance (CL)
- Surface roughness (ϵ)

Additional parameters considered for stepped seals

- Step height (SH)
- Distance to contact (DTC)
- Flow direction (LTSD or STLD)*

Flow parameters

- Overall pressure ratio (P_R)
- Inlet stagnation pressure (P_U)
- Fluid temperature distribution (T)
- Flow rate (W)

*LTSD = Large to Small Diameter.
STLD = Small to Large Diameter.

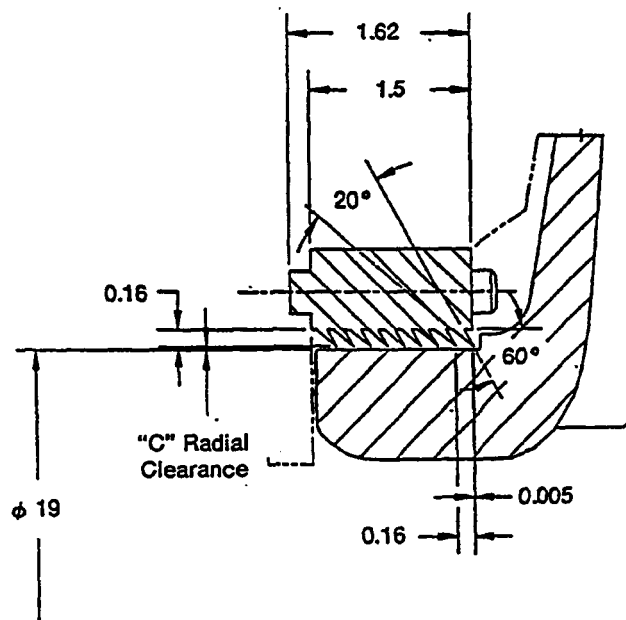
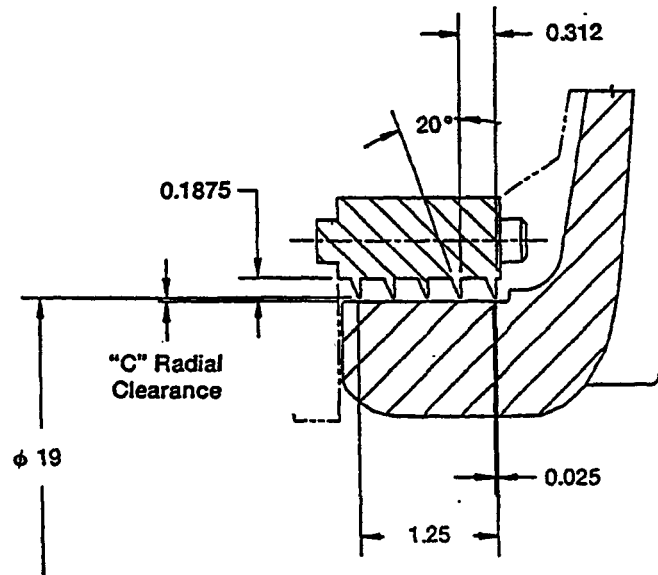
KTK - Labyrinth Seal

Code - Parameter Ranges

Parameter Ranges of Data in Labyrinth Seal Data Base

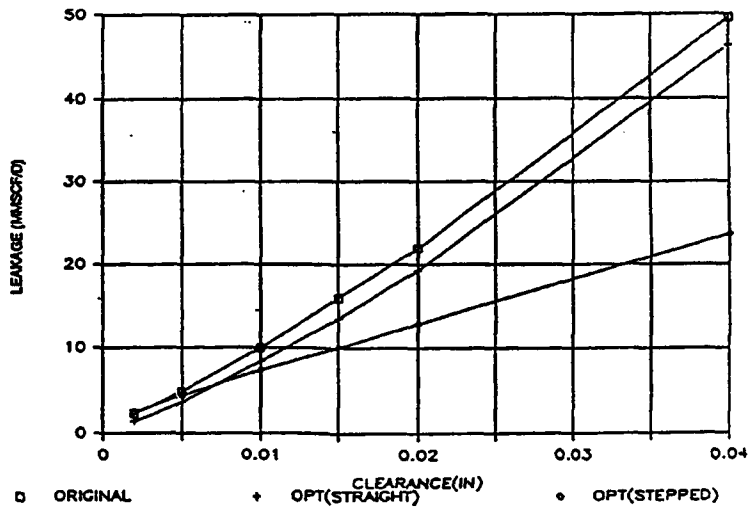
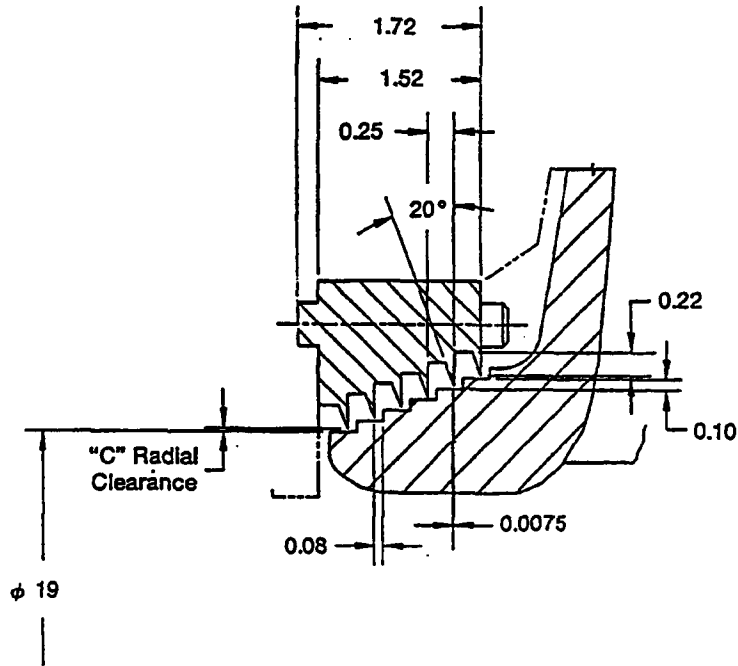
Parameter		Seal Type		Stepped Seal	
		Single knife	Straight seal	STLD dir.	LTSD dir.
KN	min	1	2	2	2
	max	1	12	6	6
KT/CL	min		0.21	0.21	0.50
	max	3.3	4.4	2.64	1.50
Kθ	min	30	60	50	50
	max	90	90	90	90
KH/CL	min	--	2.7	5.1	5.1
	max	--	31.3	29.4	28.0
KP/CL	min	--	4.0	6.4	9.2
	max	--	56.3	53	40
ε/(2CL)	min	0	0	0	0
	max	0	0.030	0	0.030
SH/CL	min	--	--	2.0	4.0
	max	--	--	29.4	12.5
DTC/CL	min	--	--	0.85	4.1
	max	--	--	40	19.4
(KP-KT)/CL	min	--	3.5	6.2	8.9
	max	--	55.0	51.8	38.5

KTK - Labyrinth Seal Code - Optimization



KTK - Labyrinth Seal

Code - Optimization (Continued)

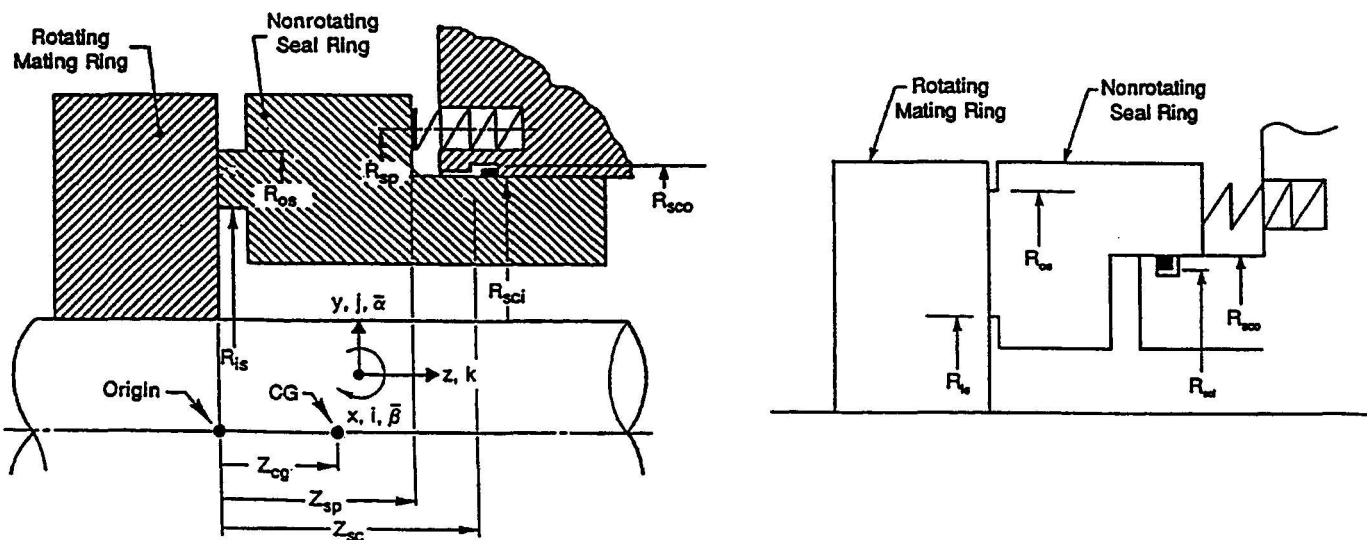


Leakage versus Clearance - TCP, SSO, FP-172 Inlet Seal
 (PU = 795 psia, PD = 715 psia, $\Delta P = 80$ psi)

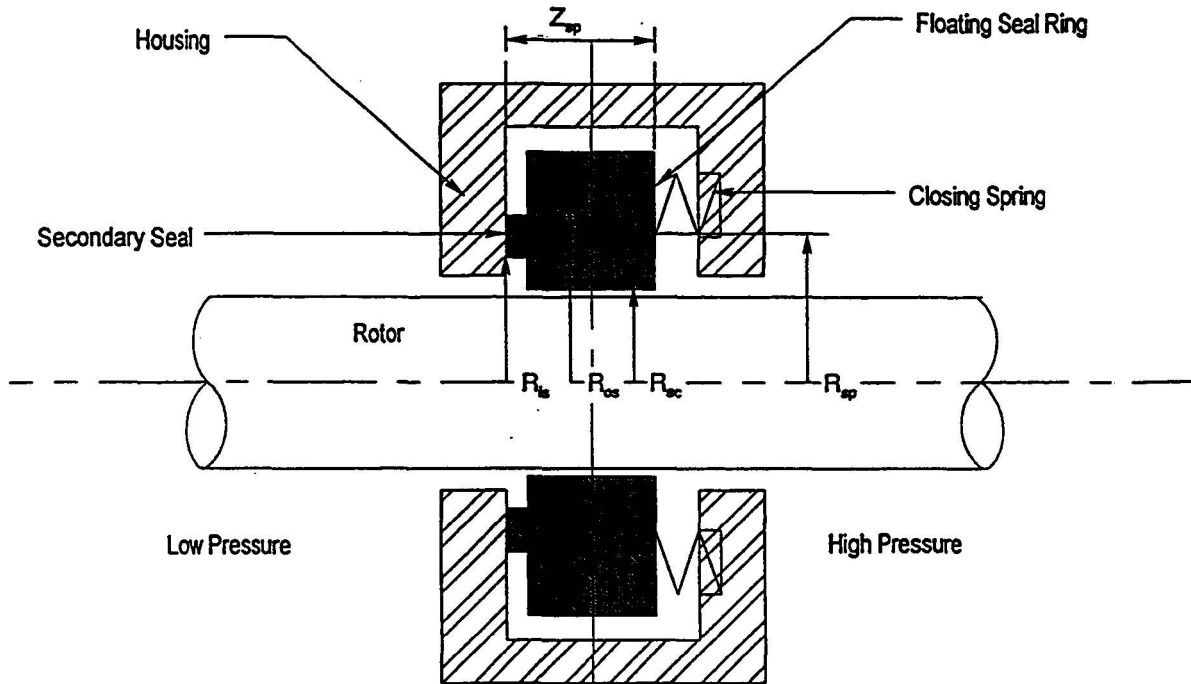
DYSEAL - Dynamic Response of Face and Ring Seals

- ▶ 5 DOF for face seals, 2 for ring seals
- ▶ Piston ring, O-ring, Contact face secondary seals
- ▶ Coulomb friction of secondary seals
- ▶ Interface represented by cross-coupled stiffness and damping
- ▶ Forward integration in time algorithms based on Newmark's method
- ▶ Continuation Option
- ▶ Plotting included

DYSEAL - Face Seal Configurations



DYSEAL - Ring Seal Configurations



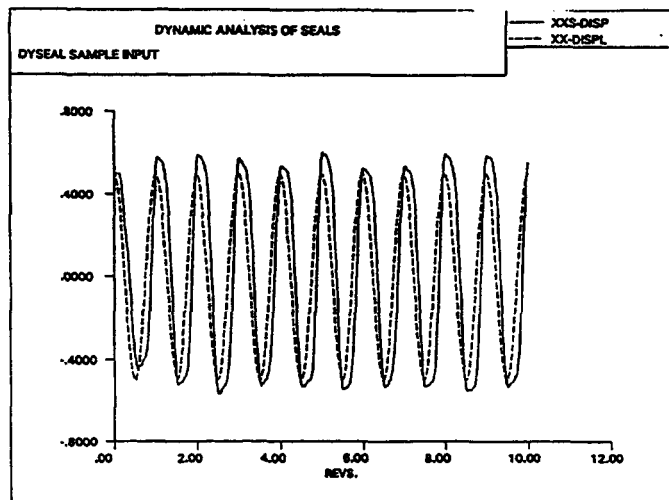
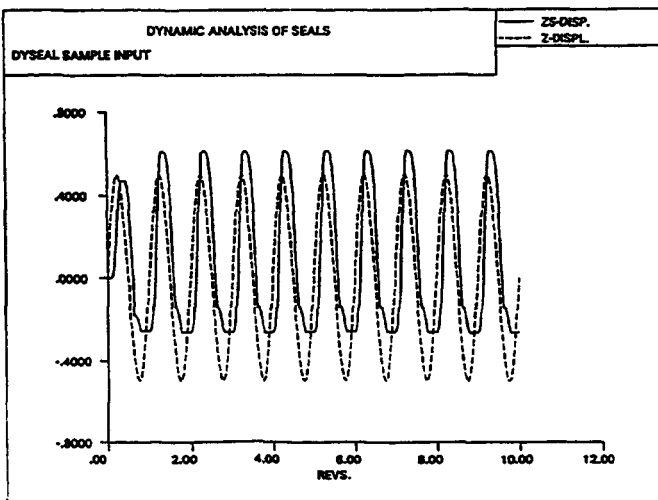
DYSEAL - Interface Stiffness and Damping Coefficients

$F \setminus \Delta$	X	Y	Z	β	α	$F \setminus \Delta$	X	Y	Z	β	α
F_x	K_{xx}	K_{yy}	← Ring Seals			F_x	D_{xx}	D_{yy}	← Ring Seals		
F_y	K_{yx}	K_{yy}	← Ring Seals			F_y	D_{yx}	D_{yy}	← Ring Seals		
F_z	Face Seals →		K_{zz}	$K_{z\beta}$	$K_{z\alpha}$	F_z	Face Seals →		D_{zz}	$D_{z\beta}$	$D_{z\alpha}$
M_x	Face Seals →		$K_{\beta z}$	$K_{\beta\beta}$	$K_{\beta\alpha}$	M_x	Face Seals →		$D_{\beta z}$	$D_{\beta\beta}$	$D_{\beta\alpha}$
M_y	Face Seals →		$K_{\alpha z}$	$K_{\alpha\beta}$	$K_{\alpha\alpha}$	M_y	Face Seals →		$D_{\alpha z}$	$D_{\alpha\beta}$	$D_{\alpha\alpha}$

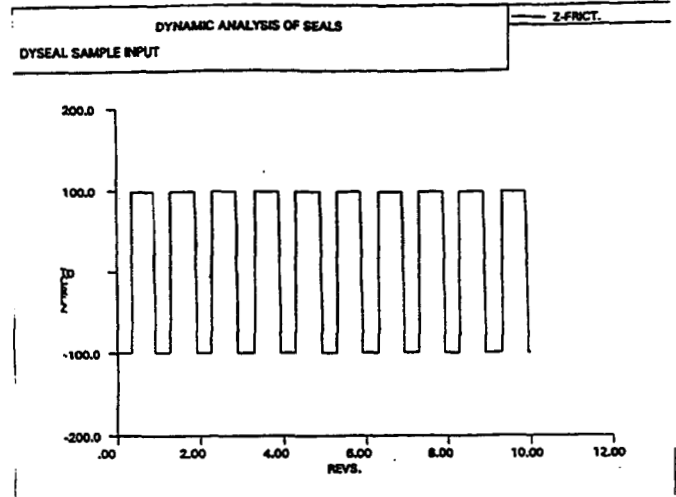
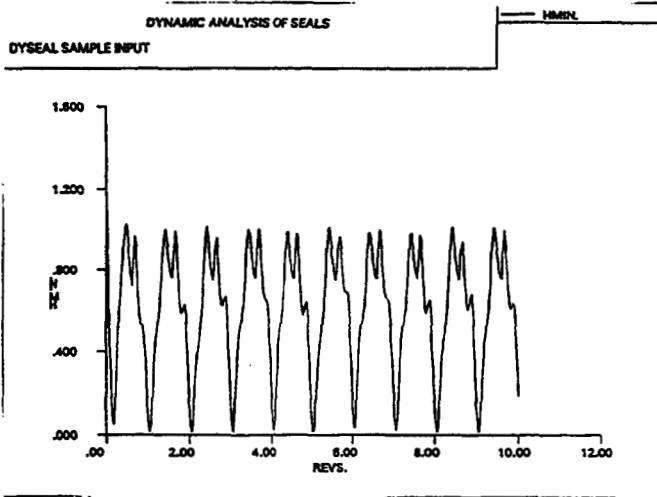
DYSEAL - Output

- ▶ Seal Ring - x, y, z, a, b
- ▶ Shaft - x, y, z, a, b
- ▶ Film thickness,
- ▶ Minimum film thickness
- ▶ Friction Forces and Moments- x, y, z, a, b
- ▶ CG, Mass, I_t , I_p
- ▶ Closing Forces
- ▶ Continuation parameters

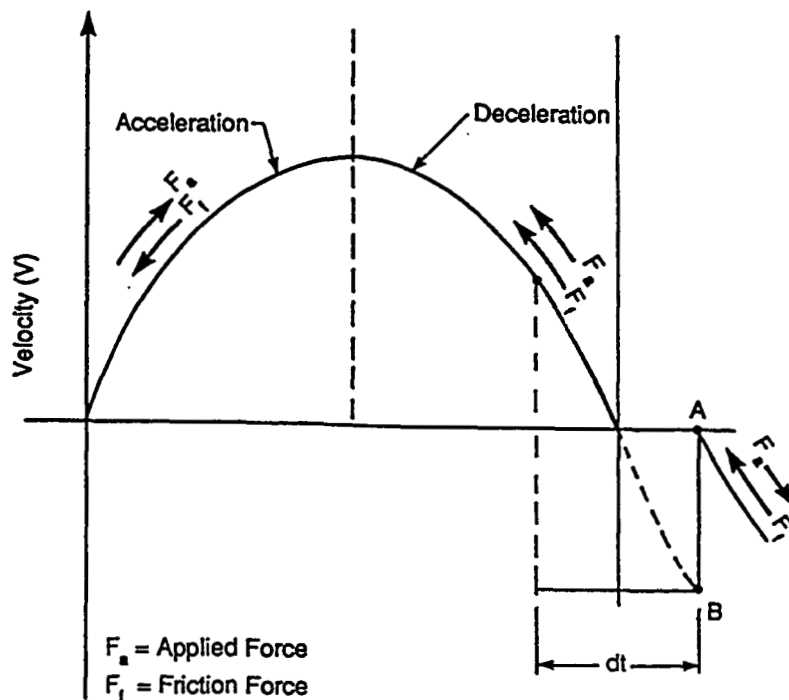
DYSEAL - Examples of Plotted Output



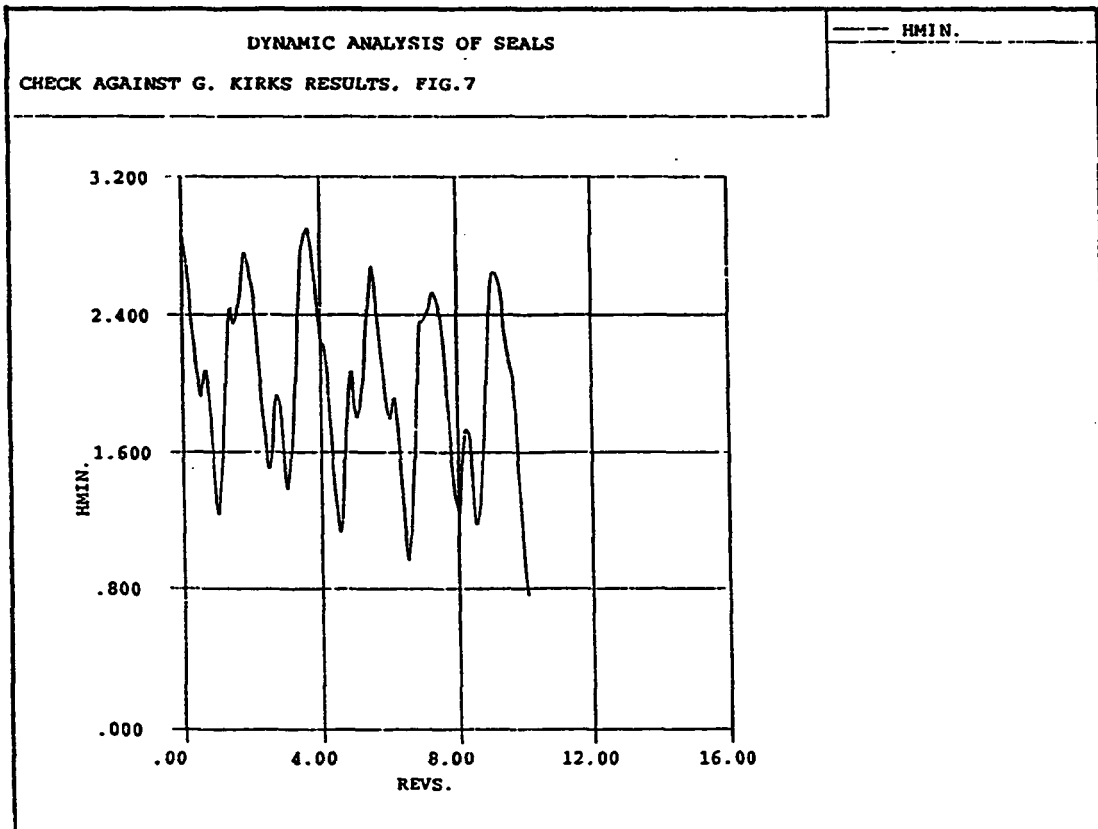
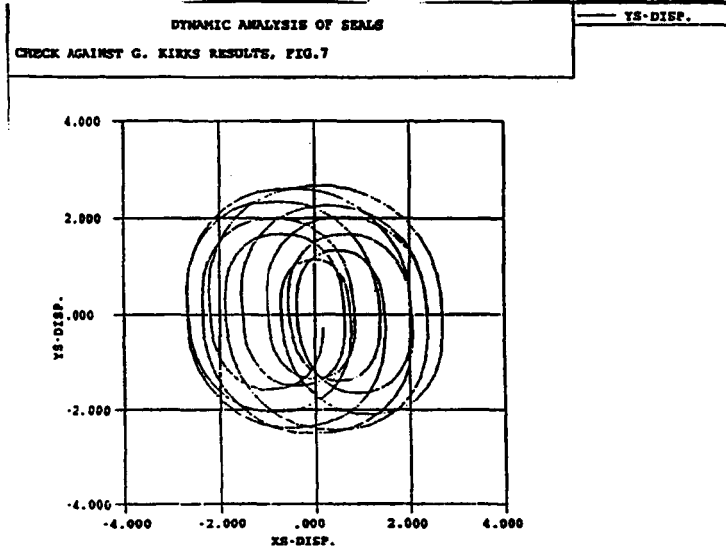
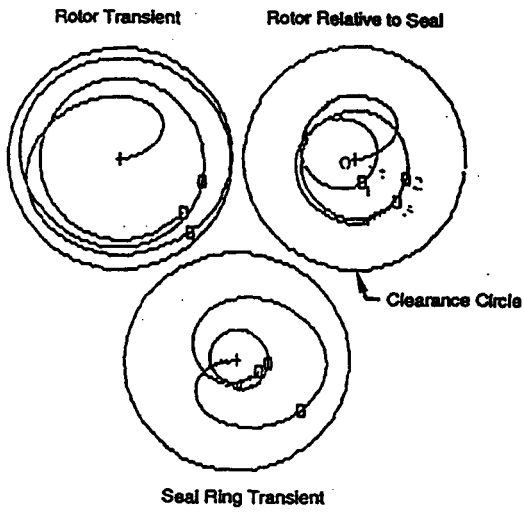
DYSEAL - Examples of Plotted Output (Continued)



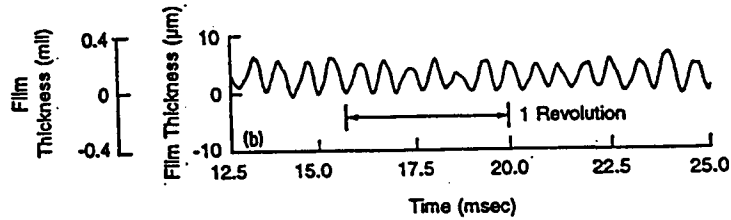
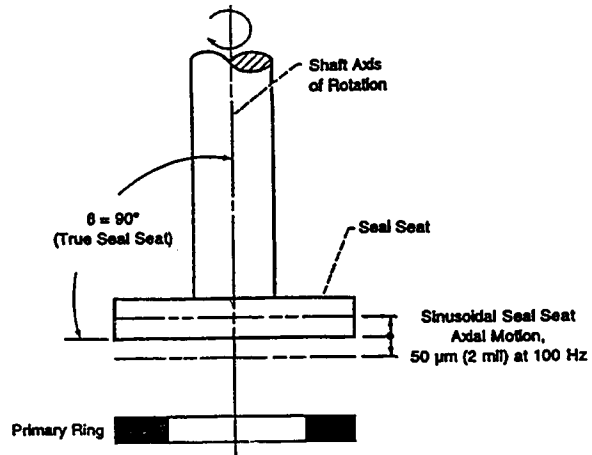
DYSEAL - Friction Algorithm



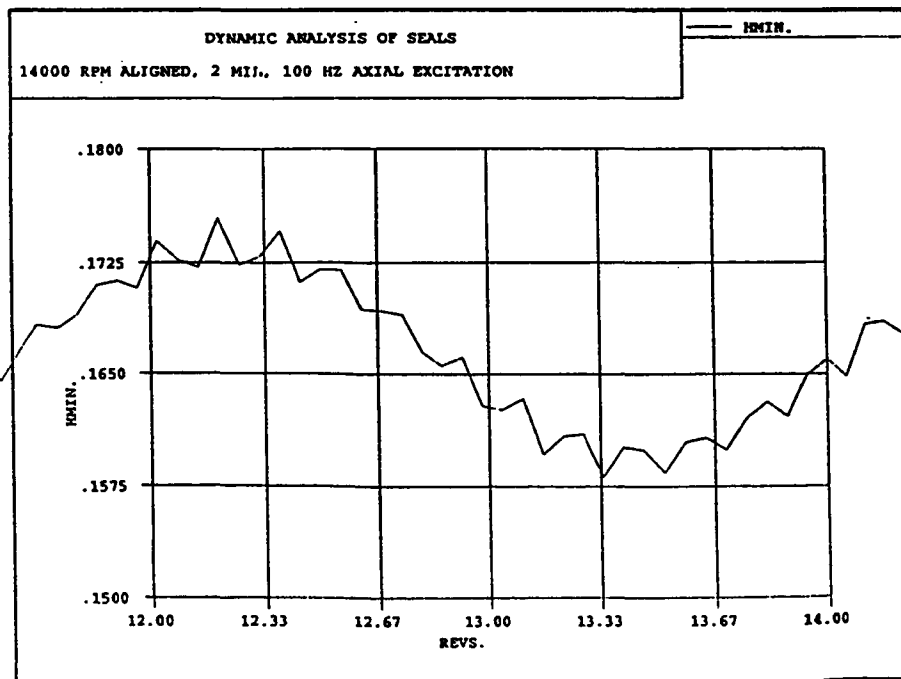
DYSEAL - Ring Seal Check



DYSEAL - Face Seal Check



b) Sinusoidal Seal Seat Mode; Amplitude = $50 \mu\text{m}$ (2 mil); Frequency = 100 Hz



COMPARISON OF SPIRALG PERFORMANCE PREDICTIONS WITH A
SPREAD SHEET SOLUTION

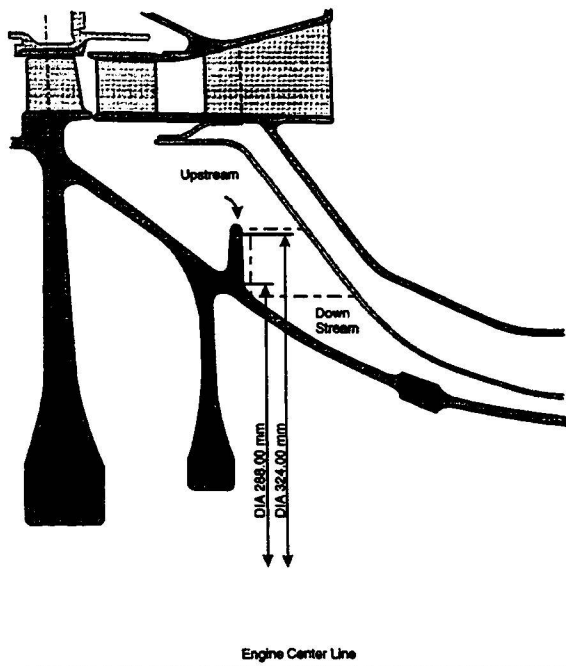
Martyn G. Roberts
Atlanta Engineering
Rolls-Royce, Inc.
Atlanta, Georgia

59-37
39451

The aero design of an inward pumping spiral groove face seal using an in-house spread sheet was compared with predictions from the NASA code SPIRALG. The high pressure compressor exit of an aero gas turbine was chosen as the location for the candidate seal. This is a challenging environment as rotational velocity, pressure drop, and temperature are high.

This presentation compares the resulting lift forces, leakages, and friction loss for various ride heights. Within practical ranges of ride height, the lift force predictions agreed well. However, both leakage and friction loss predictions were significantly different.

Design Constraints



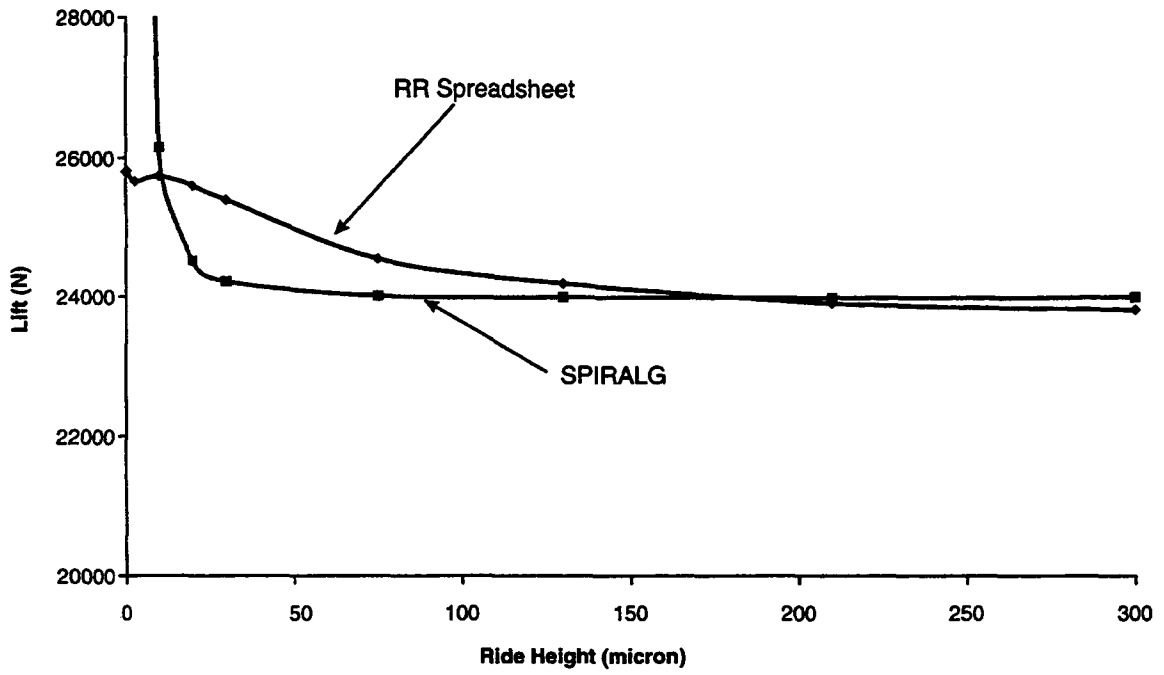
Velocity = 320 m/s (1000ft/s)

Temperature = 700°C (1300°F)

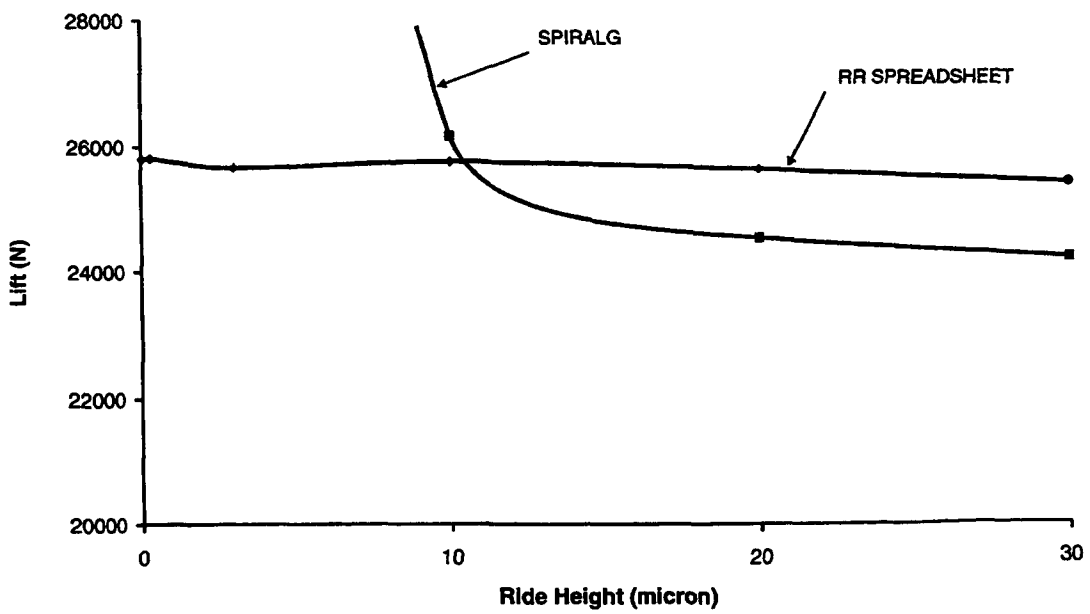
Pressure Drop = 1350 kPa (200 psi)

RR Spreadsheet based on:
E.A. Muijderman, Spiral Groove Bearings
Philips Technical Library 1966

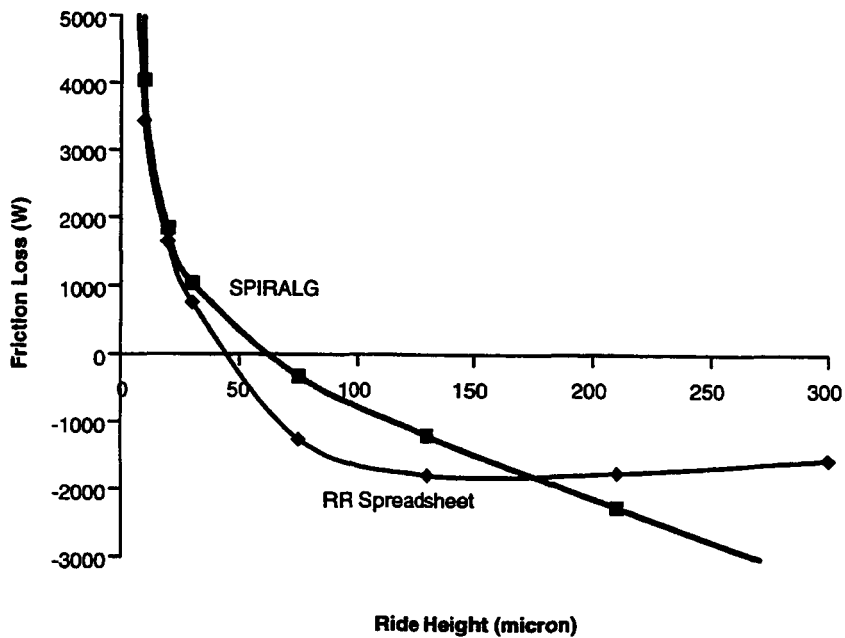
Lift Force



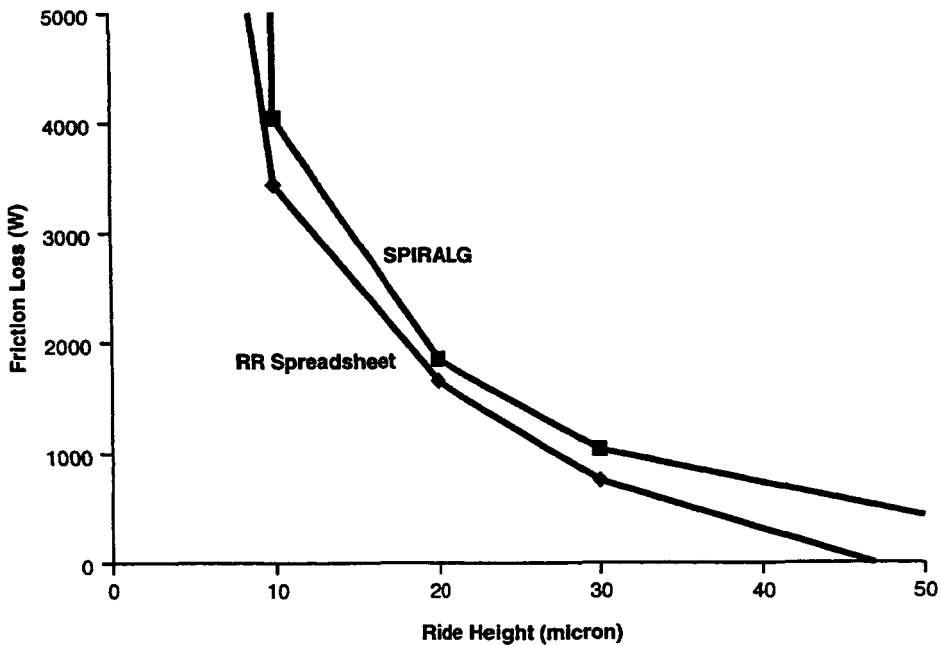
Lift Force



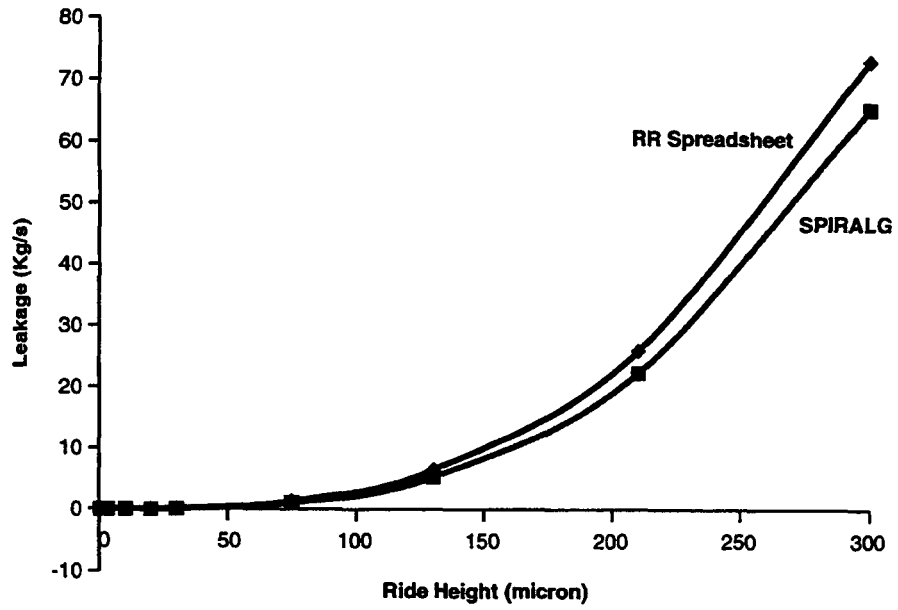
Friction Loss



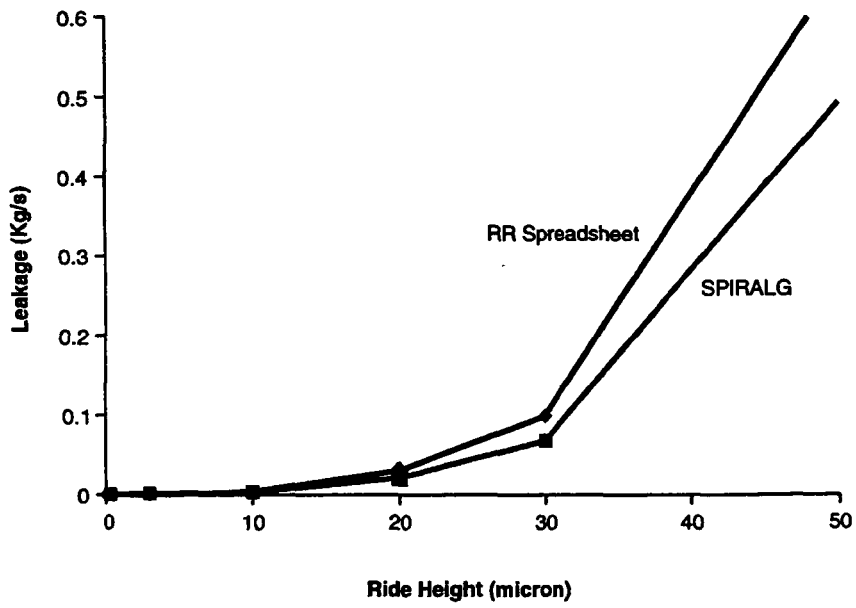
Friction Loss



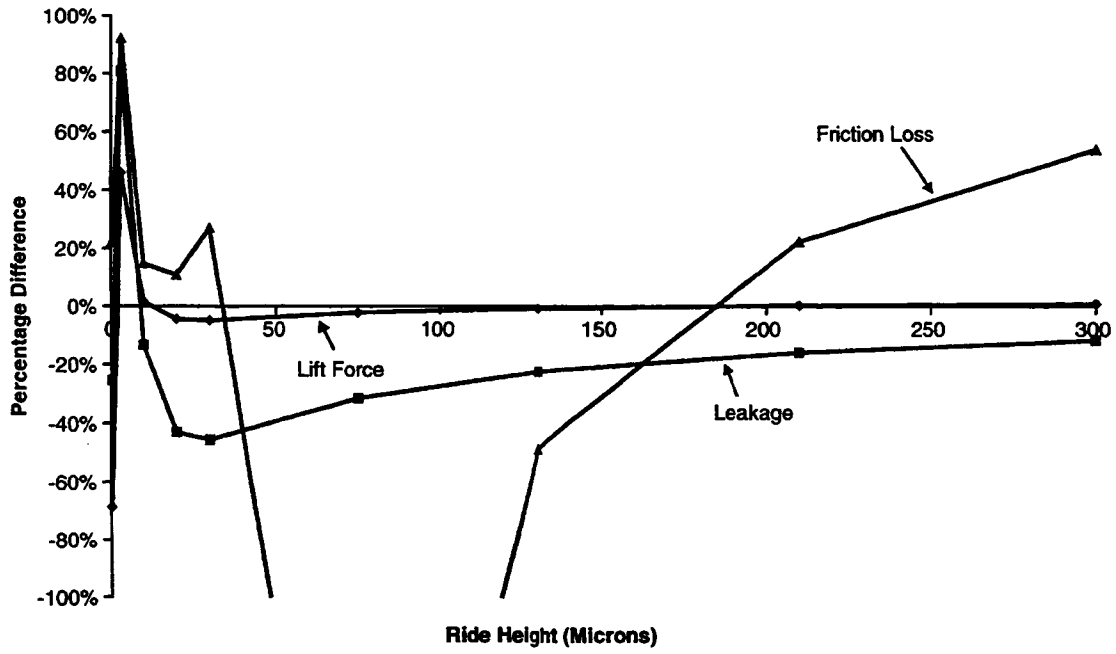
Leakage



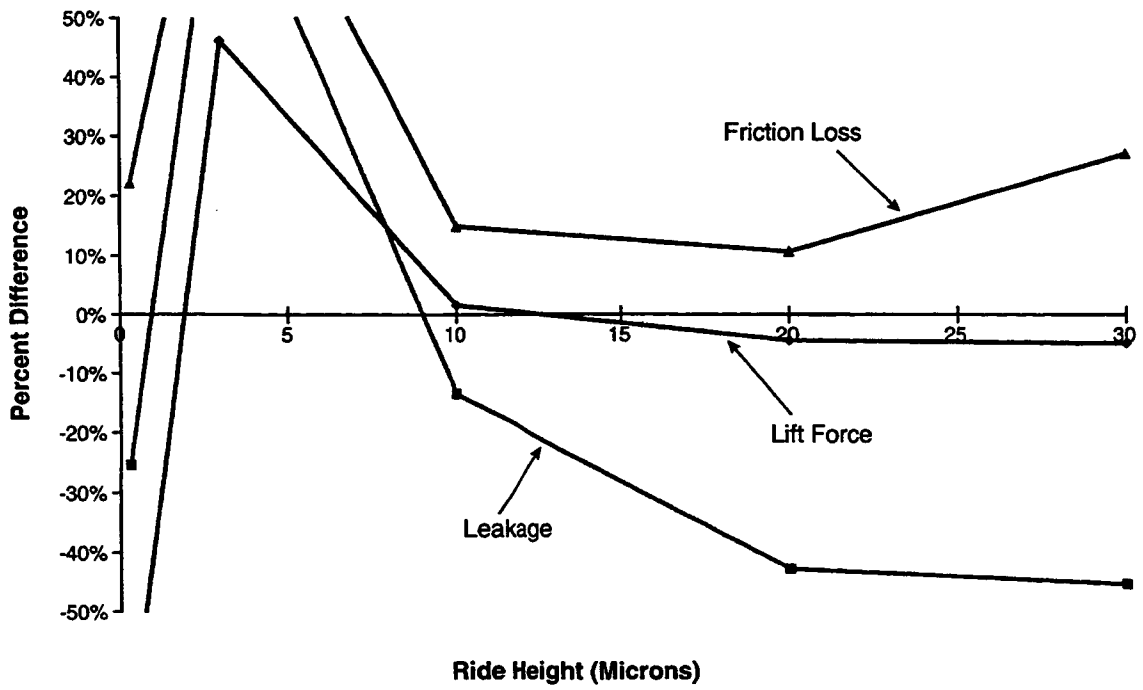
Leakage



Prediction Differences (1)



Prediction Differences (2)



COMPARISON OF CODE PREDICTIONS TO TEST MEASUREMENTS FOR TWO ORIFICE
COMPENSATED HYDROSTATIC BEARINGS AT HIGH REYNOLDS NUMBERS

John E. Keba
Rocketdyne Division
Rockwell Corporation
Canoga Park, California

510-37
39452

ABSTRACT

Rotordynamic coefficients obtained from testing two different hydrostatic bearings are compared to values predicted by two different computer programs. The first set of test data is from a relatively long ($L/D=1$) orifice compensated hydrostatic bearing tested in water by Texas A&M University (TAMU Bearing No.9) under Dr. Dara Childs (1). The second bearing is a shorter ($L/D=.37$) bearing and was tested in a lower viscosity fluid by Rocketdyne Division of Rockwell (Rocketdyne "Generic" Bearing) at similar rotating speeds and pressures (2). Computed predictions of bearing rotordynamic coefficients were obtained from the cylindrical seal code "ICYL" (3), one of the industrial seal codes developed for NASA-LeRC by Mechanical Technology Inc., and from the hydrodynamic bearing code "HYDROPAD" (4) developed by Dr. Luis San Andres of Texas A&M University.

The comparison highlights the difference the bearing has on the accuracy of the predictions. The TAMU Bearing No. 9 test data is closely matched by the predictions obtained for the HYDROPAD code (except for added mass terms) whereas significant differences exist between the data from the Rocketdyne "Generic" bearing the code predictions. The results suggest that some aspects of the fluid behavior in the shorter, higher Reynolds Number "Generic" bearing may not be modeled accurately in the codes.

The ICYL code predictions for flowrate and direct stiffness approximately equal those of HYDROPAD. Significant differences in cross-coupled stiffness and the damping terms were obtained relative to HYDROPAD and both sets of test data. Several observations are included concerning application of the ICYL code.

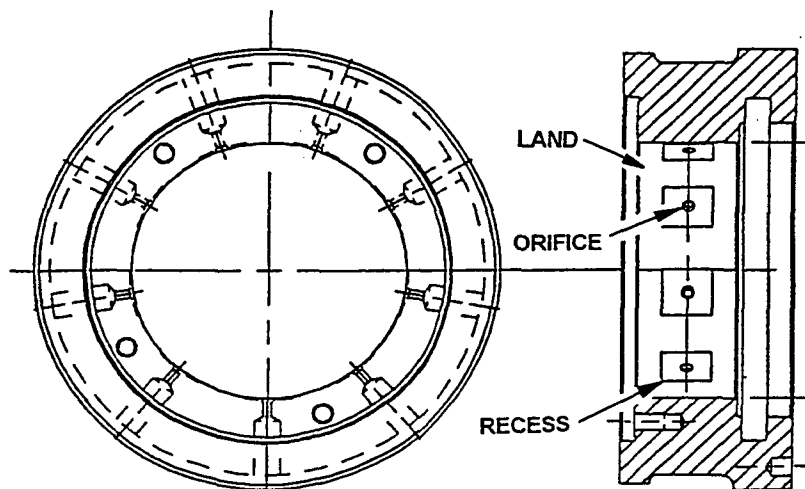
REFERENCES

1. Unpublished data. Testing was conducted in the Hybrid Bearing Test Stand at Texas A&M under Rocketdyne Div., Rockwell sponsorship. For a description of the test method, see: D. W. Childs, "Theory Versus Experiment for the Rotordynamic Coefficients of Annular Gas Seals: Part 1 -- Test Facility and Apparatus", ASME Trans., Vol. 108, July 1986.
2. Unpublished data. Testing conducted by Rocketdyne Div. Rockwell. For description of test method, see TECHNOLOGY TEST BED ENGINE -- EXPERIMENTAL VERIFICATION OF ROTORDYNAMIC ANALYSIS, FINAL REPORT; John E. Keba, Report No. RSS-8856-24, Rocketdyne Div., Rockwell. Prepared for NASA-Marshall Space Flight Center under Contract No. NAS8-40000 Task 31.
3. USERS MANUAL FOR COMPUTER CODE ICYL - CYLINDRICAL SEALS LUBRICATED BY INCOMPRESSIBLE FLUIDS, Antonio F. Artiles, Report No. 92TM13 Rev. July 1993, Mechanical Technology Incorporated. Prepared for NASA-Lewis Research Center under Contract No. NAS3-25644.
4. "HYDROPAD -- User's Manual", L. S. San Andres, Texas A&M University, Oct. 1992.

INTRODUCTION

BEARING GEOMETRY

	(units)	TAMU No. 9	Rocketdyne GENERIC
Nominal Diameter (D)	inch	3.00	2.69
Length(L)	inch	3.00	1.0
Clearance (radial) (h_0)	inch	.00475	.0049
Recess Geometry			
No. of Recesses		5	9
Depth	inch	.010	.020
Axial length	inch	1.064	.485
Circumferential length	inch	1.064	.485
Area Ratio		.200	.250
Orifice Geometry			
Throat Diameter	inch	.098	.085
Exit Chamfer		Counter Bore	Sharp Edge
Surface Roughness			
Land -- between	μ in	13	12
Land -- side	μ in	13	12
Rotor	μ in	13	6



ORIFICE COMPENSATED HYDROSTATIC BEARING

BEARING TEST CONDITIONS

	(units)	TAMU No. 9	Rocketdyne GENERIC
TEST FLUID		WATER	HFC-134a
Temperature	°F	130	100
Viscosity	lbm/ft-sec	340. E-6	122.5 E-6
Density	lbm/cu ft	61.5	71.7
SHAFT SPEED	rpm	10,200 to 24,600	0 to 24,000
Rotational Re	$\omega R h / \nu$	to 23,000	to 67,000
ΔP	psi	600 to 1000	800 to 1600
FLOWRATE	GPM	29 max.	39 max.
Flow Re	$Q / (\pi D \nu)$	to 15,000	to 72,000

SIGNIFICANT DIFFERENCES BETWEEN DATA SETS

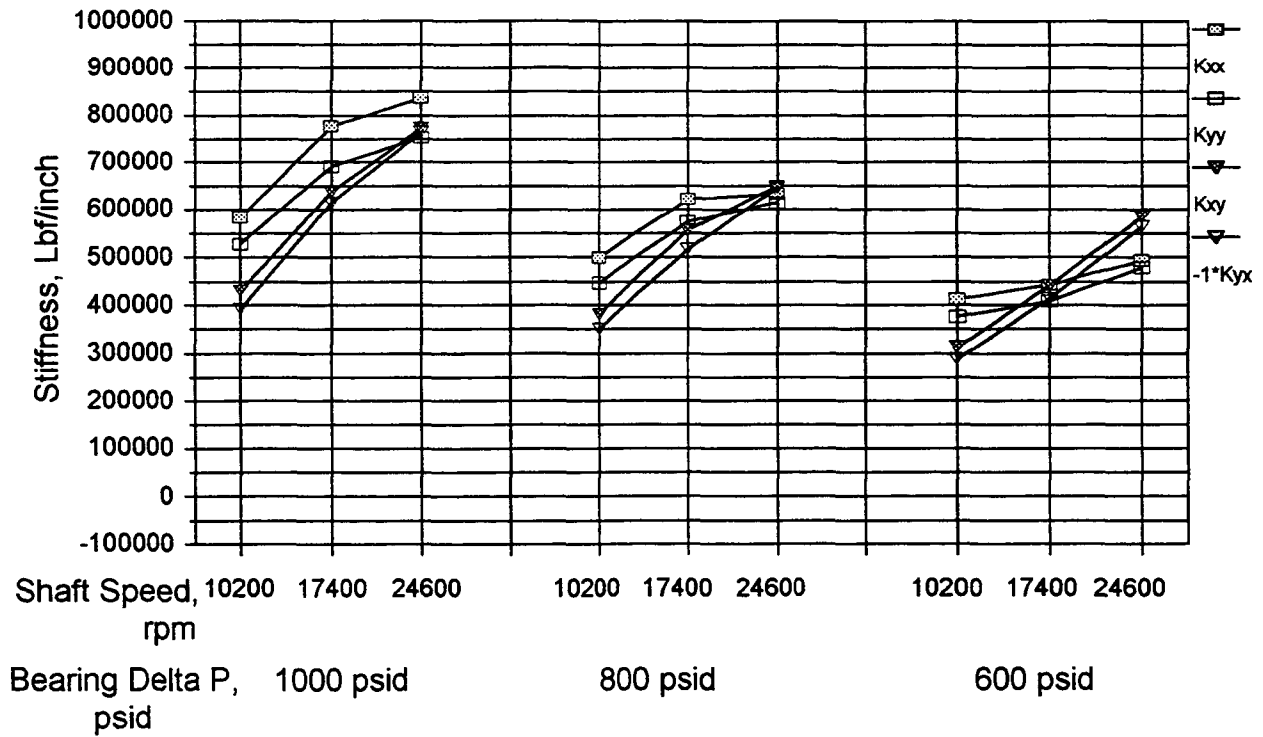
	TAMU No. 9	GENERIC
<u>GEOMETRY</u>		
Land Axial Length to Film Thickness Ratio	200:1	50:1
Orifice Exit Geometry:		
Orifice Diameter	.098 inch	.085 inch
Recess Depth	.010 inch	.020 inch
Exit Geometry	Counter Bore	Sharp Edge
<u>OPERATING CONDITIONS</u> (Compared at 800 psid, 24,000 RPM)		
Pressure Ratio: (Precess-Pout)/(Pin-Pout)	.58	.32
Fluid Compressibility:		
Bulk Modulus (adiabatic)	320,000 psi @ 68 °F	45,000 psi @ 950 psig, 100 °F
Density Change - ρ_{out} / ρ_{in}	Negligible	1.075 @ 800 psid, 30°F ΔT
Reynolds No.		
Rotational	22,200	67,000
Flow (avg. axial on lands)	12,300	49,800

PREDICTIONS VERSUS RESULTS -- TAMU BEARING NO. 9

MEASURED BEARING PERFORMANCE

- Direct and Cross-Coupled Stiffnesses relatively large, approximately equal, and both strongly dependent on speed and bearing ΔP .

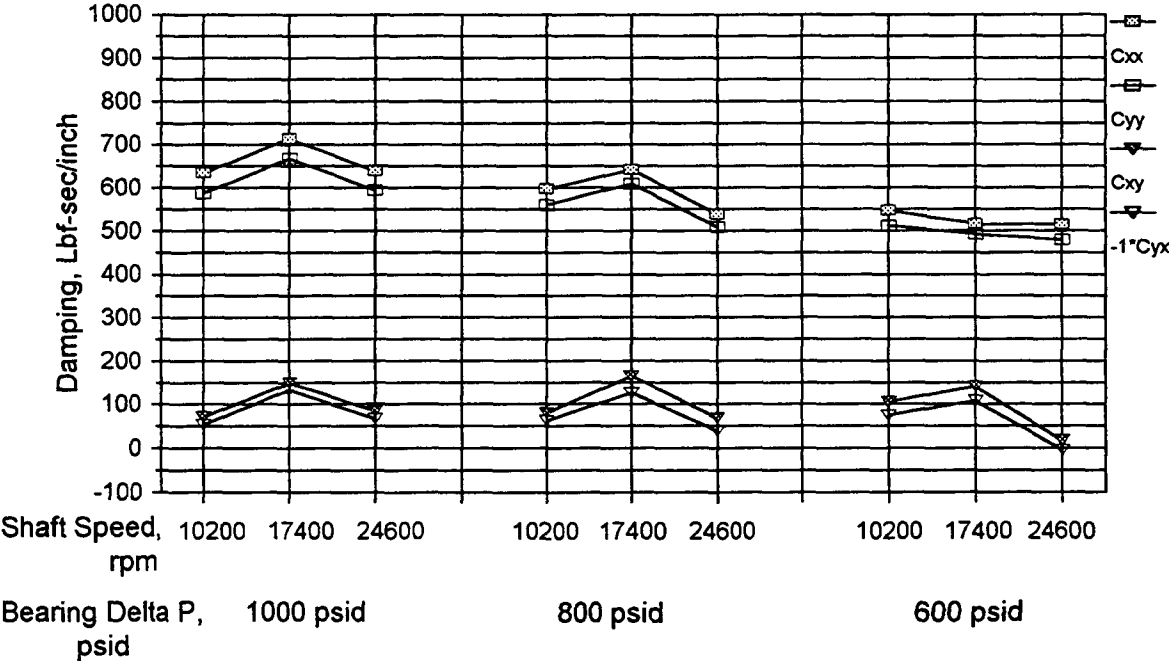
TAMU Test Series 9
Stiffness vs. Speed and Pressure



MEASURED BEARING PERFORMANCE (con't)

- Direct damping large, relatively insensitive to speed and bearing ΔP

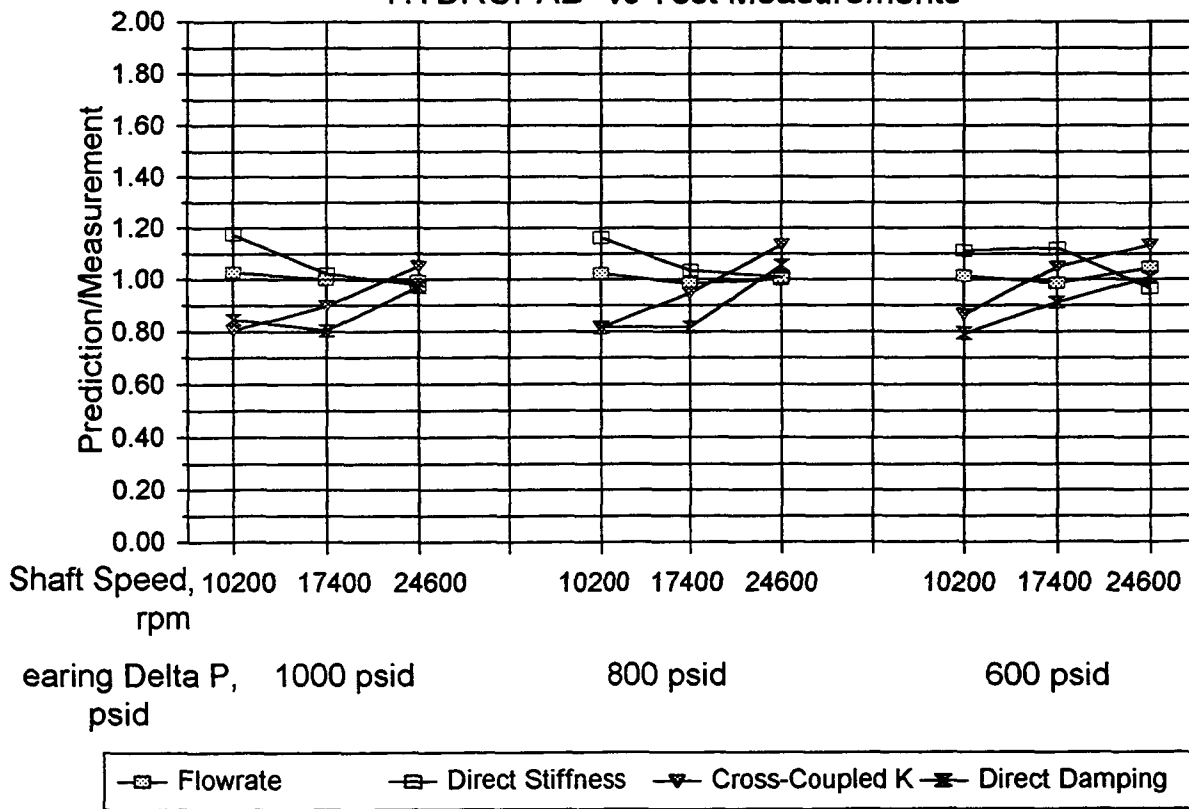
TAMU Test Series 9
Damping vs. Speed and Pressure



HYDROPAD PREDICTIONS

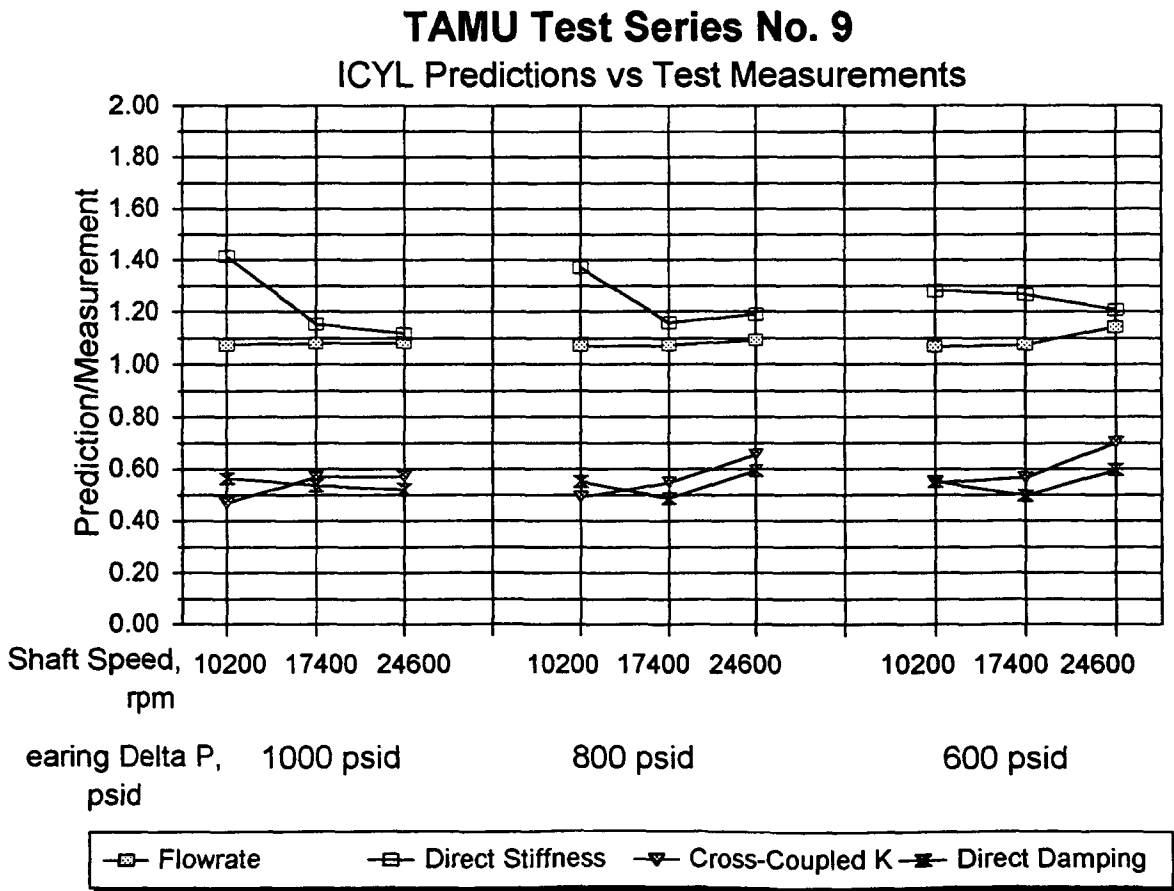
- Orifice Flow Coefficient selected to match flow data at one operating point.
 - Match of flow prediction to data at other operating conditions shows that orifice coefficient is constant.
- Direct Stiffness, Direct Damping and Cross-coupled stiffness predictions were within +/- 20% of test measurements
 - Measured cross-coupled stiffness and direct damping increased less with speed than predicted

TAMU Test Series No. 9
HYDROPAD vs Test Measurements



ICYL PREDICTIONS

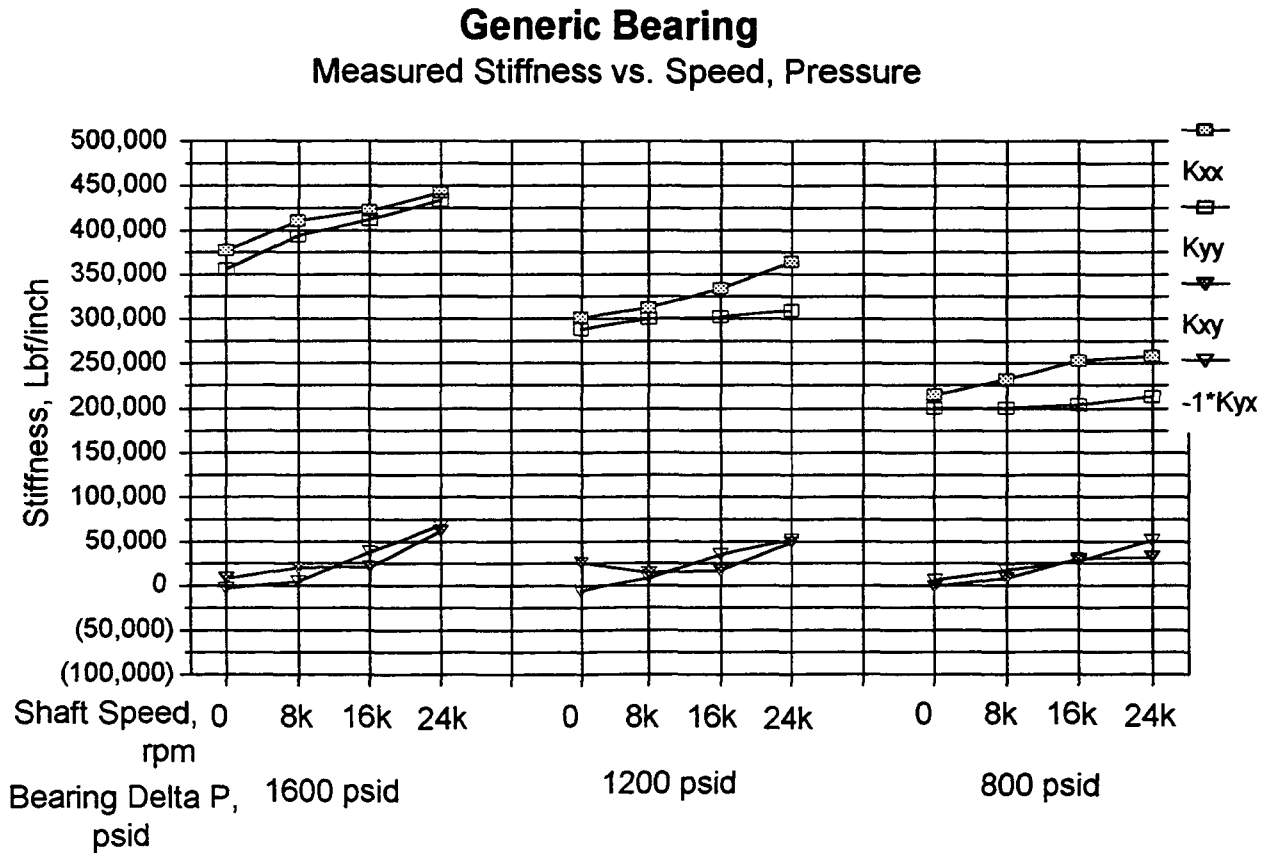
- Orifice Flow Coefficient matched to measured flow data
 - Independent of operating conditions
- Direct Stiffness within 20% of test data except at lowest speed
- Cross-Coupled Stiffness and Direct Damping approximately 50% of measured values



PREDICTIONS VERSUS TEST RESULTS -- "GENERIC" BEARING

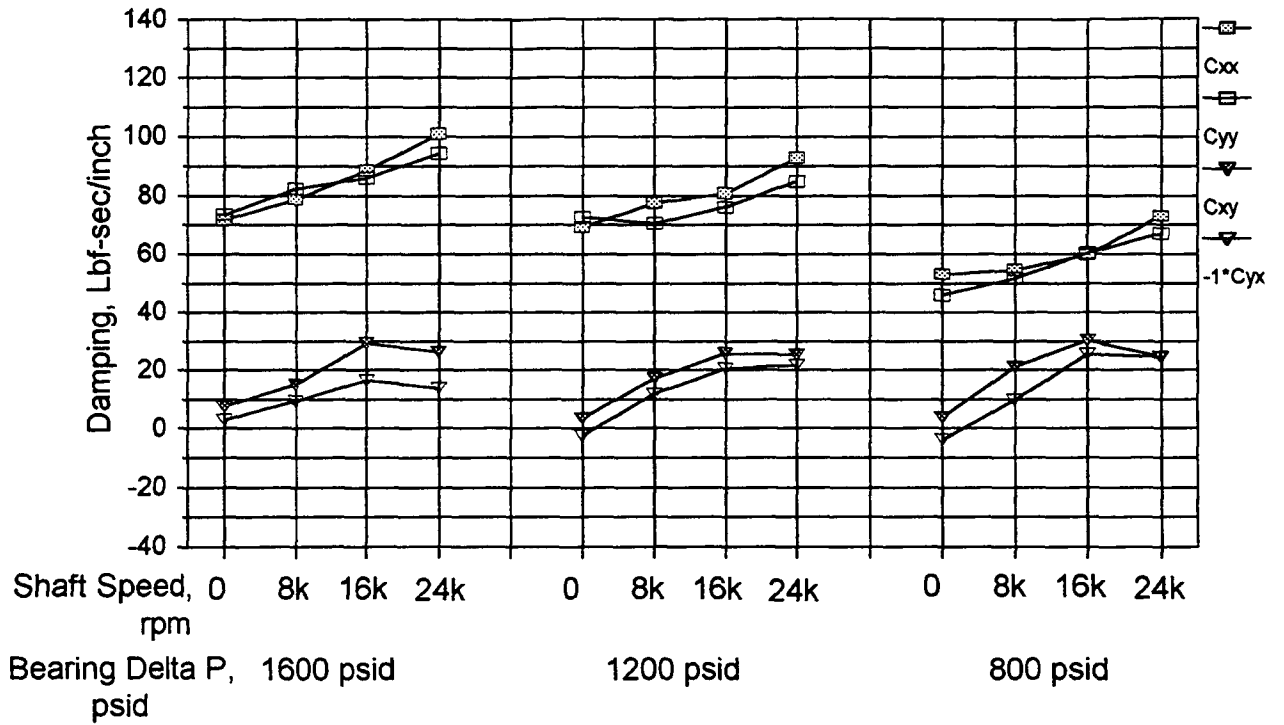
MEASURED BEARING PERFORMANCE

- Direct stiffness roughly one-half of TAMU No. 9 bearing at similar operating conditions
- Cross-Coupled Stiffness and Direct Damping about one-tenth of TAMU No. 9
 - Direct Damping is speed dependent



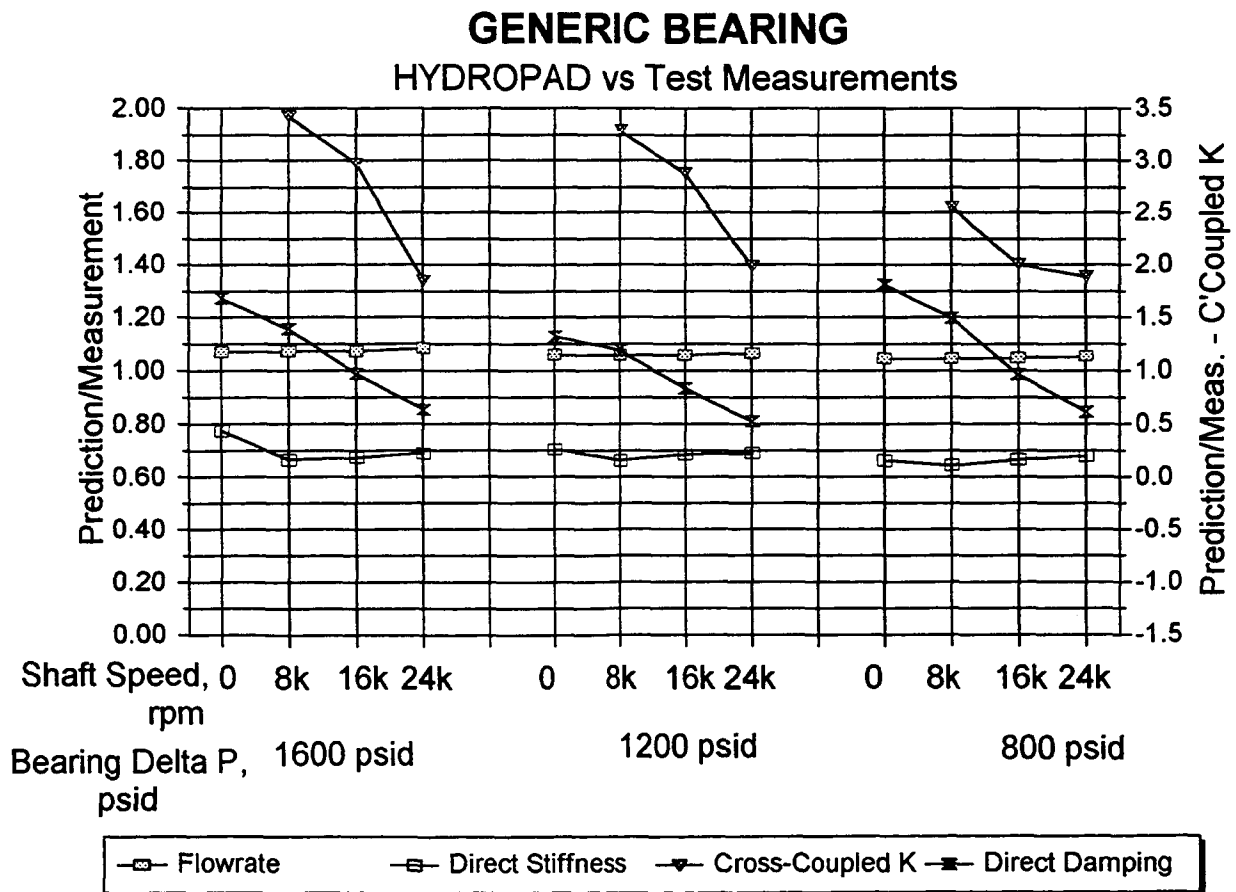
MEASURED BEARING PERFORMANCE (con't)

Generic Bearing
Measured Damping vs. Speed, Pressure



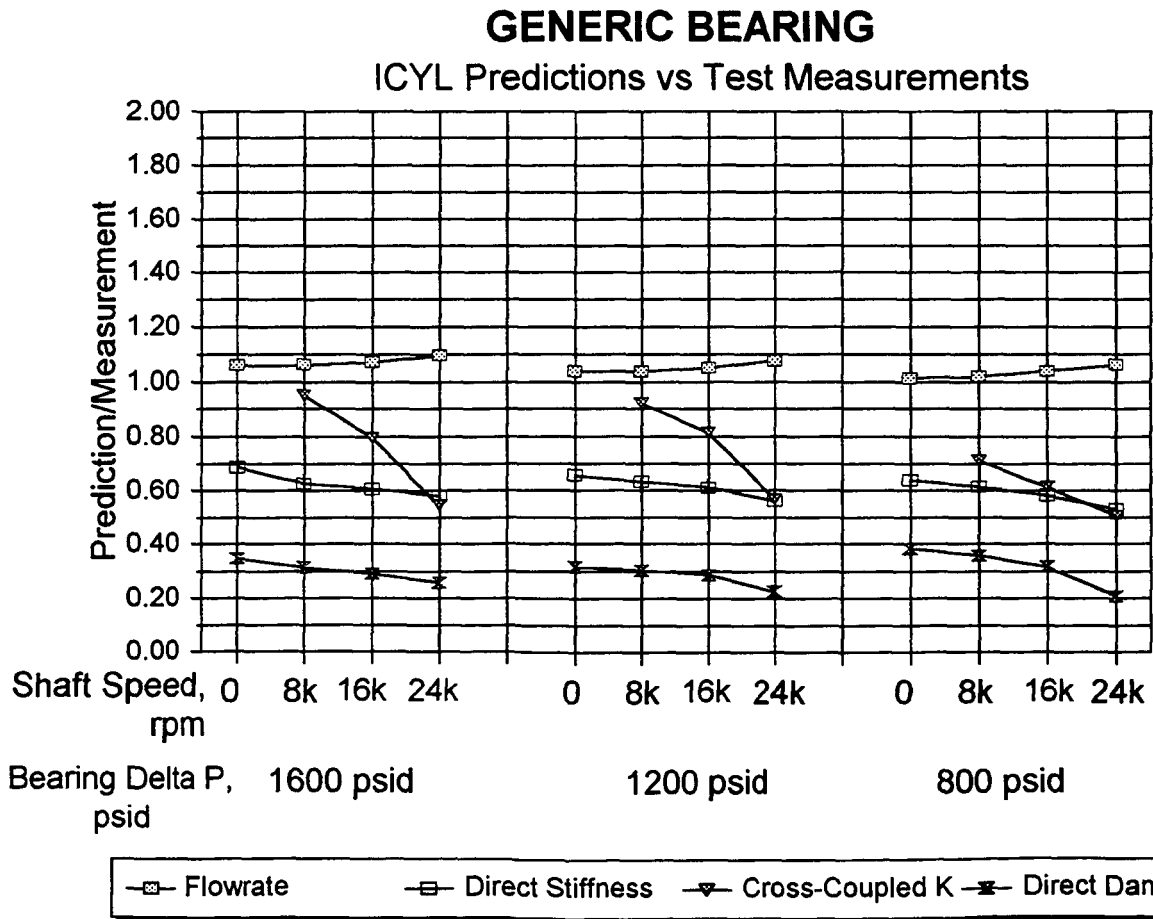
HYDROPAD PREDICTIONS

- Orifice Flow Coefficient selected to match flow data
 - Coefficient significantly smaller than TAMU bearing because of sharp edge geometry
- Direct Stiffness underpredicted by constant ratio
- Direct Damping overpredicted at low speed, under predicted at higher speeds
- Cross-Coupled stiffness overpredicted but magnitude still small compared to Direct Stiffness
- Discrepancies not pressure dependent



ICYL PREDICTIONS

- Orifice Flow Coefficient matched to measured flow data
 - Independent of operating conditions
- Direct Stiffness underpredicted, similar to HYDROPAD prediction
- Direct Damping roughly one-third of measured value
- Cross-Coupled Stiffness magnitudes are small
- Discrepancies are not pressure dependent



NOTES REGARDING ICYL USAGE

Code was run on Silicon Graphics IRIS workstation

- Provided faster execution but lacked interactive input and graphics capability of PC/OS2

Bearing modeled as follows:

- Bearing symmetric about axial center plane (ISYM =1)
- Pressures at circumferential start of model equal to pressures at end (IPER=1)
- Grid mesh size (TAMU Bearing Model) --
 - Axial - 7 total on half bearing; 5 on land including step, 2 in recess
 - Circumferential - 8 per recess sector: 5 between recesses including steps, 3 in recess
- Friction factor used IFRICT=0. (Smooth, Ng-Elrod turbulence model. Perturbed equations would not solve with IFRICT=3. Solution time with IFRICT=4 was approximately 45 minutes per case; similar results obtained)

Results from ICYL

- Flowrate must be multiplied by 2 to obtain the quantities presented.
Flow balance checked correctly (against orifice flow calculation) when factor of 2 applied

CONCLUSIONS

- **GOOD PREDICTION OF TAMU BEARING PERFORMANCE**
 - ICYL prediction of direct stiffness accurate
- **SIGNIFICANT DISCREPANCIES FOR “GENERIC” BEARING**
 - Underprediction of direct stiffness unexpected
 - Direct damping error is speed dependent
- **SHORT, HIGH CLEARANCE BEARING AND LOW VISCOSITY FLUID MAY BE CAUSE**
 - High Reynolds Number and short lands result in inertia dominated flow losses which have greater uncertainty
 - Model assumes fully developed flow in land -- entrance region error may become significant in short bearings

Low pressure ratio of GENERIC bearing causes stiffness prediction to be more sensitive to errors in predicted pressure losses in land region
 - Effect of fluid downstream of test bearing may be significant with shorter bearing

SCISEAL: A CFD CODE FOR ANALYSIS OF FLUID DYNAMIC FORCES
IN SEALS

M.M. Althavale, Y.-H. Ho, and A.J. Przekwas
CFD Research Corporation
Huntsville, Alabama

511-34

39453

OUTLINE

- **Objectives**
- **Current Status**
- **Code Capabilities**
- **Selected Results**
- **Concluding Remarks**

ACKNOWLEDGEMENTS

- **Code Development Done Under LeRC Contract NAS3-25644**
 - **Technical Monitor: R.C. Hendricks, LeRC**
 - **Program Manager: A. Liang, LeRC**
 - **MTI Manager: W. Shapiro, MTI**
- **Technical Help, Encouragement from the Following People:**
 - **Drs. A.K. Singhal, Y.G. Lai, CFDRC**
 - **Dr. B. Steinetz, LeRC**
 - **from Allison, UTRC, and GEAE**

OBJECTIVES (CFDRC)

- **Develop Verified CFD Code for Analyzing Seals**
- **Required Features Include:**
 - **Applicability to a Wide Variety of Seal Configurations such as: Cylindrical, Labyrinth, Face, and Tip Seals**
 - **Accuracy of Predicted Flow Fields and Dynamic Forces**
 - **Efficiency (Economy) of Numerical Solutions**
 - **Reliability (Verification) of Solutions**
 - **Ease-of-Use of the Code (Documentation, Training)**
 - **Integration with KBS**

SCIENTIFIC CODE DEVELOPMENT

- Task 1: Develop a 3D CFD Code (SCISEAL) for Cylindrical Seals**
- **for Annular, Tapered, Stepped**
 - **Verification of Code Accuracy**
 - **Rotordynamic Coefficient Calculations**

- Task 2: Augmentation of SCISEAL**
- **Incorporation of Multi-Domain Capabilities**

Note: Starting CFD Code = REFLEQS (developed by CFDRC under a contract from NASA MSFC/ED32)

STATUS 3RD SEALS WORKSHOP

- **Single Domain 3D Code**
 - **colocated grids**
 - **high-order schemes**
 - **rotating and moving grid systems**
 - **turbulence models, including 2-layer model**
- **Seal Specific**
 - **grid generation**
 - **pre-processing, geared for cylindrical seals**
- **Rotordynamics**
 - **whirling rotor method for centered seals**
 - **perturbation method for centered as well as eccentric seals**
- **Extensive Validation Effort**
 - **long and short annular seals**
 - **labyrinth flows**
 - **entrance loss coefficients**

AUGMENTATION IN SCISEAL AND PRESENT STATUS

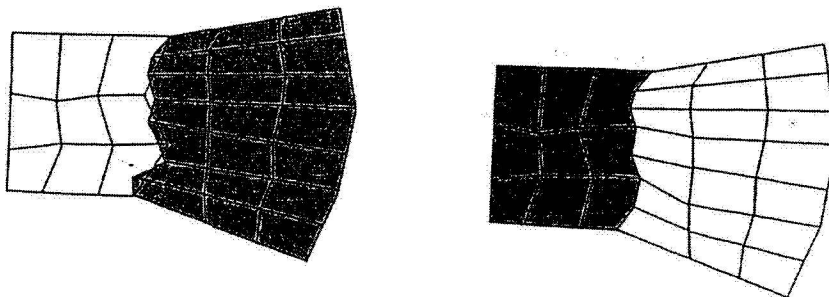
- **Major Item: Incorporation of Multi-Domain Formulation**
 - **flow treatment completed**
 - **all flow models extended to multi-domain**
 - **additional:**
 - **2D/3D switchable for efficiency in planar/axisymmetric solutions**
 - **conjugate heat transfer capability (completed in a separate contract)**
 - **local refinement multi-to-one grid interfaces**
- **Rotordynamics**
 - **whirling rotor method transferred, extended to multi-domain grids and user input grids**
 - **perturbation model transferred for cylindrical seals**
- **Validation Effort Continued**
 - **whirling seal flow solutions obtained and compared with experiments (single domain code)**
 - **several rim seal + disc cavity + labyrinth seal computations performed and compared (multi-domain code)**

MULTI-DOMAIN APPROACH

- **The Multi-Domain Method is Fully Implicit and Conservative**
- **The Approach has been Successfully Demonstrated on a Variety of 2D and 3D Flows**
- **Implicitness is Very Important to Speed Up Convergence for Low Speed Elliptic-Type Flows and Flows with Many Sub-Domains**
- **Has been Implemented for One-to-One and One-to-Many Zonal Connections**

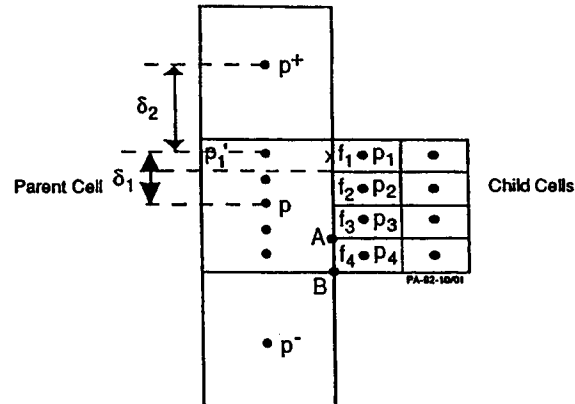
MULTI-DOMAIN ZONAL INTERFACE TREATMENT

- **Illustration of Patched Grid Matching Between Two Domains**



MULTI-DOMAIN INTERFACE TREATMENT (Cont.)

- **Basic Interface Stencil**



- **Implicitness and Conservation**

CURRENT CODE CAPABILITIES

- **Seals Code has:**
 - **Finite Volume, Pressure-Based Integration Scheme**
 - **Colocated Variables with Strong Conservation Approach**
 - **High-Order Spatial Differencing - up to Third-Order**
 - **Up to Second-Order Temporal Differencing**
 - **Comprehensive Set of Boundary Conditions**
 - **Variety of Turbulence Models ($k-\epsilon$, Low Re $k-\epsilon$, Multiple Scale $k-\epsilon$, 2-Layer Model), Surface Roughness Treatment**
 - **Multi-Domain Capability with Multi-to-One Interface Treatment**
 - **Conjugate Heat Transfer**
 - **Moving Grid Formulation for Arbitrary Rotor Whirl**
 - **Rotordynamic Coefficient Calculation Methods, CFD Based for Centered Seals Circular Whirl**
 - **Small Perturbation: Centered & Eccentric Seals**

SEAL SPECIFIC CAPABILITIES

- **Preprocessor - Geared for Seals Problems**
- **Easy, Quick Geometry Definition and Grid Generation**
- **Four Types of Cylindrical Seals:**
 - **Annular, Axial Step-Down, Axial Step-Up, and Tapered**
- **One Line Commands for**
 - **Automatic Grid Generation**
 - **Integrated Quantities: Rotor Loads, Torque, etc.**
 - **Rotordynamic Coefficients**

CODE VALIDATION AND DEMONSTRATION

- **Code has been Validated for a Large Number of Benchmark Problems**
 - **a list of 33 relevant problems**
- **Extensive Validation Effort Conducted for Practical Seals:**
 - **annular and tapered seals**
 - **labyrinth seals (stepped and straight)**
- **Turbine Main Gas Path and Secondary Path Interaction**
 - **rim seal ingestion (UTRC)**
 - **large scale rig (UTRC)**
 - **T-56 Stage 1-2 (Allison)**

VALIDATION CASES

1. Fully-developed flow in a pipe and channel.
2. Developing laminar flow in a narrow annulus between two cylinders. Slug flow at inlet, fully-developed flow at outlet.
3. Laminar flow between rotating cylinders. Below critical Taylor number, tangential flow only.
4. Flow between two cylinders, rotating inner cylinder. Taylor vortex flow, Laminar and turbulent.
5. 2-D driven cavity flow, Reynolds number up to 10,000. Comparisons with numerical results by Ghia et.al.
6. 3-D driven cavity flow.
7. Couette flow under different pressure gradients. With and without heat transfer.
8. Planar wedge flow in a slider bearing.
9. Laminar flow over a back step. Reattachment length comparison with experiments by Armaly and Durst.
10. Laminar flow in a square duct with a 90° bend. Comparison with experimental data by Taylor et.al.
11. Shock reflection over a flat plate.
12. Turbulent flow in a plane channel. Fully-developed solution at exit compared with experiments by Laufer.
13. Turbulent flow induced by rotating disk in a cavity. Comparison with experiments by Daily and Nece.
14. Centripetal flow in a stator-rotor configuration. Comparison with experiments by Dibelius et.al.
15. Flow between stator and whirling rotor of a seal. 2-D results for 0, 0.5, and synchronous whirl frequencies

VALIDATION CASES

16. **Flow over a bank of tubes.**
17. **Turbulent flow in an annular seal. Comparison with experiments by Morrison et.al.**
18. **Turbulent flow in a 7-cavity labyrinth seal. Comparison with experiments by Morrison et.al.**
19. **Turbulent compressible flow and heat transfer in turbine disk cavities Athavale et.al.**
20. **3-D driven cavity flow with lid clearance and axial pressure gradient. Control of flow through vortex imposition.**
21. **Flow in cavities on a rotor for an electrical motor. Interaction of Taylor vortices with driven cavity flow.**
22. **Flow in infinite and finite length bearings (without cavitation). Comparison of calculated attitude angles with theory.**
23. **Flow and rotordynamic coefficient calculation for straight, incompressible seals. Comparison with results from other numerical and analytical solutions; Dietzen and Nordmann.**
24. **Flow and rotordynamic coefficients in tapered compressible flow seals. Comparison with bulk-flow theory results; Nelson.**
25. **Rotordynamic Coefficients in a long annular incompressible flow seal. Comparison with experimental data; Kanemori and Iwatsubo.**
26. **Calculation of entrance loss coefficients in the entrance region of a generic seal. Effect of flow and geometry on the loss coefficient values; Athavale et.al.**
27. **Flow coefficient and pressures in a 5 cavity, straight knife, look-through labyrinth seal. Comparison with experimental data ; Witting et.al.**
28. **Flow coefficients and pressures in a 3 cavity, tapered knife, look-through labyrinth seal. Comparison with experimental data; Tipton et.al.**
29. **Flow coefficients and pressures in a 2 cavity, straight-knife, stepped labyrinth seal. Comparison with experimental data; Tipton et.al.**

VALIDATION CASES

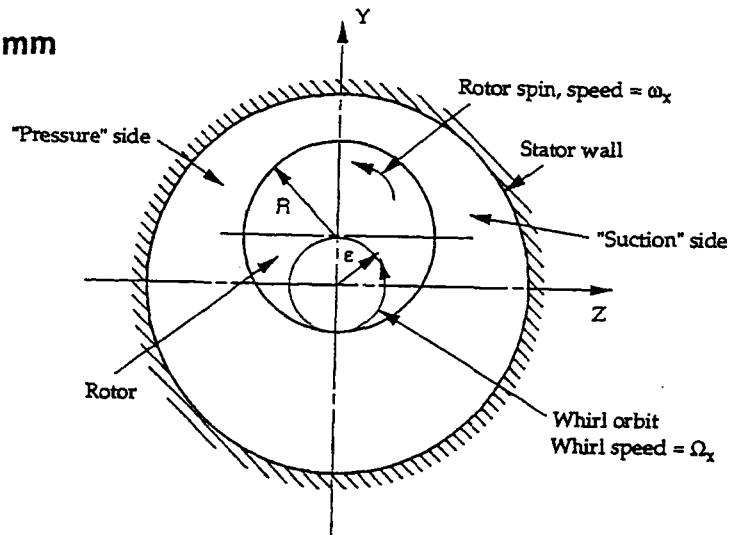
30. **Turbulent flow in a whirling annular seal, comparison with experimental data, Morrison et. al.**
31. **Rim seal ingestion computation, comparison with experimental data, Graber et. al.**
32. **Simulation of turbine disk cavity flow and interaction with main path flow, Allison T-56 engine, turbine stage 1-2 cavity and labyrinth seal.**
33. **Flow interaction in a multiple disc cavity rim seal rig with intra-cavity and secondary main path flow interactions. Comparisons with experimental data from Daniels and Johnson.**

SELECTED RESULTS

- **Several Annular and Labyrinth Seal Results Presented Earlier**
- **Presented Here are Results for**
 - **whirling annular seal (Morrison, Texas A&M, 1992 & 1995)**
 - **rim seal gas ingestion (Graber et. al., UTRC, 1987)**
 - **Allison engine turbine cavity (Munson and Forry, Allison)**
 - **large scale rig UTRC/MSFC (Daniels and Johnson, UTRC, 1993)**

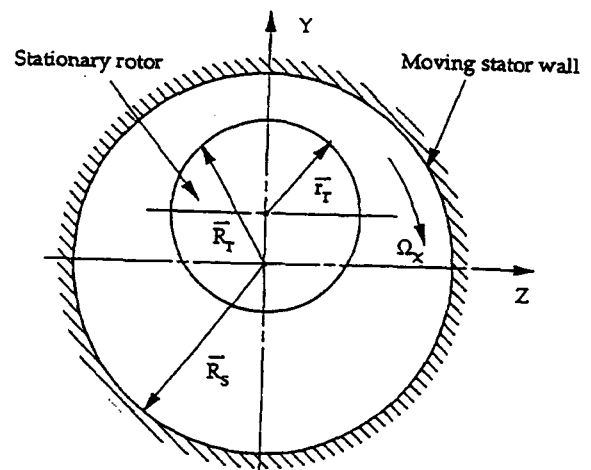
WHIRLING ANNULAR SEAL - PROBLEM DESCRIPTION

- $R = 82.5 \text{ mm}$
- Nominal Clearance $C = 1.27 \text{ mm}$
- $\varepsilon = 0.5 C$
- Seal Length $L = 37.3 \text{ mm}$
- Working Fluid: Water
- $Re = 24,000$
- $T_a = 6,600 \text{ (rpm = 3,600)}$
- $U_m = 7.49 \text{ m/sec}$
- Flow Rate = 4.83 liters/sec



WHIRLING ANNULAR SEAL - COMPUTATIONAL MODEL

- Rotating Frame of Reference
- Grid = 40x20x15
- Incompressible + Standard k- ε model
- Inlet Boundary: seal entrance (measured profiles)
- Downstream Boundary: seal exit (fixed p)
- Periodic Boundary is assumed in the circumferential direction



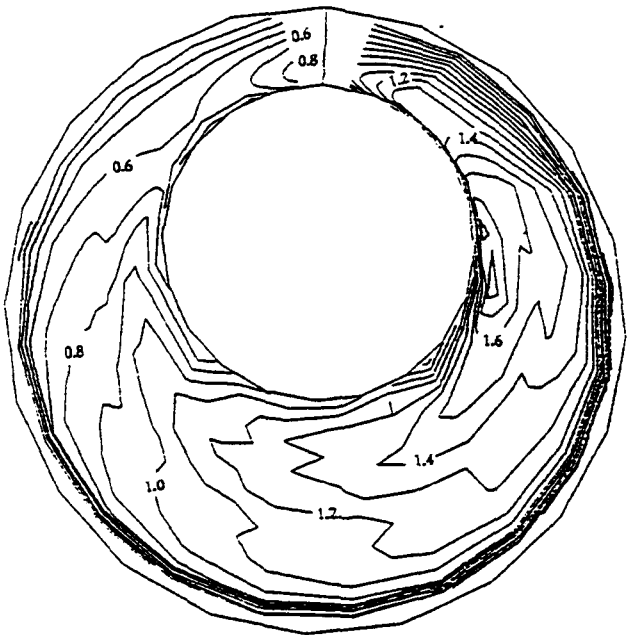
Results: Velocity Distributions and Pressure Along the Seal Length

WHIRLING ANNULAR SEAL RESULTS

Contours of U_{axial}/U_m at Several Axial Stations

Pressure side

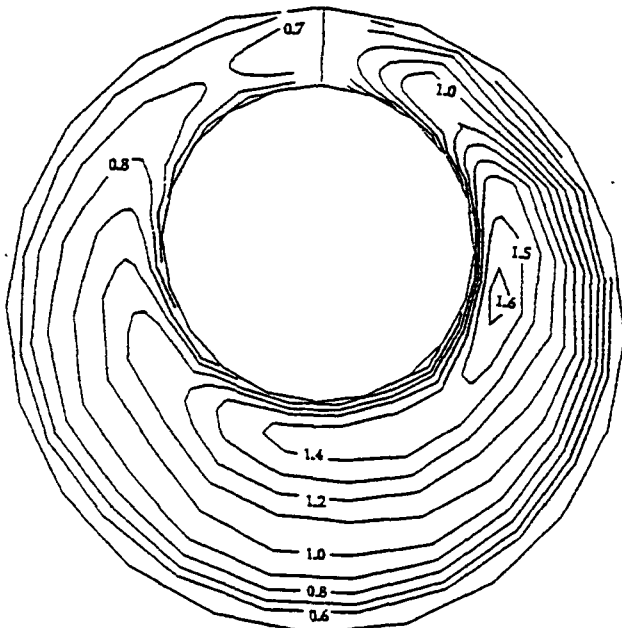
Suction side



(a) $x/L = 0.00125$

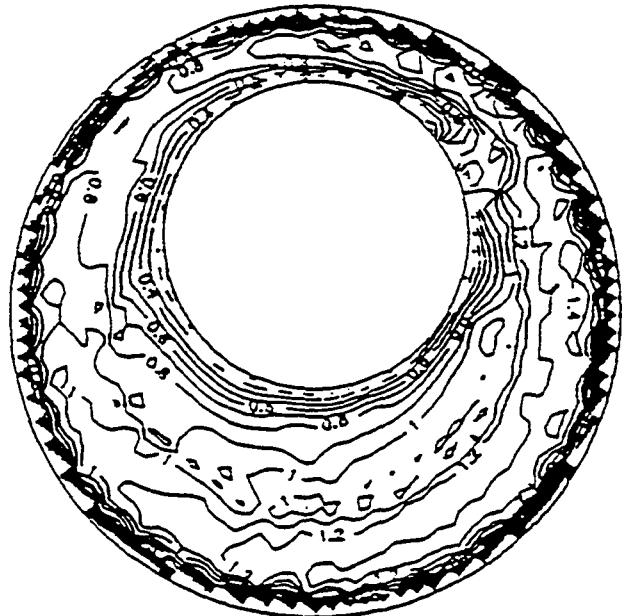


$x/L = 0.0$



(b) $x/L = 0.2125$

Numerical

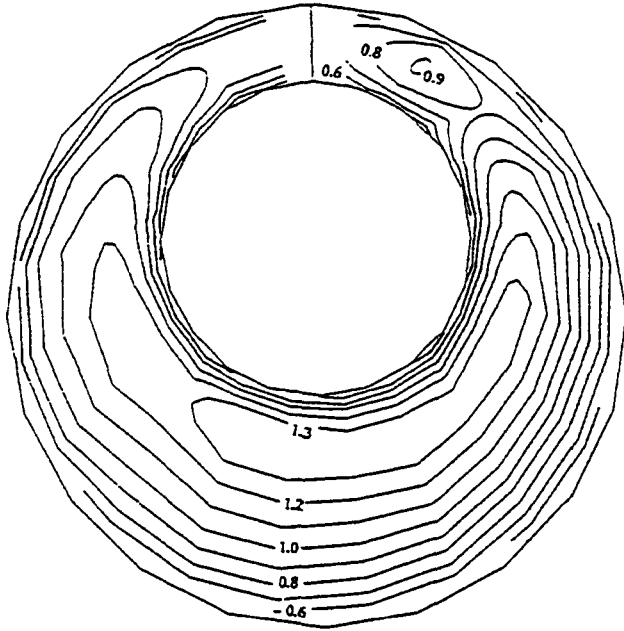


$x/L = 0.22$

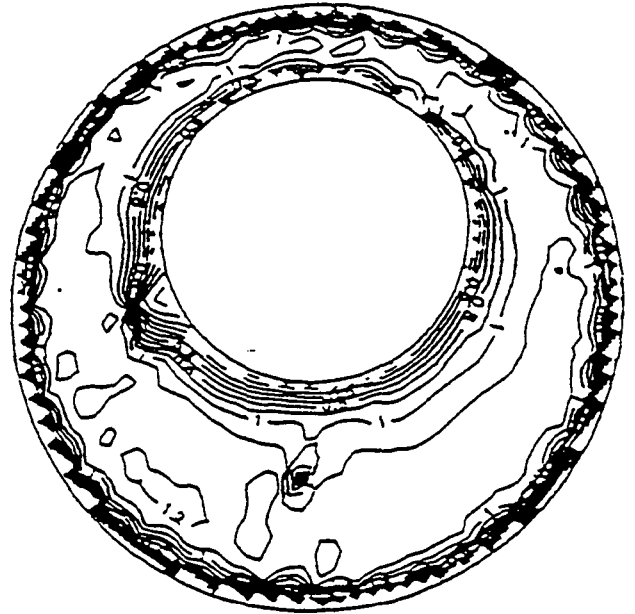
Experimental

WHIRLING ANNULAR SEAL RESULTS

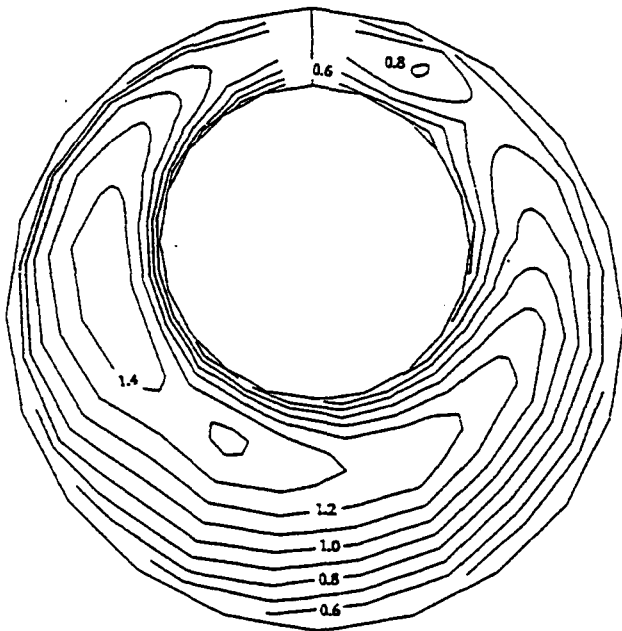
Contours of U_{axial}/U_m at Several Axial Stations



(c) $x/L = 0.4875$



$x/L = 0.49$



(d) $x/L = 0.7625$

Numerical

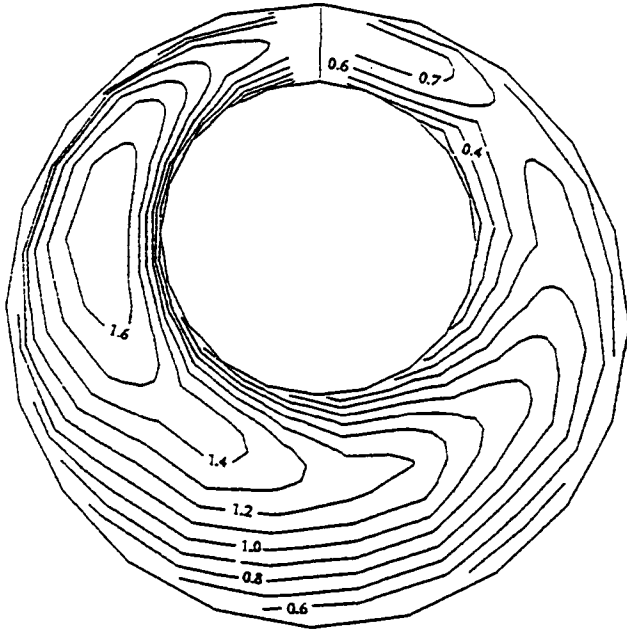


$x/L = 0.77$

Experimental

WHIRLING ANNULAR SEAL RESULTS

Contours of U_{axial}/U_m at Several Axial Stations



(e) $x/L = 0.9875$

Numerical

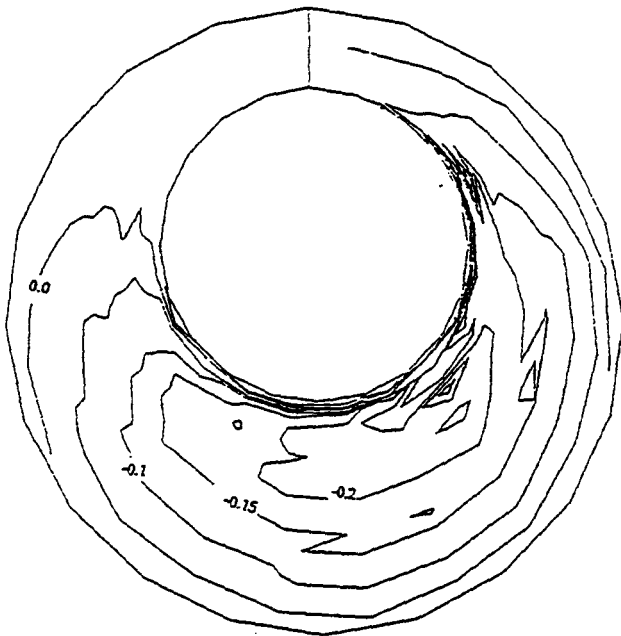


$x/L = 0.99$

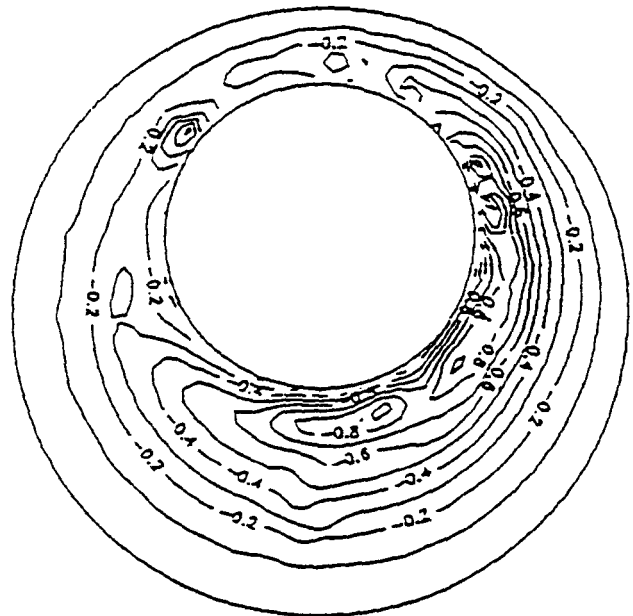
Experimental

WHIRLING ANNULAR SEAL RESULTS

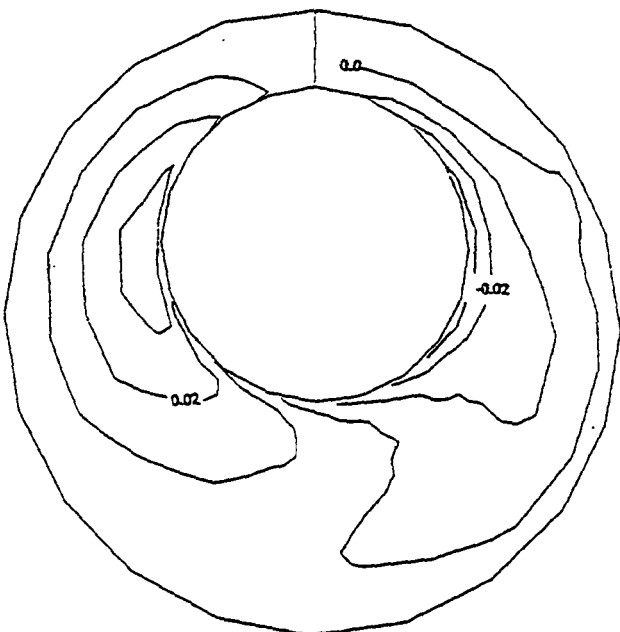
Contours of U_{radial}/U_m at Several Axial Stations



(a) $x/L = 0.00125$

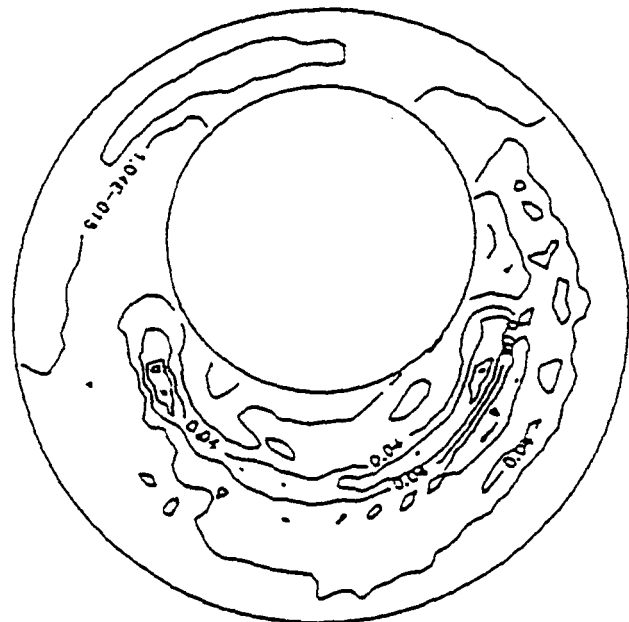


$x/L = 0.0$



(b) $x/L = 0.2125$

Numerical

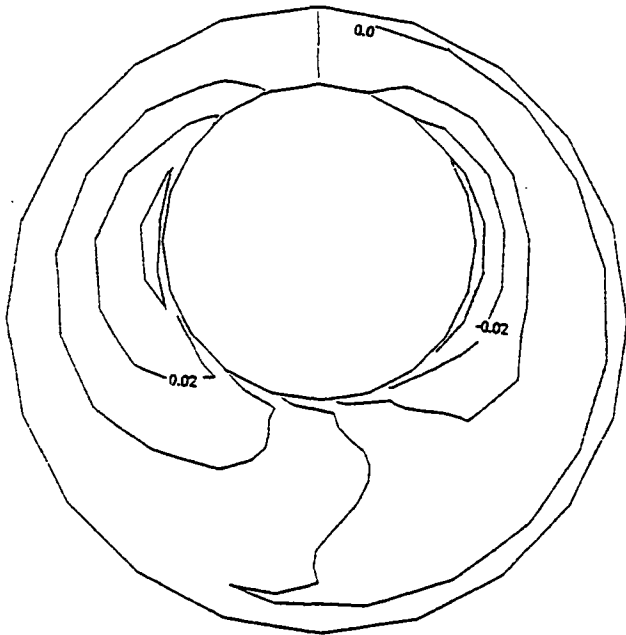


$x/L = 0.22$

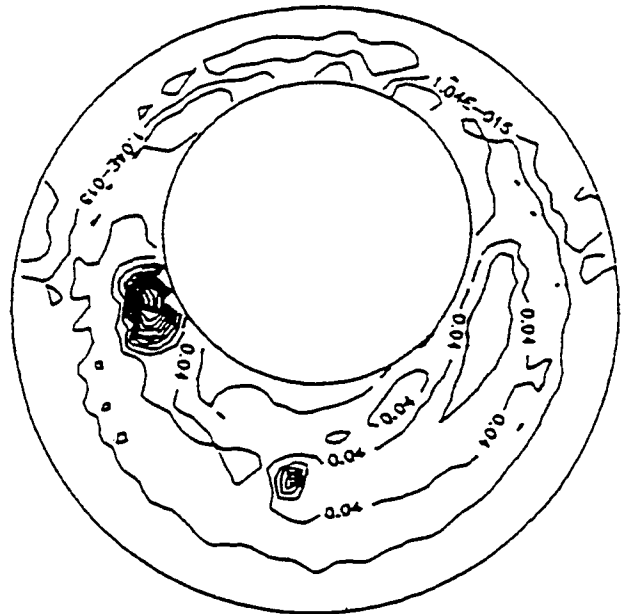
Experimental

WHIRLING ANNULAR SEAL RESULTS

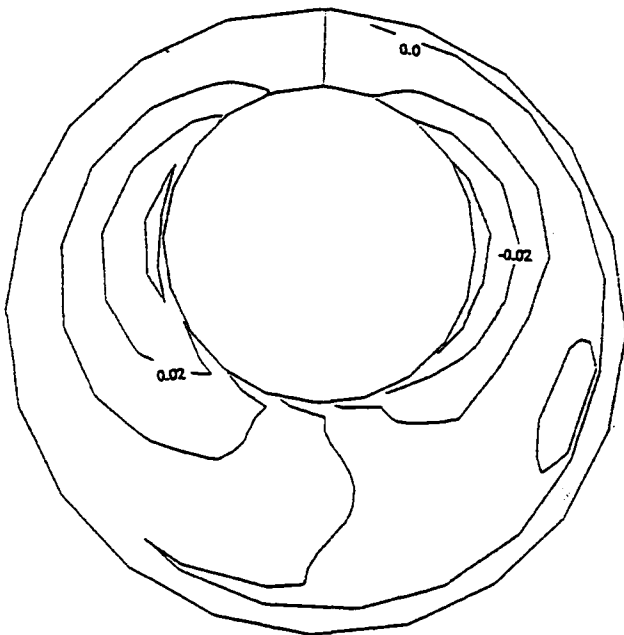
Contours of U_{radial}/U_m at Several Axial Stations



(c) $x/L = 0.4875$

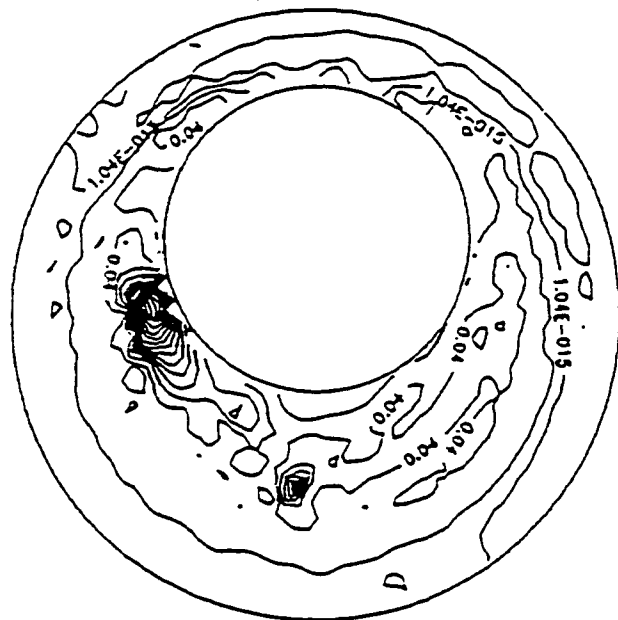


$x/L = 0.49$



(d) $x/L = 0.7625$

Numerical

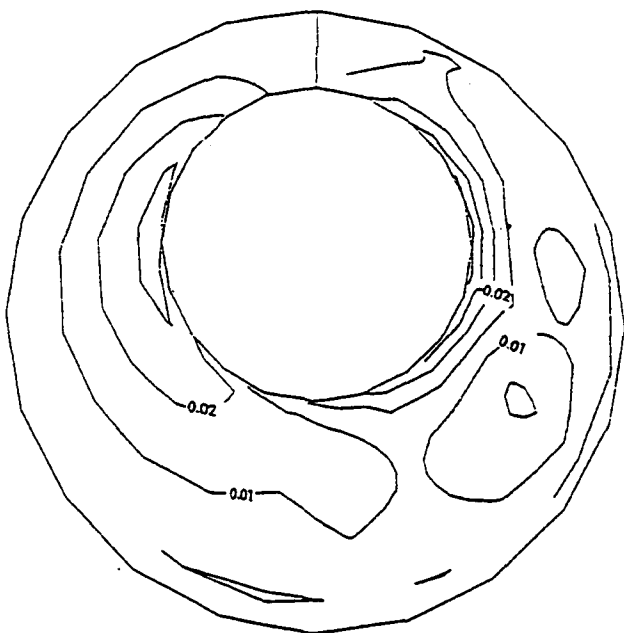


$x/L = 0.77$

Experimental

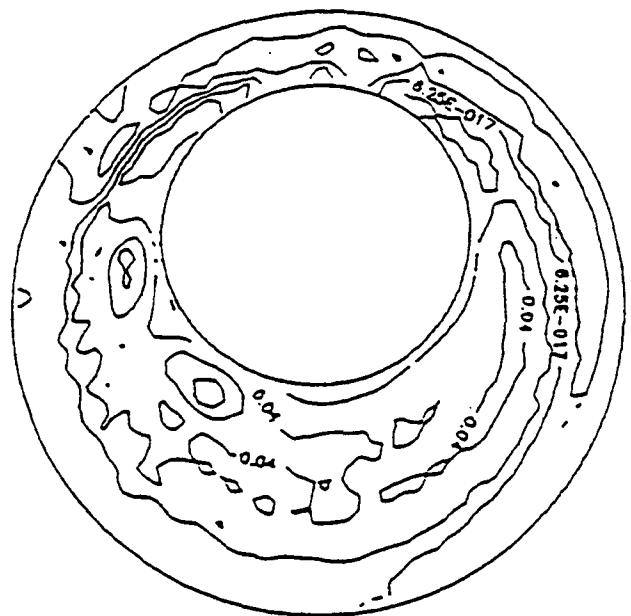
WHIRLING ANNULAR SEAL RESULTS

Contours of U_{radial}/U_m at Several Axial Stations



(e) $x/L = 0.9875$

Numerical

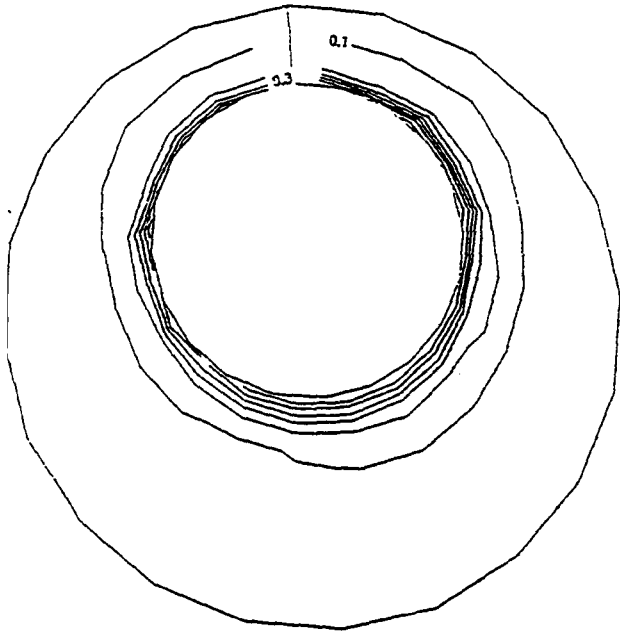


$x/L = 0.99$

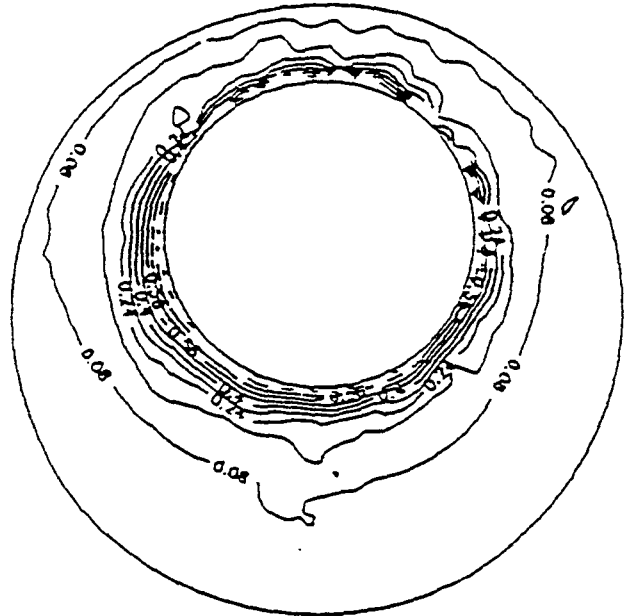
Experimental

WHIRLING ANNULAR SEAL RESULTS

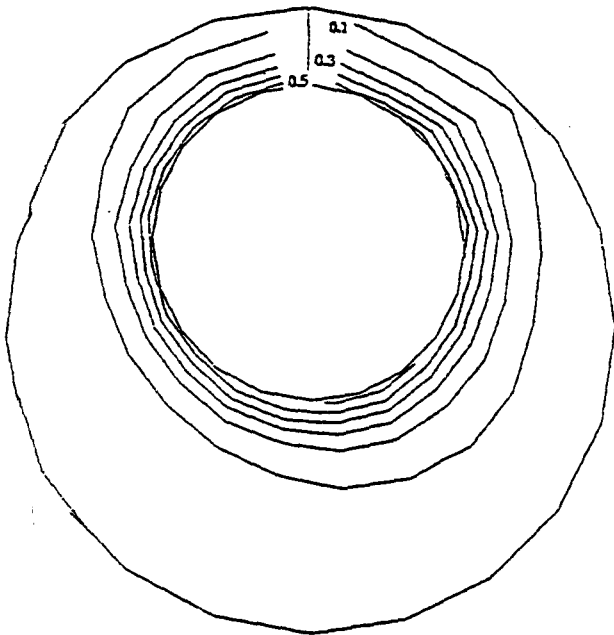
Contours of U_θ/W_{sh} at Several Axial Stations



(a) $x/L = 0.00125$

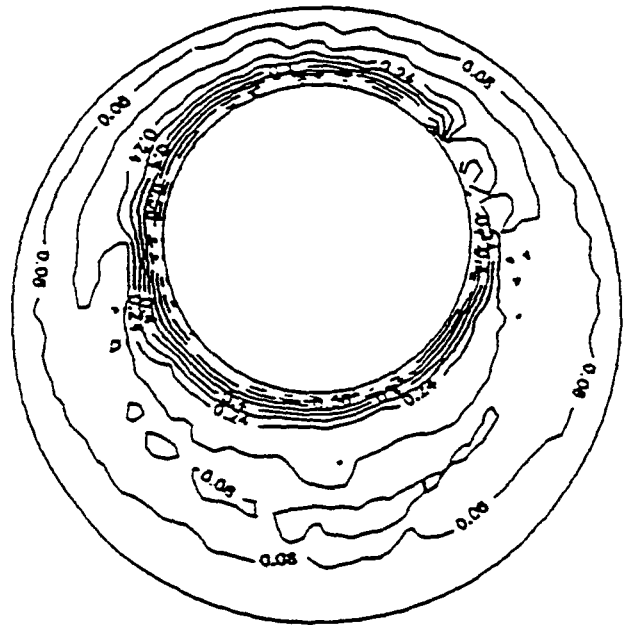


$x/L = 0.0$



(b) $x/L = 0.2125$

Numerical

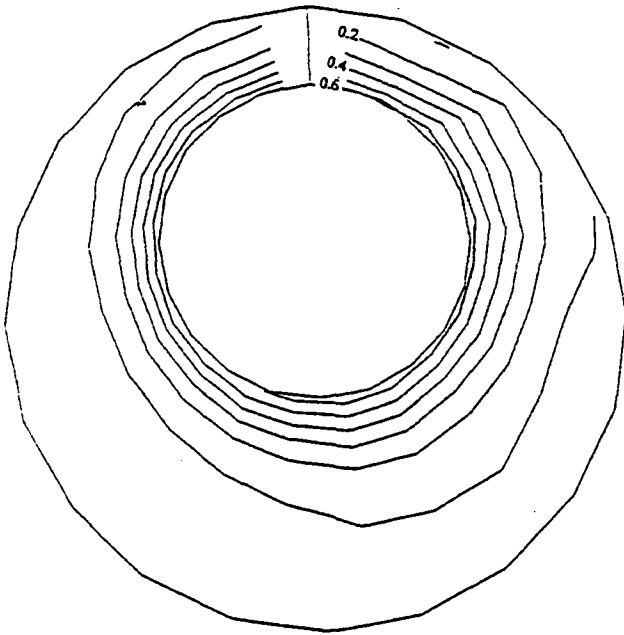


$x/L = 0.22$

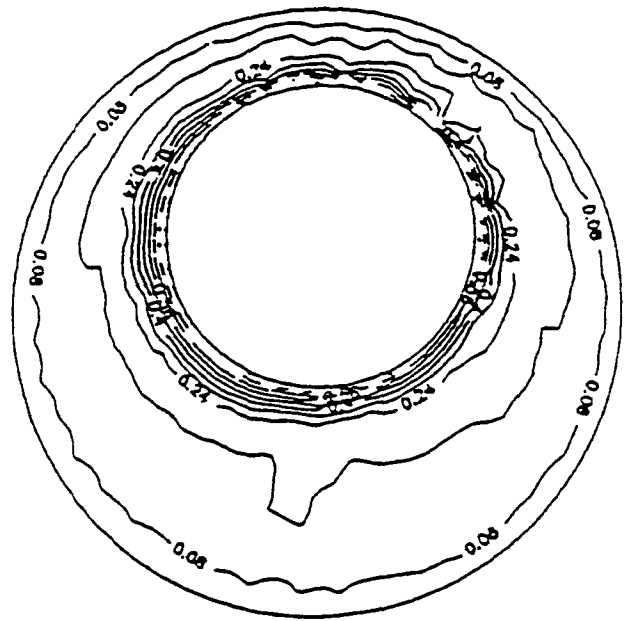
Experimental

WHIRLING ANNULAR SEAL RESULTS

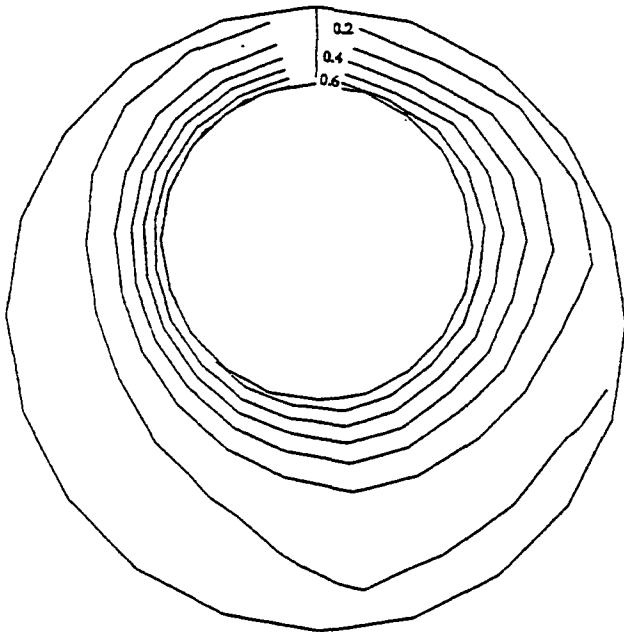
Contours of U_θ/W_{sh} at Several Axial Stations



(c) $x/L = 0.4875$

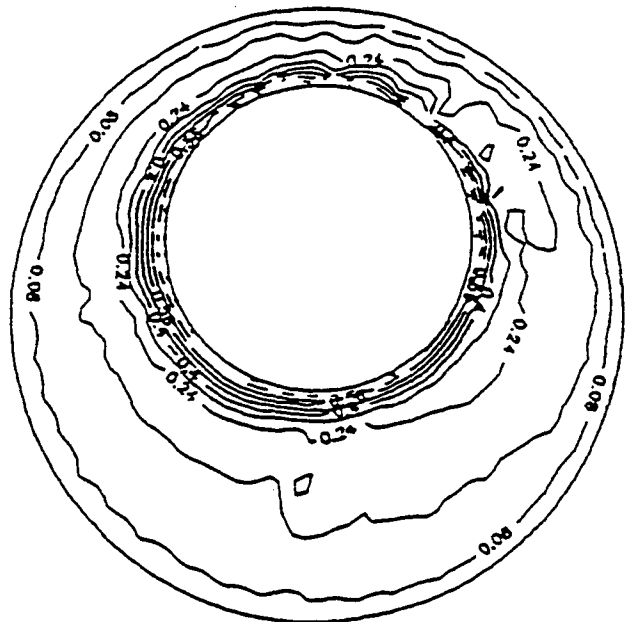


$x/L = 0.49$



(d) $x/L = 0.7625$

Numerical

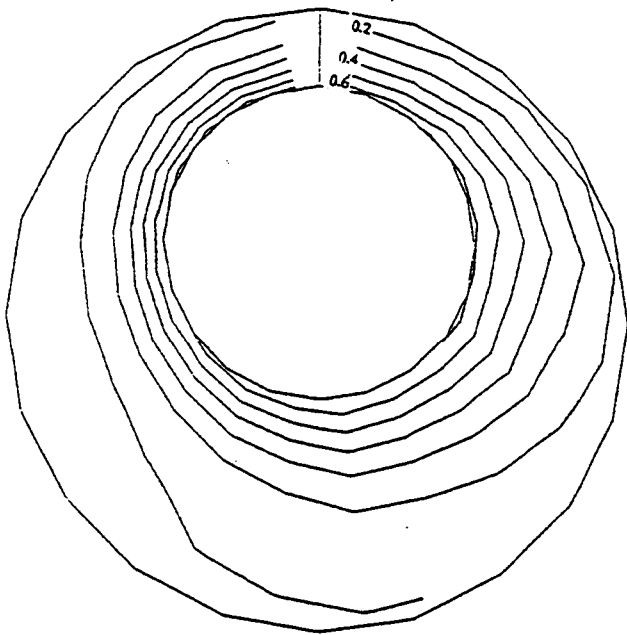


$x/L = 0.77$

Experimental

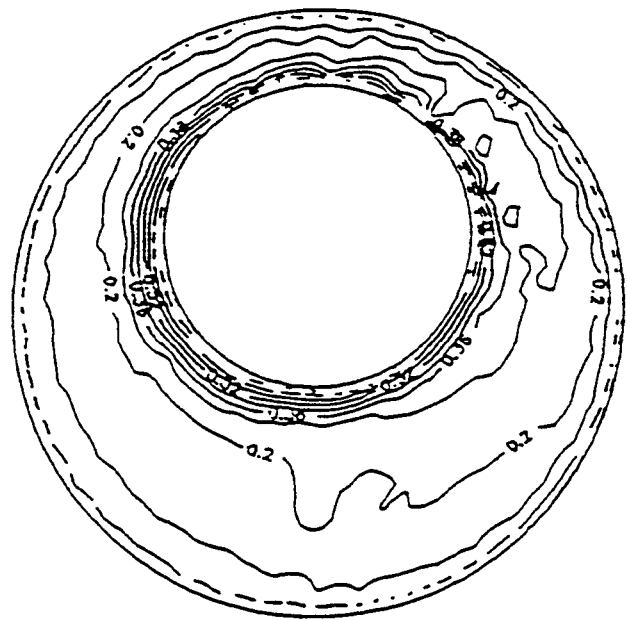
WHIRLING ANNULAR SEAL RESULTS

Contours of U_θ/W_{sh} at Several Axial Stations



(e) $x/L = 0.9875$

Numerical

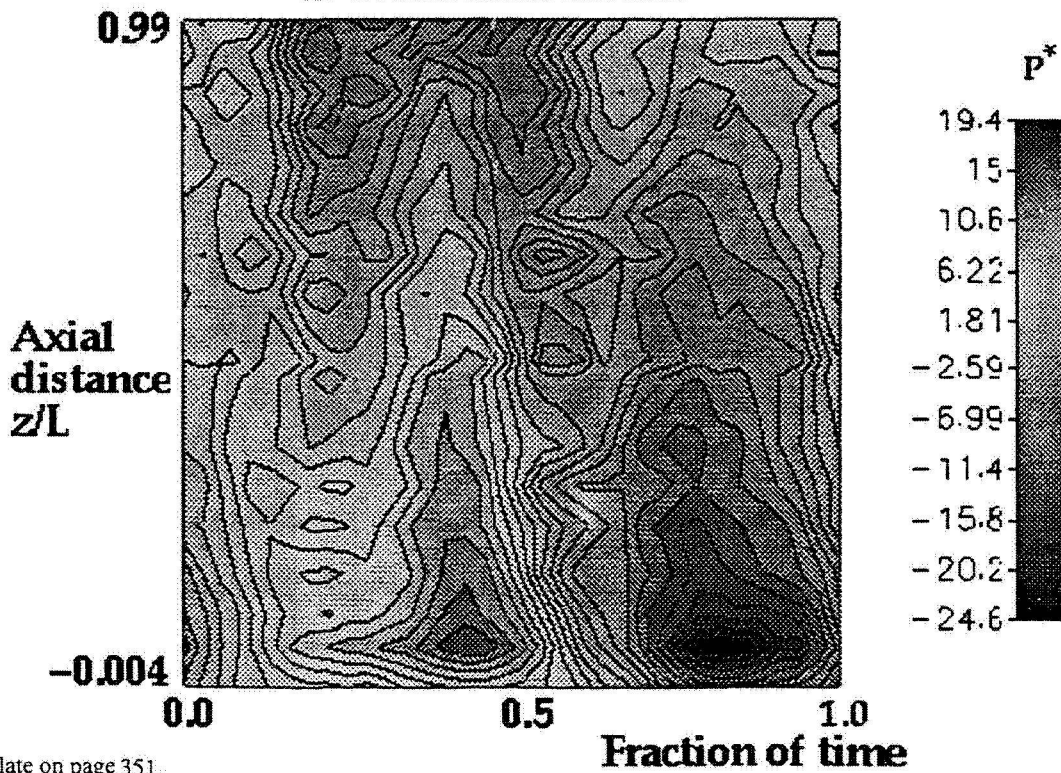
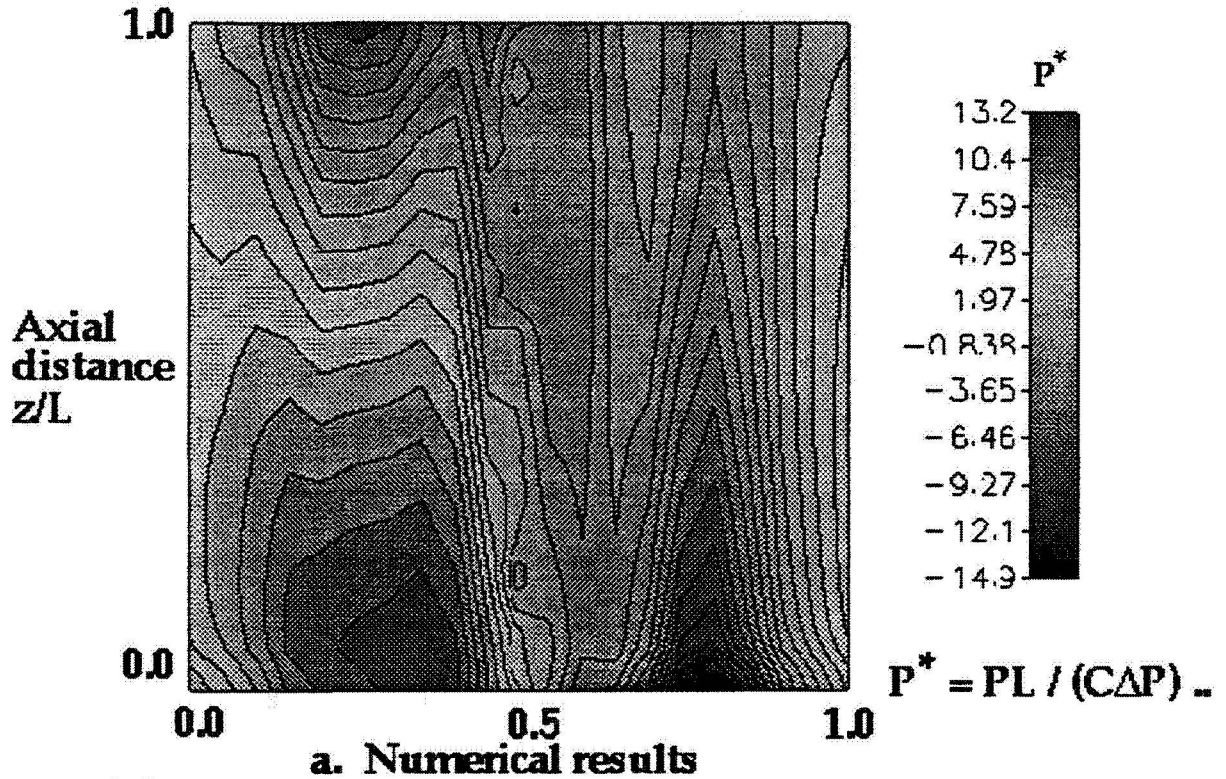


$x/L = 0.99$

Experimental

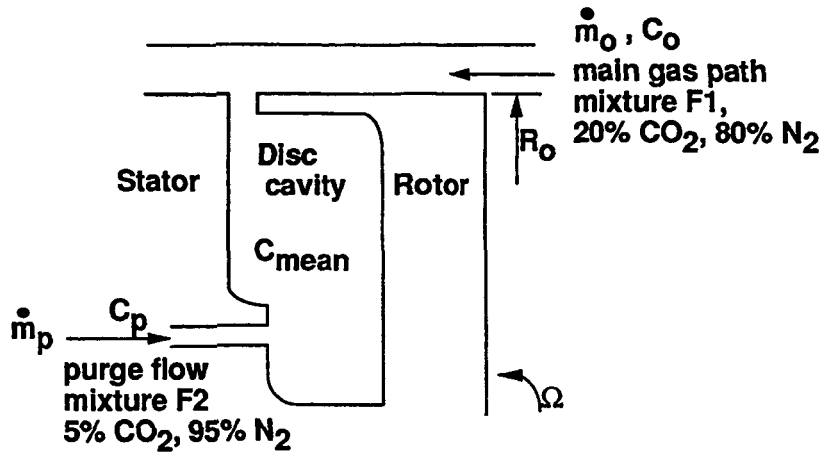
Pressures on the stator wall

← Direction of rotor motion in absolute frame



See color plate on page 351.

RIM SEAL - PROBLEM DESCRIPTION



$$\eta_t = \text{nondimensional purge mass flow} = \left(\frac{\dot{m}_p}{4\pi\mu R_o} \right) (Re_t)^{-0.8}$$

$$\phi = \text{cooling effectiveness} = \frac{C - C_o}{C_p - C_o}$$

$$Re_t = \text{tangential Reynolds number} = \frac{\Omega R_o^2}{\nu}$$

RIM SEAL INGESTION COMPUTATIONS

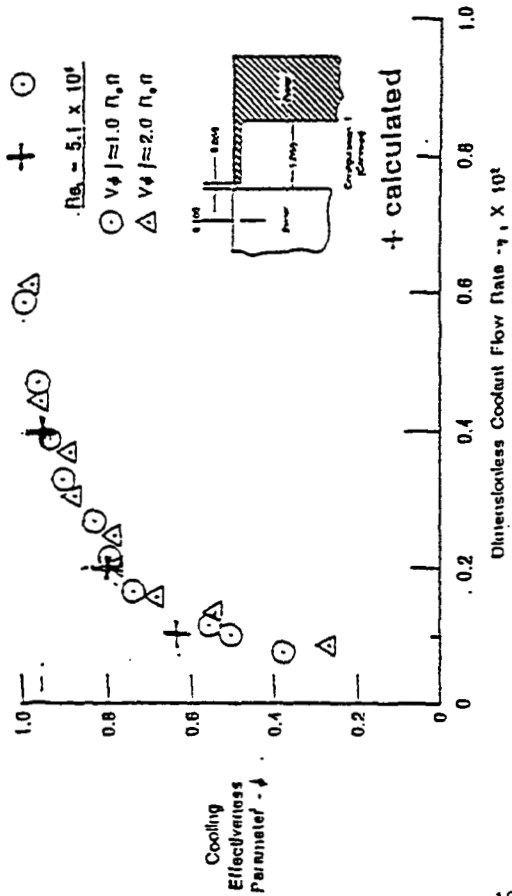
- Variation of Cooling Effectiveness due to Purge Mass Flow
- Fixed Inlet Swirl Reynolds Number
- Four Configurations Tested (reported by UTRC in AFWAL-TR-87-2050, Sept. 1987)
- Each Configuration Tested at Two Purge Flow Rates
- Ingestion Experiments Simulated Using Passive Scalar Transport of Inert Species

COMPUTATIONAL CONDITION

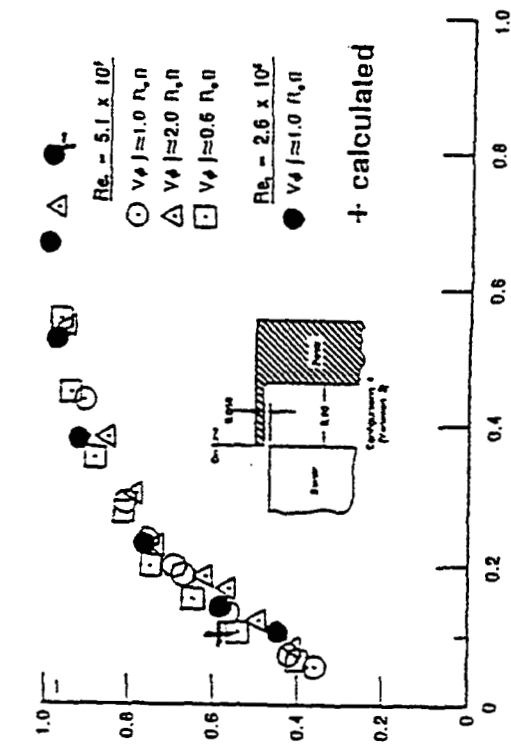
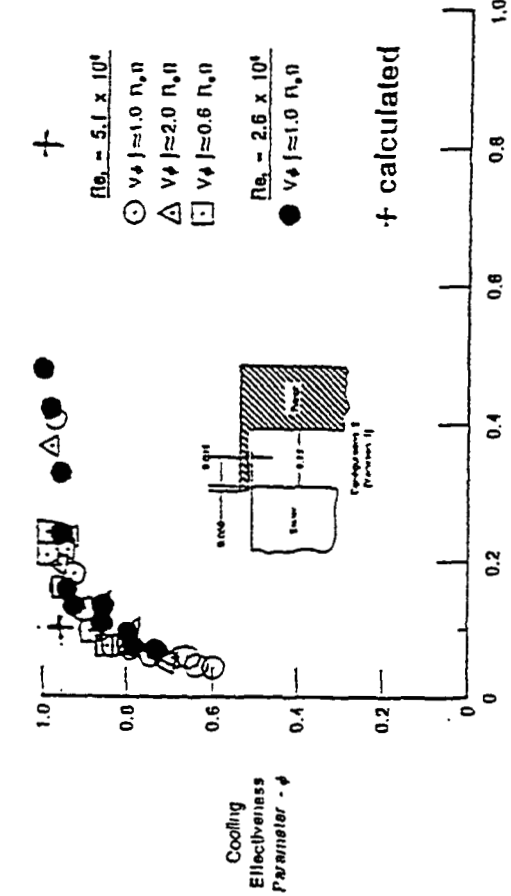
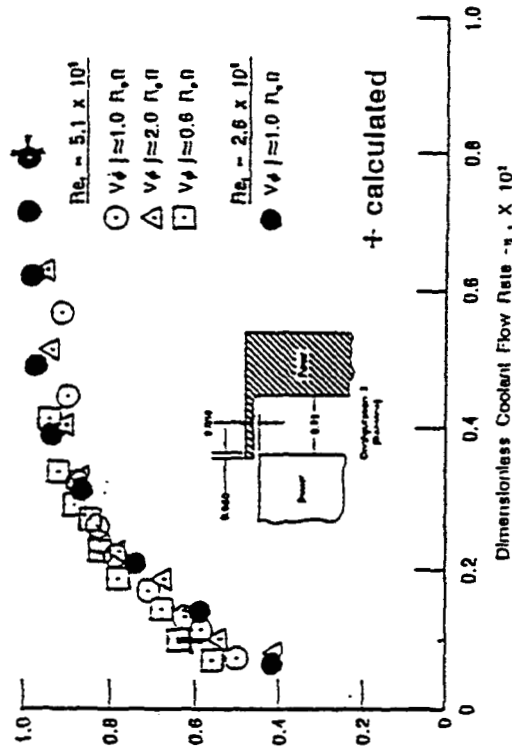
- **Two Purge Flow Rates $\eta_t = 1 \times 10^{-3}$, 8×10^{-3}**
- **Rotor Speed - 2450 rpm, $Re_t = 5.0 \times 10^5$**
- **Inlet Swirl = Rotor Tangential Velocity**
- **Axial Velocity Range 120-150 m/s for the Four Configurations**
- **Computational Grids: 50-60 cells in axial direction
60-70 cells in radial direction**

RIM SEAL FLOW ANALYSIS

Comparison of Calculated and Experimental Data (from AFWAL-TR-87-2050)



181



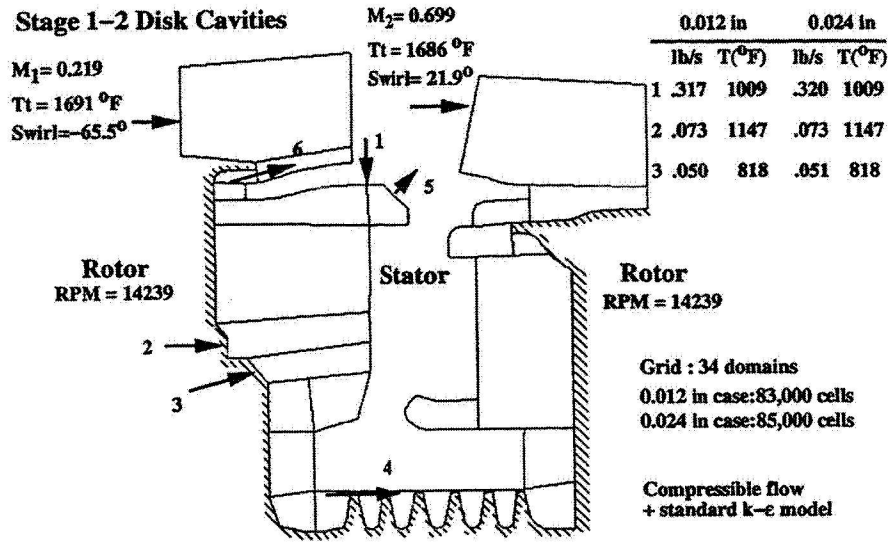
Configuration 1

Configuration 2

Configuration 3 (Baseline)

Configuration 4

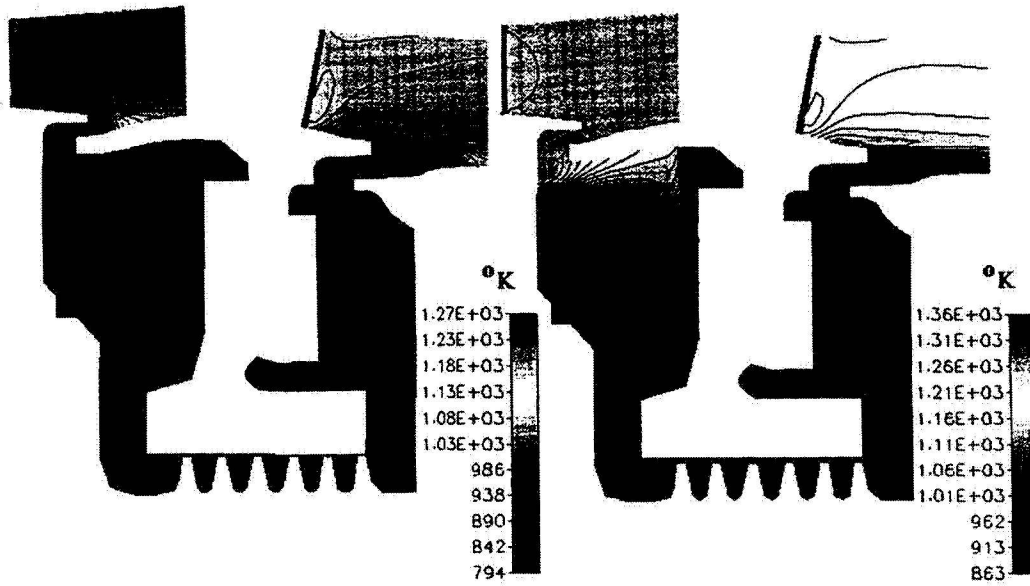
Allison Engine Tubine Cavity



Two labyrinth seal clearances are simulated (0.012 in and 0.024 in)

Temperature

Stage 1-2 Disk Cavities



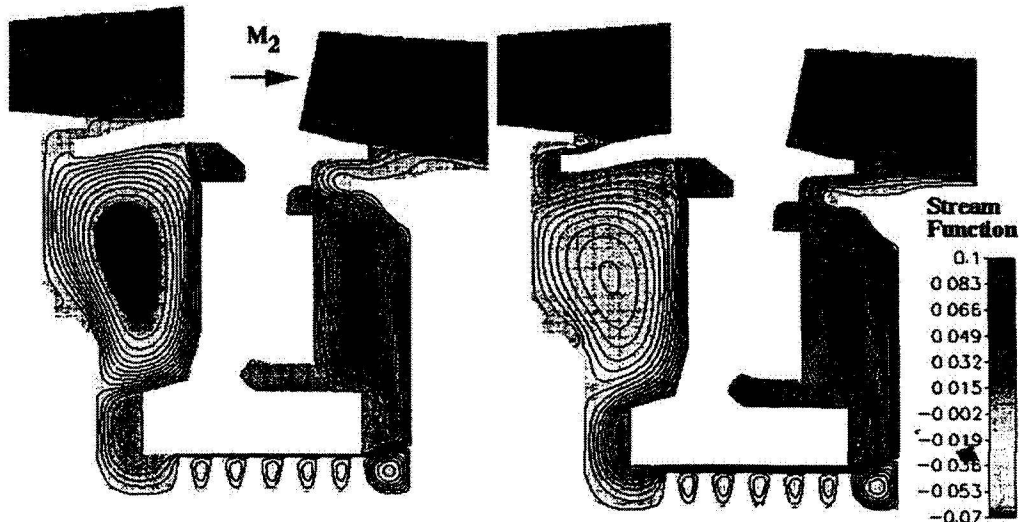
Labyrinth seal clearance = 0.012 in

Labyrinth seal clearance = 0.024 in

See color plate on page 348.

Stream Function

Stage 1-2 Disk Cavities



Labyrinth seal clearance = 0.012 in Labyrinth seal clearance = 0.024 in

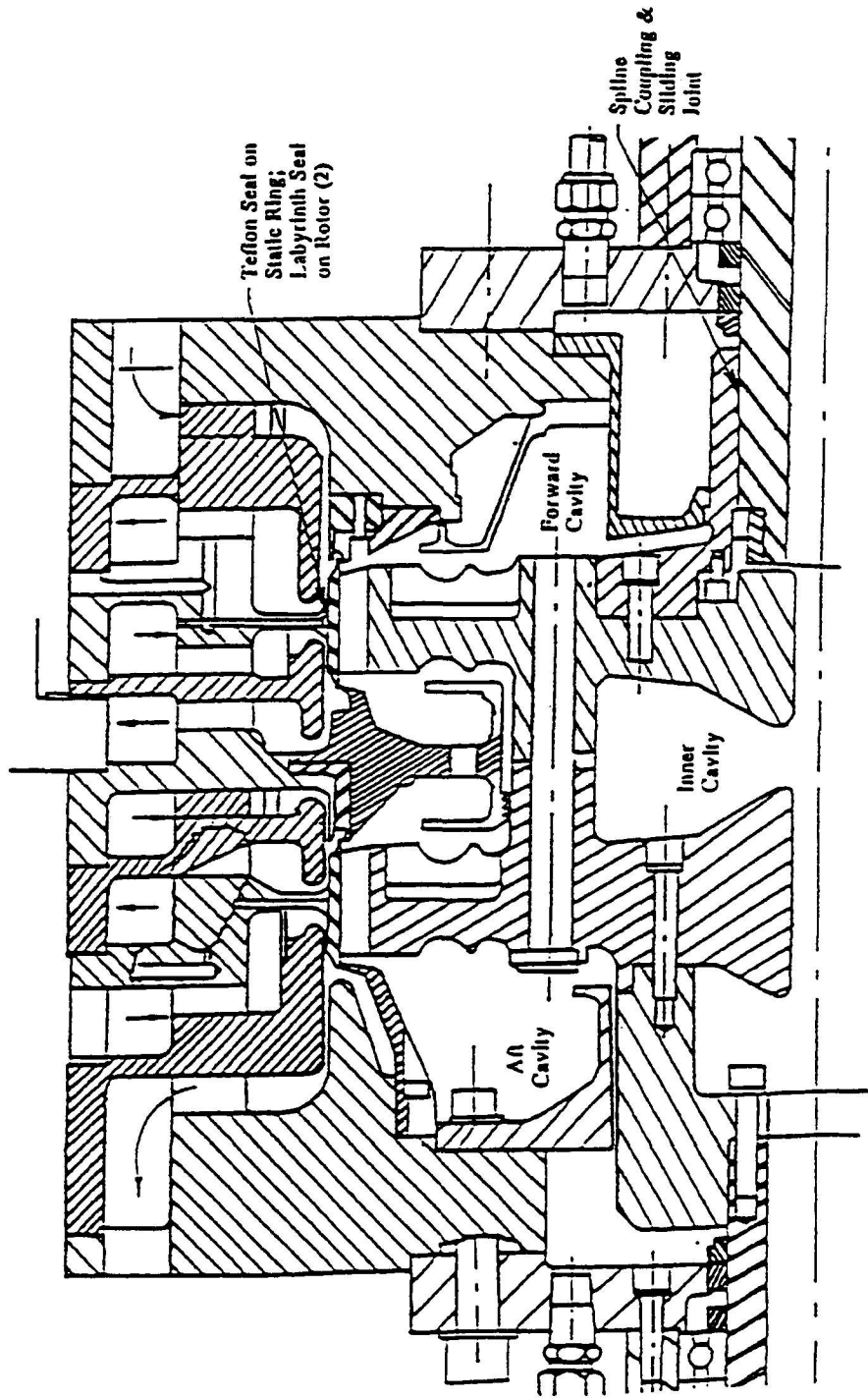
Note: The magnitude is greater than 0.1 in the free stream region (red color with no contours)

See color plate on page 349.

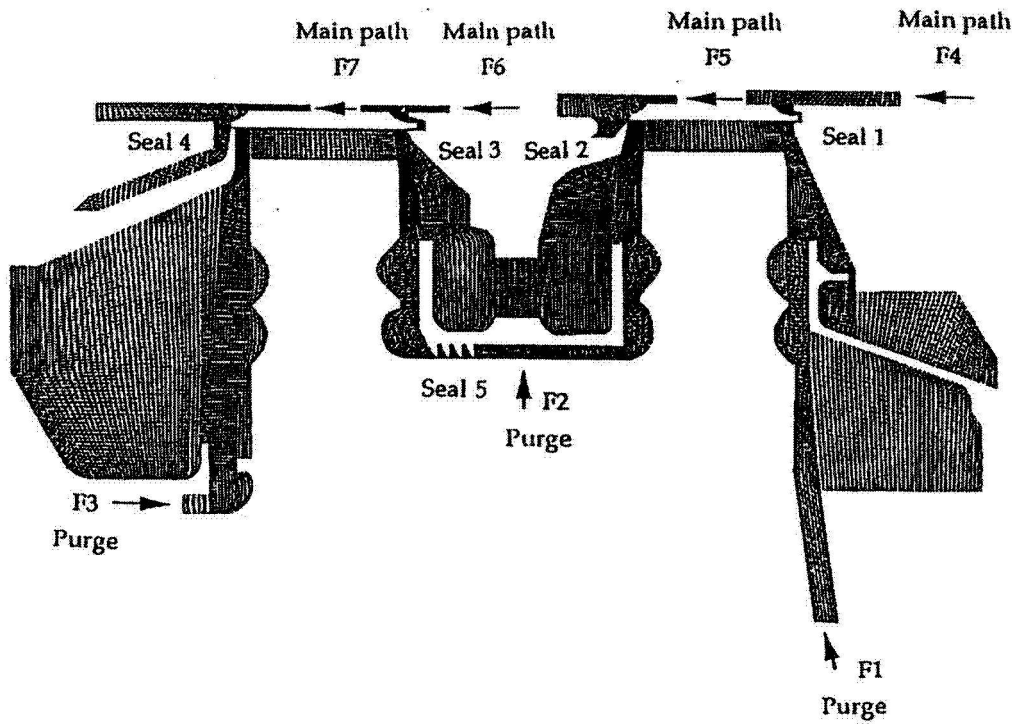
UTRC LARGE SCALE RIG - PROBLEM DESCRIPTION

- 2 Rotor, 4 Cavity Configuration in the UTRC Large Scale Rig by Daniels and Johnson
 - simulates the turbine section of the SSME HPFTP
 - 4 rim seals with associated main-path flows
 - purge flows at 3 locations
 - different concentrations of tracer gas (CO_2) injected in different flow streams and measured at several locations
 - flow rates in main path and flow paths measured and varied for parametrics
 - shanks of the blades also simulated by openings in the rotors with curved passages under the blade platforms.

UTRC LARGE SCALE MODEL RIG

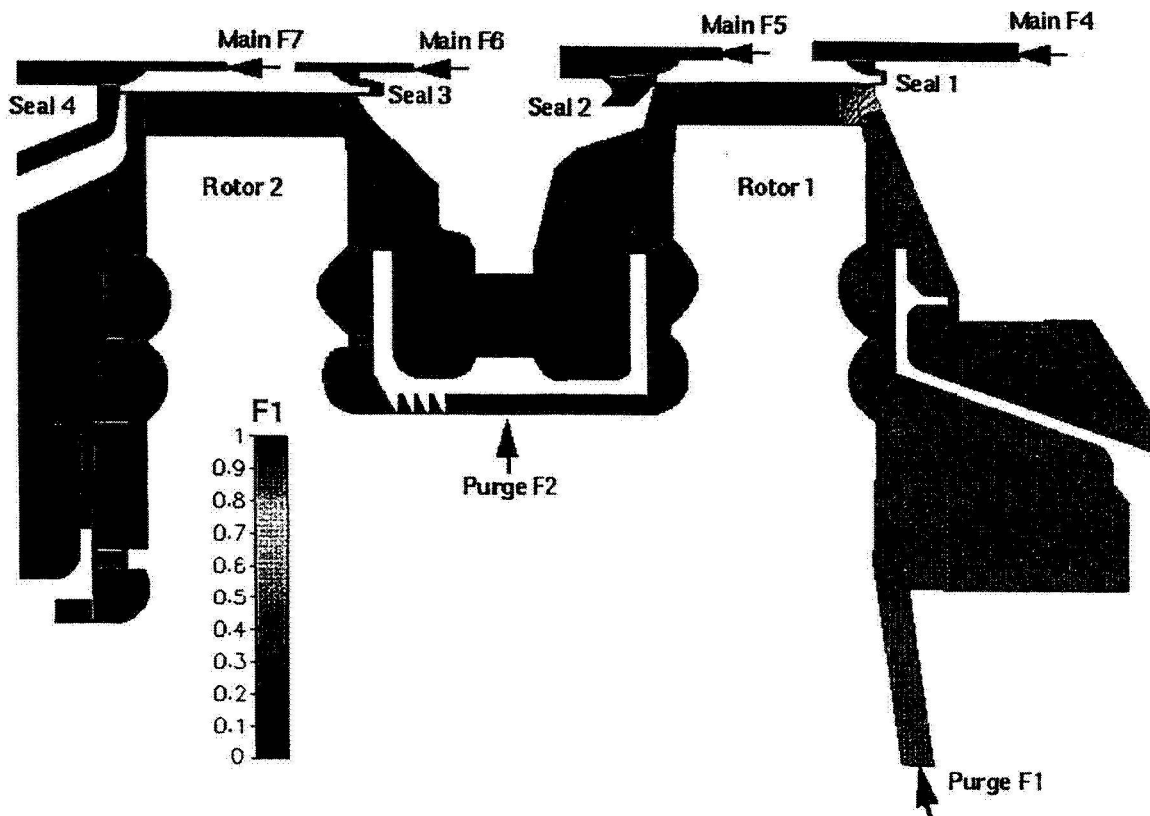


UTRC LARGE SCALE RIG - FLOW DOMAIN



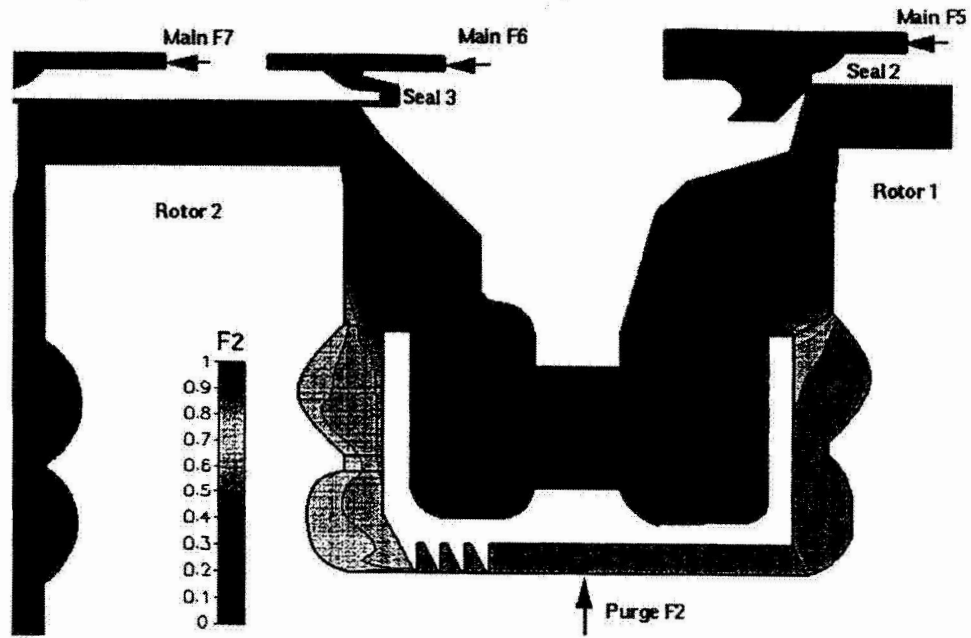
Mixture Fraction (Concentrations)

Computed Values of F1 Concentrations, Run No. 202



Mixture Fraction (Concentrations)

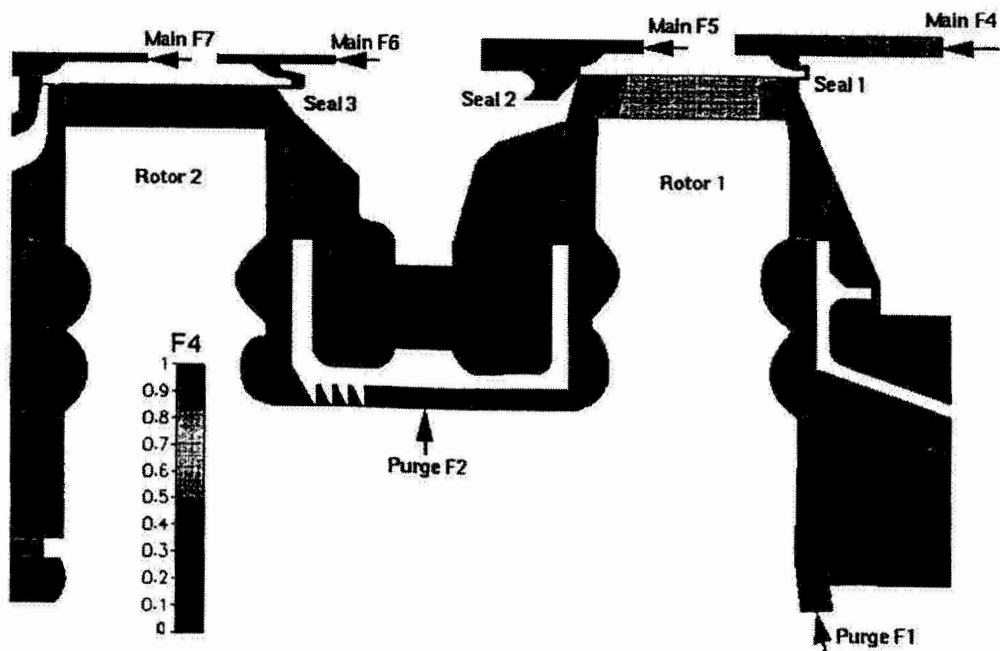
Computed Values of F2 Concentrations, Run No. 202



See color plate on page 345.

Mixture Fraction (Concentrations)

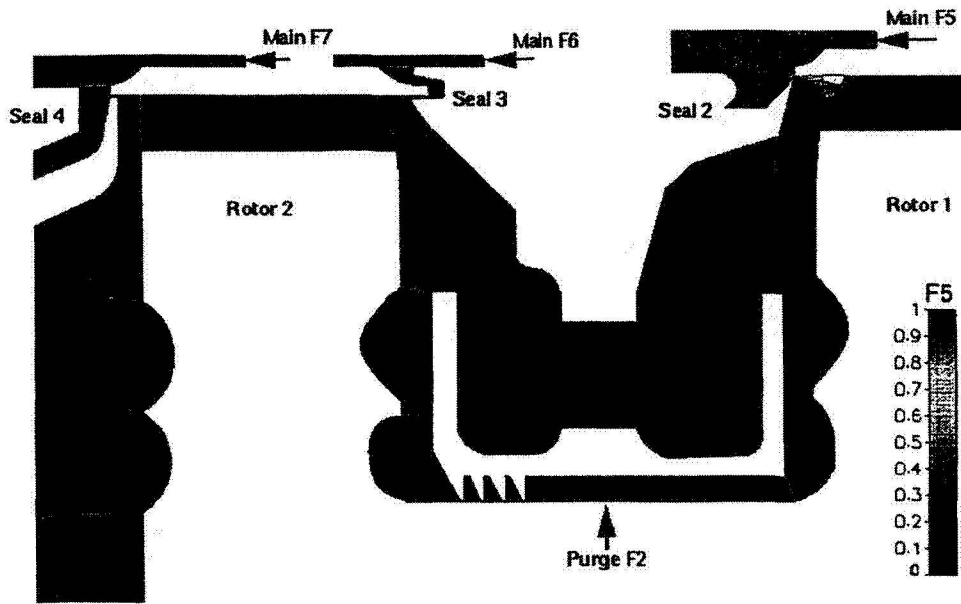
Computed Values of F4 Concentrations, Run No. 202



See color plate on page 346.

Mixture Fraction (Concentrations)

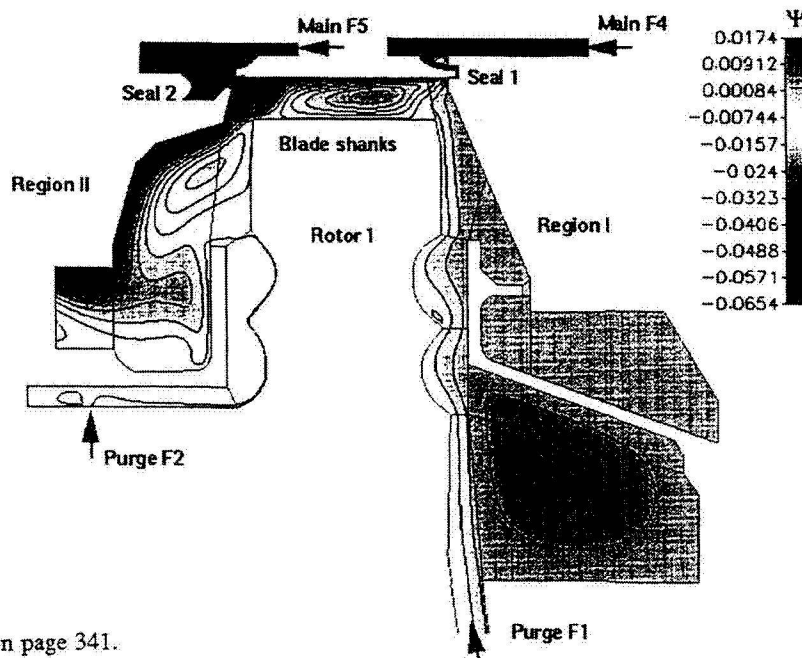
Computed Values of F5 Concentrations, Run No. 202



See color plate on page 347.

Streamfunction Plot

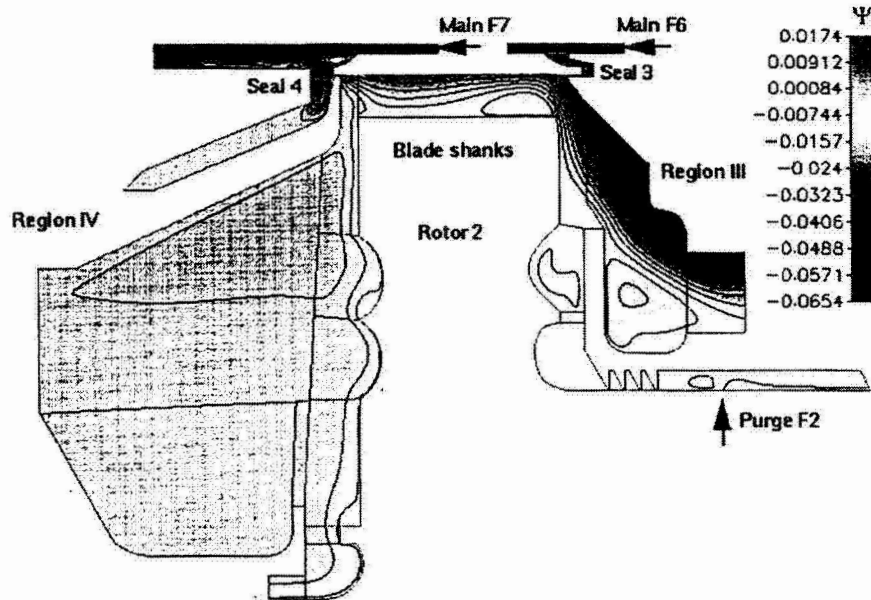
Regions I, II and Blade Shanks, Run No. 202



See color plate on page 341.

Streamfunction Plot

Regions III, IV and Blade Shanks, Run No. 202



See color plate on page 342.

CONCLUDING REMARKS

- **A 3D CFD Code, SCISEAL, Developed and Validated**
 - Capabilities Include Cylindrical Seals
 - Employed on Labyrinth Seals, Rim Seals, Disc Cavities
- **State-of-the-Art Numerical Methods**
 - Colocated Grids
 - High-Order Differencing
 - Turbulence Models, Wall Roughness
- **Multi-Domain Solution Methodology**
 - Efficient Solutions for Complicated Flow Geometries
 - entrance region & seal clearance
 - stepped and straight labyrinth seals
 - rim seals
 - face seals
 - conjugate heat transfer
 - passive scalar transport
 - 2D/3D problem treatment

CONCLUDING REMARKS (Cont.)

- **Seal Specific Capabilities**
 - **Rotor Loads, Torques, etc**
- **Rotordynamics Coefficient Calculations**
 - **Full CFD Based Solutions - Centered Seals**
 - **Small Perturbations Method - Eccentric Seals**
- **Extensive Validation Effort**

THERMOHYDRODYNAMIC ANALYSIS OF CRYOGENIC LIQUID TURBULENT
FLOW FLUID FILM BEARINGS

Luis San Andres
Mechanical Engineering Department
Texas A&M University
College Station, Texas

512-34
39454

Computational programs developed for the thermal analysis of tilting- and flexure-pad hybrid bearings, and the unsteady flow and transient response of a point mass rotor supported on fluid film bearings are described. The motion of a cryogenic liquid on the thin film annular region of a fluid film bearing is described by a set of mass and momentum conservation, and energy transport equations for the turbulent bulk-flow velocities and pressure, and accompanied by thermophysical state equations for evaluation of the fluid material properties. Zeroth-order equations describe the fluid flow field for a journal static equilibrium position, while first-order (linear) equations govern the fluid flow for small amplitude-journal center translational motions. Solution to the zeroth-order flow field equations provides the bearing flow rate, load capacity, drag torque and temperature rise. Solution to the first-order equations determines the rotordynamic force coefficients due to journal radial motions.

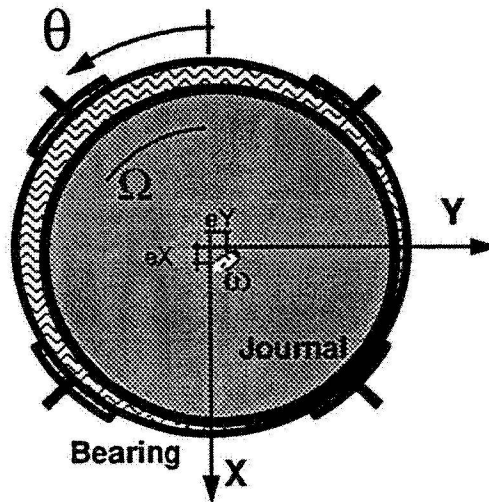
The hydroflect program calculates the static load and dynamic force coefficients for the following bearing geometries:

1. hydrostatic bearings with orifice compensation and rectangular recesses (single row or two-parallel recess row),
2. annular pressure seals (damper seals) (cylindrical and multilobe),
3. plain cylindrical hydrodynamic bearings (cylindrical and multilobe),
4. fixed arc hydrodynamic bearings with arbitrary preload,
5. tilting-pad journal bearings,
6. flexure-pad journal bearings (hydrostatic and hydrodynamic),
7. cylindrical pad bearings with a simple elastic matrix (ideal foil bearing).

Hydroflect includes the following thermal models:

- adiabatic surfaces, i.e. insulated journal and bearing surfaces.
- isothermal journal at specified temperature and insulated (adiabatic) bearing.
- isothermal bearing at specified temperature and insulated (adiabatic) journal.
- isothermal journal and bearing surfaces.
- isothermal journal and radial heat flow through bearing (stator).
- adiabatic journal and radial heat flow through bearing (stator).

Numerical computations and comparisons to experimental results from the open literature are detailed. The major features of the programs are also described. Some interesting results for herringbone journal bearings operating at large journal eccentricities are presented and the limitations of the Narrow Groove Theory are unveiled.



Computational programs developed for the thermal analysis of tilting- and flexure-pad hybrid bearings, and the unsteady flow and transient response of a point mass rotor supported on fluid film bearings are described. The motion of a cryogenic liquid on the thin film annular region of a fluid film bearing is described by a set of mass and momentum conservation, and energy transport equations for the turbulent bulk-flow velocities and pressure, and accompanied by thermophysical state equations for evaluation of the fluid material properties. Zeroth-order equations describe the fluid flow field for a journal static equilibrium position, while first-order (linear) equations govern the fluid flow for small amplitude-journal center translational motions. Solution to the zeroth-order flow field equations provides the bearing flow rate, load capacity, drag torque and temperature rise. Solution to the first-order equations determines the rotordynamic force coefficients due to journal radial (lateral) and angular motions.

The *hydroflect* program calculates the static load and dynamic force coefficients for various bearing and annular seal geometries of interest for operating conditions on the laminar, transition zone and turbulent flow regions. Numerical computations and comparisons to experimental results from the open literature are detailed. The major features of the programs are also described. Some interesting results for herringbone journal bearings operating at large journal eccentricities are presented and the limitations of the Narrow Groove Theory are unveiled.

Program name: ***hydroflex***

Date: January 1, 1995 (latest release), January 1, 1994 (original release)

Program Capability:

The ***hydroflex*** program calculates the static load and dynamic force coefficients for the following bearing geometries:

1. hydrostatic journal bearings with orifice compensation and rectangular recesses (single row or two-parallel recess row, cylindrical or pads),
2. annular pressure seals (damper seals),
3. plain hydrodynamic journal bearings (cylindrical and multilobe),
4. fixed arc hydrodynamic journal bearings with arbitrary preload,
5. tilting-pad journal bearings,
6. flexure-pivot tilting-pad journal bearings (hydrostatic and hydrodynamic),
7. pad journal bearings with a simple elastic matrix (ideal foil bearing).

hydroflex includes the following thermohydrodynamic models:

- adiabatic surfaces, i.e. insulated journal and bearing surfaces.
- isothermal journal at specified temperature and insulated (adiabatic) bearing.
- isothermal bearing at specified temperature and insulated (adiabatic) journal.
- isothermal journal and bearing surfaces.
- isothermal journal and radial heat flow through bearing (stator).
- adiabatic journal and radial heat flow through bearing (stator).

The extended computer program ***hydrotran*** embodies ***hydroflex***, and calculates the dynamic (transient) force response of a rigid rotor supported on fluid film bearings. The code calculates at each time step of numerical integration the unsteady bulk-flow field and the fluid film bearing forces due to prescribed time-varying external loads. The transient analysis is restricted to isothermal flows and rigid pad bearings.

***hydroflex* calculates**

- 1) bearing flowrate or seal leakage
- 2) friction torque, power dissipation and temperature rise
- 3) load capacity (fluid film forces and moments) if journal eccentricity is given, or journal equilibrium eccentricity components if the external loads are given.
- 4) 16 complex impedance coefficients due to dynamic journal center

displacements and journal axis rotations. The real and imaginary parts of the impedances correspond to the stiffness and damping coefficients evaluated at a specified excitation frequency. Inertia coefficients are also determined from evaluation of impedances at two whirl frequencies.

- 5) stability indicator or whirl frequency ratio for lateral journal motions and equivalent stiffness at operating speed.
- 6) pressure and temperature fields on the bearing surface, and density and viscosity field variations, within ranges of fluid flow Reynolds numbers and Mach numbers.

for

- 1) isothermal flow with barotropic fluid,
- 2) thermohydrodynamic adiabatic or radial heat flow and/or isothermal journal and bearing surfaces in the single phase flow regime.

with the following fluids:

- 1) liquid hydrogen, 2) liquid nitrogen,
- 3) liquid oxygen, 4) liquid methane,
- 5) water, 6) oil,
- 7) air , 8) barotropic liquid.

For cryogenic liquids, the fluid properties (density, viscosity and specific heat) are calculated with the miprops program from NBS Standard Database 12.

hydroflex handles the following boundary conditions at the bearing exit planes:

- 1) periodic pressure asymmetry in the axial direction.
- 2) local discharge end seal effects via an orifice like model to simulate wear-ring hydrostatic bearings or annular seals.
- 3) inlet specified circumferential pre-swirl velocity distribution.

The axial clearance functions included are of the type:

- a) uniform, b) tapered,
- c) stepped, or, d) arbitrary via spline interpolation.

Cylindrical bearings can be specified as multi-lobe geometries, and bearing pads can have a specified assembly preload.

For tilting-pads and flexure-pad bearings, pad mass moment of inertia and flexure rotational stiffness and damping coefficientc are needed for full specification of the bearing geometry.

Method:

The motion of a fluid on the thin film annular region of a fluid film bearing is described by a set of mass and momentum conservation, and energy transport equations for the turbulent bulk-flow velocities and pressure, and accompanied by thermophysical state equations for evaluation of the fluid material properties. Zeroth-order equations describe the fluid flow field for a journal static equilibrium position, while first-order (linear) equations govern the fluid flow for small amplitude journal center translational motions and journal axis angular motions. Solution to the zeroth-order flow field equations provides the bearing flow rate, load capacity, drag torque and temperature rise. Solution to the first-order equations determines the rotordynamic force coefficients due to journal lateral and angular motions.

Features:

Fully Developed, Laminar and/or Turbulent Bulk-Flow Model
Liquid of Variable properties, functions of pressure and temperature with realistic thermophysical equations of state.

Governing Equations:

Mass conservation equation,

Bulk-Flow Momentum equations in circumferential and axial directions

Energy Transport equation for Mean Flow Temperature with radial heat flow through the bearing sleeve and adiabatic journal (shaft).

Turbulence Closure Model: Bulk-Flow with friction parameters based on Moody's friction factor equations for roughened surface conditions.

Numerical method of solution: Control volume – finite difference (SIMPLEC) method.

Limitations and Restrictions: Does not include elastic deformations due to thermal effects.

Documentation:

- Complete technical report (185 pp.)
- Tutorial and User's Manual (60 pp.)
- Examples Manual (app. 250 pp.) : Test cases and output.
- On-line HELP available while running program in interactive mode.

Input:

- keyboard input – menu driven with error checking.
- data files created by program

Output:

- monitor (screen) and ASCII data files
- dump files store all information on running session
- field data files for plotting pressure, film thickness and temperature as $Z=Z(X,Y)$ surfaces.

Language: FORTRAN77. Source code provided.

Hardware: programs developed for standard fortran in workstations and VAX computers. PC version (486 or higher recommended) will soon be available.

Users: NASA Research Centers and contractors, Pratt & Whitney, Rockwell International, and U.S. Air Force – Phillips Laboratories.

Developers: Texas A&M Tribology Group – Turbomachinery Laboratory
Mechanical Engineering Department
Texas A&M University
College Station, TX 77843–3123
phone: (409) 845–0160, fax : (409) 845–1835
e–mail: andres@epbiris.tamu.edu

Available to U.S. companies from the Texas A&M University System
Technology Licensing Office.
Texas A&M University
College Station, TX 77843–3123
phone: (409) 847–8682, fax : (409) 845–1402

Sponsors of Development:

NASA Lewis Research Center, Pratt and Whitney
Rockwell International, TAMU Turbomachinery Research Consortium

Other Programs: Earlier versions of thermohydrodynamic program include:

hydrosealt : hydrostatic bearings and annular seals (1994),

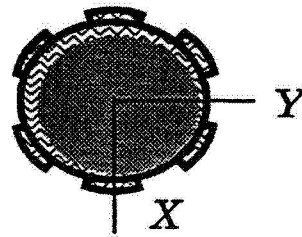
hsealt: annular seals (1992),

hydrobeart: hydrostatic bearings (1992)

same codes without (t) extension handle isothermal fluid film bearings.

hydroflex

Bulk-Flow Code
for Process Fluid Bearings



Hydrostatic bearings
Damper seals / Annular seals
Cylindrical pad journal bearings

Tilting pad journal bearings
Flexure pad hybrid bearings

*Unsteady flow and forced bearing
response to transient
forces (shocks and periodic loading)*

hydrotran

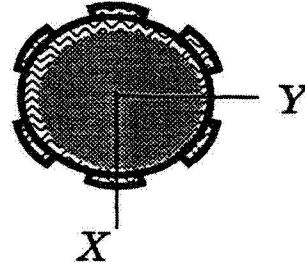
for
Cryogenics: LH₂, LO₂, LN₂, CH₄
Water Oils Perfect Gas
or Fluid $\rho, \mu = f's (P, T)$

Laminar, transition & turbulent flows
Arbitrary clearance function
Single phase, subsonic flow
Arbitrary rotor position

32 force impedance coefficients ($K+iwC$)

Simple compliance bearing structure

Reynolds Numbers in Cryogenic Fluid Film Bearings.



*Cryogenic Liquids have very low viscosity
Rotor Speeds as high as 35,000 cpm
Pressure Differential as large as 5,000 psi
Bearing geometries of $R/c = 1000$ approx.
and intentionally rough bearing surfaces.*

$Re_c = \rho \Omega R c / \mu$: Shear Flow Reynolds # due to journal rotation.

$Re_p = m / 2\pi D \mu$: Pressure Flow Reynolds # due to axial flow.

$Re_s = \rho \Omega c / \mu$: Squeeze film flow or Advection flow Reynolds #.

$M = V_{fluid} / V_{sound}$: Mach Number.

TYPICAL VALUES (HJBs):

	Re_c	Re_p	Re_s	M
LO2	126,189	55,112	201.00	0.10
LH2	51,178	186,000	84.12	0.3-0.6
LN2	96,904	58,276	154.3	0.08

Classical Lubrication Analysis is not Valid !

***Fluid Inertia and Turbulence need to be
accounted as well as actual fluid properties.***

Analytical Turbulent Bulk-Flow Model for Variable Properties, Fluid Film Bearings:

*Fully Developed Flow,
Single-Phase liquid,
Local friction factors
as turbulence descriptors,
Liquid of Variable Props:
state equations for material
properties $f(P,T)$*



*Hirs, Moody, Colebrook
friction factors formulation
for surface roughness
characterization.*



NBS code for LH2, LOX props.

Mass conservation:

$$\delta(\rho H U_i) / \delta x_i + \delta(\rho H) / \delta t = 0$$



Momentum conservation: *circumferential(X_1) and axial(X_2)*

$$-H \delta P / \delta x_i = \mu \{ \kappa_i U_i - \kappa_j V_j \} / H + D(\rho \cdot H \cdot U_i) / Dt \quad i=1,2$$

Energy Transport:

$$C_p D(\rho \cdot H \cdot T) / Dt + D(\rho \cdot H \cdot s) / Dt = -Q_s + H \cdot \beta \cdot T \cdot DP / Dt + R \cdot \Omega \cdot \tau_{1z}$$

where (U_1, U_2, P, T) fluid velocities, pressure and temperature, and,

$D() / Dt = \delta() / \delta t + U_1 \delta() / \delta X_1 + U_2 \delta() / \delta X_2$ is the material derivative.

s : fluid speed, Q_s =heat to journal and bearing, $V_1 = \Omega \cdot R, V_2 = 0$

τ_{1z} is journal surface shear stress, Ω : rotational speed.

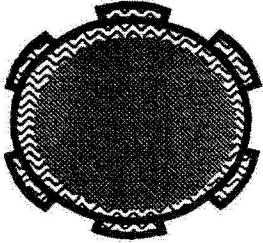
β : volumetric expansion coefficient, κ_i, κ_j : turbulent shear factors.

hydrosealt & hydroflex: Capabilities

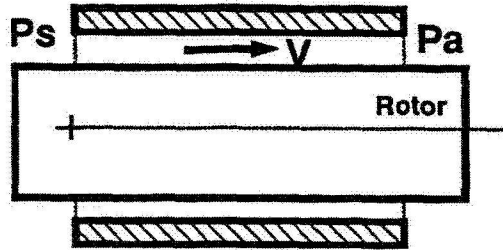
Code Capabilities		<i>hydrosealt</i> 93	<i>hydroflex</i> 94
cylindrical (360deg) hydrostatic JB	✓		
annular seals	✓		
cylindrical pad journal bearing	✓		TILTING PADS
hydrostatic bearing pads	✓	RIGID	FLEXURE PADS
cryogenic liquid	✓		
asymmetric bearing: axial direction	✓		
Isothermal-barotropic	✓		
Thermal effects—energy equation	✓	Adiabatic	Radial Heat Flow
force coefficients #:	✓	48	32 ($K+i\omega C$)
compliant bearing surface			✓
asymmetric sump pressures	✓	via Fourier Series	
misaligned journal		✓	
rectangular recesses		Position and area user defined	
Laminar Flow Turbulent flow	✓		transition regime
Works for conventional lubricants	✓	Air, Water, Oil	
Force Response to Transient Loads			✓ <i>hydrotran</i>

hydroflex: geometries of bearings & seals

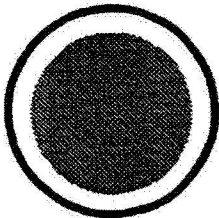
Fixed Geometry:



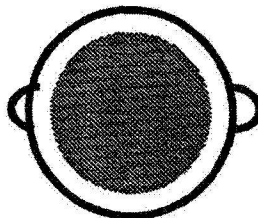
hydrostatic bearing
360deg or pads



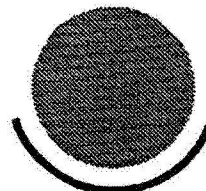
annular pressure seal



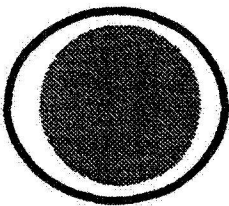
Plain JB



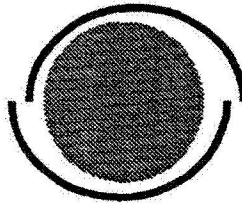
JB with axial grooves



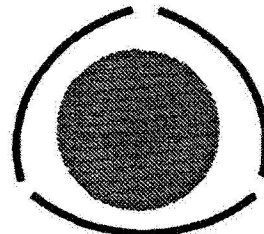
Partial arc JB



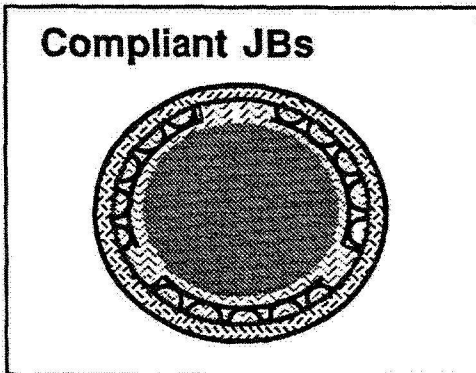
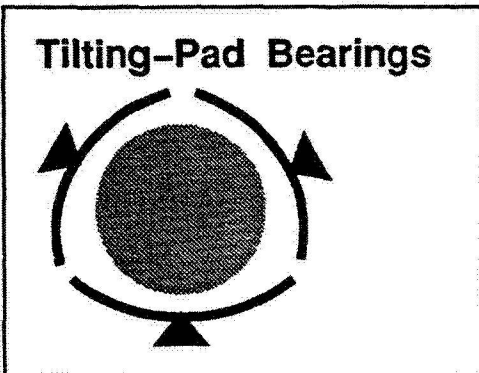
Elliptic JB



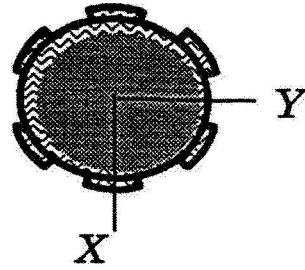
2 lobe JB
w or w/o offset



3 lob JB w or w/o
offset



Comparisons of *hydro* codes with experimental results



○ **Hydrostatic Bearings:**

- LO₂ HJBs : Redeclyff and Vohr (1969)
- LH₂ HJBs : Butner and Murply (1986)
- H₂O HJB: Chaomleffel and Nicholas (1988)
- H₂O HJBs: Childs et al. (1988–1994), 36 test cases.
- Oil HJB: Adams et al. (1992) – laminar flow

○ **Annular Pressure Seals:**

- H₂O, conv-div, Childs and Lindsey (1993)
- H₂O, Kanki and Kawakami (1984)
- air, Childs, Yang and Alexander (1994)

○ **Journal Bearings (oil):**

- Tonnesen and Hansen (1981) axially grooved
- Robison and San Andres (1995) plain cylindrical
- GAS DiMotte (1994) cylindrical

○ **Tilting Pad Bearings (oil):**

- Static Taniguchi et al. (1990)
- Static Ha et al. (1994) – turbulent
- Dynamic Someya (1988)

○ **Flexure Pad Bearings (oil):**

- Static Walton and San Andres (1995)
- Hydrostatic Childs (planned 4 q /1995)

Users of *hydrosealt*, *hydroflex* and *hydrotran* codes:

- NASA Lewis Research Center

NASA Marshall Space Flight Center
and contractors (Sverdrup, SRS)

USAF Phillips Laboratory

- Rocketdyne Division, Rockwell Int.

Pratt and Whitney, United Technologies.

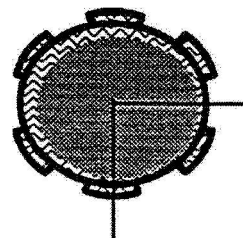
- Texas A&M Turbomachinery Laboratory

TAMU Turbomachinery Research Consortium
(US members)

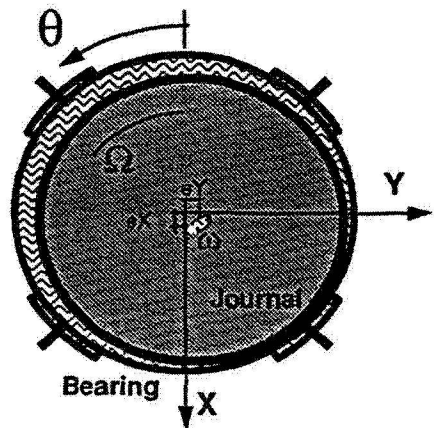
Texas A&M Technology Licensing Office licenses the codes to U.S. companies at nominal cost.

Funding for development:

Rockwell Int., 1989–91
Pratt&Whitney, 1992
NASA LeRC, 1993–95



***Fixes to improve
Dynamic Stability
in HJBs.***



Pneumatic Hammer

- a) *Limit recess axial length
reduce recess volume*
- b) *Use end seal restrictors or wear rings.*
- c) *Change type of fluid inlet restriction, i.e.
inherent compensation.*

Hydrodynamic Instability

- a) *Use rough bearing surface* TEST-OK
- b) *Fluid injection against shaft rotation* TEST-OK
- c) *Introduce bearing asymmetry* TEST-OK
- d) *Use flexible pad bearing geometry, i.e.
flexure pivot- tilting pad bearings* TESTs
PLANNED

At low frequencies avoid HAMMER EFFECTS by keeping recess volumes small and limit maximum supply pressure so that

$$(P_r - P_a) \beta_p \ll 1.00$$

where $\beta_p = (1/\rho)(\delta\rho/\delta P)$ is the liquid compressibility coefficient

***Reduced load capacity and direct stiffness
are to be trade off for dynamic stability***

Flexure Pivot Tilting Pad Hydrostatic Bearing

Advantages *over conventional tilting pad bearings.*

No pad flutter.

No wear of pivot.

No stack-up of manufacturing tolerances.

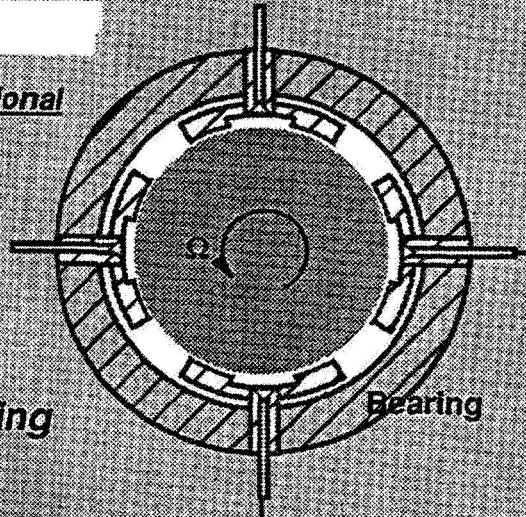
No leakage and lubrication problems at ball-socket joint.

No hydrostatic pad-rotor "grabbing" effect.

Control of cross-coupled stiffness coefficients.

Tolerance of rotor axial misalignment.

Accuracy of machining with CNC milling and wire-EDM manufacturing.



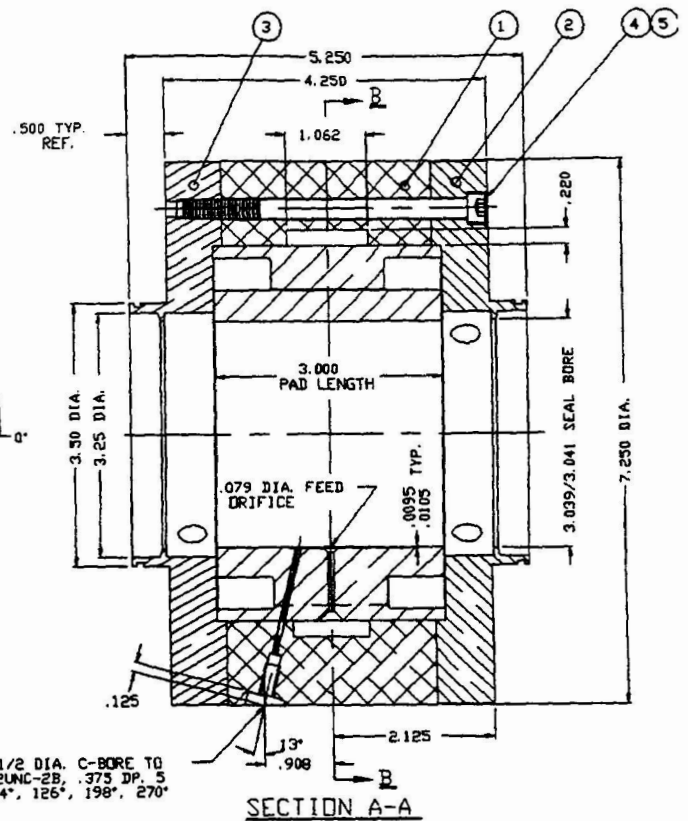
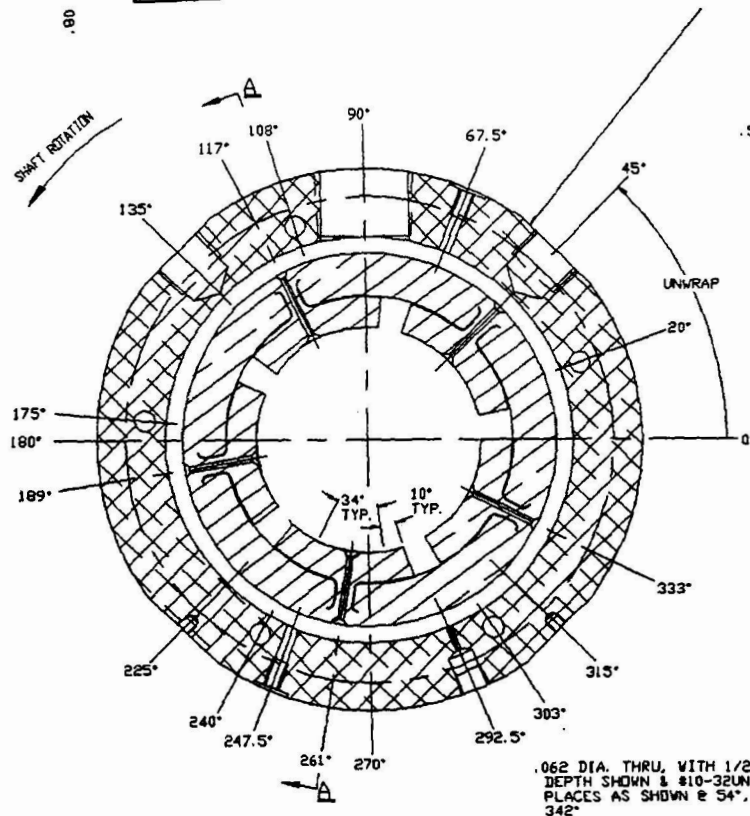
Major advantage of tilt-pad and flexure-pad bearings over fixed geometry bearings:

No restriction for hydrodynamic stability.

**Flexure-Pivot, Tilting Pad
Hydrostatic Journal Bearing (KMC, Inc.)**

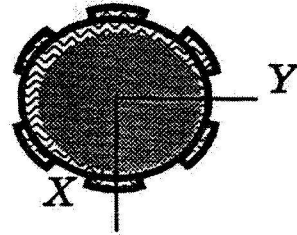
Dynamic tests in water planned for 12/95.

Objective: Reduce WFR for high speed operation.



.062 DIA. THRU, WITH 1/2 DIA. C-BORE TO DEPTH SHOWN & #10-32UNC-2B, .375 DP, 5 PLACES AS SHOWN @ 54°, 126°, 198°, 270° 342°

Advances 1995: Modeling of Bearings for Process Liquid Applications



Damper Seals:

*Thermohydrodynamics
of Two-Phase Flows*

*Liquid boiling occurs due to
thermal effects in damper
seals with low exit pressures*

*Hydrodynamics of
Sonic Flow Operation*

*LH2 fluid bearings may
operate at Mach \rightarrow 1.00
Compressibility is an issue*

Hydrostatic Bearings:

*Liquid injection opposite
to journal rotation*

*Experimental results
are favorable. How to modify
bulk flow model ?*

Foil Bearings

*Models are qualitative and highly approximate.
Demonstrated too low load capacity for primary
power.
Will there ever be parameter identification
tests?*

THE ACOUSTIC INFLUENCE OF CELL DEPTH ON THE ROTORDYNAMIC
CHARACTERISTICS OF SMOOTH-ROTOR/HONEYCOMB-STATOR
ANNULAR GAS SEALS

Dara W. Childs
Mechanical Engineering Department
Texas A&M University
College Station, Texas

513-34
ABS ONLY
39455

A two-control volume is employed for honeycomb-stator/smooth-rotor seals, with a conventional control-volume used for the through flow and a "capacitance - accumulator" model for the honeycomb cells. The control volume for the honeycomb cells is shown to cause a dramatic reduction in the effective acoustic velocity of the main flow, dropping the lowest acoustic frequency into the frequency range of interest for rotordynamics. In these circumstances, the impedance functions for the seals can not be modeled with conventional (frequency-independent) stiffness, damping, and mass coefficients. More general transfer functions are required to account for the reaction forces, and calculated here as a lead-lag term for the direct force function and a lag term for the cross-coupled function. These first order functions are simple compared to transfer functions for magnetic bearings or foundations. For synchronous response to imbalance, they can be approximated by running-speed-dependent stiffness and damping coefficients in conventional rotordynamic codes. Correct predictions for stability and transient response will require more general algorithms, presumably using a state-space format.

WALL SHEAR STRESS, WALL PRESSURE AND NEAR WALL VELOCITY FIELD RELATIONSHIPS IN A WHIRLING ANNULAR SEAL

Gerald L. Morrison, Robert B. Winslow, and H. Davis Thames III
Turbomachinery Laboratory
Texas A&M University
College Station, Texas

514-34
39456

ABSTRACT

The mean and phase averaged pressure and wall shear stress distributions were measured on the stator wall of a 50% eccentric annular seal which was whirling in a circular orbit at the same speed as the shaft rotation. The shear stresses were measured using flush mounted hot-film probes. Four different operating conditions were considered consisting of Reynolds numbers of 12,000 and 24,000 and Taylor numbers of 3,300 and 6,600. At each of the operating conditions the axial distribution (from $Z/L = -0.2$ to 1.2) of the mean pressure, shear stress magnitude, and shear stress direction on the stator wall were measured. Also measured were the phase averaged pressure and shear stress. These data were combined to calculate the force distributions along the seal length. Integration of the force distributions result in the net forces and moments generated by the pressure and shear stresses. The flow field inside the seal operating at a Reynolds number of 24,000 and a Taylor number of 6,600 has been measured using a 3-D laser Doppler anemometer system. Phase averaged wall pressure and wall shear stress are presented along with phase averaged mean velocity and turbulence kinetic energy distributions located 0.16c from the stator wall where c is the seal clearance. The relationships between the velocity, turbulence, wall pressure and wall shear stress are very complex and do not follow simple bulk flow predictions.

NOMENCLATURE

c	Nominal clearance between rotor and stator, 1.27 mm
D	Rotor diameter, 163 mm
e	Rotor eccentricity ratio
$F_{R,XY}^*$	Radial resultant force, $F/LD\Delta P$
$F_{R,Z}^*$	Axial resultant force
$F_{R,\phi}^*$	Azimuthal resultant force
L	Rotor length, 35.6 mm
$M_{R,XY}^*$	Resultant moment about radial line, $M/LD^2\Delta P$
$M_{R,Z}^*$	Resultant moment about axial line
P	Pressure
P^*	Nondimensional Pressure, $PL/c\Delta P$
P_{mean}	Time averaged pressure
P_{mean}^*	Nondimensional Mean Pressure $(P_{mean} - P_{Z/L=1.00})/\Delta P$
r	Distance above centered rotor surface
Re	Reynolds number = $2\rho U_{mean} c/\mu$
T	Wall shear stress
T^*	Nondimensional Stress, $Tc/\mu W_{sh}$
T_{mean}^*	Time averaged nondimensionalized shear stress, $T_{mean} c/\mu W_{sh}$
Ta	Taylor number = $(\rho W_{sh} c/\mu)(2c/D)^{1/2}$
U	Mean axial velocity
U^*	Nondimensional mean axial velocity, U/U_m
U_m	Average mean axial velocity, $Q/\pi Dc$, 7.4 m/s
uu	Axial velocity variance
V	Mean radial velocity
V^*	Nondimensional mean radial velocity, V/U_m

vv	Radial velocity variance
W	Mean azimuthal velocity
W^*	Nondimensional mean azimuthal velocity, W/W_{sh}
W_{sh}	Rotor surface velocity
ww	Azimuthal velocity variance
Z	Axial distance downstream of the seal entrance
ΔP	Pressure drop from seal entrance to exit
θ	Shear stress direction, $0^\circ =$ downstream direction, $90^\circ =$ direction of rotor rotation
κ	Turbulence kinetic energy, $(uu+vv+ww)/2$
κ^*	Nondimensional turbulence kinetic energy, κ/U_m^2
μ	Absolute viscosity, 7.84×10^{-4} kg/m-s
ρ	Density, 999 kg/m ³
$\Phi_{R,M}$	Direction of resultant axial moment
$\Phi_{R,MXY}$	Direction of resultant radial moment
$\Phi_{R,XY}$	Direction of radial force
<>	Phase averaged quantity

INTRODUCTION

Noncontacting seals for rotating components in turbomachines can only minimize leakage from high to low pressure regions; they can not prevent it. This is inherently so due to the seal clearances between the rotating and stationary components that comprise them. Two such seals commonly used in turbomachines today are the labyrinth and annular seals.

Labyrinth seals can produce less leakage than annular seals for a given clearance and length, thereby, providing higher efficiencies. However, the higher leakage rates in annular seals can be desirable for they result in more damping and hence increased rotordynamic stability (Allaire et al., 1978). Annular seals are geometrically similar to plain journal bearings but present a different flow structure dominated by turbulence, fluid inertia effects and large axial flows. In fact, there is great potential for them to be used as support elements in high speed cryogenic turbopumps (Van Pragenau, 1990). Consequently, it is of great interest to learn more about these seals.

A simple annular seal consists of a smooth shaft rotating concentrically inside a stationary, smooth cylinder. Typically, however, annular seal applications are much more complex. For example, seal surface finishes may be hydraulically smooth but have high relative roughnesses compared to the small clearances present. Built in misalignments and/or misalignments resulting from dynamic or static loading during operation can cause a shaft to rotate eccentrically inside its housing (Chen and Jackson, 1987). The destabilizing forces that cause the eccentricity can lead to a phenomenon called whirl in which the rotor center precesses around the center of the stator.

Due to these flow field complexities the importance of having a solid understanding of both the fluid mechanics and rotordynamics of annular seals becomes apparent. Especially since they affect seal performance and, therefore, the efficiency and reliability of the turbomachinery in which they are installed. Much

of the previous work on these seals has focussed primarily on rotordynamic effects. In recent years Morrison, et al. (1994) have performed measurements on the velocity field and turbulence characteristics in the clearance of a whirling annular seal. They completed an extensive 3-D laser Doppler anemometer investigation of the flow field inside an annular seal with a whirl ratio of 1.00 and an eccentricity ratio of 0.50. They ran two Reynolds Number conditions (12,000 and 24,000) with a Taylor Number of 6,600. Prominent features found include: a peak axial velocity that begins in the suction side of the seal at the inlet and rotates around to the pressure side of the seal at the exit; a vena contracta on the suction side of the rotor; a highly 3-dimensional flow with large radial velocities near the inlet of the seal (made evident by recirculation zones at the inlet); and, no significant increase in tangential velocity with whirling motion when compared to statically eccentric seals. In order to further characterize these clearance flows it is necessary to investigate the hydrodynamic wall pressures and shear stresses on the stator wall that surrounds the seal.

The purpose of this study is to experimentally determine mean and phase averaged characteristics of both the pressure and shear stress along the stator wall of an annular seal using piezoresistive pressure transducers and hot-film anemometers respectively. This data will complement the existing flow field data of Thames, (1992) and Morrison, et al., (1994) while providing the boundary conditions necessary to develop more accurate Computational Fluid Dynamics (CFD) models and bulk flow models used for predicting annular seal flow fields. The further development of these models are necessary so they can be used to design new turbomachines with improved leakage characteristics based upon better understanding of rotordynamic stability.

FACILITIES

The experimental facility used for this investigation is comprised of a water storage and supply system, the seal rig test section for modelling the annular seal environment, and the piezoresistive pressure and hot-film anemometry instrumentation. These flow facilities have been previously described by Morrison, et al. (1994).

Water is pumped to the test rig from a 10 m³ tank at a flow rate of 2.43 and 4.86 l/s and at a constant inlet pressure of 138 kPa resulting in an axial Reynolds numbers of 12,000 and 24,000. The flow rate and pressure are controlled by ball and gate valves both upstream and downstream of the rig. Flow rates are monitored by a turbine flow meter. A 70 kW rated heat exchanger connected to the supply pump by-pass line provides cooling of the working fluid to maintain the operating temperature window of 30 ± 4°C. All water supplied to the test rig is filtered by a 10 micron filter bank near the discharge of the supply pump.

Figure 1 is a schematic of the seal rig that simulates the seal environment and where the pressure and shear stress measurements are made. The test section is a stainless steel design which comprises two main parts. The first is the inlet where a stainless steel plate with 3.2 mm holes, and a fine nylon mesh are held. These pieces straighten and further filter the flow before it reaches the plenum in front of the seal. The second main part of the test section is where the stator and rotor are mounted. The rotor (D=0.163m) is mounted on an overhung shaft that is driven by an electric motor controlled by a variable frequency drive operated at 1,800 and 3,600 rpm for this test case resulting in a Taylor numbers of 3,300 and 6,600. The clearance between the rotor and stator has a nominal value of 1.27 mm (0.050 in.) and the rotor has a length of 35.6 mm. The seal is mounted on a brass bushing that has been

machined to provide an eccentricity ratio of 50%. This results in the rotor whirling in a circular orbit at the same speed as the shaft rotation.

Brass instrument supports have been machined to fit into the optical window opening of the rig which is normally used for laser Doppler anemometer measurements. Four blocks were drilled and tapped to house the pressure transducers (Figure 2), and four similar blocks were fabricated to hold the shear stress probes. These blocks provide several axial measurement locations from approximately six clearances upstream to five clearances downstream of the seal resulting in axial distributions of the wall pressures and shear stresses. Figures 3-5 illustrate the measurement grids used for the pressure, shear stress, and velocity measurements. The block measurement surfaces were machined to fit flush with the stator wall so as not to disturb the flow.

Olivero-Bally et al. (1993) measured wall pressure fluctuations in turbulent boundary layers. They studied noise cancellation techniques and used pinhole mounted transducers to improve the spatial resolution of the wall pressure data in the low and high frequency range respectively. Pressure measurements were made in both air and water with piezoresistive transducers. In order to minimize spatial averaging effects, the transducers were mounted in plexiglass housings with 0.3 mm diameter flush mounted pinholes. Their study indicated that by placing flush mount pressure transducers behind a small pinhole the spatial resolution can be increased without degrading the frequency response characteristics over certain frequency ranges. This technique was used in the present study using mounting blocks as shown in Figure 2. Kulite flush mount piezoresistive transducers were mounted in the blocks. The large cavity ended 1 mm from the block surface and a 0.40 mm diameter hole was drilled through. The assembly was mounted in the test section and the pressure transducers loosened in their mounts in order to purge any air from the cavity. This assured adequate frequency response (1 kHz) for the present study.

The mean pressures were measured with both a ScaniValve system and by recording the DC voltages from the Kulite transducers mounted in the brass blocks. Both gave the same results. The pressure transducers were calibrated each day *in situ* by connecting a pneumatic dead weight tester to the test section and pressurizing the test section with known pressures. The calibrations obtained were repeatable from day to day. Uncertainties on the pressure measurements are 1.5 kPa.

Hanratty and Campbell (1983) completed an extensive review of wall shear stress measurement techniques including the hot-film probe. According to the authors, the positioning of the probe relative to the wall is one of the greatest sources of error in using heated films. Pessoni (1974) found that the displacement of a commercial probe from the test section surface by 0.1 mm in a 2.5 cm air tunnel resulted in 30 to 40% deviations in the calibrations. Pessoni suggests either calibrating the probe *in situ* or in a plug of larger area and transferring the entire plug to the test section as was done in this study.

The hot-film probes used in this study (TSI 1237W) consist of a 3 mm diameter rod with the end cut off square. On this end the sensing element (a small rectangular film) is mounted. This rod is mounted in the brass blocks so that the end of the rod is flush with the block surface. The probes were calibrated in a facility consisting of two parallel smooth plates which allows calibration of the probes while seated in the brass blocks. Pressure taps on the back side of the calibrator are used to measure the axial pressure distribution which verifies that dP/dX is constant indicating that the flow between the plates is fully developed. The mean shear stress

on the wall is calculated in a channel of height h for a pressure drop ΔP along length L as follows (Haritonidis, 1989):

$$\bar{\tau}_w = \frac{\Delta P h}{L 2}$$

A Rapid Systems A/D converter possessing 4 channels, each with 8 bit resolution was used to measure the AC component of the hot-film and pressure transducer signals at a sampling rate of 2,000 samples/second with a low-pass filter of 1,000 Hz. The external trigger was connected to an electronic proximator probe situated at the keyway of the main seal/rotor shaft between the electric motor and the overhung shaft on which the seal is mounted. Thirty-two averages were necessary for the current study to obtain repeatable phase averaged results. The DC value of the signal was measured using an analog voltmeter.

Determination of the shear stress was complex since the shear stress calibration was highly non-linear. The fluctuating voltages could not be multiplied by a constant to obtain τ_w as they were for the pressure conversions. Rather, the instantaneous voltages were added to the mean voltages and then converted to the total instantaneous shear stress using the calibration curve. The mean shear stress was then calculated and subtracted from the total instantaneous shear stress to give the fluctuating shear stress component. Root-mean-squared (rms) values were calculated using these fluctuating values and an averaging scheme was also implemented to determine the phased average shear stresses and phase averaged rms values.

The flush mount hot-film probes used in this study had a rectangular sensing area which made them sensitive to the direction of the shear stress much in the same way a single hot wire is sensitive to the velocity direction. To record the shear stress direction the probes were rotated, within specially designed probe mounts which kept them flush, to find a minimum in voltage. When the long side of the hot-film is aligned with the mean shear stress vector a minimum in heat transfer from the film occurs (Ludwig, 1950). Hence, by slowly rotating the film in the flow, a minimum in voltage is noticeable. To isolate this direction with reasonable accuracy, the probe was rotated to an identical larger voltage on each side of the minimum voltage. The angles for these two voltages were then bisected to determine the minimum voltage angle. The probe was turned to this angle before the data acquisition was initiated. Uncertainties on the shear stress measurements are 10% on the magnitude and 5° on the direction.

The flow field measurements presented in this paper were extracted from the data measured by Thames (1992) of which part was presented in Morrison, et al.(1994). Descriptions of the laser anemometer system are included in those publications along with uncertainty estimates. Those uncertainties are ± 0.001 for $\langle \kappa^* \rangle$ and 0.015, 0.058, and 0.013 for $\langle U^* \rangle$, $\langle V^* \rangle$, and $\langle W^* \rangle$ respectively.

All of the data presented have been non-dimensionalized. The mean pressures were non-dimensionalized by the pressure drop from just at the seal entrance to the exit plane of the seal (values given in Table I). This was selected based upon various seal performance data available which non-dimensionalize well using this parameter. The fluctuating pressures were non-dimensionalized by $c\Delta P/L$. The shear stresses were non-dimensionalized by $\mu W_{sl}/c$ based upon Stokes law of friction:

$$\tau = \mu \left[\frac{\partial U}{\partial y} + \frac{\partial V}{\partial x} \right]$$

where the velocity gradients are represented by W_{sl}/c . These non-

dimensionalization values produce non-dimensional fluctuating pressures and shear stresses with comparable amplitudes. However, as shown in Table I, the non-dimensional pressures and shear stresses differ in dimensional value by the first being approximately two orders of magnitude larger. The mean velocities and κ were nondimensionalized by using the bulk flow velocity, U_m (7.4 m/s) except for the azimuthal velocity which was nondimensionalized by W_{sh} (30.9 m/s). Further information about the test facility, measurement procedure, and data availability on MS-DOS disks and hardcopy format are available in Thames (1992), Winslow (1994) and from G.L. Morrison.

RESULTS

The magnitude and direction of the mean wall shear stress along the length of the stator are shown in Figures 6 and 7 respectively. The shear stress magnitude plot shows at least an eight fold rise in T_m^* just inside the seal. This is followed by a less rapid decay to a value of about half the maximum by $Z/L=0.2$. This rapid rise and fall in shear stress is due to a *vena contracta* present on the seal rotor near the entrance (Morrison, et al.(1994)) which forces the fluid through a very small clearance which then increases downstream of the *vena contracta*. In addition, the rotor is accelerating the fluid tangentially, thus producing a very large wall shear stress at the entrance to the seal followed by the decrease as the cross-sectional region available for flow increases. From $Z/L=0.2$ to 0.7 the shear stress remains relatively constant with a trend towards increasing caused by the tangential velocity increasing due to the rotor's viscous drag. The exception to this is for the high Reynolds number, low Taylor number case where the shear stress actually decreases in this region. This is due to the flow becoming more fully developed in the axial direction which decreases the wall shear stress and the lack of rotor speed to generate an offsetting increase in wall shear stress by imparting larger tangential velocities to the fluid. At the exit the wall shear stress increases to values equal to the maximum inlet shear stress.

Figure 7 shows that the direction of the shear stress is strongly dependent upon the Reynolds and Taylor numbers and their ratio. This plot also indicates regions just before the entrance plane ($Z/L < 0.0$) the shear stress, is in the upstream direction, marked by Θ angles greater than 90° for all cases except the one with the largest Re/Ta ratio (7.3). (Recall that 90° represents the rotor direction, and 0° represents the downstream or axial direction.) Although it is not known exactly why there is a small degree of backflow indicated by the inlet plenum shear stress directions, research by Morrison et al.(1994) may suggest that a backward flowing region is created upstream of the seal when the radially accelerating flow is blocked from entering the clearance by large axial and azimuthal flows, and is thus deflected by the stator in the upstream direction.

For the largest Re/Ta ratio, 24,000/3,300, the axial momentum is much larger than the tangential momentum, hence, the shear stress is oriented primarily in the downstream direction. There is a slight increase in Θ as the flow progresses through the seal due to the increase in tangential momentum as the flow progresses through the seal. For the cases where the Taylor number contribution to the flow field development is greater, the direction of the mean shear stress vector changes significantly as the flow enters the seal, from a direction mostly tangential in the direction of the rotor, to one that is predominantly downstream. In the seal interior the angles increase gradually as the rotor continues to increase the azimuthal velocity by means of friction until the exit. Θ increases into the exit plenum since the cross section increases

causing the axial velocity to decrease (and to be more evenly distributed) compared to the azimuthal velocity.

Once the flow enters the seal, the shear stress direction becomes downstream with $\Theta=10^\circ$ for $Re/Ta=3.6$ and $\Theta=30^\circ$ for $Re/Ta=1.8$. The Θ distribution for $Re/Ta=3.6$ is the same for both Reynolds and Taylor number combinations with Θ increasing from 10° at the inlet to 20° just upstream of the exit. Once the flow exits the seal, Θ increases to 40° as the axial velocity decreases due to the increased clearance. The Θ axial distribution for the $Re/Ta=1.8$ case is very similar with Θ being twice as large as the $Re/Ta=3.6$ case. Hence it appears that once the Re/Ta ratio is small enough the product $\Theta Re/Ta$ produces a non-dimensional axial distribution.

The non-dimensional mean pressure distribution is shown in Figure 8. The values of ΔP used to non-dimensionalize the mean pressures are shown in Table I. The overall dimensional pressure drop increases with increasing Reynolds number and Taylor number. Doubling the Reynolds number results in a larger ΔP increase than doubling the Taylor number. The axial mean pressure distribution in Figure 8 shows a sudden decrease in pressure at the seal inlet as the flow accelerates into the small clearance and encounters the *vena contracta*. The percentage of overall pressure drop occurring at the seal entrance increases with increasing Re/Ta ratio with the two Reynolds and Taylor number combinations having a ratio of 3.6 producing the same non-dimensional axial pressure distribution however, the dimensional pressure drop for the high Reynolds number and Taylor number case is four times larger than the low Reynolds and Taylor number case. From $Z/L=0$ to 0.25 the pressure remains constant for the two largest Re/Ta ratios and increases for the smallest ratio. This result is due to the pressure recovery generated by the reduction in *vena contracta* size over this region producing a larger cross-section for the axial flow of fluid. This pressure recovery is offset by frictional headloss generated by the wall shear stresses. For the Re/Ta ratios of 3.6 and 7.3, the pressure recovery and headloss are equal resulting in a region of constant pressure. For the 1.8 Re/Ta ratio, the pressure recovery is larger resulting in a slight pressure increase. From $Z/L=0.3$ to the seal exit the pressure decreases at a relatively constant rate with the rate increasing with decreasing Re/Ta ratio.

The ratio of rotor speed to flow rate or Ta/Re appears to be a significant factor in the development of the annular seal flow field. This correlation implies that the influence of the rotor on the flow depends strongly on the relative residence time of the flow in the seal clearance with respect to the rotor surface speed, W_{sh} . In other words, the longer the length of time a given volume of fluid takes to pass through the seal, the more time the seal has to impart azimuthal momentum to that volume.

This phenomenon is seen in many of the shear stress and pressure plots which show similar trends (in shape, but not necessarily magnitude). The mean shear stress direction plot (Figure 7) exhibits this correlation particularly well. The direction curves for the cases with 3.6 Re/Ta fall nearly on top of each other while the curve of the low Re/Ta ratio shows the largest angles and the curve of the large Re/Ta ratios show the smallest angles, once again suggesting that the ratio of the rotor speed to the flow rate is proportional to the influence that the seal has on the flow field.

FORCE AND MOMENT CALCULATIONS

A simple integration scheme was used to determine the shear stress and pressure load distributions on the stator wall, calculated from the mean and phase averaged fluctuating shear stresses and pressures. The axial, azimuthal and radial force

distributions on the stator wall as well as the resulting net forces and moments were calculated.

Axial and azimuthal forces were calculated from the shear stress measurements while both the shear stress and pressure measurements were used to calculate radial or X-Y plane forces. The axial or Z direction is considered positive in the downstream direction. The azimuthal or Φ direction is considered positive in the direction of seal rotation, where 0° represents the maximum clearance, -180° to 0° represents the pressure side of the seal (the clearance is decreasing in time from the maximum to the minimum), and 0° to 180° represents the suction side. The X axis points towards $\Phi=0^\circ$ and the Y axis points towards $\Phi=90^\circ$. (See Figure 19).

Moments of the resultant pressure and radial shear stress forces are calculated about the axial midpoint of the seal ($Z/L=0.5$), while moments created by the axial stresses are calculated about the Z axis (seal center line). The angles of the moments are defined in the same manner as those of the forces.

FORCES, MOMENTS, AND DISTRIBUTED LOADS

Figures 9-12 represent the non-dimensional distributed forces (per Z/L length) along the stator wall, and the directions of these forces. Forces shown are in the axial, azimuthal and radial or X-Y planes.

F*, Shear Stress Distributed Loads: The shear stress generated axial load distributions of Figure 9 show trends that are much like those of the mean shear stress plot, Figure 6. For the $Re=12,000$, $Ta=3,300$ case there is a peak near the seal entrance (0.027) before a gradual decay near $Z/L=0.2$ (0.016). There is a load decrease past $Z/L=0.2$ to a value of 0.014 by $Z/L=0.6$, before rising gradually toward the exit plane where it peaks at 0.025 and then decreases in the exit plenum (0.021). The resultant non-dimensional axial force for the 50% eccentricity seal is 0.0238. The resultant non-dimensional moment (due to the axial force distribution and summed about the seal center line) and its direction in the radial plane is 0.4715 at -68° .

The $Re=24,000$, $Ta=6,600$ case exhibit almost identical behavior as the $Re=12,000$, $Ta=3,300$ case again showing the importance of Re/Ta . There is a peak at the seal inlet (0.024) before a small decay to $Z/L=0.25$ (0.014). The remainder of the seal interior experiences relatively stable distributed forces (constant near 0.016) to near $Z/L=0.7$. Here the value increases out to the exit (0.026). The resultant non-dimensional axial force is 0.0227. The resultant non-dimensional moment and its direction in the radial plane are 0.1753 at -64° .

When the low Reynolds number (12,000) is coupled with the large Taylor number (6,600) the entrance and exit effects upon the axial load distribution are significant. There is a large peak near the seal entrance (0.057) which is about twice the value seen for the two cases already presented. This peak is followed by a rapid decay near $Z/L=0.2$ to a value (0.020) almost equal to that observed previously. The load remains fairly constant at 0.02 (just slightly larger than the previous cases) until $Z/L=0.7$ where it increases out to the exit (0.045) reaching a value again almost twice the previous cases. The resultant non-dimensional axial force is 0.0329. The resultant non-dimensional moment and its direction are 0.3300 at -40° .

The high Reynolds number (24,000), low Taylor number (3,300) case develops the least axial load distribution of the four cases. There is a very small increase near the seal entrance (0.019) followed by a decrease near $Z/L=0.2$ to 0.012. The seal interior ($Z/L=0.2$ to 0.8) exhibits variations in the load distribution about a

value of 0.012. A slight increase at the exit plane (0.017) is observed before decreasing into the exit plenum. The resultant non-dimensional axial force is 0.0180. The resultant non-dimensional moment and its direction are 0.1102 at 172°.

F*, Shear Stress Distributed Loads: The shear stress generated azimuthal load distribution magnitudes (Figure 10) follow the same trends as the axial loads with the high Reynolds number (24,000) and low Taylor number (3,300) case generating the least load, the two cases with the same Re/Ta ratio (12,000/3,300 and 24,000/6,600) produce the same non-dimensionalized azimuthal force distribution which is larger than the first case, and the largest non-dimensional forces being generated by the Re=12,000, Ta=6,600 case.

The Re=24,000, Ta=3,300 case does not possess any distinct trend other than the force increases through the seal beginning at less than 0.001 at the seal entrance. By Z/L=0.25 the azimuthal force distribution has risen to a value of 0.0035. Along the interior to Z/L=0.8, the value falls to near 0.002. The value then increases out past the exit to a value of 0.0055. The resultant non-dimensional azimuthal load is 0.0033.

The two intermediate Re/Ta cases (12,000/3,300 and 24,000/6,600) exhibit the same shear stress azimuthal load distribution. After a relatively steep increase near the inlet to a maximum of 0.011 the azimuthal load distribution steadily increases to 0.017 by Z/L=0.9. At the exit the increasing trend becomes slightly steeper as value rise out into the exit plenum (0.024). The resultant non-dimensional azimuthal forces are 0.0166 and 0.0145 for the low Reynolds number and high Reynolds number cases respectively.

The low Reynolds number (12,000) and high Taylor number (6,600) case again possesses the largest non-dimensional load distribution. After a sharp increase near the inlet to a maximum of 0.025, the azimuthal load decreases to 0.028 then gradually increases to 0.04 at Z/L=0.7. At the exit this rising trend increases rapidly as the value rises to its maximum at the exit plane (0.075). The resultant non-dimensional azimuthal loads is 0.0553.

F*, Pressure Distributed Loads and Φ : The pressure produced radial force distributions, Figure 11, show a large increase in value from the inlet plenum to the entrance with a maximum value of 0.76 for the Re=24,000, Ta=3,300 case. The force decreases until near Z/L=0.7 where the value rises from 0.05 to 0.2. The force direction angle (Figure 12) switches from the pressure side (-180° to 0°) at the seal entrance to the suction side (0° to 180°) at the exit for all the cases. However, the high Re, low Ta seal switches sides in a direction opposite to that of the other cases. The angles change from -150° at Z/L=0.65, passes through -180° to 90° at Z/L=0.8, a change of 120°. The resultant non-dimensional force and its direction are 0.212 at -139°. The resultant non-dimensional moment and its angle are 0.0040 at -28°.

The pressure force distributions and load angles for the Re/Ta cases 12,000/3,300 and 24,000/6,600 are almost identical. There is a large increase in value from the inlet plenum to the entrance with maximum values reaching 0.96 and 1.1 for the low and high Reynolds numbers respectively. The load distribution decreases at a constant rate from Z/L=0.1 to 0.65 reaching minimums near 0.1. The values then rise from 0.1 to 0.45 at the exit. The force direction angle switches from the pressure side at the seal entrance to the suction side at the exit. The switch progresses from -110° at Z/L=0.65, passing through 0° and stopping at 55° at Z/L=0.8. This progression is in the opposite direction compared to the high Reynolds number, low Taylor number case. The resultant non-dimensional forces and their directions are 0.252

at -88° and 0.264 at -98°. The resultant non-dimensional moments and their angles are 0.0062 at -28° and 0.0066 at -39° for the low and high Reynolds number cases respectively.

For the Re=12,000, Ta=6,600 case the pressure force distribution shows a large increase in value from the inlet plenum to the entrance with a maximum of 1.5. The force distribution decreases until near Z/L=0.7 where the value rises from 0.25 to 0.9. The force direction angle switches from the pressure side at the seal entrance to the suction side at the exit although the switch is less severe than the other cases. The load angles range from -180° inside the inlet plenum, passes through 0° to 35° at the exit. The resultant non-dimensional force and its direction are 0.484 at -72°. The resultant non-dimensional moment and its angle are 0.0100 at -49°.

The shear stress produced radial force distribution is not presented in this paper since it comprises less than 1% of the total force and 6% of the moment. The data and a description are presented in Winslow(1994).

Resultant Forces and Moments Tables II and III provide listings of the total resultant forces, moments, and their respective directions for the various test cases and eccentricities. The three force components are represented in Table II: axial (F^*_{RZ}), radial (F^*_{RXY}), and azimuthal ($F^*_{R\phi}$). The radial component comprises the sum of the shear stress and pressure components, while the axial and azimuthal components consist of the shear stress forces only. The direction for the total radial force is represented by Φ_{RXY} . Two moments are represented in Table III, the total moment due to the axial shear stresses (M^*_{RZ} , calculated about the seal center line) and the total radial moment attributed to the radial shear and pressure stresses (M^*_{RXY} , calculated about Z/L=0.5). The directions for the total axial and radial moments are represented by Φ_{RM} and Φ_{RMXY} respectively.

PHASE AVERAGED MEASUREMENTS

Figures 13-18 show contour plots of the phase averaged wall pressure, wall shear stress, axial velocity, azimuthal velocity, radial velocity, and turbulence kinetic energy (κ) over one cycle (rotation) of the seal along its entire length for Re=24,000 and Ta=6,600. The measurement grids for these data have been presented in figures 3-5. The velocity components and κ were measured 0.16c above the stator by Thames (1992) using a 3-D laser Doppler anemometer system described in Morrison, et al. (1994) and Thames (1992). The phase averaged wall pressure has relatively low amplitudes upstream of the seal. Upon entering the seal, the phase averaged wall pressure increases in amplitude dramatically. The highest value (16) occurs from 30 to 50% of the cycle on the pressure side of the seal and decreases to the minimum value (-16) from 70 to 100% of a cycle on the suction side. The locations of the maximum and minimum pressures remain the same over the first half of the seal length with the magnitudes decreasing from 16 to 6 by Z/L=0.5. As the flow continues through the seal, the amplitude of the phase averaged wall pressure decreases becoming more uniform around the seal with the pressure and suction regions switching near the seal exit.

The phase averaged wall shear stress is shifted approximately 1/4 of a cycle from the wall pressures with the maximum (24) occurring at the seal entrance from 50% to 80% of a cycle and the minimum (-12) occurring from 0 to 30%. The positive value is located between the high and low pressure locations with the pressure decreasing in the direction of the rotor motion. This is a region of low azimuthal velocity with large azimuthal and axial gradients in the axial velocity (Figures 15 &

16). The phase averaged wall shear stress becomes more uniform through the central portion of the seal with the maximum positive value of 10 and a minimum of -6. The amplitudes increase near the seal exit to values as large as at the inlet with the minimum shear stress shifting to 0% cycle and the maximum centering itself around 50% of the cycle.

The phase averaged axial velocity contours are presented in Figure 15. Bulk flow models predict maximum axial velocity at the location of maximum clearance (0% of a cycle). However, for this flow field the axial velocity has a magnitude of twice the bulk flow velocity and is located at 60-70% of a cycle in a region where the phase averaged pressures are transitioning from maximum to minimum and have a value near zero. The minimum axial velocity in the inlet is on the "pressure side" of the seal from 30-40% of a cycle in a high pressure region but not at the maximum pressure location. As the flow progresses through the seal, the axial velocity becomes almost uniform at $Z/L=0.5$. However, the axial flow begins to maximize on the "pressure side" of the seal around 30% of a cycle reaching a maximum for this azimuthal region at the seal exit. Likewise, a region of minimum axial velocity is located on the "suction side" of the seal. An explanation for this behavior is the flow will preferentially accelerate towards both the largest clearance as happens for a statically eccentric seal and for the minimum pressure. However, for this whirling case, the large minimum pressure is located on the suction side near the minimum clearance. This low pressure causes the flow to deviate from the maximum clearance location but not entirely into the low pressure region. This is due to the small clearance present at the minimum pressure location not being able to accept all of the fluid. Thus the bulk of the leakage occurs between the two locations.

Phase averaged azimuthal velocities (Figure 16) exhibit different behavior from the axial velocities. The minimum at the seal entrance occurs at the maximum clearance (0%) and the maximum occurs just before the minimum clearance passes by at 40% of a cycle. This does follow intuition since the minimum azimuthal velocities occur when the rotor is farthest away from the stator. There is a slight migration of the minimum value locations as the flow progresses downstream accompanied by an ever increasing average value in $\langle W^* \rangle$. At the exit plane, the minimum value is located around 15% of a cycle and the maximum azimuthal velocity is located near 60%. The maximum values of $\langle W^* \rangle$ tend to follow the locations of minimum $\langle U^* \rangle$ throughout the seal. This is due to the lower values of $\langle U^* \rangle$ resulting in longer residence times within the seal allowing the rotor induced tangential shear stresses to cause increased azimuthal velocities.

Figure 17 presents the phase averaged radial velocities. Other than the large values at the seal inlet caused by the flow rushing into the seal, the radial velocities are very small. The phase averaged turbulence kinetic energy, $\langle \kappa^* \rangle$, in Figure 18 maximize at the seal inlet where the axial velocity is maximum, the azimuthal pressure variation is largest, and the *vena contracta* is present. This is due to the large velocity gradients resulting in lots of shearing effects generating vorticity and turbulence. The levels drop rapidly once the flow passes over the *vena contracta* and both the axial and azimuthal velocity gradients begin to decrease. $\langle \kappa^* \rangle$ becomes relatively uniform at the center of the seal. By the exit of the seal $\langle \kappa^* \rangle$ has reached a minimum centered around 0% and has a local maximum at 40% of a cycle. This increase in turbulence is due to the axial velocity reestablishing peaks near the exit resulting in local velocity gradients. In fact $\langle \kappa^* \rangle$ maximized between the minimum and maximum values of $\langle U^* \rangle$ at the exit plane.

CONCLUSIONS

The stator wall pressure and shear stress distributions are directly linked to the mean flow field and turbulence levels observed 0.16c above the stator. The mean pressure decreases rapidly at the seal inlet as the flow accelerates into the small channel. The rush of fluid into the seal from the plenum causes a *vena contracta* to form immediately inside the seal inlet. The turbulence produced by the *vena contracta* and the large mean velocity gradients associated with the sudden acceleration into the seal result in large levels of stator wall pressure, shear stress, and flow fluctuations. Contour plots of the phase averaged flow field show that at the seal inlet the pressure is high on the pressure side of the seal and low on the suction side with the shear stress being approximately 90° out of phase. As the flow progresses through the seal the level of pressure and shear stress fluctuations decrease due to the turbulence levels in the seal decreasing and the axial and tangential mean velocities becoming more uniform around the seal circumference resulting in smaller velocity gradients. At the seal exit the axial velocity has become largest on the pressure side of the seal as compared to the suction side at the seal inlet. This results in the phase averaged pressure actually becoming negative on the pressure side and positive on the suction side at the seal exit. It is the axial locations of maximum azimuthal variation in $\langle U^* \rangle$ which corresponds to the areas of maximum $\langle P^* \rangle$ and $\langle T^* \rangle$ variation. Overall, the flow field is very complex with significant interplay between the mean velocity, turbulence, wall pressure, and wall shear stress. A simple assumption of no azimuthal variance of pressure or shear stress is shown to be invalid as is the assumption that the axial velocity will be maximum at the maximum clearance location. This makes the modeling of the flow field inside whirling annular seals a very difficult task.

For all cases the mean pressure decreases rapidly at the seal entrance plane as a large volume of fluid accelerates from the entrance plenum into the small clearance, causing a *vena contracta* to form immediately inside the seal inlet. The turbulence produced by the *vena contracta* and the large axial and azimuthal velocity gradients associated with the sudden acceleration into the seal, result in large levels of stator wall pressure and shear stress fluctuations. At the seal entrances these shear stresses are typically about 90° (lagging) out of phase with the pressures; this pattern does not always hold downstream, but is highly dependent on the test conditions.

The direction of the mean shear stress varies for the different flow cases. The high rotor speed turns the angle more in the direction of the seal rotation whereas the high flow rate tends to turn the direction more downstream through the seal.

A strong correlation between the ratio of the Reynolds number and the Taylor number is seen to exist as the pressure and shear stress characteristics behave similarly for test conditions with identical ratios. This parameter, Re/Ta , apparently accounts for the effects of rotor speed and flow rate on the annular seal environment that are encountered during seal tests.

The flow field in a whirling annular seal tends to induce forces and moments on the stator wall (and hence the rotor) that are significant for the high eccentricity case studied, and can create complications when operating these seals in turbomachines. Pressure and shear stress induced forces and moments are shown to exist on the stator that can push the seal away from areas of high pressure, and can tilt the seal away from alignment due to regions of high and low pressure and shear stresses that cause force imbalances around the seal. Such occurrences can lead to

undesirable contact of the seal on the stator wall, or to instabilities in seal performance.

In summary, the annular seal flow field is very complex with significant interaction between the mean velocities, turbulence, wall pressures, wall shear stresses, and forces. This makes the modeling of the flow field inside whirling annular seals a very difficult task.

ACKNOWLEDGEMENTS

This research was supported by the NASA Lewis Research Center, the Turbomachinery Research Consortium at Texas A&M University, and the Exxon Education Foundation.

REFERENCES

Allaire, P.E. Lee, C.C., and Gunter, E.J., 1978, "Dynamics of Short Eccentric Plain Seals with High Axial Reynolds Numbers," *Journal of Spacecraft and Rockets*, Vol. 15, pp. 341-347.

Chen, W.C., and Jackson, E.D., 1987, "A General Theory for Eccentric and Misalignment Effects in High-Pressure Annular Seals," *ASLE Transactions*, Vol. 30, pp. 293-301.

Hanratty, T.J., and Campbell, J.A., 1983, "Measurement of Wall Shear Stress," *Fluid Mechanics Measurements*, Hemisphere Publishing Corporation, pp. 559-611.

Haritonidis, J.H., 1989, "The Measurement of Wall Shear Stress," *Advances in Fluid Mechanics Measurements*, Lecture Notes in Engineering, Springer-Verlag, pp. 229-261.

Ludwig, H., 1950, "Instrument for Measuring the Wall Shearing Stress of Turbulent Boundary Layers," NACA TM 1284.

Morrison, G.L., DeOtte, R.E., and Thames, H.D., "Experimental Study of the Flow Field Inside a Whirling Annular Seal," *STLE Tribology Transactions*, Volume 37, 1994, pp. 425-429.

Olivero-Bally, P., Forestier, B.E., Focquenoy, E., and Olivero, P., 1993, "Wall-Pressure Fluctuations in Natural and Manipulated Turbulent Boundary Layers in Air and Water," *Flow Noise Modeling, Measurement, and Control*, ASME Publication, Winter Annual Meeting, New Orleans, La., pp. 63-74.

Pessoni, D.H., 1974, "An Experimental Investigation into the Effects of Wall Heat Flux on the Turbulence Structure of Developing Boundary Layers at Moderately High Reynolds Numbers," Ph.D. Dissertation, Mechanical and Industrial Engineering Department, University of Illinois, Urbana.

Thames, H.D., 1992, "Mean Flow and Turbulence Characteristics in Whirling Annular Seals," Master's Thesis, Texas A&M University, College Station, TX, 77843.

Van Praegenau, G.L., 1990, "Damping Bearings for Turbomachinery," NASA TP 3092, Vol. II, *Advanced Earth-to-Orbit Propulsion Technology Conference*, Huntsville, Ala., pp. 155-162.

Winslow, Robert W., 1994, "Dynamic Pressure and Shear Stress Measurements on the Stator Wall of Whirling Annular Seals,"

Master of Science Thesis, Texas A&M University, College Station, TX, 77843.

Table I. Non-dimensionalizing parameters.

Re	Ta	ΔP kPa	U_m m/s	W_{sh} m/s
12,000	3,300	20.6	3.7	15.5
12,000	6,600	32.8	3.7	30.9
24,000	3,300	59.8	7.4	15.5
24,000	6,600	80.9	7.4	30.9
		$\Delta Pc/L$ kPa	$\mu W_{sh}/c$	$\frac{\Delta Pc/L}{\mu W_{sh}/c}$
12,000	3,300	0.74	9.52	0.013
12,000	6,600	1.17	19.1	0.016
24,000	3,300	2.13	9.52	0.0044
24,000	6,600	2.89	19.1	0.0066

Table II. Summary of total non-dimensional forces and directions.

Re	Ta	$F_{R,Z}^*$	$F_{R,XY}^*$	$\Phi_{R,XY}$	$F_{R,\phi}^*$
12,000	3,300	0.0238	0.252	-88°	0.0166
12,000	6,600	0.0329	0.484	-72°	0.0553
24,000	3,300	0.0180	0.212	-139°	0.0033
24,000	6,600	0.0227	0.264	-98°	0.0145

Table III. Summary of total non-dimensional moments and directions.

Re	Ta	$M_{R,Z}^*$	$\Phi_{R,M}$	$M_{R,XY}^*$	$\Phi_{R,MXY}$
12,000	3,300	0.472	-68°	0.0064	-27°
12,000	6,600	0.330	-40°	0.0103	-52°
24,000	3,300	0.110	172°	0.0040	-28°
24,000	6,600	0.175	-64°	0.0067	-38°

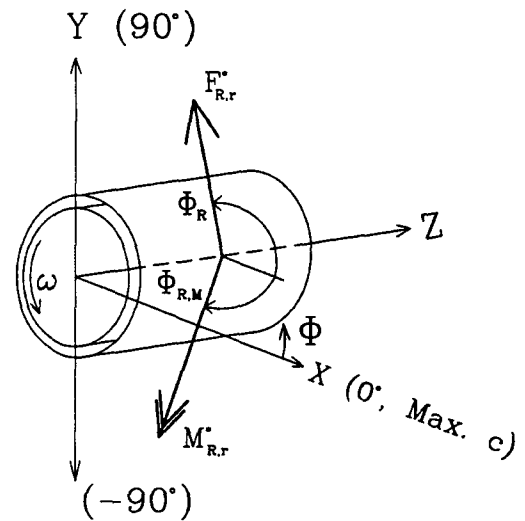


Figure 20. The directions of a set of resultant force and moment vectors on the stator wall (at $Z/L=0.5$), and the X, Y, and Z axes are defined.

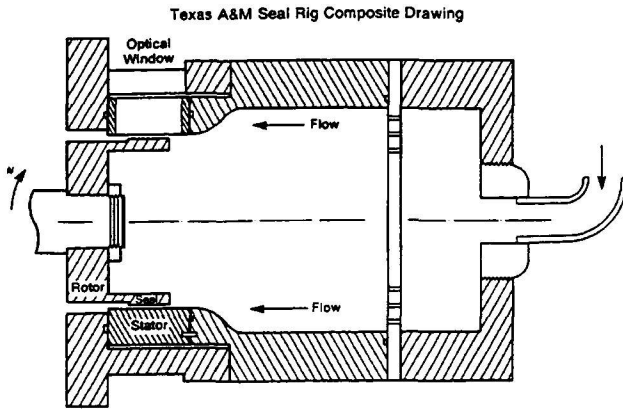


Figure 1. Seal test facility.

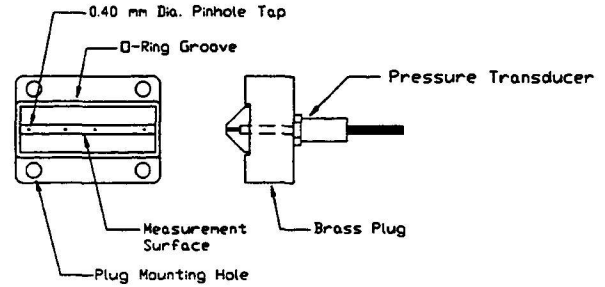


Figure 2. Pressure transducer mounting block.

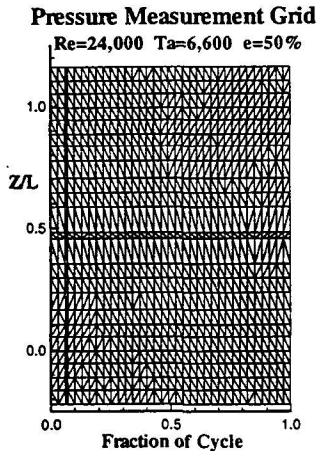


Figure 3. Phase averaged wall pressure measurement grid.

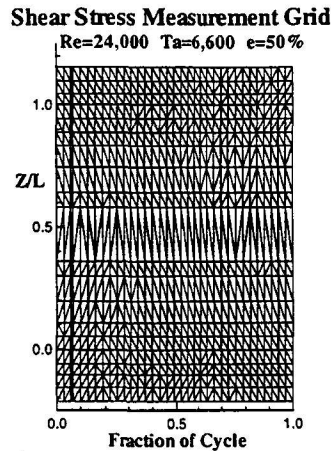


Figure 4. Phase averaged wall shear stress measurement grid.

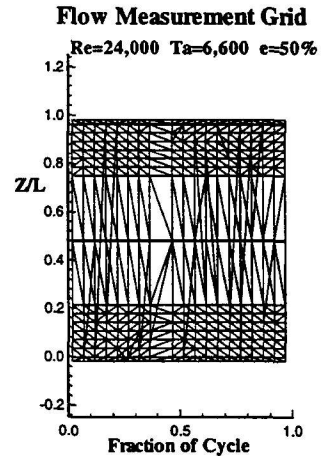


Figure 5. Phase averaged velocity field measurement grid.

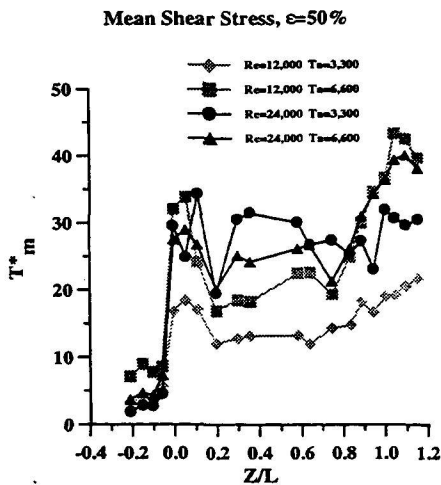


Figure 6. Non-dimensional, mean shear stress profiles for the 50% eccentricity seal.

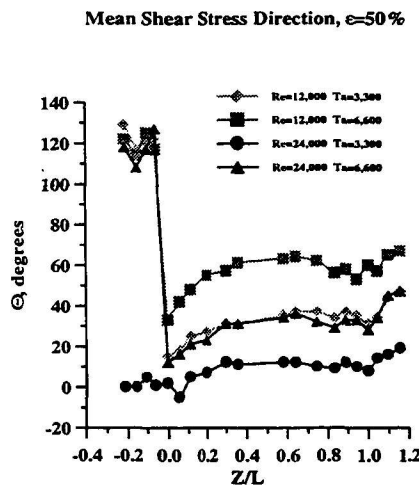


Figure 7. Mean shear stress direction profiles for the 50% eccentricity seal.

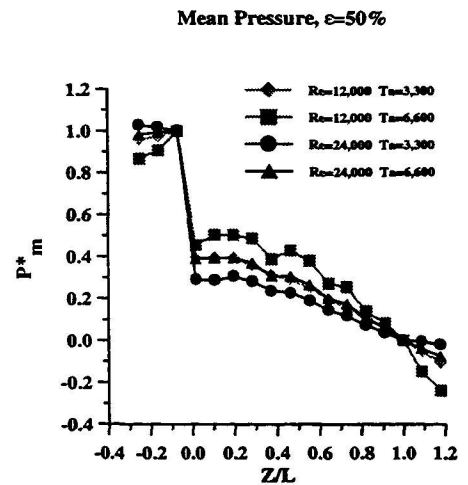


Figure 8. Non-dimensional, mean pressure profiles for the 50% eccentricity seal.

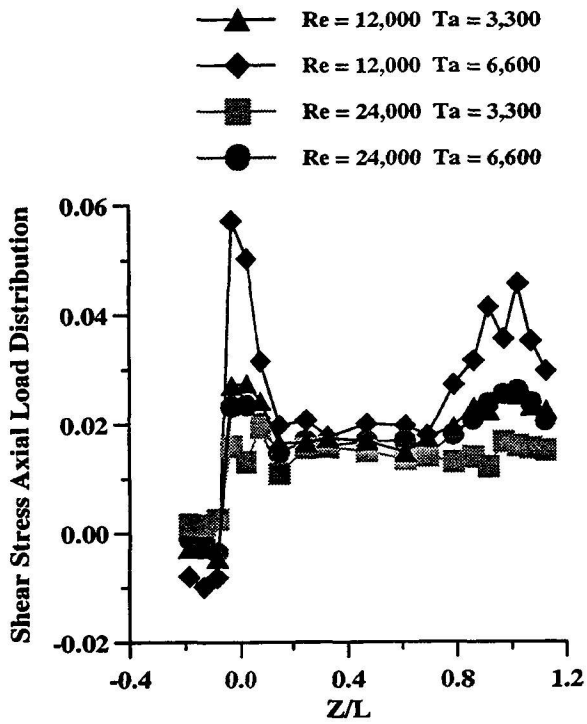


Figure 9. Shear stress axial load distribution.

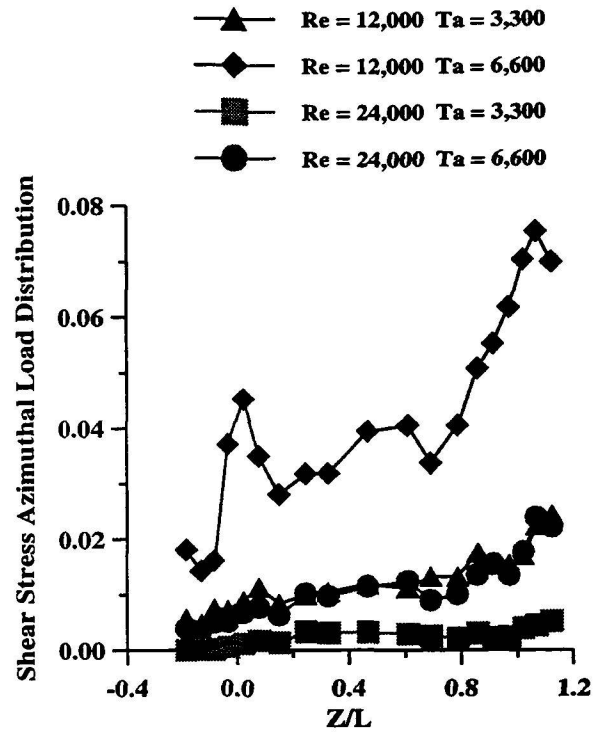


Figure 10. Shear stress azimuthal load distribution.

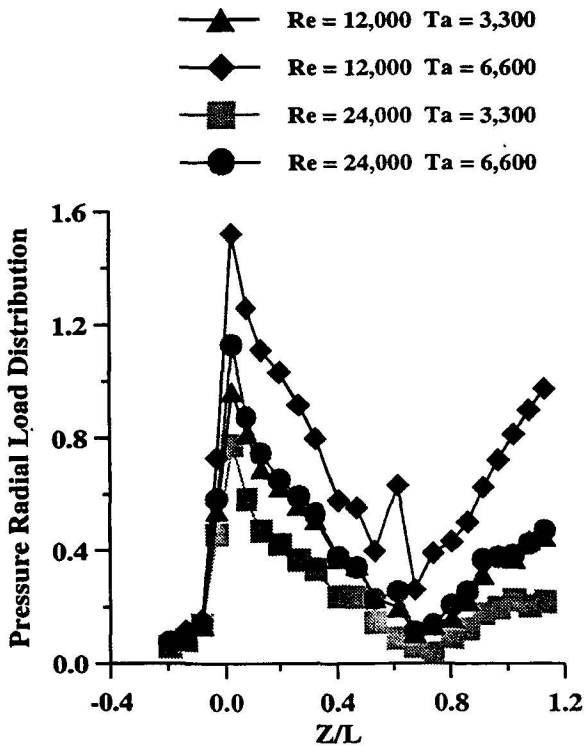


Figure 11. Pressure radial load distribution.

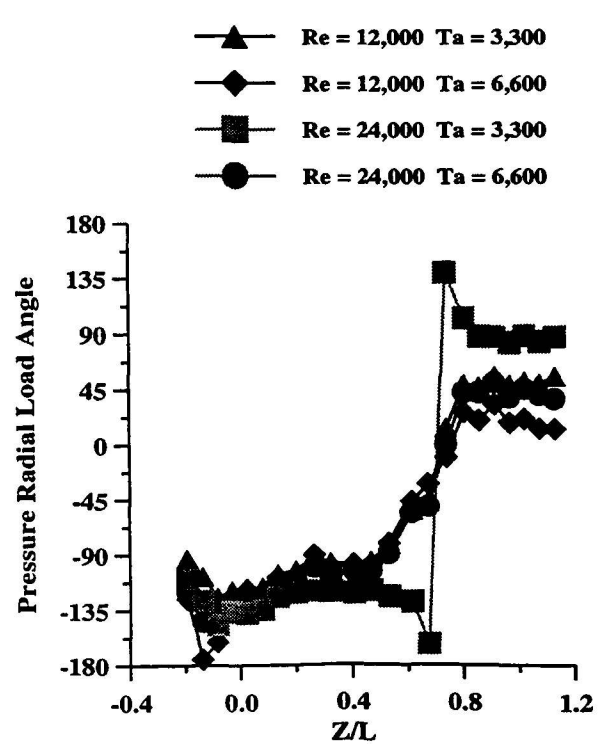


Figure 12. Pressure radial load angle of application.

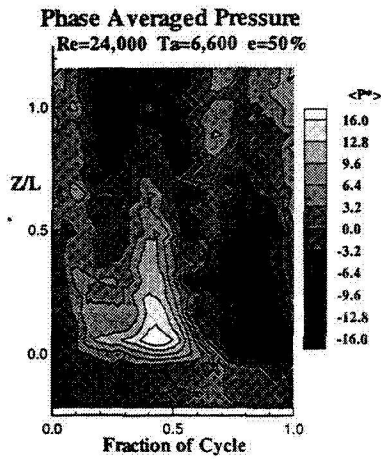


Figure 13. Phase averaged stator wall pressure.

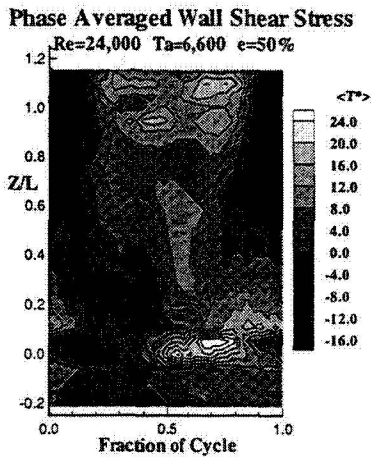


Figure 14. Phase averaged stator wall shear stress.

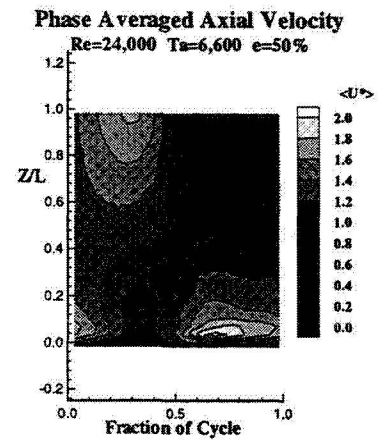


Figure 15. Phase averaged mean axial velocity located 0.16c above the stator.

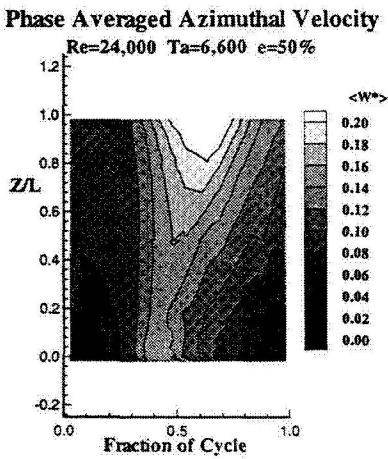


Figure 16. Phase averaged mean azimuthal (tangential) velocity distribution located 0.16c above the stator.

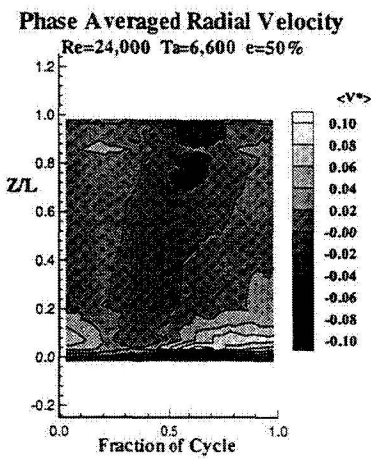


Figure 17. Phase averaged mean radial velocity distribution located 0.16c above the stator.

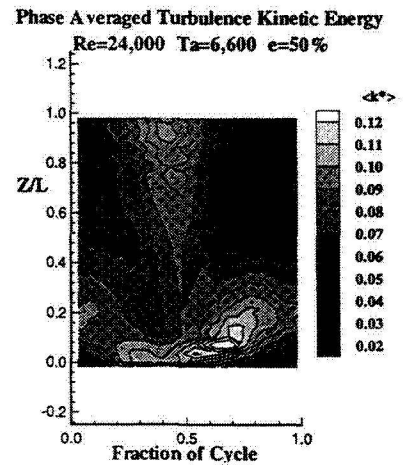


Figure 18. Phase averaged turbulence kinetic energy distribution measured 0.16c above the stator.

P&W CRYOGENIC FLUID-FILM BEARING AND SEAL TECHNOLOGY DEVELOPMENT
AND IMPLEMENTATION

Philip C. Pelfrey
Pratt & Whitney
West Palm Beach, Florida

515-37
39457

This presentation will summarize Pratt & Whitney's past, present, and future activities toward cryogenic fluid-film bearing and seal technology development and implementation. The three major areas of focus for this technology are analytical models and design tools, component testing, and technology implementation. The analytical models and design tools area will include a summary of current tools along with an overview of P&W's new full 3-D Navier-Stokes solution for hydrostatic bearings, HYDROB3D. P&W's comprehensive component test program, including teaming with the Air Force Phillips Laboratory, NASA's Marshall Space Flight Center, and Carrier Corporation, will be outlined. Component test programs consisting of material development and testing, surface patterns/roughness, pocket and orifice geometry variations, and static and dynamic performance of both journal and thrust bearings will be summarized. Finally, the technology implementation area will show the benefits and plans for P&W to incorporate this technology into products.

Overview

P&W's past, present, and future activities toward cryogenic fluid-film bearing and seal technology development and implementation. The three major areas of focus are:

- analytical models and design tools
- component testing
- technology implementation

Analytical Models & Design Tools – Past

- Reddecliff & Vohr (PN0317 & PN0345 – circa 1967)
 - static and dynamic performance for hydrostatic journal bearings (reynolds equation, finite difference)
 - accounted for turbulence, compressibility, and inertia
 - convergence problems at higher ecc. and clearances
- HYDROB (Kocur)
 - static and dynamic performance of hydrostatic journal and thrust bearings with or without grooves (reynolds equation, finite element)
 - better turbulence, compressibility, and inertia modeling
 - no convergence problems
- HYDROBEART (San Andres)
 - static and dynamic performance for hydrostatic journal brgs
 - Navier–Stokes, 2–D bulk–flow (finite difference)
 - barotropic properties, thermohydrodynamic analysis

Analytical Models & Design Tools – Present

- HYDROSEALT (San Andres)
 - adds multiple pad capabilities
 - includes plain journal bearings
 - calculates moment coefficients
 - non–symmetrical vent pressures and circumferential pressure gradients
 - non–uniform pocket sizes and orifice diameters
- RSR Software Library
 - includes 2–D bulk–flow (incompressible) for thrust bearings (Navier–Stokes)
- Note: Still use HYDROB for compressible thrust bearings

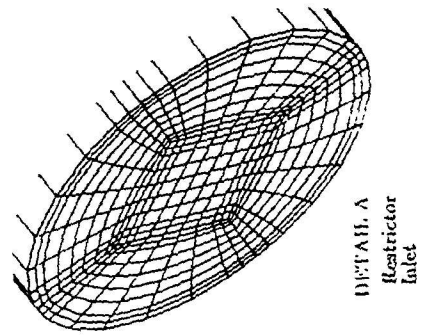
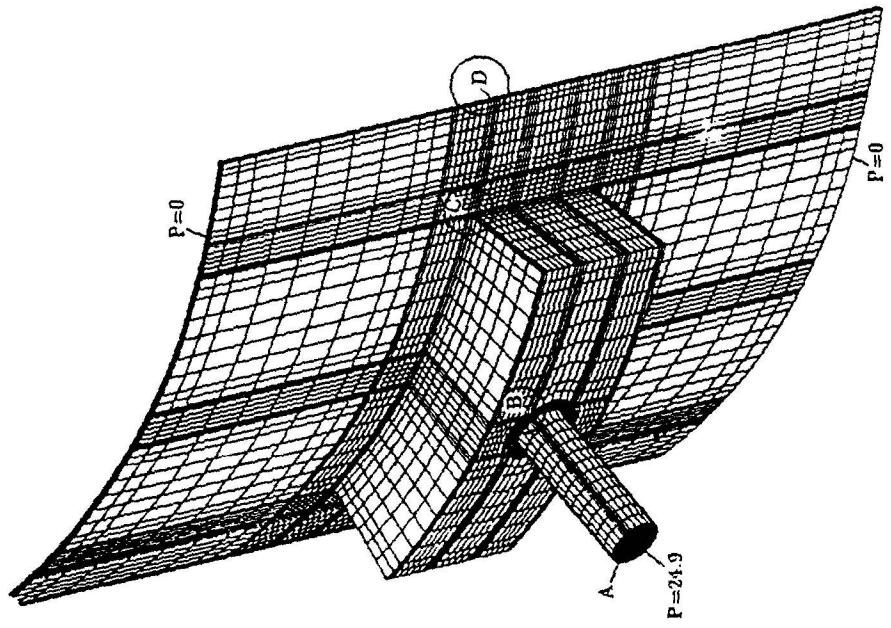
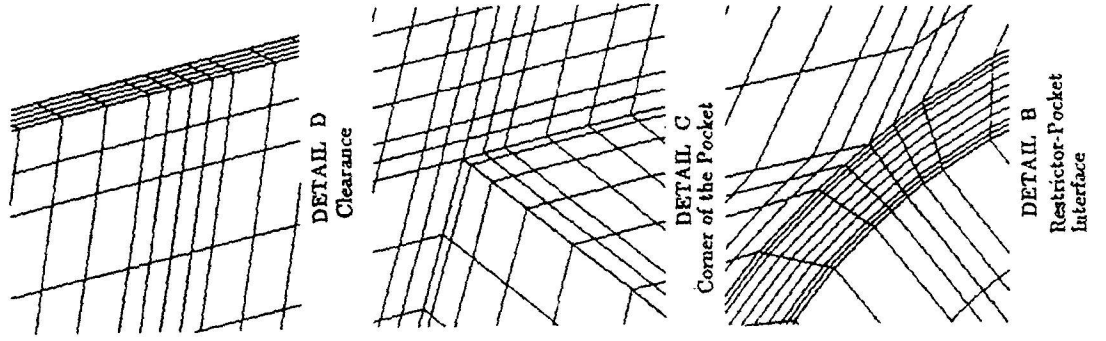
Analytical Models & Design Tools – Future

- **HYDROFLEX & HYDROTRAN (San Andres)**
 - adds transient analysis
 - adds compliant pad capability
 - 2-D bulk-flow
- **MTI Seal Codes**
- **HYDROB3D (Braun/Dzodzo)**
 - full solution of 3-D Navier-Stokes equations (finite difference/finite volume)
 - journal and thrust bearing analysis
 - accounts for compressibility, turbulence, and inertia
 - does not assume uniform pocket pressure

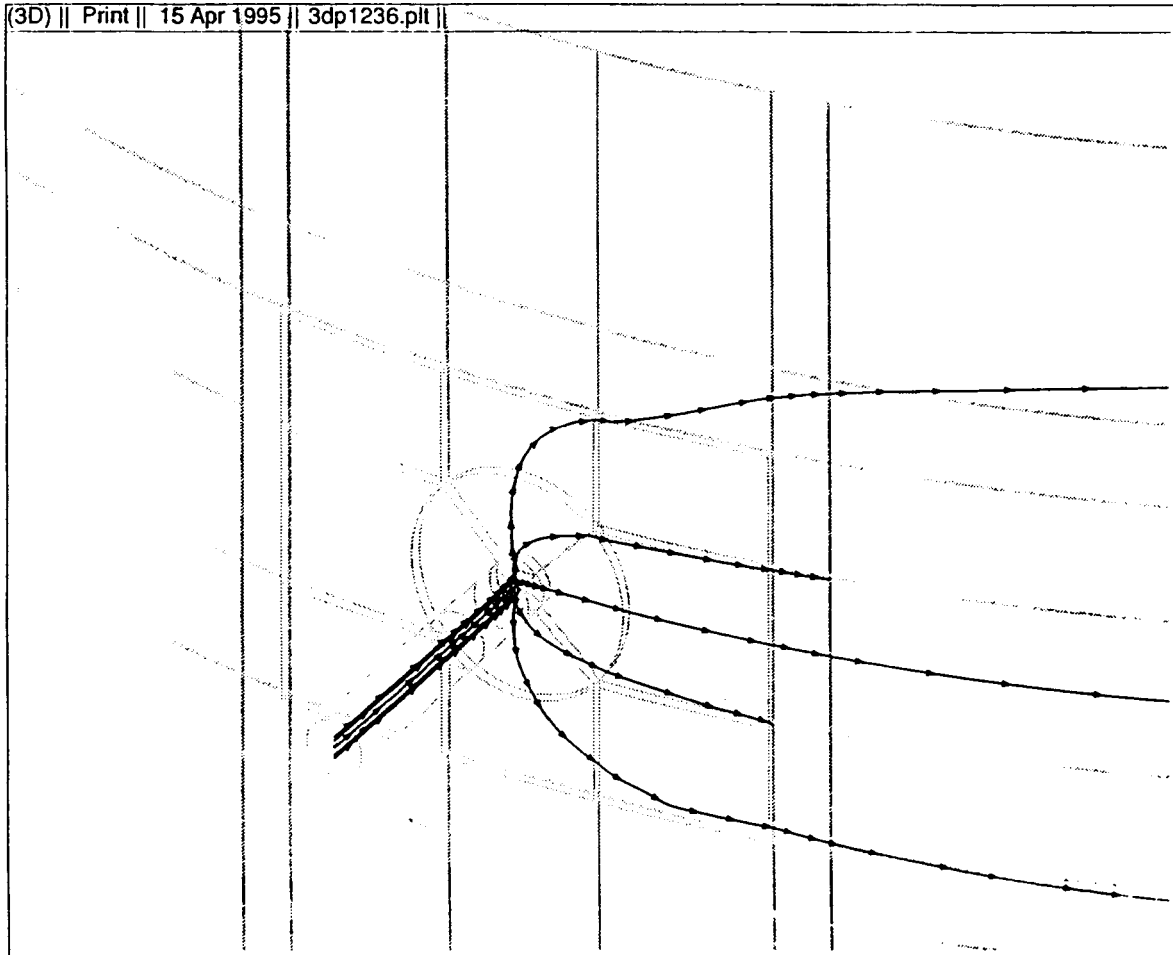
Parallel Processing

- **500 engineering workstations working in parallel over our computer network**
- **Equivalent power of 50 Cray XMP super computers (valued at 1.2 billion dollars)**
- **500 workstations cost us only 8.5 million dollars**
- **Overnight results to solutions which previously took weeks**

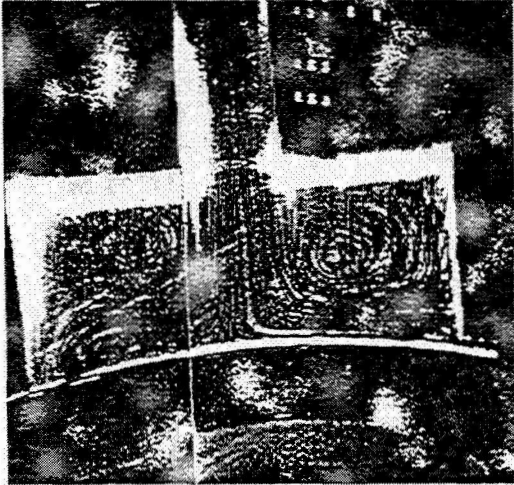
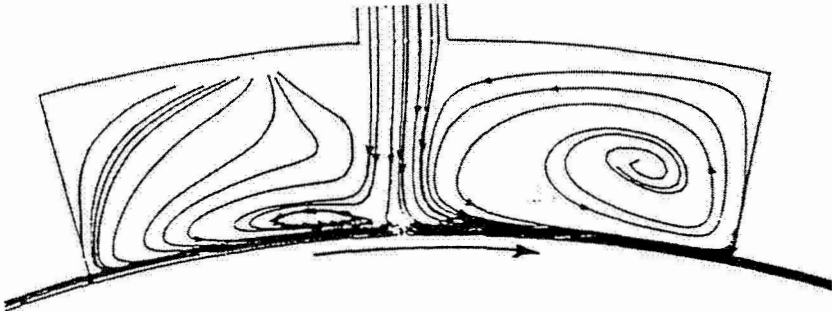
Sample 3--D Hydrostatic Bearing Mesh



Sample 3-D Hydrostatic Bearing Results



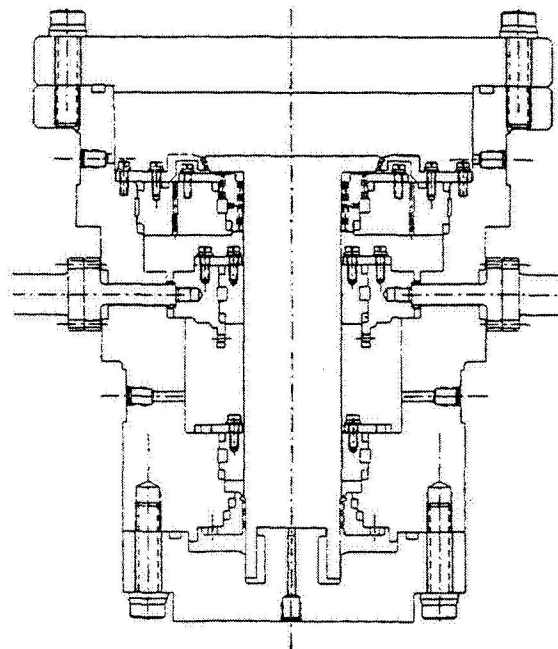
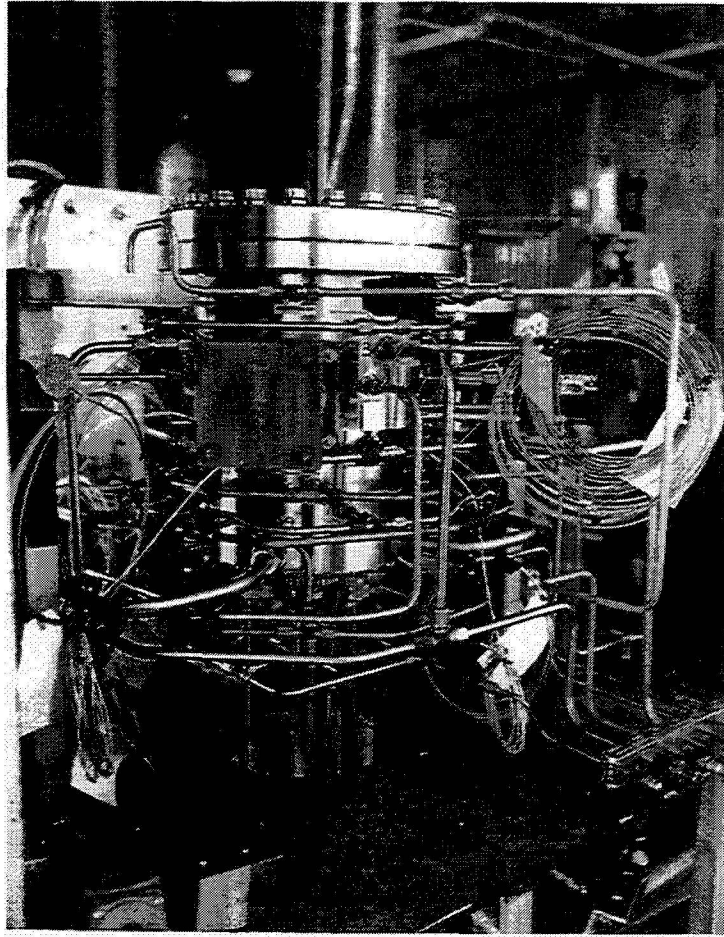
Comparison of Results to Flow Visualization



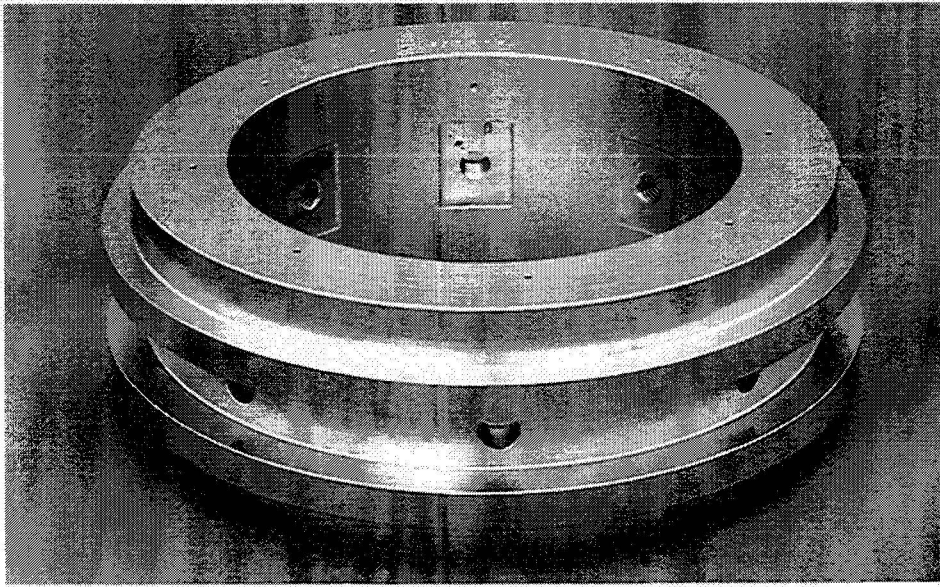
Component Testing

- Liquid hydrogen and HFC R134a material testing (Phillips Laboratory/ARPA TRP)
- Liquid oxygen material testing (NASA/MSFC)
- Performance testing (P&W/ARPA TRP)
- ARPA TRP
 - Dual–Use Hydrostatic Bearing Technology Program
 - P&W (Lead), Phillips Lab, and Carrier Corporation
 - Four year, 15 million dollar program
 - Under contract with NASA/MSFC

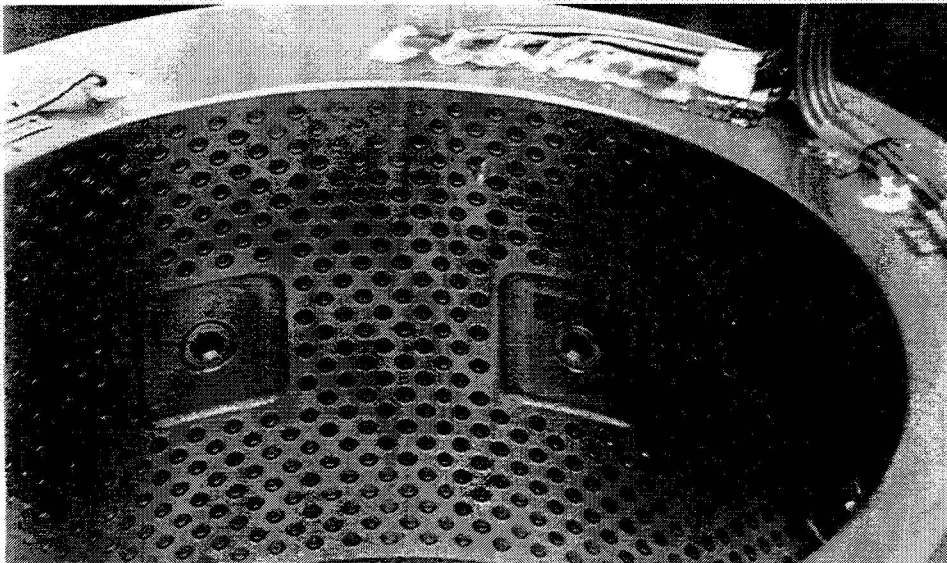
Component Test Rig



Sample Components

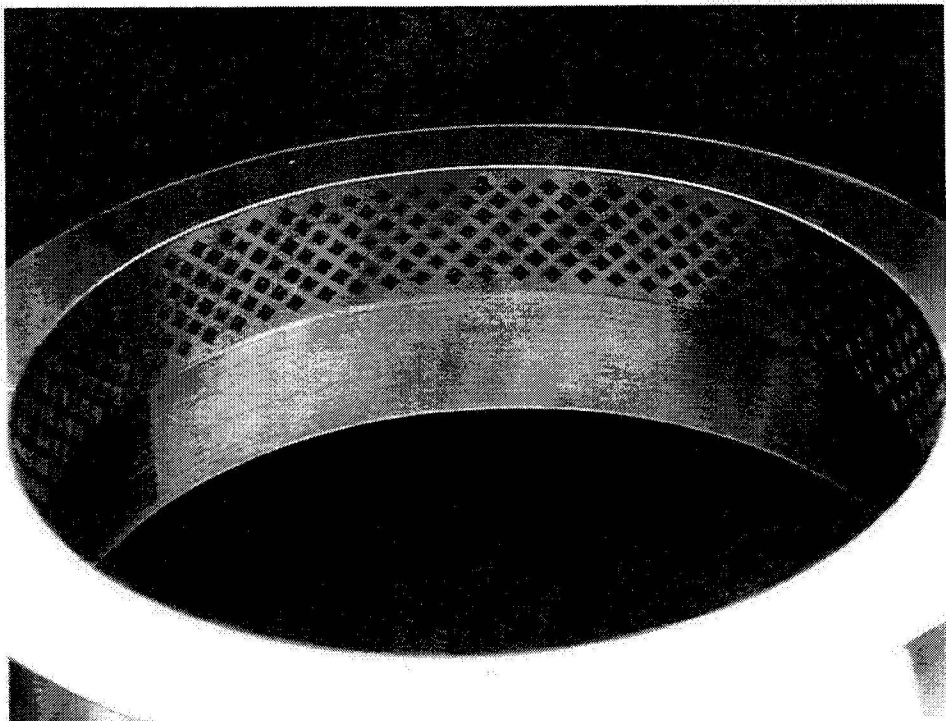
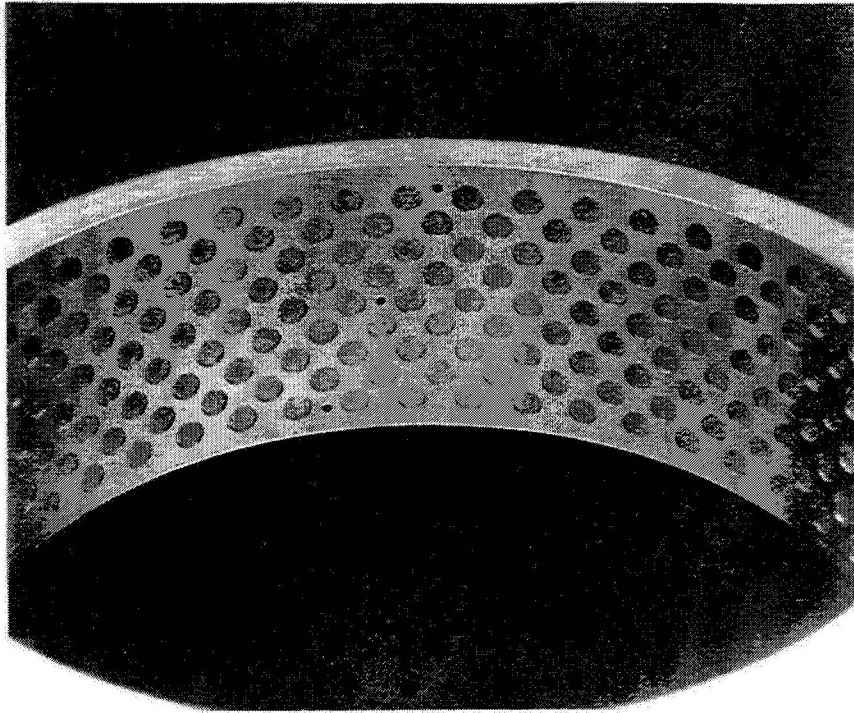


Liquid Hydrogen Bearing



Liquid Oxygen Bearing

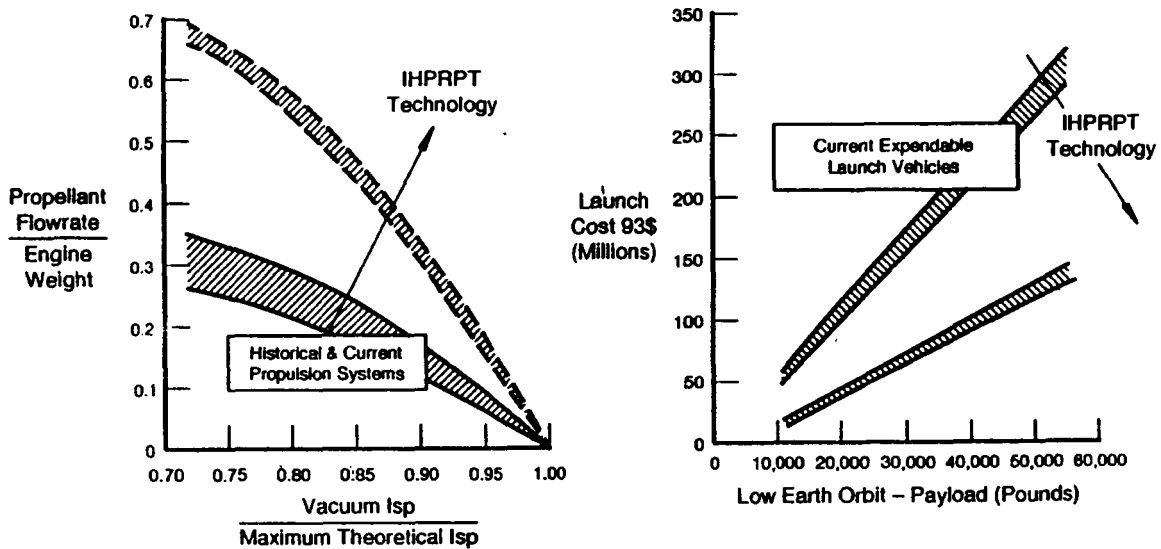
Surface Patterns



Technology Implementation

A rocket engine utilizing fluid-film bearing supported turbopumps has the ultimate effect of lowering launch costs as shown in the IHPRPT Vision:

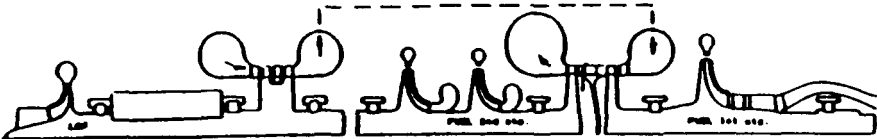
Payoffs: Reduced Vehicle Cost & Weight
Increased Payload



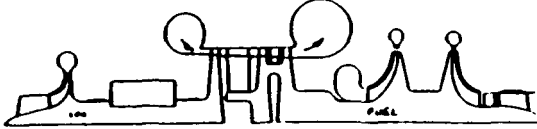
Technology Implementation

Fluid-film bearings enable smaller/lighter turbopumps through:

- No bearing DN limitation
- No sub-critical rotor limitations



Rolling Element / Subcritical



Hydrostatic / Subcritical



Hydrostatic / Supercritical

Technology Implementation

<u>Feature</u>	<u>REB Turbopump</u>	<u>FFB Turbopump</u>
# unique parts	342	24
# total parts	1,960	65
Overall size (inches)	42	10
Weight (lbs)	1,000	90
Operating clearances	10's of mils	mils
Speed (rpm)	35,000	much higher
Impellers	shrouded	unshrouded

Summary

- Technology development activities at Pratt & Whitney are focused on code development, component testing, and technology implementation.
- Analytical models and design tools are merging due to parallel processing
- Technology development is focused on end-product.

INTERSTAGE DISK-CAVITY/BRUSH SEAL NUMERICAL FLOW VISUALIZATION STUDY

V.V. Kudriavtsev and M.J. Braun
Department of Mechanical Engineering
The University of Akron
Akron, Ohio

516-34
39458

ABSTRACT

This paper presents results and model developments that are directed towards the computational fluid dynamics simulation of the secondary flow system in a gas turbine engine. Numerical flow visualization results of the 2-D axisymmetric rotational fluid flow ($Re=10^5$) in a generic cross section of an interstage turbine cavity are displayed. The core flow is driven by an imposed pressure drop along the vane row of the main flow path. Three interconnected disk cavities separated by a brush seal are located along the secondary flow path. A new computational algorithm was developed in order to predict the flow patterns and leakages for different seal and cavity configurations. The code is based on the numerical solution of the transient laminar Navier-Stokes equations, written in primitive variables and approximated on a nonuniform rectangular collocated grid. The program uses a mass and momentum conservative formulation as well as a set of boundary conditions for pressure and conservation of mass. The pressure solution uses the Poisson equation under a direct implementation procedure.

OBJECTIVE

The main purpose of this study is to present an integrated brush seal/disk cavity flow model to demonstrate the effectiveness of this approach and to emphasize the necessity for further work in this direction

INTRODUCTION

Recently, there has been a significant increase in the studies concerning the detailed physics of rotational flows in disk cavities, Przekwas et al., (1994), Virr et al., (1993), Athavale et al., (1993).

One of the main motivations for studying this problem is its direct application to gas turbine secondary flow systems management, in particular the rim and interstage cavities.

Improved efficiency of the gas turbine performance has been directly traced to improvements in the secondary flow path system, which can be simulated both through improved experimental, and novel computational methodologies.

A problem closely related to the current study is the flow in a cavity with rotating walls. This case has been extensively studied by Chew(1985), Farthing et al., (1992) and Ong and Owen(1991).

Chew(1985) treated some fundamental aspects of the heat transfer in centrifugally driven, steady-state free convection flow in a cylindrical cavity with a non-uniform disk-temperature distribution. In numerical and experimental studies performed by Owen and his associates, a rotating cavity with axial cooling air throughflow was used for the determination of heat transfer(Ong and Owen, 1991), and flow structures(Farthing et al., 1992).

Owen and Onur(1983) observed that at certain rotational velocities a non-axisymmetric vortex breakdown could occur and circulation inside the cavity becomes weaker as the Rossby number is reduced. The effect of the mainstream flow on the cavity flow has been studied numerically by Vaughan and Turner(1987). They showed that for certain conditions, a laminar 3-D solution gives a sinusoidally varying ingress-egress cycle in the rim seal area.

Ko et al., (1993) studied the axisymmetric sub-problem of a generic rotor-stator cavity. This work illuminated the presence of the main flow induced recirculation zone in the cavity gap area.

Athavale et al., (1993) performed numerical calculations to predict the rotational cavity flows with long clearance sections. The appearance of Taylor vortices was observed for supercritical rotational Reynolds numbers.

In the secondary flow systems, cavities are usually separated from the main stream, and each other by different types of seals, mostly labyrinths and honeycombs. There has been a number of previous studies that showed a marked improvement in sealing efficiency when the labyrinth seal was replaced by a brush seal,

Carfile et al., (1993) and Chupp and Dowler (1993).

Unfortunately, to date, brush seal theory has not been developed extensively, and a reliable numerical model that would allow widespread parametric design is still missing. Very few of the previous studies of this type of seal have involved theoretical, and numerical work. Most of the existing studies are experimental in nature. Chupp, et. al., (1991,1994) and Hendricks et. al., (1991) pioneered a simple theoretical leakage flow model through the brush seal.

However, simple models can not fully account for the effects of changes in the details of the brush geometries. The only available numerical simulations that analyze brush seal flows based on the composition of the brush are those of Braun and Kudriavtsev(1992, 1993a,b), and Kudriavtsev (1993). In these works the brush seal was simulated as a segment of densely packed cylinders, and the Navier-Stokes equations were directly applied to the flow upstream,

in-between, and downstream of these cylinders, Fig. 2.

These studies demonstrated that although fluid flow through the brush can be successfully 'micro-modeled', such direct brush modeling can be prohibitively expensive computationally, Kudriavtsev and Braun (1994). These authors searched for improved computational methodologies which eventually allowed the development of several simplified numerical models, such as brush partitioning(Kudriavtsev and Braun, 1994), and brush representation by a variable porosity porous body.

All studies reviewed here were concerned with the cases when either the disk cavity, or the seal were analyzed separately. Hendricks (Przekwas et al., (1994)) proposed that these two components be integrated in one computational algorithm, thus increasing the physical accuracy of the simulation.

BRUSH - POROUS BODY

The brush body can be modeled approximately as a saturated porous medium using Darcy's formula

$$-\frac{\partial P}{\partial x} = \frac{\mu}{k} U$$

and/or the Brinkman assumptions (Burmeister, 1993)

$$-\frac{\partial P}{\partial x} = \frac{\mu}{k} U - \frac{c \bar{\rho}}{\sqrt{k} \epsilon^3} \nabla^2 U$$

where ϵ is the porosity of the porous media, k is the permeability, U is the speed, and P is the pressure .

In the present study this approach is used to investigate numerically the flow through the brush.

The main purpose of this study is

to present an integrated brush seal/disk cavity flow model,

to demonstrate the effectiveness of this approach, and to emphasize the necessity for further work in this direction.

PROBLEM FORMULATION AND DETAILS OF THE SOLUTION PROCEDURE

The present study considers the fluid flow in a rotational interstage cavity(IC). Such cavity consists of a combination of the main flow path, front cavity with the rotating wall, stationary vane, and back cavity with a rotating wall.

The cavities are separated by a brush seal affixed to the lower axial wall of the vane, Fig. 1a.

The main flow is driven by a pressure drop imposed along the main flow path. This pressure drop is also the driving cause for the leakage flow through the brush seal that separates the high(front cavity) and low(back cavity) pressure zones.

Governing Equations

The 3-D Navier-Stokes equations(Schlichting(1978)) are applied here, while we are assuming rotational symmetry of the flow.

To account for the pressure drop in the mainstream across the vane row, we introduce a local flow resistance in the form of the Darcy's Law.

Thus, the permeability coefficient k_x is calculated based on apriori specified data regarding the pressure drop across the vane's blade row, Eq. 1a.

Main Flow path and Cavity Space.

The governing equations for the fluid flow in the disk cavity and along the mainstream flow path can be formulated in dimensionless conservative form as

$$\frac{\partial u}{\partial t} + \frac{\partial(vu)}{\partial r} + \frac{\partial(uu)}{\partial x} = -\frac{\partial p}{\partial x} + \frac{1}{Re} \left(\frac{\partial^2 u}{\partial r^2} + \frac{1}{r} \frac{\partial u}{\partial r} + \frac{\partial^2 u}{\partial x^2} \right) - \frac{1}{k_x Re} u \delta_{xy}$$

$$\frac{\partial v}{\partial t} + \frac{\partial(vv)}{\partial r} + \frac{\partial(uv)}{\partial x} - \frac{(w)^2}{r} = -\frac{\partial p}{\partial r} + \frac{1}{Re} \left(\frac{\partial^2 v}{\partial r^2} + \frac{\partial}{\partial r} \left(\frac{v}{r} \right) + \frac{\partial^2 v}{\partial x^2} \right)$$

$$\frac{\partial w}{\partial t} + \frac{\partial(vw)}{\partial r} + \frac{vw}{r} + \frac{\partial(uw)}{\partial x} = \frac{1}{Re} \left(\frac{\partial^2 w}{\partial r^2} + \frac{\partial}{\partial r} \left(\frac{w}{r} \right) + \frac{\partial^2 w}{\partial x^2} \right)$$

For such systems, the pressure equation was determined by Ivanushkin et al., (1980) using the momentum equation integration technique first described by Welch et al., (1966) and then exemplified by Roache(1982) for Cartesian coordinates.

PRESSURE EQUATION:

$$\begin{aligned} \frac{\partial^2 p}{\partial x^2} + \frac{1}{r} \frac{\partial p}{\partial r} + \frac{\partial^2 p}{\partial z^2} = & - \left(\frac{\partial^2 (u^2)}{\partial x^2} + \frac{\partial^2 (v^2)}{\partial r^2} \right. \\ & \left. + 2 \frac{\partial^2 (uv)}{\partial x \partial r} + 2 \frac{v^2}{r^2} \right) - \left(\frac{\partial D}{\partial t} + u \frac{\partial D}{\partial x} + v \frac{\partial D}{\partial r} \right) \\ & + \frac{1}{\text{Re}} \left(\frac{\partial^2 D}{\partial x^2} + \frac{1}{r} \frac{\partial D}{\partial r} + \frac{\partial^2 D}{\partial r^2} \right) \\ & + \frac{\partial}{\partial r} \left(\frac{w^2}{r} \right) + \frac{1}{k_x \text{Re}} \frac{\partial u}{\partial x} \delta_{xy} \end{aligned}$$

were D is the dilation term

$$\frac{\partial v}{\partial r} + \frac{v}{r} + \frac{\partial u}{\partial x} = D$$

$\delta_{xy} = 1$ for the vane's blade row flow area, while $\delta_{xy} = 0$ for the rest of the computational domain.

The Brush Region.

For this portion of the flow additional modifications were introduced into the main system of governing equations.

Momentum equations for the brush region

$$\frac{1}{\epsilon} \frac{\partial u}{\partial t} + \frac{\partial(vu/\epsilon^2)}{\partial r} + \frac{\partial(uu/\epsilon^2)}{\partial x} = -\frac{\partial p}{\partial x} + \frac{1}{\text{Re}} \left(\frac{\partial^2(u/\epsilon)}{\partial r^2} + \frac{1}{r} \frac{\partial(u/\epsilon)}{\partial r} + \frac{\partial^2(u/\epsilon)}{\partial x^2} \right) - \frac{u}{k_u \epsilon \text{Re}} \quad (7)$$

$$\frac{1}{\epsilon} \frac{\partial v}{\partial t} + \frac{\partial(vv/\epsilon^2)}{\partial r} + \frac{\partial(uv/\epsilon^2)}{\partial x} - \frac{(w/\epsilon)^2}{r} = -\frac{\partial p}{\partial r} + \frac{1}{\text{Re}} \left(\frac{\partial^2(v/\epsilon)}{\partial r^2} + \frac{\partial(v/\epsilon)}{\partial r} \left(\frac{1}{r} \right) + \frac{\partial^2(v/\epsilon)}{\partial x^2} \right) - \frac{v}{k_v \epsilon \text{Re}} \quad (8)$$

$$\frac{1}{\epsilon} \frac{\partial w}{\partial t} + \frac{\partial(vw/\epsilon^2)}{\partial r} + \frac{(wv/\epsilon)}{r} + \frac{\partial(uw/\epsilon^2)}{\partial x} = \frac{1}{\text{Re}} \left(\frac{\partial^2(w/\epsilon)}{\partial r^2} + \frac{\partial(w/\epsilon)}{\partial r} \left(\frac{1}{r} \right) + \frac{\partial^2(w/\epsilon)}{\partial x^2} \right) - \frac{w}{k_w \epsilon \text{Re}} \quad (9)$$

In a view of the modifications of the momentum equations the pressure equation takes now the form

$$\begin{aligned} \frac{\partial^2 p}{\partial x^2} + \frac{1}{r} \frac{\partial p}{\partial r} + \frac{\partial^2 p}{\partial r^2} = - \left(\frac{\partial^2(u^2/\epsilon^2)}{\partial x^2} + \frac{\partial^2(v^2/\epsilon^2)}{\partial r^2} + 2 \frac{\partial^2(uv/\epsilon^2)}{\partial x \partial r} + 2 \frac{(v/\epsilon)^2}{r^2} \right) \\ - \left(\frac{1}{\epsilon} \frac{\partial D}{\partial t} + u \frac{\partial D}{\partial x} + v \frac{\partial D}{\partial r} \right) + \frac{1}{\text{Re} \epsilon} \left(\frac{\partial^2 D}{\partial x^2} + \frac{1}{r} \frac{\partial D}{\partial r} + \frac{\partial^2 D}{\partial r^2} \right) + \\ \frac{\partial}{\partial r} \left(\frac{(w/\epsilon)^2}{r} \right) + \frac{1}{k_u \text{Re} \epsilon} \frac{\partial u}{\partial x} + \frac{1}{k_v \text{Re} \epsilon} \frac{\partial v}{\partial r} \end{aligned} \quad (10)$$

Pressure equation for the brush region

where D is a slightly modified dilation term

$$\frac{\partial(v/\epsilon)}{\partial r} + \frac{(v/\epsilon)}{r} + \frac{\partial(u/\epsilon)}{\partial x} = D \quad (11)$$

where $k_{u,v,w}$ are the three nondimensional permeability coefficients (Darcy numbers) of the brush seal with respect to the different directions. On inspection of Eqs. 6 through 10 one notices that k , also called the Darcy number, plays quite a prominent role principally characterizing the sealing capability of the brush. Accuracy in its determination is important, and can be established via three different methods.

DETERMINATION OF THE DARCY NUMBER

The Darcy number (k), plays quite a prominent role principally characterizing the sealing capability of the brush.

Accuracy in its determination is important, and can be established via three different methods.

The Numerical Approach. This approach requires numerical modeling of the Navier-Stokes equations through the brush segment, Fig. 2, following the methodology described by Braun and Kudriavtsev (1992,1993a,b), obtaining values of the average pressure drops, and finally calculating permeability using Eq. 1a.

The Theoretical Approach.

Brush permeability can be calculated using Ergun's(1952) formula

$$k = \frac{d^2 \epsilon^3}{A(1-\epsilon)^2} \quad (12)$$

where $A=150$.

Kuwahara et al., (1994) performed numerical studies of a matrix of 10x10 inclined cylinders and squares. It was found that the calculated permeability is almost identical to the (linear term) variable k in Ergun's equations (Eqs.12, 13).

The authors determined that $A=153$ when $\epsilon \in (0.08-0.84)$ for the square rods, and $A=143$ when $\epsilon \in (0.5-0.75)$, for the circular rods.

It was found that two-dimensional and three-dimensional models lead to almost identical expressions for permeability(Kuwahara et. al (1994)).

The format of the empirical Ergun's expression(1952) allows to account also for the variation of a brush packing density under real engine conditions, i.e. variable pressure difference across the seal.

$$-\frac{dP}{dx} = \frac{A(1-\epsilon)^2}{d_p^2 \epsilon^3} \left[\mu U_D + 0.143 U_D^2 \epsilon^{-3/2} k^{1/2} \bar{p} \right]$$

From Eq. 13 one can see that for constant bristle diameter (d), the Darcian leakage velocity U_D is a direct function of the average porosity and pressure differential. The change in the pressure differential is linked with the change in average porosity due to the deflection of the bristles under the pressure. Thus, we can account for the potential movement of the bristles through the change in porosity ϵ .

The Experimental Approach.

Experimental leakage flow data can be used to obtain brush seal effective permeability using Eq. 1a. In this case dP/dX is an experimental pressure gradient that is function of the brush thickness. However, in this case we will obtain "effective" seal permeability, since a large component of the leakage flow rate comes through the clearance between the brush and rub-runner, while the backing and front plates impose an additional flow resistance. Materials presented in the paper of Carlile et al., (1993) provide enough information for estimation of a brush seal permeability coefficient k_U .

Boundary conditions, 1

In Fig. 1a one can find a sketch of the computational domain with specified boundary conditions. The main flow enters the computational domain with zero radial velocity v , zero circumferential velocity w (preswirl), and an axial velocity $u=1$. The normalizing reference velocity is $U_0=100$ m/s. The maximum rotational velocity at the disk tip is $w=1$ where again, the normalizing velocity is $U_0=100$ m/s. The rotational velocity along the radial disk walls is a linear function of the radial coordinate

$$w(r) = r / r_m * w_{top} \quad (\text{where } w_{top} = u_{top} = 1) \quad (14)$$

The rotational velocity at the shaft surface (bottom of a cavity) is constant

$$w_{shaft} = r_{shaft} / r_m * w_{top} \quad (15)$$

where r_m is cavity (disk) tip radius and r_{shaft} is shaft radius. On the surface of the stationary vane $u=v=w=0$. At the main stream outflow, one can impose $\frac{\partial v}{\partial x} = \frac{\partial w}{\partial x} = 0$, which

accounts for developed flow conditions, and the axial velocity gradient is calculated through the mass balance of the continuity equation

$$\frac{\partial u}{\partial x} = - \left(\frac{\partial v}{\partial r} + \frac{v}{r} \right) \quad (16)$$

The pressure boundary conditions on the stationary walls are determined from the momentum equations, assuming that $u=v=w=0$. Thus

$$\frac{\partial p}{\partial x} = \frac{1}{Re} \left(\frac{\partial^2 u}{\partial x^2} + \frac{1}{r} \frac{\partial u}{\partial r} + \frac{\partial^2 u}{\partial x^2} \right) \quad (17)$$

Boundary Conditions, 2

$$\frac{\partial p}{\partial r} = \frac{(w)^2}{r} + \frac{1}{\text{Re}} \left(\frac{\partial^2 v}{\partial r^2} + \frac{\partial}{\partial r} \left(\frac{v}{r} \right) + \frac{\partial^2 v}{\partial x^2} \right) \quad (18)$$

Since at the interstage cavity inlet(Fig. 1a) $u=1=\text{const}$ and $v=0$, one can write

$$\frac{\partial p}{\partial x} = -u \frac{\partial u}{\partial x} + \frac{1}{\text{Re}} \frac{\partial^2 u}{\partial x^2} \quad (19)$$

At the cavity exit(Fig. 1a)

$$\frac{\partial p}{\partial x} = -v \frac{\partial u}{\partial r} - u \frac{\partial u}{\partial x} + \frac{1}{\text{Re}} \left(\frac{\partial^2 u}{\partial r^2} + \frac{1}{r} \frac{\partial u}{\partial r} + \frac{\partial^2 u}{\partial x^2} \right) \quad (20)$$

Thus the pressure conditions are calculated along all the boundaries of the computational domain using Neumann type boundary conditions.

In the gas turbine the flow along the main flowpath is driven due to the pressure difference between the nozzle guide vane and the turbine exhaust. For the interstage cavity under consideration the most part of the pressure drop in the area where the vane blade row is located. In the 2D formulation it is not possible to account for this effect. We used a distributed flow resistance (in the Darcy law format) to account for this pressure drop along the main flow path.

Solution Parameters and Computational Grid

For this study we had chosen constant permeability $k_U=6.0 \times 10^{-13}$. One can obtain this value by using Ergun Equation with $\epsilon=0.216$ and $d=0.075$ mm.

A nonuniform grid 207x145 (Fig. 1c) was superimposed over the computational domain of Fig. 1a.

In order to provide enhanced flow resolution the grid had an increased density near the cavity walls and in the area adjacent to the brush seal.

Numerical experiments indicated that this grid size constituted the minimum requirement for the accurate resolution of the complex vortex separation processes that are taking place within the interstage cavity.

The overall grid contained 23 separate regions along the axial direction, and 14 such regions along the radial direction. Inside each one of these regions the grid steps are uniform, but different from region to region.

Figure 1c presents the computational mesh used for all the flow simulations discussed in this paper. The sketch of the grid imposed over the domain of the brush seal is shown in Fig. 1b.

TABLE 1
Physical Characteristics and Parameters used in the Numerical Computations

Brush seal Darcy number	$Da=k_u=6 \times 10^{-7}$
Rotational ratio	$R=w_{\max}/U_{in}=1.$
Main flow Reynolds number	$Re_m=1.2 \times 10^5$
Vane flow Darcy number	$Da=k_x=10^{-4}$
Computational domain dimensions:	
Normalizing length	$L_0=1 \text{ mm},$
Nondimensional Axial size	$l_x=28.1$
Nondimensional Radial size	$l_r=34.48$
Nondimensional Shaft Radius	$r_{\text{shaft}}=160.0$
Nondimensional Tip Cavity Radius	$r_m=183.48$
Brush seal characteristics:	
Brush permeabilities	$e=k_u/k_v=0.01$
Permeability (k_x)	$k_{\text{Ergun}}=6.0 \times 10^{-13}$
	$k_{\text{exp}}=5.0 \times 10^{-13}$
	[k_{exp} calculated from Carlile, Hendricks & Yoder(1993) data].
Bristle diameter	$d=0.075 \text{ mm}$
Brush seal porosity	$\epsilon=0.216$
Brush seal clearance	$l_{cl}=0.08 \text{ mm}$

RESULTS AND DISCUSSION, 1

In Figs. 3a, and 3b one can find the global flow patterns that occur in the interstage cavities presented in Fig. 1. Figure 3a shows the flow when the side disk walls of the cavity are rotating, while Fig. 3b presents the version of the same flow when the velocity of the side walls is zero. These flows, whether they contain or not the disks rotational effects, are generally extremely complicated even for the simplified geometry used here. One can see four interacting vortices of different sizes in the front cavity, three major vortices in the seal cavity, several more vortices and a shear layer in the downstream cavity. The three vortices in the vane cavity are generated by the shear layer that fills the smaller downstream cavity. A small gap induced recirculation zone (GRZ) similar to the one presented by Ko et al., (1993) and Guo et al., (1994) is present in the area where the vane cavity is bound by the main flow stream. Generation of this zone provides the mechanism by which flow leaves the back cavity. A comparison between the flow patterns of Fig. 3a and Fig. 3b indicates a slight increase in the vortex structure complexity when rotation is not present; also the corner vortices that are located near the rotating walls are much stronger. Thus, it appears that for the geometry and flow parameters that were considered in this study, the rotational effects have limited influence on the global interstage cavity flow structure. To further support this conclusion we present in Fig. 3c the contour images of the flow field when the side walls are rotating. The dark area zones are indicative of regions that have not been penetrated by the effects of the rotating side disks, and thus the w -component of the velocity is still close to zero. One can also see that since the mainstream w -velocity field was set equal to zero (boundary conditions), the main stream ingress into the interstage cavity areas prevents the development of strong rotation effects. Note that rotational components are strong only in the lower corners of the interstage cavity. It is also worth mentioning that in the area surrounding the brush seal, the flow rotational component is considerably diminished in value.

In Figs. 4a, and 4b one can see details that reveal the flow structure in the brush seal area for the cases with rotating (Fig. 4a), and respectively non-rotating side walls (Fig. 4b). One can again appreciate the complex flow formations that are taking place in the area where the brush seal is located. Because of the brush high resistance to flow passage, part of the secondary flow is reversing its direction towards the rotating wall. This effect becomes especially strong when the front cavity wall is rotating. It can

RESULTS AND DISCUSSION, 2

be seen that the flow entering the area between the front plate and the shaft is skewed and generally non-uniform. A major part of this flow is heading towards the clearance, where the velocity magnitude is several times higher than elsewhere. Part of the flow enters the brush (porous medium), and starts a slow motion along the brush walls. First downward and inside, and then upward, outside of the brush backing plate (BP). From Figs. 4a, and 4b we can clearly see that the radial component of the brush flow is comparable in size to the axial component. Thus the assumption that the radial component is negligible and the brush flow can be represented by the flow pattern of an axial cross-section, clearly does not hold. If one studies further the area near the BP and the gap between the BP and the shaft, one finds very complex flow structures, probably real, that could never be visualized if a set of simplified calculations (uniform inflow and specified outflow boundary conditions), or bulk calculations were made. We refer in particular to the secondary vortex that is splitting behind the BP, with part of it entering the gap area, meeting the leakage flow and reversing its direction.

The powerful leakage flow stream, is instrumental in shaping the flow pattern that fills the seal cavity, Figs. 5 and 6. This flow stream remains attached to the shaft surface, whether the shaft rotates or not. Note that the cavities' lateral walls are attached to the shaft, and when the shaft rotates so do the side walls. Figures 5a, and 5b demonstrate different flow patterns that appear in the seal cavity as the process progresses in time. The flow is completely past the transient developmental stage (from rest to steady state). However, its shape keeps evolving in time, proving that while a steady state is not existent, a quasi steady-state, somewhat periodic behavior has set in. When the shaft is rotating, Fig. 5a, we can clearly observe three secondary vortices of continuous and periodic changing flow patterns, which exchange momentum by means of the appearance and disappearance of the small middle vortex. In the case of the stationary shaft, Fig. 5b, one can distinguish two main secondary vortices. The second one of the two exhibits an elongated backward moving finger that interposes between the first main vortex and the leakage flow stream emerging from under the brush. The rotation of the shaft seems to stimulate the development of the two main vortices, and suppresses the minor vortices and their effects.

Extremely interesting is the flow formation that appears under high shaft rotation, and small flow leakage from the brush. Figure 5c presents just such a case. The decrease in leakage can follow from a strong reduction in seal clearance or

RESULTS AND DISCUSSION, 3

decreased brush permeability. The disappearance of the strong axial flow along the shaft allows the formation of Taylor vortices, between the inner rotating shaft and outer stationary cylinder(vane). This form of fluid instability creates three almost equal length vortices that fill the entire cavity between the vane and the rotating shaft. In effect, the apparition of the Taylor formations indicate the domination of the rotational effects upon the axial flow shear layer that contains the leakage fluid. Again, it is proven that the integrated cavity/seal approach allows increased insight in the many complicated flow features that are influencing the global flow field.

Figure 6 delivers a very intuitive insight into the effect of the rotating shaft on the patterns and penetration of the rotational effect into the flow of the seal cavity. The periodic nature of the flow can be observed again, together with the fact that the zone of higher rotational component(white color) penetrates inside the cavity, increasing its size, Figs. 6.1, 6.2, and 6.3, only to start returning to its initial size and location, as the flow cycles (Figs. 6.4, 6.5, 6.6, and 6.7) .

Quantitative mapping of the pressure development in the front and back cavities as well as in the seal cavity, Figs. 7a, 7b, and 7c support our qualitative conclusion that flow in the interstage cavity is periodic in nature. Thus, Fig. 7a shows variations of the pressure drop across the brush seal and in-between the front and back cavities. One can clearly assess the periodic variation of the pressure that is associated with a corresponding variation in the flow patterns. Figure 7b demonstrates the periodic behavior of the maximum velocity in the brush seal clearance area and at the seal cavity outflow boundary. In Fig. 7c the periodic nature of the rotational component in the front cavity is on display. Corroborated, all these data allows the important conclusion, that for high main flow Reynolds numbers(always the case in the gas turbine flow path) the fluid flow has a periodic oscillatory nature that require time-dependent terms in the governing equations. These terms are routinely omitted by some researchers (Ko et al., (1993), Iacovides and Launder(1991), Guo et al., (1994)).

CONCLUSIONS

The present paper presents work-in-progress results and model developments that are directed towards the computational fluid dynamics simulation of the secondary flow system of the gas turbine engine.

A computational algorithm and computer program (FLOCON) has been developed to model complex interstage gas turbine cavity flow with the brush seal inserted between adjacent cavities. A combination of two flow models, the first, for the brush seal (porous media assumption), and the second, for the interstage cavity (rotational axisymmetric flow) was successfully implemented into a single computational entity.

- The core flow is driven by an imposed pressure drop along the vane row of the main flow path.**
- Three interconnected disk cavities separated by a brush seal are located along the secondary flow path.**
- A new computational algorithm was developed in order to predict the flow patterns and leakages for different seal and cavity configurations.**
- The code is based on the numerical solution of the transient laminar Navier-Stokes equations, written in primitive variables and approximated on a nonuniform rectangular collocated grid.**
- The program uses a mass and momentum conservative formulation as well as a set of boundary conditions for pressure and conservation of mass. The pressure solution uses the Poisson equation under a direct implementation procedure.**

CONCLUSIONS

- **A time dependent Alternating Direction Implicit(ADI) method is also used for the solution of all primitive variables.**
- **This integrated computational approach allows the simulation of the rotating disk cavity vortex flow periodic features, as well as their impact on leakage flow and sealing effectiveness. In the present study this approach is used to numerically investigate the flow through the brush.**

The proposed integrated approach allows solutions for complex flow features that otherwise would not be accounted for. The results of the present study indicate that for some conditions rotational effects may be of minor effect for the brush seal flow and the global flow pattern. It was found that the flow in the brush seal penetrates inside the porous brush body and has stronger near wall(backing and front plates) absolute velocities.

Also, the axial velocity component is comparable with the radial velocity component due to lower flow resistance along the bristles. This fact brings up the conclusion that brush seal modeling when the brush is only represented by its axial (horizontal) cross-section is not self supporting.

In general, it was found that flow in the cavity has periodic nature, for both pressure, velocity and vortex formations.

REFERENCES, 1

Athavale, M.M., Przekwas, A.J., Hendricks, R.C., 1993, "Driven Cavity Simulation of Turbomachinery Blade Flows with Vortex Control", AIAA-93-0390, 31st Aerospace Sciences Meeting & Exhibit, Jan 11-14, 1993, Reno, NV

Braun, M.J., Kudriavtsev, V.V., 1993a, "A Numerical Simulation of a Brush Seal Section and Some Experimental Results", Int. Gas Turbine and AeroEngine Congress, Cincinnati, 1993, ASME Paper 93-GT-398, 1-12, (also Transactions of the ASME, Journal of Turbomachinery, Vol. 117, No.1, Jan. 1995, pp. 190-202)

Braun, M.J., Kudriavtsev, V.V., 1993b, "Numerical Visualization of Flow Structures in Dense Banks of Cylinders Located in a Channel", Third Int. Symposium on Experimental and Numerical Flow Visualization, 1993 ASME Winter Annual Meeting, New Orleans, Louisiana, Nov. 28 - Dec. 3, 1993/Eds. B. Khalighi, M.J. Braun, C.F. Freitas, D.H. Fruman, pp. 1-8, (accepted for the publication - ASME Journal of Fluids Engineering, March-1995)

Braun M.J., Kudriavtsev, V.V., 1992, "Experimental and Analytical Investigation of Brush Seals", Seals Flow Code Development-92, NASA CP-10124, Proceedings of a workshop held at NASA Lewis Research Center, August, 5-6, 1992, pp. 181-195.

Burmeister, L.C., 1993, "Convective Heat Transfer, John Wiley & Sons, pp.44-51.

Carlile, J.A., Hendricks, R.C., Yoder, D.A., 1993, "Brush Seal Leakage Performance with Gaseous Working Fluids at Static and Low Rotor Speed Conditions", 1993, Journal of Engineering for Gas Turbines and Power, Vol. 115, pp. 397-403

Chew, J.W., 1985, "Computation of Convective Laminar Flow in Rotating Cavities", J. Fluid Mech., Vol.153, p.339

Chupp, R.E., Dowler, C.A., "Performance Characteristics of Brush Seals for Limited-Life Engines", 1993, Journal of Engineering for Gas Turbines and Power, Apr. 1993, Vol. 115, pp. 390-396

Chupp, R.E., Holle, G.F., Dowler, C.A., 1991, "Simple Leakage Flow Model for Brush Seals", AIAA Paper No. 91-1913

Chupp, R.E., Holle, G.F., 1994, "Generalizing Circular Brush Seal Leakage Through a Randomly Distributed Bristle Bed", ASME Paper 94-GT-71, International Gas Turbine and AeroEngine Congress & Exposition, The Hague, Netherlands, June 13-16, 1994

Ergun, S., 1952, "Fluid Flow Through Packed Columns", Chem. Eng. Prog., Vol.48, No.2, pp. 89-94

Farthing, P.R., Long, C.A., Owen, J.M., Pincombe J.R., 1992, "Rotating Cavity with Axial Throughflow of Cooling Air: Flow Structure", ASME Journal of Turbomachinery, Vol. 114, pp. 237-246

Guo, Z., Rhode, D.L., Davis, F.M., 1994, "Computed Eccentricity Effects on Turbine Rim Seals at Engine Conditions with a Mainstream", ASME-94-GT-31, Int. Gas Turbine and Aeroengine Congress & Exposition, The Hague, Netherlands, June 13-16, 1994

REFERENCES, 2

Hendricks, R.C., Schlumberger, J., Braun, M.,J., Choy, F.C., Mullen, R.L., 1991, "A Bulk Flow Model of a Brush Seal System", ASME Paper No. 91 GT-325, 36th ASME International Gas Turbine and Aeroengine Congress & Exposition, Orlando, FL, June 3-6

Iacovides, H., Launder, B.E., 1991, "Parametric and Numerical Study of Fully Developed Flow and Heat Transfer in Rotating Rectangular Ducts", Journal of Turbomachinery, Jul. 1991, Vol. 113, pp. 331-338

Ivanushkin, S.G., Kim, L.V., Kondrashov, V.I., Tomilov, V.E., 1980, "Internal Transient Problems of Convective Heat Transfer", Tomsk University Publishers, Tomsk, pp. 1-150 (in Russian)

Ko, S.H., Rhode, D.L., Guo, Z., 1993, "Computed Effects of Rim Seal Clearance and Cavity Width on Thermal Distributions", ASME Paper 93-GT-419

Kudriavtsev, V.V., 1993, "Numerical Analysis of the Transient Fluid Flows in the Brush Seal Elements of the Aerospace Turbomachinery", Ph.D. Dissertation, Moscow Aviation Institute (in Russian)

Kudriavtsev, V.V., Braun, M.J., 1994, "Advances in Brush Seal Numerical Modeling", SAE Aerospace Atlantic '94 Conference and Exposition, SAE-TP-941208, /Advanced Dynamic Seals, Dayton, Ohio, pp.1-13 (Also AIAA Journal of Propulsion and Power, to be published in 1996).

Kuwahara, F., Nakayama, A., Koyama, H., 1994, "Numerical Modelling of Heat and Fluid Flow in a Porous Medium", Heat Transfer, 1994, Vol.5., Proceedings of the Tenth International Heat Transfer Conference, Brighton, UK, Paper-11-PP-18, pp. 309-314,

Ong, C.L., Owen, J.M., 1991, "Prediction of Heat Transfer in a Rotating Cavity with a Radial Outflow", ASME Journal of Turbomachinery, Vol. 133, pp.115-122

Owen, J.M., Onur, H.S., 1983, "Convective Heat Transfer in a Rotating Cavity", ASME Journal of Engineering for Power, v. 105, pp. 265-271

Przekwas, A.J., Athavale, M.M., Hendricks, R.C., 1994, "Progress in Advanced Modeling of Turbine Engine Seal Flows", AIAA-94-2803, 30th Joint Propulsion Conference

Roache, P.L., 1982, Computational Fluid Mechanics, Hermosa Publishers.

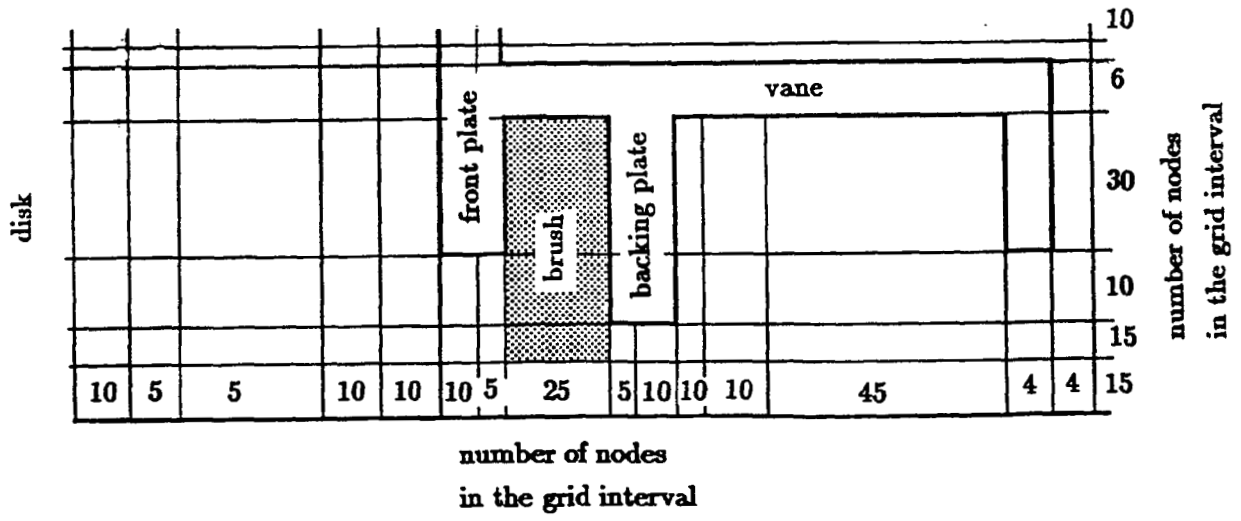
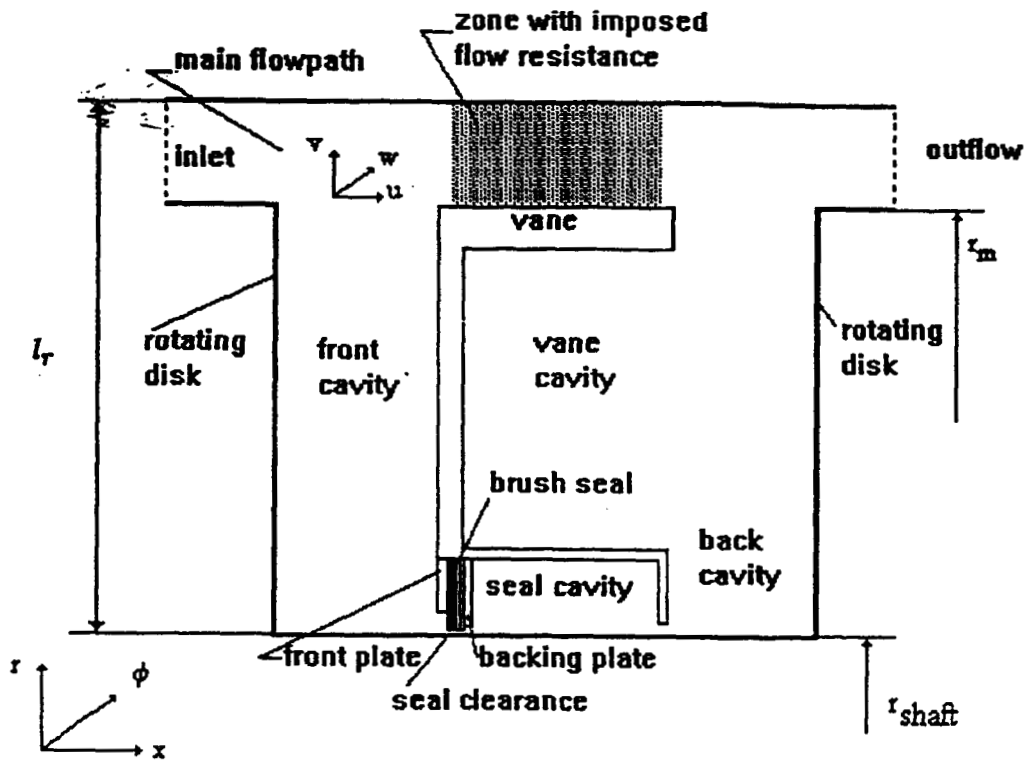
Schlichting, H., 1978, Boundary-layer Theory, N.Y., McGraw-Hill

Torrance, K.E., 1968, "Comparison of Finite-Difference Computations of Natural Convection", Journal Research NBS: Mathematical Sciences, N72B, 281.

Vaughan, C.M., Turner, A.B., 1987, "Numerical Prediction of Axisymmetric Flow in a Rotor-Stator System with an External Mainstream Flow", Proceedings 5th Int. Conf. on Numerical Methods in Laminar and Turbulent Flows, Swansea, UK.

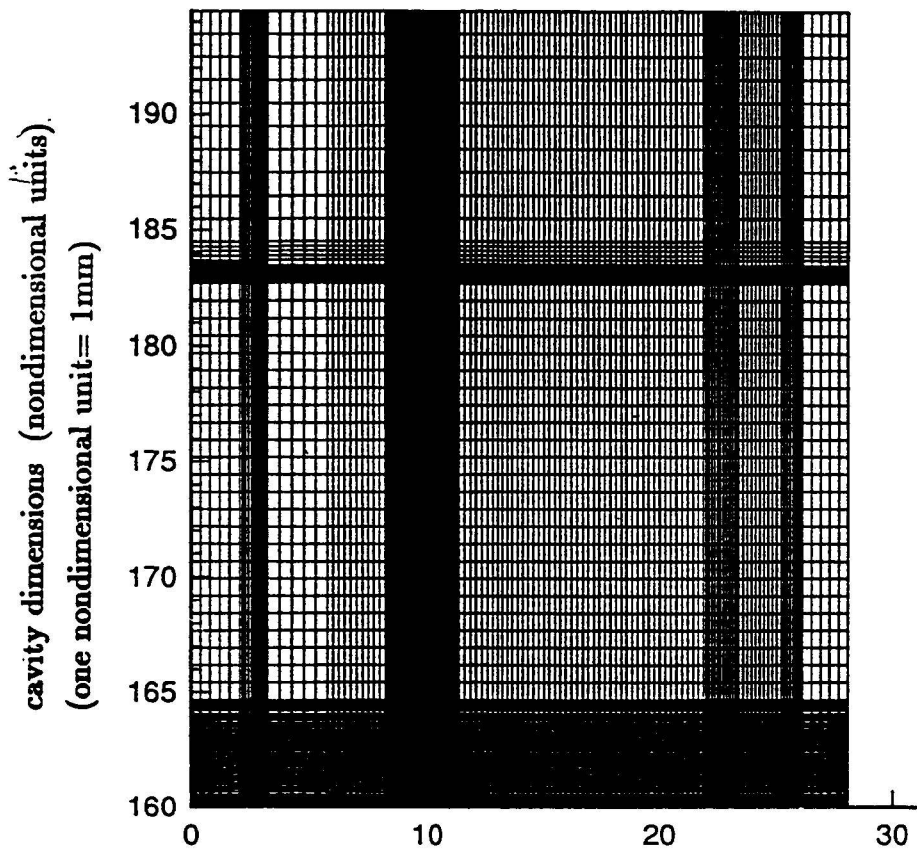
Virr, G.P., Chew, J.W., Coupland, J., 1993, "Application of Computational Fluid Dynamics to Turbine Disk Cavities", ASME Paper No. 93-GT-89.

Welch, E.J., Harlow, F.H., Shannon, J.P., Daly, B.J., 1966, "The MAC Method: A Computing Technique for Solving Viscous, Incompressible, Transient Fluid Flow Problems Involving Free Surfaces", Technical Report, Los Alamos Scientific Laboratory, LA-3425,UC-32, TID-4500



B) GRID INTERVALS AROUND THE BRUSH SEAL

FIGURE 1(A,B,C). SIMULATED INTERSTAGE CAVITY



C) COMPUTATIONAL GRID (209 x144)

FIGURE 1(A,B,C). SIMULATED INTERSTAGE CAVITY

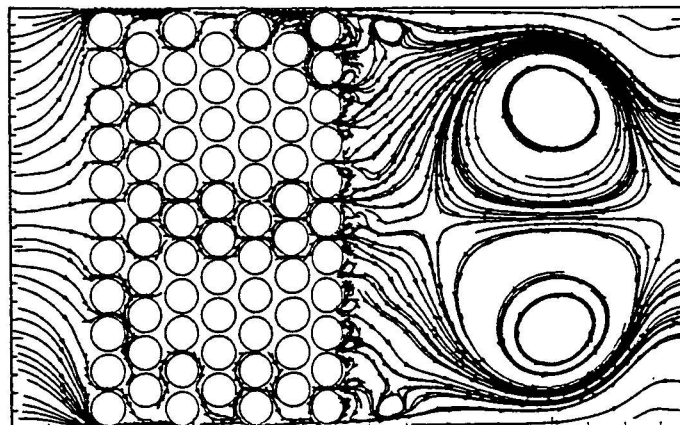


FIGURE 2 FLOW THROUGH THE SIMULATED BRUSH SEGMENT
LOCATED IN THE CHANNEL

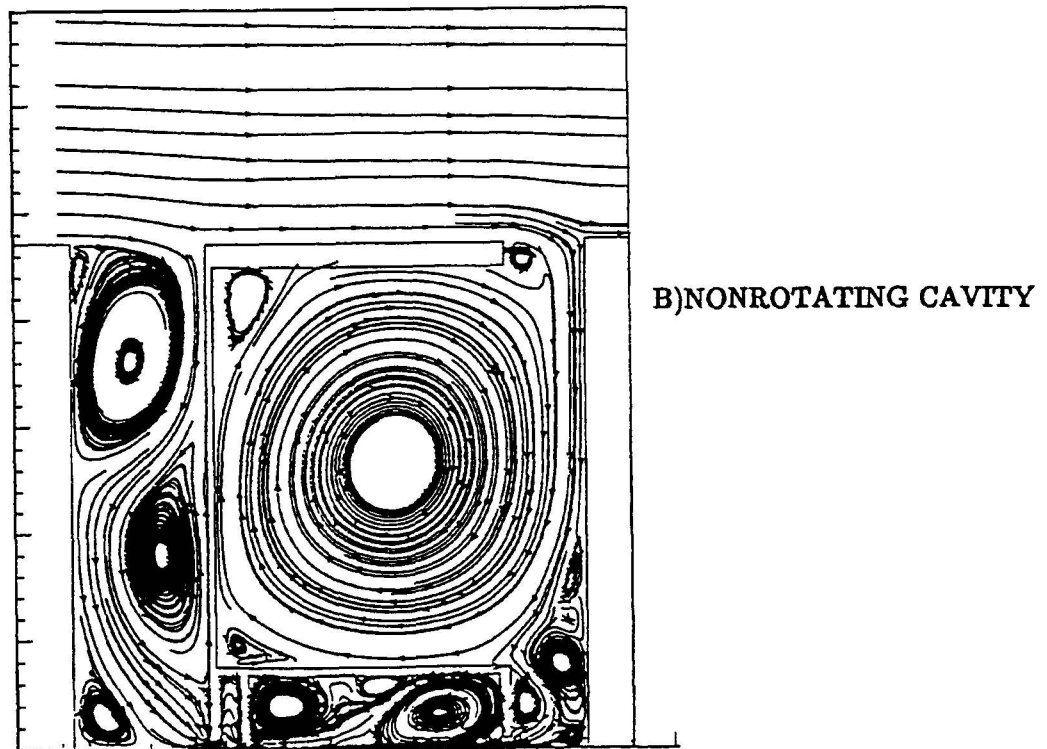
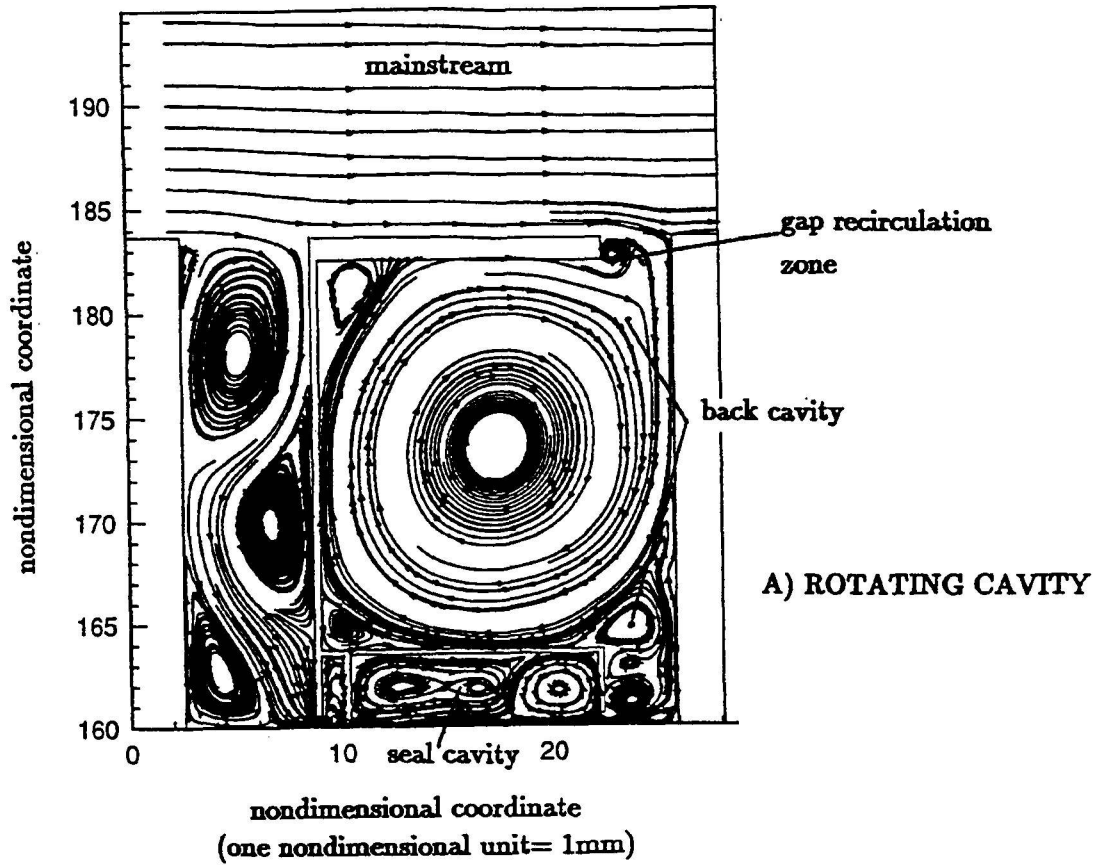


FIGURE 3 A,B). FLOW PATTERNS IN THE INTERSTAGE SEAL CAVITY

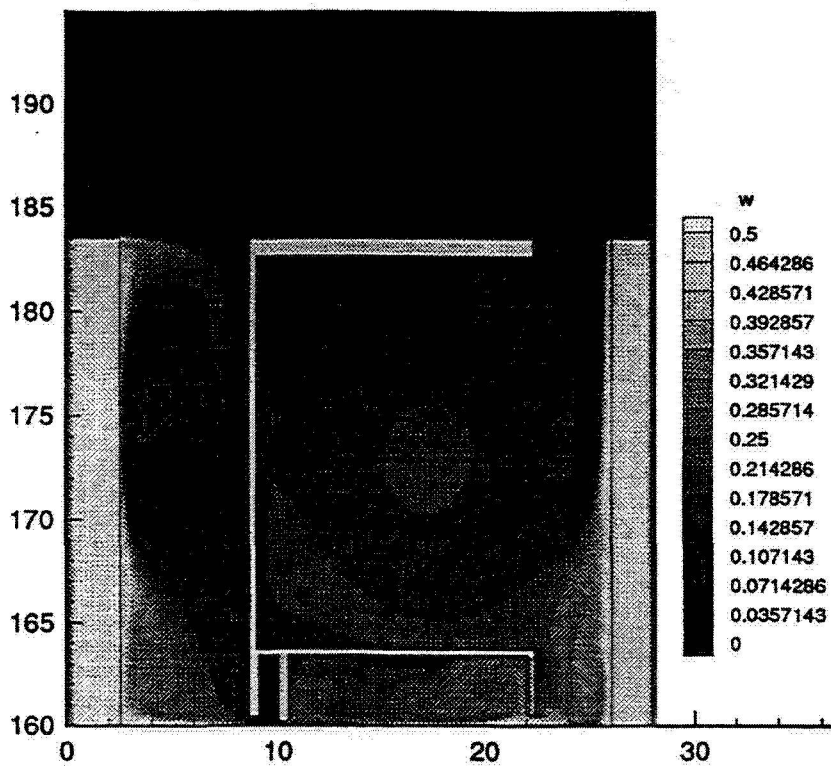


FIGURE 3 C FLOW PATTERNS IN THE INTERSTAGE SEAL CAVITY

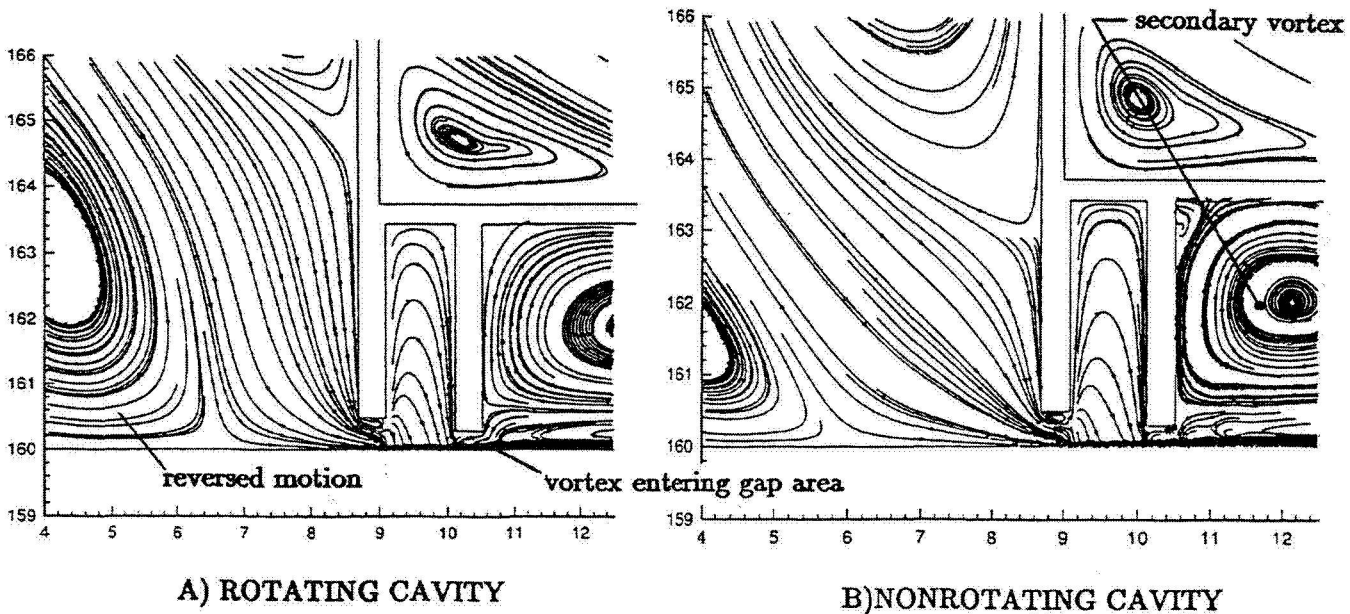


FIGURE 4(A,B) FLOWFIELD IN THE AREA SURROUNDING THE BRUSH SEAL

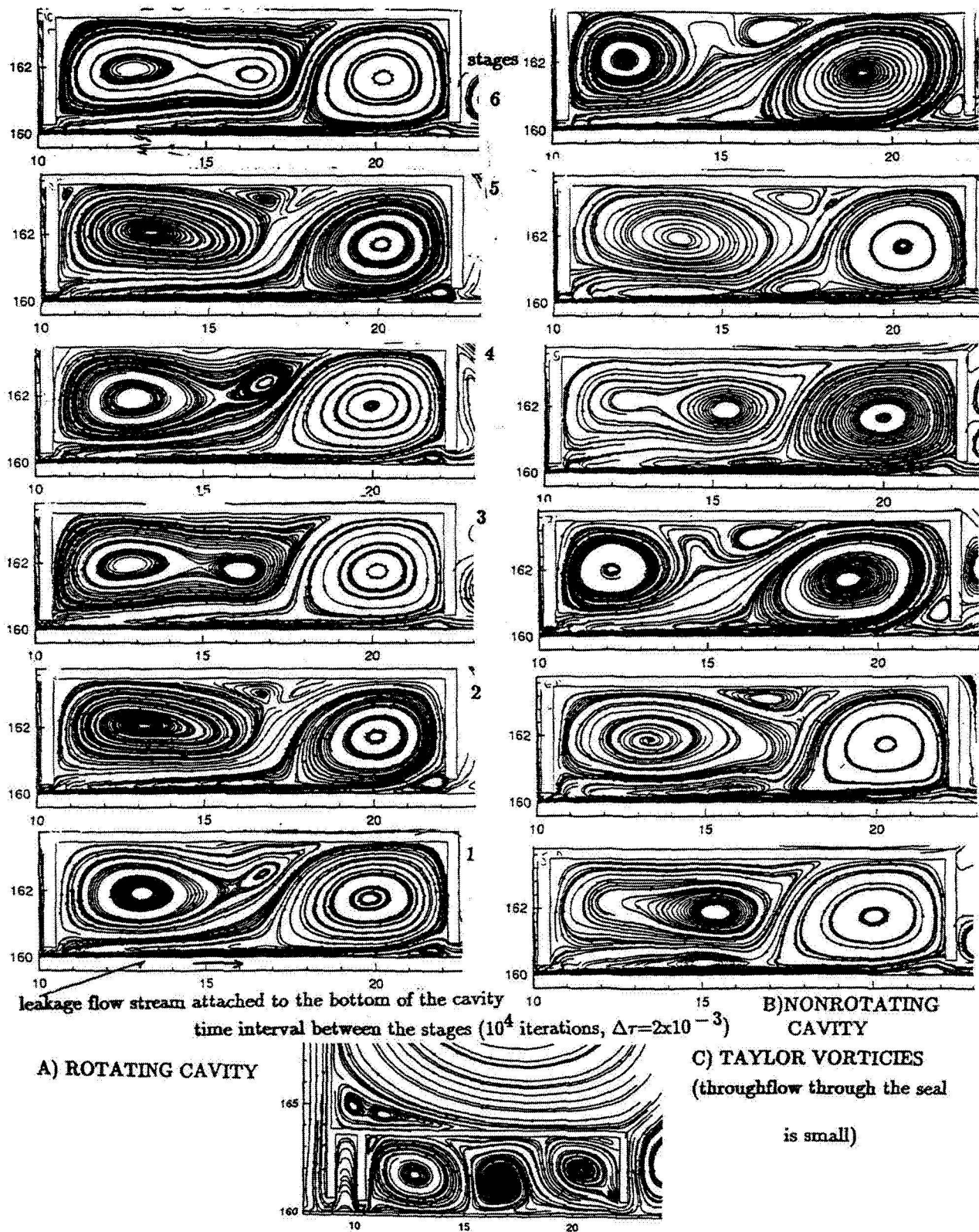


FIGURE 5(A,B,C). FLOW PATTERNS IN THE SEAL CAVITY

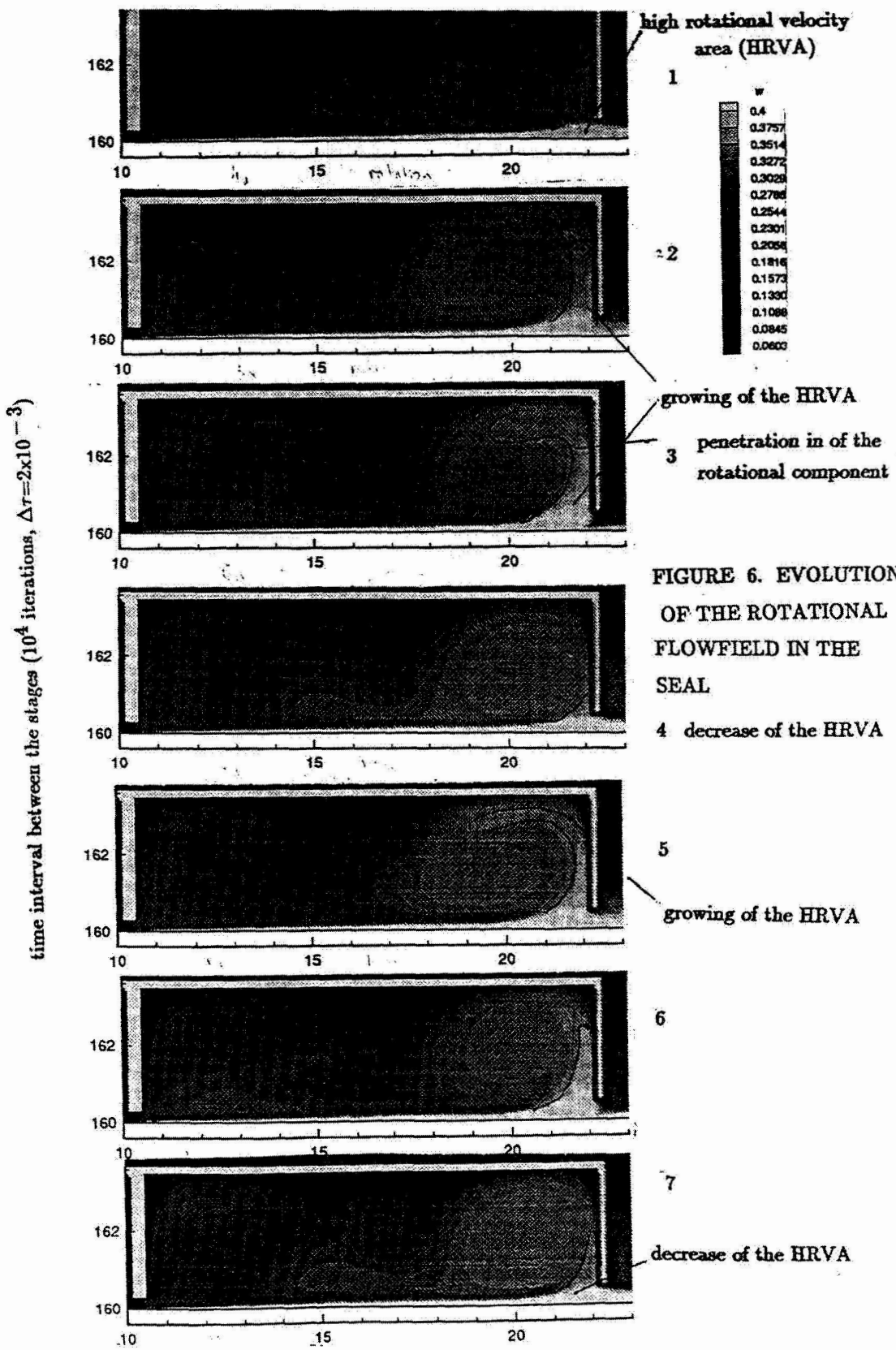
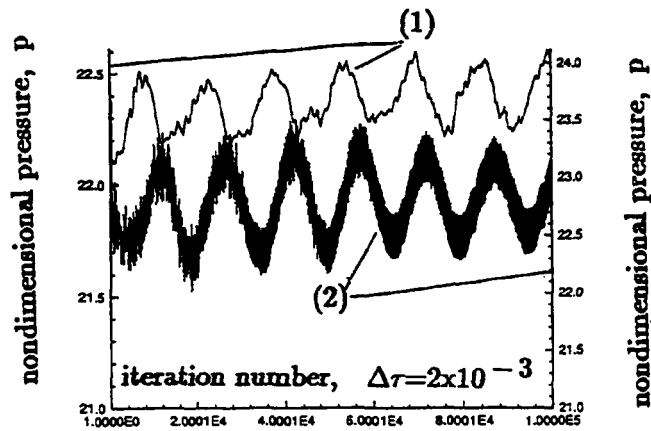
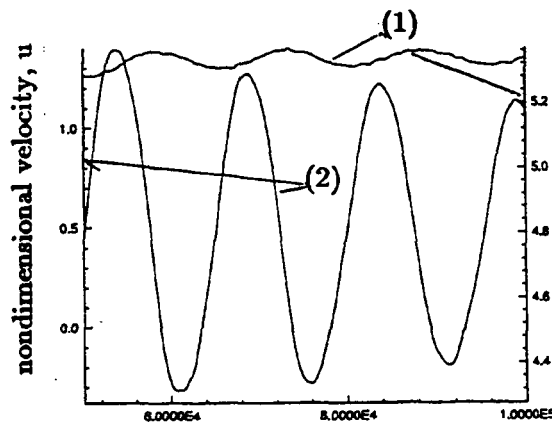


FIGURE 6. EVOLUTION OF THE ROTATIONAL FLOWFIELD IN THE SEAL

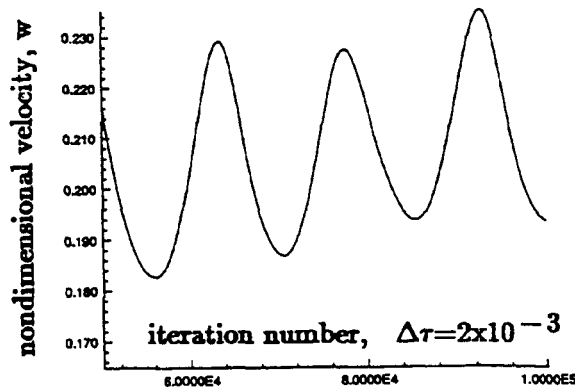


$$P(\text{dimensional}) = p \times \rho u_0^2$$

A) PRESSURE DROPS ACROSS THE BRUSH SEAL (1) and BETWEEN THE FRONT AND BACK CAVITIES(2)



B) AXIAL VELOCITY COMPONENT U
 (1) BRUSH SEAL CLEARANCE
 (2) SEAL CAVITY OUTFLOW



C) ROTATIONAL COMPONENT W (center of the front cavity)

FIGURE 7(A,B,C) PERIODIC FEATURES OF THE FLUID FLOW

TWO-DIMENSIONAL DYNAMIC SIMULATION OF A CONTINUOUS FOIL BEARING

M.J. Braun, F.K. Choy, M. Dzodzo, and J. Hsu
Department of Mechanical Engineering
The University of Akron
Akron, Ohio

517-37

39459

1 SCOPE OF WORK

In this paper, the two dimensional (radial and circumferential) transient Navier-Stokes equations are used to solve the hydrodynamic problem in conjunction with the time dependent motion of the journal, and the deformable, spring supported foil, Fig. 1A. The elastic deformation of the foil and its supports are simulated by a finite element model. The time-dependent Navier-Stokes formulation is used to solve for the interaction between the fluid lubricant, the motion of the journal and the deformable foil boundary. The steady state, the quasi-transient and the full transient dynamic simulation of the foil-fluid-journal interaction are examined on a comparative basis. For the steady state simulation, the fluid lubricant pressures are evaluated for a particular journal position, by means of an iterative scheme until convergence is achieved in both the fluid pressures and the corresponding foil deformation. For the quasi-transient case, the transient motion of the journal is calculated using a numerical integration scheme for the velocity and displacement of the journal. The deformation of the foil is evaluated through numerical iteration in feedback mode with the fluid film pressure generated by the journal motion until convergence at every time step is achieved. For the full transient simulation, a parallel real-time integration scheme is used to evaluate simultaneously the new journal position and the new deformed shape of the foil at each time step. The pressure of the fluid lubricant is iterated jointly with the corresponding journal position and the deformed foil geometry until convergence is achieved. A variable time-stepping Newmark-Beta[1] integration procedure is used to evaluate the transient dynamics at each time step of the bearing (Choy et al.[2,3], Braun et al.[4]).

For simplicity in the numerical solution, an infinitely long bearing (two dimensional in the radial and the circumferential directions) is used for the purpose of parametric demonstration.

2 NOMENCLATURE

h	characteristic length; $h=R_s/1000$	
J	Jacobian of the coordinate transformation; $y^j=y^j(x^j)$	
$[K]_g$	Matrix stiffness: foil and its support in global coordinates	
$[M_f]$	Mass matrix of the foil	
M_j	Mass of the journal	
P	dimensionless pressure; $P=p/\rho(\nu/h)^2$	
R_s	shaft radius	
S	source term	
t	time	
U_i	dimensionless Cartesian velocity vector component; $U_i=u_i/h/\nu$	
U_i	dimensionless covariant velocity components (normal to	the cell faces), $U_1\beta_1^i+U_2\beta_2^i$
x^j	curvilinear coordinate	
X^j	dimensionless general curvilinear coordinate; $X^j=x^j/h$	
$y_j^{1,2}$	displacement of the journal	
y^j	Cartesian coordinate	

- Y^j dimensionless Cartesian coordinate; $Y^j=y^j/h$
 β_j^i cofactor of the i-th row and j-th column of the Jacobian matrix
 ν kinematic viscosity
 ρ density
 τ dimensionless time; $\tau=t\nu/h^2$
 $\delta y^{1,2}$ displacement of the foil

3 THE ANALYTICAL MODEL

The transient fluid lubricant behavior is modeled by the joint solution of the continuity equation

$$\frac{\partial}{\partial X^i} (U_k \beta_k^i) = \frac{\partial U_1}{\partial X^1} + \frac{\partial U_2}{\partial X^2} = JS_m \quad (1)$$

where $U_j = U_1 \beta_1^j + U_2 \beta_2^j$, and the momentum equations

$$\frac{\partial U_i}{\partial \tau} + \frac{\partial}{\partial X^i} [U_j U_i - \frac{1}{j} (\frac{\partial U_i}{\partial X^m} \beta_k^j \beta_k^m + \frac{\partial U_k}{\partial X^m} \beta_i^m \beta_k^j) + P \beta_i^j] = 0 \quad (2)$$

where β_j^i represents the cofactor of the i-th row and j-th column in the Jacobian matrix J of the coordinate transformation $y^i = y^i(x^j)$; y^i is the reference Cartesian coordinate system. The finite volume method based on the finite difference method was applied for the numerical simulation which uses nonorthogonal coordinates (Fig. 1B) and a collocated grid. The SIMPLE procedure of Patankar and Spalding[5] was used for solving the set of equations. The code developed by Dzodzo[6] has been used after imposing modifications for the boundary conditions. The collocated control volume cells, corresponding to the arbitrary coordinates x^1, x^2 and the reference Cartesian coordinate y^1, y^2 system are presented in Fig. 1B. For the steady state and the quasi-transient cases, assuming the foil deformation follows closely the effects of the journal motion, the deformation of the foil is modeled by a combination of bending elements supported by external linear springs, Fig. 1A. The foil structural model is developed by installing the localized bending elements stiffness matrix into the global matrix. The deformation of the foil is calculated by solving the force equations as

$$\begin{Bmatrix} \delta y^1 \\ \delta y^2 \end{Bmatrix} = [K]_g^{-1} \begin{Bmatrix} F_{y^1} \\ F_{y^2} \end{Bmatrix} \quad (3)$$

where $[K]_g$ is the global stiffness matrix of the foil structure, and F_{y^1} and F_{y^2} are the y^1 and y^2 direction forces acting on the foil through the fluid lubricant. These forces are evaluated by integrating the fluid pressure at the foil boundary, for the i-th location, as

$$F_{y^1} = (1/2) \left(\int_{\theta_{i-1}}^{\theta_i} p \cos \theta d\theta + \int_{\theta_i}^{\theta_{i+1}} p \cos \theta d\theta \right) \quad (4)$$

and

$$F_{y^2} = (1/2) \left(\int_{\theta_{i-1}}^{\theta_i} p \sin \theta d\theta + \int_{\theta_i}^{\theta_{i+1}} p \sin \theta d\theta \right) \quad (5)$$

The transient motion of the journal in the y^1 and y^2 directions can be represented with the following equations

$$\ddot{y}_j^1 = (1/M_j) \left(\int_0^{2\pi} P \cos \theta d\theta + f_{u^1}(t) \right) \quad (6)$$

and

$$\ddot{y}_j^2 = (1/M_j) \left(\int_0^{2\pi} P \sin \theta d\theta + f_{u^2}(t) \right) \quad (7)$$

In Eqs. 6 and 7, $f_{y1}(t)$ and $f_{y2}(t)$ are the forces due to mass imbalance in the Y^1 and Y^2 directions. The accelerations \ddot{y}_j^1 and \ddot{y}_j^2 are then integrated numerically to evaluate the velocity and displacement of the journal at each time steps. For the full-transient case, the transient motion of the foil is evaluated in parallel with the transient motion of the journal.

$$\begin{Bmatrix} \delta\dot{y}^1 \\ \delta\dot{y}^2 \end{Bmatrix} = [M_f]^{-1} \left(\begin{Bmatrix} F_{y1} \\ F_{y2} \end{Bmatrix} - [K]_s \begin{Bmatrix} \delta y^1 \\ \delta y^2 \end{Bmatrix} \right) \quad (8)$$

Both foil and journal transient equations, Eqs. 6 and 7 and the foil Eq. 8 are solved simultaneously. Taking into account the load forces and initial conditions of both the journal and the foil, the transient motion of the journal and the foil were calculated independently by using the Newmark Beta integration procedure.

4 DISCUSSION OF RESULTS

To demonstrate the above developed procedure, a 4in(10.16cm) diameter bearing was used as an example. A thin circular foil of 0.01in(0.254mm) thickness is supported at 60 equally spaced locations around the outer circumference, Fig. 1A, by radial linear springs with a stiffness of 50,000lb_f/in(8.756*10⁶N/m). The radial clearance between the foil and the journal is 0.003in (0.0762mm) and the fluid lubricant has a dynamic viscosity of 1.26*10⁻⁶lb_f-s/in² (8.68*10⁻³kg/s-m), and density of 2.846*10⁻²lb_m/in³ (787.7kg/m³). A vertical load of 500lb_f was applied to the journal operating at rotational speeds ranging from 1000 to 4000 rpm.

Figure 3 shows, for various operational speeds, the comparison between the steady state journal equilibrium positions for a rigid journal bearing and the same dimension compliant foil bearing. Note that in both cases, the equilibrium positions shift towards the bearing center as speed increases(Choy et al.[2], Braun et al.[4]). However, for the foil bearing due to the deformation of the foil, Fig. 3, the equilibrium position of the journal is shifted in the direction of the occurrence of the deformation. This shift, appears to occur in order to maintain a certain minimal radial clearance, necessary to the build-up of the self acting pressure wedge(similar to the pressure distribution mechanism in the rigid journal bearing). Figures 4A and 4B depict the fluid film pressure distribution in the bearing clearance for both the foil and rigid journal bearings. Note that in Fig. 4A, for the foil bearing, when the journal speed decreases to 1000rpm, the positive pressure recedes circumferentially and achieves a higher peak pressure than that of the rigid bearing, Fig. 4B. The explanation can be found only when one considers Figs. 3 and 4 together. By inspection, one can see that as the lower speeds are characterized by steady state shaft positions further away from the geometric center, the smaller minimum clearances exhibited by the compliant foil bearing will generate the higher peaks observed in fig. 4A. Figure 5A presents the stiffness characteristics of both the rigid journal and foil bearings at various operating speeds. Note that at the lower operating speed of 1000 rpm, the cross-coupled stiffness, $K_{xy}(K_{y^1y^2})$ for the foil bearing is substantially lower(40%) than that of the rigid bearing. As the speed increases, to 4000rpm, the two curves run with almost parallel slopes, and thus the difference between their magnitudes remains relatively constant. However, their absolute magnitude has now increased to 1.2*10⁶lb/in (2.1*10⁸N/m). Under these circumstances the reduction in the $K_{xy}(K_{y^1y^2})$ of the foil bearing represents only 10% difference from that of the rigid bearing. At the same time, the direct stiffness, $K_{xx}(K_{y^1y^1})$ and $K_{yy}(K_{y^2y^2})$, remain relatively the same. This reduction in the cross coupling stiffness of the foil bearing shows that this device offers improved stability when compared to the rigid bearing. For damping, Fig. 5B shows a reverse trend, as the foil bearing exhibits lower direct damping characteristics, $C_{xx}(C_{y^1y^1})$ and $C_{yy}(C_{y^2y^2})$, than those of the rigid bearing. However, this trend is not as pronounced as the effects observed in the stiffness characteristics of Fig. 5A. This phenomenon is further corroborated by the stability characteristics exhibited by the logarithmic decrement graph shown in Fig. 6. A study of this figure shows that the foil bearing provides a better stability at lower speed, and its advantage decreases with respect to the rigid bearing, as speed increases.

In order to verify the linear steady state analysis performed in the previous example, a time transient analysis was carried out for the same foil bearing. Figure 7A depicts the quasi-transient simulation(without the inertia effects of the foil) of the journal motion with a mass imbalance eccentricity of $e_m=0.005$ in. at a rotational speed of 1,000rpm. During the transient motion, the journal moves quickly into its steady state elliptical orbit as predicted by the linear stability analysis, Fig. 6, and proves the system to be highly stable. Figure 7B shows the journal motion for the same case using the full transient simulation, i.e., including the foil inertia effects. Note that the full transient progresses quickly into the steady state orbit, in the same manner as the quasi-transient, but with a relatively smaller orbit amplitude. The most likely explanation is, that due to the transient motion of the foil, a higher damping effect is being generated in the system, which in turns, results in smaller vibration amplitudes.

In order to examine the nonlinearities of the foil bearing, the same analysis is performed for a journal rotational speed of 4,000rpm, where the linear analysis predicts an unstable behavior. During this simulation, the quasi-transient procedure fails to converge to a reasonable result as the calculated deformed shape of the foil changes considerably from one time step to another in an irrational and discontinuous manner. This phenomenon is possibly due to the fact that during the quasi-transient analysis, the foil deformed position is iterated together with the fluid pressure, and forced to converge at the same time. Such a procedure implicitly assumes that the foil will move instantly to its deformed position following the motion of the journal and pressure changes without any delay. However, due to the presence of the mechanical inertia of the fluid in the gap between the journal and the foil, and due to foil's own mechanical inertia, such motion is practically impossible, especially at higher speeds. To confirm this theory, the full transient analysis was performed at 4,000 rpm. Figure 8A depicts the orbit of the journal motion and the corresponding foil deformation at consecutive time steps. The change in the lubricant pressure curve during this transient motion is shown in Fig. 8B. Note that now, both the resulting foil deformation and the corresponding pressure are continuous and follow in a logical manner. Thus one may conclude from this exercise that, when higher speed and/or nonlinearity behavior are involved, a full transient simulation is required to provide an adequate prediction of the performance of the system.

Figure 9 shows the journal motion for the full transient case at 4,000 rpm. Note that, due to the instability of the system, the journal motion goes into a "limit cycle" type orbit. Note that the deformed shape of the foil is smoothly continuous and even though we are witnessing a limit cycle behavior, the clearance between the shaft and the foil shows that the system has overcome instability and it can function without damage in this state. This outcome is probably due to the compliance of the foil. Due to this large deformation, the converging and diverging zones of the fluid are substantially different than those of a rigid journal bearing, and the existence of the large deformation in the foil further confirms the necessity of a flexible foil transient model to accurately predict the performance of the system.

5 CONCLUSIONS

A numerical model to simulate the steady state and transient dynamics of a foil bearing was developed. Results from the foil bearing analysis are compared to those from a rigid journal bearing. The conclusions drawn from this study are as follows:

1. The dynamics of the fluid film can be effectively simulated using the Navier-Stokes equations, and any limitations concerning inertia effects have been eliminated. The procedure allows a natural calculation of the damping coefficients and is compatible with the dynamic formulation of the problem.
2. The foil bearing can provide better system stability than a rigid journal bearing.
3. The location of the journal equilibrium position can change substantially, on comparison with the rigid bearing, due to the possible large deformation of the foil. The peak pressure in a foil bearing will be higher than of its rigid counterpart for the lower velocities(1000rpm), while for the higher ones(Figs. 4),

the pressure generating the load carrying capacity, and the pressure peaks will be lower and distributed more evenly around the circumference of the bearing.

4. For cases without large foil deformation or journal eccentricity, the linear steady state analysis is accurate, and sufficient.

5. When higher rotational speed and/or nonlinearity are involved, a full transient simulation(foil-fluid-rotor) is required in order to provide an adequate prediction of the performance of the system. The quasi-transient(without foil inertia) or the linear analysis will not be able to provide an accurate simulation of the event.

6 ACKNOWLEDGMENT

The work presented in this paper was supported in part by NASA Lewis Research Center, Cleveland, Ohio under grant NAG3-1366. The continuous support of NASA Technical Project monitor, Mr. Jim Walker, is greatly appreciated.

7 REFERENCES

1. N.M. Newmark, "A Method for Structural Dynamics", J. of the Engineering Mechanics Division, Trans. ASCE, EM3, July 1959, pp. 67-94.
2. F.K. Choy, M.J. Braun, and Y. Hu, "Nonlinear Effects in a Plain Journal Bearing - Part 1 : Analytical Study" ASME Journal of Tribology, Vol. 113, No.3, pp.555-562, July 1991.
3. F.K. Choy, M.J. Braun, and Y. Hu, "Nonlinear Transient and Frequency Response Analysis of a Hydrodynamic Journal Bearing", ASME Journal of Tribology, Vol. 114, No. 3, July 1992, pp. 448-454.
4. M.J. Braun, F.K. Choy, and Y. Hu, "Nonlinear Effects in a Plain Journal Bearing - Part 2 : Results" ASME Journal of Tribology, Vol. 113, No.3, pp.563-570, July 1991.
5. S.V. Patankar, and D.B. Spalding, "A Calculation Procedure for Heat, Mass and Momentum Transfer in Three-Dimensional Parabolic Flows", Int. J. Heat Mass Transfer, Vol. 15, p. 1787.
6. M. Dzodzo, "Laminar Natural Convection in Some Enclosures of Arbitrary Cross Section", Ph'D Thesis, Faculty of Mechanical Eng., University of Belgrade

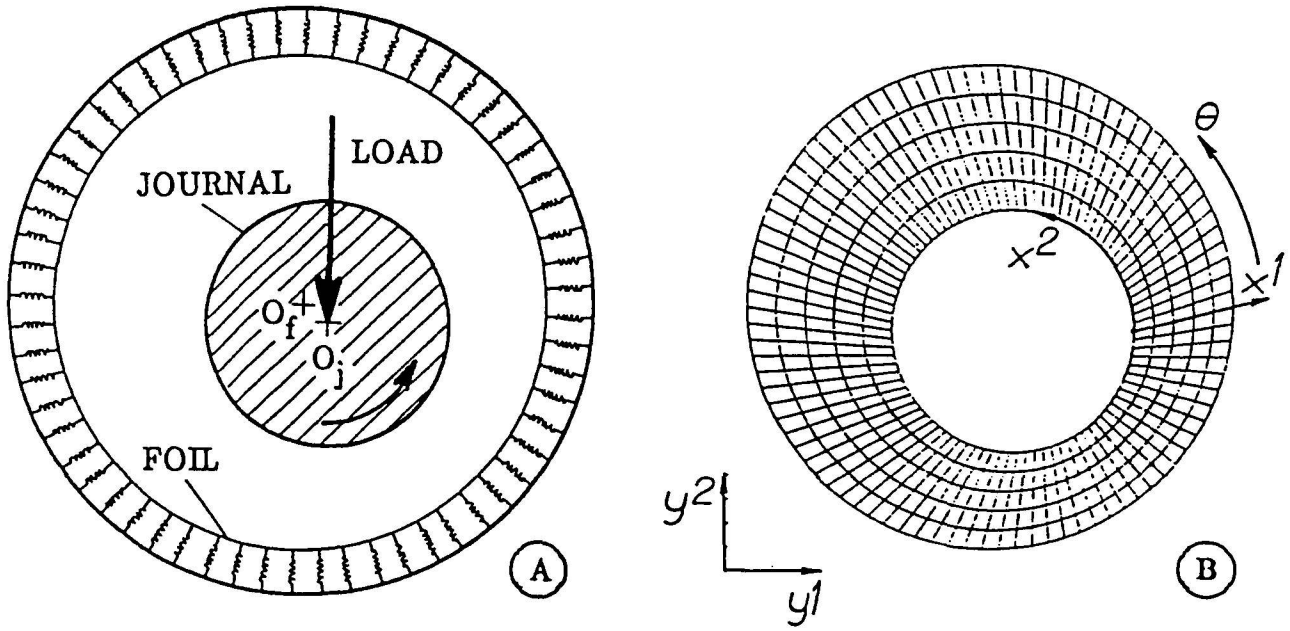


FIGURE 1. Analytical Model of the Foil Bearing System:
 (A) The Foil Bearing; B) The Fluid Lubricant Model

STEADY STATE ANALYSIS

TRANSIENT ANALYSIS

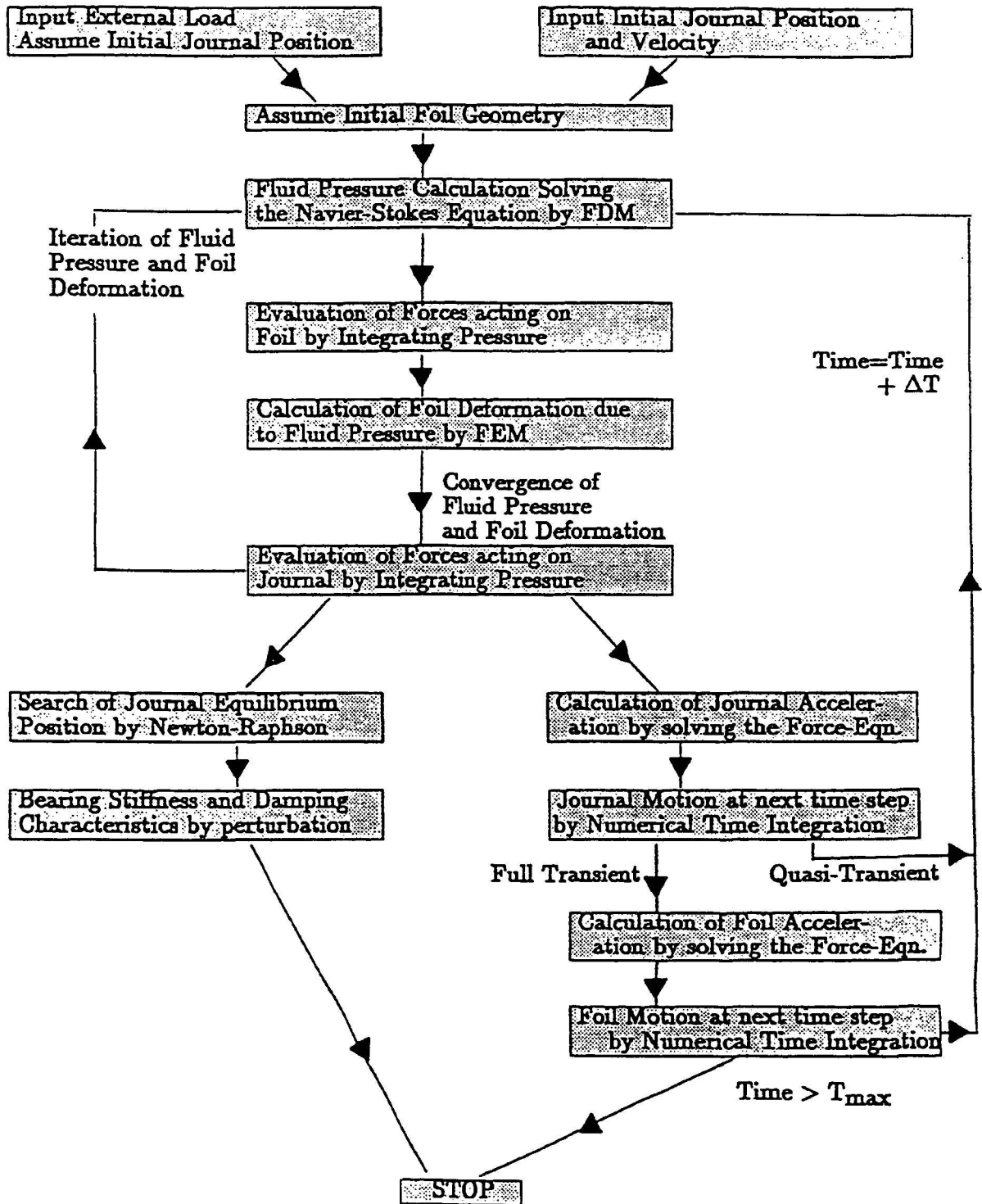


FIGURE 2. Flow Chart for the Steady-State, Quasi-Transient, and the Transient Numerical Simulations

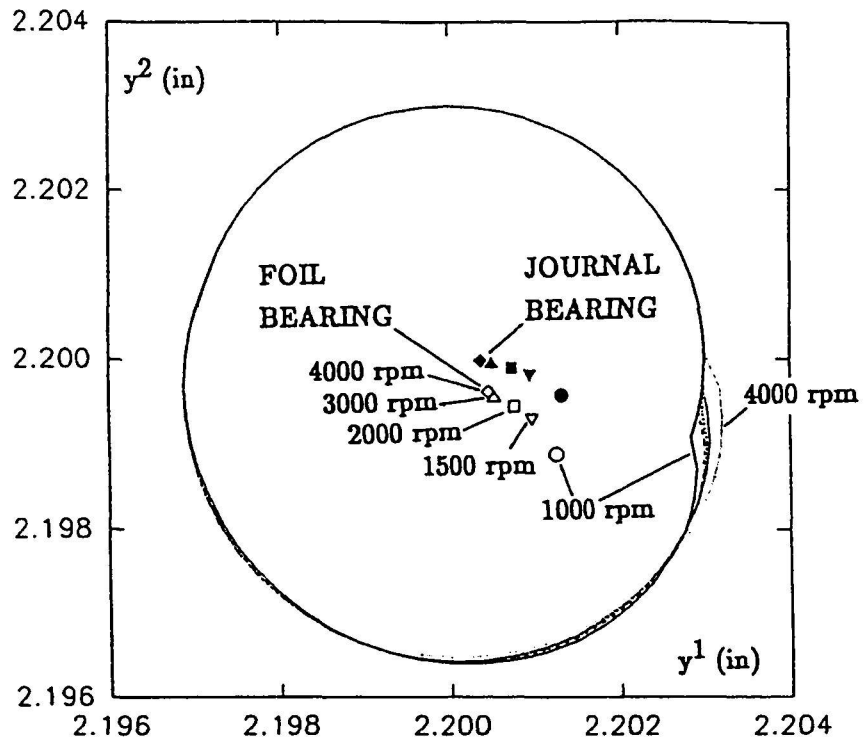


FIGURE 3. Equilibrium Position of the Journal for the Rigid and the Compliant Foil Bearings

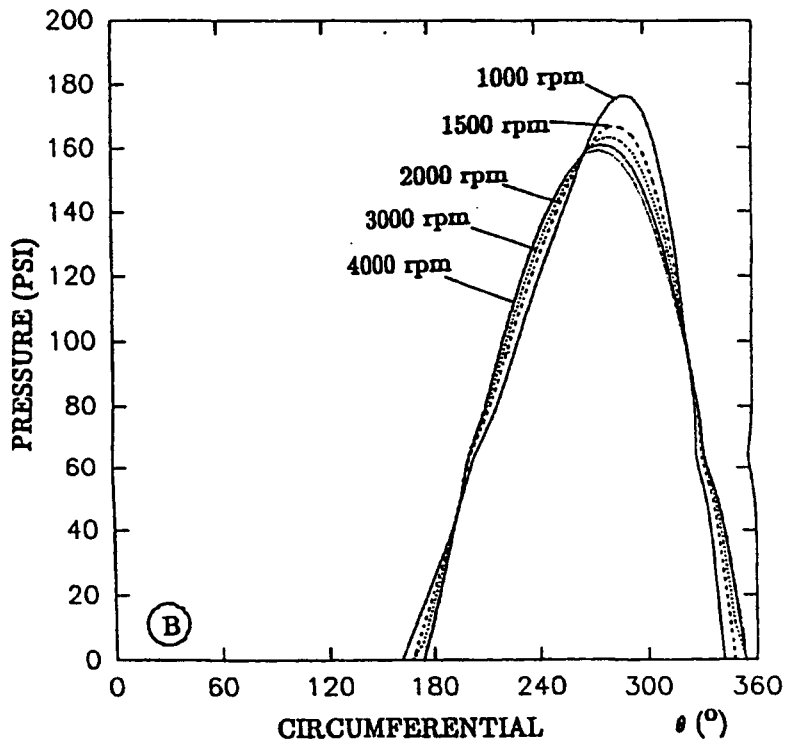
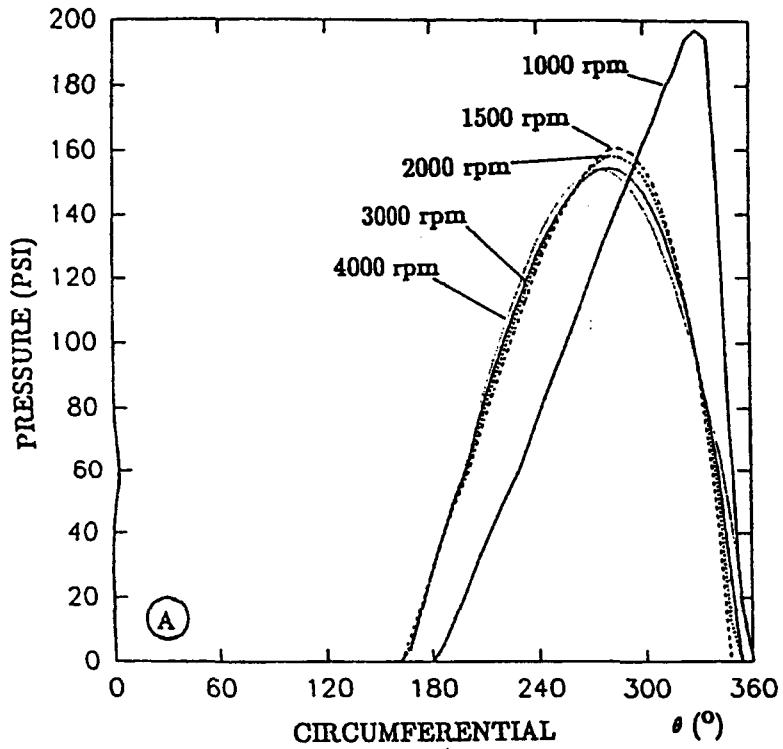


FIGURE 4. Pressure Profile with Various Operating Speeds: (A) Compliant Foil Bearing; (B) Rigid Bearing

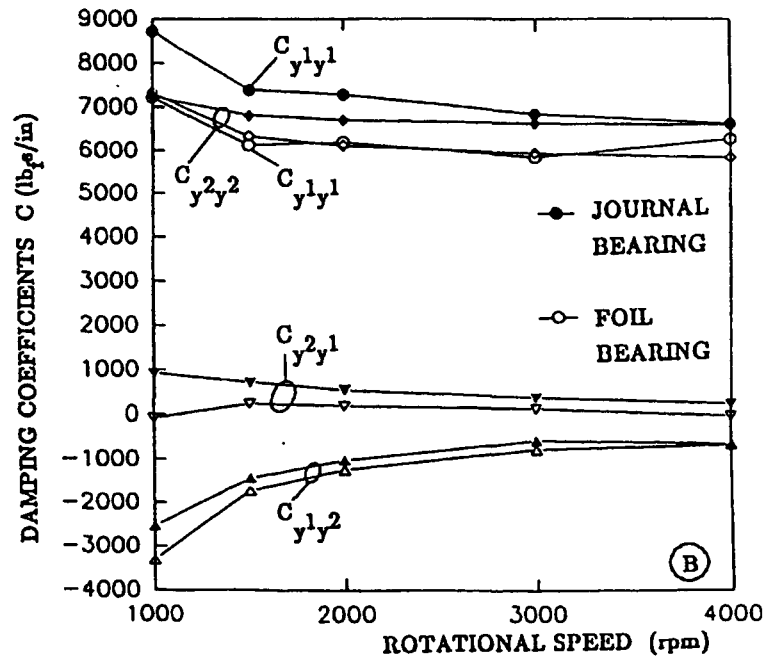
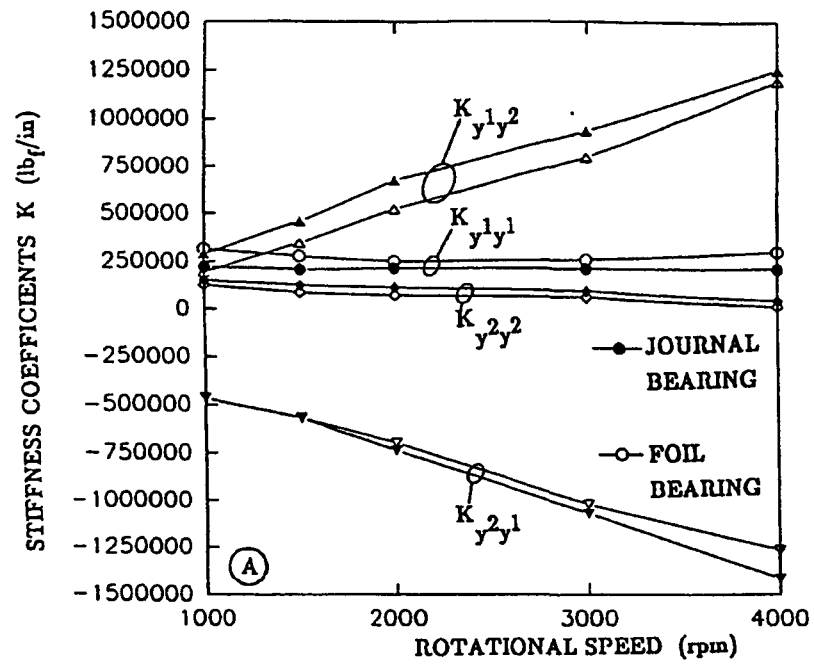


FIGURE 5. Bearing Characteristics for both the Rigid and the Compliant Foil Bearings. (A) Stiffness; (B) Damping

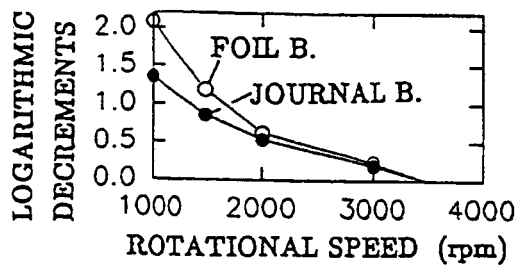


FIGURE 6. Logarithmic Decrement of the Journal Stability for the Rigid and the Compliant Foil Bearings

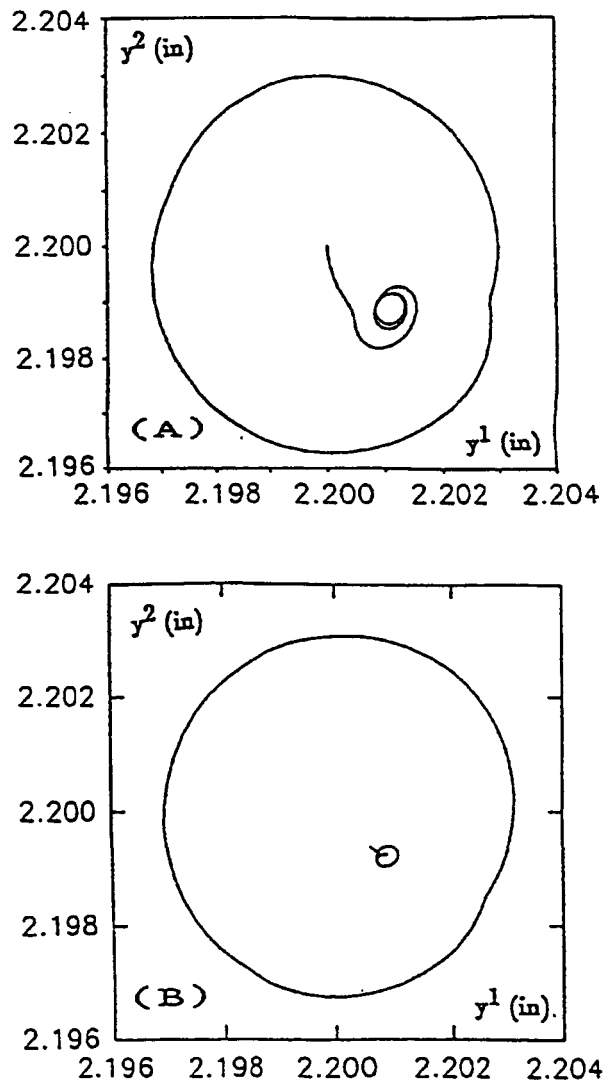


FIGURE 7. Transient Trajectories of the Journal Center at 1000 rpm. (A) Quasi-Transient; (B) Full Transient

CONSEQUENT DEFORMED FOIL SHAPE
 AT TIME STEP 4580, 4620, AND 4660

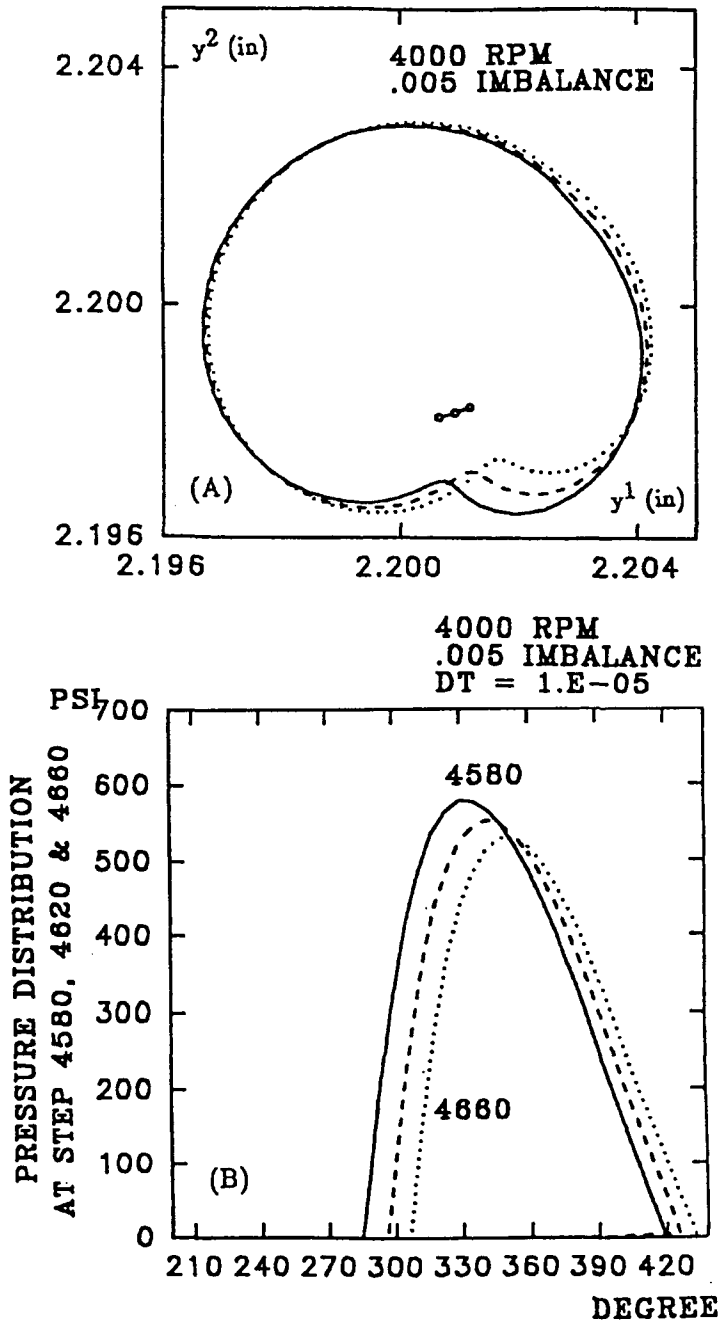


FIGURE 8. Full Transient Model at 4000rpm. (A) Foil Deformation and Journal Motion; (B) Fluid Pressure Profile

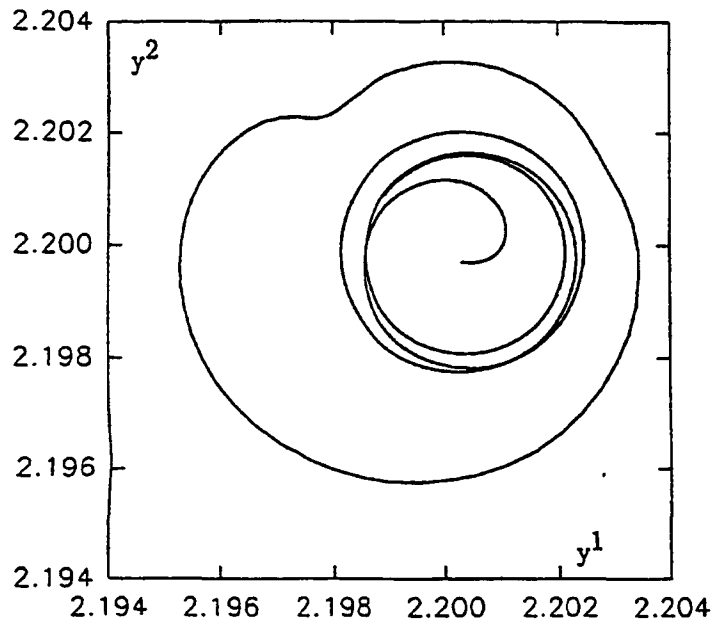


FIGURE 9. Full Transient Orbit of the Journal at 4000rpm

THREE DIMENSIONAL FLOW AND PRESSURE PATTERNS IN A HYDROSTATIC
JOURNAL BEARING

M.J. Braun and M.B. Dzodzo
Department of Mechanical Engineering
The University of Akron
Akron, Ohio

518-34
39460

The flow in a hydrostatic journal bearing (HJB) is described by a mathematical model that uses the three dimensional non-orthogonal form of the Navier-Stokes equations. Using the u , v , w , and p , as primary variables, a conservative formulation, finite volume multi-block method is applied through a collocated, body fitted grid. The HJB has four shallow pockets with a depth/length ratio of 0.067 . This paper represents a natural extension to the two and three dimensional studies undertaken prior to this project (see literature review, Braun, and Dzodzo,1995).

The geometry of the HJB configuration can be seen in Fig. 1. The figure presents the pockets positioned symmetrically in the axial direction, while the adjacent lands are connected circumferentially. The present approach takes into account the finite width of the pockets and bearing lands, thus requiring a three dimensional treatise of the flow for the entire bearing. The process is steady-state, the fluid is Newtonian, and incompressible.

The governing equations of motion were cast in a dimensionless form. The characteristic length (h), is of the order of magnitude of the clearance and has been chosen to be 0.001in(0.0254mm). The equations are written in a general form for a non-orthogonal body fitted coordinate system in accordance with a formulation first presented by Peric(1985). The three dimensional approach to the problem required the application of the multi-block technique, in order to accommodate the geometry of the bearing. A literature review, as well as some details about the concept and application of the multi-block approach are presented by Rizzi et al.(1993). The individual blocks contain collocated control volume cells anchored in a system of corresponding local arbitrary coordinates. The local system of coordinates is then referenced to a global Cartesian system.

The case presented here is that of a hydrostatic jet dominated flow which generates a flattened central vortical cell(CVC) in the downstream part of the pocket, while a fluid turn-around zone(TAZ) occupies all the upstream space, Fig. 2, thus preventing any exit flow through the upstream port. Figure 3 presents the non-dimensional pressure distribution($P=p/\rho(\nu/h)^2$) in a bearing unwrapped format. Most significantly, the pressure in the pocket varies strongly across its circumferential direction, while axially its variation is less pronounced. These results are validated by experimental evidence. It is worth noting that the present day industrial codes consider the pressure in the pocket constant, fact that influences considerably the stiffness and damping predictions.

REFERENCES

Braun, M.J., Dzodzo, M., 1995, "Effects of the Feedline and Hydrostatic Pocket Depth on The Flow Patterns and Pressure Distribution", ASME Journal of Tribology, Vol. 117, No. 2, pp. 224-233.

Peric, M., 1985, "A Finite Volume Method for the Prediction of Three-Dimensional Fluid Flow in Complex Ducts", Ph.D. Thesis, University of London.

Rizzi A., Eliasson P., Lindblad I., Hirsch C., Lacor C., Haeuser J., 1993, "The Engineering of Multiblock/Multigrid Software for Navier-Stokes Flows on Structured Meshes," Computers Fluids, Vol. 22, No. 2/3, pp. 341-367.

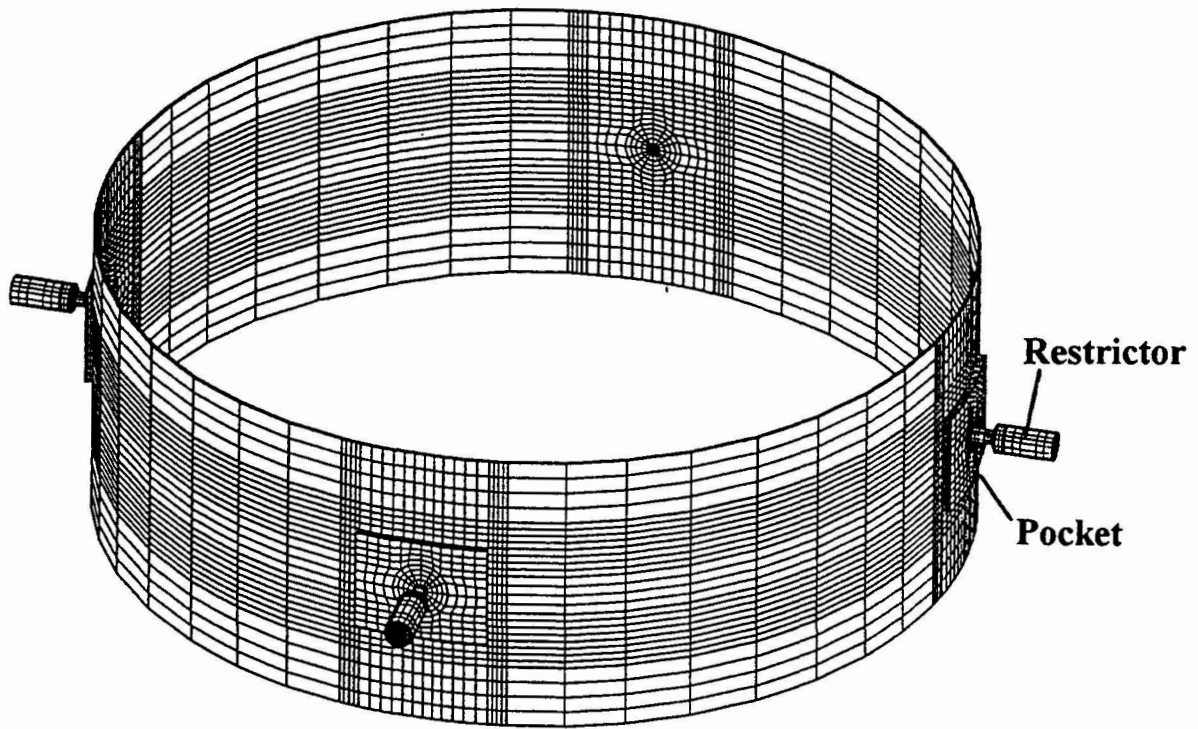


Figure 1 Three Dimensional Computational Grid

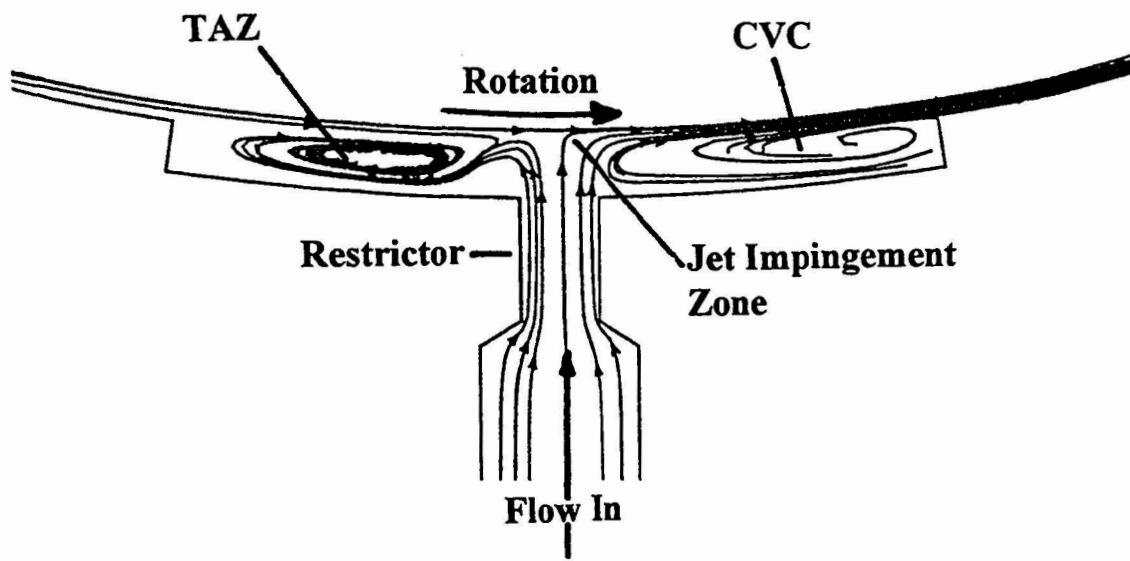
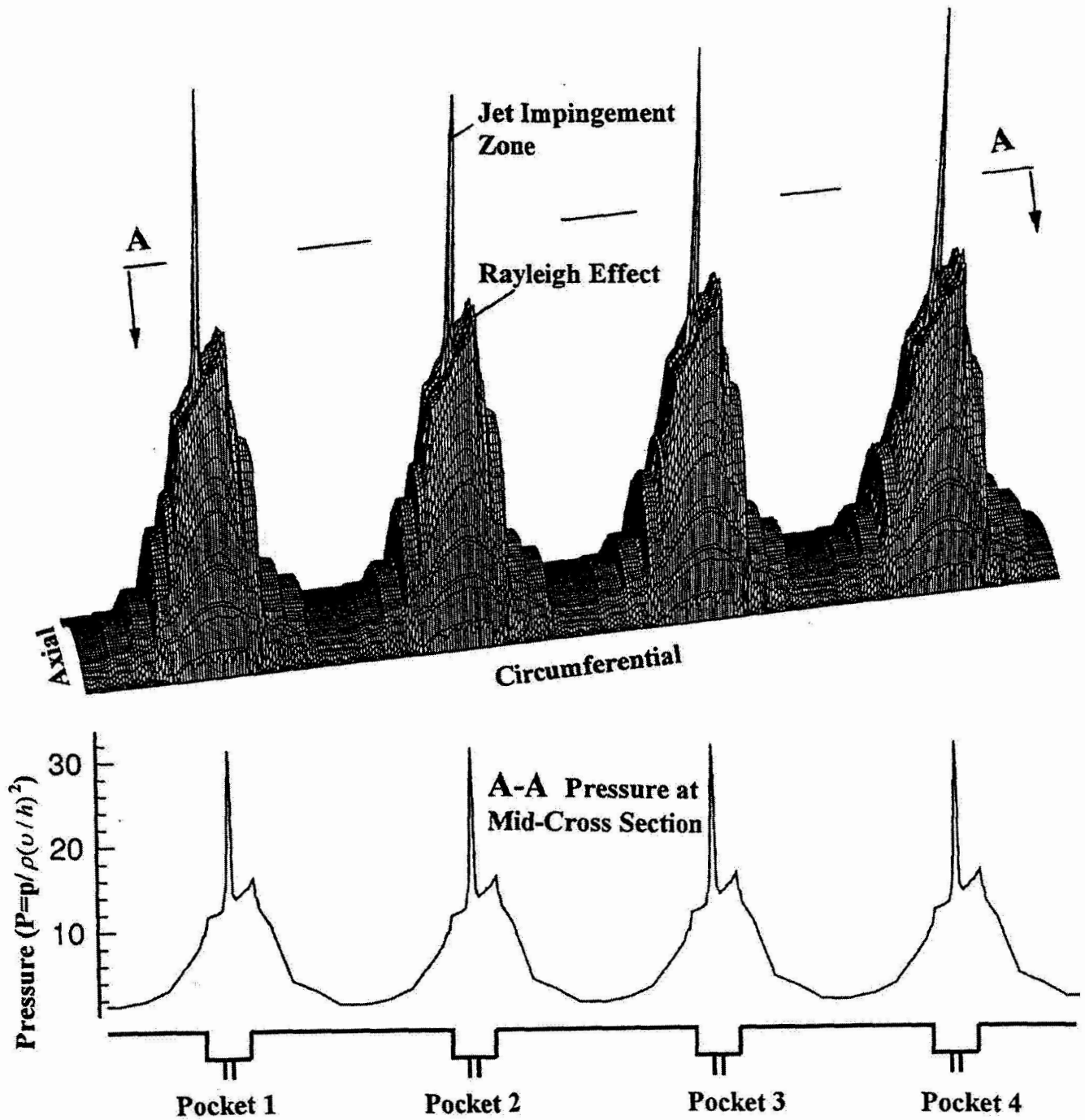


Figure 2 Flow at the Mid-Cross Section of a Hydrostatic Pocket



**Figure 3 Pressure Map in the Hydrostatic Journal Bearing
(Unwrapped Geometry)**

THREE DIMENSIONAL FLOW AND PRESSURE PATTERNS IN A SINGLE POCKET OF A HYDROSTATIC JOURNAL BEARING

M.J. Braun and M.B. Dzodzo
Department of Mechanical Engineering
The University of Akron
Akron, Ohio

519-34
39461

ABSTRACT

The flow in a hydrostatic pocket is described by a mathematical model that uses the three dimensional Navier-Stokes equations written in terms of the primary variables, u , v , w , and p . Using a conservative formulation, a finite volume multi-block method is applied through a collocated, body fitted grid. The flow is simulated in a shallow pocket with a depth/length ratio of 0.02.

The flow structures obtained and described by the authors in their previous two dimensional models are made visible in their three dimensional aspect for the Couette flow.

It has been found that the flow regimes formed central and secondary vortical cells with three dimensional corkscrew-like structures that lead the fluid on an outward bound path in the axial direction of the pocket. The position of the central vortical cell center is at the exit region of the capillary restrictor feedline. It has also been determined that a fluid turn around zone occupies all the upstream space between the floor of the pocket and the runner, thus preventing any flow exit through the upstream port.

The corresponding pressure distribution under the shaft presented as well. It was clearly established that for the Couette dominated case the pressure varies significantly in the pocket in the circumferential direction, while its variation is less pronounced axially.

FORMULATION OF THE MATHEMATICAL MODEL

Geometry. The typical geometry of a shallow hydrostatic pocket incorporated in a single pocket HJB-like configuration can be seen in Fig. 1. The figure presents the pocket positioned symmetrically in the axial direction, while the adjacent lands are connected circumferentially. A cross section A-A through this pocket is presented in Fig. 2, where we show only a portion of the lands. The figure shows the relative relationship between the pocket, restrictor, and the lands. At the bottom of the pocket there is a capillary feedline of length L_2 and diameter B . The pocket projected footprint is of length L . The most influential physical parameter of such a configuration is its aspect ratio D/L . The physical dimensions of the pocket and its environment are presented in Table 1. In earlier papers presented by Braun and Dzodzo(1994a,b,c, 1995a,b), and Dzodzo et al.(1994) the geometry introduced the assumption that the cavity width is much larger than its length or depth, thus reducing the problem to a two dimensional case of coordinates (Y_1, Y_2) . The present approach takes into account the finite width of the pocket, thus requiring a three dimensional treatise of the flow. The process is steady-state, the fluid is Newtonian, with constant properties, and incompressible.

Dimensionless Equations for the Fluid Model. To obtain a certain degree of generality in the discussion of the results, the governing equations of motion are cast in a dimensionless form. The characteristic length has been chosen to be $h=0.001\text{in}$ (0.0254mm). The equations are written in a general form for a non-orthogonal body fitted coordinate system in accordance with a formulation first presented by Peric(1985).

The three dimensional approach to the problem required the application of the multi-block technique, Fig. 3, in order to accommodate the geometry of Fig. 1. A literature review, as well as some details about the concept and application of the multi-block software are presented by Rizzi et al. (1993). The individual blocks contain collocated control volume cells anchored in a system of corresponding local arbitrary coordinates X^1, X^2, X^3 that are presented in Fig. 3. The local system of coordinates is then referenced to the global Cartesian system represented by Y_1, Y_2, Y_3 .

Using these notations, and the dimensionless variables defined in the nomenclature, the continuity equation takes the form

$$\frac{\partial}{\partial X^i} (U_k \beta_k^j) = \frac{\partial U_1}{\partial X^1} + \frac{\partial U_2}{\partial X^2} + \frac{\partial U_3}{\partial X^3} = 0, \quad (1)$$

where $U_j = U_1 \beta_1^j + U_2 \beta_2^j + U_3 \beta_3^j$

The momentum equations for Cartesian velocity components $U_i (i=1,2,3)$ can be written as

$$\frac{\partial}{\partial X^j} [U_j U_i - \frac{1}{j} (\frac{\partial U_i}{\partial X^m} \beta_k^j \beta_k^m + \frac{\partial U_k}{\partial X^m} \beta_i^m \beta_k^j) + P \beta_i^j] = 0 \quad (2)$$

where β_j^i , represents the cofactor of the i -th row and the j -th column in the Jacobian matrix J . This matrix performs the necessary coordinate transformation $Y_i = Y_i(X^j)$ where Y_i represents the Y_1, Y_2, Y_3 reference Cartesian system of coordinates. The advantage of this formulation is its readiness to naturally interface with the irregular geometry of the pocket as presented by Braun and Dzodzo(1995a,b).

Boundary Conditions. The boundary conditions on the lands, at their open ends are:

$$\frac{\partial U_1}{\partial Y_3} = \frac{\partial U_2}{\partial Y_3} = \frac{\partial U_3}{\partial Y_3} = 0; Y_3 = 0 \text{ and } Y_3 = 1000; 0 \leq X^2 \leq 2 \quad (3)$$

The boundary conditions were imposed by using the explicit step-space extrapolation(Shyy (1985)). The velocities U_1, U_2 and U_3 at $Y_3=0$ and $Y_3=1000$ for the current iteration, were assumed to be equal to the corresponding velocities of the neighboring interior cells (in Y_3 direction) from the previous iteration. By using these boundary conditions even the recirculation zones at the outlet cross sections can be predicted. The pressure in both the circumferential and axial directions at the open boundaries of the lands were assigned to a reference environment pressure,

$$P=0; Y_3=0 \text{ and } Y_3=1000, 0 \leq X^2 \leq 2 \quad (4)$$

The boundary pressure condition at the inlet of the restrictor($Y_2=0$) was assigned to be $P=247.3$ for the case of the Couette dominated flow and $P=1235.8$ for the case of the jet dominated flow. The dimensional pressure and velocity correspondents are given in Table 2. The velocity boundary conditions at the inlet of the restrictor ($Y_2=0$) are:

$$\frac{\partial U_1}{\partial Y_2} = \frac{\partial U_2}{\partial Y_2} = \frac{\partial U_3}{\partial Y_2} = 0; Y_2 = 0 \quad (5)$$

The explicit step-space extrapolation (Shyy, 1985) was used, in the same way as for the lands' outlet boundaries, but applied now in the Y_2 direction. The resulting velocity distribution at the inlet of the restrictor was an almost parabolic fully developed velocity profile. The tangential velocity at the shaft surface($X^2=2$) was $U_o = Re = 8$. This condition resulted in boundary conditions at the rotating shaft surface of the form

$$U_1 = -U_o * \sin \alpha; U_2 = U_o * \cos \alpha; U_3 = 0, \text{ at } Y_1 = Y_{1c} + R * \cos \alpha \text{ and } Y_2 = Y_{2c} + R * \sin \alpha \quad (6)$$

where $Y_{1c,2c}$ represent the position of the center of the shaft, and the angle α can be determined from Eqs. 6. The rest of the boundary conditions along the stationary walls are set to $U_1 = U_2 = U_3 = 0$.

RESULTS AND DISCUSSION

Due to the interaction between the penetrating jet coming through the restrictor and the shear layer carried by the shaft, the flow is eminently three dimensional. Its complicated structure is the resultant of the mergence between Poiseuille and Couette driven flows, as well as the influence of the axial boundary conditions. The Poiseuille portion of the flow is caused by the pressure differential between the inlet of the restrictor and the pocket bottom, while the Couette motion is engendered by the shear layer generated by the motion of the shaft. Depending on the relationship between the axial

boundary conditions (e.g either symmetric pressure, or different pressures at the axial ends), significant differences may appear in the structure of the axial flow and the pressure distribution on the lands.

Figure 5 presents a two dimensional cross section in the circumferential direction through the three dimensional flow in the pocket(Figs. 1, 2 and 3). This cross section is located at the mid-distance between the two axial ends of the pocket/shaft assembly. The physical situation involves a flow structure dominated by a high shear Couette flow interacting with a relatively low pressure gradient($P=243.7$ at the restrictor inlet) Poiseuille flow. The figure presents the central portion of the shallow pocket at the location where the restrictor merges with the pocket floor. It can be seen that the diameter of the restrictor forms a large gap in the pocket at the point of enjoinment. The shear layer is moving almost as a rigid body with the shaft and creates two recirculation zones at the location where it merges with the incoming jet. This central portion presents a modified vortical cell(MOVC), similar to the central vortical cell in a deep pocket presented by Braun and Dzodzo (1995a,b), but now completely shifted from the downstream portion of the pocket to the exit region of the capillary restrictor feedline. This change in location causes the effective diameter of the restrictor to be severely diminished, and thus strongly influences the local flow discharge coefficient. The downstream of the MOVC contains a flattened recirculation pillow as evidenced by Fig. 6, and the corresponding Detail A.

The detail of the SVC can be better observed in Fig. 7. The dominance of the Couette flow causes a very remarkable and somewhat little expected effect. Thus a study of Detail A shows that at the upstream exit of the pocket no fluid exits the pocket in the circumferential direction, but is rather turned around by the shear layer which occupies the entire clearance, forming a so called turn around zone(TAZ). This situation is entirely responsible for the birth of the SVC. In fact SVC serves to satisfy flow continuity and re-directs the flow in the axial direction of the pocket(just like MOVC).

Figure 8 was obtained by introducing tracer particles at an arbitrary location of the capillary restrictor entry, and then follow their path as they move towards the exit of the pocket. Figure 8a presents the three dimensional trajectory of a particle as it moves and gets trapped first in the MOVC, then leaves it, and enters the SVC. Once the particle reaches the SVC core, it spirals outwards axially, and leaves the confines of the pocket. Another example of spiral flow moving axially out can be seen in Fig. 8b. One can conclude that for the Couette dominated flow the fluid is generally trapped in the pocket and than it axially corkscrews its way out.

A three dimensional picture of the pressure formed under the shaft in the case of the Couette dominated flow can be seen in Fig. 9. The Rayleigh effect at the downstream exit of the pocket is clearly visible in the (A-A) cross section of Fig. 9b. The pressure increases all along the circumferential length of the pocket, starting at the upstream end, and reaching a level approximately 33% higher at its downstream end. This figure presents clear proof that previous assumptions of constant pressure across the pocket, or that the pressure is constant in the first half of the pocket are not correct.

CONCLUSIONS

An analytical formulation using 3-D Navier-Stokes equations is used for the determination of the flow patterns in shallow hydrostatic pocket with adjoined lands, Fig. 1. The laminar, steady-state, constant properties, Navier-Stokes equations are cast in a formulation that permits a body fitted coordinates numerical implementation. The results confirm the findings of the 2-D models of Braun et al.(1993, 1994b) and Braun and Dzodzo (1994a,b,c,d and 1995a,b) and extends the numerical simulation to the case of the three dimensional flow. The findings of the numerical simulation of a shallow hydrostatic pocket can be summarized as follows

- in the Couette dominated flow the TAZ occupies all the space between the floor of the pocket and the runner with the consequence that no flow exits through the upstream port
- the three dimensional flow shows that the flow trapped either in the MOVC or SVC eventually finds its way out in the axial direction. In the Couette dominated flow the fluid is trapped for long periods in the pocket area as it axially corkscrews its way out of the pocket(Fig. 8). Thus the fluid tracers are zig-zagging several times from the downstream to the upstream edge of the pocket while moving slowly towards the axial edges of the pocket.

• the pressure under the runner in the case of the Couette dominated flow increases significantly from the upstream to the downstream ends of the pocket, with a strong spike in the region of the Rayleigh step end. For the circumferential speeds used in this paper ($U=8$), the inertial pressure drops are more pronounced on the axial edges of the pockets as a consequence of the dominant axial outflow from the pockets.

REFERENCES

- Braun, M.J., Dzodzo, M., 1994a, Numerical Predictions of Discharge Coefficients in a Hydrostatic Bearing," *Advanced Earth-to-Orbit Propulsion Technology - 1994*, ed. R.J. Richmond R.J. and Wu S.T., Alabama, May 17-19, NASA CP-3282, Vol. II, pp. 412-420
- Braun, M.J., Dzodzo, M., 1994b, "Effects of Hydrostatic Pocket Shape on The Flow Patterns and Pressure Distribution" 5th International Symposium on Transport Phenomena and Dynamics of Rotating Machinery (ISROMAC-5), Vol. A, pp. 88-106, May 8-12, Maui, Hawaii.
- Braun, M.J., Dzodzo, M., 1994c, "Effects of the Feedline and Hydrostatic Pocket Depth on the Flow Pattern and Pressure Distribution", Paper No. 94-Trib-27, ASME/STLE Tribology Conference, Maui, Hawaii, October 16-19.
- Braun, M.J., Dzodzo, M., 1995a, "Effects of the Feedline and Hydrostatic Pocket Depth on The Flow Patterns and Pressure Distribution", *ASME Journal of Tribology*, Vol. 117, No. 2, pp. 224-233.
- Braun, M.J., Dzodzo, M., 1995b, "Effects of Hydrostatic Pocket Shape on The Flow Patterns and Pressure Distribution", *International Journal of Rotating Machinery*, Vol. 1, No. 3, (in press)
- Dzodzo M., Braun, M.J., Hendricks R.C., 1994, "Pressure and Flow Characteristics in a Shallow Hydrostatic Pocket with Rounded Pocket/Land Joints", *Proceedings, 4th International Tribology Conference, AUSTRIB'94*, G.W. Stachowiak, ed., Uniprint the University of Western Australia, Perth, Australia, Vol. 2, pp. 587-592.
- Peric, M., 1985, "A Finite Volume Method for the Prediction of Three-Dimensional Fluid Flow in Complex Ducts", Ph.D. Thesis, University of London.
- Rizzi A., Eliasson P., Lindblad I., Hirsch C., Lacor C., Haeuser J., 1993, "The Engineering of Multiblock/Multigrid Software for Navier-Stokes Flows on Structured Meshes," *Computers Fluids*, Vol. 22, No. 2/3, pp. 341-367.
- Shyy, W., 1985, "Numerical Outflow Boundary Condition for Navier-Stokes Flow Calculations by a Line Iterative Method", *AIAA Journal*, Vol. 23, No. 12, December, pp. 1847-1848.

TABLE 1. The geometrical characteristic of the pockets

	D_{less}	in	m
L	448.6	0.4486	0.01139444
D	9	0.009	0.0002286
C	2	0.002	0.0000508
B	50	0.050	0.00127
L_2	292	0.292	0.0074168
R	1500	1.5	0.0381
W_P	350	0.350	0.00889
W_L	325	0.325	0.008255
h	1	0.001	0.0000254

TABLE 2. The runner velocities and the restrictor inlet pressure

(for $\rho=900 \text{ kg/m}^3$, $\mu=9 \cdot 10^{-2} \text{ kg/ms}$ ($\nu=\mu/\rho=100 \cdot 10^{-6} \text{ m}^2/\text{s}$) and $h=25.4 \cdot 10^{-6} \text{ m}$)	
$Re=U_0$	8
Linear speed	31.46 m/s
Rot. speed	7885 rpm
Inlet pressure	
$P=247.3$	$34.5 \cdot 10^5 \text{ Pa}$ (500 psi)
$P=1235.8$	$172.4 \cdot 10^5 \text{ Pa}$ (2500 psi)

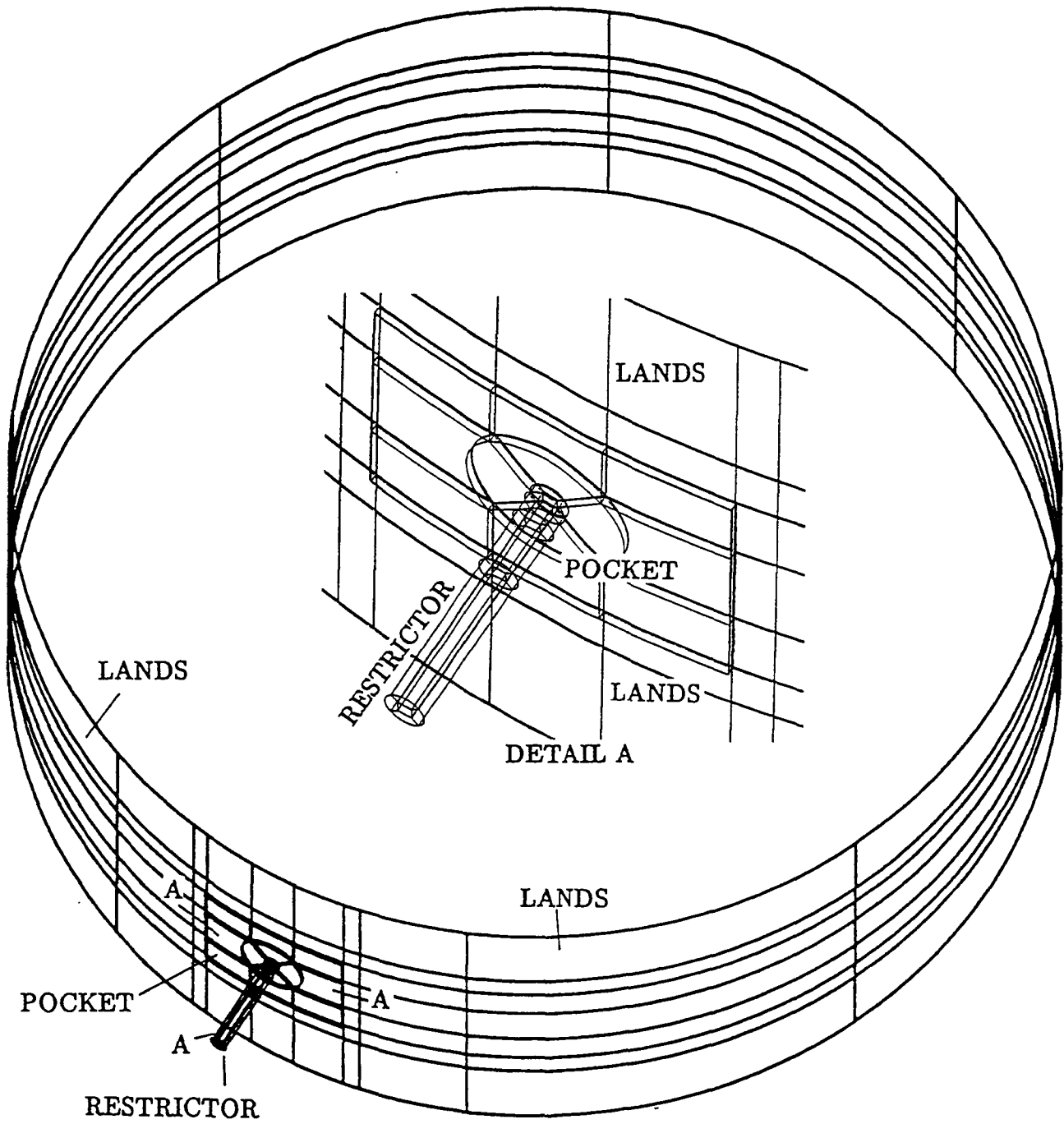


Fig. 1 Shallow hydrostatic pocket with adjoining lands

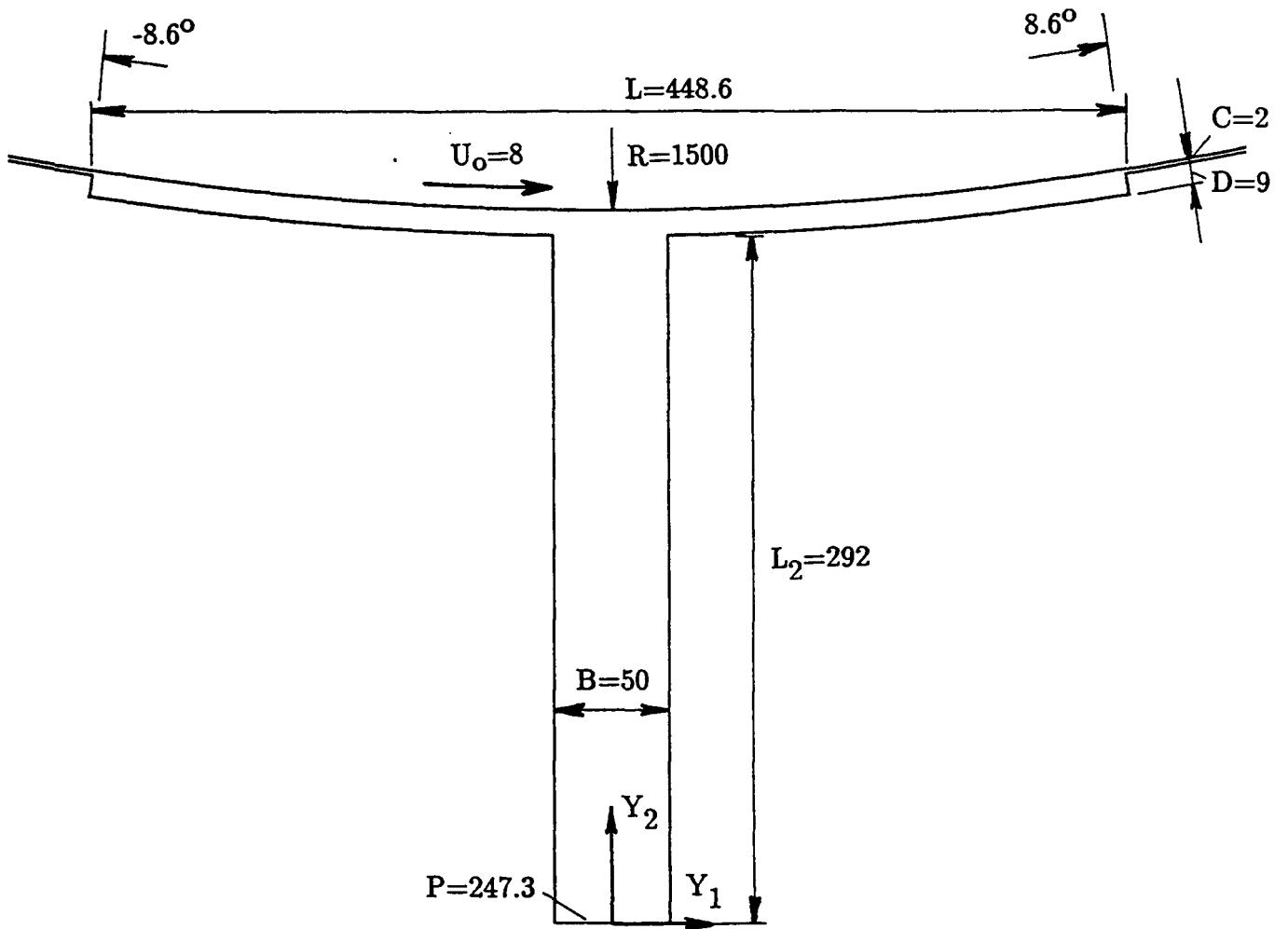


Fig. 2 Circumferential cross section through the shallow hydrostatic pocket (see also Figs. 1 and 3, cross section A-A)

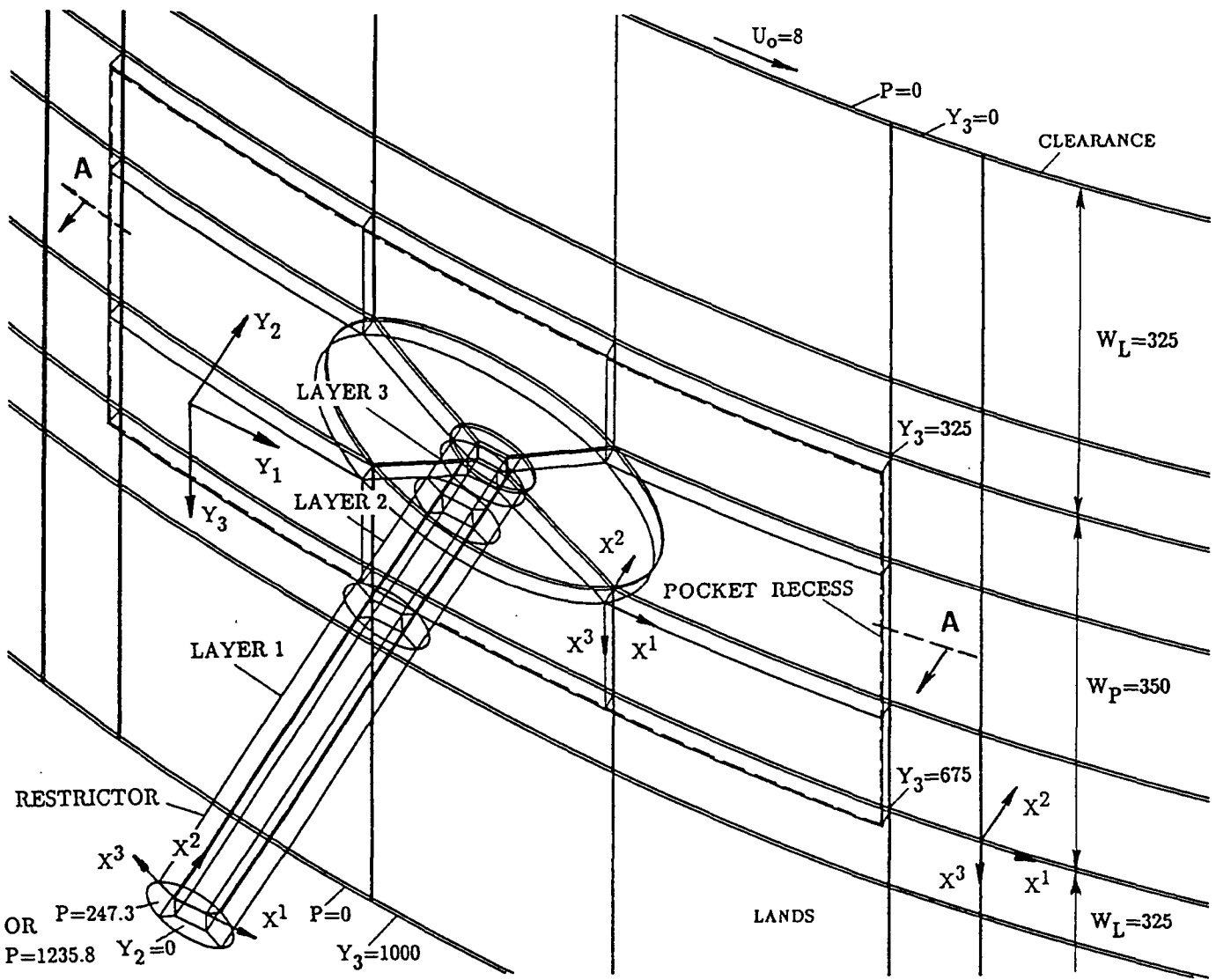


Fig. 3 Three dimensional view of the block structure of the hydrostatic pocket and a portion of the lands

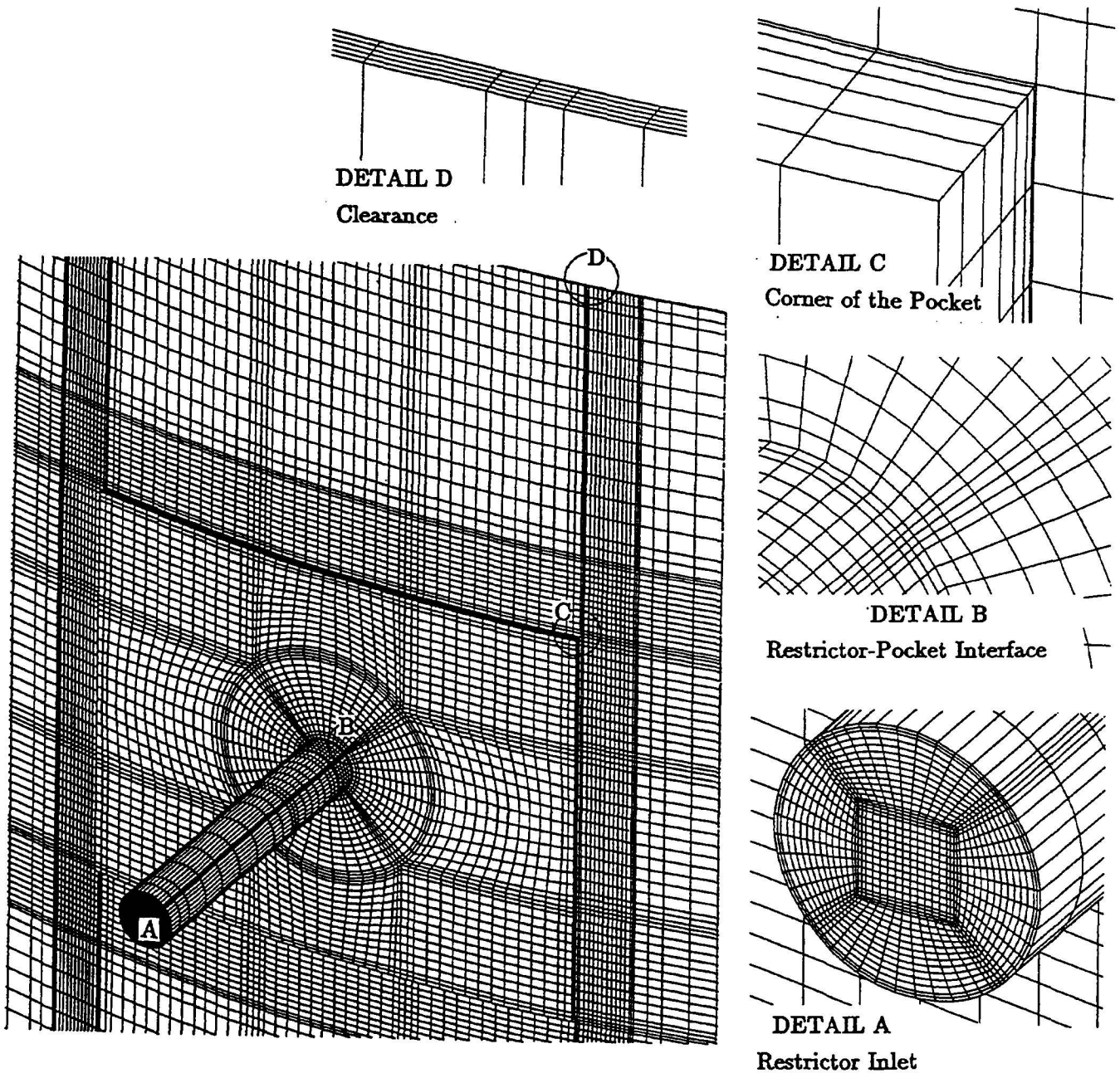


Fig. 4 Cell distribution inside the blocks of Fig. 3

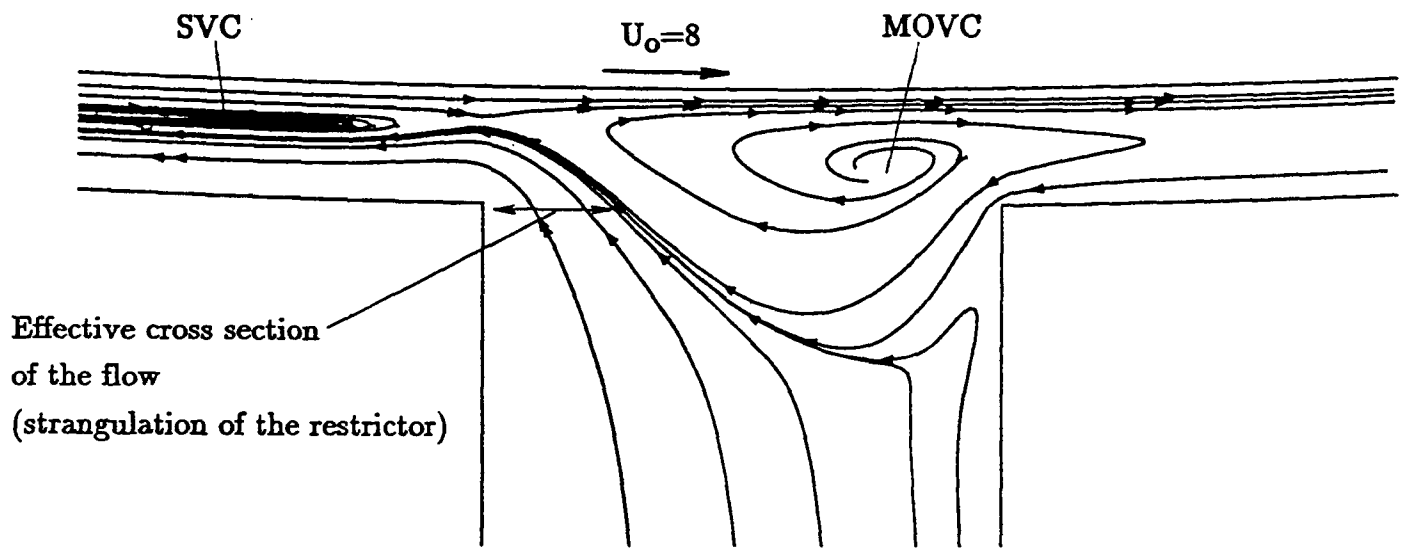


Fig. 5 Flow structure in the central portion of the pocket. Modified oblong (MOV) and secondary vortical cells (SVC) for Couette dominated flow

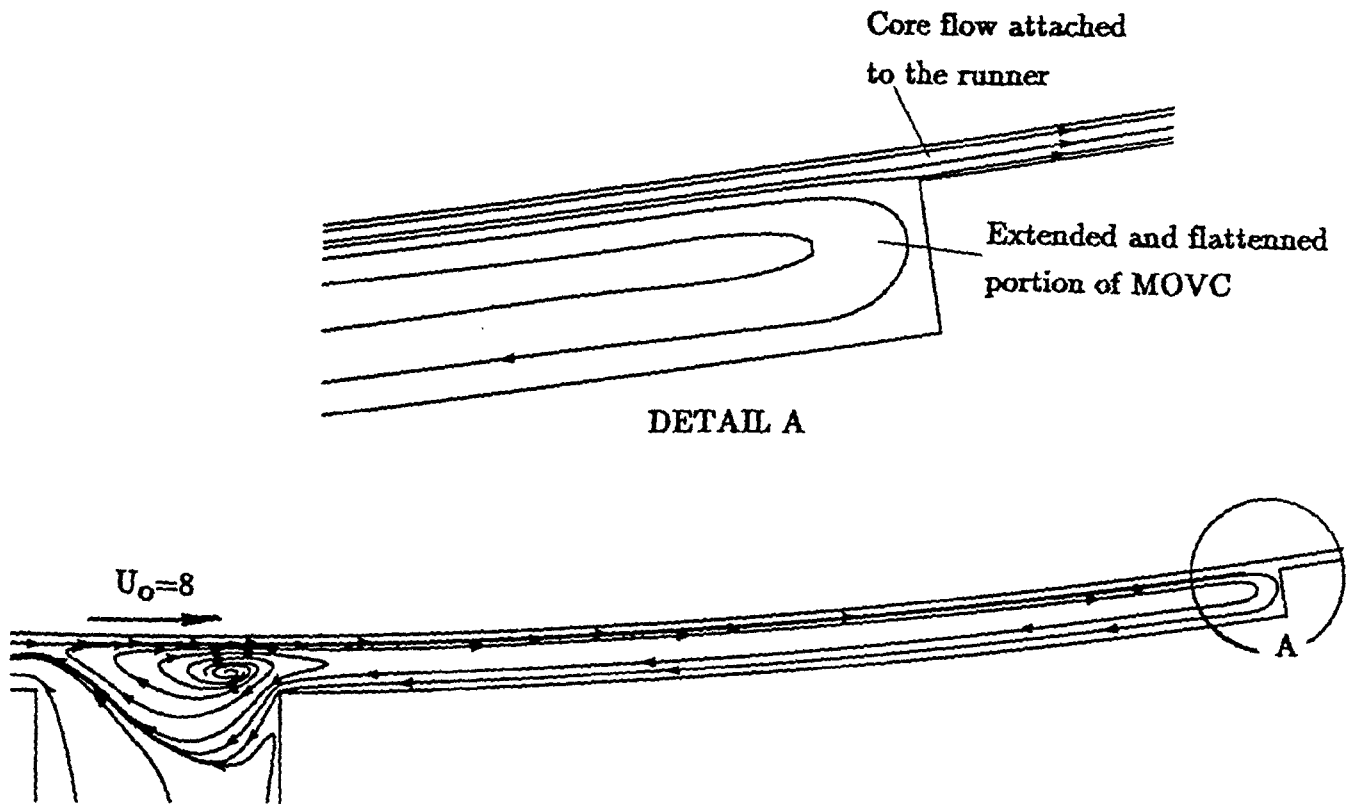


Fig. 6 Structure of the modified oblong vortical cell in the downstream section of the Couette dominated flow

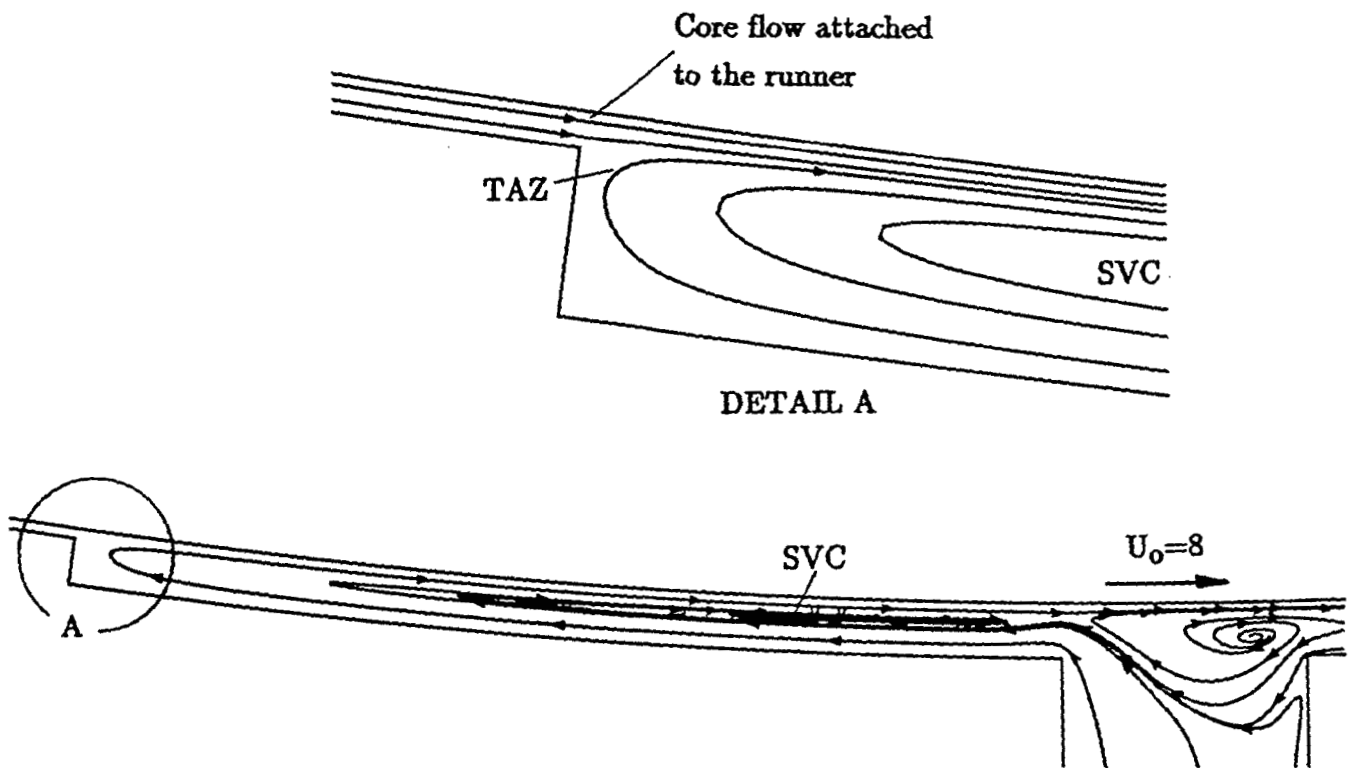


Fig. 7 Structure of the secondary vortical cell in the upstream section of the Couette dominated flow

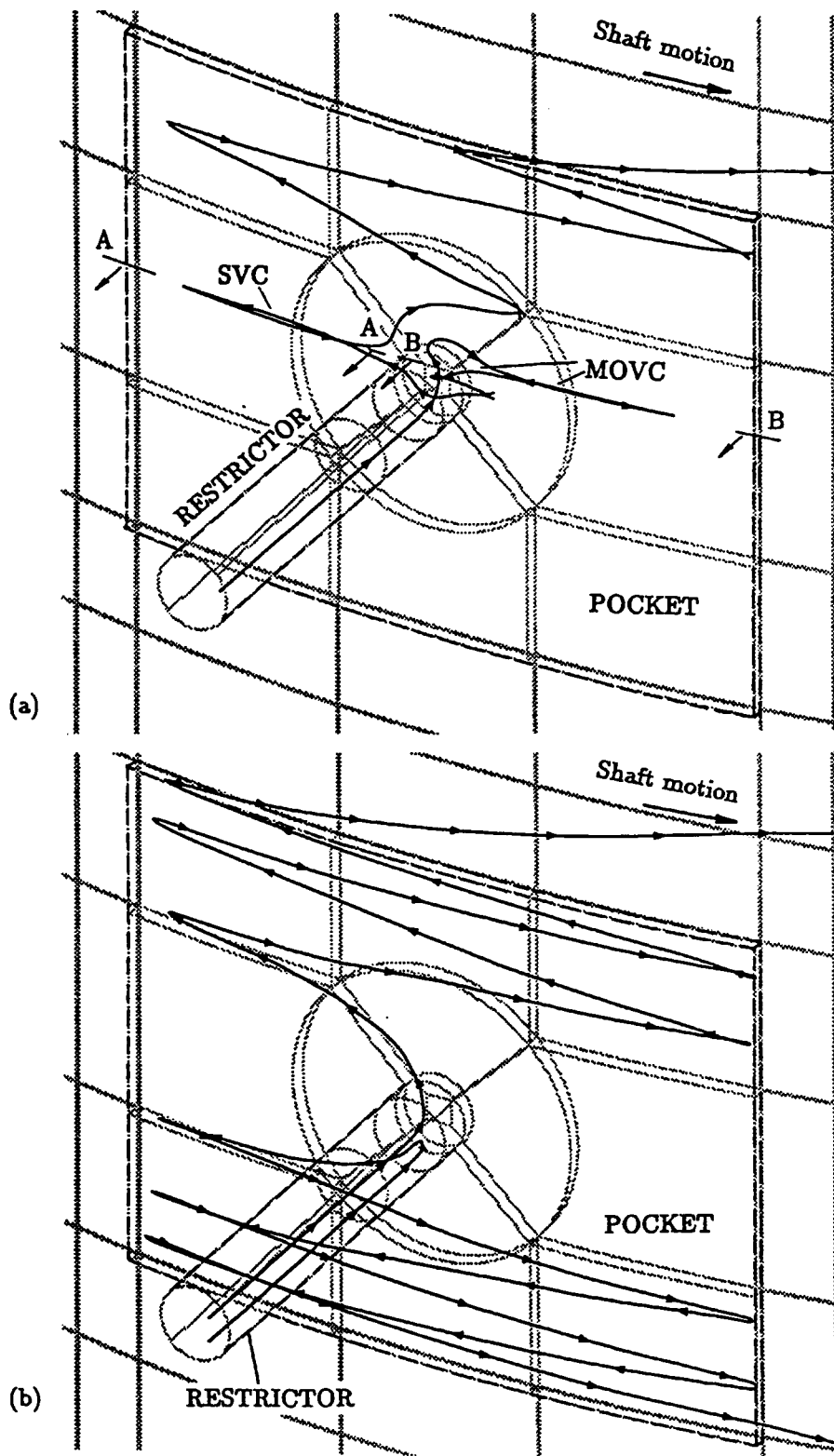
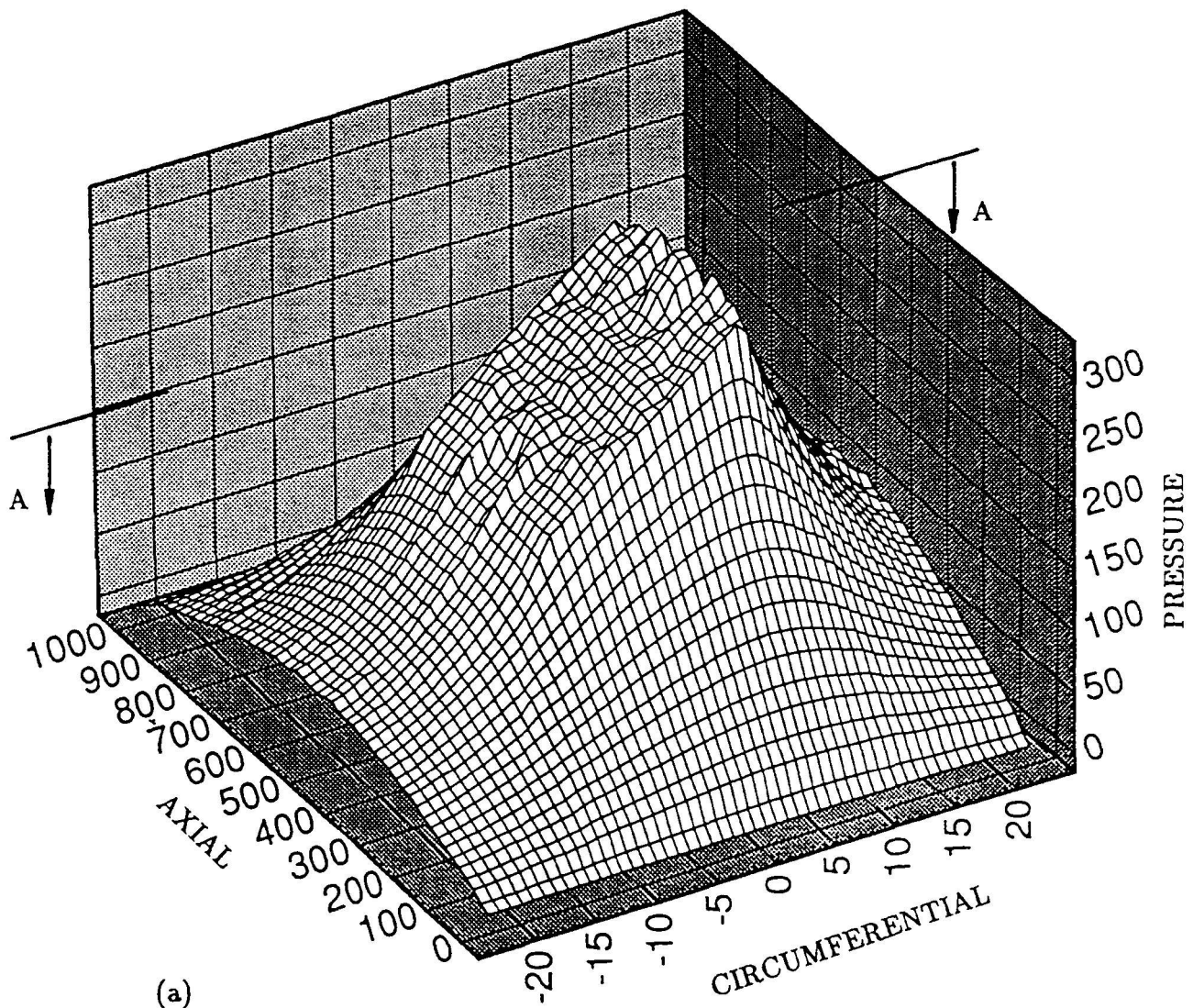
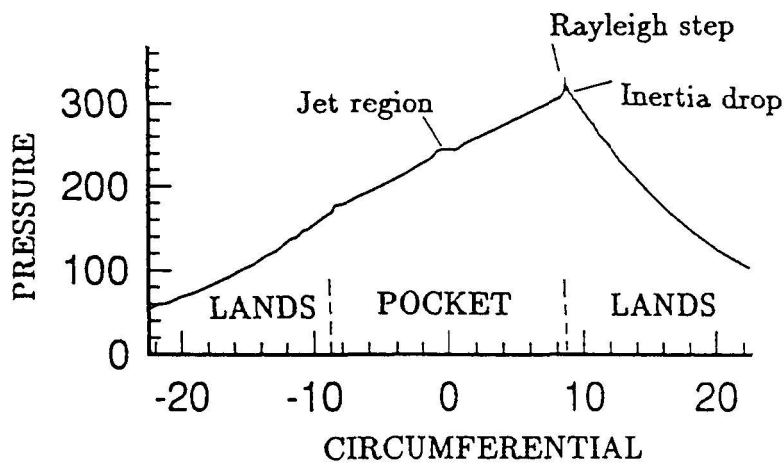


Fig. 8 (a) Particle streakline visualizing the three dimensional MOV, the SVC and their interaction

(b) Particle streaklines visualizing the spiral flow moving axially out of the pocket for Couette dominated flow



(a)



(b)

Fig. 9 (a) Pressure distribution formed under the shaft in the case of the Couette dominated flow

(b) Pressure distribution in the A-A (Fig. 1 and 3) cross section

LIQUID ANNULAR SEAL RESEARCH

520-37

Alan B. Palazzolo, Balaji Venkataraman, and Sathya S. Padavala
Department of Mechanical Engineering
Texas A&M University
College Station, Texas

39462

and

Steve Ryan, Pat Vallely, and Kerry Funston
NASA George C. Marshall Space Flight Center
Marshall Space Flight Center, Alabama

ABSTRACT

This paper highlights the accomplishments on a joint effort between NASA - Marshall Space Flight Center and Texas A&M University to develop accurate seal analysis software for use in rocket turbopump design, design audits and trouble shooting. Results for arbitrary clearance profile, transient simulation, thermal effects solution and flexible seal wall model are presented. A new solution for eccentric seals based on cubic spline interpolation and ordinary differential equation integration is also presented.

INTRODUCTION

Development of the SSME-ATD-HPOTP required accurate simulation for vibration control. Component modeling of liquid annular seals is a critical step in accomplishing this task. This is particularly true for the intentionally "roughened bore" annular seals which provide damping and reduce cross-coupled stiffness. Seal modeling software was developed which included the following features to more realistically simulate the fluid-structure interaction forces:

- Arbitrary clearance profile in the axial and circumferential directions
- Fluid compressibility for LH2 and LOX modeling
- Hir's and Moody's Friction Factor modeling
- Eccentric Operation
- Thermo-hydrodynamic coupled solution for concentric and eccentric operations
- Transient motion
- Flexible wall modeling

Bulk flow continuity, momentum and energy equations are solved in a coupled manner. Constitutive thermophysical relations for LH2 and LOX are obtained from the NIST Database, MIPROPS. A simple and efficient dependence in the eccentric problem is developed using cubic spline interpolation. The resulting n th order two point boundary value problem consists of ordinary differential equations for the zeroth order (steady state) and first order (perturbation) cases. Leakage, torque, horse power loss, stiffness, damping and inertia dynamic coefficients are calculated by the software. Both direct and cross-coupled coefficients are provided.

GOVERNING EQUATIONS

The 2-D bulk flow mass continuity, momentum and the energy equations for the seal are given by,

Mass continuity:

$$\frac{\partial(\rho h)}{\partial t} + \frac{\partial(\rho h u)}{\partial z} + \frac{\partial(\rho h v)}{\partial q} = 0 \quad (1)$$

Axial momentum :

$$\frac{\partial(\rho h u)}{\partial t} + \frac{\partial(\rho h u^2)}{\partial z} + \frac{\partial(\rho h u v)}{\partial q} = -h \frac{\partial p}{\partial z} + [\tau_{zy}]_0^h \quad (2)$$

Circumferential momentum :

$$\frac{\partial(\rho h v)}{\partial t} + \frac{\partial(\rho h u v)}{\partial z} + \frac{\partial(\rho h v^2)}{\partial q} = -h \frac{\partial p}{\partial q} + [\tau_{qv}]_0^h \quad (3)$$

Energy equation :

$$C_p \left[\frac{\partial(\rho h T)}{\partial t} + \frac{\partial(\rho h u T)}{\partial z} + \frac{\partial(\rho h v T)}{\partial q} \right] + Q_s = T \beta h \left\{ \frac{\partial p}{\partial t} + v \frac{\partial p}{\partial q} + u \frac{\partial p}{\partial z} \right\} + R \Omega [\tau_{qv}]_h - v [\tau_{qv}]_0^h - u [\tau_{zy}]_0^h \quad (4)$$

RESULTS

Figure 1 shows the general solution path employed. A structural FE model of the entire LOX pump was developed at NASA-MSFC and predicted the operating clearance distribution in Figure 2. The variation of clearance in the axial and circumferential directions raised concerns related to effects on the rotordynamic coefficients. An arbitrary clearance profile version of the code was developed, patterned on the geometry shown in Figure 3. Subsequent simulations revealed only slight deviations of the dynamic coefficients from their values for an average clearance model, as typified in Figure 4. Further concerns on seal distortion led to examination of the elliptical clearance profiles in Figure 5. The results in Figure 6 again show only slight influence on dynamic coefficients except for high "ellipticities".

Past investigations of bearing flexibility effects on direct damping have shown considerable reductions. Consequently, efforts were made to analyze seal flexibility effects. Figure 7 shows a diagram of the general 2-D, axisymmetric, 4-node, isoparametric FE model employed to obtain seal deformations. Figure 8 contains a computation flow diagram for the determination of dynamic coefficients with flexibility effects.

Figures 9, 10, 11 show comparisons of direct and cross coupled stiffnesses and direct damping between Iwatsubo's published results and the current approach. The results show some significant changes with the inclusion of flexibility. Figures 12-15 show the effects of flexible, rigid, constant properties and thermo-hydrodynamic modeling on the dynamic coefficients of an SSME-ATD HPOTP damping seal. Modeling assumptions are seen to exhibit significant influence on the dynamic coefficients.

Sudden transient vibrations were observed in the development stages of the SSME-ATD HPOTP. The seal code was updated to provide forces due to transient shaft motions. The forces were determined by direct solution of the momentum and continuity equations and by integrating the spatially varying dynamic coefficients, multiplied by increments in position, velocity and acceleration. The dynamic coefficients were obtained at any spatial position by interpolating from a radial/circumferential grid. The latter, approximate approach was found to be nearly as accurate and many times more efficient than the direct solution approach. Spatial variation of the direct stiffness is illustrated in Figure 16. Transient forces were applied to the single mass (Jeffcott) rotor model in Figure 17. Numerical integration was used to predict the locus of the rotor in response to ramp and ramp/sinusoidal type external loads. Figures 18-21 show that

(a) A model employing concentric linear coefficients may produce significant error for large motions.

(b) The "integrated" dynamic coefficient approach yields responses that are nearly identical with direct solution of the continuity and momentum equations.

SUMMARY

This manuscript has highlighted the development of advanced software for the prediction of dynamic forces and force coefficients in liquid annular seals. Effects of variable clearance profile, seal flexibility, thermo-hydrodynamic modeling and transient motions have been included. Future work includes CFD modeling of seal and impeller related fluid forces.

ACKNOWLEDGEMENTS

The authors gratefully acknowledge NASA's Marshall Space Flight Center and the NASA/ASEE Summer Faculty Program for sponsoring this research.

REFERENCES

Iwatsubo, T., Yang, B.S., 1987, "The Effects of Elastic Deformation on Seal Dynamics," *The 1987 ASME Design Technology Conferences - 11th Biennial Conference on Mechanical Vibration and Noise*, Sep.27-30, Boston, Massachusetts, pp. 435-440.

Venkataraman, B., and Palazzolo, A.B., 1995, "Thermo-hydrodynamic Analysis of Turbulent Cryogenic Annular Seals with Large Eccentric Motion," presented at the 1995 Society of Tribologists and Lubrication Engineers (STLE) Annual Meeting in Chicago, Illinois, May 14-19, 1995 and accepted for publication in the STLE Tribology Transactions.

Venkataraman, B., and Palazzolo, A.B., 1995, "Effects of Wall Flexibility on the Rotor-dynamic Coefficients of Turbulent Cryogenic Annular Seals," accepted for publication in the ASME JOURNAL OF TRIBOLOGY and to be presented at the 1995 Joint ASME/STLE Tribology Conference, Kissimmee, Florida, October 8-11, 1995.

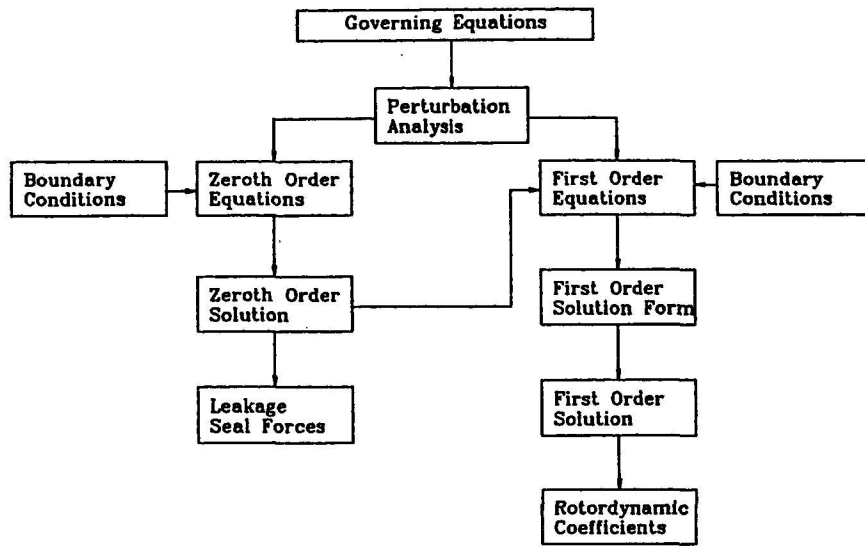


Figure 1 Flow Chart of Solution Procedure

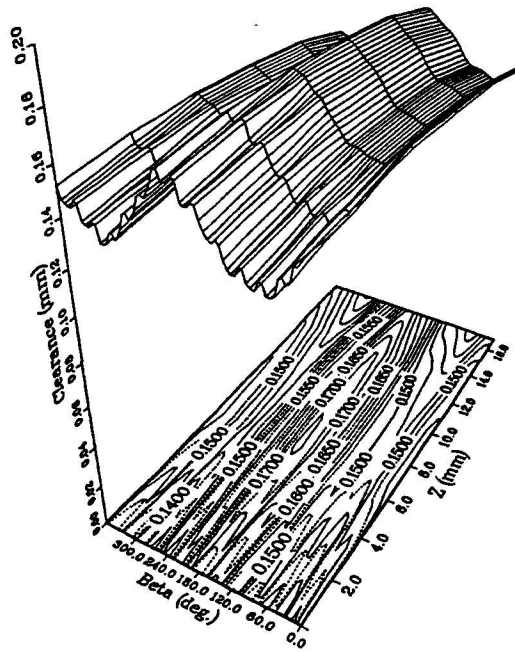


Figure 2 Predicted Clearance Profile for Seal, Unit 3-01

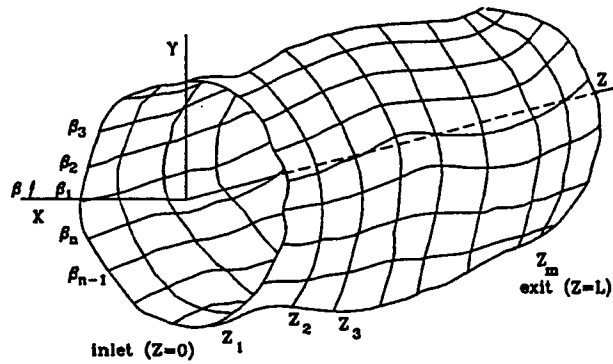


Figure 3 Grid for Numerical Integration

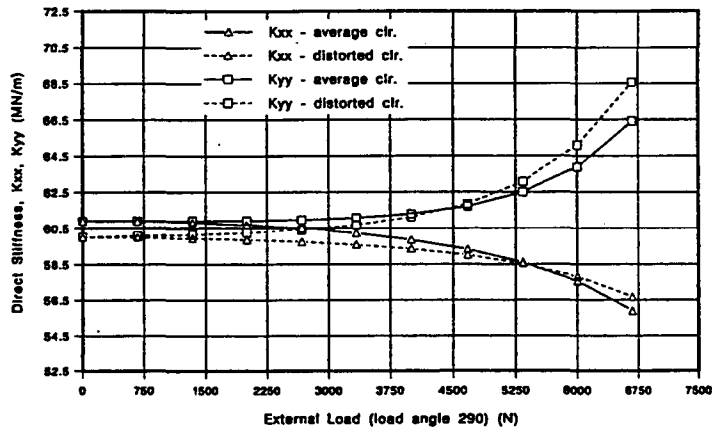


Figure 4a Direct Stiffness for Distorted Seal, Unit 3-01

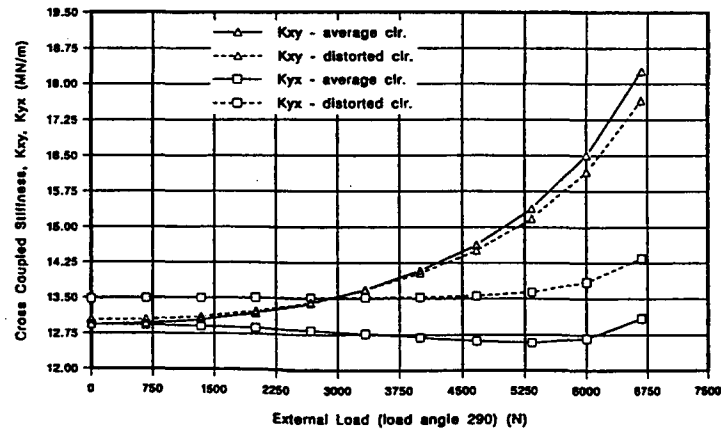


Figure 4b Cross Coupled Stiffness for Distorted Seal, Unit 3-01

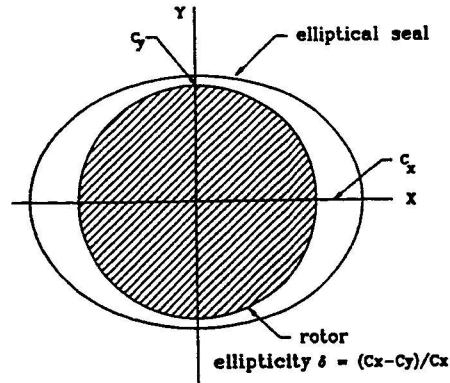


Figure 5 Elliptical Seal

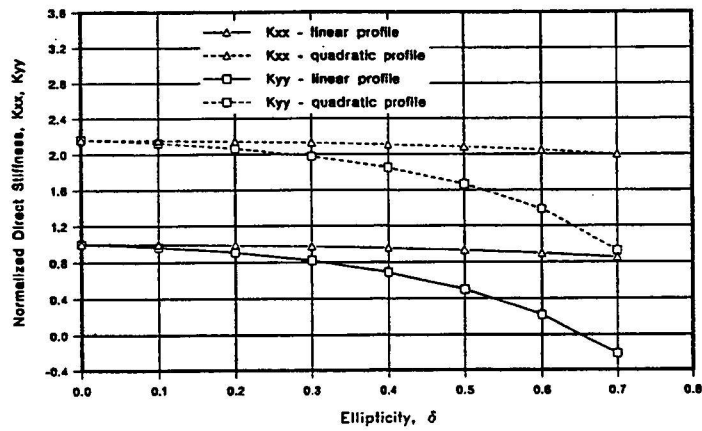


Figure 6a. Normalized Direct Stiffness for Elliptical Seal (Curved)

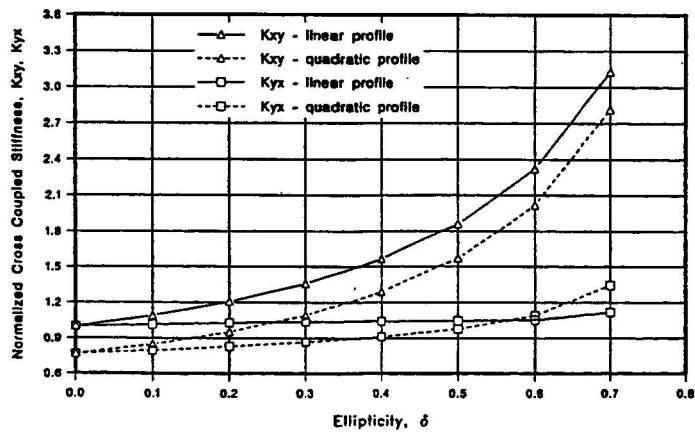


Figure 6b Normalized Cross Coupled Stiffness for Elliptical Seal (Curved)

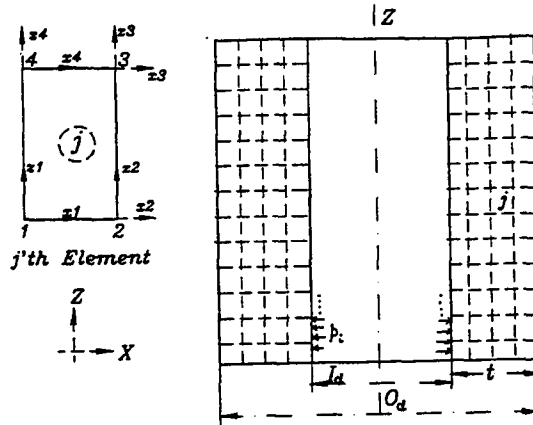


Figure 7 Finite Element Axisymmetric Model of the Seal

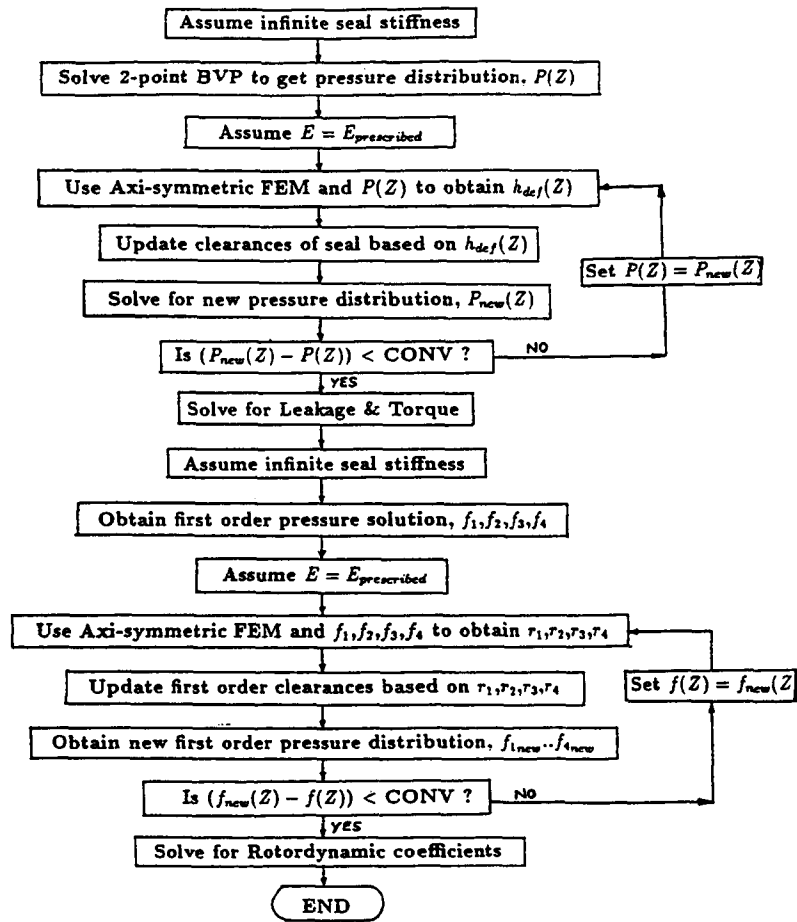


Figure 8 Flow diagram for the numerical solution

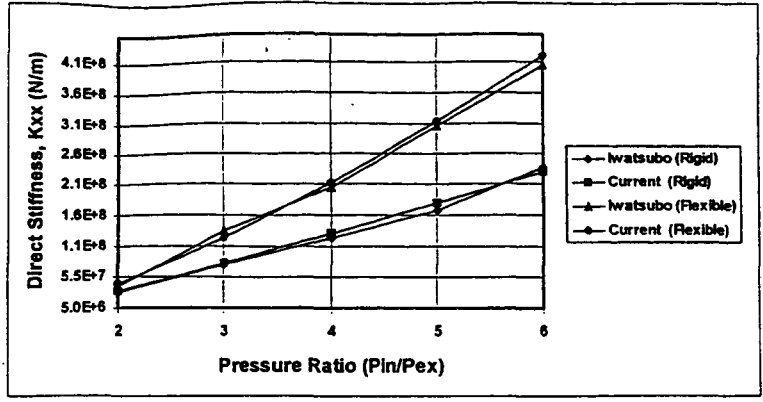


Figure 9 Comparison of Direct Stiffness with Iwatsubo and Yang (1987).

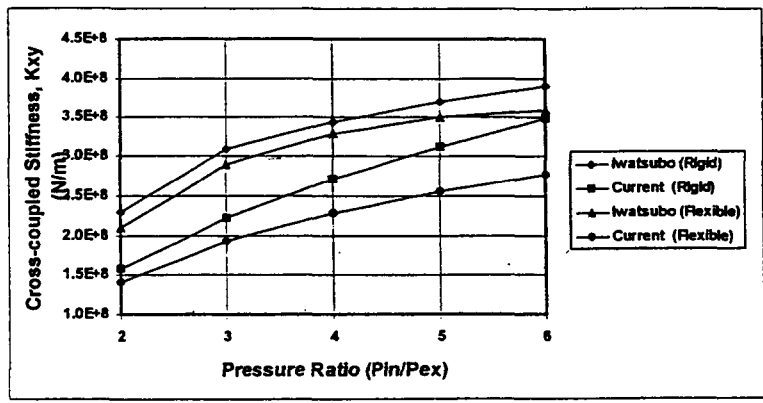


Figure 10 Comparison of Cross coupled Stiffness with Iwatsubo and Yang (1987).

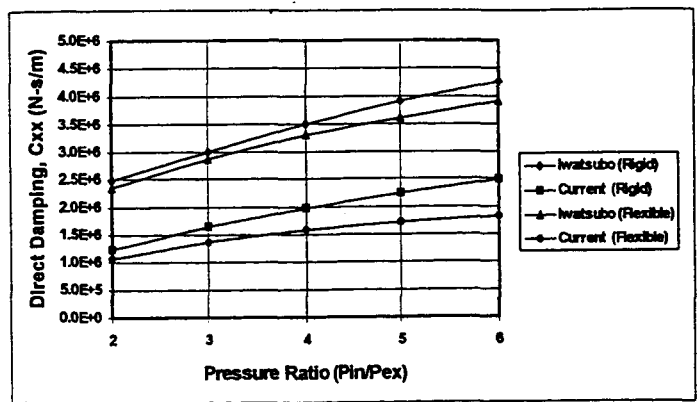


Figure 11 Comparison of Direct Damping for Iwatsubo and Yang (1987)

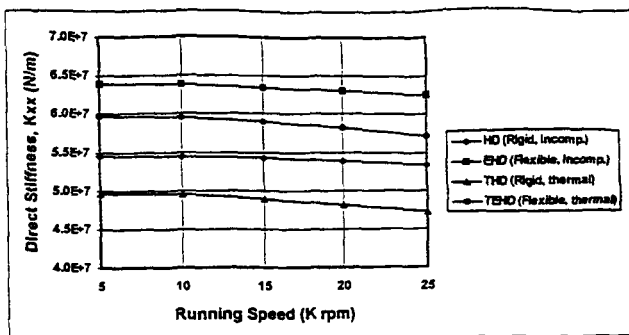


Figure 12 Comparison of Direct Stiffness between flexible and rigid models for UNIT 3-01 Seal.

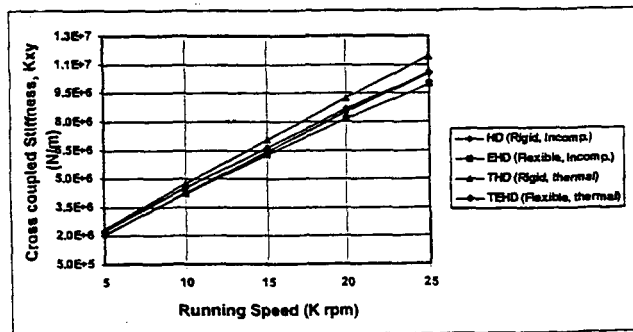


Figure 13 Comparison of Cross coupled Stiffness between flexible and rigid models for UNIT 3-01 Seal.

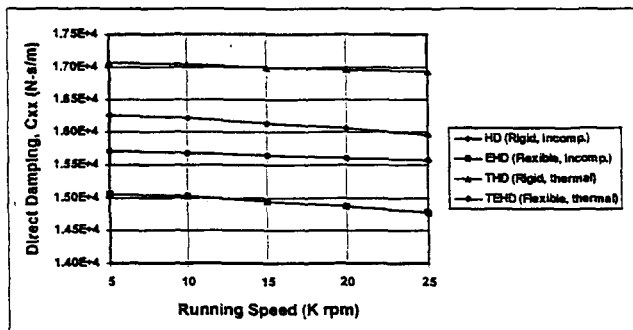


Figure 14 Comparison of Direct Damping between flexible and rigid models for UNIT 3-01 Seal.

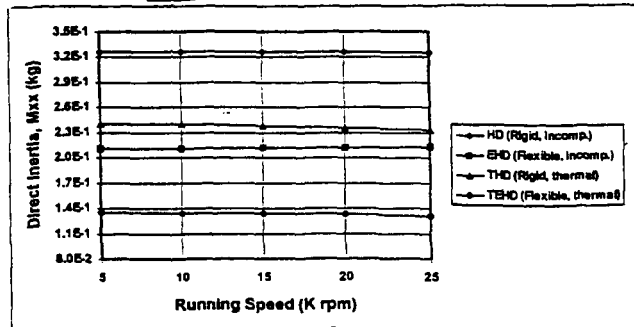


Figure 15 Comparison of direct inertia between flexible and rigid models for UNIT 3-01 Seal.

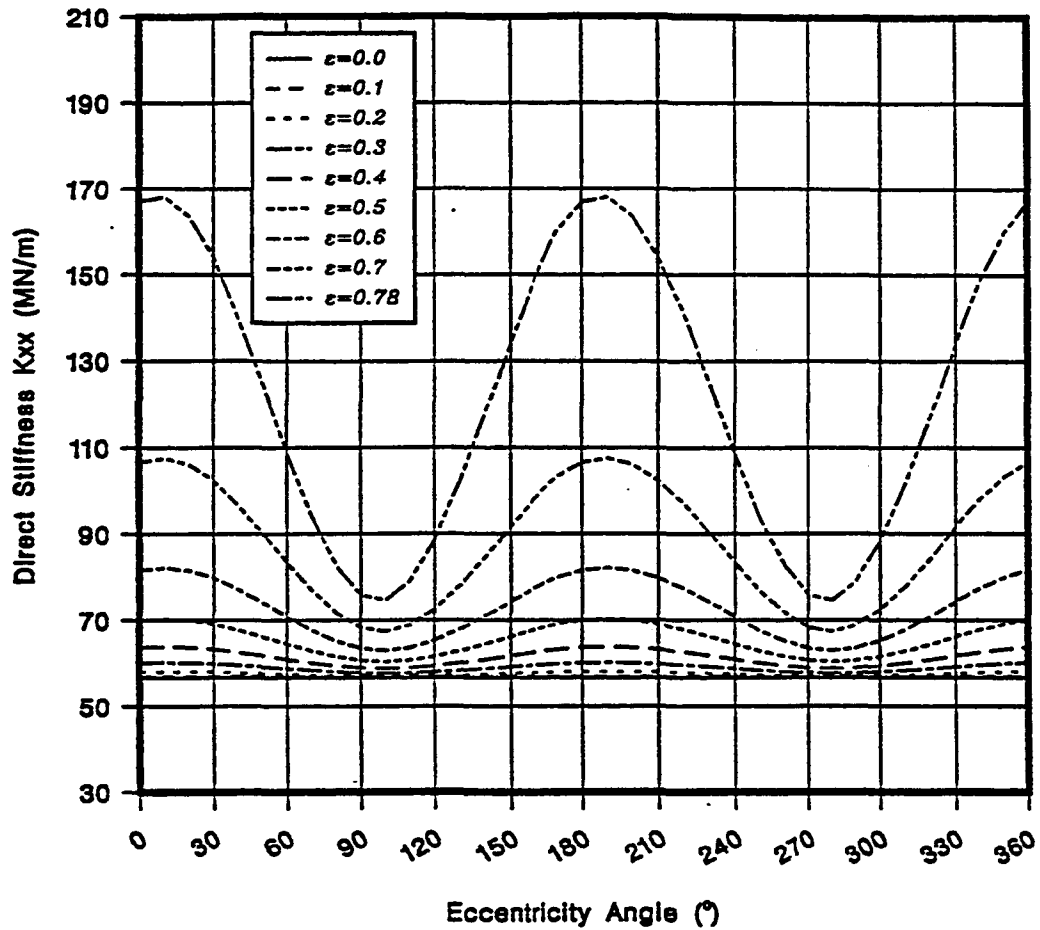


Figure 16 Variation of K_{xx} for Unit 3-02 as a Function of Rotor Position

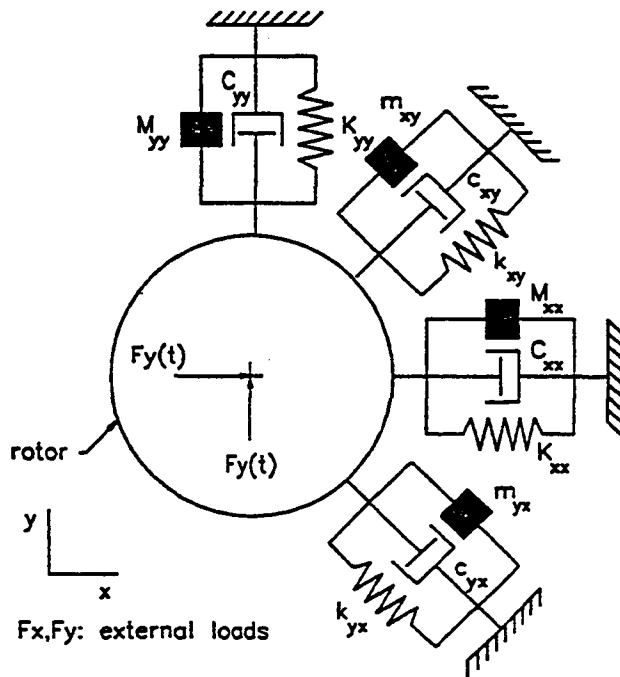


Figure 17 Rotor-Seal Model Used for Simulation

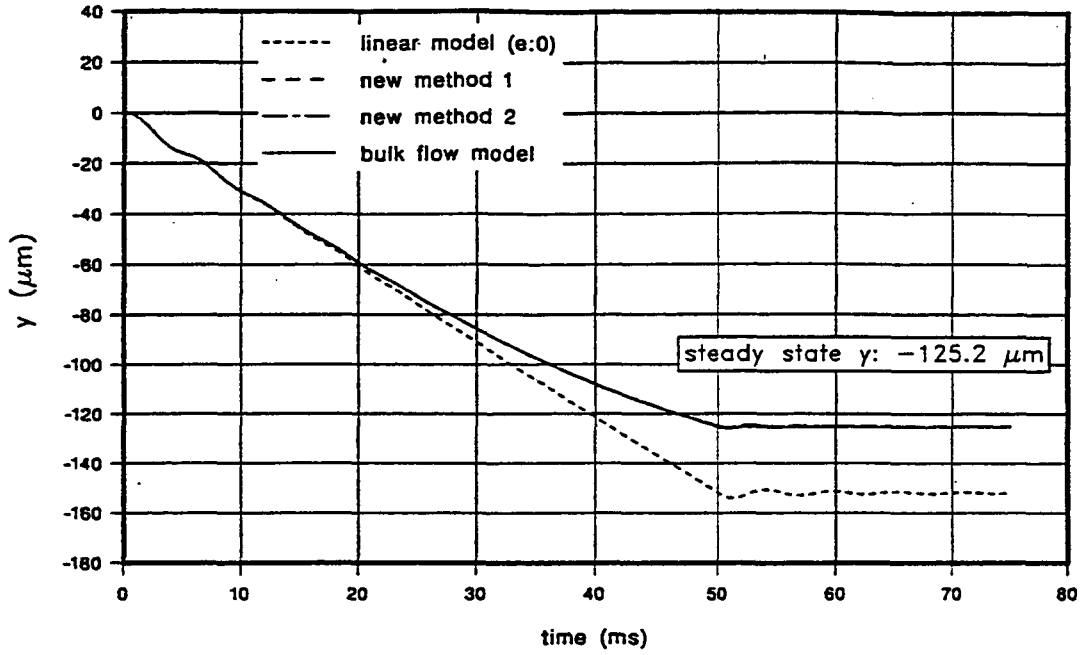


Figure 18

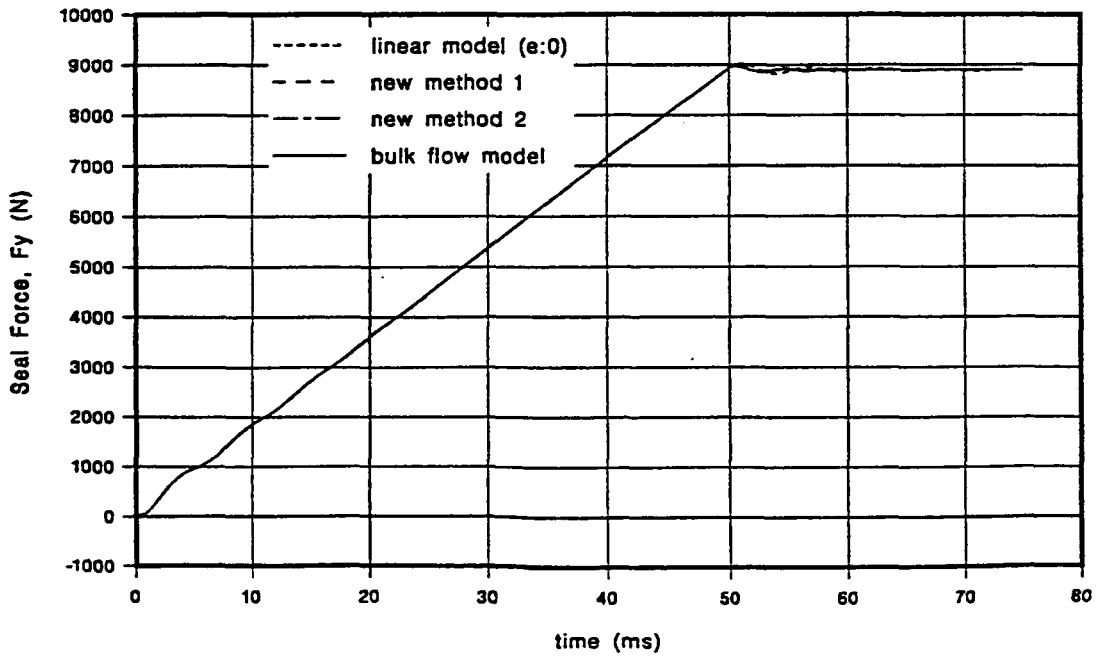


Figure 19 Gradually Applied Load, 8900 N (2000 lb), Disp. (y), Seal Force (Fy)

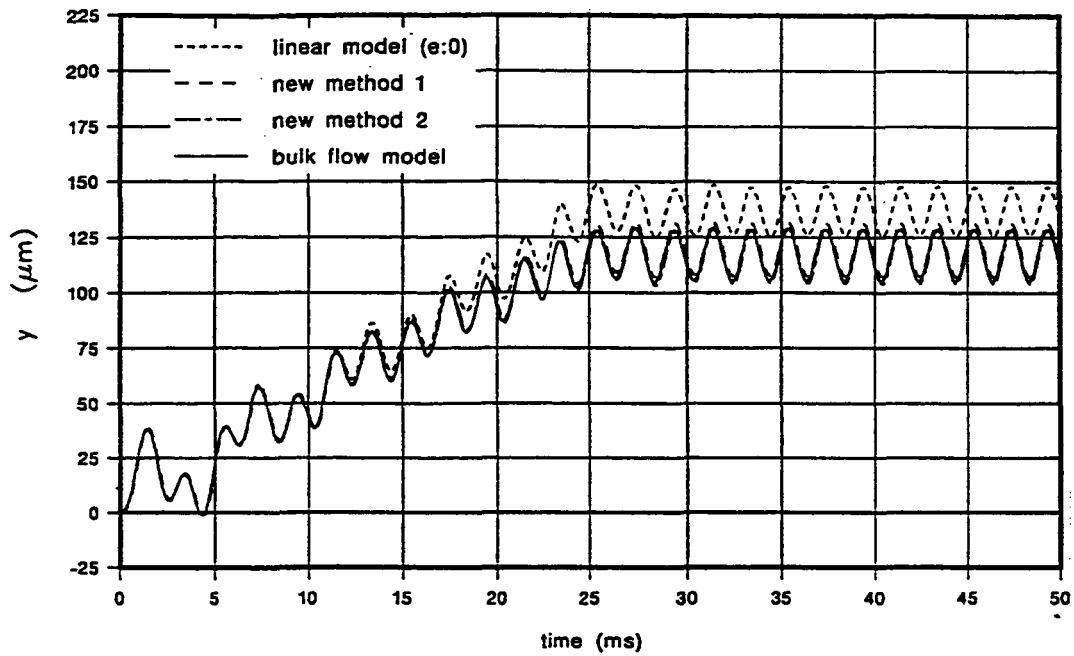


Figure 20

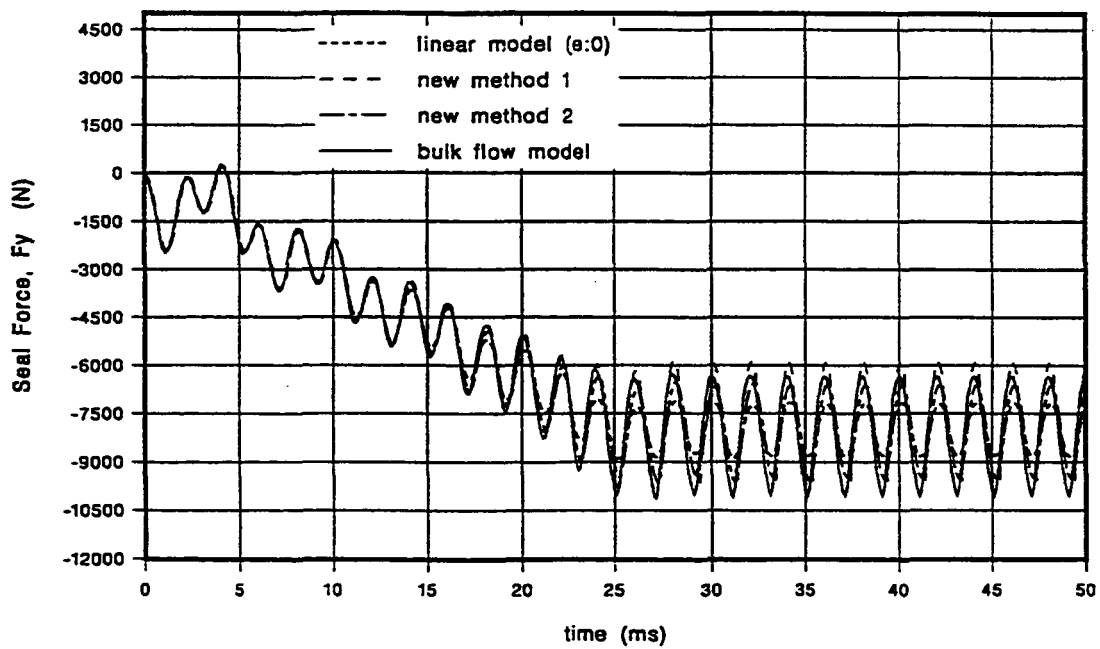


Figure 21 High Frequency Load (Eccentric), 4450N at 500Hz, Disp. (y), Force (F_y)

SEALS RESEARCH AT ALLIEDSIGNAL

M. Rifat Ullah
AlliedSignal Engines
AlliedSignal, Inc.
Phoenix, Arizona

5, 37

39463

A consortium has been formed to address seal problems in the Aerospace sector of AlliedSignal, Inc. The consortium is represented by makers of Propulsion Engines, Auxiliary Power Units, Gas Turbine Starters, etc. The goal is to improve Face Seal reliability, since Face Seals have become reliability drivers in many of our product lines. Several research programs are being implemented simultaneously this year. They include: Face Seal Modeling & Analysis Methodology; Oil Cooling of Seals; Seal Tracking Dynamics; Coking Formation & Prevention; and Seal Reliability Methods.

Air/Oil Seals Must Be Improved, Now!

- Consortium formed across Aerospace
- Products: Propulsion, APU, Starters etc.
- Focus: Face Seals
- Goal: 10x Life Improvement
- Strategy: Address Root Causes

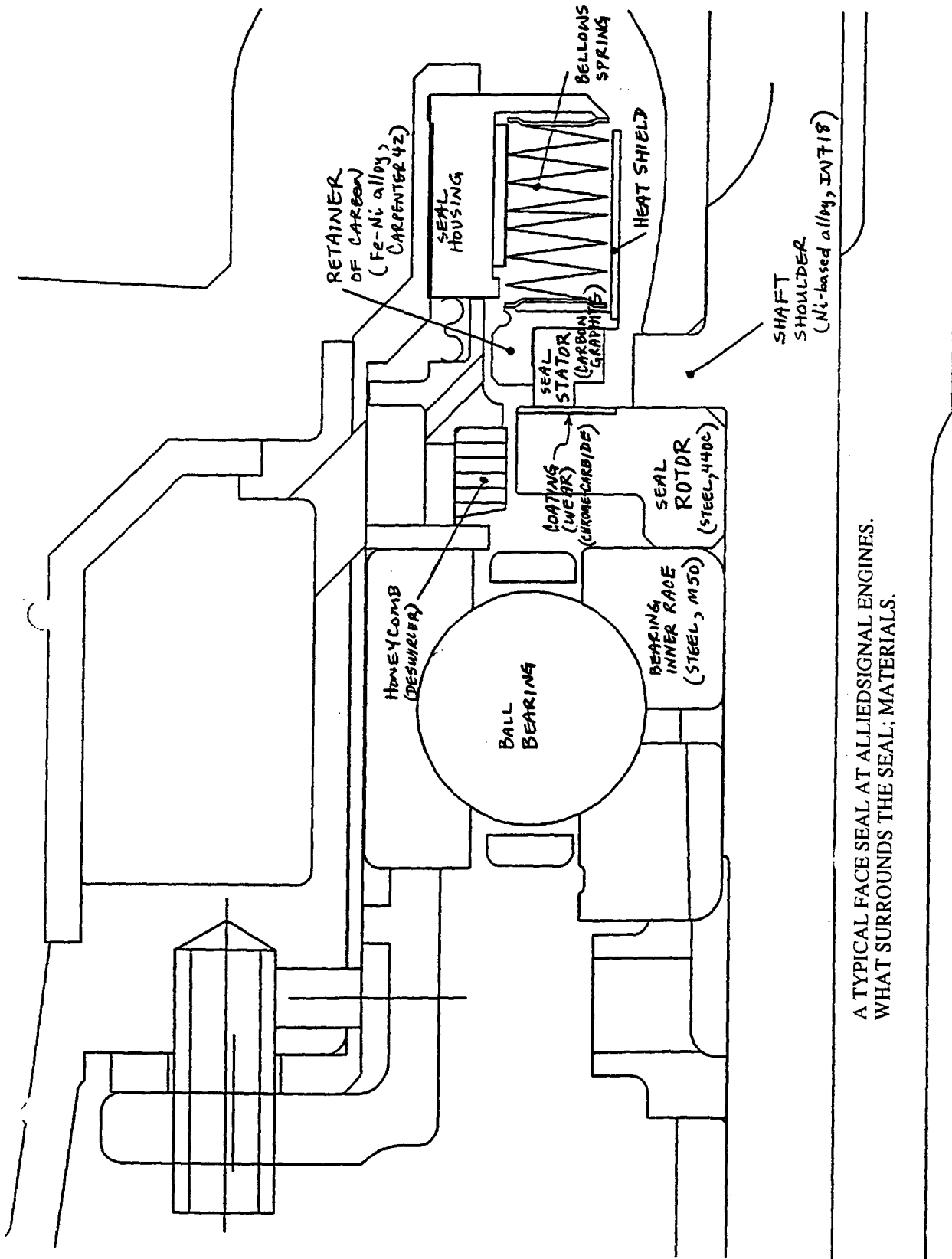
Root Causes & Their Effects

- **Causes:**

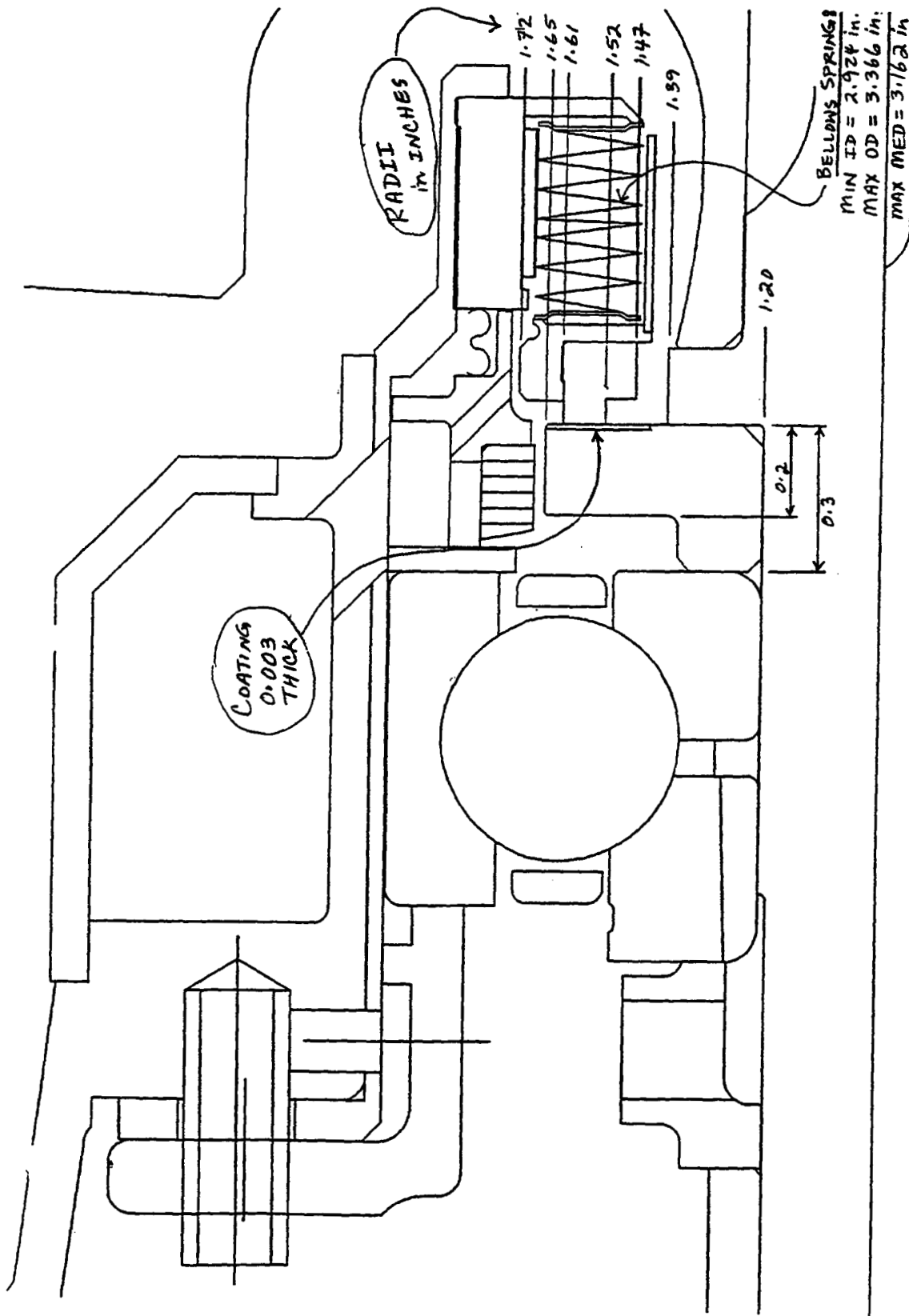
- » High Temperature in Seals
- » Incorrect Tracking Dynamics
- » Coking Propensity of Oil

- **Effects:**

- » Leakage (oil & air)
 - Smell of Oil or Smoke in Cabin
 - High Oil Consumption, etc.
- » Wear



A TYPICAL FACE SEAL AT ALLIED SIGNAL ENGINES.
 WHAT SURROUNDS THE SEAL; MATERIALS.



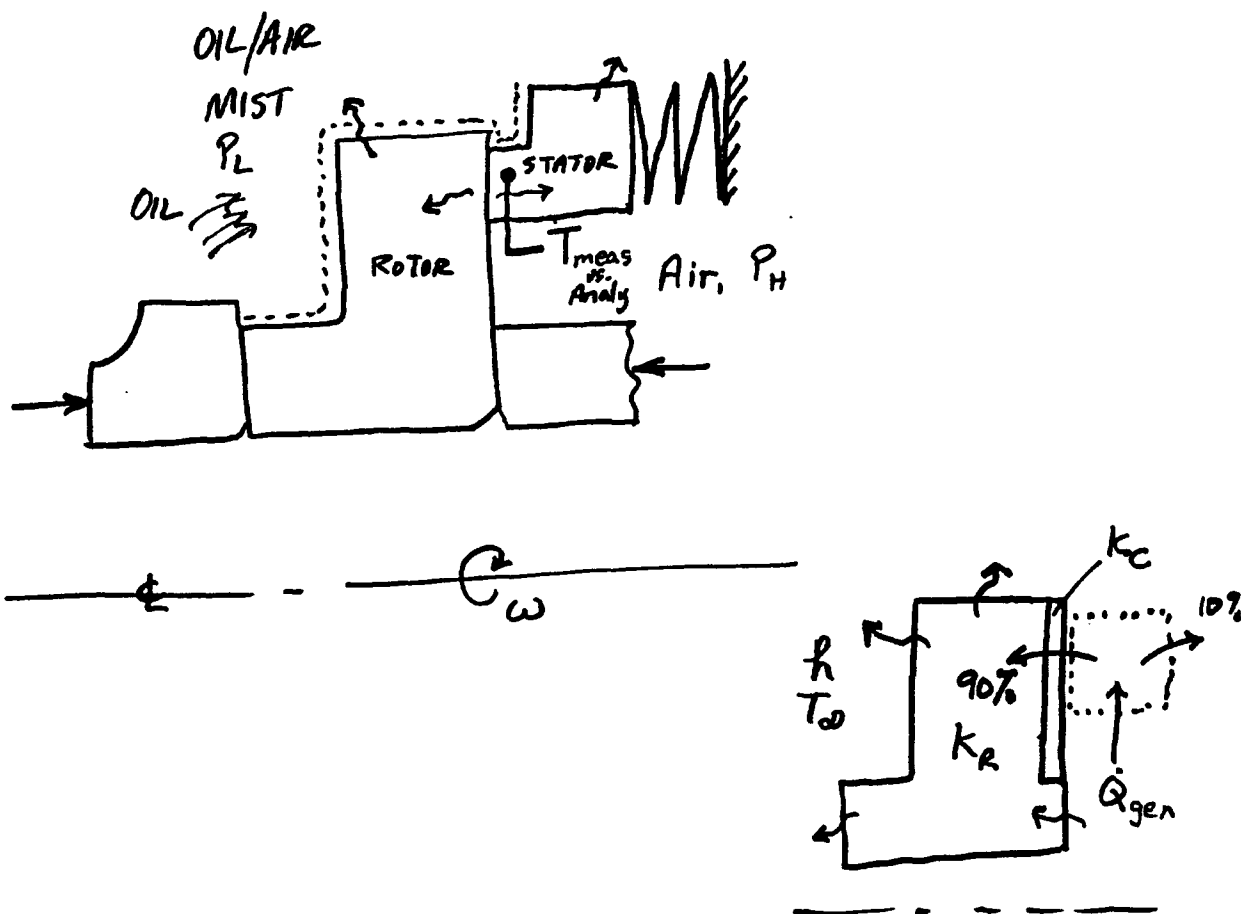
TYPICAL GEOMETRY OF SEAL (ALL DIMENSIONS IN INCHES)

Activities This Year

- Programs On-going:
 - » Thermal Modl/Ana Methods
 - » Oil Cooling Heat Transfer
 - » Tracking Dynamics Modl/Ana Methods
 - » Coking Chemistry, Causes & Resolution
 - » Reliability Methods
- Most Pgms have 1995 Year End Deadlines...Future Recomms to follow

Thermal Modl/ Ana Methods

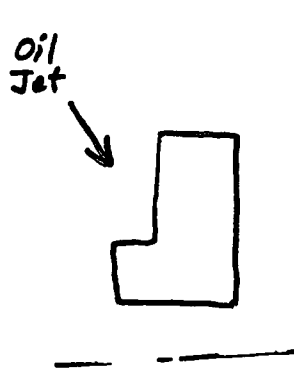
- Predictive Tools Dev: Temperatures, Deformations, Stresses, Leakages
- Steady-State in 1995
- Includes:
 - » Selection of Seal Codes
 - » Experimental Verification of Models



THERMAL MODELING/ANALYTICAL METHODS ARE BEING DEVELOPED AND REFINED THAT WILL PREDICT SEAL PERFORMANCE

Oil Cooling Heat Transfer

- Experimental Heat Trans (AZ St. Univ.)
- Overall Heat Transfer Coeffs in 1995
- To Be Used in Seal Models & Analyses
- Includes:
 - » Oil Jets
 - » Oil Splash (conventional method)
 - » Proprietary Cooling Scheme

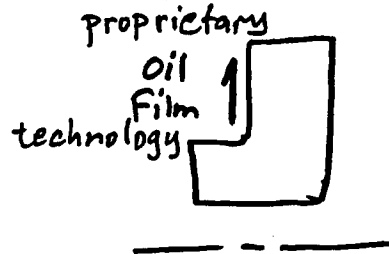


HEAT TRANSFER COEFFN.

OVERALL
SPACE AVERAGED

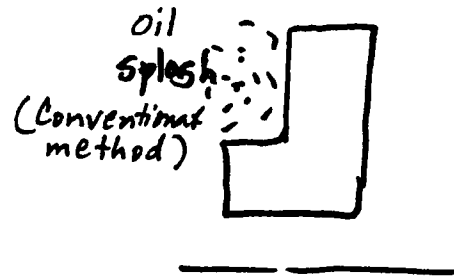
(LUMPED CAPACITANCE METHOD)

$Bi < .1$



$$Re_r \begin{cases} 30,000 \\ 7.5 \times 10^6 \end{cases}$$

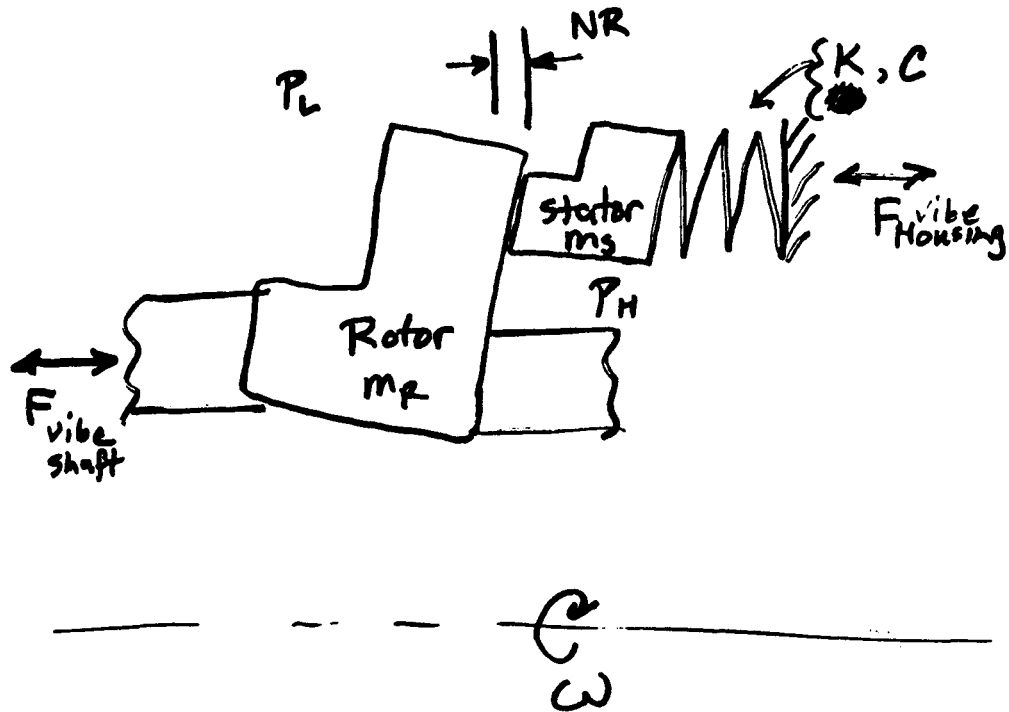
$$Pr \begin{cases} 88 \\ 24 \end{cases}$$



EXPERIMENTAL HEAT TRANSFER WORK IS UNDERWAY TO MEASURE COOLING EFFECTIVENESS, AND TO DEVELOP DESIGN DATA

Tracking Dyn. Modl/ Ana Methods

- Predictive Tools Dev: Tracking Response, Face Loads
- Steady-State in 1995
- Includes:
 - » Selection of Tracking Models
 - » Experimental Verification of Models



RIG TESTS ARE BEING PERFORMED TO CALIBRATE/CHARACTERIZE MODELS THAT WILL PREDICT SEAL/ROTOR SEPARATION AS A FUNCTION OF THE DESIGN PARAMETERS

Coking Chemistry: Causes & Resolution

- Understand Coking Mechanisms, Precursors
- Develop Tests to Measure Coking Propensity
- Develop Practical Solutions
- Scope Includes (With UDRI):
 - » Test Methods Dev
 - » Oil Components Analysis
 - » Recommend Additive Packages (proprietary)
 - » Smart Filter (proprietary)

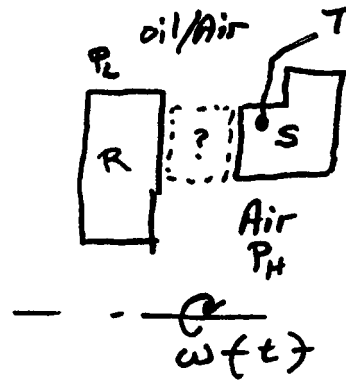
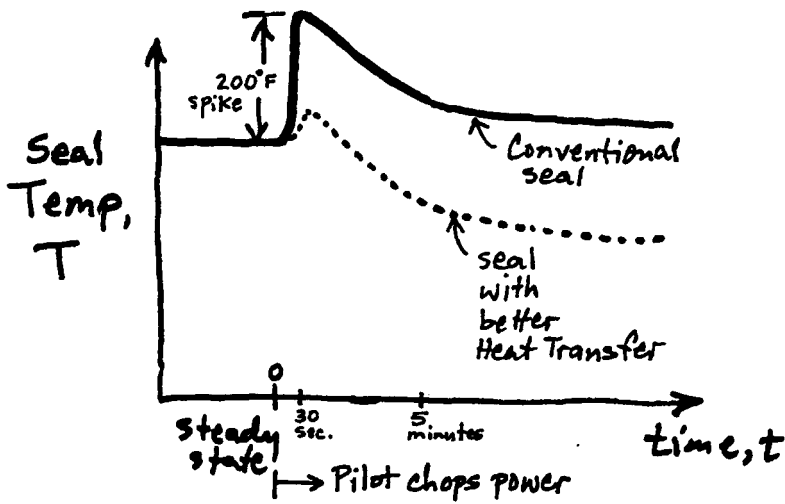
Reliability Methods

- Predictive Tools Dev: Seal Life, Failure Modes
- Baseline Today's Seals...Compare Effects of Future Improvements
- Weibull Methods
- Scope Includes:
 - » Reliability Database Development & Cleanup
 - » Process Definition (RawData -to- Life Pred)

Future Research Needs...

- Partial List....
 - » Transient Behavior of Seals (Temperature Spiking Problem)
 - » Friction & Wear Measurements With Realistic Geometries
 - » Efficient Oil Scavenging from Seal Compartments

THIS IS AN EXAMPLE OF A FUTURE RESEARCH NEED AT ALLIEDSIGNAL
(MANY SUCH NEEDS HAVE BEEN IDENTIFIED)



spike appears
strong function of
 $(P_H - P_L)$ as power is chopped,
but weak function
of speed during power chop.

A TRANSIENT TEMPERATURE SPIKING PROBLEM HAS BEEN OBSERVED IN AIR/OIL FACE SEALS. CAUSES UNKNOWN SO FAR. WHAT CAUSES IT AND HOW TO PREVENT THIS POTENTIALLY DAMAGING PHENOMENON?

INNOVATIVE SEALING TECHNOLOGY FOR NEXT GENERATION SUBSONIC ENGINES

John Munson
Allison Engine Company
Indianapolis, Indiana

522-07

and

39464

Bruce Steinetz
NASA Lewis Research Center
Cleveland, Ohio

The next generation of subsonic engines can be expected to continue the historical trend towards increased thrust to weight (T/W) and decreased specific fuel consumption (SFC). Development programs currently underway throughout the gas turbine industry such as DoD's Integrated High Performance Turbine Engine Technology (IHPTET), and more recently NASA's Advanced Subsonic Transport (AST) programs, have altered these trends in both pace and magnitude. Advanced seals and sealing technologies have become a prominent part of these efforts due to the large potential performance gains which can be realized.

Allison has recently completed a study for NASA the goal of which was to quantize the potential performance benefits which might accrue through the use of advanced seals in future subsonic gas turbine engines. For the study a two engines were analyzed, a small turboshaft and a larger turbofan engine to help assess the effect of engine size on the results. Engines were analyzed stage by stage with the most sensitive areas highlighted. Leakage characteristics for advanced seals were then substituted into secondary airflow models, and the leakage reductions documented. These leakage reductions were then converted to changes in performance, i.e. increased range, decreased takeoff gross weight, etc. and presented. It was found that the development and use of a relatively few advanced seals, less than 5, could for example reduce SFC by 10% or more.

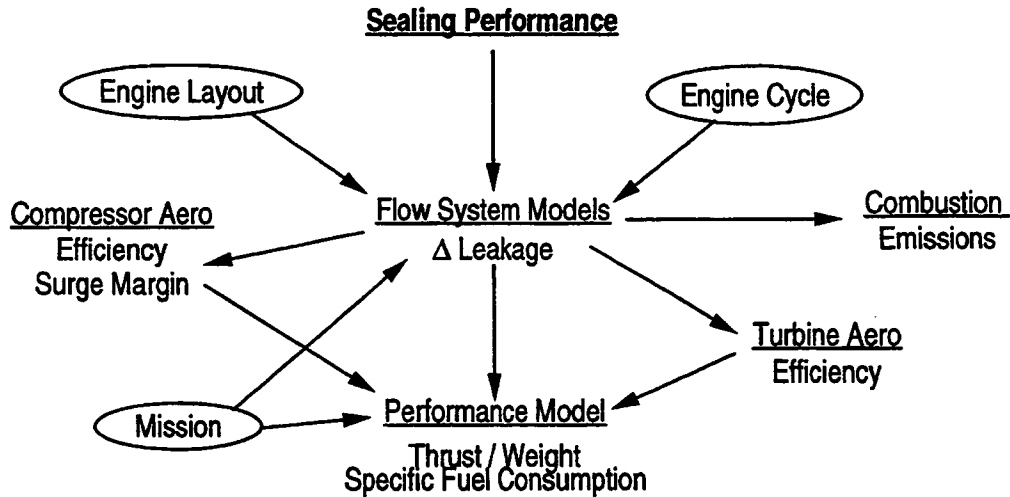
Improved Sealing Technology Provides the Best Avenue for Large Improvements in Performance

- Supportive of NASA - AST Program Goals
 - ◆ 8-10% Fuel efficiency improvements in future subsonic commercial transports (EIS 2005)
 - ◆ Reduced emissions
- Supportive of IHPTET goals
- Relatively low cost technology (large benefit / cost ratio)
- Close correlation between leakage reduction and % performance improvement

Program Objectives

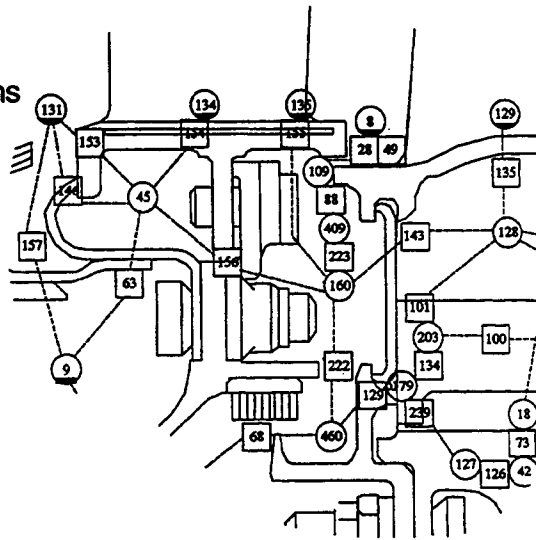
- Define sensitivity between performance gain and leakage reduction
- Considered 2 engines, small turboshaft & regional turbofan
- Baseline seal and engine technology defined by current Allison AE-3007, and LHTEC T801
- Analytically demonstrate the effect on engine performance provided by incorporation of advanced sealing concepts
- Identify technology hurdles and propose development plan to mature sealing technologies for 2005 EIS date

Analytical Procedure



Definitions

- Selected 2 modern engines to define baseline, both contain latest seal technologies
 - ◆ Brush Seals
 - ◆ Abradable / Abrasive blade tip systems
 - ◆ Mechanical / Carbon sump seals
- **What is Leakage ?**
 - ◆ Overboard airflows
 - ◆ Any airflow which exits or enters from the engine main power stream
 - ◆ Blade & vane cooling flows specifically exempted
- Assumption - cooling flows are exactly correct



Results Reported Based on Simplified Duty Cycle

<u>Regional</u>			<u>Turboshaft</u>		
<u>Point</u>	<u>Condition</u>	<u>Duration</u>	<u>Point</u>	<u>Condition</u>	<u>Duration</u>
Idle	SLS 103°F Day	34%	Idle	SL Stand Day	5%
Cruise	0.7M, 20K Stand	33%	50% MCP	SL " "	40%
Max	SL, ISO+18°F	33%	MCP	SL " "	46%
			IRP	SL " "	9%

Advanced Engines

- Regional 20 - 24,000 pound thrust class
 - ◆ - Increased cycle pressure ratio ~ 40:1
 - ◆ - Increased turbine inlet temperature ~ 2900°F
 - ◆ - Increased bypass ratio ~ 15:1
- Small turboshaft
 - ◆ - Compressor unchanged
 - - Rebladed gasifier / power turbine
 - ◆ - Increased power turbine mechanical speed
 - ◆ - Increased turbine inlet temperature ~ 2900°F

Leakage in Regional Engine Concentrated at Relatively Few Locations

- 50% of leakage through 2 turbine blade / vane gaps
- Top 5% leaks account for 75% of total leakage flow
- Effort at few locations can yield large returns

Leakage Location	Mission Weighted Rank	Weighted % of Total Leakage	Weighted % Core Flow	
Front sump 0 seal buffer	0.00	0.02	0.00	
Front sump inershaf seal	0.01	0.30	0.02	
Front sump #4 seal	0.00	0.01	0.00	
Front sump #4 seal buffer	0.09	2.24	0.16	
Comp discharge overboard	0.12	3.04	0.22	
Preswirlr Overboard	0.18	4.55	0.32	
Center sump #5 seal	0.00	0.01	0.00	
Center sump #6 seal	0.00	0.01	0.00	
Combustor to 1st nozzle inner	0.12	2.47	0.18	
1st nozzle to 1st blade *	1.00	24.94	1.79	
1st blade to 2nd nozzle *	0.22	5.39	0.38	
2nd nozzle to 2nd blade *	0.77	19.26	1.38	
2nd blade to 3rd nozzle *	0.37	9.13	0.65	
3rd nozzle to 3rd blade *	0.33	8.34	0.59	
3rd blade to 4th nozzle *	0.02	0.58	0.04	
4th nozzle to 4th blade *	0.15	3.79	0.27	
4th blade to 5th nozzle *	0.04	0.90	0.07	
5th nozzle to 6th blade *	0.11	2.64	0.19	
6th blade to rtbs	0.04	1.06	0.08	
Combustor to 1st nozzle outer	0.05	1.05	0.08	
1st nozzle to 1st blade *	0.03	0.75	0.05	
1st blade to 2nd nozzle *	0.21	5.21	0.38	
2nd nozzle to 2nd blade *	0.15	3.72	0.27	
2nd blade to 3rd nozzle *	0.01	0.29	0.02	
3rd nozzle to 3rd blade *	0.00	0.00	0.00	
3rd blade to 4th nozzle *	0.00	0.00	0.00	
4th nozzle to 4th blade *	0.00	0.00	0.00	
4th blade to 5th nozzle *	0.00	0.00	0.00	
5th nozzle to 6th blade *	0.00	0.00	0.00	
6th blade to rtbs	0.01	0.30	0.02	
Total Leaks (Blade tip Exclud)		100.00	7.160285	

Smaller Turboshaft Uses Proportionally More Air

- Leakage is still relatively concentrated
- Top 5 leaks account for 50% of leakage
- Leakage somewhat more distributed throughout engine

Leakage Location	Ranking Mission Weighted	% Mission Weighted	Weighted % Core Flow
Front sump #1 seal buffer	0.08	1.66	0.27
Front sump vent	0.06	1.13	0.18
Front sump #2 seal buffer	0.04	0.91	0.15
Intershaft seal	0.06	1.23	0.20
Comp 1st stage	0.26	5.20	0.85
Combustor to 1st nozzle inner	0.16	3.30	0.54
1st nozzle to 1st blade "	0.55	11.10	1.81
1st blade to 2nd nozzle "	1.00	20.43	3.35
1st blade to 2nd nozzle "	1.00	20.43	3.35
2nd blade to 3rd nozzle "	0.55	11.21	1.83
2nd blade to 3rd nozzle "	0.55	11.21	1.83
3rd nozzle to 3rd blade "	0.39	8.13	1.34
3rd blade to 4th nozzle "	0.33	6.78	1.10
4th nozzle to 4th blade "	0.09	1.80	0.29
4th blade overboard	0.21	4.36	0.72
1st nozzle to 1st blade	0.33	6.80	1.11
1st nozzle / 1st blade trk	0.07	1.45	0.24
1st blade to 2nd nozzle	0.31	6.31	1.03
2nd nozzle / 2nd bld trk	0.22	4.49	0.73
Total Leaks (Blade tip Excluded)		100.00	16.35

Engine Performance Improvements Impact Entire Aircraft

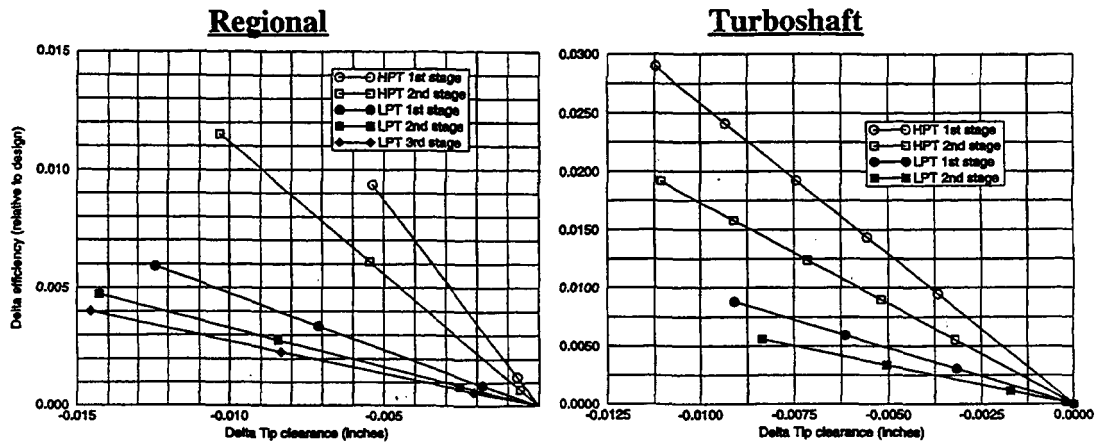
- Regional based on 120 - 150 seat aircraft optimized for minimum takeoff gross weight
 - ◆ Twin engine
 - ◆ 1600 NM range
 - ◆ McDonnell-Douglas MD-80 used as starting point for model
- AH-64 Apache used as model for helicopter airframe
 - ◆ Helicopter equipped with 1016 Lb payload
 - ◆ Fuel for 260 NM mission + 30 min reserve
 - ◆ Takeoff gross weight 14612 Lbs

Smaller Engine Shows Greater Sensitivity to Leakage

	<u>Regional</u>				<u>Turboshaft</u>					
	Δ SFC	Δ Fn/Wgt	Δ TOGW	Δ MFB	Δ SFC	Δ HP	Δ TOG- W	Δ Fuel Burn	Δ Pay- load	Δ Range
	%/PT	%/PT	%/PT	%/PT	%/PT	%/PT	%/PT	%/PT	%/PT	%/PT
CDP -> O/B	1.5	-2.8	0.4	2.0	-	-	-	-	-	-
CDP -> HPT	0.7	-2.1	0.2	1.1	1.530	-3.280	0.99	2.497	-39.7	-20.1
INT -> HPT	0.3	-1.6	0.2	0.6	-	-	-	-	-	-
INT -> O/B	-	-	-	-	0.870	-1.770	0.55	1.410	-22.8	-3.78
η LPC	-	-	-	-	0.984	-1.667	0.58	1.560	-20.6	-10.4
η HPC	1.0	-1.9	0.2	1.3	0.732	-1.309	0.44	1.170	-16.1	-8.20
η HPT	0.8	-0.9	0.1	1.0	1.624	-2.446	0.93	2.554	-30.6	-15.6
η LPT	0.8	-0.9	0.1	1.0	1.167	-1.174	0.60	1.784	-15.4	-8.00

Small coefficients per %Increase in bleed flows, or %Decrease in component efficiency

Blade Tip Clearances Strongly Effect Turbine Performance



- Small turboshaft shows almost 2X sensitivity
- Similar analysis performed for centrifugal (turboshaft), and axial (regional) compressors

Seal Technology Requirements

- Must be near term to meet EIS 2005 goal
- Currently under development somewhere
- Required materials currently available
- Risk / Cost considerations
- Size / Space / Physical constraints limit applicability
- Desire more than one approach, if possible

Seal / Seal Technology Strategy

Priority Sealing Locations

Interstage blade / vane gaps

compressor (axial)

turbine

Compressor Discharge

Blade tips

compressor (axial)

compressor (centrifugal)

turbine (unshrouded)

turbine (shrouded)

Seal Technologies

Overlap treatment

Brush Seals

Film Riding Seal

Active Clearance Control

"Smart Metal"

Case Cooling

Demonstration of Potential Regional Performance Gains

	<u>ΔFlow</u>	<u>ΔSFC</u>	<u>ΔFn/Wgt</u>	<u>ΔTOGW</u>	<u>ΔMFB</u>
FR Rim	-2.50%	-1.80%	5.43%	-0.50%	-2.8%
Comp Int	-	-1.10%	3.40%	-0.40%	-1.4%
Tot'l Rim	-2.50%	-2.90%	8.83%	-0.90%	-4.2%
Comp End	-0.20%	-0.33%	0.61%	0.09%	-0.4%
Preswirl	-0.32%	-0.49%	0.91%	-0.13%	-0.6%
Tot'l Face	-0.52%	-0.82%	1.52%	-0.22%	-1.0%
Tot'l FR	-3.02%	-3.72%	10.35%	-1.12%	-5.2%
HPT Tip	-	-1.60%	3.36%	-0.48%	-2.1%
Grand Tot	-3.02%	-5.32%	13.71%	-1.60%	-7.3%

Demonstration of Potential Small Engine Gains

	<u>ΔFlow</u>	<u>ΔSFC</u>	<u>ΔHP</u>	<u>ΔPAYLD</u>	<u>ΔRNG</u>
FR Rim	-3.27%	-5.00%	10.7%	130%	65.7%
Intershaft	-0.32%	-0.28%	0.56%	7.30%	3.78%
HPT Tip	-	-1.78%	2.67%	33.5%	17.1%
<u>Comp Tip</u>	<u>-</u>	<u>-3.96%</u>	<u>6.90%</u>	<u>85.3%</u>	<u>43.3%</u>
Tot'l Tip	-	-5.74%	9.57%	118.8%	50.4%
Grand Tot	-3.60%	-11.0%	20.8%	256%	120%

Conclusions

- Large gains possible through development & use of advanced seal technology
- Large gains are attainable through the use of only a few advanced seals
- Even larger gains than demonstrated are possible with "clean sheet" approach to secondary flow system design
- No matter what else is done with engine cycle, etc. identified losses due to sealing remain
- Better seals are an inexpensive way to substantially boost engine performance

FRACTIONAL WHIRL MOTION IN WAVE JOURNAL BEARINGS

Florin Dimofte and Robert C. Hendricks
NASA Lewis Research Center
Cleveland, Ohio

523-37

39465

ABSTRACT

Unloaded gas, plain journal bearings experience sub-synchronous whirl motion due to fluid film instabilities and wall contact usually occurs immediately after the onset of the whirl motion. An alternative is the wave journal bearing which significantly improves bearing stability. The predicted threshold where the sub-synchronous whirl motion starts was well confirmed by the experimental observation. In addition, both a two-wave and a three-wave journal bearing can operate free of sub-synchronous whirl motion over a large range in speeds. When the sub-synchronous whirl motion occurs, both the two-wave and three-wave bearing can run in a whirl orbit well within the bearing clearance. At large clearances and wave amplitudes a two-wave bearing, unlike other bearings, can exhibit a sub-synchronous whirl movement at both low and high speeds, but can run extremely stable and without whirl at intermediate speeds. Moreover, in these cases, the whirl frequencies are close to a quarter of the synchronous speed. The three-wave bearing can exhibit sub-synchronous whirl motion only after a specific threshold when the speed increases and the whirl frequencies are close to half of the synchronous speed.

INTRODUCTION

The whirl motion of the shaft inside a gas journal bearing is a result of an unstable condition of the lubricant fluid film. The frequency of this motion is, in most cases, equal or less than one-half of shaft frequency and is called "Sub-Synchronous Frequency Whirl" (SSFW). Unloaded plain journal bearings are very susceptible to the SSFW. Plain journal bearings experiencing SSFW usually develop an unstable motion and wall contact occurs immediately after the onset of the whirl motion resulting in bearing failure. This phenomena was observed soon after gas bearing applications were developed starting in the middle 1950's. Due to its importance for bearing life the SSFW was also well analyzed as a fluid film instability condition. Among others, Castelli and Elrod [1] and Constantinescu [2] contributed work that theoretically established when SSFW occurs.

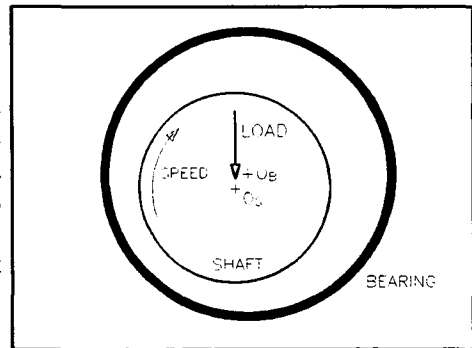


FIG. 1 PLAIN JOURNAL BEARING

Unlike the plain journal bearing (Fig.1), a wave journal bearing (Fig.2 shows a three-wave bearing) reduces the journal bearing sensitivity to SSFW. A wave journal bearing [3] is a bearing with a slight, but precise variation in the circular profile of a journal bearing such that a waved profile is circumscribed on the inner bearing diameter and having a wave amplitude equal to a fraction of the bearing clearance. Fig. 2 shows a three-wave bearing. The clearance and the wave and the wave's amplitude are greatly exaggerated in Fig.1 and 2 so that the concept may be visualized.

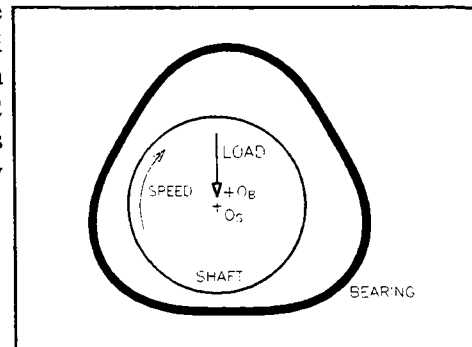


FIG. 2 THREE-WAVE JOURNAL BEARING

BEARING STABILITY

In a bearing stability calculation, as a first approach, the rotor can be

considered rigid and symmetrical, and supported by two identical bearings. Therefore, each bearing carries a mass M that is one-half of the rotor mass. The motion equation of the center of the shaft inside the bearing can be written as:

$$\begin{bmatrix} (Z_{xx} - M \nu^2) & Z_{xy} \\ Z_{yx} & (Z_{yy} - M \nu^2) \end{bmatrix} \begin{bmatrix} x \\ y \end{bmatrix} = 0$$

where the bearing is represented by its four impedance coefficients, Z_{jk} ($j = x, y; k = x, y$) which can be calculated by using a small perturbation technique [4], and ν is the whirl frequency.

The threshold of instability occurs when the determinant of the matrix is zero and the corresponding mass, M_c , is the mass required to develop the SSFW movement of the shaft inside the bearing. The bearing can run free of half frequency whirl movement when its actual allocated mass is less than the critical mass (M_c).

TEST RIG

A bench test rig was assembled to provide information about how a journal bearing behaves when SSFW movement occurs [5]. The bearing tester uses a commercial spindle capable of 30,000 RPM with a run-out of less than 1 micron. The rig was set up with the shaft oriented vertically such that the test bearing could easily run in an unloaded condition (Fig. 3). Air at surrounding atmospheric conditions, was used as the lubricant. The test bearing is supported by double thrust levitation air bearing plates that allow the bearing to move very freely in the radial direction (Fig. 4). Two pairs of displacement sensors allow measurement of bearing orbits with respect to the shaft at two locations, just above and just below the test bearing. This configuration allows the bearing threshold susceptibility to SSFW to be precisely observed and provides information

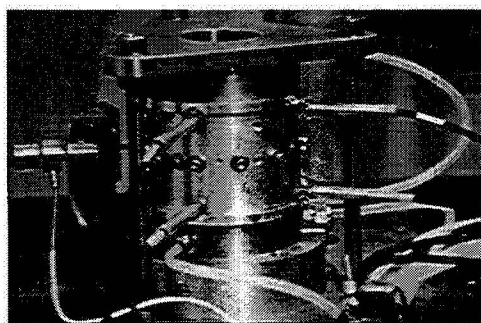


FIG. 4 BEARING FOR SSFW TEST

how the bearing behaves under SSFW.

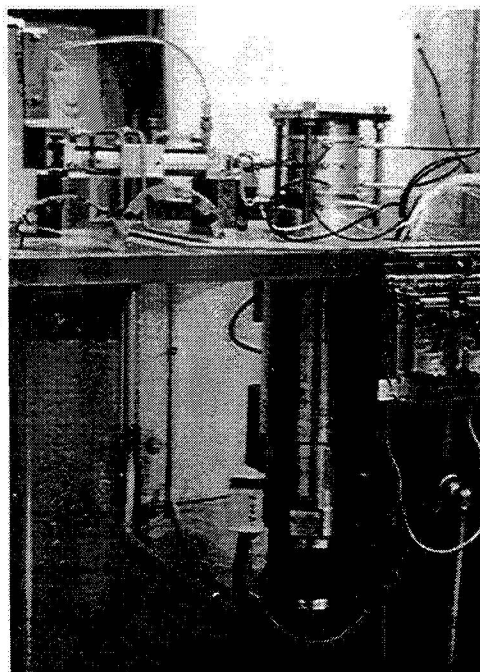


FIG. 3 TEST RIG

RESULTS AND DISCUSSION

A plain journal bearing with 50 mm diameter, 58 mm length, and 0.038 mm radial clearance was tested [6]. The maximum out of round was 0.0012 mm which results in the ratio of the distortion amplitude to the radial clearance of 0.034. The test results confirm that the plain journal bearing is very susceptible to SSFW. The whirl movement appeared soon after the shaft started to turn (e.g. 355 RPM). The motion was unstable because its orbit increased very rapidly and the shaft rubbed the bearing wall as can be seen in the bottom screen of Fig. 5. The upper screen of Fig. 4 shows the tracks of two displacement sensors, one in the top and the other in the bottom, fixed in the same vertical plane. Both of these tracks followed the same path showing a translatory movement of the bearing which is close to a harmonic motion. The frequency of the bearing motion was 2.96 Hz or half of the shaft frequency.

Then, both a three- and a two-wave journal bearing were tested. The three-wave bearing had a radial clearance of .037 mm and a corresponding ratio of the wave amplitude ratio to the radial clearance of 0.343. This bearing ran free of SSFW up to a threshold speed between 740 and 960 RPM. One of the observed threshold can be seen in

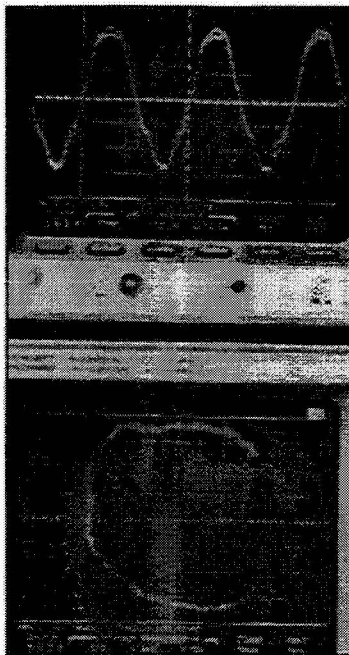


FIG. 5 SSFW OF A PLAIN BEARING AT 335 RPM, WHIRL FREQUENCY = 2.9 Hz

Fig. 6. When the radial clearance was reduced to 0.015 mm the three-wave bearing ran free of SSFW up to a speed of 11900 RPM. The wave amplitude ratio was, in this case, only 0.168. These experimentally observed thresholds of SSFW were in very good agreement with the theoretical prediction as can be seen in Fig. 7 [6]. Moreover, as speed increases, the whirl orbit is stable keeping a safe range well within the bearing clearance (see bottom screen in Fig. 8). The three-wave bearing profile limits the maximum amplitude of the shaft center (upper screen of Fig. 8) that modifies the shape of the orbit from circular to a three side orbit (bottom screen of Fig. 8).

The test of a two-wave bearing with 0.038 mm radial clearance and a wave amplitude ratio of 0.442 shows that the bearing operates very stable at intermediary speeds such as 10000 RPM (Fig. 9) while experiencing SSFW at both low and high speeds such as 600 and 24000 RPM respectively (Fig.10 and Fig. 11). When the SSFW occurs the bearing runs stable in a manner similar to the three wave bearing. However the dominant sub-synchronous whirl frequency, in this case, is close to a quarter of the synchronous shaft speed. In addition the half frequency and moreover the synchronous frequency are also present as can be better seen in the upper part of Fig. 11. When the wave amplitude ratio was decreased to 0.214, the whirl frequency increases close to half of the synchronous frequency like in both plain and three wave journal bearings.

CONCLUDING REMARKS

1. The observed thresholds at which the SSFW occurs correspond with the predicted thresholds.
2. An unloaded journal bearing with an altered circular profile, such as a wave bearing, allows operation over a range of speeds under which the bearing can run free of SSFW. When this movement occurs the radius of the SSFW increases up to a size where the equilibrium between the radial force generated by the whirl movement and the pressure force in the film is established. The equilibrium radius is smaller than the bearing clearance and the bearing can run stably and safely.
3. At large clearances and wave amplitudes a two-wave bearing, unlike other bearings, can exhibit a sub-synchronous whirl movement at both low and high speeds, but can run extremely stable and without whirl at intermediate speeds. Moreover, in these cases, the whirl frequencies are close to a quarter of the synchronous speed. The three-wave bearing can exhibit the sub-synchronous whirl motion only after a specific threshold when the speed increases and the whirl frequencies are close to half of the synchronous speed.

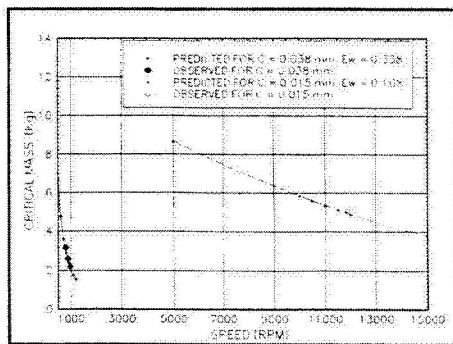


FIG. 7 PREDICTED AND OBSERVED THRESHOLD OF SSFW FOR THREE-WAVE BEARINGS.

4. At smaller clearances both two- and three-wave bearings exhibit half synchronous whirl frequency and increased onset whirl thresholds.

REFERENCES

1. Castelli, V. and Elrod, H.G., "Solution of the Stability Problem for 360 Deg Self-Acting, Gas-Lubricated Bearings," Journal of Basic

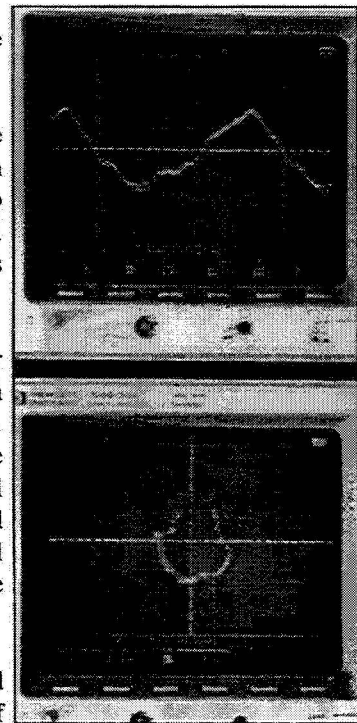


FIG. 6 THRESHOLD OF SSFW OF A THREE-WAVE BEARING AT 921 RPM, WHIRL FREQUENCY = 7.58 Hz.

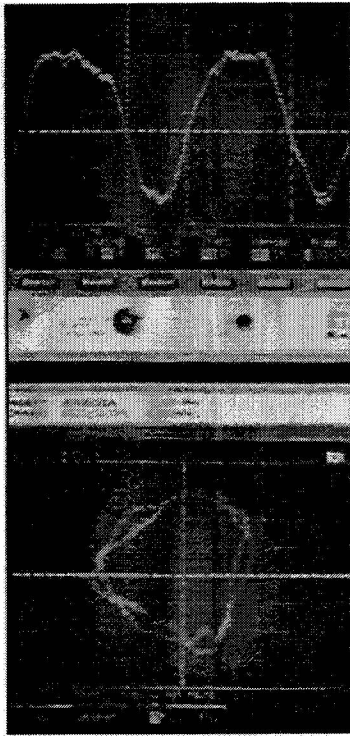


FIG. 8 SSFW OF A THREE-WAVE BEARING AT 1391 RPM, WHIRL FREQUENCY = 10.21 Hz

Engineering, Trans. ASME, Series D, Vol 87, 1, pp. 199-212, (1965).

2. Constantinescu, V.N., "On Hydrodynamic Instability of Gas-lubricated Journal Bearings," Journal of Basic Engineering, Trans. ASME, Series D, Vol 87, 3, pp. 579-588, (1965).

3. Dimofte, F., "Wave Journal Bearing with Compressible Lubricant; Part I: The Wave Bearing Concept and a Comparison with a Plain Circular Journal Bearing", presented to STLE 1993 Annual Meeting, May 17-20, 1993, Calgary, Canada, to be published in STLE Tribology Transactions No. 1, Jan. 1995.

4. Dimofte, F., "Effect of Fluid Compressibility on Journal Bearing Performance," STLE Tribology Trans. Vol. 36, 3, pp. 341-350, (1993).

5. Dimofte, F., Addy, H., E., Jr., and Walker, J., F., "Preliminary Experimental Results of a Three Wave Journal Air Bearing", Proceeding of Advanced Earth-to-Orbit Propulsion Technology Conference held at NASA Marshall Space Flight Center, Huntsville, AL, May 17-19, 1994, NASA CP 3282, Vol II, pp.375-384, 1994.

6. Dimofte, F., "Predicted and Experimental Observed Fluid Film Instability of an Unloaded Gas Journal Bearing" to be presented to the 15th Canadian Congress of Applied Mechanics CANCAM 95, University of Victoria, Victoria, BC, May 28 - June 2, 1995.

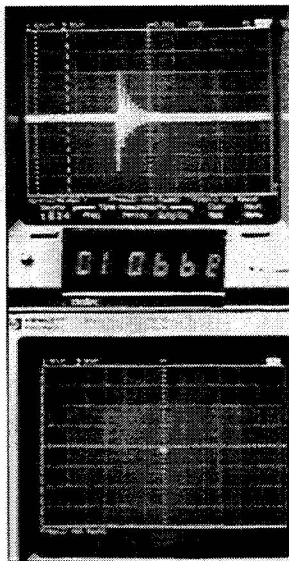


FIG. 9 SYNCHRONOUS WHIRL OF A TWO-WAVE BEARING AT 10668 RPM AFTER AN IMPACT.

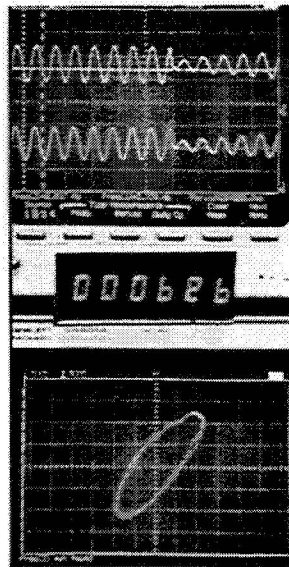


FIG. 10 SSFW OF A TWO-WAVE BEARING AT 626 RPM, WHIRL FREQUENCY = 2.81 (2.77) Hz

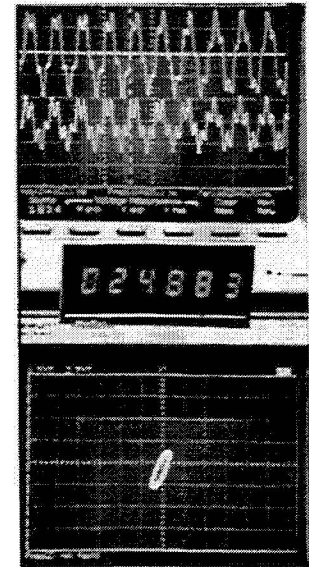


FIG. 11 SSFW OF A TWO-WAVE BEARING AT 24883 RPM, WHIRL FREQUENCY = 103.1, 206.2, AND 412.4 Hz

Streamfunction Plot

Regions I, II and Blade Shanks, Run No. 202

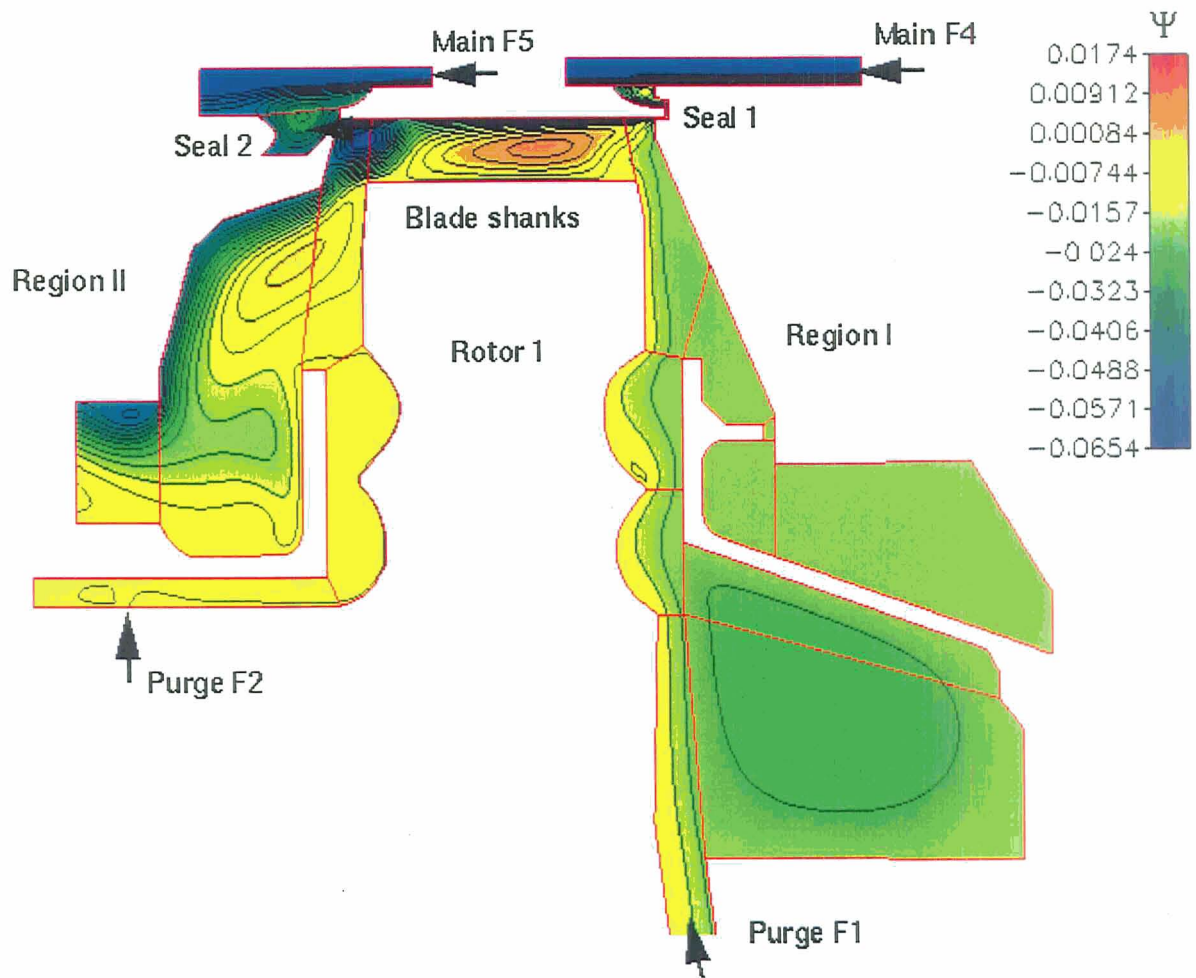


Figure 3 —(a) Streamline pattern in regions I, II and the connecting blade shank region. (b) Streamline pattern in regions III, IV, connecting blade shank region and the slot in the stator support. (c) Flow detail at seals 1, 2, and blade shank region to illustrate the complex vortical structure and Mainpath flow ingestion.

Streamfunction Plot

Regions III, IV and Blade Shanks, Run No. 202

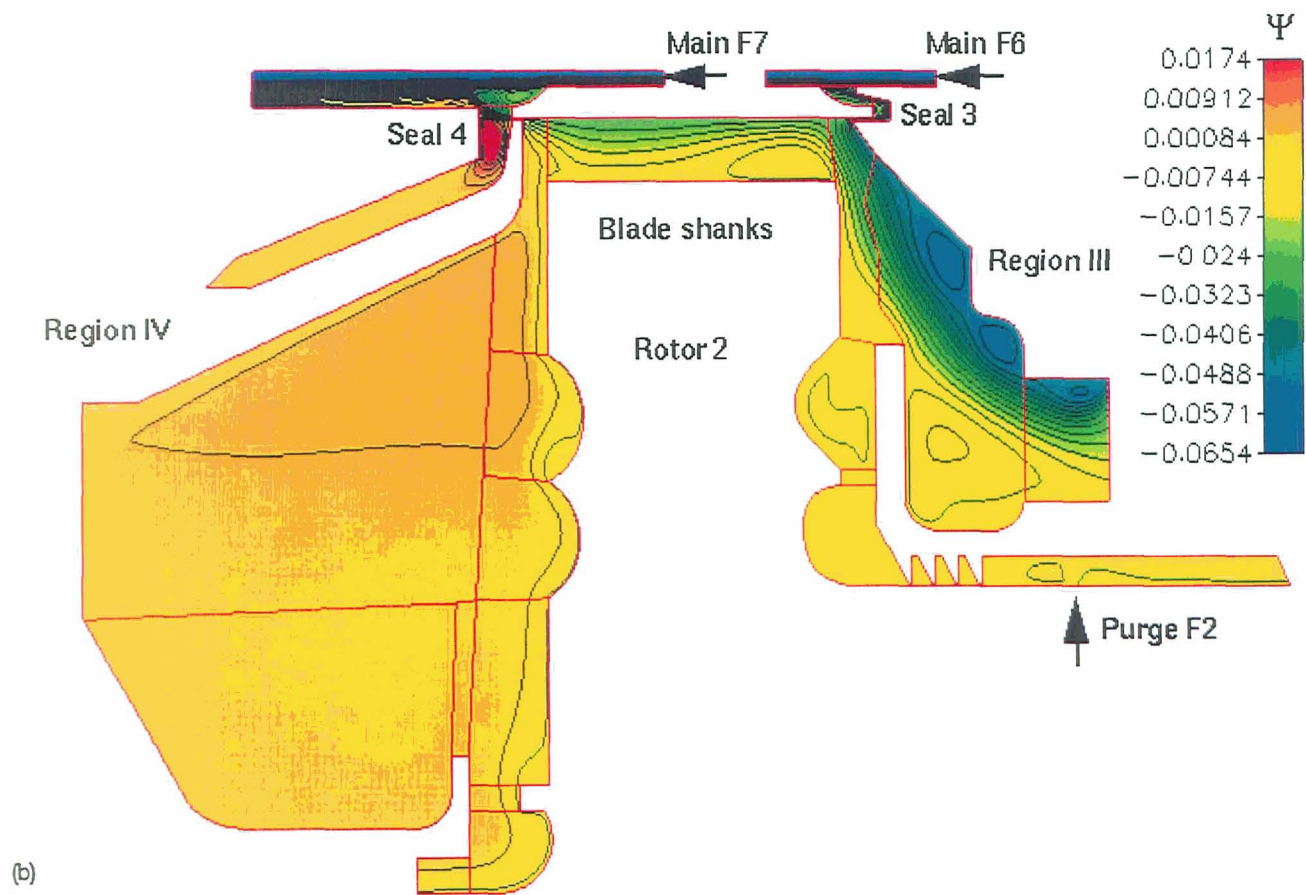


Figure 3 —(a) Streamline pattern in regions I, II and the connecting blade shank region. (b) Streamline pattern in regions III, IV, connecting blade shank region and the slot in the stator support. (c) Flow detail at seals 1, 2, and blade shank region to illustrate the complex vortical structure and Mainpath flow ingestion.

Streamfunction Plot

Detail in Blade Shanks on Rotor 1, Run No. 202

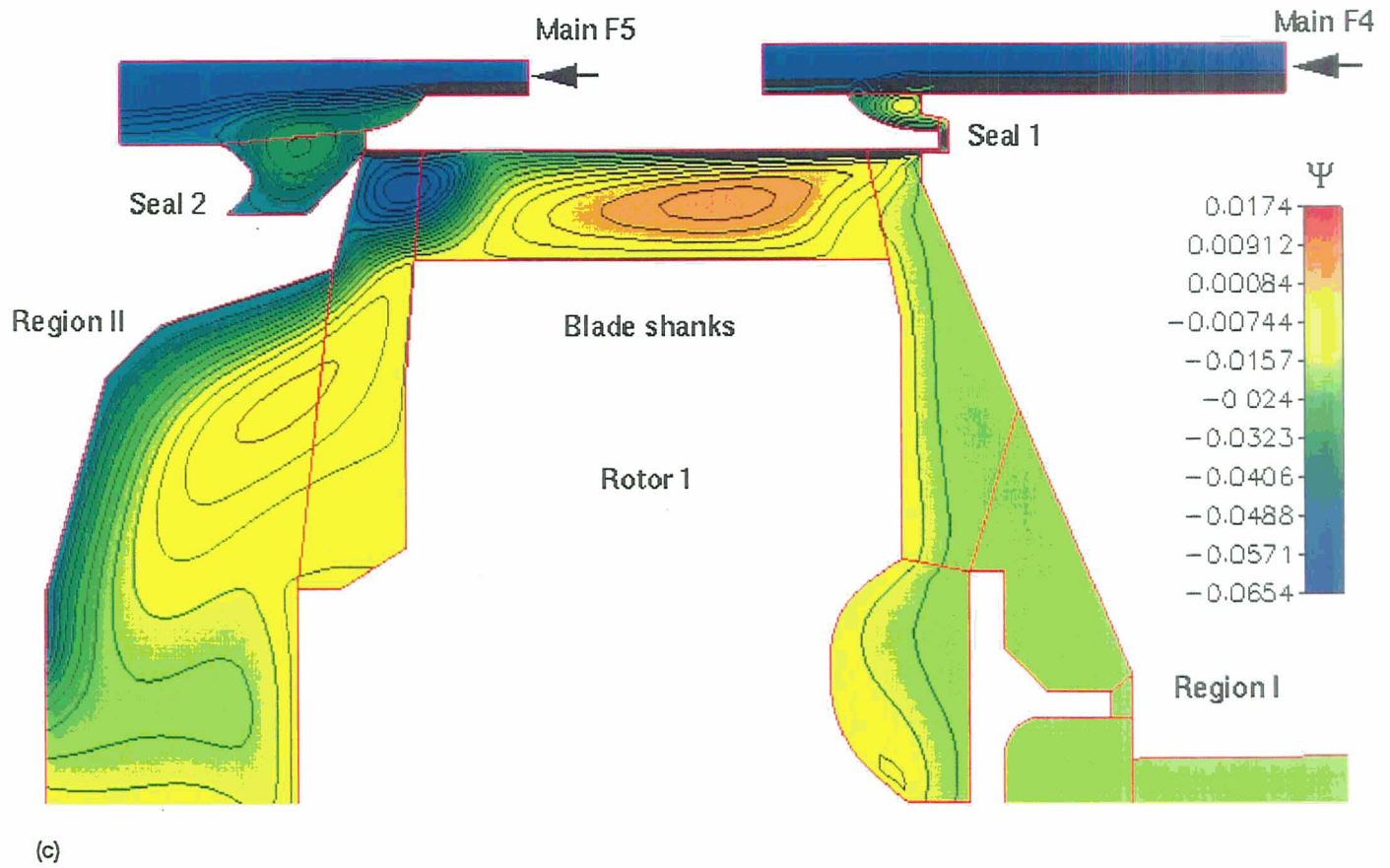
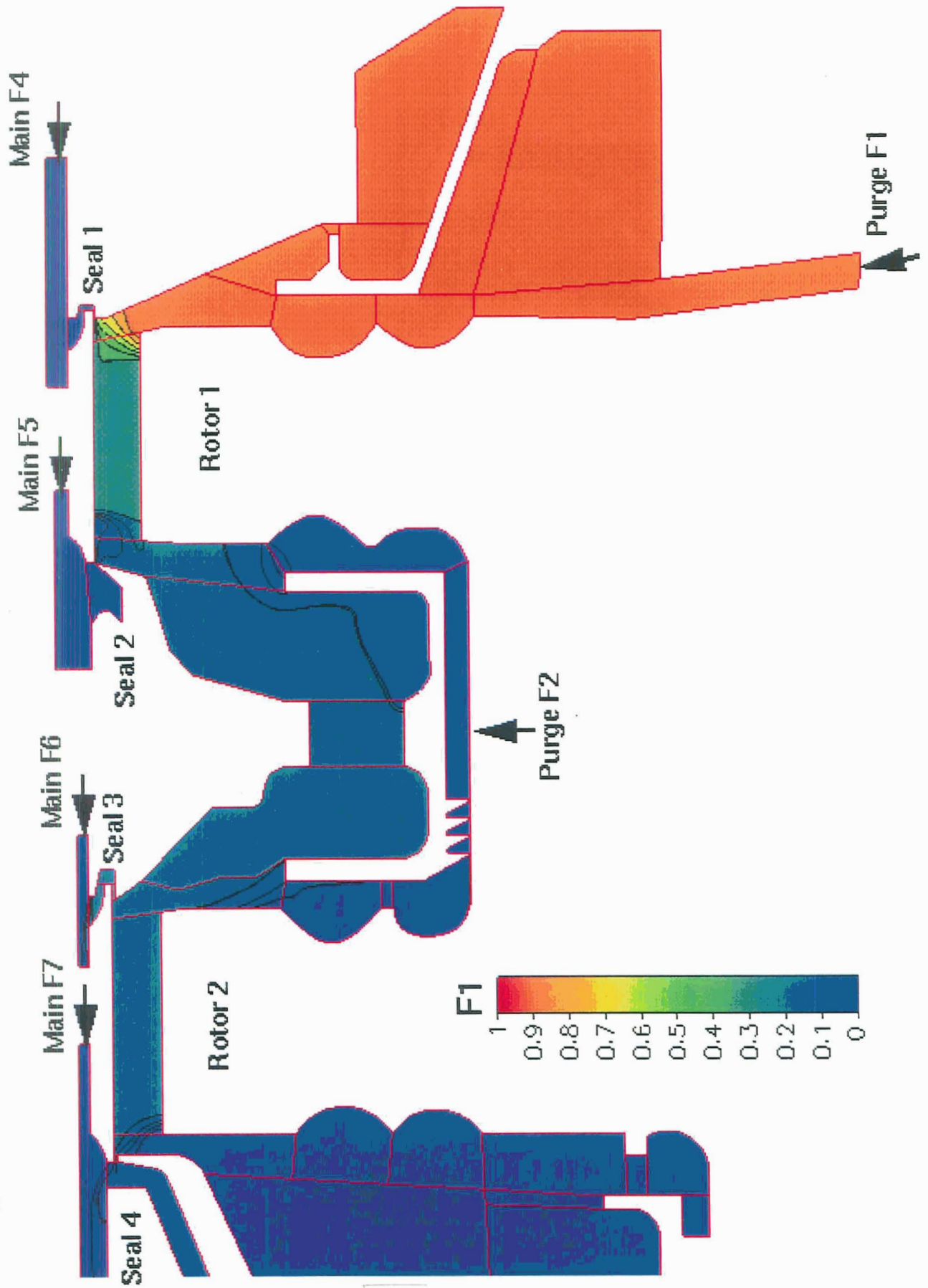


Figure 3 —Concluded. (c) Flow detail at seal 1, 2, and blade shank region to illustrate the complex vortical structure and main-path flow ingestion.

Mixture Fraction (Concentrations)

Computed Values of F1 Concentrations, Run No. 202



Mixture Fraction (Concentrations)

Computed Values of F2 Concentrations, Run No. 202

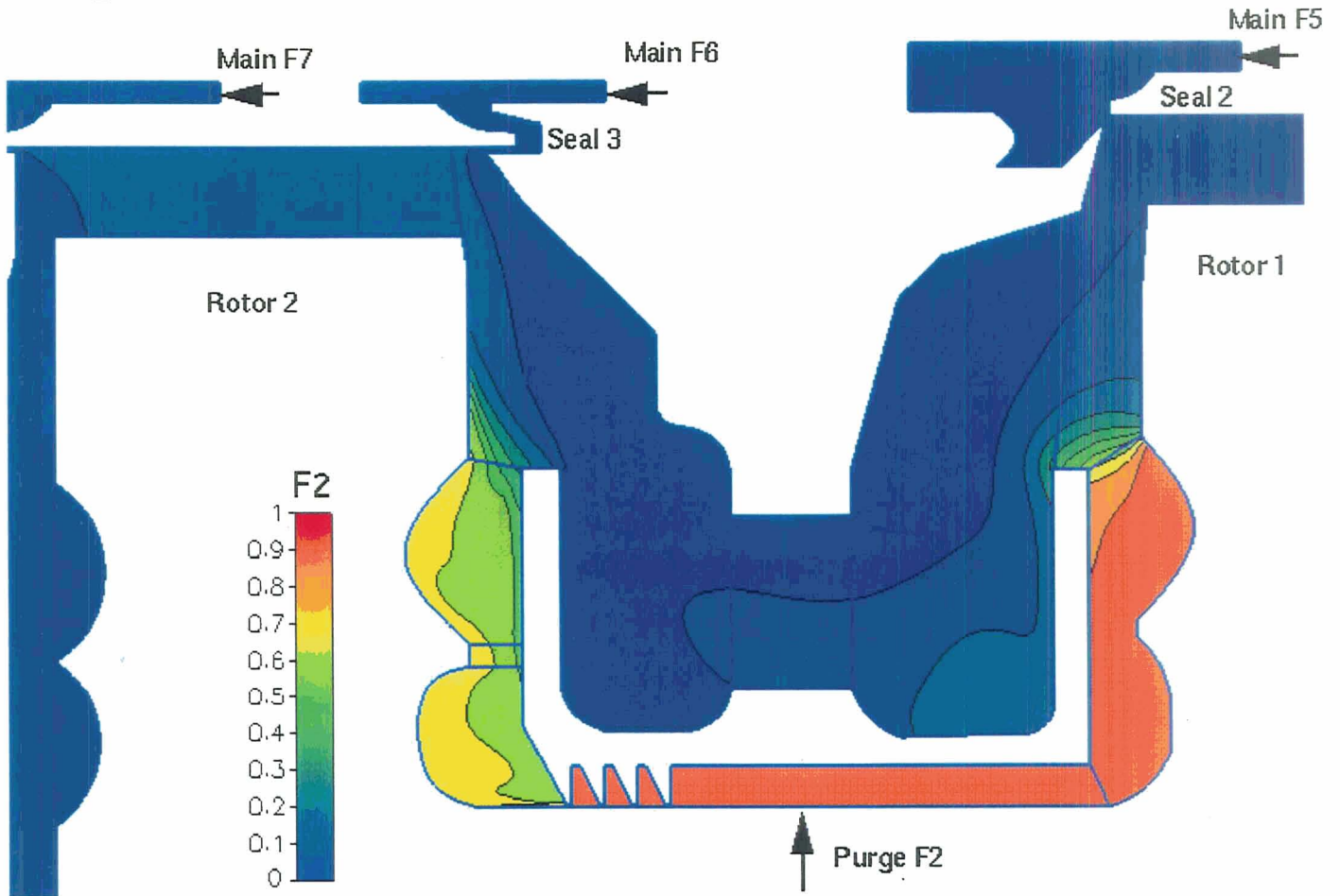


Figure 3 Ingestion of main-path flow in multiple gas-turbine disc cavities
UTRC/MSFC Large Scale Rig

Mixture Fraction (Concentrations)

Computed Values of F4 Concentrations, Run No. 202

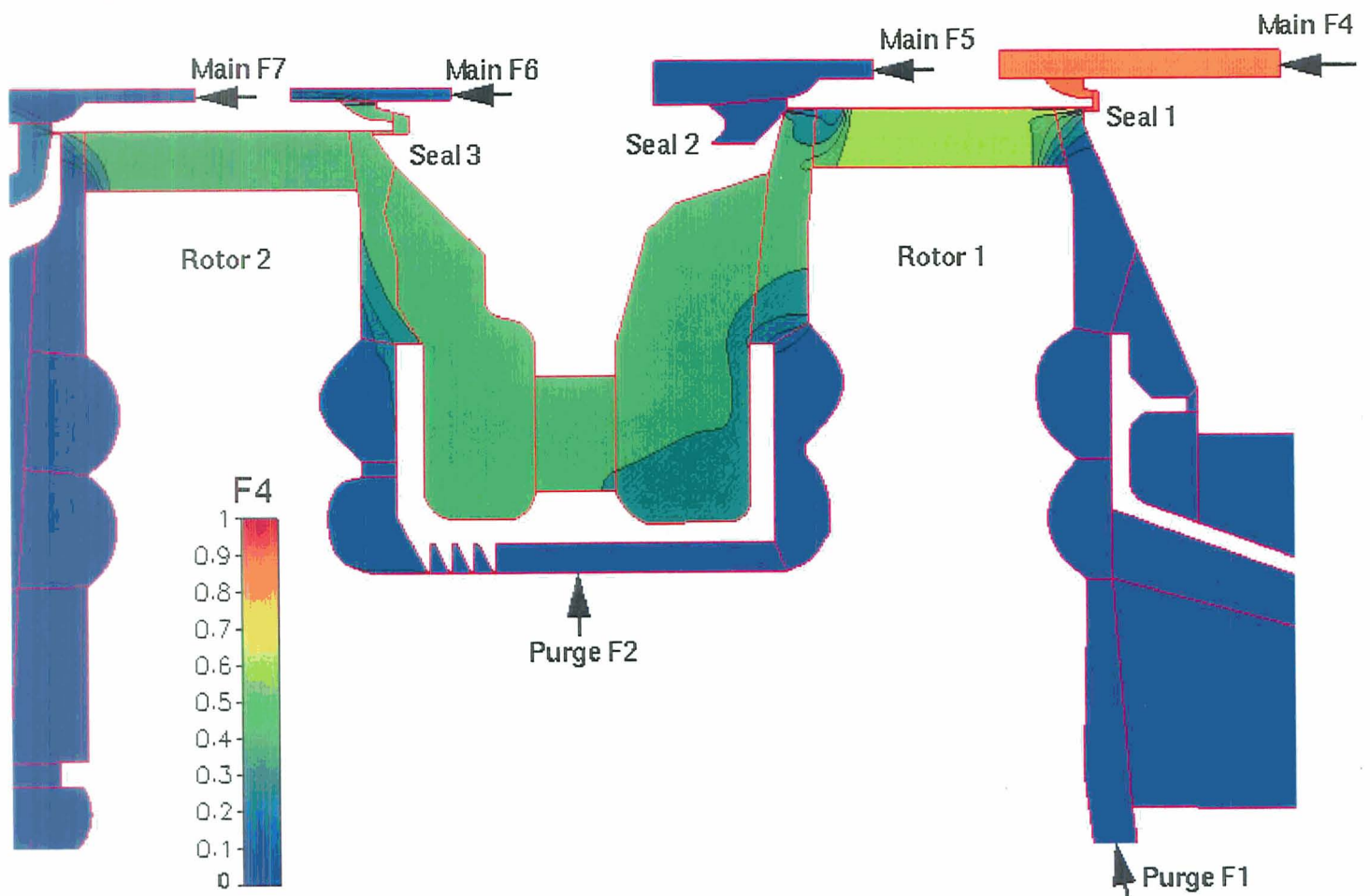


Figure 3 Ingestion of main-path flow in multiple gas-turbine disc cavities
UTRC/MSFC Large Scale Rig

Mixture Fraction (Concentrations)

Computed Values of F5 Concentrations, Run No. 202

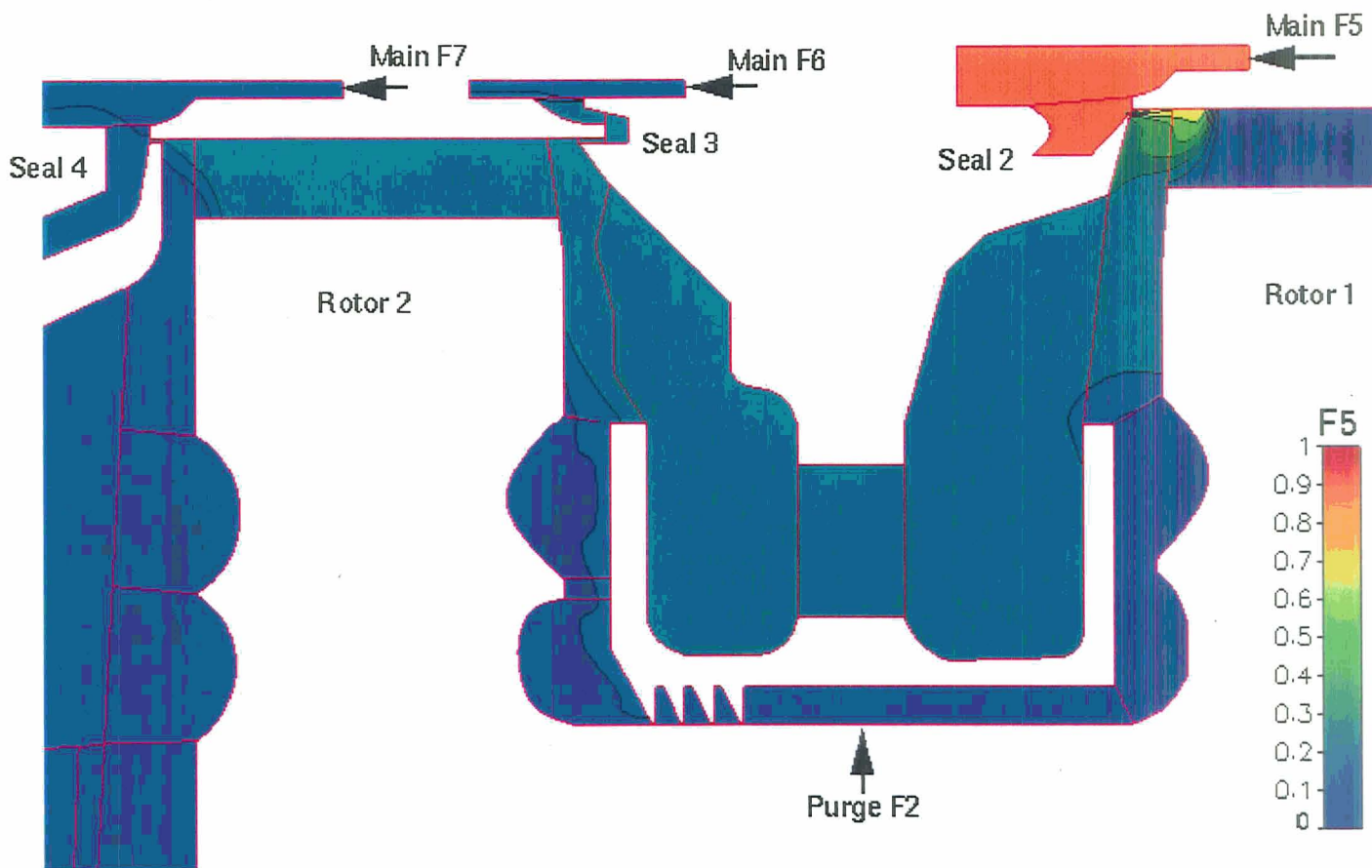
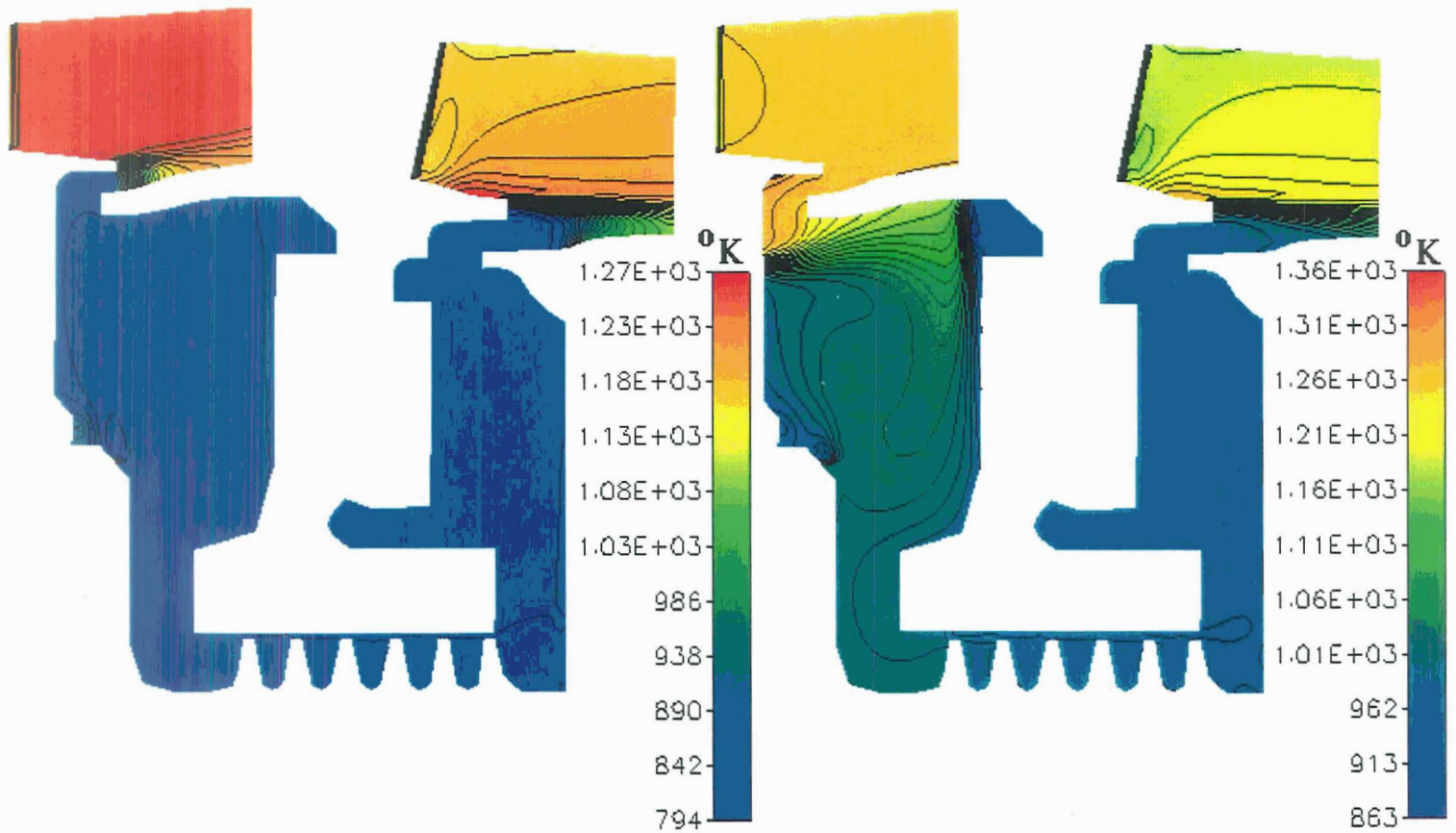


Figure 3 Ingestion of main-path flow in multiple gas-turbine disc cavities
UTRC/MSFC Large Scale Rig

Temperature

Stage 1-2 Disk Cavities



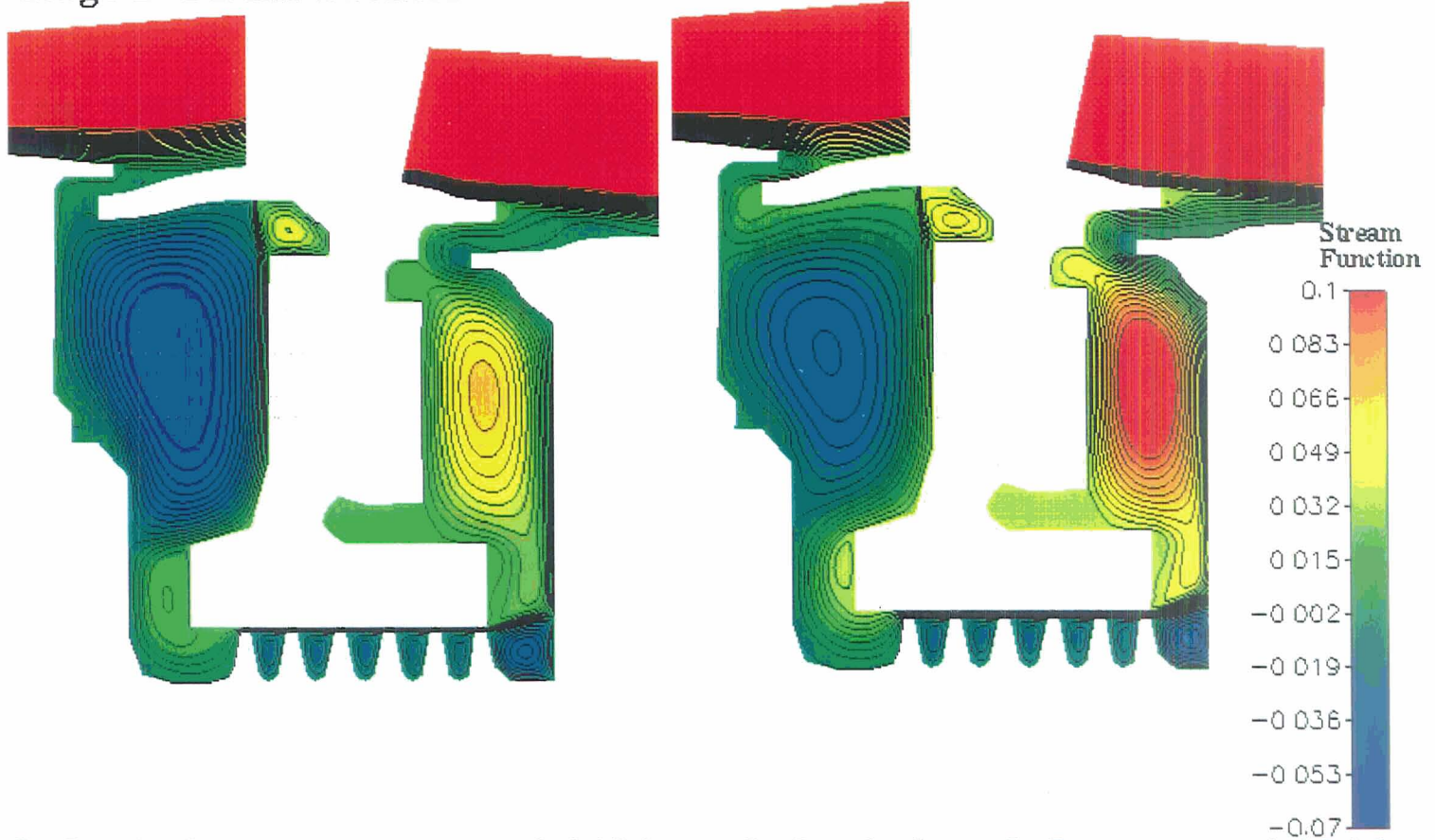
Labyrinth seal clearance = 0.012 in

Labyrinth seal clearance = 0.024 in

Figure 6

Stream Function

Stage 1-2 Disk Cavities



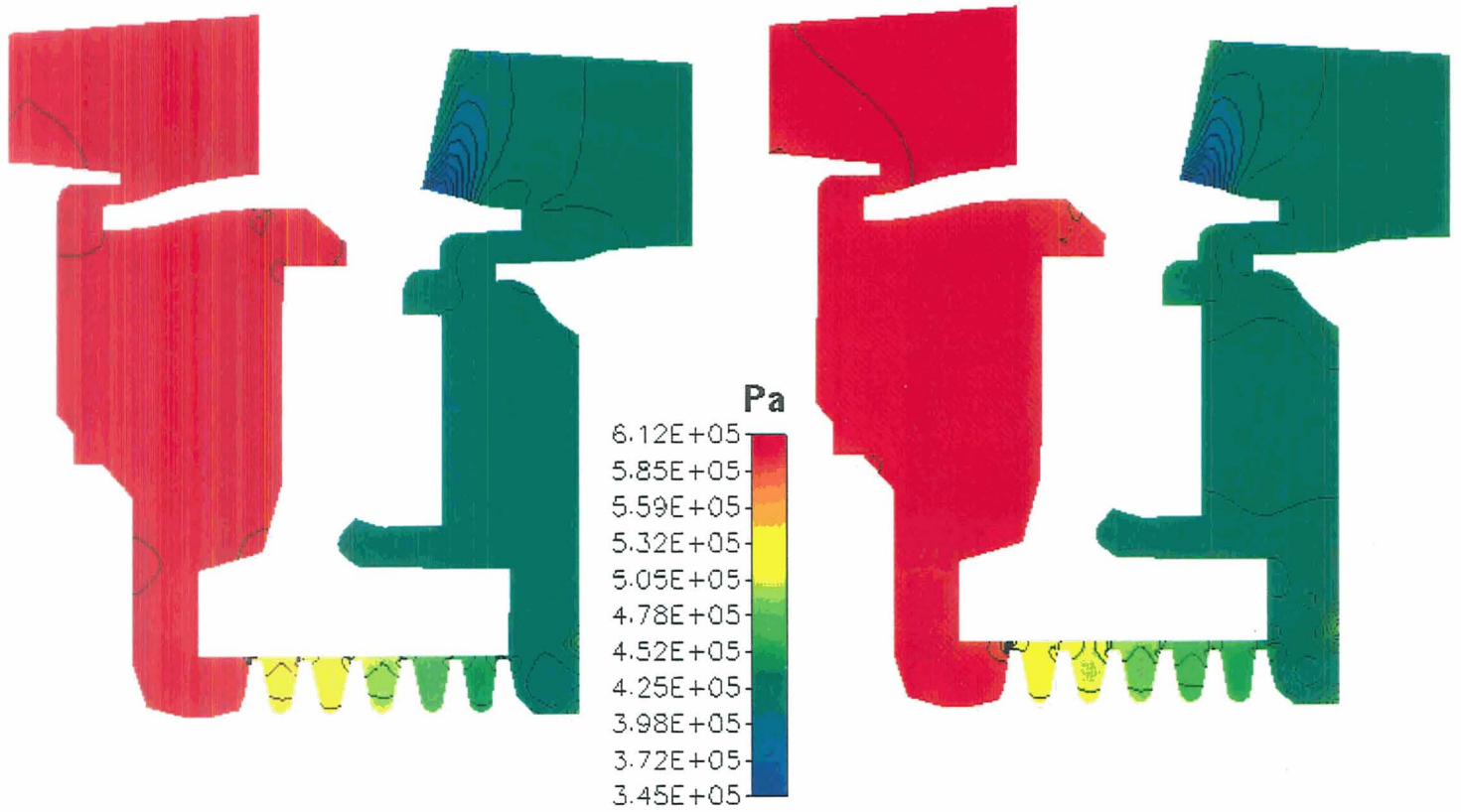
Labyrinth seal clearance = 0.012 in Labyrinth seal clearance = 0.024 in

Note: The magnitude is greater than 0.1 in the free stream region (red color with no contours)

Figure 7

Pressure

Stage 1-2 Disk Cavities

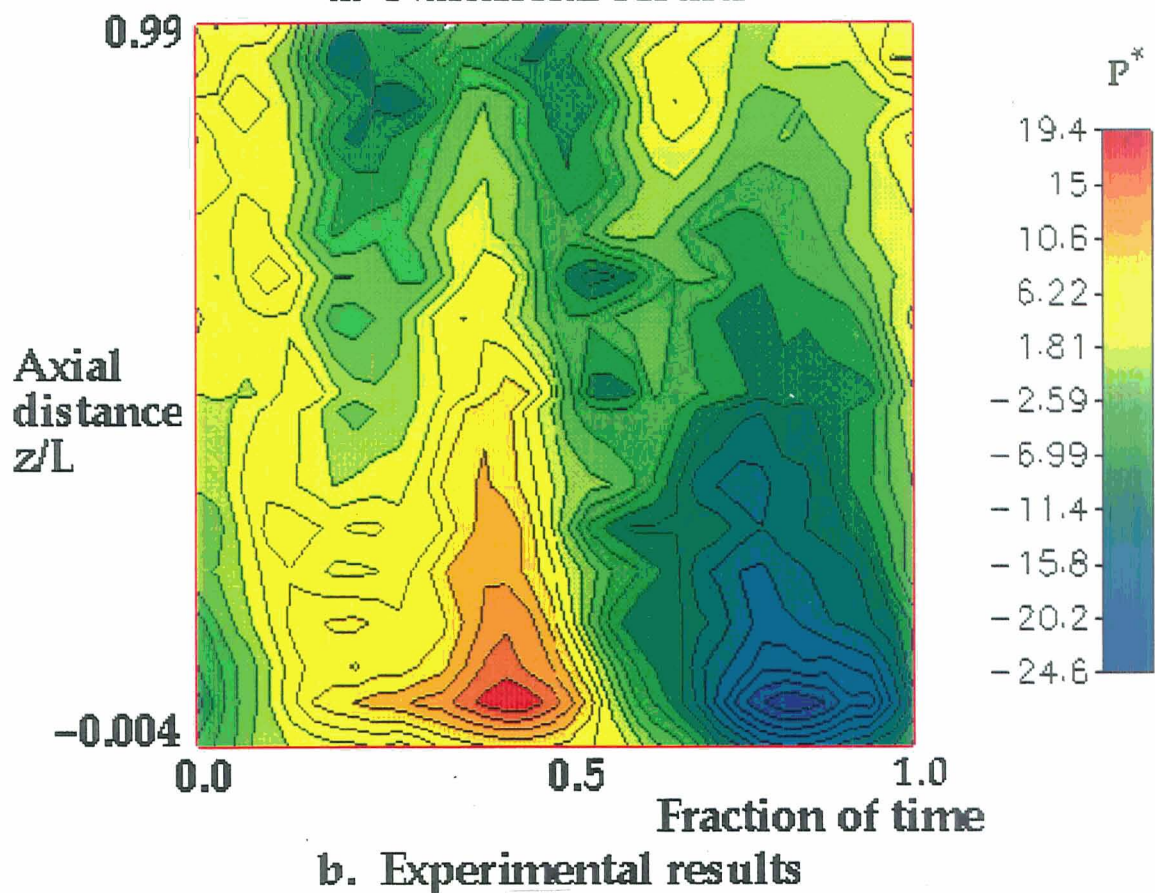
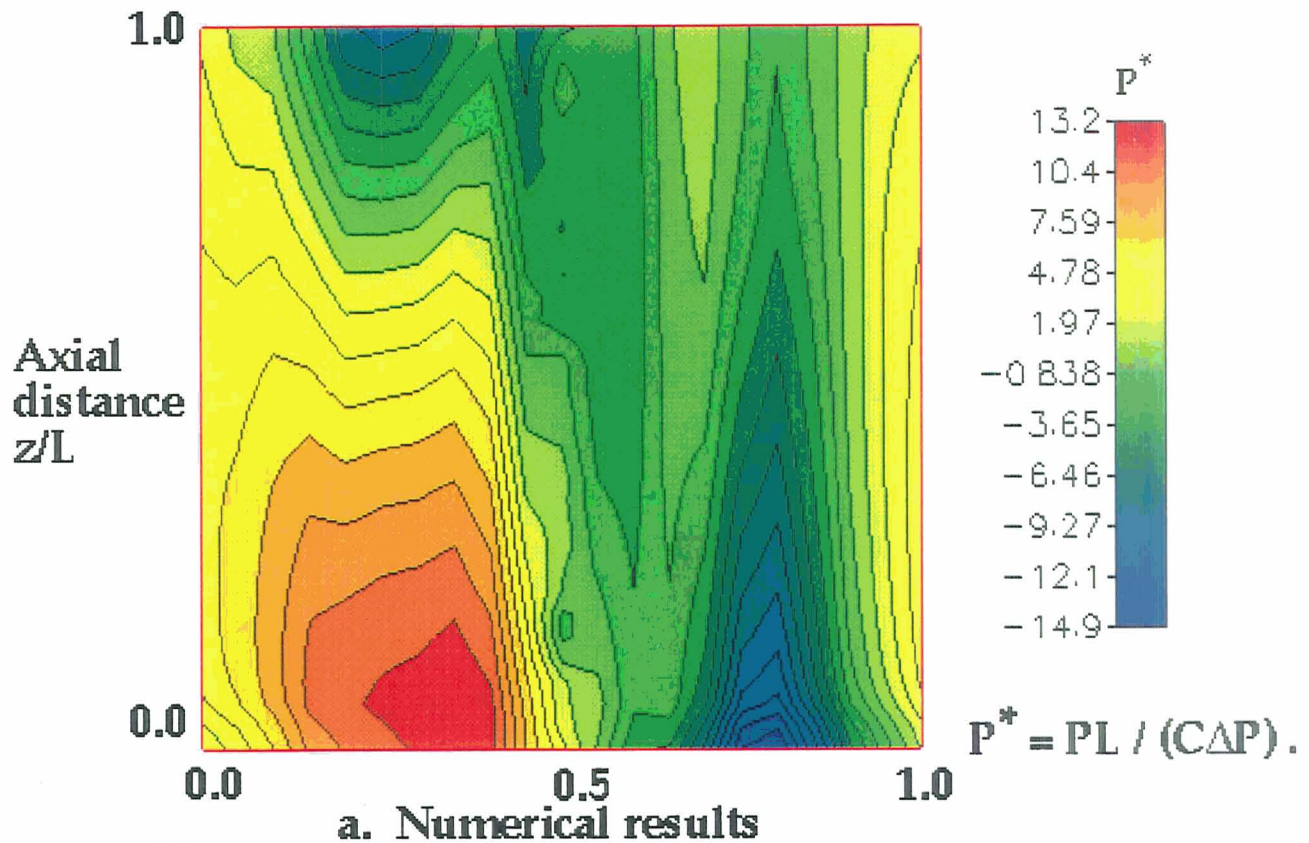


Labyrinth seal clearance = **0.012 in**

Labyrinth seal clearance = **0.024 in**

Pressures on the stator wall

← Direction of rotor motion in absolute frame



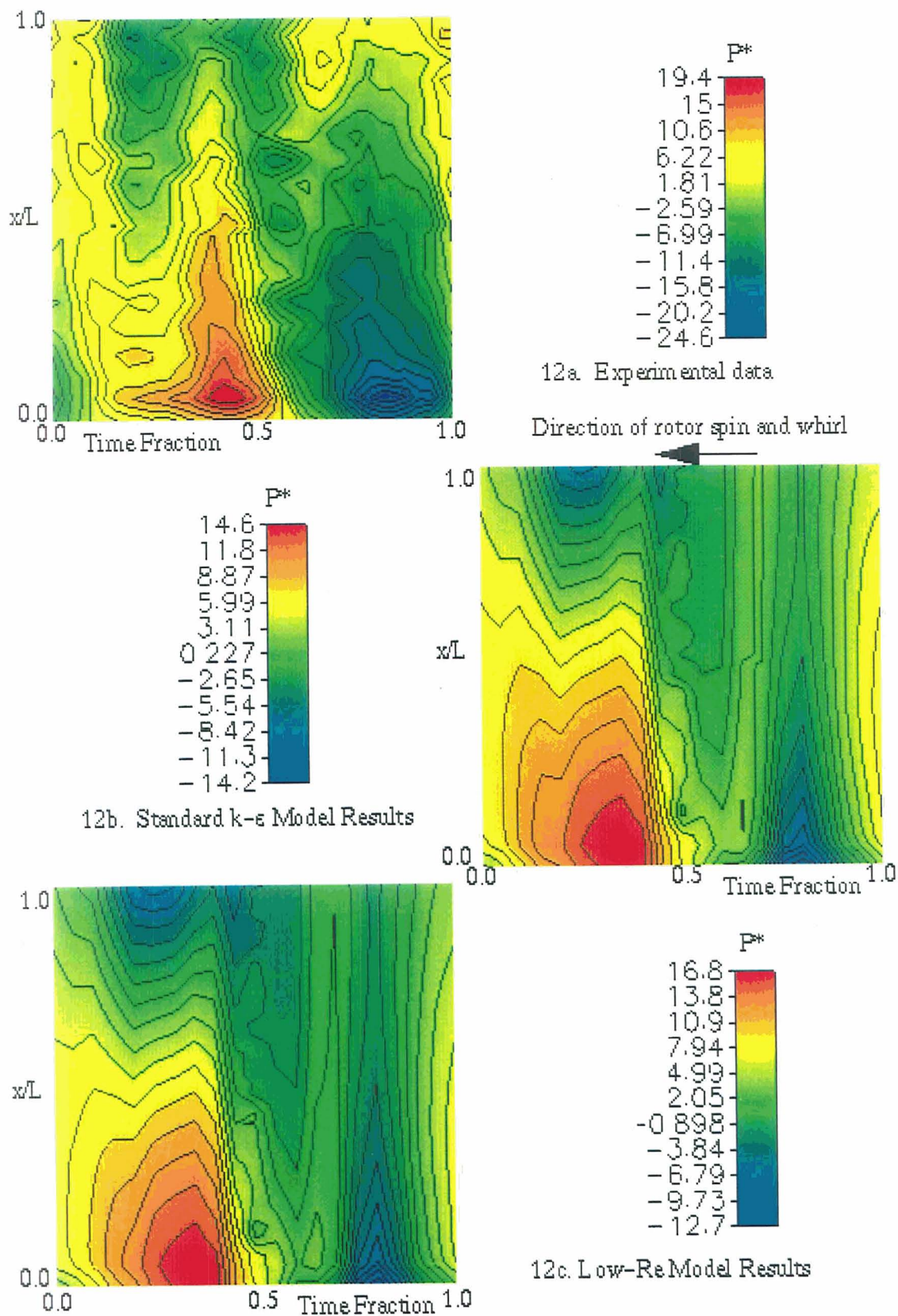


Figure 12. Stator Wall Pressures as a Function of the Axial and Tangential Distance. Time Fraction 0.5 is at Minimum Clearance, 0.0 to 0.5 is Pressure Side, 0.5 to 1.0 is Suction Side.

REPORT DOCUMENTATION PAGE

Form Approved
OMB No. 0704-0188

Public reporting burden for this collection of information is estimated to average 1 hour per response, including the time for reviewing instructions, searching existing data sources, gathering and maintaining the data needed, and completing and reviewing the collection of information. Send comments regarding this burden estimate or any other aspect of this collection of information, including suggestions for reducing this burden, to Washington Headquarters Services, Directorate for Information Operations and Reports, 1215 Jefferson Davis Highway, Suite 1204, Arlington, VA 22202-4302, and to the Office of Management and Budget, Paperwork Reduction Project (0704-0188), Washington, DC 20503.

1. AGENCY USE ONLY (Leave blank)	2. REPORT DATE March 1996	3. REPORT TYPE AND DATES COVERED Conference Publication	
4. TITLE AND SUBTITLE Seals Code Development Workshop		5. FUNDING NUMBERS WU-242-20-06	
6. AUTHOR(S) Robert C. Hendricks and Anita D. Liang, compilers		8. PERFORMING ORGANIZATION REPORT NUMBER E-9945	
7. PERFORMING ORGANIZATION NAME(S) AND ADDRESS(ES) National Aeronautics and Space Administration Lewis Research Center Cleveland, Ohio 44135-3191		10. SPONSORING/MONITORING AGENCY REPORT NUMBER NASA CP-10181	
9. SPONSORING/MONITORING AGENCY NAME(S) AND ADDRESS(ES) National Aeronautics and Space Administration Washington, D.C. 20546-0001		11. SUPPLEMENTARY NOTES Responsible person, Robert C. Hendricks, organization code 5300, (216) 977-7507.	
12a. DISTRIBUTION/AVAILABILITY STATEMENT Unclassified - Unlimited Subject Categories 07, 16, 20, and 99 This publication is available from the NASA Center for Aerospace Information, (301) 621-0390.		12b. DISTRIBUTION CODE	
13. ABSTRACT (Maximum 200 words) Seals Workshop of 1995 industrial code (INDSEAL) release include ICYL, GCYLT, IFACE, GFACE, SPIRALG, SPIRALI, DYSEAL, and KTK. The scientific code (SCISEAL) release includes conjugate heat transfer and multidomain with rotordynamic capability. Several seals and bearings codes (e.g., HYDROFLEX, HYDROTRAN, HYDROB3D, FLOWCON1, FLOWCON2) are presented and results compared. Current computational and experimental emphasis includes multiple connected cavity flows with goals of reducing parasitic losses and gas ingestion. Labyrinth seals continue to play a significant role in sealing with face, honeycomb, and new sealing concepts under investigation for advanced engine concepts in view of strict environmental constraints. The clean sheet approach to engine design is advocated with program directions and anticipated percentage SFC reductions cited. Future activities center on engine applications with coupled seal/power/secondary flow streams.			
14. SUBJECT TERMS Seals; Rotordynamics; Bearings; Tribology; Secondary flow			15. NUMBER OF PAGES 370
			16. PRICE CODE A16
17. SECURITY CLASSIFICATION OF REPORT Unclassified	18. SECURITY CLASSIFICATION OF THIS PAGE Unclassified	19. SECURITY CLASSIFICATION OF ABSTRACT Unclassified	20. LIMITATION OF ABSTRACT